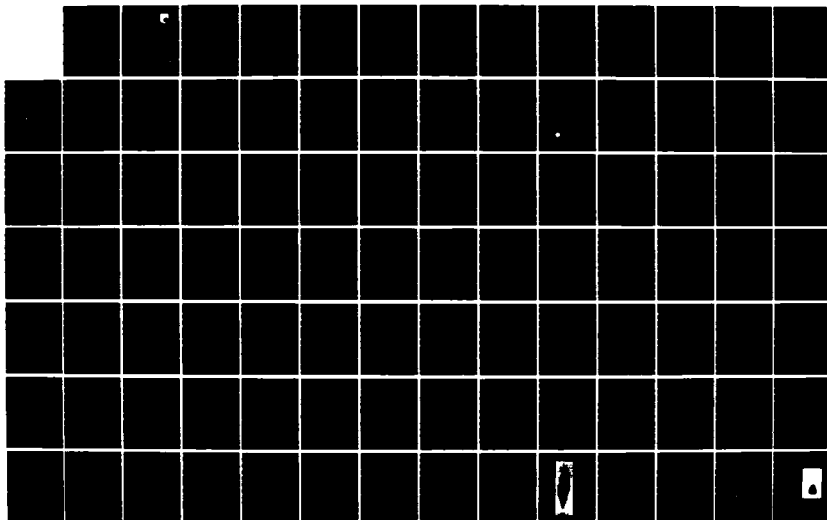
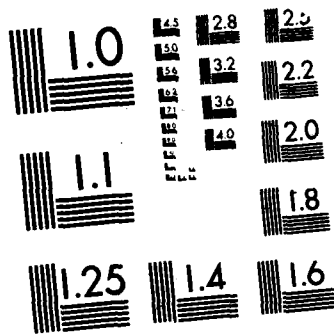


AD-A173 414 LASER OPTICS/COMBUSTION DIAGNOSTICS(U) SYSTEMS RESEARCH 1/3
LABS INC DAYTON OH RESEARCH APPLICATIONS DIV
L P GOSS ET AL JUL 86 SRL-6603 AFMAL-TR-86-2023
UNCLASSIFIED F33615-80-C-2054 F/B 21/2 NL





AD-A173 414

AFWAL-TR-86-2023

LASER OPTICS/COMBUSTION DIAGNOSTICS

L. P. GOSS
G. L. SWITZER

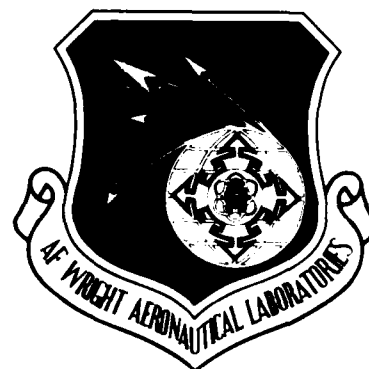
Research Applications Division
Systems Research Laboratories, Inc.
2800 Indian Ripple Road
Dayton, OH 45440-3696

July 1986

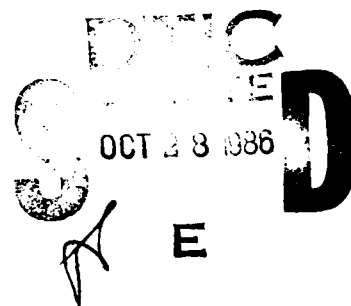
Final Report for Period 2 September 1980 - 2 October 1985

Approved for public release; distribution unlimited.

AERO PROPULSION LABORATORY
AIR FORCE WRIGHT AERONAUTICAL LABORATORIES
AIR FORCE SYSTEMS COMMAND
WRIGHT-PATTERSON AIR FORCE BASE, OH 45433-6563



DTIC FILE COPY



86 10 28

NOTICE

When Government drawings, specifications, or other data are used for any purpose other than in connection with a definitely related Government procurement operation, the United States Government thereby incurs no responsibility nor any obligation whatsoever; and the fact that the government may have formulated, furnished, or in any way supplied the said drawings, specifications, or other data, is not to be regarded by implication or otherwise as in any manner licensing the holder or any other person or corporation, or conveying any rights or permission to manufacture use, or sell any patented invention that may in any way be related thereto.

This report has been reviewed by the Office of Public Affairs (ASD/PA) and is releasable to the National Technical Information Service (NTIS). At NTIS, it will be available to the general public, including foreign nations.

This technical report has been reviewed and is approved for publication.

W. M. Roquemore

W. M. ROQUEMORE
Fuel Combustion
Fuels and Lubrication Division
Aero Propulsion Laboratory

Arthur V. Churchill

ARTHUR V. CHURCHILL
Chief, Fuels Branch
Fuels and Lubrication Division
Aero Propulsion Laboratory

FOR THE COMMANDER

Robert D. Sherrill

ROBERT D. SHERRILL, Chief
Fuels and Lubrication Division
Aero Propulsion Laboratory

If your address has changed, if you wish to be removed from our mailing list, or if the addressee is no longer employed by your organization please notify AFWAL/POSF, W-PAFB, OH 45433 to help us maintain a current mailing list.

Copies of this report should not be returned unless return is required by security considerations, contractual obligations, or notice on a specific document.

UNCLASSIFIED

SECURITY CLASSIFICATION OF THIS PAGE

ADA 173 414

REPORT DOCUMENTATION PAGE

1a. REPORT SECURITY CLASSIFICATION Unclassified			1b. RESTRICTIVE MARKINGS	
2a. SECURITY CLASSIFICATION AUTHORITY			3. DISTRIBUTION/AVAILABILITY OF REPORT Approved for public release; distribution unlimited.	
2b. DECLASSIFICATION/DOWNGRADING SCHEDULE			5. MONITORING ORGANIZATION REPORT NUMBER(S) AFWAL-TR-86-2023	
4. PERFORMING ORGANIZATION REPORT NUMBER(S) 6603 Final			7a. NAME OF MONITORING ORGANIZATION Aero Propulsion Laboratory (AFWAL/POSF) Air Force Wright Aeronautical Laboratories	
6a. NAME OF PERFORMING ORGANIZATION Systems Research Laboratories, Inc.		6b. OFFICE SYMBOL (If applicable)	7b. ADDRESS (City, State and ZIP Code) Wright-Patterson AFB, OH 45433-6563	
6c. ADDRESS (City, State and ZIP Code) 2800 Indian Ripple Road Dayton, OH 45440-3696			9. PROCUREMENT INSTRUMENT IDENTIFICATION NUMBER F33615-80-C-2054	
8a. NAME OF FUNDING/SPONSORING ORGANIZATION Aero Propulsion Laboratory		8b. OFFICE SYMBOL (If applicable) AFWAL/POSF	10. SOURCE OF FUNDING NOS.	
8c. ADDRESS (City, State and ZIP Code) Wright-Patterson AFB, OH 45433-6563			PROGRAM ELEMENT NO. 62203F 61102F	PROJECT NO. 3048 2308
11. TITLE (Include Security Classification) Laser Optics/Combustion Diagnostics (Unclass.)			TASK NO. 05 S1	WORK UNIT NO. 02 23
12. PERSONAL AUTHOR(S) L. P. Goss, G. L. Switzer				
13a. TYPE OF REPORT Final Report		13b. TIME COVERED FROM 80Sept02 TO 85Oct02	14. DATE OF REPORT (Yr., Mo., Day) July 1986	
15. PAGE COUNT 288				
16. SUPPLEMENTARY NOTATION				
17. COSATI CODES			18. SUBJECT TERMS (Continue on reverse if necessary and identify by block number)	
FIELD	GROUP	SUB. GR.	Simultaneous Temperature-Concentration Measurements, Coherent Anti-Stokes Raman Spectroscopy (CARS), Applications of Nd:YAG and Dye Lasers, Hardened CARS System. (continued)	
21	02			
20	06			
19. ABSTRACT (Continue on reverse if necessary and identify by block number) Coherent anti-Stokes Raman spectroscopy (CARS) instruments have been developed for the simultaneous measurement of temperature and species concentrations in turbulent-diffusion, sooty hydrocarbon flames. Contour maps of average temperature, rms temperature, average concentration, and rms concentration have been obtained on a laboratory-scale burner. Simultaneous N ₂ and O ₂ measurements by the CARS technique were made with a dual-dye-laser setup. A combination of the laboratory CARS system and a laser-Doppler-velocimetry (LDV) system was completed and tested on a Bunsen-burner premixed flame. Measurements indicated that simultaneously obtained velocity and temperature data were Favre averaged due to density weighting of the seed particles. Temperature-velocity correlations were obtained and compared to literature values on similar burners obtained with a combined fine-wire thermocouple and LDV. Normal-gradient and counter-gradient transport were observed in the premixed flame. An environmentally hardened CARS system was developed and employed to measure temperatures in the near-wake recirculating-flow region of a bluff-body-stabilized diffusion flame. Time-averaged temperature profiles and probability distribution functions (pdf's) were obtained. (continued)				
20. DISTRIBUTION/AVAILABILITY OF ABSTRACT UNCLASSIFIED/UNLIMITED <input type="checkbox"/> SAME AS RPT <input checked="" type="checkbox"/> DTIC USERS <input type="checkbox"/>			21. ABSTRACT SECURITY CLASSIFICATION Unclassified	
22a. NAME OF RESPONSIBLE INDIVIDUAL W. M. Roquemore, Ph.D.			22b. TELEPHONE NUMBER (Include Area Code) (513) 255-6813	22c. OFFICE SYMBOL AFWAL/POSF

DD FORM 1473, 83 APR

EDITION OF 1 JAN 73 IS OBSOLETE.

UNCLASSIFIED

SECURITY CLASSIFICATION OF THIS PAGE

UNCLASSIFIED

SECURITY CLASSIFICATION OF THIS PAGE

Block 18. SUBJECT TERMS (Continued)

Combustion Diagnostics, Laser Doppler Velocimetry (LDV), Temperature-Velocity Correlations, Simultaneous Temperature-Velocity Measurements, *Dye Injection*

Block 19. ABSTRACT (Continued)

and interpreted in terms of the flow field characteristics. A comparison of temperature data obtained by means of the CARS technique and using three thermocouples of different design was made. This comparison indicated that the physical design of the thermocouple probe is important and may influence the flow and, thus, the temperature.

UNCLASSIFIED

SECURITY CLASSIFICATION OF THIS PAGE

PREFACE

This report was prepared by L. P. Goss, Ph.D., and G. L. Switzer and covers work performed during the period 2 September 1980 through 2 October 1985 under Contract F33615-80-C-2054. The contract was administered under the direction of the Air Force Wright Aeronautical Laboratories, Aero Propulsion Laboratory (AFWAL/POSF), Wright-Patterson Air Force Base, OH, with W. M. Roquemore, Ph.D., Government Project Monitor.

Accession For	
NTIS GRA&I	<input checked="checked" type="checkbox"/>
DTIC TAB	<input type="checkbox"/>
Unannounced	<input type="checkbox"/>
Justification	
By	
Distribution/	
Availability Codes	
Dist	Avail. and/or Special
A-1	

TABLE OF CONTENTS

<u>Section</u>	<u>Page</u>
1 INTRODUCTION	1
2 FUNDAMENTAL LABORATORY STUDIES	3
2.1 10-Hz CARS Instrument	3
2.2 Error Analysis of CARS Thermometry and Species-Concentration Measurements	13
2.3 Effects of Turbulence upon CARS Signal Production	47
2.4 Simultaneous CARS Thermometry and Species- Concentration Measurements	85
2.5 Multiple-Species Measurements	121
2.6 Alternate CARS Temperature Methods	130
2.7 Determination of Raman Linewidths from CARS Spectra	142
2.8 Blackbody Thermometric Probe	149
2.9 Thermometry and Species-Concentration Measurements by Laser-Deflection Techniques	164
2.10 Combined CARS-LDA Instrument	187
3 HARDENED CARS SYSTEM DEVELOPMENT	244
REFERENCES	279

LIST OF ILLUSTRATIONS

<u>Figure</u>	<u>Page</u>
1 Nonresonant Spectra Used for Distortion of Calculated CARS Spectrum and Resulting Fitted Temperatures of Distorted Spectra. The initial temperature of the calculated CARS spectrum was 2000 K	32
2 Averaged Nonresonant Spectrum Used for the Normalization of the Distorted CARS Spectra. The initial temperature for the CARS spectrum was 2000 K	34
3 Single-Shot Spectrum of the Nonresonant Sample and Reference	35
4 Super-Radiant Dye Laser Employed for CARS Studies	38
5 Temperature PDF Obtained in a Near-Stoichiometric Flame. $T = 2069 \pm 68$ K	41
6 Temperature Uncertainty as a Function of Temperature Due to a 6.4% Intensity Uncertainty	43
7 Plot of Relative Uncertainty of Ratio R_T with 4% Uncertainty in Temperature	46
8 Optical Schematic of CARS Setup for Simultaneous Temperature- N_2 and Relative- O_2 Concentration Measurements	122
9 Right-Angle Reference Scheme Employed for O_2 - N_2 Studies	123
10 Relative O_2 -Number Density Error Versus Temperature for Integration Method of Number-Density Determinations	129
11 Temperature Histogram Obtained at Location 9.5 cm above Burner Surface	131
12 N_2 -Number-Density Histogram Obtained at Location 9.5 cm above Burner Surface	132
13 O_2 -Number-Density Histogram Obtained at Location 9.5 cm above Burner Surface	133
14 Correlation Plot of O_2 - N_2 Versus Adiabatic Calculations (Solid) Obtained at Location 9.5 cm above Burner Surface	134
15 Variation in Nonresonant Susceptibility (χ_{nr}) as Function of Temperature	137
16 Variation of (a) Peak and (b) Integrated CARS Intensity of Q-Branch of N_2 with Temperature	139

LIST OF ILLUSTRATIONS (Concluded)

<u>Figure</u>	<u>Page</u>
17 Plot of Variation of Temperature with Log of Integrated CARS Signal of Q-Branch of N_2	141
18 Uncertainty of Temperature Determined by Integrated CARS Intensity as Function of Temperature	143
19 High-Temperature Blackbody Probe	150
20 Spectral Radiance of Blackbody at Various Temperatures (K) . . .	153
21 Transmission Attenuation of Quartz Fiber	155
22 Schematic Diagram of Receiver Optics	156
23 Spectral Response of InGaAs Detector	157
24 (a) Response of Blackbody Probe to Change in Temperature, (b) Photograph Depicting Speed at Which Heat Source Was Removed from Probe	159
25 Transfer Function of Blackbody Probe	160
26 CARS Temperature pdf's in the Near-Wake Region of the Bluff Body	265

LIST OF TABLES

<u>Table</u>	<u>Page</u>
I Results of Dye-Laser Comparison	39
II Hardened-CARS-System Software	245

Section 1

INTRODUCTION

This report describes the results of experimental and theoretical investigations of the coherent anti-Stokes Raman scattering (CARS) technique as a diagnostic tool for the study of turbulent flames.

The study of turbulent combustion on a fundamental level requires detailed spatially resolved information on the instantaneous values (acquired simultaneously) of a large number of scalar quantities such as temperature, species concentration, velocity, and pressure. Measurement of such scalar quantities is essential for producing the single and joint moments required by various modeling theories.

The CARS technique has been shown to be an important diagnostic tool for the measurement of temperature and major flame species concentrations. When this technique is combined with a laser Doppler anemometer (LDA), simultaneous temperature and velocity measurements can be made.

The objectives of this program were to utilize CARS and other promising laser optical techniques for obtaining data needed in the evaluation of combustion models and to investigate methods of improving the diagnostic capabilities of these techniques. The program was divided into two parts, Part A consisting of fundamental laboratory evaluation of CARS and other techniques and Part B consisting of the hardened CARS system effort.

Section 2 of this report describes the fundamental laboratory equipment and studies which were undertaken including:

- 1) 10-Hz CARS instrument
- 2) Error analysis of CARS thermometry and species-concentration measurements
- 3) Turbulence effects on CARS signals
- 4) Simultaneous species-concentration and thermometry in a turbulent flame
- 5) CARS multiple-species measurements
- 6) Alternative CARS thermometry methods
- 7) Determination of Raman linewidths from CARS spectra
- 8) Development of a blackbody probe
- 9) Thermometry and species-concentration measurements by laser-deflection techniques
- 10) Combined CARS/LDA instrument

Section 3 describes the construction, evolution, and application of the hardened CARS system for combustion diagnostics on the AFWAL-APL large-scale tunnel facility.

Section 2

FUNDAMENTAL LABORATORY STUDIES

2.1 10-Hz CARS INSTRUMENT

The CARS system is described in a paper entitled, "10-Hz Coherent Anti-Stokes Raman Spectroscopy Apparatus for Turbulent Combustion Studies," which was published in the Review of Scientific Instruments (see following pages). Subsequent modifications to this system included: 1) addition of a TN6132 DARSS detector having a larger dynamic range and no memory effects, which resulted in a reduction in the number of signal splits required to cover the intensity range needed, and 2) electronic modifications which were required in combining the CARS and LDA instruments to permit simultaneous velocity and temperature measurements (see Section 2.9).

10-Hz coherent anti-Stokes Raman spectroscopy apparatus for turbulent combustion studies

L. P. Goss, D. D. Trump, B. G. MacDonald, and G. L. Switzer

Systems Research Laboratories, Inc., 2800 Indian Ripple Road, Dayton, Ohio 45440-3696

(Received 4 October 1982; accepted for publication 25 January 1983)

A 10-Hz coherent anti-Stokes Raman spectroscopy (CARS) instrument capable of simultaneous thermometry and N_2 -concentration measurements in a turbulent flame has been designed and constructed and is described in detail. The instrument employs the doubled output of a pulsed Nd:YAG laser for pumping a broadband dye laser and also for the CARS pump beam. The broadband dye laser is used to excite, during a single pulse, the entire Q Branch of N_2 , the CARS signal of which is recorded by a multichannel analyzer. Special problems which were encountered with the multichannel analyzer include signal retention and limited dynamic range. The former was greatly reduced by employing cleansing scans between laser firings, and the latter was circumvented by employing a multiple beamsplitter arrangement in which the CARS signal was divided into four separate intensity regions, each of which covered a specific temperature range. The 10-Hz operation of the instrument required the use of a mass storage device such as an 800-bits-per-inch tape. CARS data recorded and digitized by the multichannel analyzer were transferred via machine-coded instructions to a minicomputer for storage on tape. Analysis of the CARS data consisted of a nonlinear least-squares fit of the CARS bandshape for thermometry and integration of the CARS signal for N_2 concentrations. CARS measurements in a near-stoichiometric premixed propane flame and a turbulent diffusion flame are reported. Results of calibration measurements indicate that uncertainties of 4% in temperature and 6% in concentration are obtainable with this instrument.

PACS numbers: 82.40.Py, 82.60.Cx

INTRODUCTION

The study of turbulent combustion on a fundamental level requires detailed spatially resolved information on the instantaneous values (acquired simultaneously) of a large number of scalar quantities such as temperature, species concentration, velocity, and pressure. It is important to measure such scalar quantities in order to produce the single and joint moments required by various modeling theories. The goal of the present study was to develop a nonperturbing experimental technique for measuring these quantities in turbulent flame systems. Coherent anti-Stokes Raman spectroscopy (CARS) is an attractive experimental technique for this purpose because it can provide time-resolved (~ 10 ns) and spatially resolved (~ 0.1 mm³) measurements of temperature and major flame species, simultaneously, without appreciably perturbing the flame. This paper describes a 10-Hz system which has been developed for making CARS measurements in turbulent, sooty flames.

I. THEORETICAL CONSIDERATIONS

Coherent anti-Stokes Raman Spectroscopy (CARS) has received considerable attention during the last several years as a possible technique for remote combustion diagnostics because of its applicability to practical combustion systems, e.g., furnaces,¹ internal combustors,² and combustion tunnels.³⁻⁵ Spontaneous Raman spectroscopy has also been widely investigated in this regard^{6,7}; however, due to the weak signal strength and incoherent character of this technique, its use is generally limited to relatively clean flames.

CARS is a nonlinear, lightwave mixing process capable

of high spatial and temporal resolution and is described in detail in Refs. 8 and 9. The fundamental concepts of the theory are included here for purposes of discussing the practical application of the technique. Laser beams at frequencies ω_1 and ω_2 (pump and Stokes, respectively), having a frequency difference equal to a Raman resonance of the molecular species being probed, are focused and mixed to generate a laser-like CARS signal through the third-order susceptibility. The third-order susceptibility which governs CARS can be expressed in abbreviated form as

$$\chi^{(3)} = \chi_n + \chi_r, \quad (1)$$

where χ_n is the nonresonant contribution and χ_r is the Raman resonant contribution to the third-order susceptibility. χ_r , far from electronic resonance, is given by

$$\chi_r = \frac{2c^4}{h\omega_2^4} N \sum_{v,J} \frac{\Delta(v,J) \left(\frac{d\sigma}{d\Omega} \right)_{v,J}}{\omega_r - \delta - i\Gamma(v,J)}, \quad (2)$$

where N is the total number density of the species being probed; $\Delta(v,J)$ is the population difference between the states involved in the Raman transition; ω_r is the frequency of the Raman transition; δ is the frequency difference between ω_1 and ω_2 ; $\Gamma(v,J)$ is the HWHM of the Raman transition; and $(d\sigma/d\Omega)_{v,J}$ is the Raman-scattering cross section. The CARS intensity distribution is given by¹⁰

$$I_1(\omega_1) \sim \int d\omega'_1 T(\omega_1 - \omega'_1) \int d\omega_1 I_1(\omega_1) \times \int d\omega_2 I_1(\omega'_1 - \omega_1 + \omega_2) I_2(\omega_2) |\chi_3(\omega_1 - \omega_2)|^2, \quad (3)$$

where T is the slit function, and I_1 and I_2 are the spectral densities of the pump and Stokes sources, respectively. In broadband CARS, the Stokes bandwidth is normally sufficiently large that I_2 can be taken outside the integrals, and Eq. (3) can then be expressed as

$$I_3(\omega_3) \sim I_1^{\text{Tot}} I_2 \int \hat{I}_1(\omega_3 - \delta) |\chi_3(\delta)|^2 d\delta, \quad (4)$$

where I_1^{Tot} is the total pump intensity (integrated over all frequencies); I_2 is the Stokes intensity per unit frequency interval; \hat{I}_1 is the pump-intensity distribution convolved over the slit function; and the variable of integration δ varies over all values of detuning $\omega_1 - \omega_2$.

For calculation of a CARS spectrum, the third-order susceptibility is generated according to Eqs. (1) and (2) and subsequently convolved over the pump-laser linewidths and the appropriate slit function as dictated by Eq. (4). Figure 1(a) shows $|\chi^{(3)}|^2$ for N_2 at 1700 K before convolution over

the pump linewidth and slit function. The spectral constant,¹¹ nonresonant susceptibilities,¹² and Raman-linewidth variation with temperature and J level¹³ were employed for this calculation. Figure 1(b) shows the convolved spectrum utilizing the experimentally observed 0.4-cm⁻¹ HWHM Gaussian pump linewidth and a 4.0-cm⁻¹ HWHM Gaussian slit function.

Temperatures are derived from the spectral distribution of the CARS radiation which is determined either by scanning the Stokes frequency through the spectral region of interest or by exciting the molecular transitions in a single laser shot with a broadband Stokes beam.¹⁴ The second method has allowed the CARS technique to be applied to turbulent time-varying flames¹⁵ in which the nonlinear nature of the CARS process prevents the use of scanning techniques.

Species concentration measurements are accomplished on a major flame species by integrating the CARS signal¹⁶ while monitoring laser-power variations by means of a power reference. A minor species concentration can be determined from the bandshape of the CARS signal¹² or through background subtraction of the nonresonant signal and then integration of the resonant CARS signal.¹⁷ Care must be taken when performing density measurements in turbulent flames to insure that refractive-index effects are not so large as to cause problems with the external power-referencing scheme. The variation of the refractive index can cause beam steering, beam defocusing, and focal shifting. The magnitude of these effects is determined by the strength of the turbulence and the distance through the turbulence which the beams must travel before their foci. Preliminary measurements on the small-scale burner reported in this paper and on a large-scale practical combustor¹⁸—including both turbulence intensity measurements and external referencing after the flame—indicated that the refractive index effects were small and did not influence the density determinations. If these effects were to become a problem—such as in the case of measurements performed in internal combustors or in very large turbulent flames—then an *in situ* referencing scheme would be required.¹⁸⁻²⁰ This would involve either incorporation of a second dye laser to produce the nonresonant signal¹⁸ or employment of polarization analyzers and associated half-wave plates to monitor, selectively, the nonresonant signal produced at the same frequency as the resonant CARS signals.^{19,20} In either case, the added complexity required by this method of referencing was not warranted in the flames under study.

In turbulent flames the local flame temperature can vary several thousand times a second, therefore, a simultaneous measurement of the temperature and species concentration is required. Simultaneous measurements were first reported in Ref. 21, and the design of the CARS instrument discussed in this paper is a result of these earlier studies.

II. EXPERIMENTAL TECHNIQUE AND APPARATUS

A. Optics

Figure 2 is an optical schematic of the 10-Hz CARS apparatus. The pump source is the frequency-doubled out-

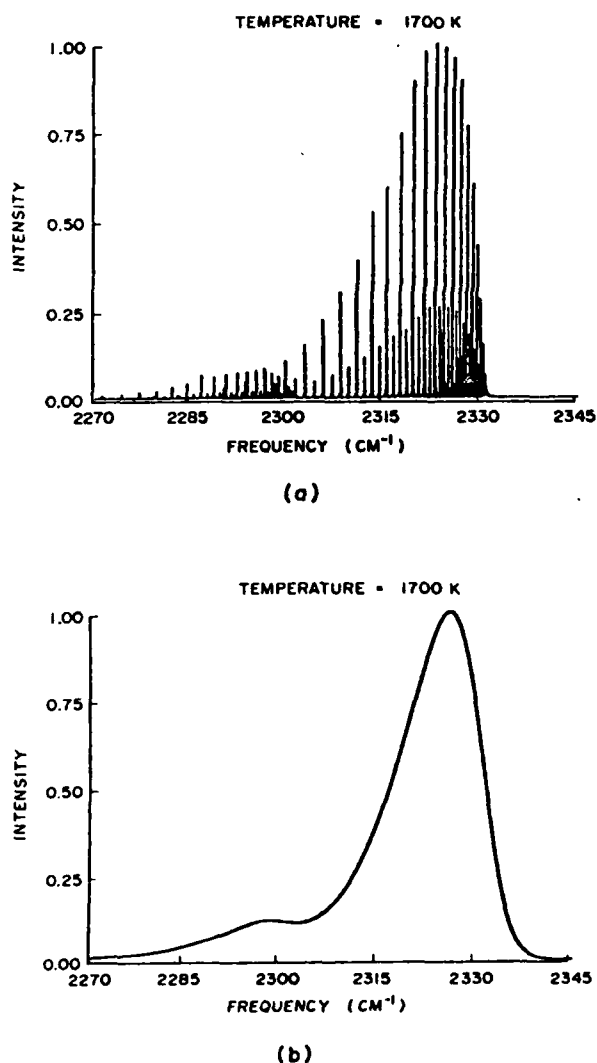


FIG. 1. $|\chi^{(3)}|^2$ (a) for N_2 at a temperature of 1700 K, and (b) convolved over a 4.0-cm⁻¹ Gaussian slit.

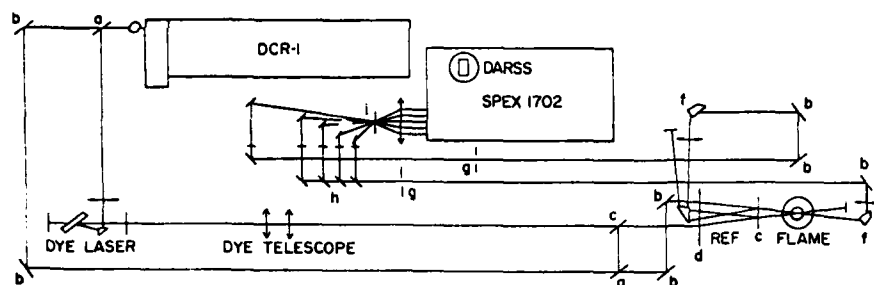


FIG. 2. CARS optical schematic. Arrows indicate lenses. (a) 50% beamsplitter for 532 nm, (b) total reflector, (c) dichroic, green reflector, red transmitter, (d) 50-cm lens, (e) 20% beamsplitter, (f) Pellin-Broca prism, (g) iris, (h) beamsplitter array (0.1%, 1%, 10%, and total reflector), (i) 532-nm filter.

put from a Quanta-Ray DCR-1 Nd:YAG laser. This laser produces ~ 210 mJ of 532-nm radiation at a repetition rate of 10 Hz. For studies of N_2 , the laser power is typically adjusted to 70 mJ for optimum signal levels. The 532-nm output serves as the pump beam (ω_1) for the CARS signal and also as the pump for the broadband dye laser. A beam splitter removes 50% of the 532-nm beam for pumping of the broadband dye laser which serves as the Stokes beam (ω_2). For excitation of the N_2 Raman transition at 2331 cm^{-1} , the dye-laser output is centered at 607.3 nm by concentration tuning of the laser dye, Sulfarhodamine 640. The optimum concentration was found to be ~ 40 mg/l in methanol. The broadband emission displayed by the dye laser was $\sim 130\text{ cm}^{-1}$ HWHM. This laser has a conversion efficiency of about 30% when operated in a longitudinal pumping configuration with no amplifier stage. No improvements were realized through the use of an amplifier stage, implying that the dye was not being saturated at the powers employed.

To achieve spatial resolution a BOXCAR²² mixing configuration was adopted. With this approach, the primary pump beam is split a second time by a 50% beam splitter, one-half being combined with the Stokes beam by a dichroic mirror and the remaining half being made parallel with the Stokes and pump beams; all are crossed and focused by a 50-cm focal length lens. To assure that the dye laser focuses at the same point as the pump beams, the focal point for the pump beams is located by a knife edge and the dye beam is focused at this point by adjusting its beam divergence with a telescope.

Due to the nonlinear dependence of the CARS signal upon the power density as well as the mode structure of the pump and Stokes lasers, the reference scheme must reproduce the spatial and temporal characteristics of the sample-beam focal volume to a high degree.²¹ To accomplish this task a retroreflecting power reference was incorporated into the CARS system. The reference is formed by a 20% beam splitter which is positioned in front of the focal point, perpendicular to the incident beams. That portion of the laser beams reflected by the splitter produces a second focus that generates a CARS signal from atmospheric N_2 , which serves as the power reference for the concentration measurements. With this arrangement the correlations between sample and reference intensities are consistently 94%–97%.

Both the reference and sample signals are recollimated and passed through Pellin-Broca prisms to separate the 532-nm radiation from the CARS signal. The CARS signal is coupled to a Spex $\frac{1}{2}$ -m monochromator through a series of

beam splitters which are used as an optical method of increasing the dynamic range of the detection electronics.

Single-shot spectra are obtained by employing a Tracor-Northern DARSS Reticon detector. This device (see Sec. II B) becomes nonlinear above 2000 counts/pulse. The lower end of the dynamic range is determined by electronic noise and is about 200 counts. In turbulent combustion media, however, a dynamic range of 10 is not adequate to account for the large variations in temperature and number density. The beam-splitter arrangement allows this limitation to be overcome by simultaneously imaging four different sample beams on the face of the Reticon. Each of the four peaks represents a different fraction of the total CARS intensity. The effect of temperature upon the CARS intensity is shown in Fig. 3. By choosing the correct beam-splitter combinations, the entire CARS intensity and, therefore, temperature range can be covered by a single detector. As displayed in Fig. 3, the temperature range is divided into four separate regions, 300–600, 600–1000, 1000–1600, and 1600–2300 K. When the CARS signal is generated from a hot part

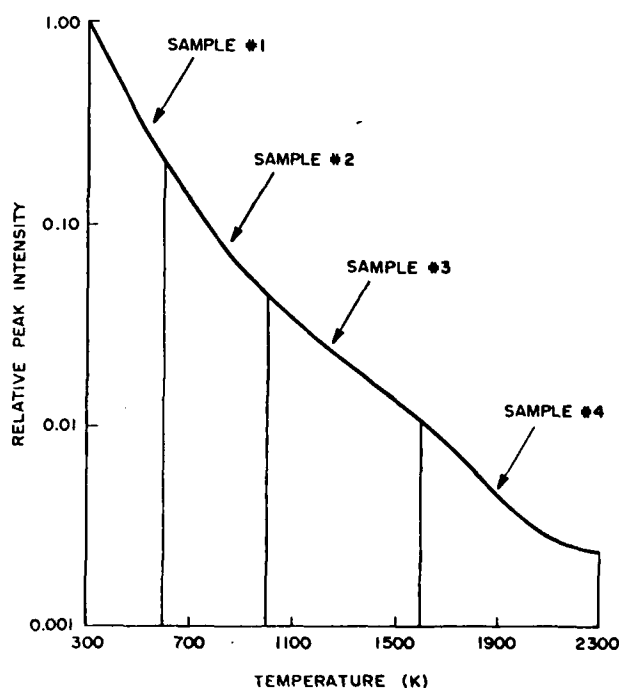


FIG. 3. Relative intensity-vs-temperature plot for N_2 Q branch. The intensity temperature of each region of the four sample peaks is depicted.

of the flame, the peak carrying the largest fraction of the signal is in the proper count range on the Reticon and is used to measure temperature and species concentration. When the CARS signal originates from a cooler portion of the gas, however, this peak is off scale (greater than 2000 counts), and one of the other three peaks is used for the measurement. This is demonstrated in Fig. 4.

In order to position the four sample beams and the reference beam on the Reticon simultaneously, the slits are removed from the monochromator. The five beams are then crossed 10 cm in front of a 10-cm focal length lens and enter the monochromator in a parallel fashion. The full expansion of all five beams on the collecting mirror of the monochromator could not be realized; thus, a certain amount of resolution was lost. The measured dispersion for this arrangement of the instrument was 2.4 cm^{-1} per channel element of the Reticon, with a $\sim 4.0\text{-cm}^{-1}$ HWHM measurement resolution.

B. Data-acquisition system

The basic components of the CARS data-acquisition system are shown in Fig. 5. The heart of the system is a Tracor-Northern 1710 multichannel analyzer with a plug-in optical spectrometer and an intensified gated diode-array rapid-scanning-spectrometer (DARSS) detector. The detector incorporates a Reticon solid-state line scanner and a monolithic, self-scanning, 512-element, linear photodiode array in a dual in-line package. The DARSS detector provides thermoelectric cooling (for reduced dark counts) and has a gatable, continuously variable-gain image intensifier. This detector displays little of the troublesome blooming encountered with vidicons.²³ The data from linear dynamic range measurements obtained for the DARSS detector are shown in Fig. 6. These data were obtained by averaging 100 shots of room-temperature N_2 CARS signals. The input intensity was varied by insertion of calibrated neutral-density filters. The points on this plot indicate the signal counts extending above the background levels for both the peak and integrated detector responses. These data suggest a maximum peak count constrained to ~ 2000 for linear operation. The lowest acceptable number of signal counts which indicated no interference from background-noise sources was ~ 200 . Thus, for single-shot operation the useful dynamic range of the detector is ~ 10 .

The TN-1710 is microprocessor controlled by an LSI-11. The mainframe of the analyzer contains 16 Kbytes of volatile memory and will accept plug-in modules to provide additional capabilities. The TN-1710 analyzer is supported by a Model 42 Teletype, Shugart dual 8-in. diskette drive, and a Hewlett-Packard 7004B X-Y plotter.

A Tracor-laser synchronizer was fabricated to synchronize the laser firing to the TN-1710 data-acquisition cycle. Upon a trigger from the TN-1710, the laser synchronizer generates four signals; two signals (20-V pulses) fire the laser flashlamps and Q switch, while the other two signals (TTL) trigger the TN-1710 data-acquisition electronics and gate the detector for background light reduction. Four variable delays are provided for adjusting the relative timing of the four signals. The laser may be fired in a single-shot mode or

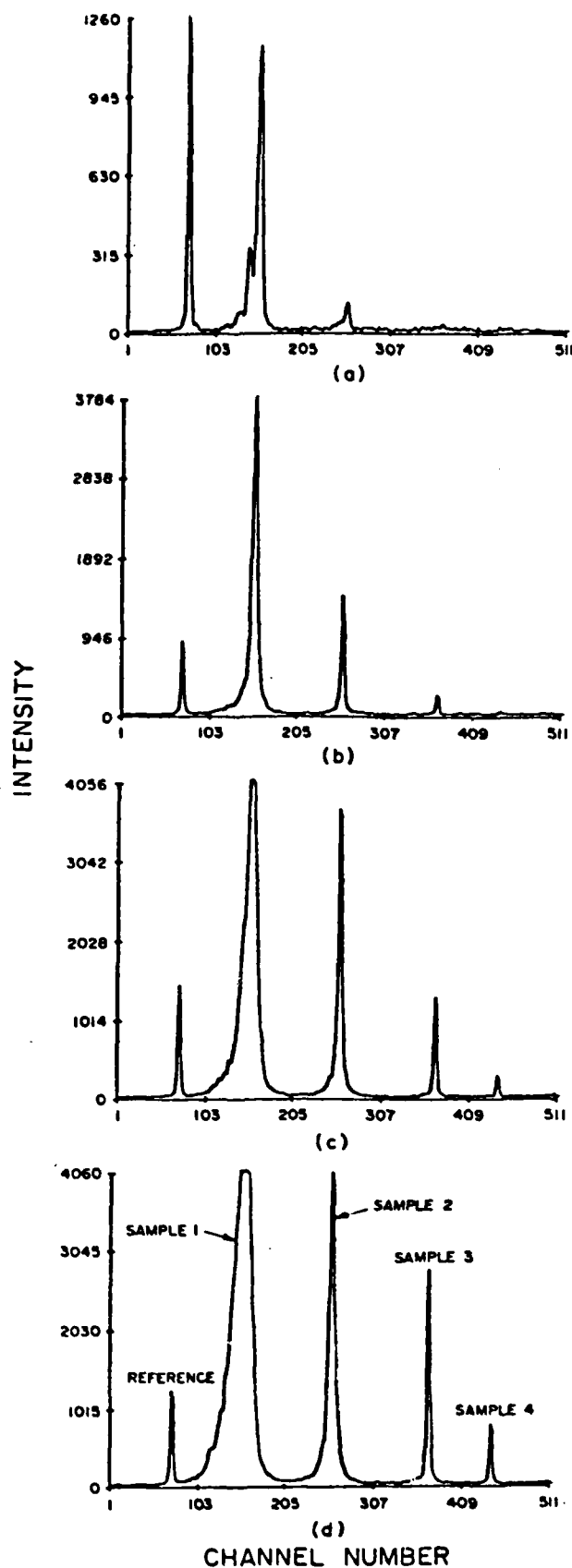


FIG. 4. Single-shot spectra obtained in turbulent diffusion flame, depicting variation of CARS intensity and how splitting arrangement insures that CARS signal is always on scale for at least one of the four sample peaks.

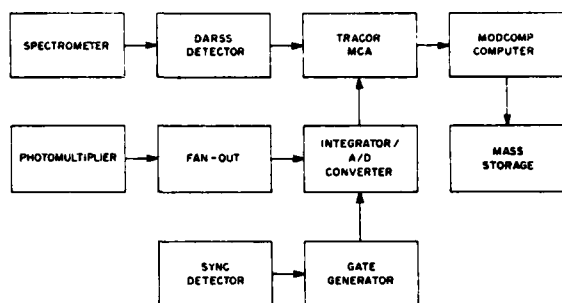


FIG. 5. Block diagram of the CARS-system data-acquisition electronics.

its firing can be controlled by the TN-1710 console or be program control. The synchronizer allows the laser flash-lamps to be pulsed continuously, regardless of laser firing mode, to maintain the laser cavity at a constant temperature.

The video signals from the DARSS detector are digitized and stored in a special memory of the TN-1710. This memory (spectral data memory, SDM) consists of 8 Kbytes of data memory partitioned to accept up to sixteen individual spectra. From the SDM, data are transferred in 16-bit parallel fashion to a Modular Computer Systems (ModComp) 7840 Classic Series Minicomputer. The transfer program (machine code) of the TN-1710 controls the handshaking and data transfer on the sending side. On the receiving (ModComp) side, FORTRAN in conjunction with a direct memory processor channels the information to either a 5-Mbyte disk drive or an 800-bpi magnetic-tape transport. When 512-channel spectra are being taken at 10 Hz, a disk can be filled in 8 min and a tape can be filled in 32 min. The use of the direct memory processor allows rapid data storage with minimum central-processor time. The flow of control during data transfer is diagrammed in Fig. 7.

In addition to the spectral data from the TN-1710, the data-acquisition system can acquire 10-Hz integrated data from a photomultiplier tube. The desired CARS signals are

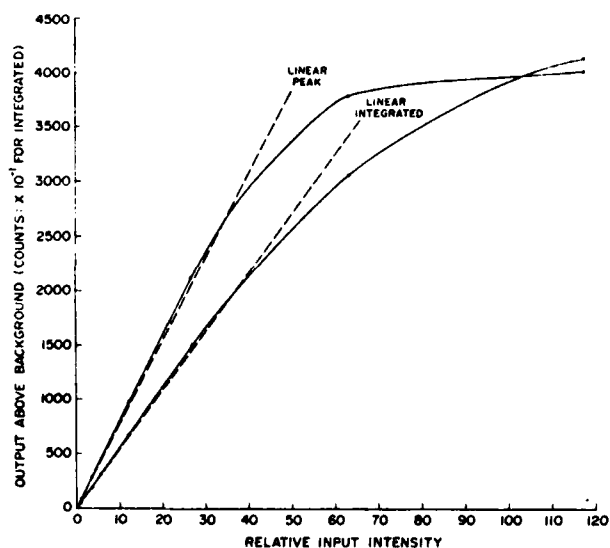


FIG. 6. DARSS-dynamic-range comparison for peak and integrated intensities in pulsed operation.

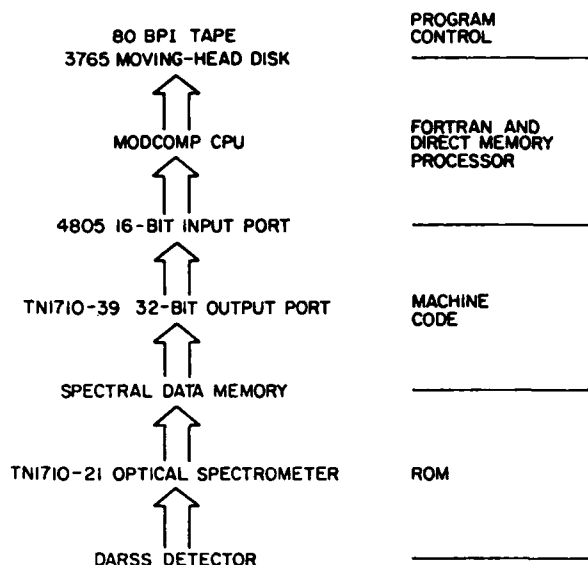


FIG. 7. Sequence of data storage, transfer, and restorage for 10-Hz operation.

time-multiplexed via different lengths of fiber-optic cable to a single photomultiplier tube. The tube signals are fed to a LeCroy 428-F Fan-Out which splits the PMT output into twelve parts, allowing up to twelve different CARS signals to be derived from a single PMT. Each of the twelve signals drives one channel of a 12-channel integrator/analog-to-digital converter (LeCroy Camac Model 2249SG). Each channel is individually gated to capture a single pulse from the pulse train of the photomultiplier tube. The custom-built gate generator provides 12 individually adjustable (start time and duration) gates, all triggered by a common sync signal from a pin diode which monitors the laser event. Instructions in the TN-1710 data-acquisition program cause it to address and read out the requested number of A/D converter channels sequentially. This information is deposited into the SDM, replacing the last 12 channels of the 512-channel spectral information and transferred along with the DARSS data to the ModComp 7840 Computer.

A significant problem was discovered with the DARSS detector during testing for 10-Hz operations, namely, that the detector possesses a memory allowing information from one laser shot to be carried over to the next. The image-lag effect demonstrated in Fig. 8 consists of two components—the intensifier phosphor-decay time ($TC \sim 10$ ms) and a second component due to the Reticon which results in an 8%–10% carryover of signal from one scan to the next. The phosphor-decay component is important when the detector is being scanned rapidly, > 20 Hz. However, since the detector is operated at 10 Hz for this application, the Reticon component represents the dominant image-lag problem. The Reticon lag component, as demonstrated in Fig. 8, is reduced only by scanning and not by increased time exposure. Since it is reduced only by the number of scans of the DARSS detector, then any scheme to reduce its effect would require that the DARSS be scanned several times between laser pulses to reduce any image lag. The total number of scans, however, is

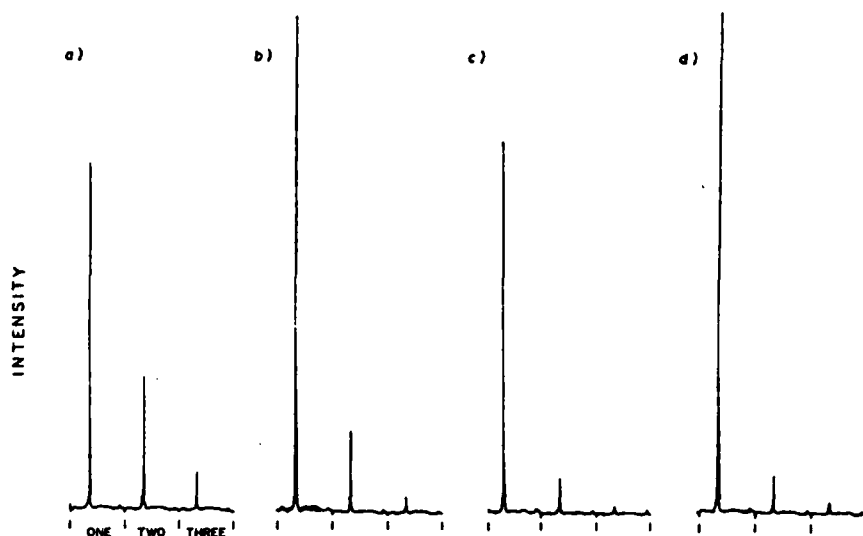


FIG. 8. Plot of relative intensities of three consecutive scans of the DARSS detector exposed to a single laser shot at different time delays. Time delays (a) 20 ms, (b) 33 ms, (c) 50 ms, and (d) 100 ms.

limited by the need for at least 60 ms of integration time and the time required for data transfers. Since the integration time could not be lowered, a concerted effort was made to minimize data-transfer time to allow maximum flexibility for anti-image lag schemes. A machine-code program was required for data transfer since a transfer program written in FLEXTRAN, the Tracor's high-level language (similar to BASIC), required 21 s for transfer of all 512 channels of each spectrum. The machine-code program which makes use of available machine registers and machine-coded instructions having lower addressing modes and correspondingly lower execution times requires 22 ms to transfer the 512-channel spectrum.

Once data-transfer time had been minimized, an anti-image-lag scheme was devised. The scheme represented a compromise between performing a large number of scans

that would totally erase the retained image and maintaining a long integration time that would permit the entire signal to be acquired. Through the use of the external exposure input of the optical spectrometer, a special data-acquisition cycle was developed which reduced the image-lag problem to less than 1% signal bleedover. This acquisition cycle appears in Fig. 9(a). After each laser shot, the detector integrates for 60 ms to acquire the full CARS signal. The detector is then scanned and its output digitized and deposited into the SDM. If the ModComp is ready, the spectrum is transferred via the I/O ports. Otherwise, the program loops for a time equal to the transfer time, which keeps the laser firing rate at 10 Hz. The detector is scanned to reduce image lag; and after a small delay, the detector is scanned once again to further cleanse it of any retained images. The detector is then ready for the next CARS signal. The result of the anti-image-lag

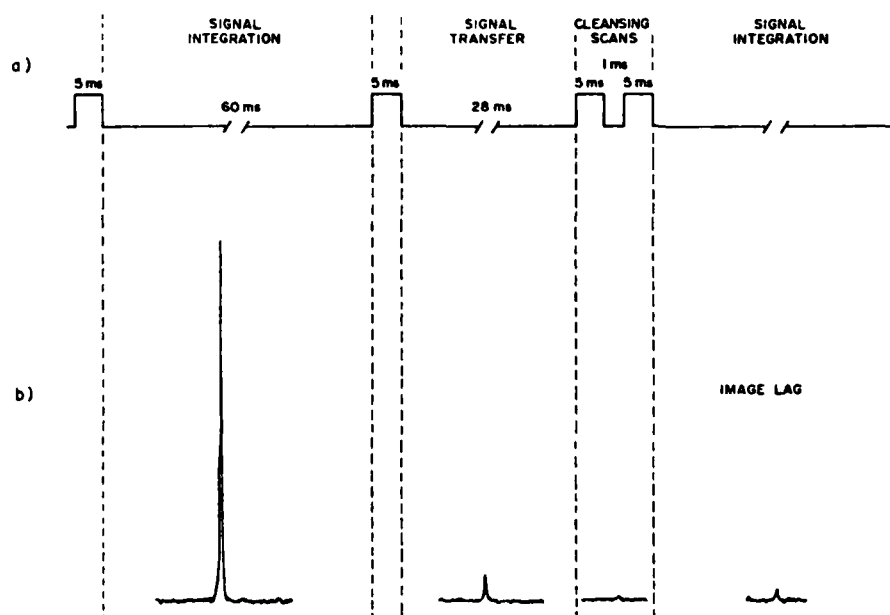


FIG. 9. (a) Data-acquisition cycle employed to minimize image lag problems. (b) Plot of relative intensities resulting from the anti-image lag data-acquisition scheme.

acquisition cycle is shown in Fig. 9(b). The 10-Hz antilag acquisition system was employed for all data acquisition reported in this paper.

C. Data reduction

As discussed in Sec. II B, the raw spectra are stored in a mass-storage device (by the ModComp computer, typically tape) and retained for analysis at a later time. This analysis includes conversion of the raw single-shot spectra to temperatures and species concentrations from which histograms, contour maps, and correlation plots can be constructed.²⁴

The data reduction consists of fitting the observed spectral bandshape in order to obtain temperatures and integrating the CARS signal to obtain concentrations. However, since four sample (flame) CARS peaks are generated during a single shot, the program must decide which peak is in the proper intensity range for temperature fitting. The basic program can be broken down into the following five subprograms: (1) initial parameter setup; (2) peak selection; (3) temperature fitting; (4) concentration determination; and (5) data storage.

The initial parameter setup involves first determining the sample reference intensity correlations for each of the four CARS peaks in ambient air, which consists of ratioing the integrated sample signal by the integrated-power-reference value for a total of 200 shots. This measurement is needed for calibration of the flame-concentration data and for determining the error in the concentration measurement. Next, the initial temperature guesses are made for each of the four peaks. Each peak covers a narrow range of temperatures (typically less than 600 K) from 300 to 2300 K; the initial temperature guess will vary depending upon the beam-splitting combination employed. The program then searches through the file of spectra to be reduced and selects, for each of the four peaks, one spectrum in which the peak intensity falls between 200 and 2000 counts. Next, each of these spectra is frequency fit (using a fitting procedure similar to the temperature fit discussed below) to determine the starting channel, frequency, and boundaries of that CARS peak. This procedure establishes the boundary conditions for each peak to be used by the peak-selection subprogram.

The peak-selection subprogram performs the task of determining which of the four peaks recorded during a single shot will be used for temperature fitting. Each peak is tested to determine whether its intensity falls within the 200–2000 count range. Next, the initial parameters and boundary conditions which were determined in the setup subprogram are applied to the peak in the correct intensity range. Normalization for diode-sensitivity variation and dye-laser tuning is then performed, and the CARS spectrum is ready for temperature fitting.

The temperature-fitting subprogram employs a nonlinear least-squares fit of the temperature.²⁵ The fit is based upon the iterative equation

$$\Delta T = (J^+ J)^{-1} J^+ \Delta \phi, \quad (5)$$

where J and J^+ are the Jacobian matrices defined by

$$J = \begin{pmatrix} \frac{dI(1)}{dT} \\ \vdots \\ \frac{dI(n)}{dT} \end{pmatrix}, \quad J^+ = \frac{dI(1)}{dT} \dots \frac{dI(n)}{dT} \quad (6)$$

and $\Delta \phi$ is the difference matrix defined by

$$\Delta \phi = I_o(1) - I_c(1), \dots, I_o(n) - I_c(n) \quad (7)$$

where the subscripts o and c represent observed and calculated intensities, respectively. The temperature subprogram begins with the initial temperature guess and forms the necessary matrices for the iterative equation. The correction, ΔT , to the guessed temperature is determined and a new temperature calculated. The new temperature is then used as the temperature guess and the iterative cycle repeated until the temperature correction, ΔT , becomes small—typically three cycles of the iteration are required. To reduce the time required for temperature fitting, a CARS-spectra library was calculated and stored for use by the fitting routine. Instead of calculating the CARS spectrum for each cycle, the temperature-fitting subprogram retrieves the spectrum from the library. This reduces the data-analysis time per spectrum from 30 min to 3 s on the ModComp Classic 7840 Computer.

Once the temperature has been fit the concentration can be determined from the integrated area of the CARS signal. The N_2 number density is given by²⁴

$$N_T = N_{300} \sqrt{\frac{(R_T)(I_T)}{I_{300}}}, \quad (8)$$

where N_T is the N_2 number density at temperature T ; N_{300} is the N_2 number density at 300 K; R_T is the ratio of the bandshapes of the CARS spectrum at 300 K to the CARS spectrum at temperature T ; I_T is the experimentally measured integrated CARS intensity at temperature T ; and I_{300} is the experimentally measured integrated CARS intensity at 300 K. The ratio R_T takes into account the change in the Raman linewidths and population redistribution with temperature. Once the spectral data file has been reduced to temperature and species-concentration data, the results are stored on mass storage by the data-storage subprogram, and analysis of the next file of raw CARS spectra begins.

Approximately 3 s of CPU time per spectrum is required for the data analysis discussed above. Data reduction is generally accomplished at night when the ModComp computer can be solely dedicated to this task. At this rate approximately one tape of CARS data (30 min of 10-Hz data) can be reduced overnight.

III. SYSTEM CALIBRATION AND EXPERIMENTAL RESULTS

To calibrate the 10-Hz CARS system in a known flame environment, a premixed near-stoichiometric mixture of propane and air was burned in a concentric-tube burner. This flame has been studied extensively by two-line fluorescence and sodium-line reversal and is known to have a steady, flat temperature distribution across its profile.¹⁸ The burner was operated at an air flow of 1.75 std. l/min of air and 0.082 std. l/min of propane. This corresponds to a fuel-to-air ratio

of 0.0767 and an equivalence ratio of 1.20. Adiabatic flame calculations for a propane-air mixture predict an average temperature of 2195.6 K and an N_2 concentration of 2.535×10^{18} molecules/cm³. The average temperature measured by the CARS technique was 2174.0 ± 90 K, with an N_2 concentration of $2.637 \times 10^{18} \pm 0.139 \times 10^{18}$ molecules/cm³. Because of the flame stability at the measurement location, the observed deviations given for these measurements are due solely to the uncertainty of the measuring technique. Uncertainties of 4% in temperature and 5.2% in concentration are thus obtainable with this apparatus. These results are in agreement with error-analysis results for this instrument which will be reported in the near future.²⁶

The temperature histogram of the experimental data is shown in Fig. 10(a). The bin size for the temperature and concentration pdfs was 100 K and 1.0×10^{18} molecules/cm³, respectively. The concentration histogram is shown in Fig. 10(b), and the correlation of the two measured parameters is shown in Fig. 10(c). Most of the data are grouped very near the adiabatic flame curve, shown in this figure as a solid line. The adiabatic equilibrium flame calculations are based upon the assumption that each homogeneous volume of gas within a flame consists of an equilibrium mixture of gases at adiabatic temperature. These calculations neglect radiative heat and mass transfer. The solid line in Fig. 10(c) is the adiabatic equilibrium calculation performed for fuel-to-air equivalence ratios between 0.1 and 3.0 using the computer code of Gordon and McBride.²⁷ Initially the fuel and air were at atmospheric pressure (750 Torr) and 298 K. The equivalence ratio of 1.2 indicates a slightly fuel-rich mixture, as demonstrated by the data which lie primarily on the lower fuel-rich curve.

To produce a turbulent flame, the burner was operated with a fuel flow of 1.9 l/min of propane surrounded by an outer air flow of 17 l/min, corresponding to a Reynolds number of 2000. The ratio of mass flows of air to fuel was ~6 to 1. The flame which was produced was thus dominated by the shear generated by the two mass flows. The flame displayed a high degree of large-scale turbulent structures, a length of 30 cm, and a large amount of sooting. For the results plotted in Fig. 11, the measurements were made 16.5 cm above the fuel tube and directly on the centerline.

The temperatures were observed to vary greatly from room temperature to near stoichiometric in this flame. A pdf of the temperature data is shown in Fig. 11(a). A 100-K bin size was used in this plot. The data show a wide temperature distribution for this flame. This wide temperature distribution and temperature fluctuations indicated by these data are typical of values obtained at downstream locations in turbulent-jet diffusion flames.²⁸ The N_2 -concentration pdf for the N_2 -concentration data is shown in Fig. 11(b). The bin size in this plot is 1.0×10^{18} molecules/cm³. The concentration shows a dominant peak at 3.0×10^{18} molecules/cm³, which corresponds to the hot-flame zones, the higher concentrations of N_2 being due to low-temperature regions. The cross correlation between the simultaneous temperature and N_2 concentration is shown in Fig. 11(c). Superimposed on these data are results from the adiabatic flame calculation for the propane-air flame. The upper line corresponds to a fuel-lean

mixture and the lower, to a fuel-rich mixture. The turning point in the higher-temperature region corresponds to a stoichiometric mixture. As can be seen, the experimental data follow the adiabatic flame calculations. The average temperature at this flame location was 1335 K, with a standard deviation of 521 K. Notice that the entire temperature range from 300 to 2300 K was measured, indicating that the CARS

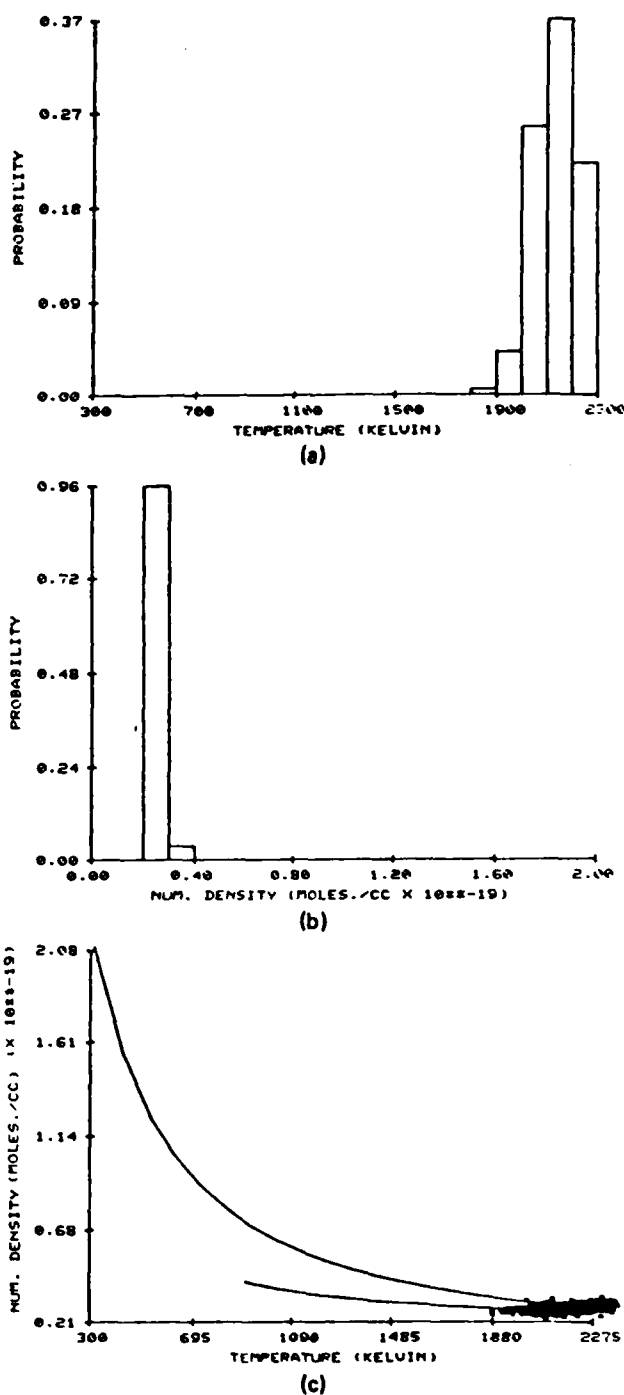


FIG. 10. Data obtained in the near-stoichiometric premixed flame. (a) Temperature pdf, (b) concentration pdf, and (c) correlation plot of temperature and concentration vs adiabatic-equilibrium-calculation results (solid)

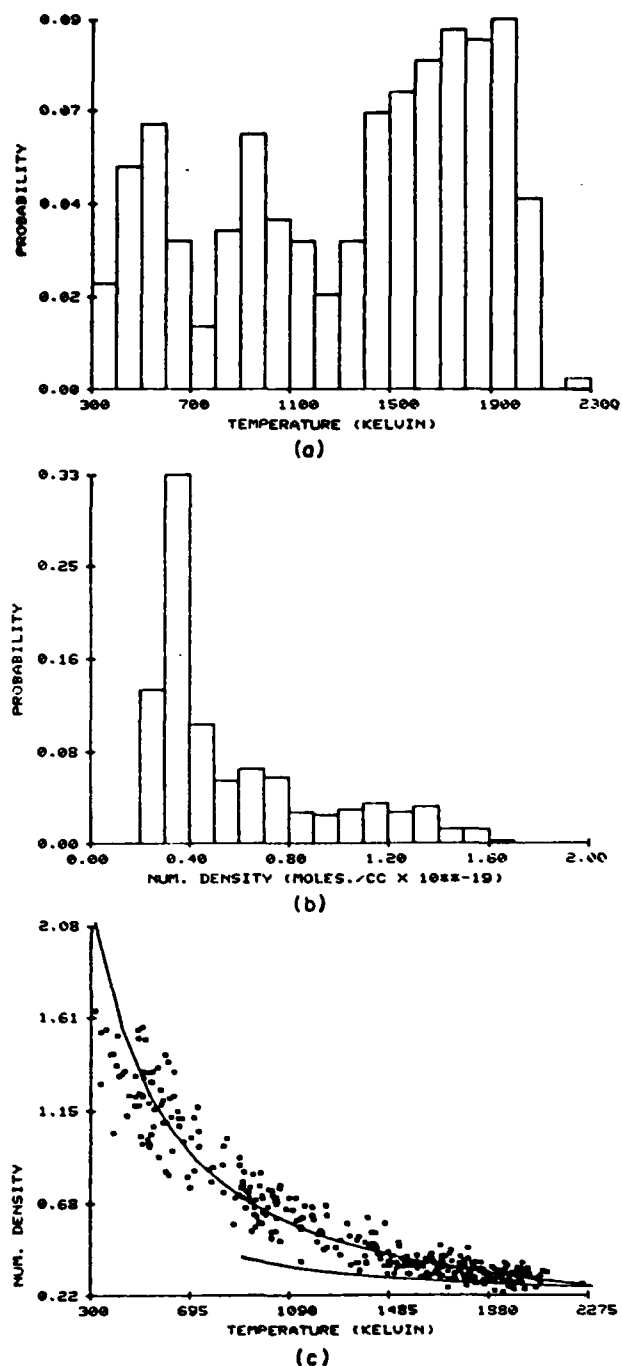


FIG. 11. Data obtained in R , ~2000 turbulent flame. (a) Temperature pdf, (b) concentration pdf, and (c) correlation plot of temperature and concentration vs adiabatic-equilibrium-calculation results (solid).

apparatus is quite capable of obtaining temperatures and species concentrations in turbulent, sooty flame environments.

ACKNOWLEDGMENT

Work supported under USAF Contract F33615-80-C-2054.

- ¹A. C. Eckbreth, *Combust. Flame* **39**, 137 (1980).
- ²Z. A. Stenhouse, D. R. Williams, J. B. Cole, and M. D. Swords, *Appl. Opt.* **18**, 3819 (1979).
- ³J. P. E. Taran, presented at the CARS Meeting of the Institute of Physics, AERE, Harwell, March 1979.
- ⁴G. L. Switzer, W. M. Roquemore, R. B. Bradley, P. W. Schreiber, and W. B. Roh, *Appl. Opt.* **18**, 2343 (1979).
- ⁵G. L. Switzer, L. P. Goss, W. M. Roquemore, R. B. Bradley, P. W. Schreiber, and W. B. Roh, *AIAA J. Energy* **4**, 209 (1980).
- ⁶S. Lederman, *Prog. Energy Combust. Sci.* **3**, 1 (1977).
- ⁷M. Lapp and D. L. Hartley, *Combust. Sci. Technol.* **13**, 199 (1976).
- ⁸J. W. Nibler, W. M. Shaub, J. R. McDonald, and A. B. Harvey, in *Vibrational Spectra and Structure*, edited by J. R. Durig (Elsevier, Amsterdam, 1977), Vol. 6.
- ⁹A. C. Eckbreth, P. A. Bonczyk, and J. F. Verdieck, *Prog. Energy Combust. Sci.* **5**, 253 (1979).
- ¹⁰R. J. Hall, J. F. Verdieck, and A. C. Eckbreth, *Opt. Commun.* **35**, 69 (1980).
- ¹¹R. J. Hall, *Combust. Flame* **35**, 47 (1979).
- ¹²A. C. Eckbreth and R. J. Hall, *Combust. Sci. Technol.* **25**, 175 (1981).
- ¹³R. J. Hall, *Appl. Spectrosc.* **34**, 700 (1980); L. A. Rahn, A. Owyong, M. E. Coltrin, and M. L. Kowski, in *Proceedings of the Seventh International Conference on Raman Spectroscopy*, edited by W. F. Murphy (North-Holland, Amsterdam, 1980), p. 694.
- ¹⁴W. B. Roh, P. W. Schreiber, and J. P. E. Taran, *Appl. Phys. Lett.* **29**, 174 (1976).
- ¹⁵A. C. Eckbreth and R. J. Hall, *Combust. Flame* **36**, 87 (1979).
- ¹⁶W. B. Roh, Air Force Aero Propulsion Laboratory Report No. AFAPL-TR-77-47, Wright-Patterson Air Force Base, OH, August 1977.
- ¹⁷L. A. Rahn, L. J. Zych, and P. L. Mattern, *Opt. Commun.* **30**, 249 (1979).
- ¹⁸L. P. Goss and G. L. Switzer, Air Force Wright Aeronautical Laboratories Report No. AFWAL-TR-80-2122, Wright-Patterson Air Force Base, OH, February 1981.
- ¹⁹R. L. Farrow, P. L. Mattern, and L. A. Rahn, *Appl. Opt.* **21**, 17 (1982).
- ²⁰J. L. Oudar, R. W. Smith, and Y. R. Shen, *Appl. Phys. Lett.* **5**, 380 (1980).
- ²¹L. P. Goss, G. L. Switzer, and P. W. Schreiber, *AIAA Paper No. 80-1543*, 1980.
- ²²A. C. Eckbreth, *Appl. Phys. Lett.* **32**, 421 (1978).
- ²³G. W. Liesegang and P. W. Smith, *Appl. Opt.* **20**, 2604 (1981).
- ²⁴L. P. Goss, G. L. Switzer, D. D. Trump, and P. W. Schreiber, *AIAA Paper No. 82-0240*, 1982.
- ²⁵A. Kim, *J. Chem. Edu.* **47**, 120 (1970).
- ²⁶L. P. Goss, B. G. MacDonald, D. D. Trump, and G. L. Switzer (to be published).
- ²⁷S. Gordon and B. J. McBride, National Aeronautics and Space Administration Report Nos. NASA SP273, 1971 and NTIS N71-37775.
- ²⁸M. C. Drake, M. Lapp, C. M. Penny, S. Warshaw, and P. W. Gerhold, presented at the 18th Symposium (International) on Combustion, University of Waterloo, Waterloo, Canada, 17-22 August 1980 (Combustion Institute, Pittsburgh, 1981).

2.2 ERROR ANALYSIS OF CARS THERMOMETRY AND SPECIES-CONCENTRATION MEASUREMENTS

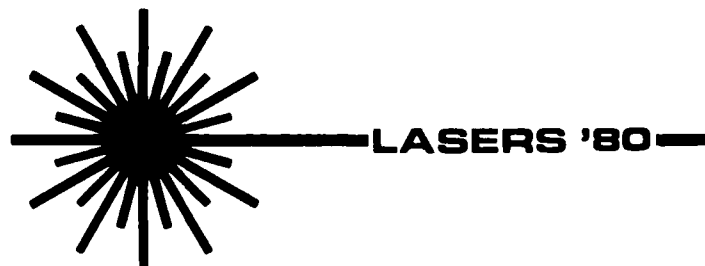
An assessment of the requirements of a CARS instrument for combustion diagnostics is given in a paper entitled, "Assessment of the Application of CARS to Combustion Diagnostics," which was published in Lasers '80. This paper, which is included on the following pages, gives a brief introduction to error analysis and the potential effects of turbulence upon CARS. A more detailed discussion follows.

ASSESSMENT OF THE APPLICATION OF CARS
TO COMBUSTION DIAGNOSTICS

L. P. Goss and P. W. Schreiber

pp. 220-235

REPRINTED FROM
PROCEEDINGS
OF THE
INTERNATIONAL CONFERENCE
ON



ASSESSMENT OF THE APPLICATION OF CARS TO COMBUSTION DIAGNOSTICS

L. P. Goss
Research Chemist
Systems Research Laboratories, Inc.
Dayton, OH 45440

P. W. Schreiber
Research Physicist
Aero Propulsion Laboratory
Air Force Wright Aeronautical Laboratories
Wright-Patterson Air Force Base, OH 45433

ABSTRACT

The application of CARS to the diagnostics of turbulent combustion media is examined, and problems incurred in thermometry and concentration measurements employing this technique are discussed. For thermometry, these problems include the dynamic-range limitations of the multichannel-analyzer detectors and the extensive computer time required to reduce Q-branch data to temperatures. Problems associated with concentration measurements include turbulence induced intensity losses and the requirement for simultaneous temperature measurements.

I. Introduction

Light-scattering and wave-mixing spectroscopic techniques are playing an ever-increasing role in the broad area of optical diagnostics. Spontaneous Raman scattering has received much attention for remote point probing of flames;¹ however, due to its low signal levels and incoherent nature, it is generally limited to investigations of relatively clean combustion media. Consequently, many flames of practical interest (e.g., hydrocarbon-fueled, turbulent diffusion flames) may be beyond its range of applicability. With the increasing emphasis on alternative--and generally less clean--fuels, new diagnostic techniques are being developed and refined. Coherent anti-Stokes Raman spectroscopy (CARS) is one such technique.

Some of the major attractions of the CARS technique include large discrimination capabilities against background luminosity, laser-induced fluorescence, and particulate interferences;² very high S/N levels which make it capable of probing practical combustion environments successfully over a broad range of operating conditions;³ and the ability to obtain temperature and species concentration instantaneously, making the technique ideal for the study of fluid-dynamic variables in turbulent combustion.⁴ It is the purpose of this paper to report on the advances that have been made toward the application of the CARS technique to the study of turbulent combustion environments.

II. Thermometry

A major application of CARS is the utilization of the technique for thermometry in flame environments. The primary species studied in flames has been N₂ because of its abundance. To determine the temperature from an N₂ Q-branch spectrum, one must calculate the CARS spectrum as a function of temperature, based upon the third-order nonlinear susceptibility, $\chi^{(3)}$, expressed by

$$\chi^{(3)} = \chi_n + \chi_r \quad (1)$$

where χ_n is the nonresonant contribution and χ_r is the Raman resonant contribution to the third-order susceptibility. χ_r is given by

$$\chi_r \propto \sum_{v,J} \frac{N \Delta(v,J) \left(\frac{d\sigma}{d\Omega} \right)_{v,J}}{\omega_r - \Delta - i\Gamma(v,J)} \quad (2)$$

where N is the total number density of the species being probed; $\Delta(v,J)$ is the population difference between the states involved in the Raman transition; ω_r is the frequency of the Raman transition, Δ is the frequency difference between the pump, ω_1 , and the probe, ω_2 ; $\Gamma(v,J)$ is the HWHM of the Raman transition; and $(d\sigma/d\Omega)_{v,J}$ is the Raman scattering cross section defined for Q-branches as

$$\left. \frac{d\sigma}{d\Omega} \right]_{v,J} = \left(\frac{\omega_2}{c} \right)^4 \frac{h}{2m\omega_0} \left[\alpha^2 + \frac{4}{45} b_J^J \gamma^2 \right] (v+1) \quad (3)$$

where α is the spherical part of the polarizability and $b_J^J \gamma^2$ is the anisotropic part which usually has a weak J dependence. The corresponding CARS power is given by⁵

$$P_a(\omega) = \int P_1(\omega_1) d\omega_1 \int P_1(\omega - \Delta) P_2(\omega_1 - \Delta) |\chi^{(3)}(\Delta)|^2 d\Delta \quad (4)$$

where P_1 is the spectral power of the pump laser and P_2 is the spectral power of the probe laser.

In the normal course of calculating a CARS spectrum, the third-order susceptibility is generated according to Eqs. (1) and (2) and then $|\chi^{(3)}|^2$ is convolved over the pump and probe laser linewidths as dictated by Eq. (4). Another convolution over the detector-slit function, however, must be made before the calculated spectrum can be compared to the experimentally observed one. A nonlinear least-squares program has been developed to fit the observed experimental spectrum as a function of temperature.⁶ The program is based upon the iterative matrix equation

$$\Delta P = (J^+ J)^{-1} J^+ \Delta \phi \quad (5)$$

where J is the Jacobian matrix whose elements are defined by $J_{ik} = dI_i/dP_k$ (I_i is the i th intensity and P_k the k th parameter); J^+ is the transpose of the J matrix; $\Delta \phi$ is the matrix with elements $\Delta \phi_i = I_{iobs} - I_{ical}$ (where I_{iobs} is the i th observed experimental intensity and I_{ical} the i th calculated intensity); and ΔP is the correction matrix whose elements contain the corrections to be made upon the parameters which are varied. Figure 1 depicts a fit that was made to a single-shot spectrum obtained from a premixed propane burner.

Effect of Linewidths Upon Temperature Measurements

As outlined above, the temperature of a combustion medium can be estimated by obtaining the best fit of a calculated spectrum to an experimentally determined one. To achieve this fit, temperature and linewidth can be used as adjustable parameters if the J dependence upon the linewidth in the Q-branch is neglected. This approach has yielded excellent results for laminar laboratory flames where the temperature has been determined by other methods such as the line-reversal technique.⁴ However, it would be advantageous to gain a better understanding of the linewidth problem to improve the reduction of CARS data to temperatures and species concentrations. The latter case presents a much more difficult problem and will be discussed later.

The primary mechanisms for spectral line broadening in a combustion medium are molecular collisions and the Doppler effect. The linewidths depend upon temperature, pressure, and composition of the medium as well as the J value of the line. Collisional effects, as demonstrated for the case of hydrogen, may cause narrowing or broadening of the spectral line.⁷ Fortunately, collisional narrowing can be neglected for most species. However, it does present a special problem for the analysis of hydrogen data, and additional work is required for proper analysis of H_2 data in combustion environments. As an approximation, the collisional linewidth can be expressed as a function of the optical collisional frequency,⁸ which yields, for the half-intensity breadth,

$$\Gamma = \frac{1}{\tau_0} \quad (6)$$

where τ_0 is the time between collisions. From kinetic theory one obtains, for a gas composed of a single species,

$$\Gamma = 4N \sqrt{\frac{\pi kT}{m}} \rho^2 \quad (7)$$

where ρ is the optical collisional diameter which may be 10 to 10^3 times greater than the value obtained from kinetic-theory experiments.¹ For N_2 this yields an estimated half-intensity breadth between 2×10^{-3} and $2 \times 10^{-1} \text{ cm}^{-1}$ at atmospheric pressure and room temperature. If one assumes that the collisional diameter is independent of the velocity of the molecules, then Γ should depend upon $T^{-1/2}$. This assumption appears to be in reasonable agreement for N_2 linewidth measurements using CARS.⁹ A review of recent

experiments and theoretical developments in the area of Raman line shapes is given by Srivastava and Zoidi.¹⁰ The theory was compared with experimental CARS data for the Δ_2 Q-branch by Rahn, Owyong, Colhin, and Koszykowski.¹¹ Although these data indicate that the J dependence is weak, a sufficient change in Γ occurs to warrant the inclusion of this effect in calculated spectra. Additional work is required to investigate the effect of neglecting the J dependence when temperatures are determined by fitting measured Q-branch spectra to calculated spectra.

As the temperature of the combustion gas increases for a given pressure, the effect of Doppler broadening becomes more important. Thus, the linewidth becomes a combination of Doppler and collisional broadening. If collisional narrowing is neglected, it can be shown that the anti-Stokes susceptibility becomes

$$\chi^{(3)}(\omega) = \sum_{v,J} K_{v,J} \left(\frac{(4/\pi) \ln 2}{\Delta\omega_D} \right)^{1/2} \int_{-\infty}^{+\infty} \frac{d\xi}{\omega_r(v,J) + \xi - \omega - i\Gamma(v,J)} \exp[-4(\ln 2) \xi^2 / \Delta\omega_D]^2 \quad (8)$$

where

$$K_{v,J} = \frac{N \Delta_J c^4}{3 \hbar \omega_s^4} \left(\frac{d\sigma}{d\Omega} \right)_{v,J}$$

and $\Delta\omega_D$ is the Doppler width for forward Raman scattering given by

$$\Delta\omega_D = \omega_J [8(\ln 2) kT / mc^2]^{1/2} \quad (9)$$

If one lets

$$t = \frac{2(\ln 2)^{1/2} \xi}{\Delta\omega_D}$$

the equation for $\chi^{(3)}(\omega)$ becomes

$$\chi^{(3)}(\omega) = \sum_{v,J} -K_{v,J} \left(\frac{(4/\pi) \ln 2}{\Delta\omega_D} \right)^{1/2} \int_{-\infty}^{+\infty} \frac{e^{-t^2} dt}{z - t} \quad (10)$$

where $z = [(\omega - \omega_r + i\Gamma(v,J)) 2(\ln 2)^{1/2} / \Delta\omega_D]$.

If $\Gamma \rightarrow 0$, it can be shown that in this Doppler limit, the expression reduces to

$$\chi^{(3)} = \sum_{v,J} K_{v,J} \left(\frac{(4/\pi) \ln 2}{\Delta\omega_D} \right)^{1/2} \left[\pi i e^{-z^2} - 2 \sqrt{\pi} e^{-z^2} \int_0^z e^{t^2} dt \right] \quad (11)$$

where

$$e^{-z^2} \int_0^z e^{t^2} dt$$

(Dawson's integral) is tabulated in Ref. (12) and $z = 2(\ln 2)^{1/2} (\omega - \omega_r) / \Delta\omega_D$. The effect of the real part is to increase the halfwidth of the Doppler line and to increase the wings. At first, the real part was estimated to be small. With this assumption the width of $|\chi^{(3)}(\omega)|^2$ in the Doppler limit becomes $\Delta\omega_D / \sqrt{2}$. Later it was shown that the real part does contribute significantly and that the halfwidth is $\sim 1.22 \Delta\omega_D$ for a Doppler-broadened CARS line.¹³

If $\Delta\omega_D \rightarrow 0$, the Gaussian function in Eq. (8) becomes a δ -function, and one obtains the ordinary collisional broadened line. However, in high-temperature regions of a combustion medium, Doppler broadening can become significant. For example, at 2000K the Doppler width for N_2 becomes 2.4×10^{-2} which is comparable to the collisional width at atmospheric pressure. The J dependence for the total linewidth would be reduced under these conditions. When it is necessary to include Doppler broadening, $|\chi^{(3)}(\omega)|$ can be estimated by using Eq. (8), if the nonresonant background is not significant. When the J dependence is known,

then the temperature can be determined by fitting calculated data to experimental data using temperature and Γ as adjustable parameters.

Experimental Setup

The laser system used most often in performing CARS measurements in combustion studies is the Nd:YAG-dye laser combination. The Air Force Wright Aeronautical Laboratories/Aero Propulsion Laboratory CARS setup used for the majority of the studies reported in this paper is shown in Fig. 2. The system consists of a Quanta-Ray Nd:YAG laser whose frequency-doubled output is used to pump a broadband dye laser and to provide the pump beams used in the CARS process. The broadband dye laser consists of an oscillator-amplifier combination with a 30% lasing efficiency. An optical delay line (M8,M9,M10) is incorporated into the scheme to provide a temporal match between the Nd:YAG- and dye-laser pulses. The Nd:YAG and dye beams in the BOXCARS orientation are crossed and focused by lens L5 into the premix burner flame. Beam splitter BS5 splits off ~ 30% of the three beams and forms the reference leg. This path is used for normalization and species-concentration determinations. The resulting CARS signals in both the sample and reference are predispersed by Pellin Broka prisms and coupled into a SPEX 1702 monochromator by periscopes PS2 and PS3.

A Tracor-Northern TN1710 DARSS reticon is used as the detector. The DARSS unit consists of a linear (one-dimensional) diode-array (reticon) detector element in conjunction with a photo-cathode intensifier. The overall sensitivity of the device is similar to that of the OMA unit, which is about 50% of a common S-20 response photomultiplier. This was found to be more than adequate for most combustion studies. The major advantages of the DARSS over the OMA are the larger linear-dynamic range, the lack of blooming or cross-talk between channels of the detector, and the better electronic support offered by the TN1710 control unit. To circumvent the single dimensionality of the Tracor-Northern DARSS detector, the entrance slit of the monochromator is rotated 90° from its usual vertical position to a horizontal position. This allows the two CARS signals to be aligned on different regions of the DARSS detector, as shown in Fig. 3. The two CARS signals are then recorded simultaneously by the DARSS and analyzed at a later date. This configuration allows simultaneous determination of temperature and species concentration.

Temperature Measurements in Turbulent Flames

To characterize a turbulent system, measurements must be made faster than the system's variation. For turbulent combustion systems this requires measurement speeds of ~ 10 kHz, if turbulent data are to be collected in real time. Such data rates are not technically feasible at present due to laser as well as detector limitations. The Nd:YAG laser systems normally employed have an optimum repetition rate of only 10 Hz which is far from the tens-of-kilohertz rate needed. However, with a 10-Hz system, many problems still must be overcome before data can be taken. The OMA device which is used will ultimately limit the repetition rate which is feasible.

A problem associated with multichannel-analyzer devices is the limitation in the linear dynamic range in single-shot operation. An estimate of the dynamic range which is required for studying a turbulent flame can be gained from consideration of the change in the intensity of the CARS signal with a temperature variation of 300 to 2200K. The change in the intensity of the fundamental band of the Q-branch of N_2 is ~ 240 for this temperature range. However, to determine a temperature from the Q-branch spectrum above 1200K, a measurement must also be made of the hotband intensity. At 2200K the hotband intensity is one-fifth that of the fundamental. Because of the background variation of the OMA detectors, a signal of at least 20 counts must be maintained in the hotband if it is to be used for temperature determination. Thus, a dynamic range of 1800 to 1 must be maintained by the OMA detector. Most OMA devices, however, have only a 200-count dynamic range during single-shot operation. Since no OMA devices--either vidicon or reticon--exist today which have the vast dynamic range required for this temperature regime, alternative approaches must be pursued.

One possible alternative is the use of two OMA detectors and a beam splitter arranged in such a way that one detector is 200 times more sensitive than the other. This would result in the changing of the single-shot dynamic range from ~ 200/1 to ~ 40,000/1. Such an approach--while possible--is cost prohibitive. A second alternative would be to monitor a parameter other than the N_2 Q-branch which is indicative of temperature. Such a parameter is the nonresonant susceptibility, $\chi_n^{(3)}$, which is described by

$$\chi_n^{(3)} = \sum_i C_i \chi_{ni}^{(3)} \quad (12)$$

where C_i and χ_{ni} are the percent concentration and the nonresonant susceptibility of the i^{th} species, respectively. The nonresonant CARS power is given by

$$P_a = K_{\text{exp}} N_T^2 |x_n^{(3)}|^2 P_p^2 P_s \quad (13)$$

where N_T is the total number density of all species present, which is inversely proportional to the temperature. Normalizing the signal with a power reference to cancel any power fluctuations of the lasers results in

$$P'_a = \frac{P_a}{P_R} = \frac{K_{\text{exp}} \left(\frac{1}{T}\right)^2 |x_n^{(3)}|^2}{K_{\text{exp}}^R \left(\frac{1}{T_R}\right)^2 |x_n^{(3)}|^2_R} \quad (14)$$

under conditions of constant pressure. Ratioing Eq. (14) to the results of a measurement made on a standard gas yields

$$\frac{P'_a}{P'^{S_T}_a} = \frac{\left(\frac{1}{T}\right)^2 |x_n^{(3)}|^2}{\left(\frac{1}{T_s}\right)^2 |x_n^{(3)}|^2_s} \quad (15)$$

and rearranging Eq. (15) to solve for the temperature yields

$$T = \frac{|x_n^{(3)}|}{|x_n^{(3)}|_s} \sqrt{\frac{P'^{S_T}_a}{P'_a}} (T_s) \quad (16)$$

The temperature is thus reduced to a simple ratio of the integrated nonresonant signal produced by the flame to that of a standard gas. It is also a function, however, of the relative change in the third-order susceptibility between the standard gas and the experimental composition. Studies of the nonresonant susceptibility for flames have indicated that $x_n^{(3)}$ can vary by as much as 40% throughout the flame.¹⁴

Equilibrium flame calculations have been made for a propane-fueled flame to determine the variation of $x_n^{(3)}$ as a function of temperature, and the results are depicted in Fig. 4. The calculations indicate that two different $x_n^{(3)}$'s can be obtained for a given temperature, depending upon whether the measurement is made in a fuel-rich or lean region. Figure 5 is a plot of the temperature as a function of $T_s \sqrt{P'^{S_T}_a / P'_a}$. This plot indicates that for a given $T_s \sqrt{P'^{S_T}_a / P'_a}$, two temperatures are possible. The largest uncertainties in the temperature according to Fig. 5 are encountered when the fuel-to-air mixture is near stoichiometric. Here the difference in temperature between the fuel-rich and lean cases is ~ 70K. By taking an average of these cases, an error of only $\pm 35K$ is incurred at the high-temperature end, making the technique quite attractive. The technique has the advantage of being independent of linewidth parameters--parameters to which the standard CARS techniques are highly sensitive. The second major advantage of such a technique is that extreme fluctuations in signal are no longer encountered. For a variation in temperature between 300 and 2200K, a variation in the CARS nonresonant signal level of only 44 would be observed. This is ~ 19 times smaller than the N_2 Q-branch variation for the same temperature range. Because the temperature determined by the nonresonant susceptibility depends upon the integrated intensity and not upon the band shape, the OMA device can be replaced by more sensitive photomultipliers. This is important for two reasons. First, while the signal levels for N_2 are relatively strong for room air, the nonresonant signal levels are ~ 10^3 times weaker. The added sensitivity of the photomultiplier compensates for the overall lower signal levels. The nonresonant signal levels can be further improved by switching from the broadband dye laser employed for N_2 to a narrow-band laser which can concentrate more of the power of the laser into a smaller region and thus increase the S/N ratio of the CARS signal. The second advantage of using photomultipliers is that the signal processing is no longer limited to the 30-Hz maximum rates of the DARSS detector. In fact 10-kHz data rates are possible at a relatively low cost. Thus, nonresonant temperature determinations offer the possibility of operating at the 10-Hz rates of available laser systems without difficulty.

Another important feature of the nonresonant technique is the reduction in processing time necessary to determine the temperature from the experimental data. In the case of an N_2 Q-branch, the spectrum must be fitted as described earlier by a nonlinear least-squares iteration. This requires, on the average, about 10 sec. per spectrum. At a rate of 10 Hz, 1 sec. of experimental data would require 100 sec. of computer processing time. To study a turbulent combustion system, data must be taken for hours at a time which would mean that hundreds of hours would be required for processing the data. However, in order to determine

temperatures from the nonresonant signal, Eq. (15) must be solved which, for a computer, is an extremely fast process. Thus, the experimental data could be processed and temperatures determined in the 100-ms between laser pulses.

To test the nonresonant method for determining temperatures, a study was conducted on a propane-air premixed burner. Measurements conducted on this flame with the nonresonant technique indicate a temperature of $2203\text{K} \pm 40\text{K}$. Previous measurements conducted on this flame with both the resonant CARS and sodium-line-reversal techniques with the same flow rates yielded temperatures of $2210 \pm 50\text{K}$ and $2240 \pm 30\text{K}$, respectively.⁶ The nonresonant method is presently being tested in turbulent combustion media at this laboratory.

III. Concentration Measurements

To obtain single-shot number densities, either an absolute or a relative measurement of the integrated CARS intensity of the Raman transition must be made. The former is extremely difficult--if not impossible--in most instances. The latter is performed through the use of a ratioing technique in which an account of the power fluctuation of the laser systems is also made. The scheme which has proven to be the most reliable for this purpose is a common lens arrangement described in Ref. 4.

Along with the concentration measurement, a simultaneous temperature measurement must be made. The magnitude of the error in the concentration measurement due to the variation of the temperature can be assessed as follows: The mole fraction on nitrogen $x(N_2)$, as determined by a CARS measurement, is given by

$$x(N_2) = 0.780 \frac{T_2 F(N_2)}{T_1} \left(\frac{P_{a2}}{P_{a1}} \right)^{1/2} \quad (17)$$

where $T_2 = T_{\text{flame}}$; P_{a2} is the anti-Stokes power at T_2 ; T_1 is the calibration temperature; P_{a1} is the anti-Stokes power at T_1 ; and $F(N_2)$ is the temperature-dependent correlation factor. The term $F(N_2)$ is a temperature-dependent quantum-mechanical function which takes into account the ideal gas law, number densities, nuclear-spin degeneracies, and number of rotational levels. $F(N_2)$ ranges from 1.0 at $T_2 = 300\text{K}$ to 2.0 at $T_2 = 2100\text{K}$. Thus, for small variances in T_2 ,

$$\left(\frac{\partial F(N_2)}{\partial T_2} \right)_{T_1} \approx 0 \quad (18)$$

Performing the necessary differentiation of Eq. (17) and simplifying yields the following relationship for the relative error in the concentration measurement:

$$E[x(N_2)] = [E(T_1)^2 + E(T_2)^2 + 1/4 E(I_2)^2 + 1/4 E(I_1)^2]^{1/2} \quad (19)$$

From this relationship, it can be seen that the major contributors to $E[x(N_2)]$ are $E(T_1)$ and $E(T_2)$. Thus, the associated error in the temperature determination due to instrumental factors as well as turbulence has a large effect upon the precision of the concentration measurement. Simultaneous determination of temperature and number density assures that the relative error introduced due to turbulence during time-averaged measurements will not enter into the concentration measurement. Simultaneous measurements are possible because the general shape of the Q-branch profile can be used to determine the temperature, while the integrated area of the Q-branch can be used to determine the concentration. Figure 6 presents data obtained from a series of simultaneous temperature and concentration measurements which were performed on a propane-fueled flame.⁴

Effect of Linewidth Upon Density Measurements

As previously discussed, density measurements can be related to the integrated CARS Q-branch spectrum of a molecule. To reduce this measurement to number density, it is also necessary to measure simultaneously the temperature of the combustion medium and the integrated CARS Q-branch spectrum of a reference cell of known molecular concentration and temperature. Unfortunately, the integrated intensity is approximately inversely proportional to the linewidth. Since the linewidth of the reference species is different from that of the combustion species, relatively large errors in the measured concentration can occur. The correction for linewidth differences is especially difficult because the composition and temperature of the two media differ greatly.

If the spectral power of the broadband dye laser is assumed to be constant, nonresonant interferences are assumed to be insignificant, and Doppler broadening as well as the J dependence of Γ_J is neglected, then the measured number density may be expressed as

$$N = \left(\frac{P_{\text{INT}}}{(P_{\text{INT}})_c} \frac{\Gamma_{\text{eff}}(T, \Gamma)}{\Gamma_{\text{eff}}(T_c, \Gamma_c)} \frac{F(T_c)}{F(T)} \right)^{1/2} N_c \quad (20)$$

where

$$\Gamma_{\text{eff}} = \frac{\Gamma}{1 + \frac{1}{F(T)} \sum_{J \neq J'} \sum \frac{\Gamma^2 G_{JJ'}(T)}{(\omega_J - \omega_{J'})^2 + 4\Gamma^2}}; \quad F(T) = \sum_J \Delta_J^2; \quad G_{JJ'} = 8\Delta_J \Delta_{J'}$$

P_{INT} is the integrated CARS power; and the subscript c refers to the corresponding calibration gas. If the interference between lines is small ($\omega_J - \omega_{J'} \gg 4\Gamma^2$), then $\Gamma_{\text{eff}} \rightarrow \Gamma$. This is usually not the case, and Γ_{eff} must be calculated or measured. Measurements based upon the assumption of a constant optical cross section and empirical data for Γ_{eff} at room temperature have been completed.¹⁵ Although the results were reasonable, it was not possible to assess the precision and accuracy of the measurements. An assessment of the errors requires that the linewidth problem and laser modes be treated in a more realistic manner, and comparisons must be made in media of known number density at combustion temperatures and pressures.

Since the Doppler width becomes comparable to the collisional width at the higher combustion temperatures, its effect upon number-density measurements should also be considered. To do this, the expression for $\chi^{(3)}$ given by Eq. (8) must be used to calculate the integrated CARS power. If $\Gamma(T, P)$ is known with sufficient accuracy, this approach is more realistic; it will be given consideration in future work. The effect of collisional narrowing, however, still must be addressed for molecules such as H_2 .

Turbulence Effects Upon CARS Intensities and a Scheme for Their Compensation

Spatial gas-density gradients typical of turbulent combustion translate directly into refractive-index gradients. Such gradients--if severe--can produce phase distortion, steering, and beam spreading¹⁶ of the incident pump and Stokes laser beams and reduce the efficiency of the CARS process. These effects can be especially severe for BOX-CARS techniques since the beams which are spatially separated and crossed only at their foci traverse different paths through the turbulent medium and, therefore, can be randomly steered with respect to each other by the turbulence. This random steering of the beams can result in a variation in beam overlap and thus in CARS efficiency. In the collinear-CARS case, beam spreading rather than steering is the effect of major concern since the pump and Stokes beams are overlapped; and even though steering of the beams does take place, the beams are steered approximately the same amount. The net effect of such steering is to introduce an uncertainty concerning the exact region where the CARS measurement is taking place. The effect of spreading the pump and Stokes beams, however, is to increase the focal spot size with a subsequent reduction in the CARS intensity. This decrease in CARS intensity due to turbulence does not affect the temperature measurement since it depends upon the band profile rather than the absolute intensity, but it has the potential to have a great effect upon the intensity-dependent concentration measurement. Thus, it is imperative that the effects of turbulence upon the generation of the CARS signal be evaluated critically if accurate number densities are to be obtained by means of this technique.

To theoretically evaluate the effect of turbulence upon the CARS intensity, two different approaches can be taken. The first involves the application of the focused-beam solution of the wave equations for the pump and Stokes waves to calculate the third-order polarization, $\mathcal{P}_a^{(3)}$. For this case the solution for the electromagnetic wave at the anti-Stokes frequency, E_a , may be placed in the integral form

$$E_a(\vec{r}, t) = 1/c \int \frac{\mathcal{P}_a^{(3)}(\vec{r}', t') d^3 \vec{r}'}{|\vec{r} - \vec{r}'|} \quad (21)$$

where $t' = t - |\vec{r} - \vec{r}'|/c$. As can be seen from Eq. (21), the evaluation of this integral requires an explicit expression for the focused pump and Stokes waves. Although approximate analytical expressions for E_p and E_s are available,¹⁸ it is not possible to carry out the integration to yield a closed form. An easier approach to the problem utilizes the plane-wave solution for the anti-Stokes intensity at the focal volume.¹⁹ This method yields the approximate solution

$$I_a(\omega_a + \delta, z) = \left(\frac{4\pi^2 \omega_a}{c^2}\right)^2 |3\chi^{(3)}|^2 z^2 I_p^2 I_s(\omega_s - \delta) \quad (22)$$

where I_a and I_s are the corresponding spectral intensities; I_p is the intensity of the monochromatic pump; and δ is the frequency deviation of the broad-band Stokes wave from the resonant condition $\omega_s = \omega_p - \omega_r$.

A complete analysis of the effect of turbulence upon the generation of CARS requires a solution of Eq. (21), which is a very difficult task. However, in a turbulent medium the focal spot increases in size and is also displaced from the nonturbulent position in a statistical way from pulse to pulse. The change in the spot size should have the greatest effect upon the CARS signal since this reduces the intensities in the focal volume. For this case, the plane-wave solution yields

$$P_{at} = A_e I_a = \left(\frac{4\pi^2 \omega_a}{c^2}\right)^2 |3\chi^{(3)}|^2 z_e^2 \left(\frac{P_p}{A_e}\right)^2 P_s \quad (23)$$

where A_e is the effective area of the focal spot and z_e is the corresponding distance over which the major portion of the CARS signal is generated. From geometrical considerations, it is reasonable to postulate that the value of z_e increases with A_e such that

$$z_e^2 = k A_e \quad (24)$$

where k is a constant. Thus, the ratio of the anti-Stokes power for a nonturbulent medium to that for a corresponding turbulent medium can be estimated from Eqs. (23) and (24) to yield

$$\frac{P_a}{P_{at}} = \frac{P_a \int_{\text{int}}}{P_{at} \int_{\text{int}}} = \frac{A_{et}}{A_e} = \left[\frac{D_{et}}{D_e}\right]^2 \quad (25)$$

where the subscript t is used for parameters corresponding to the turbulent medium and the subscript int indicates the integration over frequency.

Since turbulence affects beam propagation by inducing random fluctuations in the index of refraction within the medium, two gases having a large difference in their refractive indices can be mixed in a turbulent jet to produce a small turbulent field. Thus, to investigate the effects of turbulence upon beam propagation and the generation of CARS signals, the turbulent generator shown in Fig. 7 was employed. To make the turbulent field produced by the generator as uniform as possible, the nozzles of the generator were made by photographically producing an etching pattern on copper-clad epoxy plates. The copper was etched away in a pattern which formed six nozzles on each plate when the plate was sandwiched between separating plates. The nozzles were fed from the large openings in the plate which, in turn, were fed from the header. Alternating the orientations of the plates allowed for feeding even- and odd-numbered nozzle rows with two different gases in order to generate a turbulent mixing medium.

The CARS experimental setup for studying the turbulent effects shown in Fig. 8(a) was the same as that employed for the simultaneous temperature-species concentration measurements, with the exception that a collinear rather than a BOX-CARS arrangement was employed for the turbulence studies. The turbulent generator in these studies was placed between the focusing lens and its focus in the sample leg and kept well away from the focal region where the majority of the CARS signal is produced. This procedure ensured that any loss in the CARS signal would be due primarily to turbulence effects and not to number-density changes resulting from helium being introduced into the focal volume.

In order to study the variation in spot size after propagation through turbulence, a small portion of the pump and Stokes beams was split off from the sample path just after focus. The split beams were then coupled onto a PAR 1205 OMA detector which allowed recording of the spread of the focal spot. Figure 9 shows the effects of turbulence upon the spot size and upon the CARS intensity as recorded by the setup described above. As can be seen from Fig. 9(a), with the use of air only (and no helium flow), the focal spot is sharp and well defined; the resulting CARS signal from the sample path is strong. However, when the helium is allowed to flow, the focal spot expands drastically with a corresponding decrease in the CARS intensity in the sample leg as shown in Fig. 9(b). The effect of

introducing this type of turbulence in the beam path, in this case, was a factor-of-eleven reduction in intensity, with a corresponding 330% error in the concentration measurement.

Figure 10 shows the results of a detailed study of the variation of the CARS intensity as a function of turbulent-generator position. Along with the relative CARS signal, the relative beam spread as measured by the OMA setup is displayed. The x-axis represents the distance of the generator from the focus of a 42-cm.-focal-length lens. As indicated by the experimental curves, the relative CARS signal decreases as the distance from the generator to the focal region of the beam increases. Conversely, the beam spread increases. A calculation of the natural log of the relative intensity as a function of the natural log of the inverse of the relative beam spread indicates, however, that the intensity varies not as the square of the inverse of the beam spread [see Eq. (25)] but linearly as the inverse of the beam spread. An important clue concerning the reason for this result was obtained when it was noted that a 90-deg. rotation of the OMA, which resulted in the rectangular target being perpendicular to the beam propagation, gave little indication that the beam was spreading. Imaging the beam upon the laboratory wall allowed the visual assessment that the beam was spreading in only one direction. The spread, in fact, was perpendicular to the flow of the helium-air turbulence, indicating that the turbulence was not completely random in nature. This one-dimensional spreading by the turbulent field results in a linear inverse dependence of the CARS intensity upon the beam spread, as indicated.

Because of the large errors that can be introduced into the concentration measurement, it is imperative that some means of compensating for this turbulence be developed. What was considered to be the most promising approach was a novel reference scheme proposed by Ultee and reported by Shirley²⁰ for background-free CARS spectra, i.e., high major species concentrations or low concentrations with the background canceled. This scheme involved the use of a nonresonant signal as an *in situ* reference. In the above-cited report, it was proposed that a two-component dye laser be employed to produce both a resonant and a non-resonant signal; the temperature could be determined from the resonant, and the nonresonant could serve as a calibration source for the concentration measurement since it is a measure of the total number of molecules present in the measurement volume. It was also noted that such a measurement approach would be immune to medium extinction and refraction effects since all beams would be similarly affected, thus making it an ideal method for turbulent compensation.

The *in situ* reference scheme works in the following manner. The anti-Stokes power of the normal resonant CARS signal can be expressed as

$$P_r = C(T, \Gamma) K N_i^2 P_p^2 P_{sr} \quad (26)$$

where N_i is the concentration of the i th species being probed; P_p is the power of the pump beam; P_{sr} is the power of the Stokes beam for the resonant signal; K is the appropriate proportionality constant which depends upon the focused beam geometry; and $C(T, \Gamma)$ is a complex function which depends upon the temperature, T , and the Raman linewidth, Γ , and represents the integration of the third-order susceptibility over the frequency region of interest for the resonant signal. The nonresonant signal can be expressed in terms of

$$P_n = C'(T, \Gamma) K' N_T^2 P_p^2 P_{sn} \quad (27)$$

where N_T is the total number density of the gas being probed; P_{sn} is the power of the Stokes beam responsible for the nonresonant signal; and $C'(T, \Gamma)$ is the appropriate function for the nonresonant signal.

Ratioing Eqs. (26) and (27) results in

$$\frac{P_r}{P_n} = \frac{K N_i^2 P_{sr} C(T, \Gamma)}{K' N_T^2 P_{sn} C'(T, \Gamma)} \quad (28)$$

where the pump power has been canceled. If one assumes that the two Stokes beams fluctuate in the same manner, Eq. (28) indicates that only the nonresonant reference is required to compensate for turbulence and allow concentration measurements to be made. If the ratio of the Stokes beams does not remain constant for all laser pulses, then Eq. (28) must be modified for incorporation of a power reference. The power reference consists of making measurements on a standard gas such as room air simultaneously with the sample measurements and ratioing these values to cancel the shot-to-shot fluctuations in the Stokes beams. This results in

$$\frac{\frac{P_r}{P_n}}{\frac{P_r^S}{P_n^S}} = \frac{\frac{C(T, \Gamma) N_i^2}{C'(T, \Gamma) N_T^2}}{\frac{C(T_s, \Gamma_s) (N_i^S)^2}{C'(T_s, \Gamma_s) (N_T^S)^2}} \quad (29)$$

where s denotes the standard gas measurement.

The ratio of $C(T, \Gamma)$ to $C'(T, \Gamma)$ can be estimated from theory if the temperature is simultaneously measured and reasonable approximations for linewidths determined. For the measurements at room air presented in this paper, $C(T, P) = C(T_s, \Gamma_s)$ and $C'(T, P) = C'(T_s, \Gamma_s)$; thus, these quantities cancel. Equation (29) indicates that by ratioing the resonant and nonresonant signals of the sample and a standard reference which are simultaneously produced, the effects of turbulence on beam extinction in adverse environments can be compensated. Figure 8(b) depicts the dye-laser setup used for producing the broadband and narrow-band Stokes beams required for the experiment. A grazing-angle prism²¹ was used for beam expansion; this allowed for one-half the beam to be incident upon a total reflector which produced the broadband Stokes output and the other half to be incident upon a 600-groove/mm 5000-Å blazed grating which accounted for the narrow nonresonant Stokes output. The output of the dye laser was then amplified and directed to the turbulent region, as shown in Fig. 8(a). The broadband output of the dye laser was used to produce the N_2 Q-branch signal. The narrow-band dye was tuned away from the resonant CARS transition and used for the nonresonant CARS signals. The narrow-band Stokes beam was employed for the nonresonant signal to enhance the signal level of the weak process. The incorporation of the in situ nonresonant Stokes output results in an additional peak being displayed by the Tracor-Northern 1710-DARSS multichannel analyzer for both the sample and reference legs. The correlations of the nonresonant signals and the resonant signals in the sample and reference paths without turbulent flow were typically better than 97%.

Figure 11 depicts the results obtained by use of this scheme with and without turbulent flow. Figure 11(b) shows the display with air flow only. The two peaks at the left of the display are from the reference path which experienced no turbulence, and the two peaks at the right are from the sample path in which the generator was located. Figure 11(a) displays the results when helium is allowed to flow, forming a turbulent mixing region. As can be seen, the peaks in the sample path are lower in intensity than those obtained without helium flow; however, both the nonresonant and resonant peaks decreased by the same percentage. Thus, through normalization of the resonant signal by the nonresonant in situ reference, one can compensate for the effect of the helium-produced turbulence.

The experimental results obtained during the study are shown in Table I. In the non-turbulent study, the resonant signals in the sample and reference path were averaged for twenty shots and ratioed, which compensated for any power fluctuations for the resonant signals. The nonresonant signals obtained simultaneously with the resonant signals were averaged over the same twenty shots and ratioed, which compensated for any power fluctuations for the nonresonant signals. Similar ratios were obtained for the turbulence study on twenty single shots. Comparing the ratios of the resonant and nonresonant signals with and without turbulence indicated that although the absolute values of the resonant and nonresonant signals were decreased in the turbulent case, the ratios of resonant to nonresonant signals remained the same within experimental error (0.2714 and 0.2805, respectively). Thus, although turbulence produces a signal loss in the resonant sample path, the same percentage loss was experienced in the nonresonant sample; by ratioing the two signals, the loss was compensated. Also listed in Table I are the concentrations that were obtained with and without the compensation technique for the turbulence data. Without the compensation technique, the measured N_2 concentration was $66.24\% \pm 2.96\%$; with compensation, it was $79.43\% \pm 1.83\%$, which is well within the experimental error of the N_2 concentration in ambient air. These results show that by using this method for turbulence compensation, accurate intensity information can be obtained without regard to the severity of the refractive-index change or beam extinction. Immediate applications for this type of method lie in performing concentration measurements in supersonic, turbulent, and particle-laden environments. The extension of this technique to combustion environments is presently being investigated, and the results will be reported at a later date.²²

TABLE I
INTEGRATED INTENSITIES AND RESULTING CONCENTRATIONS FROM CARS MEASUREMENTS
MADE ON THE HELIUM TURBULENT GENERATOR

<u>No Turbulence</u> ^{*†}		
<u>Resonant</u>	Nonresonant	Ratio (R/N)
$\bar{x} = 0.3409$	$\bar{x} = 1.257$	$\bar{x} = 0.2714$
$\sigma = 0.0063$	$\sigma = 0.0355$	$\sigma = 0.0111$
<u>Turbulence</u>		
<u>Resonant</u>	Nonresonant	Ratio (R/N)
$\bar{x} = 0.2463$	$\bar{x} = 0.8788$	$\bar{x} = 0.2805$
$\sigma = 0.0215$	$\sigma = 0.0794$	$\sigma = 0.0139$
<u>Concentrations</u>		
<u>Without Compensation (%)</u>	<u>With Compensation (%)</u>	
$\bar{x} = 66.24$	$\bar{x} = 79.43$	
$\sigma = 2.96$	$\sigma = 1.83$	

* Values represent average of 20 points.

† Values normalized to corresponding intensity of power reference.

\bar{x} = average value, σ = standard deviation.

CONCLUSIONS

In conclusion, certain problems are associated with conducting both CARS thermometry and concentration measurements in turbulent combustive media. For thermometry the major problem is associated with the limited dynamic range of the OMA detector. However, this problem can be circumvented by either employing a dual OMA detector arrangement or making a measurement of the nonresonant susceptibility. The nonresonant temperature method has the following advantages: (1) it is independent of linewidth parameters; (2) the required dynamic range is reduced; (3) photomultipliers can be used for the detector, negating the need for expensive OMA devices; and (4) temperatures can be processed in real time, greatly reducing the numerical-processing time requirements. However, the nonresonant temperature method requires an integrated-intensity measurement of the CARS signal and, therefore, cannot be employed in extremely turbulent environments since intensity losses due to turbulence effects will produce large errors in the temperature measurement.

For concentration measurements, it has been shown that turbulence can induce large errors in the CARS integrated-intensity measurement. The major effect of turbulence in the case of collinear CARS is an increase in the focal spot size which results in a decrease in the energy density at the focus, with a corresponding loss in the CARS intensity. This effect can be compensated by the inclusion of a nonresonant reference which transverses the same turbulence as the normal CARS signal and thus experiences the same intensity losses. This technique, as demonstrated with helium-induced turbulence, can fully compensate for the CARS intensity losses, thus allowing measurements to be made in extremely turbulent particle-laden environments. In combustive turbulent environments, a simultaneous determination of the temperature must be performed to separate intensity losses due to temperature (and thus number-density changes) from those due to turbulence effects.

REFERENCES

1. Laser Raman Gas Diagnostics (M. Lapp and C. M. Penny, Eds.) (Plenum Press, NY, 1974).
2. A. Eckbreth and R. J. Hall, Combust. Flame **36**, 87 (1979).
3. G. L. Switzer, W. M. Roquemore, R. B. Bradley, P. W. Schreiber, and W. B. Roh, Appl. Opt. **18**, 2343 (1979).
4. L. P. Goss, G. L. Switzer, and P. W. Schreiber, Paper 80-1543 presented at the 15th AIAA Thermophysics Conference, Snowmass, CO, 14-16 July 1980.
5. R. J. Hall, Combust. Flame **35**, 47 (1979).
6. L. P. Goss and G. L. Switzer, "Application of Coherent Anti-Stokes Raman Scattering to Combustion Media," AFWAL-TR-80-2021 (Air Force Wright Aeronautical Laboratories, Wright-Patterson Air Force Base, OH, February 1981).

7. W. B. Roh, R. Weber, and P. W. Schreiber, *Opt. Commun.* 27, 142 (1978).
8. Quantitative Molecular Spectroscopy and Gas Emissivities (S. S. Penner, Ed.) (Addison-Wesley Publishing Co. Reading, MA, 1959).
9. W. B. Roh, "Coherent Anti-Stokes Raman Scattering of Molecular Gases," AFAPL-TR-77-47 (Air Force Aero Propulsion Laboratory, Wright-Patterson Air Force Base, OH, August 1977).
10. R. Srivastava and H. Zoidi, "Intermolecular Forces Revealed by Raman Scattering," in Raman Spectroscopy of Gases and Liquids (A. Weber, Ed.) (Springer-Verlag, NY, 1979).
11. L. Rahn, A. Owyong, M. Coltrin, and M. Koszykowski, "The J Dependence of Nitrogen 'Q' Branch Linewidths," presented at the 7th International Conference on Raman Spectroscopy, Ottawa, Canada, 4-9 August 1980.
12. Handbook of Mathematical Functions (M. Abramowitz and I. A. Segun, Eds.) (Power Publications, Inc., NY, 1964).
13. M. A. Henesian, L. A. Kulevsky, R. L. Byer, and R. L. Herbst, *Opt. Commun.* 18, 225 (1976).
14. A. C. Eckbreth, P. A. Bonczyk and J. A. Shirley, Experimental Investigations of Saturated Laser Fluorescence and CARS Spectroscopic Techniques for Practical Combustion Diagnostics, Technical Report UTRC R78-952665-18 (United Technologies Research Center, East Hartford, CT, February 27, 1978).
15. G. L. Switzer, W. M. Roquemore, R. B. Bradley, P. W. Schreiber, and W. B. Roh, "CARS Measurements in Simulated Practical Combustion Environments," Presented at the 178th ACS National Meeting, Washington, D.C., 9-14 September 1979.
16. B. Hogge and W. Visinsky, *Appl. Opt.* 10, 889 (1971).
17. D. Jackson, Classical Electrodynamics (John Wiley and Sons, Inc., NY, 1967), p. 186.
18. R. Schmeltzer, *Appl. Opt.* 10, 1652 (1971).
19. P. Regnier, F. Moya, and J. P. E. Taran, *AIAA J.* 12, 826 (1974).
20. J. A. Shirley, R. J. Hall, J. F. Verdick, and A. C. Eckbreth, Paper 80-1542 presented at the 15th AIAA Thermophysics Conference, Snowmass, CO, 14-16 July 1980.
21. S. Chandra and A. Compaan, *Opt. Commun.* 31, 73 (1979).
22. L. P. Goss and P. W. Schreiber, "Effects of Combustive Turbulence on CARS Signal Production." To be published.

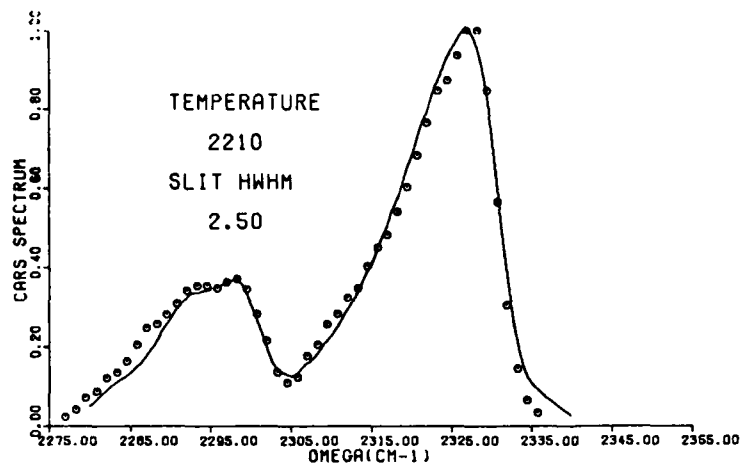


Figure 1. Temperature Fit of the Single-Shot Spectrum Obtained with the Nd:YAG-Based CARS System on a Propane-Fueled Burner.

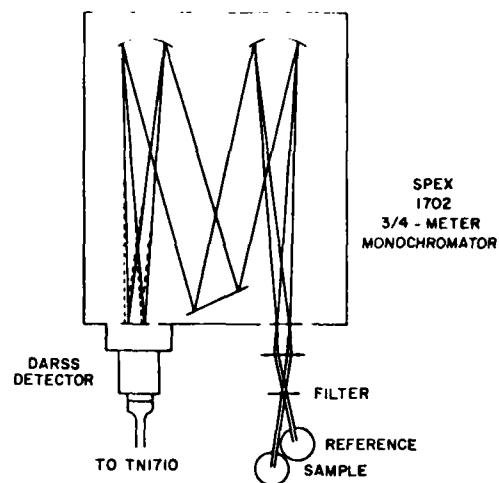


Figure 3. Optical Arrangement for Simultaneous Recording of a Sample and Reference Signal.

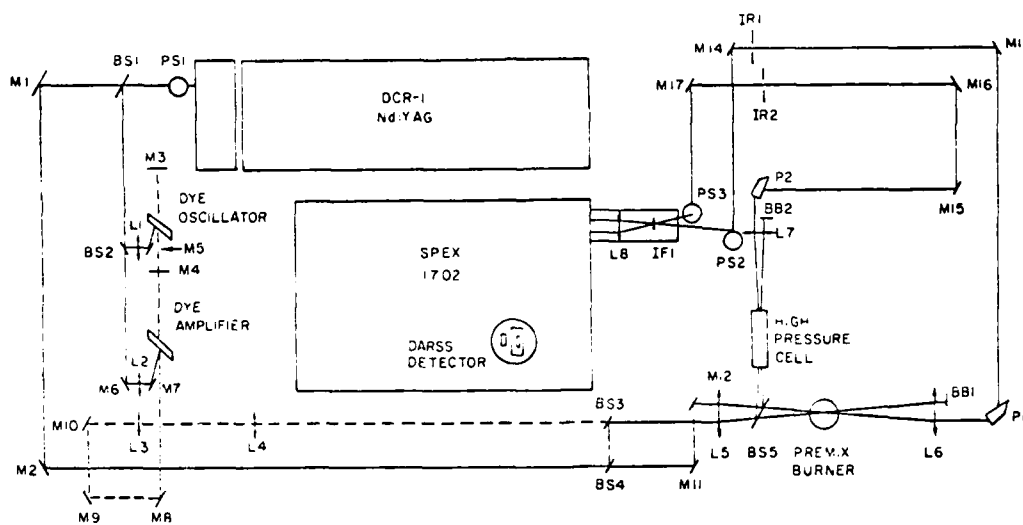


Figure 2. Diagram of the AFWAL-APL Laboratory CARS Arrangement.

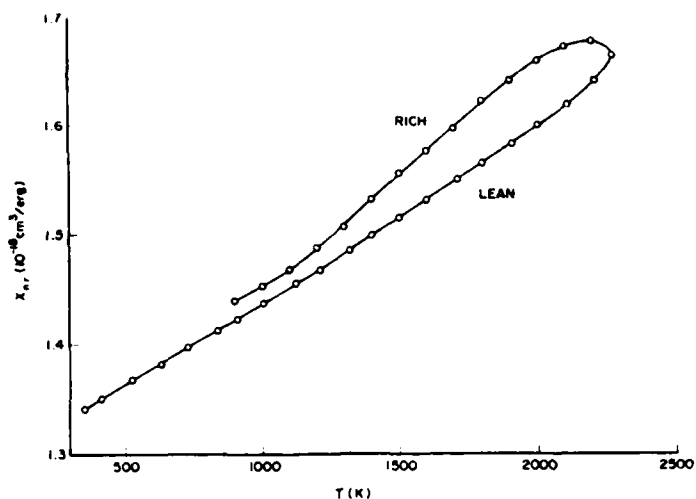


Figure 4. Variation in the Nonresonant Susceptibility (χ_{NR}) as a Function of Temperature.

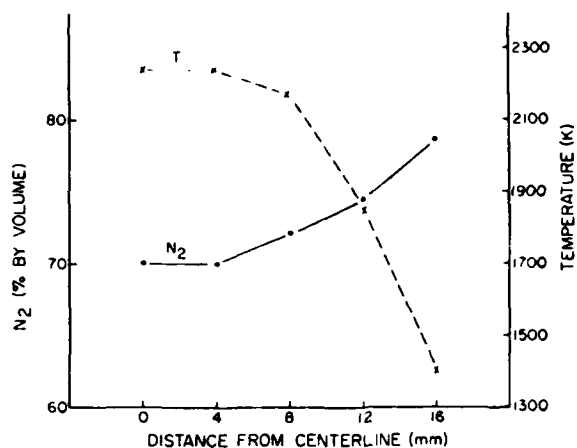


Figure 6. Horizontal Profiles of a Propane-Fueled Flame from the Centerline (0 mm) of the Flame.

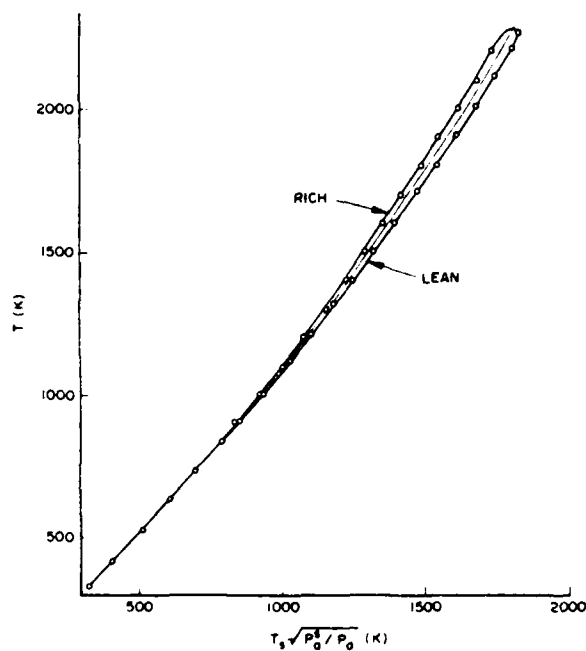


Figure 5. Correlation of the Uncorrected Temperature $T_S \sqrt{P_3^4 / P_0}$ and the Temperature Corrected for Variation of the Nonresonant Susceptibility on a Fuel-Rich and Lean Propane Flame.

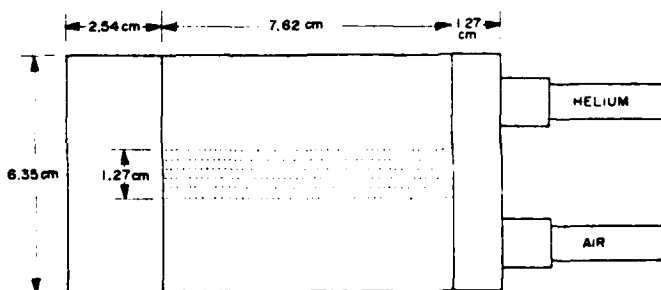
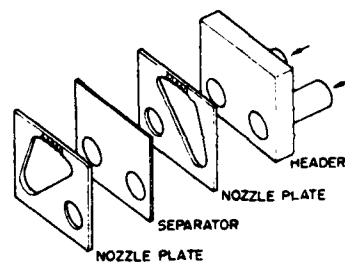


Figure 7. Diagram of the Turbulent Generator Used for the Helium Turbulence Experiments.

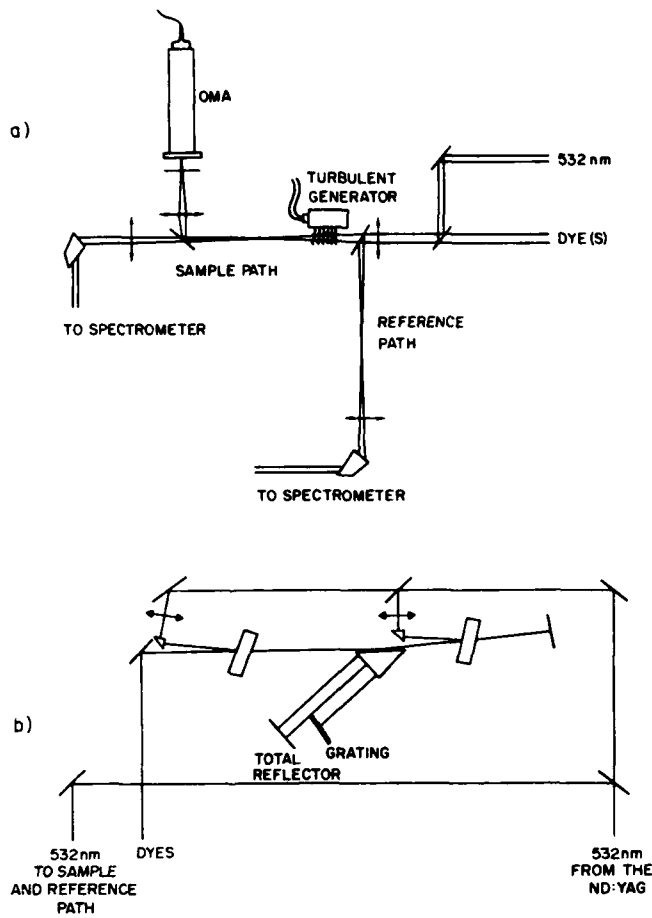


Figure 8. a) Experimental Setup for the Turbulence Studies. b) Setup Employed for the Broadband and Narrow-Band Dye Laser.

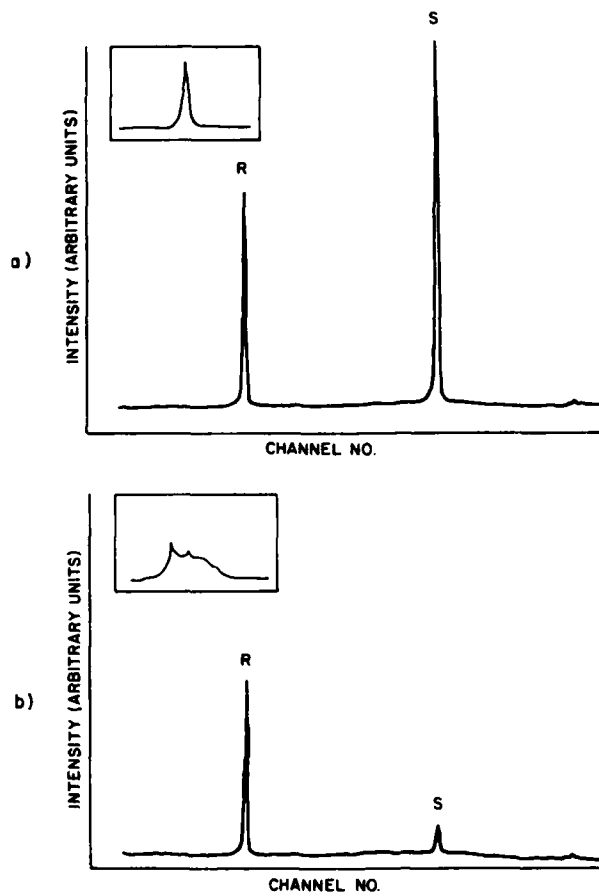


Figure 9. Beam Spread and the Resulting CARS Intensity. a) without Turbulence, b) with Turbulence. Inserts are the Beam Spreads Recorded by the OMA. R - Reference Path, S - Sample Path.

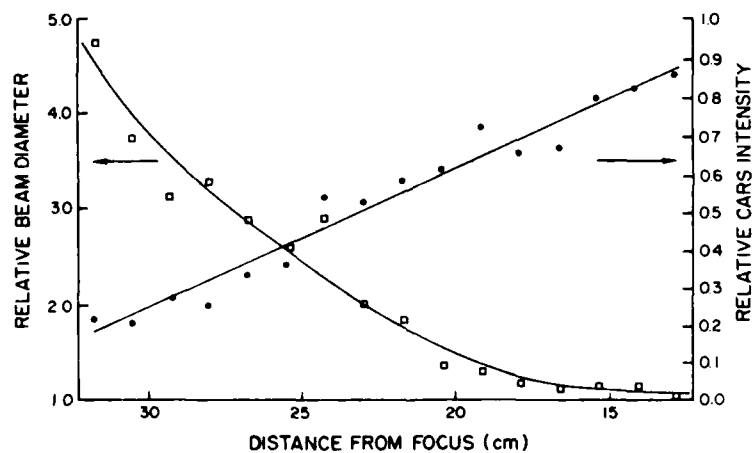


Figure 10. Variation of CARS Intensity and Beam Diameter with Horizontal Scan of Turbulent Generator.

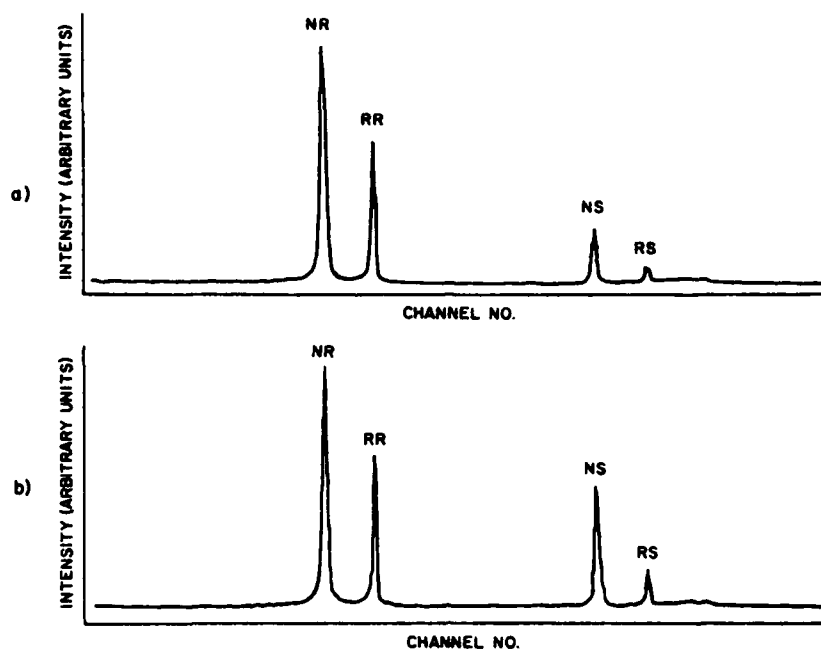


Figure 11. Display of the In Situ Reference Scheme.
(a with Flow, b) without Flow.

In an attempt to gain a better understanding of the errors incurred in CARS single-shot thermometry, an error-analysis study was undertaken. Both systematic and random errors exist which can contribute to an error in the fitted CARS temperature. These include

Systematic

slit function
spectral constants
nonresonant susceptibility
dye-laser tuning
diode sensitivity

Random

random nature of dye laser
diode background
photon statistics
stray light

Of the possible errors listed above, the dye laser is thought to be of the greatest magnitude and, thus, was the focus of this study. To estimate the error of the measurement, the following procedure was used.

A series of 200 nonresonant spectra was recorded. Processing of these spectra consisted of taking a precalculated CARS spectrum, superimposing the nonresonant spectrum from a given starting point (selectable), and fitting this distorted spectrum by a least-squares temperature-fitting program. This procedure was carried out for all 200 nonresonant spectra, as a function of the starting position. The results are shown in Fig. 1. It is quite evident from this figure that the band shape of the dye can have a tremendous effect upon the fitted temperature. In fact, a change in the starting position of only six channels from 212 to 218 produced a 185-K change in the fitted temperature. This is the systematic error mentioned earlier. Notice, however, that the temperature variance is consistently ~ 60 K. The temperature variance is

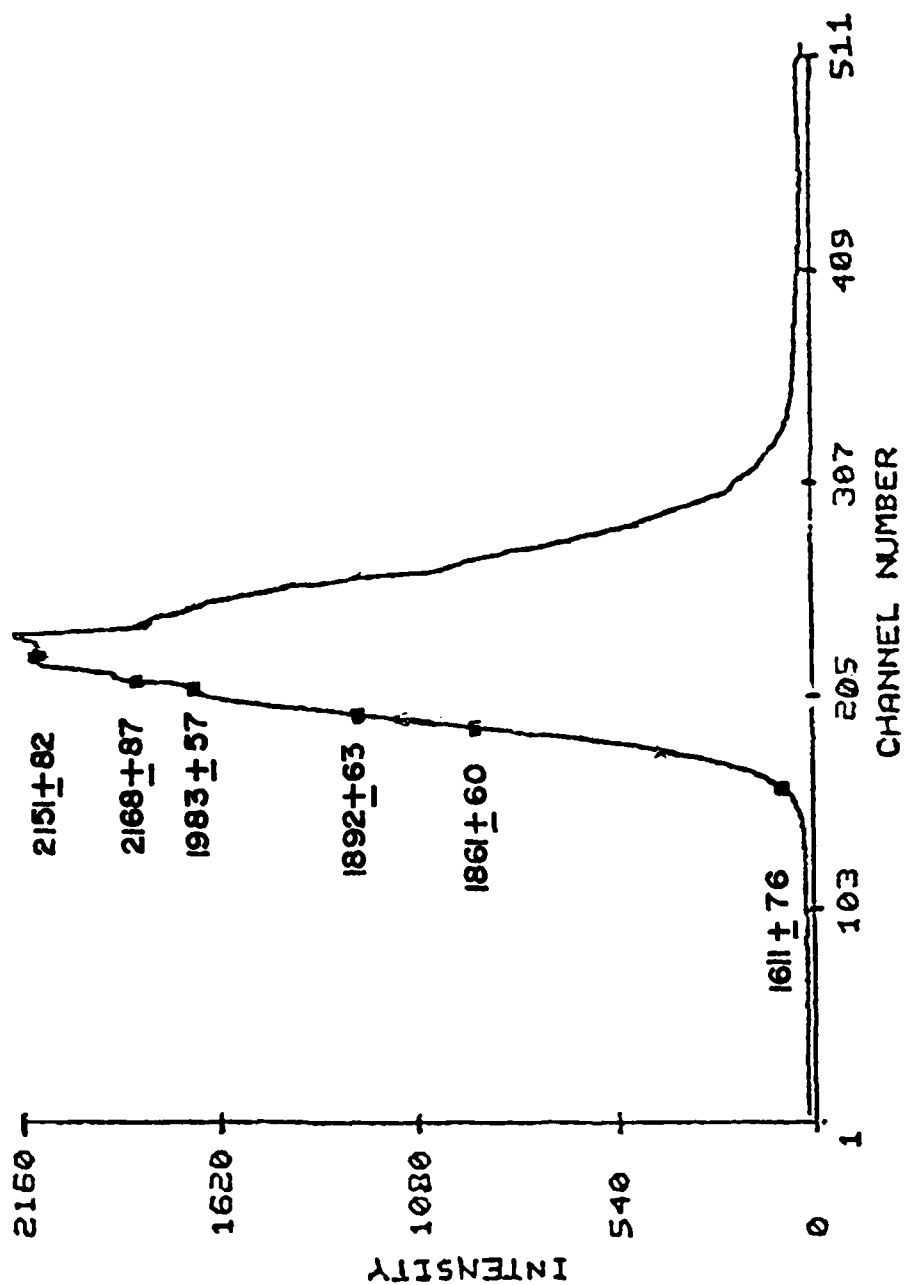


Figure 1. Nonresonant Spectra Used for Distortion of Calculated CARS Spectrum and Resulting Fitted Temperatures of Distorted Spectra. The initial temperature of the calculated CARS spectrum was 2000 K.

due to the channel-to-channel fluctuation of the dye and is the random error discussed earlier.

The next step was to attempt to eliminate the systematic error due to the dye tuning. One method of accomplishing this would be to tune the dye to the correct frequency, which can be tested via the premixed propane flame and lamp emissions. However, experience with dye tuning has shown that it is difficult to fine tune the dye by varying the concentration. A second method involved taking the average profile (200 shots) and using it to normalize the CARS spectra to account for the dye-tuning error. The results of this procedure, shown in Fig. 2, indicate that the systematic error due to dye-laser tuning can be eliminated by normalization.

Next, a nonresonant reference was tested to eliminate the systematic dye-tuning problem and the random fluctuation error of the dye waveform. The reference path was adjusted to accommodate a nonresonant cell filled with ~ 1 atm. of propane. Figure 3 displays a single shot of the sample and reference nonresonant signals. Notice in this figure that the general shape of the two nonresonant curves is similar; the individual noise on each curve, however, is different, which suggests that the random-noise error of the dye will not be eliminated by ratioing to the simultaneously obtained nonresonant reference.

To determine whether this was the case, a precalculated CARS spectrum was distorted by the sample waveform, normalized to the reference waveform, and fitted for each of the 200 nonresonant spectra. Channels 138 and 328 were the starting channels in the reference and sample, respectively. The starting temperature was 2000 K. The data indicated that while the systematic error

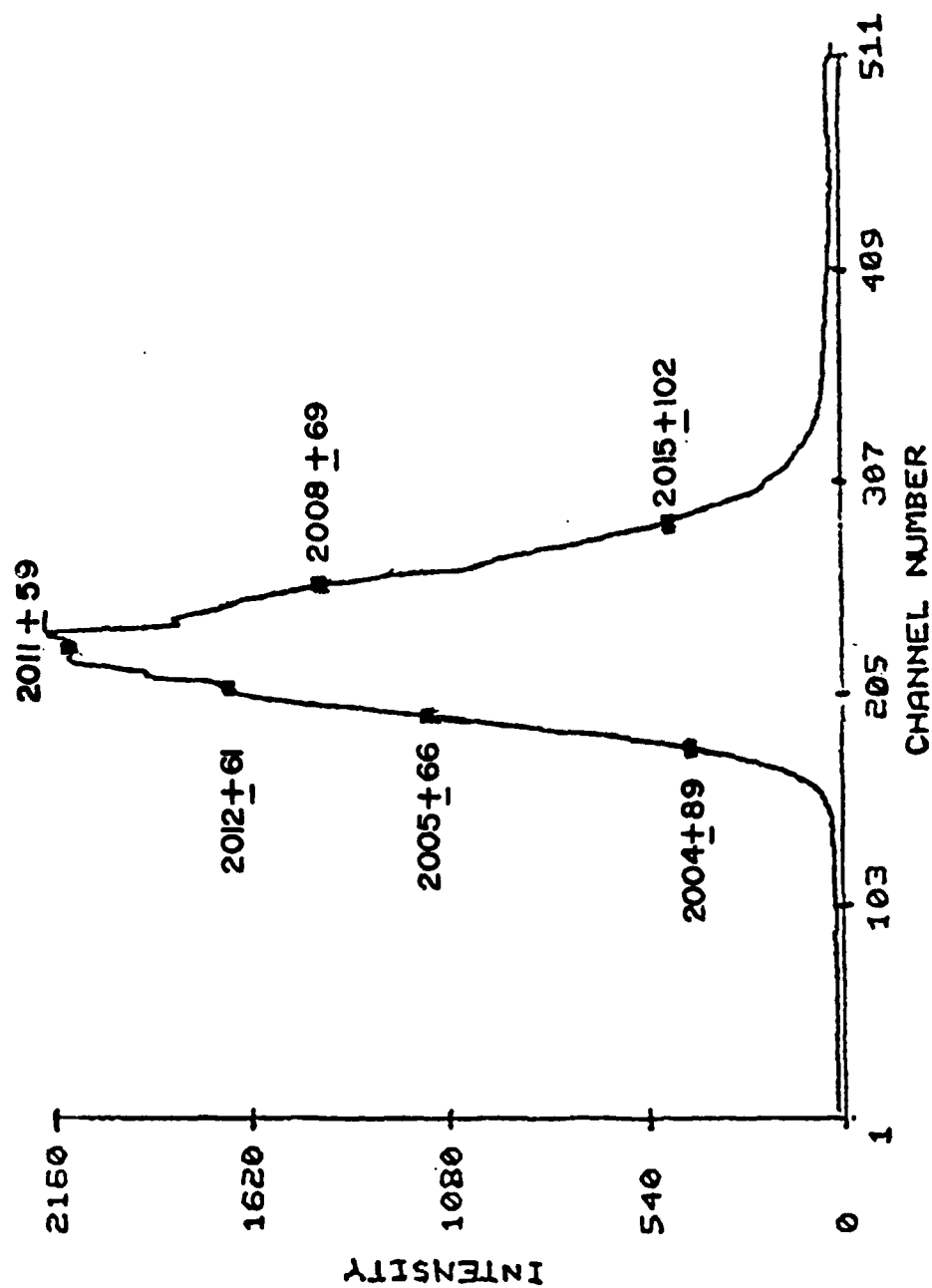


Figure 2. Averaged Nonresonant Spectrum Used for the Normalization of the Distorted CARS Spectra. The initial temperature for the CARS spectrum was 2000 K.

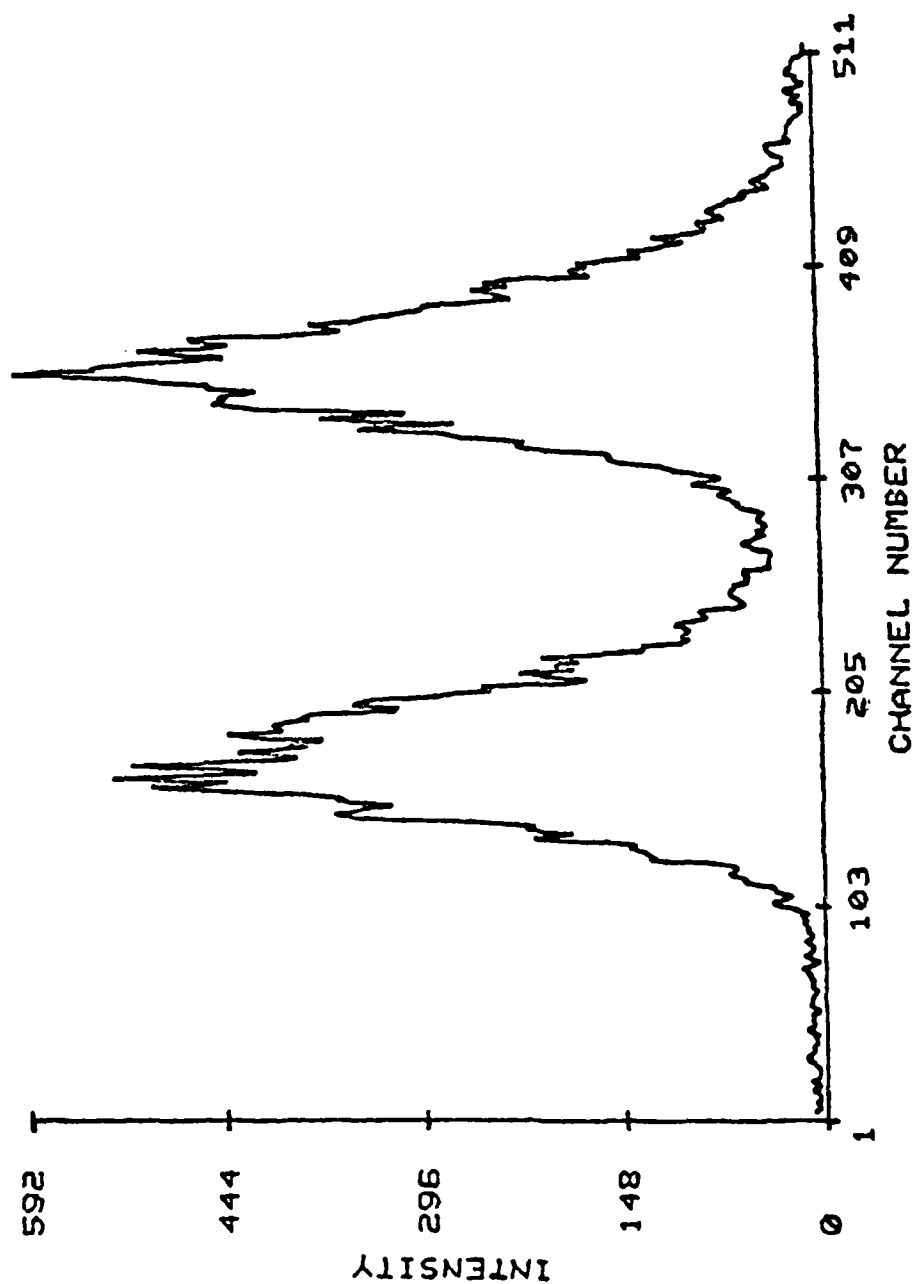


Figure 3. Single-Shot Spectrum of the Nonresonant Sample and Reference.

was reduced to 2%, the random error was actually increased. This can be explained only if the random errors in each waveform are independent and no correlation exists between the sample and reference. In this case, the error is given by

$$\sigma^2 = \sum_i \sigma_i^2$$

The errors in the individual measurement were found to be 91 and 78 K; thus,

$$\sigma^2 = (0.046)^2 + (0.039)^2$$

$$\sigma = 0.0603, \approx 121 \text{ K}$$

which corresponds to a temperature uncertainty which is in close agreement with the observed variance.

If, instead, one averages the reference spectra to eliminate the random error (reducing it by \sqrt{n} , where n is 200) and uses this average spectrum to normalize for the dye bandshape, the systematic error is greatly reduced, leaving the random error in the original dye waveform.

This study indicates that while the systematic error can be virtually eliminated by ratioing to the nonresonant profile of the sample or a nonresonant reference, the random channel-to-channel fluctuation of the dye laser cannot be ratioed out in this manner. Because of this the random error is the limiting error of the CARS measurement and can be improved only by spectra averaging and/or building a quieter dye laser. This error is $\sim 4\%$ of the measured temperature which is in good agreement with the observed experimental error obtained in propane premixed flame studies.¹

To understand the cause-and-effect relationship between the dye waveform and the random fluctuation observed in the CARS signal, a series of experiments was conducted in which the dye-laser configuration was varied and the resulting dye waveforms and nonresonant CARS signals observed. In particular, a super-radiant dye laser was tested because of the lack of frequency modes or modulation observed in these laser systems.

The super-radiant dye-laser configuration which was employed is shown in Fig. 4. The laser consists of a single oscillator and amplifier pumped in an off-axial scheme. The output coupler is removed from this laser to minimize feedback and the forming of longitudinal modes. The spontaneous emission from the oscillator is amplified and routed to the sample area where the CARS signal is formed. Since minimal feedback is set up at the oscillator, the output beam is only partially coherent and displays a high degree of divergence. This results in a much larger beam waist at the focus and a reduced CARS signal. However, the dye-laser waveform is very uniform and does not display the random fluctuations characteristic of broad-band lasers. The results of the dye-laser comparisons are given in Table I. The surprising result was that while the super-radiant dye waveform did not show the frequency modulation typical of most broad-band lasers, the nonresonant CARS signal produced by this laser system displayed some modulation. This result indicates that the mode interaction between the two pump beams is as important as that between the dye and the pump beams. This suggests that the best combination of lasers would be a single-mode Nd:YAG and a super-radiant dye.

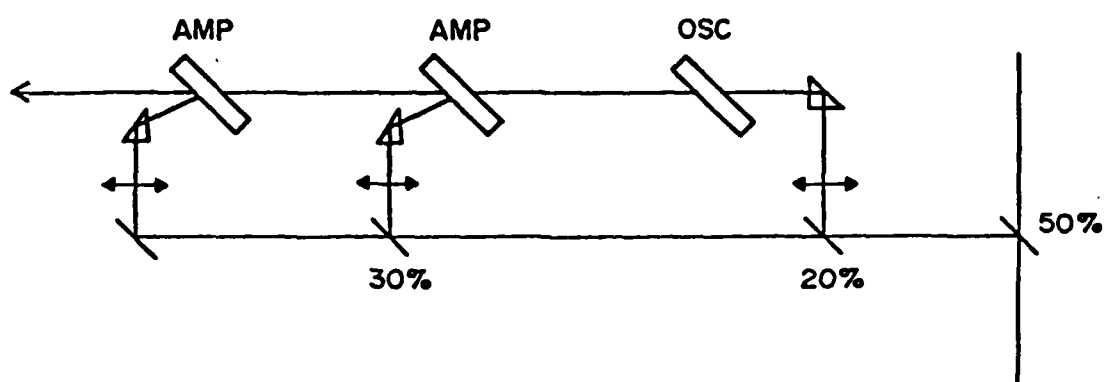


Figure 4. Super-Radiant Dye Laser Employed for CARS Studies.

TABLE I

RESULTS OF DYE-LASER COMPARISON

Dye-Laser Configuration	Average Fluctuation*
	(%)
Super-radiant (nonresonant)	4.63
Super-radiant (dye waveform)	1.29
20% Reflector dye (nonresonant) mild pump	6.24
20% Reflector dye (dye waveform) mild pump	2.97
20% Reflector dye (nonresonant) hard pump	4.16
20% Reflector dye (dye waveform) hard pump	2.51
50% Reflector dye (nonresonant) mild pump	6.06
50% Reflector dye (dye waveform) mild pump	3.10
50% Reflector dye (nonresonant) hard pump	5.87
50% Reflector dye (dye waveform) hard pump	2.83
90% Reflector dye (nonresonant) mild pump	6.26
90% Reflector dye (dye waveform) mild pump	3.83
90% Reflector dye (nonresonant) hard pump	5.60
90% Reflector dye (dye waveform) hard pump	2.94

*The average fluctuations were determined by obtaining the average profile of 200 shots and comparing this profile to each individual shot.

To document that a corresponding reduction in a resonant CARS signal would occur with a super-radiant dye laser, a stoichiometric flame was studied. If, indeed, the random dye waveform fluctuations are reduced, then a corresponding reduction of the temperature fluctuation for a constant temperature source would be observed.

Typical temperature fluctuations observed with a standard Fabry-Perot cavity dye laser are on the order of 120 K in a premixed stoichiometric flame. This can be reduced to ~ 90 K through the use of saturated amplifiers.² The temperature fluctuations observed while employing the super-radiant dye laser were ~ 65 K. The reduction in the random noise of the dye profile substantially reduced the measurement uncertainties associated with single-shot CARS thermometry. Figure 5 displays the temperature pdf obtained in the stoichiometric flame. The results of this study with the super-radiant dye laser indicate that a favorable reduction in the noise and, therefore, thermometry uncertainties can be obtained by employing such a dye-laser setup and that single-shot uncertainties of ~ 60 K can be obtained even by a low-resolution instrument.

The uncertainty in a quantity due to the uncertainty in one of its parameters is given by

$$\sigma_T^2 = \sum_i \sigma_I^2 \left(\frac{dT}{dI_i} \right)^2 \quad (1)$$

Letting T be the CARS temperature and I the intensity per channel of the observed CARS signal, then the uncertainty in the temperature due to the random fluctuation of the dye and thus the CARS signal is given in terms of the magnitude of the intensity uncertainties and the sensitivity of the temperature to a change in the intensity for each channel (or wavelength). To

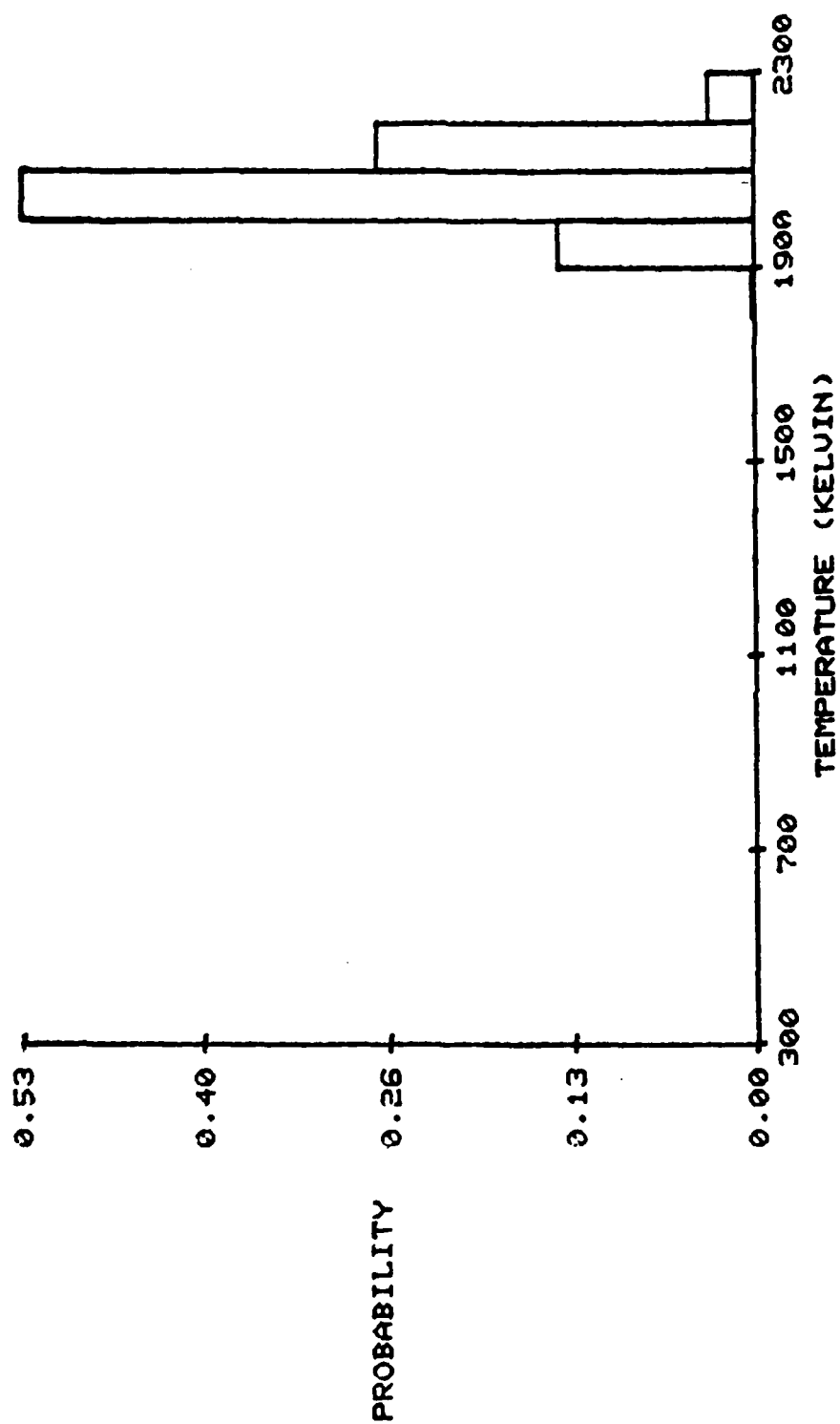


Figure 5. Temperature PDF Obtained in a Near-Stoichiometric Flame.
 $T = 2069 \pm 68$ K.

determine the temperature uncertainty due to the random fluctuations of the dye laser, the fluctuations obtained with the super-radiant dye laser were examined. The stoichiometric 1000-shot data set discussed earlier was averaged and the individual single shots compared to the averaged spectrum to determine a deviation. This yielded an experimentally measured deviation in σ_I of $3.2\% \pm 0.8\%$. This value can then be used to calculate the temperature uncertainty for the super-radiant studies. The results of this calculation indicated a temperature uncertainty of ~ 30 K. This is approximately one-half the observed value based upon 1000 shots. If, instead, the value $2\sigma_I$ is used in Eq. (1), the experimentally observed uncertainties are obtained (see Fig. 6).

According to Eq. (1) the temperature uncertainty obtained with a given dye laser depends linearly upon the channel-to-channel intensity fluctuations of that dye laser. The channel-to-channel intensity fluctuation can be expressed as

$$\sigma_I = \sqrt{\sum_i \left(\frac{I_i - I_{avg}}{N - 1} \right)^2} \quad (2)$$

where I_i is the i th channel intensity; I_{avg} is the average intensity for the i th channel; and N is the number of channels used to obtain the data. Substituting Eq. (2) into Eq. (1) indicates that the temperature uncertainty varies directly with the dye fluctuations but as the inverse square root of the number of channels or the resolution of the instrument. Thus, it appears that one can reduce σ_T by simply increasing the resolution of the CARS instrument. An increased resolution would also favor the derivative dI/dT . However, as the resolution of the instrument is increased, more and more of the mode

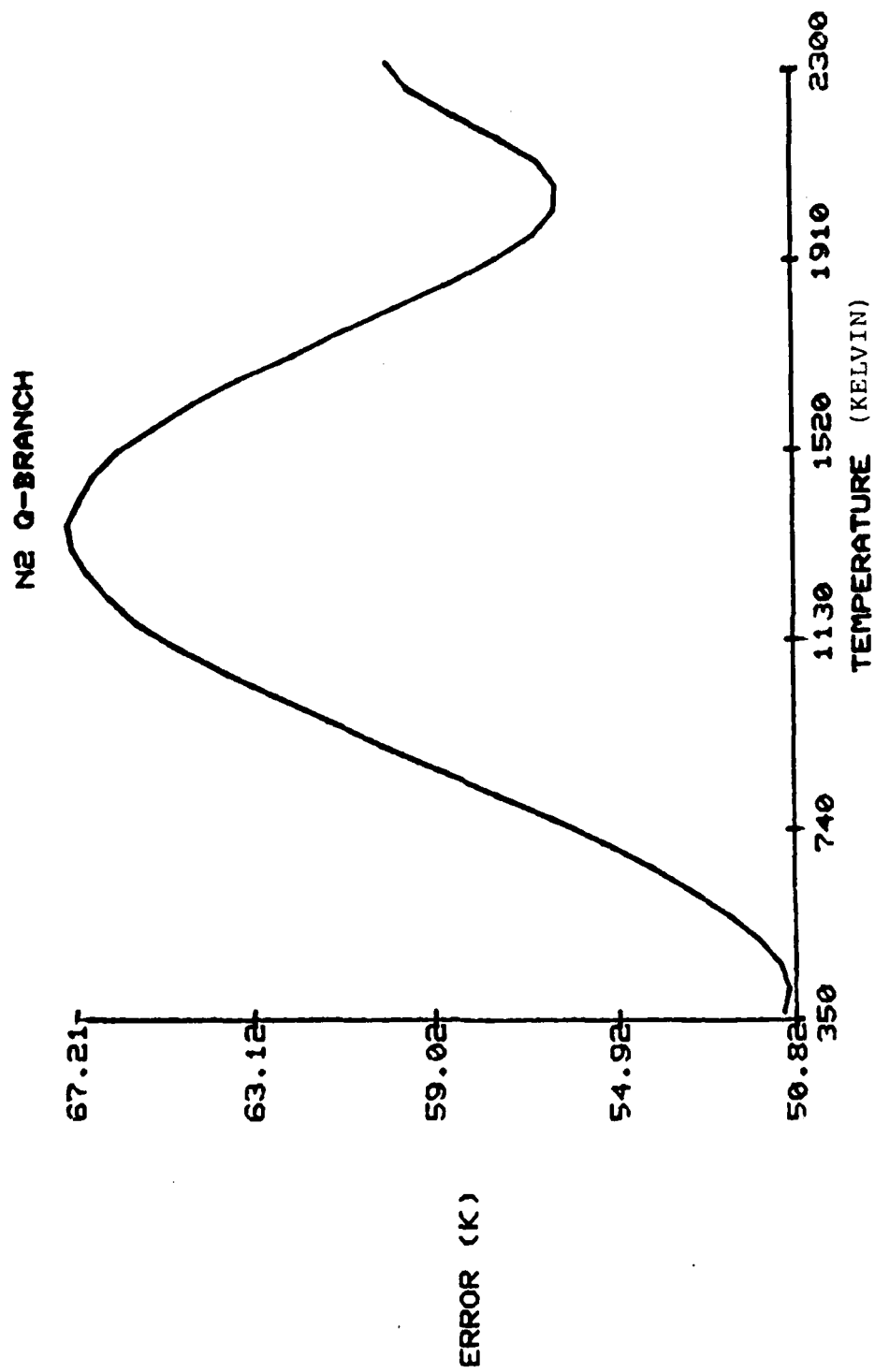


Figure 6. Temperature Uncertainty as a Function of Temperature Due to a 6.4% Intensity Uncertainty.

beating of the dye and pump lasers can be observed, increasing σ_I which results in a limit to the increase in accuracy of single-shot CARS thermometry to about 50 K with a standard dye laser. This phenomenon can be observed in the high-resolution study reported in Ref. 3. By reducing or eliminating the mode-beating modulation of the dye laser such as with the use of a super-radiant dye and using a single-mode Nd:YAG laser, better accuracies should be obtainable by converting to a high-resolution CARS instrument.

Concentration-Error Analysis

The number density as determined from the integrated-CARS-intensity measurement for a major species (concentration > 20% by volume) in an atmospheric flame is given by⁴

$$N_T = N_{300} \sqrt{\frac{R_T \cdot P_T}{P_{300}}} \quad (3)$$

where N_T is the nitrogen number density at temperature T ; N_{300} is the nitrogen number density at 300 K; R_T is the ratio of the integrated bandshapes of the CARS spectrum at 300 K to the CARS spectrum at temperature T ; P_T is the experimentally measured integrated CARS power at temperature T ; and P_{300} is the experimentally measured integrated CARS power at 300 K. The ratio R_T takes into account the change in the Raman linewidths and population redistribution with temperature. The probable error in the measurement of N_T from probable errors in R_T , P_T , and P_{300} (assuming no intensity losses due to turbulence effects) is given by

$$\Delta N_T = \left[\left(\frac{\partial N_T}{\partial R_T} \right)_{P_T, P_{300}}^2 \Delta R_T^2 + \left(\frac{\partial N_T}{\partial P_{300}} \right)_{R_T, P_T}^2 \Delta P_{300}^2 + \left(\frac{\partial N_T}{\partial P_T} \right)_{R_T, P_{300}}^2 \Delta P_T^2 \right]^{1/2} \quad (4)$$

Combining Eqs. (3) and (4), performing the differentiation, and simplifying yields

$$E(N_T) = [\frac{1}{4} E(R_T)^2 + \frac{1}{4} E(P_T)^2 + \frac{1}{4} E(P_{300})^2]^{1/2} \quad (5)$$

The uncertainty in P_T and P_{300} without turbulence and assuming no problems from photon statistics (due to the large signal levels) is the correlation error observed between the sample and reference ($\sim 6\%$).⁴

The uncertainty in R_T is due to the temperature uncertainty. R_T is defined by

$$R_T = \frac{\int \hat{I}_1(\omega_3 - \delta) |x_3'(\delta)|_{300}^2 d\delta d\omega_3}{\int \hat{I}_1(\omega_3 - \delta) |x_3'(\delta)|_T^2 d\delta d\omega_3} \quad (6)$$

This ratio takes into account the variation of the Raman linewidths and the populational redistribution with temperature. The uncertainty in R_T due to an uncertainty in T is given by⁵

$$\frac{1}{\sigma_{R_T}^2} = \frac{1}{\sigma_T^2} \left(\frac{\partial R_T}{\partial T} \right)^2 \quad (7)$$

The measured temperature uncertainty is $\sim 4\%$ with the present CARS system. For a 4% uncertainty in the temperature, the relative uncertainty in R_T is shown in Fig. 7. At 2200 K the predicted uncertainty in R_T is 6.3%. Substituting this value into Eq. (5) indicates a 5.1% uncertainty at 2200 K for the concentration measurement. The experimentally measured value is 5.3%, which is in close agreement with the predicted value.⁴

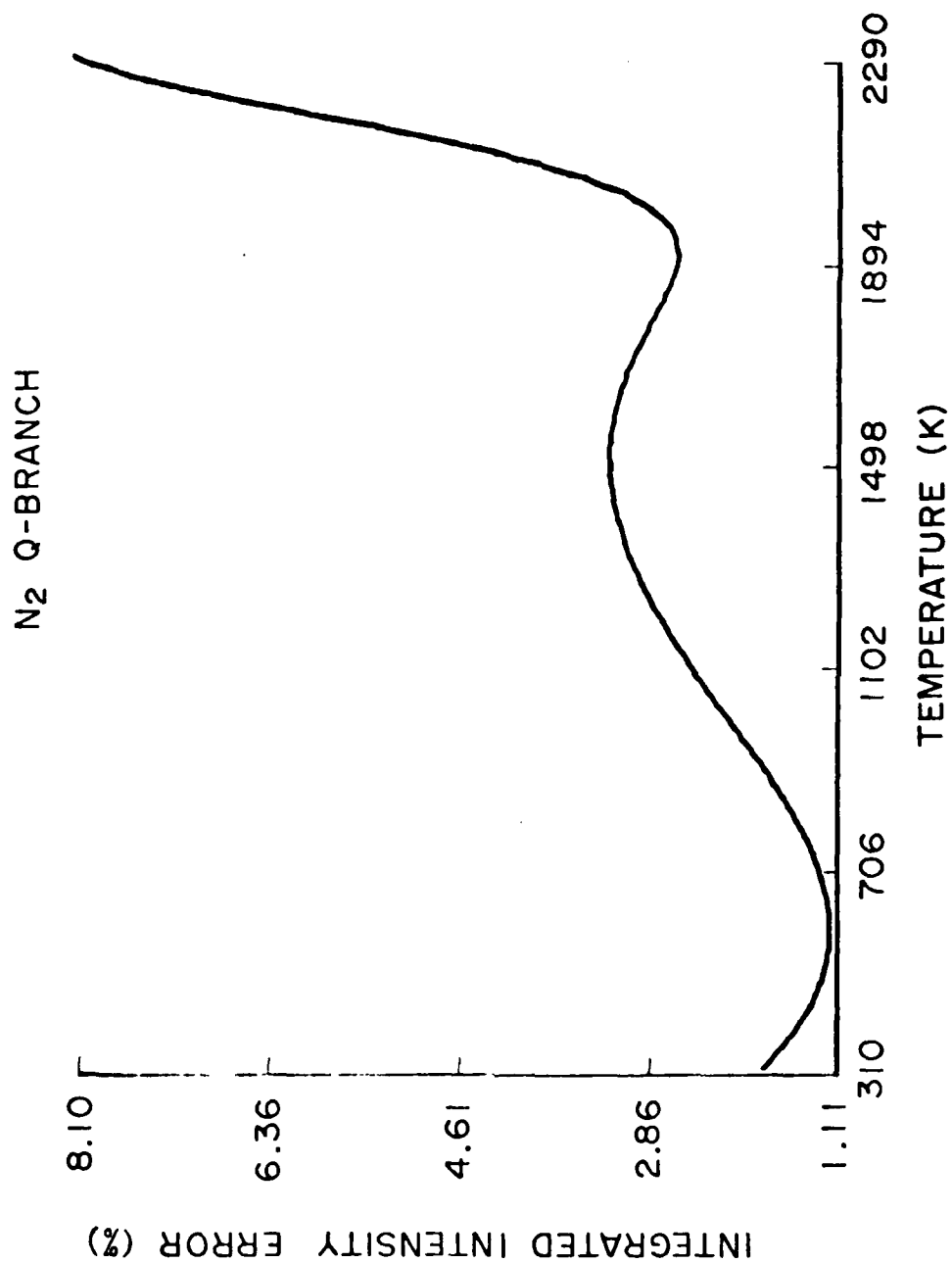


Figure 7. Plot of Relative Uncertainty of Ratio R_T with 4% Uncertainty in Temperature.

2.3 EFFECTS OF TURBULENCE UPON CARS SIGNAL PRODUCTION

A potential problem involved in making optical measurements in turbulent flame environments is the strong refractive-index gradients produced by temperature-density variations. To determine the impact of this effect upon CARS signal production, a series of studies was conducted on a helium jet and in a propane diffusion flame. The results of these studies are discussed in the paper entitled, "Effects of Turbulence upon CARS Signal Production," which appears on the following pages.

EFFECTS OF TURBULENCE UPON CARS SIGNAL PRODUCTION

L. P. Goss

and

P. W. Schreiber

ABSTRACT

The effects of turbulence-induced index-of-refraction gradients upon CARS signal production are examined in terms of the log-amplitude theory of electromagnetic-radiation propagation through turbulence based upon the works of Tatarski and Schmeltzer. Experiments in both noncombustive and combustive environments are conducted to verify the theoretical results. Turbulence effects in a practical combustor system are examined along with suggestions on methods of minimizing the influence of the turbulence-induced effects upon CARS concentration measurements.

I. INTRODUCTION

The major application of coherent anti-Stokes Raman spectroscopy (CARS) has been in the area of combustion diagnostics where the environment can present severe problems. In combustion the media can be luminescent, sooty, turbulent, have large temperature-concentration gradients, and produce intense structural and acoustic vibrations. It is necessary to evaluate these environmental effects upon diagnostic signals and to correct or eliminate them before accurate measurements can be obtained. The ability of CARS to reject luminous background signals has been demonstrated in numerous studies.¹ In addition, the effects of particle-laden environments have also been the subject of a thorough investigation.² The effects of turbulence upon CARS signal production, however, has not received much attention. One recent study in this area has demonstrated the severity of turbulence effects and introduced a technique which can compensate for the CARS signal losses incurred due to turbulence.³ The purpose of this paper is to examine the effects of turbulence upon CARS signals, to discuss how these results relate to the \log_e amplitude theory of wave propagation through turbulent media, and to present possible methods of minimizing the turbulent effects which are encountered.

L. P. Goss is with Systems Research Laboratories, Inc., 2800 Indian Ripple Road, Dayton, OH 45440; P. W. Schreiber is with the Aero Propulsion Laboratory Air Force Wright Aeronautical Laboratories, Wright-Patterson AFB, OH 45433.

To simplify the comparison between theory and experiment, collinear CARS was chosen for this study rather than a BOXCARS technique. This allowed difficult problems associated with beam wander and interaction-volume variation to be avoided. A study with BOXCARS in turbulent environments is the subject of a forthcoming paper.⁴

II. THEORY

The generation of CARS occurs in a gaseous medium when two intense collinear electromagnetic waves interact with a molecular species. The higher frequency wave, $E_p(\omega_p)$, which is called the pump wave and the lower frequency wave, $E_s(\omega_s - \delta)$, generate an anti-Stokes spectrum at $2\omega_p - \omega_s + \delta$ when E_s is tuned through the Stokes spectrum of the molecular species under investigation. The anti-Stokes spectrum can also be generated by employing a broadband source for E_s in conjunction with the narrow-band pump wave.⁵ The appropriate term in the third-order polarization which is responsible for this effect is⁶

$$P_a^{(3)}(\omega_a + \delta) = 3\chi^{(3)}(\omega_p, \omega_p, \omega_s + \delta) E_p^2 E_s(\omega_s - \delta) \quad (1)$$

where $\chi^{(3)}$ is the corresponding third-order susceptibility, ω_s is the center frequency of the Stokes radiation, δ is the deviation from ω_s , and ω_a is the center frequency of the anti-Stokes line given by $2\omega_p - \omega_s$. Similar third-order polarizations can be written at the pump and Stokes frequencies.

However, for weak interactions the amplitude of the pump and Stokes waves are not significantly affected by the medium. Thus, only the electromagnetic-wave equation at the anti-Stokes frequency must be considered in the analysis. This wave equation is

$$\nabla^2 E_a = \frac{1}{c^2} \frac{\partial^2}{\partial t^2} \left(E_a + 4\pi (\mathcal{P}_a^{(1)} + \mathcal{P}_a^{(3)}) \right) \quad (2)$$

where E_a is the anti-Stokes field and $\mathcal{P}_a^{(1)}$ is the linear polarization. For plane waves, the solution of the above equation yields for the anti-Stokes intensity

$$I_a(\omega_a + \delta, Z) = \left(\frac{4\pi^2 \omega_a}{c^2} \right)^2 |3\chi^{(3)}|^2 I_p^2 I_s(\omega_s - \delta) \frac{\sin^2(Z\Delta k/2)}{(\Delta k/2)^2} \quad (3)$$

where Z is the distance over which the CARS signal is produced and

$$\Delta k = \frac{2\omega_p \eta_p}{c} - \frac{\omega_s \eta_s}{c} - \frac{\omega_a \eta_a}{c}$$

where η_a , η_p and η_s are the indices of refraction. For most applications $Z\Delta k/2$ is small, and Eq. (3) reduces to

$$I_a(\omega_a + \delta, Z) = \left(\frac{4\pi^2 \omega_a}{c^2} \right)^2 |3\chi^{(3)}|^2 Z^2 I_p^2 I_s(\omega_s - \delta) \quad (4)$$

To obtain spatial resolution, focused beams are used and most of the CARS intensity is generated near the focal volume. For this case, the solution for E_a may be placed in the integral form⁷

$$E_a(\vec{r}, t) = 1/c \int \frac{\mathcal{P}_a^{(3)}(\vec{r}', t') d^3\vec{r}'}{|\vec{r} - \vec{r}'|} \quad (5)$$

where $t' = t - |\vec{r} - \vec{r}'|/c$. As can be seen from Eq. (1), the evaluation of this integral requires an explicit expression for the focused pump and Stokes waves. Although approximate analytical expressions for E_p and E_a are available,⁸ it is not possible to carry out the integration to yield a closed form. A complete analysis of the effect of turbulence upon the generation of CARS requires a solution of Eq. (5) which is a very difficult task. However, in a turbulent medium the focal spot increases in size and is also displaced from the nonturbulent position in a statistical manner from pulse to pulse. The change in the spot size should have the greatest effect upon the collinear CARS signal since this reduces the intensities in the focal volume. For this case, the plane-wave solution yields

$$P_{at} = A_{et} I_a = \left(\frac{4\pi^2 \omega_a}{c^2} \right)^2 |3\chi^{(3)}|^2 \left(\frac{Z_{et}}{A_{et}} \right)^2 P_p^2 P_s \quad (6)$$

where P_{at} is the anti-Stokes power, P_p is the pump power, P_s is the Stokes power, A_{et} is the effective area of the focal spot and Z_{et} is the corresponding distance over which the major portion of the CARS signal is generated. From geometrical considerations of focused Gaussian beams, it is reasonable to postulate that the value of Z_{et} increases with A_{et} such that

$$Z_{et}^2 = k A_{et} \quad (7)$$

where k is a constant. Thus, the ratio of the anti-Stokes power for a non-turbulent medium to that for a corresponding turbulent medium can be estimated from Eqs. (6) and (7). This gives

$$\frac{P_a \int_{\text{int}}}{P_{at} \int_{\text{int}}} = \frac{P_a}{P_{at}} = \frac{A_{et}}{A_e} = \left(\frac{D_{et}}{D_e} \right)^2 \quad (8)$$

where the symbol \int_{int} indicates the integrated power and the subscript t is used for parameters corresponding to the turbulent medium. While Eq. (8) defines the relationship between the integrated CARS signal and the diameter of the focused laser beams, it does not relate the beam diameters to the strength of the turbulence through which the beams propagate. This relation was ascertained from studies of laser beam propagation through the turbulent atmosphere. Gebhardt and Collins⁹ have shown that the use of certain assumptions allows the spread for both focused and collimated beams to be directly related to a parameter called the structure constant of turbulence (C_N). The results of Gebhardt and Collins were based upon the works of Tatarski,¹⁰ and a first-order Rytov approximation, modified for beam waves by Schmeltzer.¹¹ The assumptions imposed were that 1) the total energy is conserved in going from the transmitter plane to the receiver plane, 2) the resulting average intensity profile remains Gaussian in shape, 3) the turbulence has a Kolmogorov spectrum, and 4) the \log_e amplitude, ℓ , is normally distributed about a mean $\langle \ell(R) \rangle$ and has a variance equal to $C_\ell(R)$, R being the radius vector along the propagation path. With these assumptions the theory predicts that the average spread of the focal spot due to turbulence (D_t) with respect to the spot size in the absence of turbulence (D) can be expressed as

$$\frac{D_t}{D} = \exp \left(- \left(\langle \ell(0) \rangle + C_\ell(0) \right) \right) \quad (9)$$

The exact mathematical expressions for the \log_e amplitude $\langle \ell(0) \rangle$ and its variance $C_\ell(0)$ are complicated and cumbersome to work with directly. Equation

(9) is generally rewritten to include a normalization factor, $C_\ell^S(0)$, which is the variance of the \log_e amplitude for a spherical wave. This yields

$$\frac{D_t}{D} = \exp \left[- C_\ell^S(0) \left(\frac{\langle \ell(0) \rangle}{C_\ell^S(0)} + \frac{C_\ell(0)}{C_\ell^S(0)} \right) \right] \quad (10)$$

where

$$C_\ell^S(0) = 0.124 C_N^2 k^{7/6} f^{11/6} \quad (11)$$

In Eq. (11) C_N is the turbulence structure constant, k is equal to $2\pi/\lambda$, and f is the focal length of the lens. It can be shown that the normalized ratios $\langle \ell \rangle / C_\ell^S$ and (C_ℓ / C_ℓ^S) depend upon a single dimensionless parameter

$$\Omega = \left(\frac{2\pi D_0}{\lambda f} \right)^2 \quad (12)$$

where D_0 is the diameter of the beam incident upon the focusing lens. Gebhardt and Collins⁹ have tabulated the values of $\langle \ell \rangle / C_\ell^S$, and Fried and Seidman¹² have tabulated (C_ℓ / C_ℓ^S) as a function of Ω for the cases of focused and collimated beams.

Equation (10) can be simplified by considering the experimental conditions. The collinear CARS configuration employed a focusing lens with a focal length of 42 cm and an incident beam diameter of 1 cm. In this situation Ω is equal to 1.4×10^5 . The tabulated values of the normalized ratios $\langle \ell \rangle / C_\ell^S$ and (C_ℓ / C_ℓ^S) for this Ω are -2.1 and 0.0, respectively. Expressing Eq. (10) in terms of the \log_e of the ratio of the spot sizes and substituting the tabulated values of the normalized ratios $\langle \ell \rangle / C_\ell^S$ and (C_ℓ / C_ℓ^S) , yields

$$\ln \left(\frac{D}{D_t} \right) = 2.1 (0.124 C_N^2 k^{7/6} f^{11/6}) \quad (13)$$

Equation (13) assumes that the turbulence exists in the entire region from the lens to its focus. Equation (13) can be modified by a simple transformation of variables for the more general case where the turbulence is located anywhere between the lens and its focus. For this case, the values of $C_\ell^S (< \ell > / C_\ell^S)$ and $C_\ell^S (C_\ell / C_\ell^S)$ in Eq. (10) must be replaced by

$$\left[C_{\ell_1}^S \left(\frac{< \ell >_1}{C_{\ell_1}^S} \right) - C_{\ell_2}^S \left(\frac{< \ell >_2}{C_{\ell_2}^S} \right) \right] \text{ and } \left[C_{\ell_1}^S \left(\frac{C_{\ell_1}}{C_{\ell_1}^S} \right) - C_{\ell_2}^S \left(\frac{C_{\ell_2}}{C_{\ell_2}^S} \right) \right] \quad (14)$$

In Eq. (14) the value of f is replaced by f_2 , the distance from the focal spot to the near side of the turbulent medium, and f_1 the corresponding distance to the far side of the medium ($f_1 - f_2$ is the medium thickness). D_{o1} and D_{o2} are the beam diameters at f_1 and f_2 . Using these values, one obtains for $\lambda = 532\text{nm}$.

$$\ln \left(\frac{D}{D_t} \right) = 4.64 \times 10^7 C_N^2 (f_1^{11/6} - f_2^{11/6}) \quad (15)$$

Equation (8) describes the effects of changing the focal spot size upon the CARS integrated intensities. Combining Eq. (8) with Eq. (15) yields

$$\ln \left(\frac{P_a}{P_{at}} \right) = 9.28 \times 10^7 C_N^2 (f_1^{11/6} - f_2^{11/6}) \quad (16)$$

Equation (16) indicates that the \log_e of the integrated CARS power should depend upon 1) the thickness of the turbulence, 2) the displacement of the turbulence from the focal region, and 3) the structure constant of the turbulence. An examination of the tabulated ratios $(< \ell > / C_\ell^S)$ and (C_ℓ / C_ℓ^S)

indicates that because of the extremely large values of Ω employed, the normalized ratios are relatively insensitive to changes in incident beam diameters and the focal length of the lens for visible laser wavelengths. This would indicate that Eq. (16) should also be independent of 1) the focal length of the focusing lens employed for CARS production and 2) the incident beam diameter. It is these predictions which are experimentally examined for noncombustive and combustive turbulence in this paper.

III. EXPERIMENTAL

A. Turbulent Generators

Since turbulence affects beam propagation by inducing random fluctuations in the index of refraction within the medium, two gases having a large difference in their refractive indices can be mixed in a turbulent jet to produce a small turbulent field. Thus, to investigate the effects of noncombustive turbulence upon beam propagation and the generation of CARS signals, the helium-air-mixing turbulent generator reported in Ref. 3 was employed. This generator consists of alternating helium-air nozzle plates sandwiched between separating plates which allows the helium and air flows to be controlled separately. To study turbulent effects in combustion, two small burners were used. They included a small annealing torch and a flame shielded burner.¹³

B. CARS Setup

The CARS experimental setup for studying the turbulent effects shown in Fig. 1 was the same as that used for the simultaneous temperature-species concentration measurements reported in Ref. 13, with the exception that a collinear rather than a BOXCARS arrangement was used for the turbulence studies. The

turbulent generator in these studies was placed between the focusing lens and its focus in the sample leg and kept well away from the focal region where the majority of the CARS signal is produced. This procedure ensured that any loss in the CARS signal would be due primarily to turbulence effects and not to number-density changes resulting from helium or temperature variation in the focal volume.

In order to study the variation in spot size after propagation through turbulence, a small portion of the pump beam was split off from the sample path just after focus. The split beams were then magnified and coupled onto a PAR 1205 OMA detector which allowed recording of the spread of the focal spot.

IV. RESULTS AND DISCUSSION

A. Noncombustive Turbulence

Figure 2 shows the effects of turbulence upon the CARS intensity as obtained with the helium-air turbulent generator. As seen from Fig. 2(a), when only air is flowing in the turbulent generator, the focal spot is sharp and well defined and the resulting CARS signals are strong. However, when the helium is allowed to flow and mix with the air, the resulting beam spread is drastically increased, with a corresponding large drop in the sample signal as shown in Fig. 2(b). This effect can produce large errors in the concentration measurements. For this particular case there was an eleven-fold reduction in the CARS intensity, with a corresponding 330% error in N_2 concentration.

Equation (16) indicates that the perturbation of the CARS signal due to turbulence increases with the distance of the turbulent region ($f_1^{11/6} - f_2^{11/6}$) from the focal volume of the pump and probe lasers. To study this effect, the helium-air turbulent generator was placed at different positions in the sample beam path, and the relative CARS signal was recorded. Figure 3 depicts the results obtained by scanning the turbulent generator along the axis of beam propagation. The CARS signal is shown to decrease as the generator scans away from the focal region in the sample path, with a corresponding increase in the beam spread, as predicted by Eq. (16). It is apparent, however, that the relative integrated signals do not vary inversely with the square of the beam diameter. Figure 4 shows a comparison between the observed relative signal levels and those predicted from the relative beam-spread measurements, assuming a linear inverse relation between the integrated signal and the beam spread. As can be seen, the correspondence is quite good. However, Eq. (16) indicates that the integrated signal should vary inversely with the square of the beam spread. An important clue concerning the reason for this discrepancy was obtained when it was noted that a 90° rotation of the OMA gave little indication that the beam was spreading. Imaging the beam upon the laboratory wall permitted a visual assessment that the beam was spreading elliptically. The spread was perpendicular to the flow of the helium-air turbulence. Since the area of the corresponding elliptical focal spot depends upon the product of the major and constant minor axis, Eq. (8) becomes

$$\frac{P_a}{P_{at}} = \frac{D_{et} D_e}{D_e D_e} = \frac{D_{et}}{D_e} \quad (17)$$

where D_{et} refers to the major axis of the ellipse.

The ratio is thus linear in nature rather than quadratic. Equation (16) then becomes

$$\ln\left(\frac{P_a}{P_{at}}\right) = 4.64 \times 10^7 C_N^2 (f_1^{11/6} - f_2^{11/6}) \quad (18)$$

Both Eq. (16) and (18) indicated that a linear relation exists between the \log_e of the ratio of the integrated CARS power and the displacement parameter $(f_1^{11/6} - f_2^{11/6})$. A plot of the experimental data obtained from scanning the helium-air turbulent generator as $\log_e (P_a/P_{at})$ as a function of $(f_1^{11/6} - f_2^{11/6})$ is shown in Fig. 5. The data indicate reasonably straight-line behavior, as predicted. Notice, however, that the fitted line has a nonzero intercept. Equation (18) does not account for a nonzero intercept. To confirm that the nonzero intercept was not due to some error in the experimental measurement such as an uncertainty of the thickness of the turbulence, the displacement from the focus, or the CARS intensity, the relative corrections necessary to translate the experimental curve such that it intercepted zero were calculated. These calculations showed that an error of ~ 12 cm for the generator displacement from focus, a doubling of the turbulence-generator length (from 7.5 to 15 cm), or an error in the intensity of 300% (the turbulent CARS intensities should be ~ 300% lower) would be necessary to account for the discrepancy. It was estimated that the thickness of the turbulence and displacement of the generator were accurate to within 1 mm and the intensity measurements were reproducible to within $\pm 8\%$ of the integrated signals. Thus, the intercept cannot be explained in terms of an experimental error incurred during the measurement. Another interesting feature is that the same effect was

observed with the corresponding beam-spread data. The exact nature of this discrepancy is still under investigation; however, it has been empirically determined that a plot of the \log_e of the ratio of the intensity or beam diameter as a function of $(f_1^{22/6} - f_2^{22/6})$ will typically intersect near zero. Figure 6 shows the results for the beam spread and CARS intensity plotted in this manner. The corresponding empirical equation for fitting the experimental data was

$$\ln \left(\frac{P_a}{P_{at}} \right) = 2.053 \times 10^{15} C_N^4 (f_1^{22/6} - f_2^{22/6}) \quad (19)$$

where $k^{7/6} C_N^2$ has been squared in order to ensure that the units will cancel properly. As indicated by Eqs. (18) and (19), the slopes of such plots as shown in Figs. 5 and 6 can be used to obtain the structure constant of turbulence. This parameter is a measure of the strength of the turbulence through which the beam passes. The values of C_N determined from both the CARS-intensity variation and the beam-spread data for helium-air mixing are given in Table I. These values are approximately four orders of magnitude larger than those for the near-ground turbulence experienced in air which indicates extremely strong turbulence.

To determine whether the focal length of the lens employed in CARS production affected the CARS signal loss due to turbulence, a series of lenses from 15 to 50 cm was employed. The experiment was conducted with the turbulent generator located a constant distance from the focus of each lens; this ensured that the displacement parameter $(f_1^{22/6} - f_2^{22/6})$ would remain constant and thus any

variations in the CARS signal from lens to lens would be due to the different lenses employed. The results of this experiment indicated (within experimental error) that the CARS signal loss due to turbulence was independent of the focal length of the lens employed, which is consistent with the \log_e -amplitude theory.

B. Combustive-Turbulence Studies

The experimental arrangement shown in Fig. 1 was also utilized to study the effects of combustion-produced turbulence upon collinear CARS. The turbulence generator (in this case various burners) was placed between the focusing lens used for the generation of CARS and its focal point. The resulting beam spread was monitored by an OMA, and the resulting integrated CARS signal along the sample path was normalized by the CARS signal from the reference path. The results with the flames on and off were then compared to determine the various effects which combustion turbulence had upon the beams. The first combustion study conducted with such an arrangement employed the annealing torch for flame production. The main objective was to determine if effects were present when the laser beams traversed the flame and, if so, to estimate the geometrical shape of the focal spot. In order to accomplish this task, a series of simultaneous beam spread - integrated CARS intensity measurements were made as the laser beams traversed the annealing torch flame. As illustrated in Fig. 7 a plot of the \log_e of the ratio of the CARS intensity as a function of the \log_e of the corresponding beam spreads shows that, contrary to helium-air-mixing turbulence, the combustion turbulence caused the CARS signal to vary inversely with the square of the beam diameter. This result indicates that the flame-produced turbulence was random in nature. The \log_e amplitude of the CARS signal is predicted by Eq. (16) for $f^{11/6}$ and the following equation for $f^{22/6}$

$$\ln \left(\frac{P_a}{P_{at}} \right) = 8.212 \times 10^{15} C_N^4 (f_1^{22/6} - f_2^{22/6}) \quad (20)$$

A visual examination showed that the beam was, on the average, uniform in all directions. However, the variation in the data indicates that the turbulence produced by this method displayed a higher degree of fluctuation.

To determine the effects of variation of the displacement parameter on CARS signal production for combustive turbulence the annealing torch was scanned horizontally along the axis of beam propagation. The results indicated for this experiment that the CARS signal loss increased as the flame was positioned further from the focal region, which is consistent with Eq. (16) and the helium-air turbulent results. The width of the flame was 2.8 cm. The experimental data when plotted as the \log_e amplitude of the ratio of the intensities as a function of the displacement parameter $(f_1^{11/6} - f_2^{11/6})$ exhibits a behavior similar to that demonstrated with the helium-air-mixing turbulence. Again the data do not have a zero intercept as predicted by Eq. (16). Plotting the \log_e amplitude as a function of the displacement $(f_1^{22/6} - f_2^{22/6})$ results in an intercept near zero, as shown in Fig. 8. The structure constants obtained from the slope of the plots are given in Table I.

To study the effects of different flame types, an experiment was performed in which the air flow of the annealing torch burner was varied and the fuel flow kept constant. The relative air flow was varied from an initial zero flow (diffusion flame) to a relatively high flow in which the flame was highly structured and conical. By maintaining the burner at a fixed location, (and thus keeping $(f_1^{11/6} - f_2^{11/6})$ constant) only a change in the turbulence structure constant could cause the CARS signal loss to vary. The data shown

in Fig. 9 indicate that the diffusion--sooty, low-temperature, large-temperature-gradient--flames have the greatest effect upon CARS signal levels, while the high-air-flow flames have the least effect. The resulting structure constants obtained from these data and Eq. (20) are listed in Table II.

C. Turbulent Effects in Practical Combustors

In order to estimate the effect of turbulence upon CARS measurements in a practical combustion system, the Air Force Wright Aeronautical Laboratories Combustion Tunnel was used as a test case.¹⁴ The hardened CARS system¹⁵ which was built especially for studies on this combustor employed a 31-cm focal-length lens for CARS signal production. The diameter of the tunnel flame was 13 cm. Maximum turbulence effects were expected to occur when the beams were focused through the turbulent medium before the CARS signal was produced. In this arrangement f_2 is zero and f_1 is the diameter of the flame for Eq. (20). The greatest turbulence level reported in Table I was $5.27 \times 10^{-4} \text{ m}^{-1/3}$ (Eq. 20). Assuming the flame in the combustor to have the same structure constant, the intensity loss due to this turbulence is predicted to be 45%. However, the experimental data accumulated by the hardened system indicated that no noticeable turbulent effect was observed. The hardened system was designed such that the reference was placed in series with the sample beam after the combustion-tunnel path. Thus, the beams, if distorted, would indicate an intensity change in the reference when the tunnel was in use. All present data indicate, however, that if the turbulence in the tunnel affected the CARS signal, the distortion was below the normal variation encountered in the system and could not be distinguished. The turbulence effects would have to be less than 8-10%, which in this case places an upper limit on the turbulence structure constant of $\sim 3.72 \times 10^{-4} \text{ m}^{-1/3}$. In an attempt to verify this result, a premixed propane

burner was studied in the laboratory. The burner was operated such that the inner burner emitted propane and the outer burner emitted only air. This setup resulted in a flame with characteristics similar to the bluff-body-produced flame of the AFWAL combustor. CARS intensity measurements were made through different parts of the flame and the structure constants were determined according to Eqs. (16) and (20). Figure 10 displays the flame with the profiling grid superimposed. Table III lists the structure constants for this profile. The position examined in the practical combustor corresponds to location 0,165 which had a structure constant of 3.427×10^{-4} . This would lead to an intensity loss of only 7%, which is consistent with the practical combustor results.

Notice that structure-constant data indicate that the region near the fuel jet displays the largest structure constant. This effect, however, is offset by the narrower cross section (~ 3 cm) of the flame at the nozzle in the combustor, which results in a CARS signal loss of only 0.1%. Thus, although the structure constant is large, the overall turbulence effects are minimized by the small cross section. The data indicate that reliable CARS measurements could be made in this flame without interference from turbulence effects.

D. Minimization of Turbulence Effects

Equations (16) and (20) indicates several means by which the effects of turbulence upon CARS signal production can be minimized. One method would be to minimize the displacement parameter $(f_1^{11/6} - f_2^{11/6})$, either by reducing the

thickness of the turbulent region or by minimizing the displacement of the focus of the laser beams from the turbulent region. Typically, however, the thickness of the flame media and/or the measurement location cannot be varied. A second method is to examine only regions of the flame in which the structure constant, C_N , is relatively low. Unfortunately, in a few cases, this limits the regions from which reliable concentration data can be taken.

A more practical approach is to develop methods to compensate for the turbulence. A possible scheme for accomplishing this was reported in Ref. 16 and modified and experimentally verified in Ref. 3. In this scheme a nonresonant signal is used as an in situ reference, both resonant and nonresonant CARS signals being generated at the same time in the same location by laser beams which traverse the same turbulent path. Using this method, accurate concentration measurements were made even through severe turbulence. Thus demonstrating that compensation can be achieved with an in situ reference.

Immediate applications of this technique would be in the performance of concentration measurements in extremely thick, particle-laden turbulent flames or supersonic combustion environments where extreme refractive-index gradients are known to exist.

CONCLUSIONS

Experimental results with the helium-air-mixing turbulent generator indicate that 1) the effects of turbulence upon the relative CARS signals can be pronounced, 2) the CARS signal varies inversely with the elliptical area of the focal spot, 3) the relative magnitude of these effects depends upon the

structure constant of the turbulence, the displacement of the turbulence from the focal region, and the thickness of the turbulent region, and 4) the \log_e amplitude shows a $C_N^4 f^{22/6}$ dependence.

The experiments completed on combustion turbulence show the focal spot to be approximately circular and the CARS signal to vary inversely with the square of the beam diameter, as predicted by theory. In addition, the data follow reasonably well the relationship expressed by Eq. (16). However, it was again necessary to use the 22/6 power rather than the 11/6 power predicted by theory to obtain an intercept at the origin. Since the calculated structure constants are sensitive to this exponent, data are presented based upon the 22/6 power as well as the 11/6 power.

Structure constants were found to vary significantly as a function of position in a propane-air flame, being greatest in the combustion zone. In addition, fuel-rich flames had a larger structure constant than lean flames. Structure constants from a laboratory flame were used to predict CARS signal losses in the AFWAL Combustor. The results were consistent with the combustor data observed.

The effects of turbulence can be minimized by 1) reducing the thickness of the turbulent media, 2) conducting measurements in low C_N regions or 3) employing an in situ reference compensating scheme which has been used to make accurate concentration measurements--even in extremely turbulent environments.

The nonzero intercept of the \log_e -amplitude equation is the subject of a continuing study. Possible reasons for this discrepancy include 1) the

Kolmogorov spectrum does not apply for the turbulence studied, and 2) the relatively large structure constants derived from turbulent generators have taken the results out of the realm of weak turbulence. However, the success of the empirically determined equation governing the \log_e amplitude variation is encouraging. It should be possible to use this equation to obtain semi-quantitative predictions for the CARS signal losses from turbulence, if the structure constant of turbulence for the system can be estimated.

REFERENCES

1. See, for example, W. M. Tolles, J. W. Nibler, J. R. McDonald, and A. B. Harvey, Appl. Spectros. 31, 253 (1977).
2. A. C. Eckbreth and R. J. Hall, Combust. Flame 36, 87 (1979).
3. L. P. Goss and P. W. Schreiber, Invited Paper No. J.4 presented at the International Conference on Lasers 80', New Orleans, LA, December 15-19, 1980.
4. L. P. Goss and P. W. Schreiber, "Turbulence Effects on BOXCARS," to be submitted to Appl. Opt.
5. W. B. Roh, P. W. Schreiber, and J. P. E. Taran, Appl. Phys. Lett. 29, 174 (1976).
6. W. B. Roh and P. Schreiber, Appl. Opt. 17, 1418 (1978).
7. D. Jackson, Classical Electrodynamics (John Wiley and Sons, Inc., NY, 1967), p. 186.
8. R. Schmeltzer, Appl. Opt. 10, 1652 (1971).
9. F. G. Gebhardt and S. A. Collins, J. Opt. Soc. Am. 59, 1139 (1969).
10. V. I. Tatarski, Wave Propagation in a Turbulent Medium (McGraw Hill, NY, 1961).

11. R. A. Schmeltzer, Q. Appl. Math. 24, 339 (1966).
12. D. L. Fried and J. B. Seidman, J. Opt. Soc. Am. 57, 181 (1967).
13. L. P. Goss, G. L. Switzer, and P. W. Schreiber, Paper 80-1543 presented at the 15th AIAA Thermophysics Conference, Snowmass, CO, 14-16 July 1980.
14. W. M. Roquemore, R. B. Bradley, J. S. Stutrud, C. M. Reeves, and L. Krishnamurthy, Paper No. 80-67-93 presented at the Gas Turbine Conference and Products Show, New Orleans, LA, March 10-13, 1980.
15. G. L. Switzer, L. P. Goss, W. M. Roquemore, R. B. Bradley, P. W. Schreiber, and W. B. Roh, J. Energy 4, 209 (1980).
16. J. A. Shirley, R. J. Hall, J. F. Verdick, and A. C. Eckbreth, Paper No. 80-1542 presented at the 15th AIAA Thermophysics Conference, Snowmass, CO, 14-16 July 1980.

FIGURE CAPTIONS

Figure 1. Experimental CARS Setup Used for Turbulence Studies.

Figure 2. Beam Spread and Resulting CARS Intensity a) Without Turbulence, b) With Turbulence. Inserts are the beam spreads recorded by the OMA. R - Reference Path, S - Sample Path.

Figure 3. Variation of CARS Intensity and Beam Diameter with Horizontal Scan of Helium Turbulence Generator.

Figure 4. Correlation of the Relative CARS Signal as Experimentally Measured (\cdot) and as Predicted from the Measured Beam Diameters ($P_a \propto 1/D$) for a Horizontal Scan of the Helium Turbulence Generator.

Figure 5. Plot of the \log_e Amplitude of the CARS Signal Versus the Displacement Parameter $(f_1^{11/6} - f_2^{11/6})$ for a Horizontal Scan of the Helium Turbulence Generator. a - nonturbulent; at - turbulent.

Figure 6. \log_e Amplitude Plot of the CARS Signal Versus the Displacement Parameter $(f_1^{22/6} - f_2^{22/6})$ for a Horizontal Scan of the Helium Turbulence Generator. a - nonturbulent; at - turbulent.

Figure 7. Correlation of the Relative CARS Signal to the Relative Beams Spread for Combustive Turbulence. a - nonturbulent; at - turbulent.

Figure 8. \log_e Amplitude Plot of the CARS Signal Versus the Displacement Parameter $(f_1^{22/6} - f_2^{22/6})$ for a Horizontal Scan of an Annealing Torch. a - nonturbulent; at - turbulent.

Figure 9. Variation of the Relative CARS Signal as a function of the Relative Air Flow for the Premixed Propane Fueled Burner.

Figure 10. Turbulent Flame which was Used to Model the AFWAL Combustion Tunnel.

TABLE I

Turbulence Structure Constants, C_N , Determined from the CARS-Intensity and Beam-Spread Experimental Data.

Non-Combustive Turbulence

	Eq. (18)	Eq. (20)
Exp. Data	$C_N(m^{-1/3})$	$C_N(m^{-1/3})$
Beam Spread	1.113×10^{-3}	5.46×10^{-4}
CARS Intensity	1.086×10^{-3}	5.42×10^{-4}

Combustive Turbulence

	Eq. (16)	Eq. (20)
Exp. Data	$C_N(m^{-1/3})$	$C_N(m^{-1/3})$
Beam Spread	1.399×10^{-3}	4.463×10^{-4}
CARS Intensity	1.378×10^{-3}	5.27×10^{-4}

TABLE II

C_N Values Obtained from the Variation of the Relative Air Flow of an Annealing Torch.

Relative Air Flow	$\log_e \left(\frac{P_a}{P_{at}} \right)$	C_N (Eq. 16) ($\times 10^{-4} \text{ m}^{-1/3}$)	C_N (Eq. 20) ($\times 10^{-4} \text{ m}^{-1/3}$)
0.0	1.812	8.897	4.536
0.5	1.029	6.704	3.938
1.0	1.409	7.844	4.260
1.5	.859	6.125	3.764
2.0	.573	5.002	3.402
2.5	.687	5.477	3.559
3.0	.597	5.106	3.437
3.5	.308	3.667	2.913
4.0	.113	2.221	2.267
4.5	.096	2.048	2.176

TABLE III

 C_N Values From a Profile of the Turbulent Flame.

Position (mm)	C_N [Eq. (16)]	C_N [Eq. (20)]
<u>x,y</u>	<u>$\times 10^{-4} \text{ m}^{-1/3}$</u>	<u>$\times 10^{-4} \text{ m}^{-1/3}$</u>
0,5	11.68	4.772
0,5	11.42	4.768
0,25	11.34	4.753
0,35	9.53	4.356
0.45	8.86	4.201
0,55	8.93	4.216
0,65	7.83	3.949
0,75	7.19	3.782
0,85	7.31	2.813
0,95	7.05	3.745
0,105	6.93	3.634
0,115	5.86	3.415
0,125	5.76	3.383
0,135	5.59	3.335
0,145	5.88	3.420
0,155	5.61	3.340
0,165	5.91	3.427
10,165	5.28	3.240
20,165	4.69	3.054
30,165	4.62	3.031
40,165	3.87	2.774
50,165	3.82	2.757
60,165	2.79	2.356

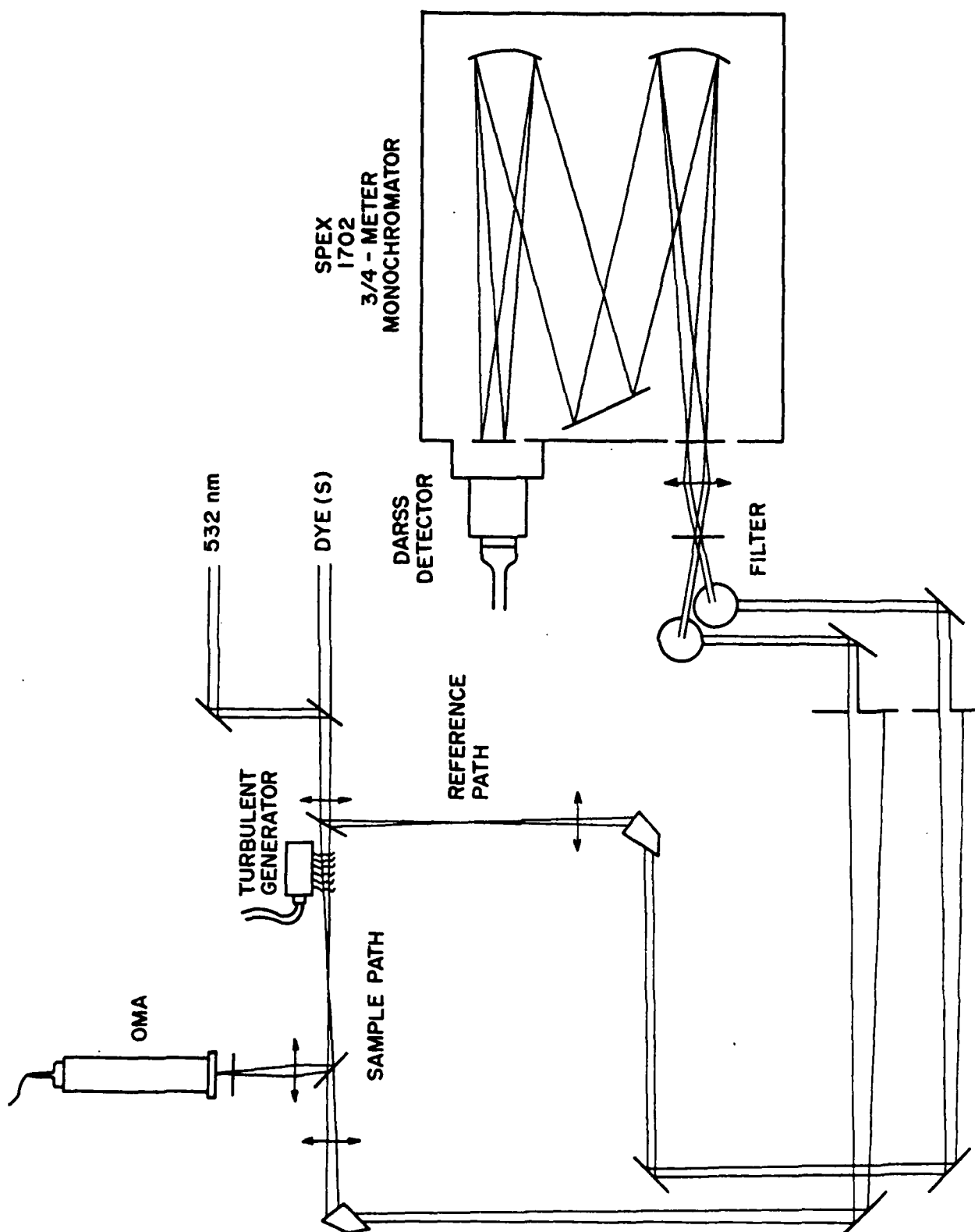


Figure 1

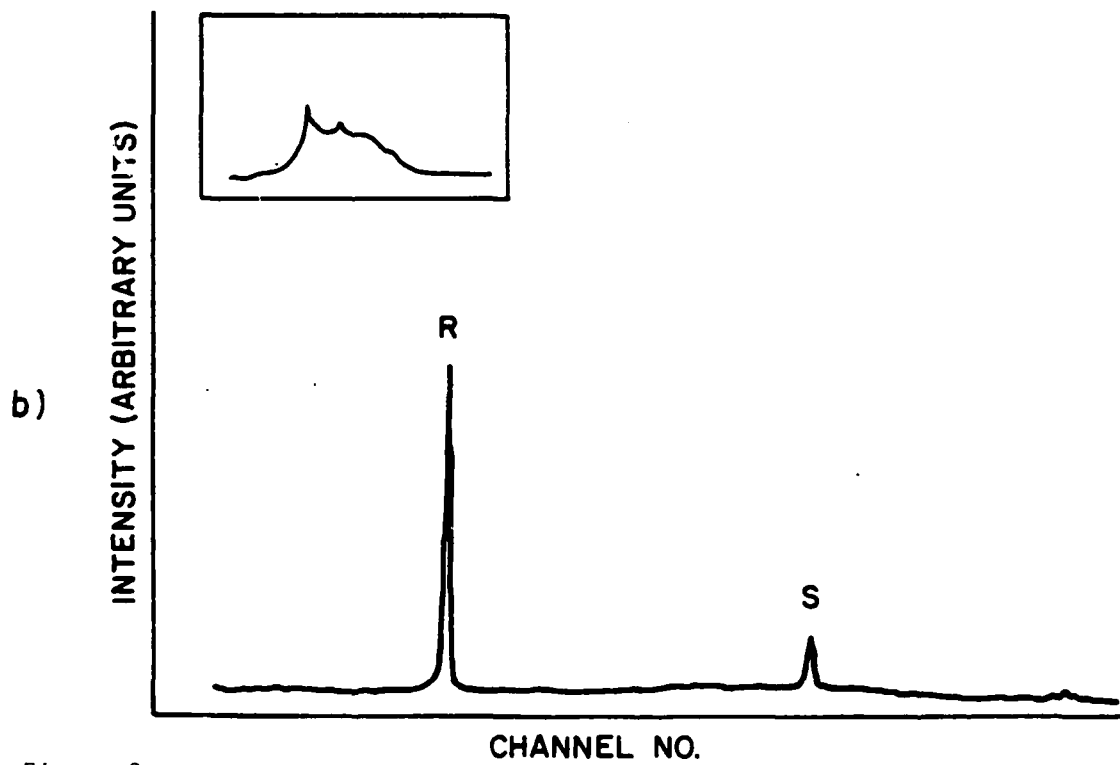
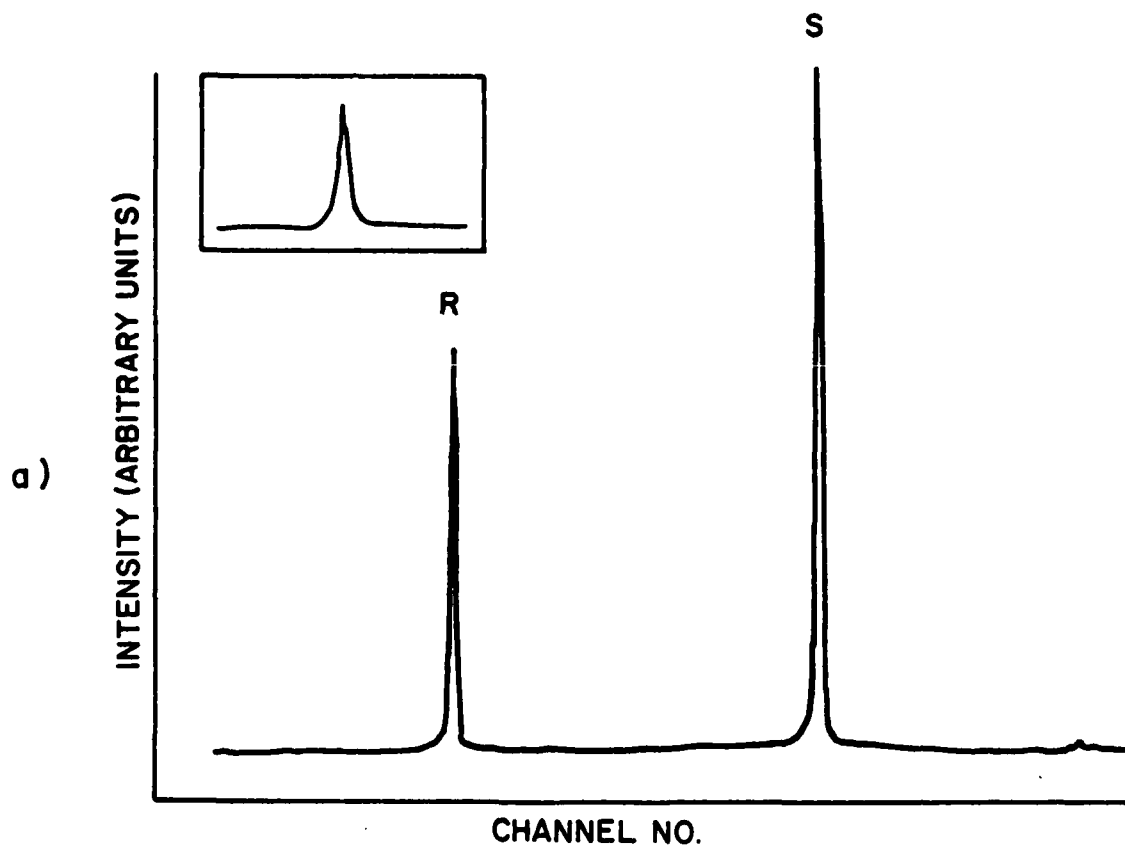


Figure 2

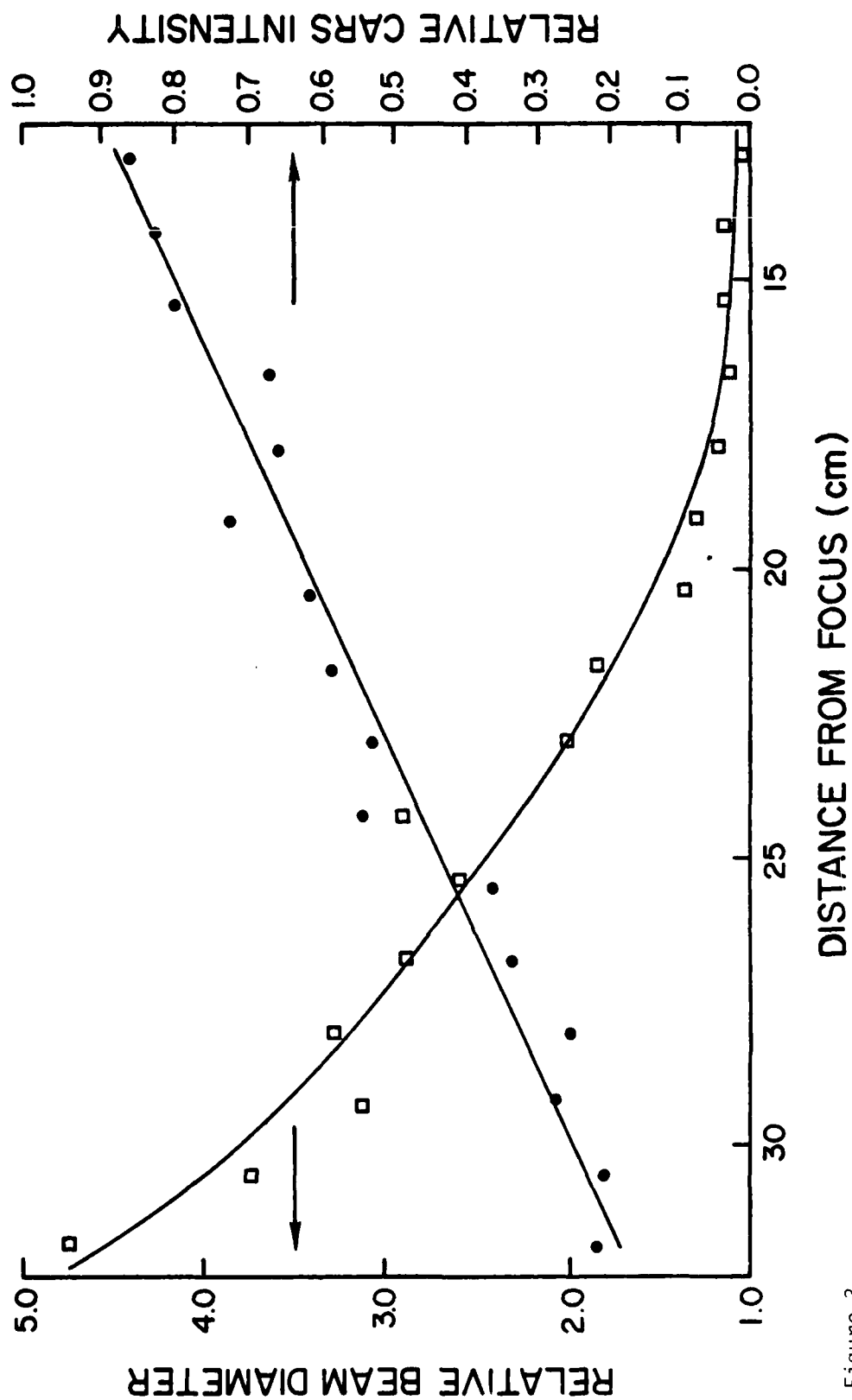


Figure 3

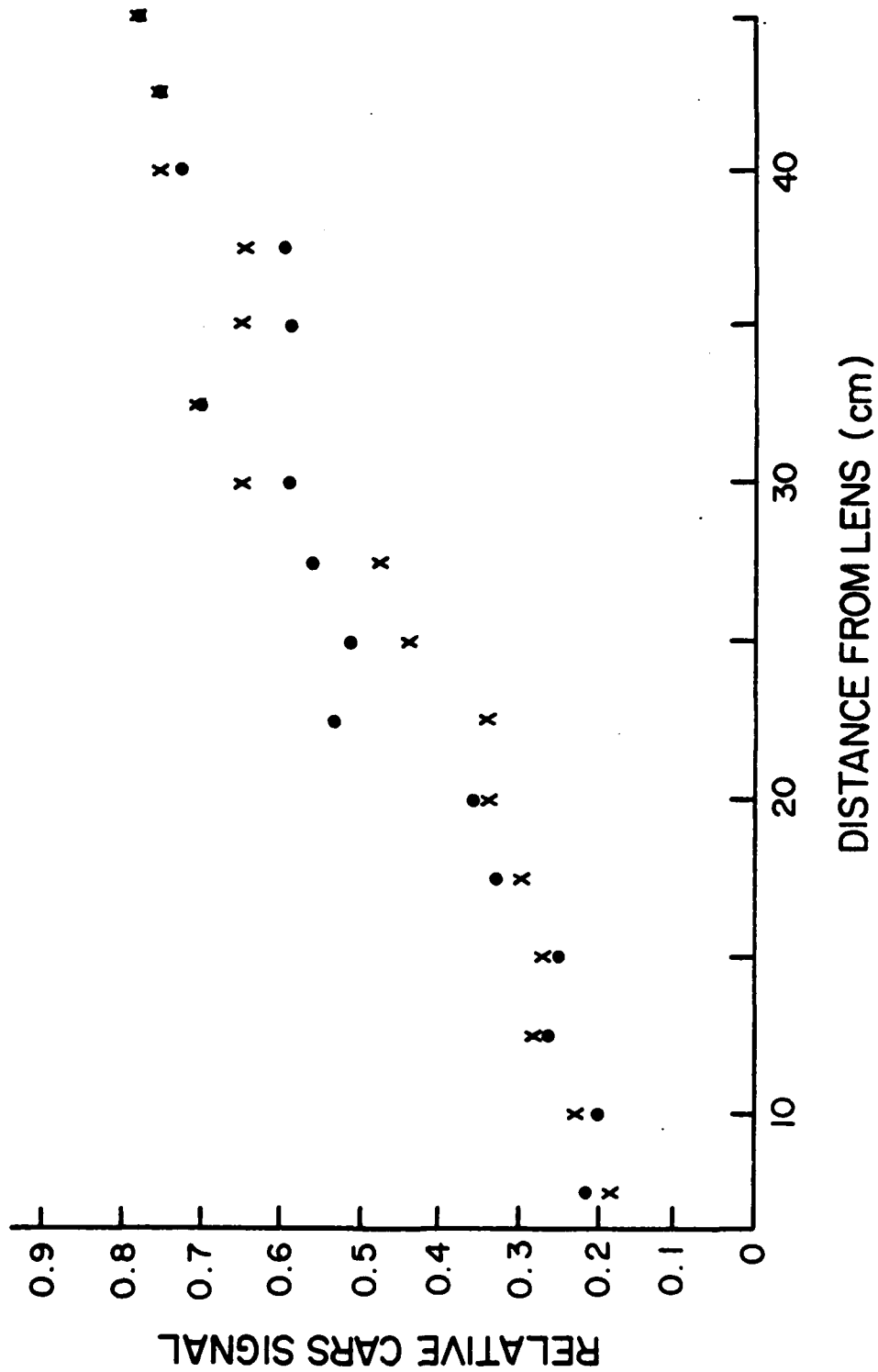


Figure 4

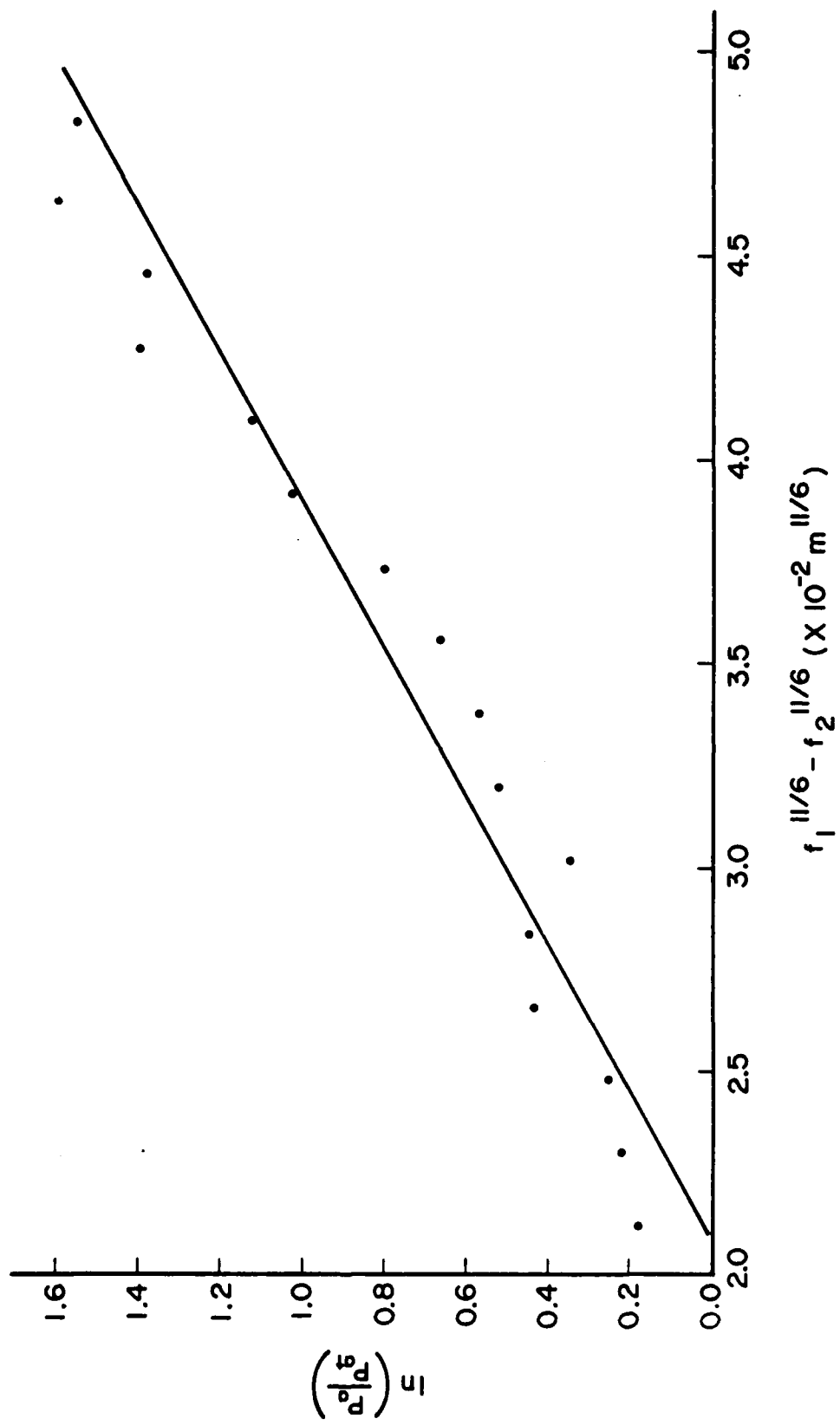


Figure 5

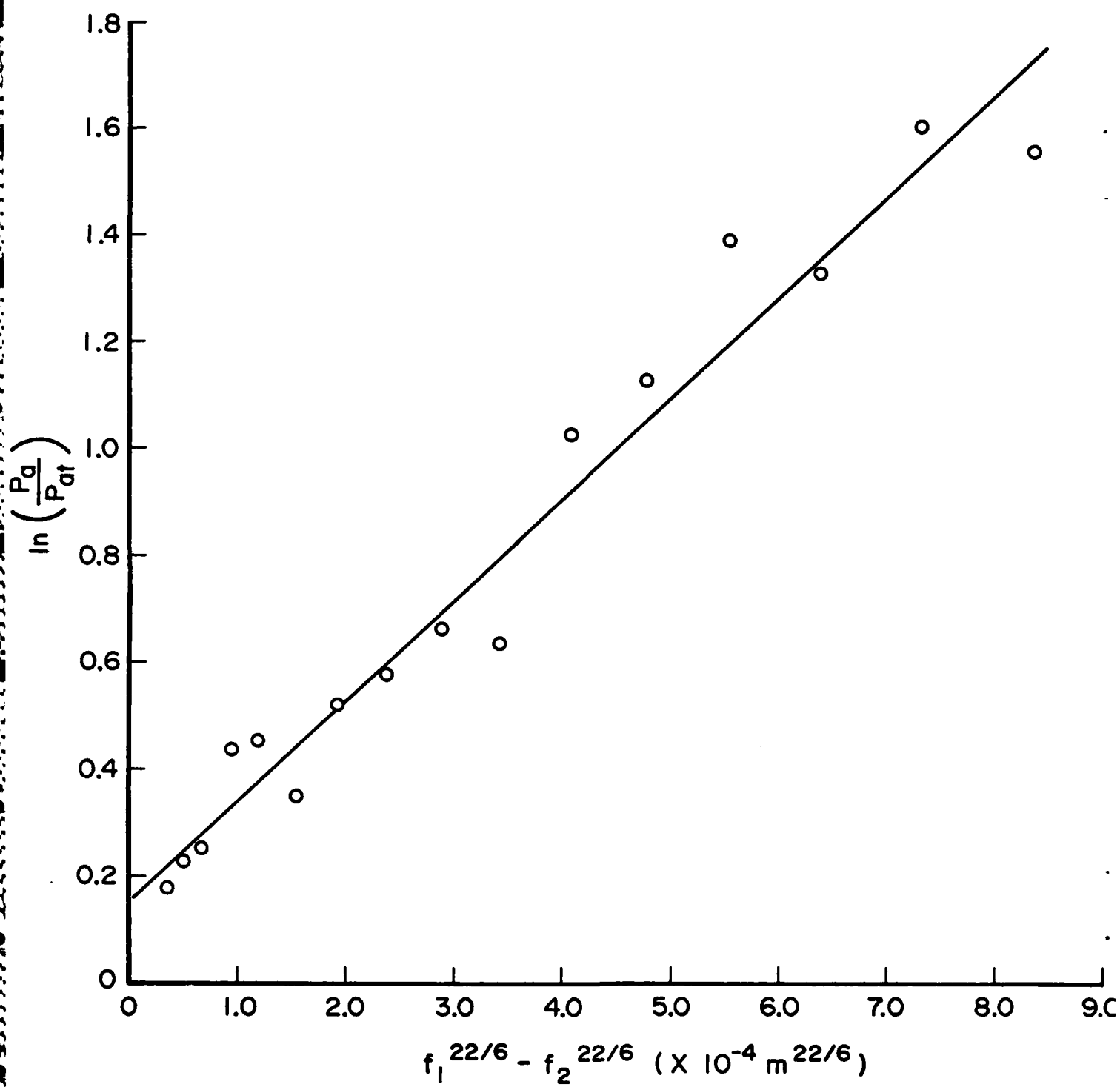


Figure 6

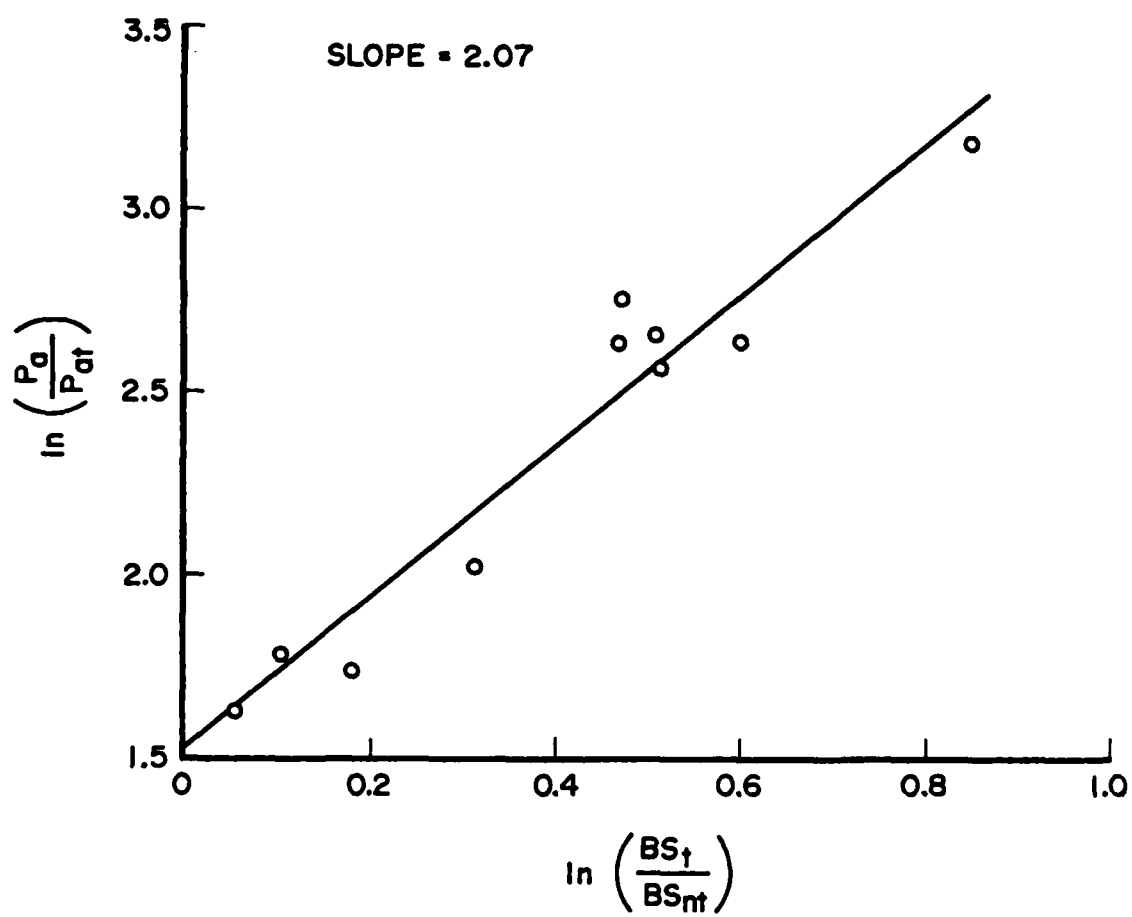


Figure 7

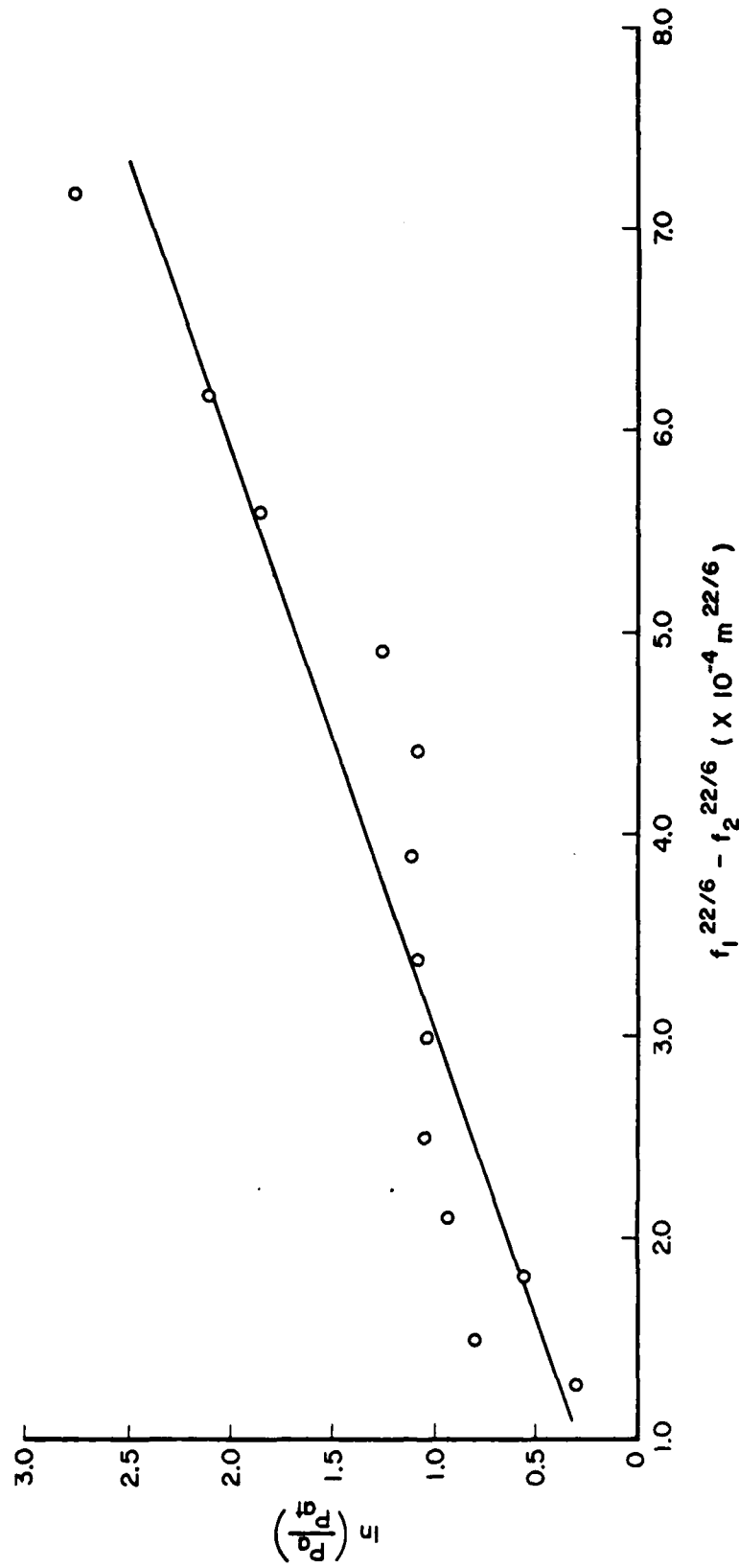


Figure 8

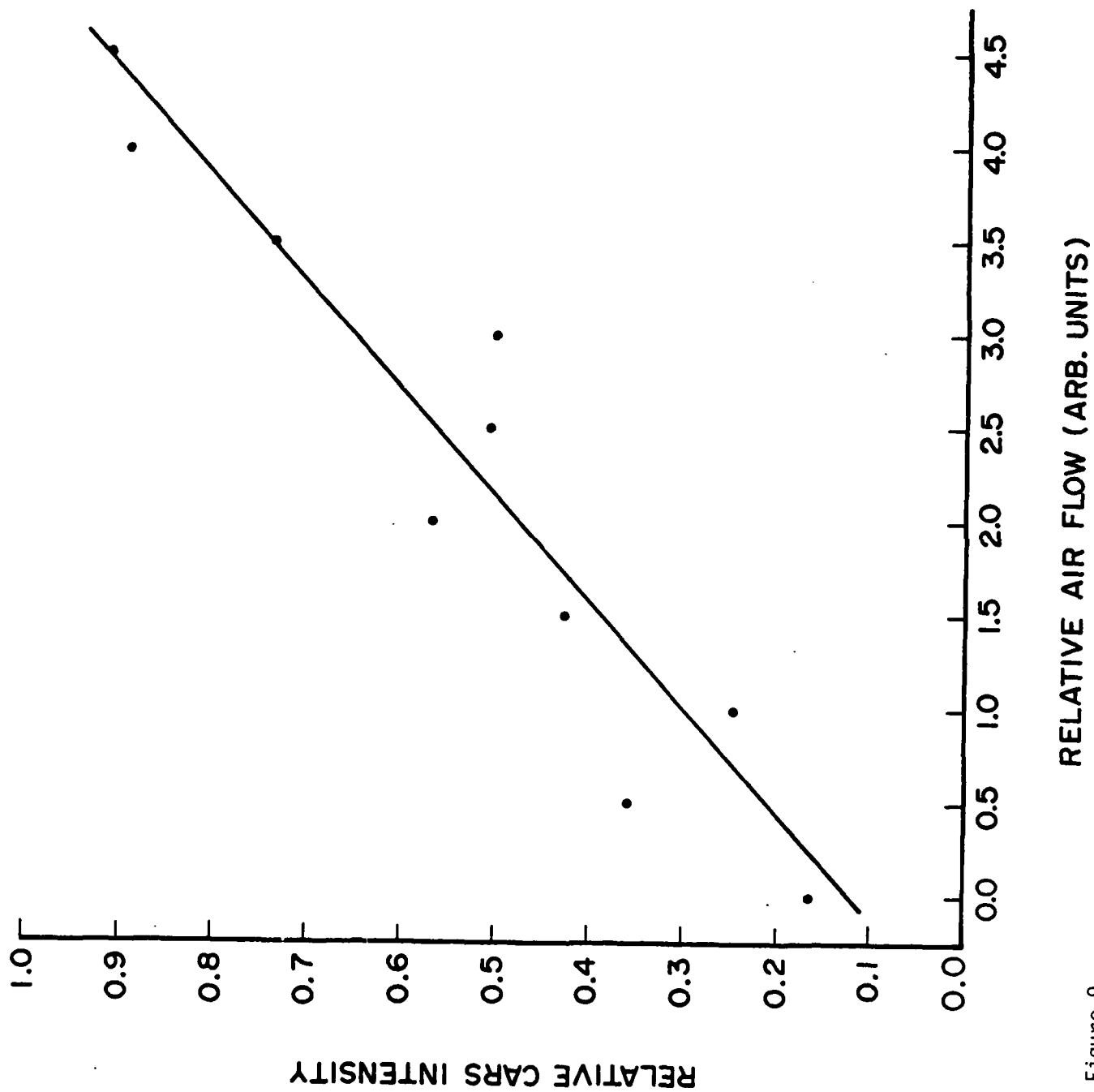


Figure 9

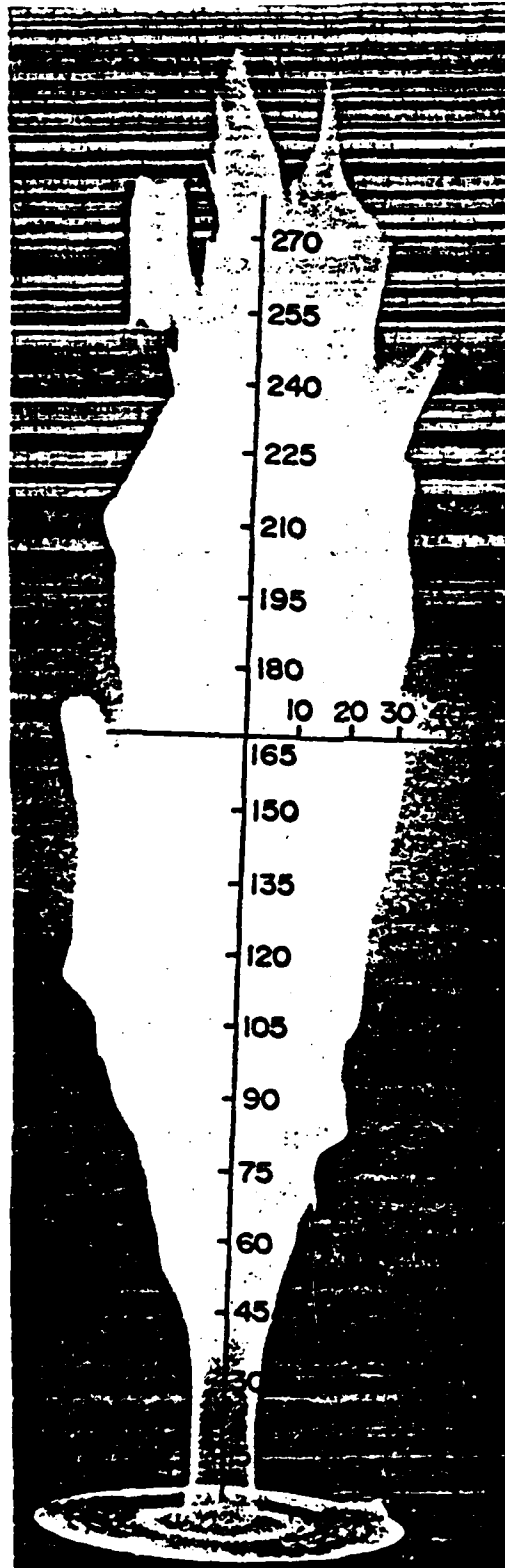


Figure 10

2.4 SIMULTANEOUS CARS THERMOMETRY AND SPECIES-CONCENTRATION MEASUREMENTS

The results of CARS thermometry and species-concentration measurements on both premixed and turbulent flames are discussed in three papers which appear on the following pages. The first paper entitled, "Flame Studies with the Coherent Anti-Stokes Raman Spectroscopy Technique," discusses measurements made on a premixed propane-air flame; in this paper single-shot thermometry and species-concentration measurements were reported for the first time. The second paper entitled, "Temperature and Species-Concentration Measurements in Turbulent Flames by the CARS Technique," demonstrates the ability of CARS to obtain data in turbulent flames. Average values, probability density functions, and correlation plots of temperature and N_2 density were obtained and compared with results from an adiabatic flame model. The third paper entitled, "CARS Thermometry and N_2 Number-Density Measurements in a Turbulent Diffusion Flame," discusses an extensive x-y profile made in a turbulent propane diffusion flame in which contour maps of the temperature, N_2 density, and fluctuations of these quantities were obtained. Probability distribution functions of temperature and N_2 density were obtained at various locations in the flame.

Flame Studies with the Coherent Anti-Stokes Raman Spectroscopy Technique

L.P. Goss* and G.L. Switzer†
Systems Research Laboratories, Inc., Dayton, Ohio
and

P.W. Schreiber‡
Air Force Wright Aeronautical Laboratories, WPAFB, Ohio

A premixed propane-air flame has been studied by the coherent anti-Stokes Raman spectroscopy technique. Single-shot thermometry has been demonstrated and the temperature uncertainty due to the broadband dye laser analyzed. A comparison with sodium-line-reversal temperatures indicates good agreement with the CARS temperatures. A retroreflecting power-reference scheme has been developed which allows simultaneous single-shot temperature and species-concentration measurements to be made in the premixed flame. An error analysis of the concentration measurements indicates that uncertainties of ~5% are obtainable with the present instrumentation.

Introduction

A PROGRAM is in progress at the AFWAL Aero Propulsion Laboratory (APL) to evaluate combustor models in environments which simulate those encountered by gas-turbine combustors. This program involves the selection and evaluation of appropriate diagnostic techniques for making time-averaged and time-resolved point measurements of velocity, temperature, and major species concentration in simulated, practical combustion environments.

Of the various optical diagnostic techniques, coherent anti-Stokes Raman spectroscopy (CARS) is considered to be one of the more promising methods for making temperature and species-concentration measurements in combustion environments. Favorable results have been obtained by various investigators using laboratory-type flame sources.¹⁻⁴ In addition, a preliminary evaluation of this technique using the large-scale AFWAL/APL combustor has been made,^{5,6} and the results are very encouraging in view of the large-scale, hostile, gas-turbine-type combustion environment in which the sensitive optical system was operated. A similar combustor evaluation has also been conducted at ONERA.⁷ Researchers at United Technologies Research Center have made successful temperature measurements using the BOX-CARS technique in a large-scale furnace-type combustor.⁸ Investigators at Shell Research Limited Thornton Research Centre have demonstrated the feasibility of using CARS to measure temperatures in a reciprocating engine.⁹

The goals of this laboratory effort are to obtain simultaneous single-shot temperatures and number densities, to determine the accuracy with which this can be accomplished, and to use these results to evaluate various model combustors. The purpose of this paper is to report the advances that have been made toward achievement of these goals.

Theoretical Considerations and Computer Codes

The third-order susceptibility which governs CARS can be expressed in abbreviated form as

$$\chi^{(3)} = \chi_n + \chi_r \quad (1)$$

where χ_n is the nonresonant contribution and χ_r is the Raman resonant contribution to the third-order susceptibility. χ_r , far from electronic resonance, is given by

$$\chi_r = \frac{2c^4}{\hbar\omega_2^2} N \sum_{v,J} \frac{\Delta(v,J) (d\sigma/d\Omega)_{v,J}}{\omega_r - \delta - i\Gamma(v,J)} \quad (2)$$

where N is the total number density of the species being probed, $\Delta(v,J)$ the population difference between the states involved in the Raman transition, ω_r the frequency of the Raman transition, δ the frequency difference between the pump ω_1 and the probe ω_2 , $\Gamma(v,J)$ the half-width at half maximum (HWHM) of the Raman transition, and $(d\sigma/d\Omega)_{v,J}$ the Raman scattering cross section.

The CARS intensity distribution is given by¹⁰

$$I_3(\omega_2) \sim \{d\omega_1^2 T(\omega_1 - \omega_2)\} d\omega_1 I_1(\omega_1) \times \{d\omega_2 I_1(\omega_2 - \omega_1 + \omega_2) I_2(\omega_2) |\chi_r(\omega_1 - \omega_2)|^2 \quad (3)$$

where T is the slit function and I_1 and I_2 are the spectral densities of the pump and Stokes sources, respectively. In broadband CARS, the Stokes bandwidth normally is sufficiently large that I_2 can be taken outside the integrals; Eq. (3) is then expressible as

$$I_3(\omega_2) \sim I_1^m I_2 \int \tilde{I}_1(\omega_1 - \delta) |\chi_r(\delta)|^2 d\delta \quad (4)$$

where I_1^m is the total pump intensity (integrated over all frequencies); I_2 is the Stokes intensity per unit frequency interval; \tilde{I}_1 is the pump intensity distribution convolved over the slit function; and the variable of integration δ varies over all values of the detuning $\omega_1 - \omega_2$.

For calculation of a CARS spectrum, the third-order susceptibility is generated according to Eqs. (1) and (2) and subsequently convolved over the pump laser linewidths and the appropriate slit function as dictated by Eq. (4). Figure 1a shows $|\chi_r^{(1)}|^2$ for N_2 at 1700 K before convolution over the pump linewidth and slit function. The spectral constants,¹¹

Presented as Paper 80-1543 at the AIAA 15th Thermophysics Conference, Snowmass, Colo., July 14-16, 1980; submitted Jan. 16, 1981; revision received Oct. 6, 1982. This paper is declared a work of the U.S. Government and therefore is in the public domain.

*Senior Chemist.

†Research Engineer.

‡Research Physicist, Aero Propulsion Laboratory.

nonresonant susceptibilities,¹² and Raman-linewidth variation with temperature and J level¹¹ were employed for this calculation. Figure 1b shows the convolved spectrum utilizing the experimentally observed 0.4-cm^{-1} HWHM Gaussian pump linewidth and a 4.0-cm^{-1} HWHM Gaussian slit function.

A nonlinear least-squares program has been developed for fitting the observed experimental spectrum as a function of temperature. It is based upon the matrix equation¹⁴

$$\Delta T = (J^T J)^{-1} J^T \Delta \phi \quad (5)$$

where J is the Jacobian matrix whose elements are defined by $J_i = dI_i/dT$ (I_i being the i th intensity and T the temperature); J^T is the transpose of the J matrix; $\Delta \phi$ is the matrix with elements $\Delta \phi_i = I_{\text{obs}} - I_{\text{cal}}$ (where I_{obs} is the i th observed experimental intensity and I_{cal} is the i th calculated intensity); and ΔT is the correction to be made to the temperature.

The fitting routine functions in the following manner: First, an initial guess of the temperature is made and a spectrum calculated. This spectrum is then used to formulate the $\Delta \phi$ matrix. Second, the Jacobian matrix is created by a numerical evaluation of the intensity-temperature derivative, and the transpose of the Jacobian and subsequent inverse of the product of the Jacobian with its transpose is formed. Next, the correction ΔT is calculated according to Eq. (5). The correction can then be made to the temperature and the resulting new temperature used as the initial guess for the next iterative cycle. The iterative process is continued until

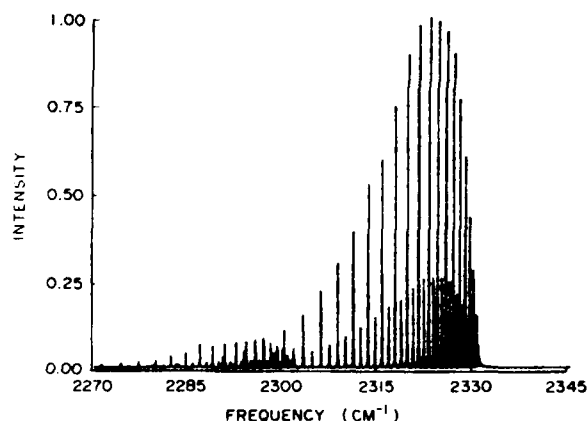


Fig. 1a $|x^{(0)}|^2$ for N_2 at a temperature of 1700 K.

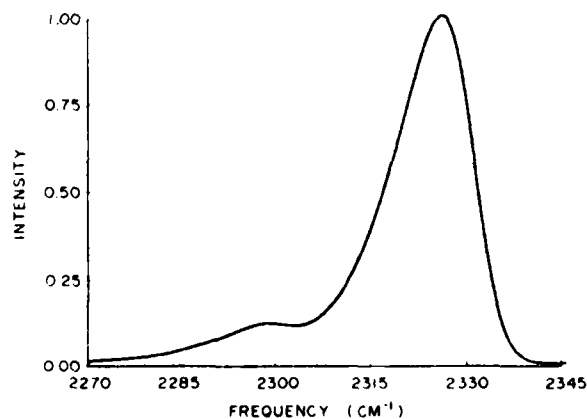


Fig. 1b $|x^{(0)}|^2$ convolved over a 4.0-cm^{-1} Gaussian slit for N_2 at a temperature of 1700 K.

variation of the calculation spectrum yields no further improvement in the fitted temperature. The dispersion—an indicator for the fitting error for each parameter—can be obtained from

$$D_i = (J^T J)^{-1} \sigma^2 / (\text{NOBS} - 1) \quad (6)$$

where $(J^T J)^{-1}$ is the i th diagonal element of the $(J^T J)^{-1}$ matrix, σ^2 the variance obtained between the observed and calculated spectra, and NOBS the total number of data points in the observed spectrum. Three cycles of this iteration are usually required for fitting the temperature. Figure 2 shows a fit that was made to single-shot data obtained from a premixed propane-air flame.

Experimental Method

The CARS experimental setup, shown in Fig. 3, consists of a Quanta-Ray Nd:YAG laser whose frequency-doubled output is used to pump an oscillator-amplifier broadband dye laser and to form the pump beams in a BOXCAR¹⁵ arrangement. The pump and probe beams are crossed and focused by a 50-cm-focal-length lens having a BOXCAR half-angle of 3 deg, which produces a measured beam-interaction length of ~ 1 mm. A retroreflecting beam splitter is positioned after the focusing lens, and the split beam is used to form the reference path. The resulting CARS signals from both the sample and reference paths are predispersed by Pellin-Broca prisms and coupled into a Spex 1702 monochromator.

A Tracor-Northern TN1710 DARSS Reticon is used as the detector for the CARS system. The DARSS consists of an intensified, gated (photocathode microchannel plate) unit coupled with a linear (one-dimensional) diode array (Reticon). The major advantages of this detector over vidicon units are the large linear dynamic range and the smaller blooming and cross talk between channels. The experimentally measured dispersion of the Spex 1702 monochromator is 2.4 cm^{-1} per $50\text{-}\mu$ DARSS channel. The combined slit function of the monochromator and DARSS detector has been determined to be Gaussian in shape with a width of 4.0 cm^{-1} HWHM. To circumvent the single dimensionality of the detector, the entrance slit of the monochromator is rotated 90 deg from its usual vertical position to a horizontal position. This allows the various CARS signals to be aligned side by side on different regions of the detector. The CARS signals are recorded simultaneously by the DARSS for analysis at a later date. This experimental configuration allows simultaneous determination of temperature and species concentration, as will be discussed later.

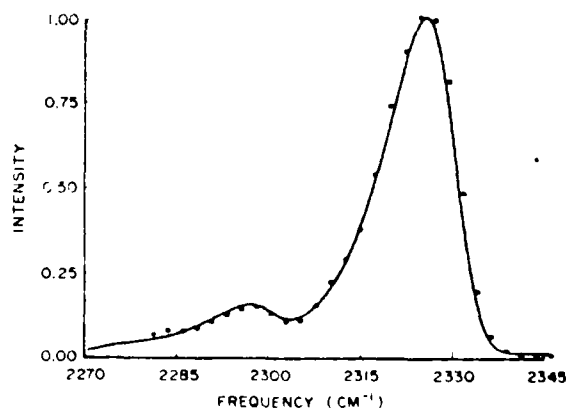


Fig. 2 Typical fit of the N_2 Q-branch bandshape. Fitted temperature was $1760\text{ K} \pm 15\text{ K}$. Dots represent experimental values, and the solid curve is theoretically calculated spectrum.

The burner employed for these studies consists of a Perkin-Elmer assembly (No. 290-0107) with an adjustable nebulizer (No. 303-0352) for seeding during sodium-line-reversal measurements. The assembly was fitted with a water-cooled argon sheath which was employed for stabilizing the flame. Both acetylene-air and propane-air premixes can be used in the burner for flame studies. The assembly was mounted on two translation stages which allowed radial and axial profiles of the flame to be constructed. The observed flame consisted of an inner and an outer portion, both of which could be independently controlled. The premixed propane-air flame, shown in Fig. 4, is conical in shape with a visible flame height of ~ 80 mm.

Single-Shot Thermometry Studies

The ability to perform single-shot thermometry is of the utmost importance in practical turbulent combustors where the temporal variation of the flame temperature can be quite large. Single-shot CARS thermometry in flames was first demonstrated at UTRC¹ and has been subsequently used in various studies.¹⁷ To obtain a temperature during a single laser shot, a substantial portion of the Q branch of N_2 must be probed. This is accomplished by the broadband dye laser discussed in the experimental section. The broadband CARS signal which is produced is detected by a multichannel analyzer—in this case, the TN1710 Reticon—and stored for data analysis. The temperature-fitting routine is used to reduce the raw CARS spectrum for temperature determination.

To test the ability of the laboratory CARS system to produce single-shot spectra of relatively hot flames, a series of studies was conducted on the premixed Perkin-Elmer burner. This burner (as will be demonstrated by its profile) provides a relatively uniform temperature distribution. For this study, the burner was operated at an airflow of 1.75 standard liters/min of air and 0.082 standard liters/min of propane. This corresponds to a fuel-air ratio of 0.0767 and an equivalence ratio of 1.20. Adiabatic flame calculations¹⁸ for this propane-air mixture predict an average temperature of 2196 K. The average temperature measured by the CARS technique for 500 individual data shots was $2174 \text{ K} \pm 90 \text{ K}$. The temperature histogram of the experimental data is shown in Fig. 5. The bin size for the temperature pdf was 100 K. These data were obtained 10 mm above the burner surface on the centerline of the inner fuel tube. Because of the flame stability at the measurement location, the observed distribution is considered to be primarily due to the uncertainty in the temperature measurement. This would indicate a 4% uncertainty in the temperature measurement. The individually fitted errors given by the dispersion indicator were all less than 30 K for the 500 measurements in the flame.

The dispersion indicator, however, is a measure only of the deviation of the observed spectrum from the calculated spectrum at a given temperature. It reflects the error in the fitted temperature—not the actual error in the temperature measurement. The actual temperature error is potentially quite complex due to the dependence of the temperature upon several parameters. One of the major sources of error for single-shot thermometry is the broadband dye laser. The broadband dye can be a source of both a random error due to

the dye nonuniformity and a systematic error due to dye tuning. Careful concentration tuning of the dye laser can essentially eliminate the systematic error. Elimination of the random error, however, is difficult to achieve. This nonuniformity is due to mode competition which is taking place under the dye gain curve. The measured deviation from channel to channel of the broadband dye as measured from the nonresonant susceptibility induced from a nonresonant gas is $\sim 20\%$. The uncertainty induced in the measurement can be determined from Eq. (7), assuming that the dye

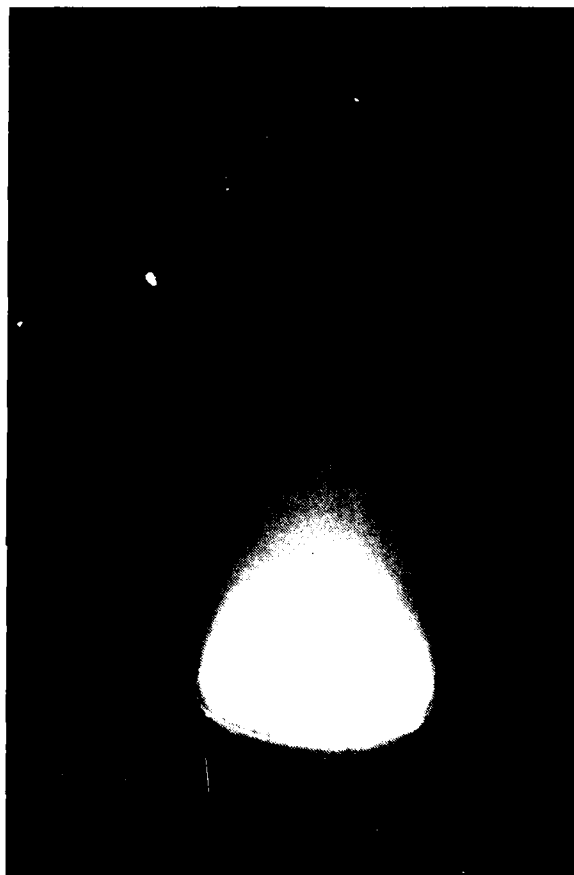


Fig. 4 Premixed near-stoichiometric propane-air flame employed in flame studies.

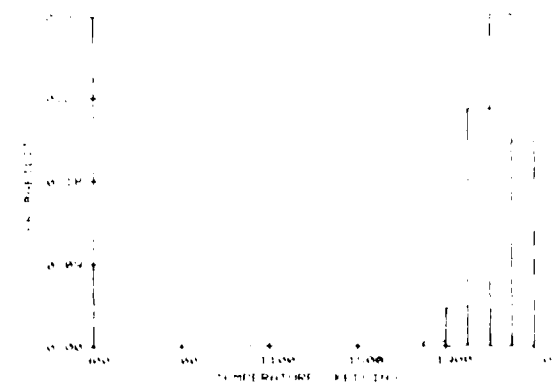


Fig. 5 Temperature pdf obtained from near-stoichiometric propane-air flame. Average temperature was $2174 \text{ K} \pm 90 \text{ K}$.

Fig. 3 Schematic of CARS apparatus employed in present studies

AD-A173 414 LASER OPTICS/COMBUSTION DIAGNOSTICS(U) SYSTEMS RESEARCH 2/3

AD-A173 414 LASER OPTICS/COMBUSTION DIAGNOSTICS(U) SYSTEMS RESEARCH 2/3

LABS INC DAYTON OH RESEARCH APPLICATIONS DIV

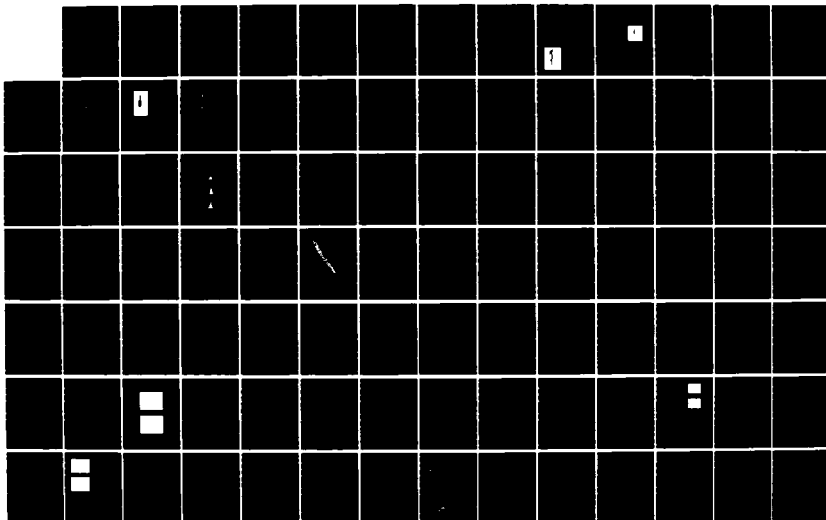
L P GOSS ET AL. JUL 86 SRL-6603 AFMAL-TR-86-2023

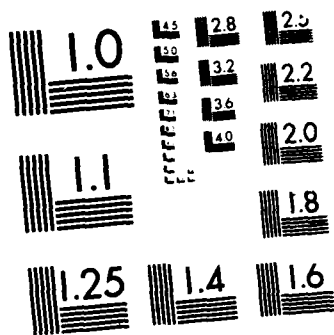
UNCLASSIFIED F33615-80-C-2054 F/G 21/2 NL

UNCLASSIFIED F33615-80-C-2054 F/G 21/2 NL

UNCLASSIFIED F33615-80-C-2054 F/G 21/2 NL

UNCLASSIFIED F33615-80-C-2054 F/G 21/2 NL





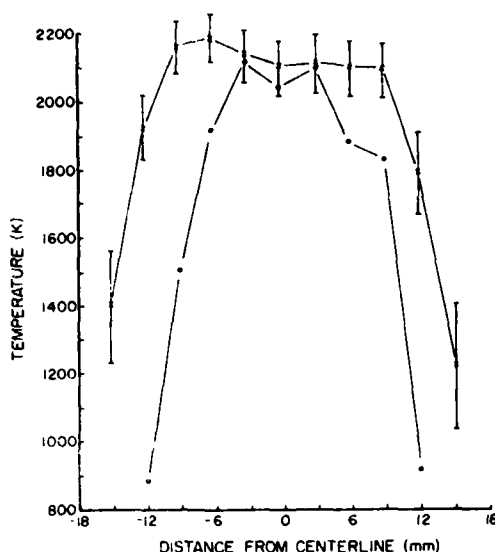


Fig. 6 Radial profiles of the premixed propane-air flame. x and o denote axial position 10 and 55 mm above burner surface, respectively. Error bars indicate observed temperature fluctuation.

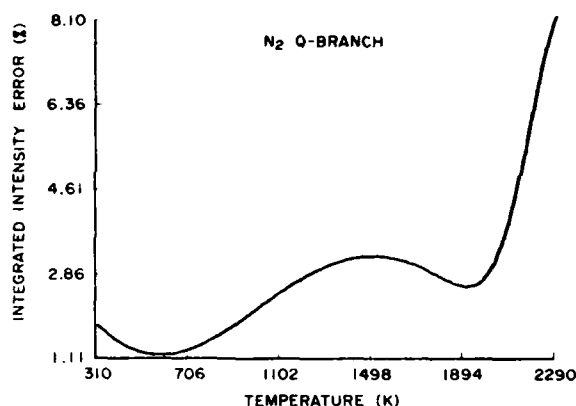


Fig. 7 Relative uncertainty in integrated bandspace ratio R_T as function of temperature for 4% uncertainty in measured temperature.

fluctuation is uncorrelated with other spectral variables¹⁷:

$$\sigma_i^2 = \frac{I}{\sigma_m^2} \sum_i \left(\frac{dI_i}{dT} \right)^2 \quad (7)$$

where σ_m^2 is the variance of the dye laser intensity from channel to channel, and dI_i/dT is the change in the CARS intensity at frequency i due to a change in the temperature. The temperature uncertainty determined from the variance of the dye laser is $\sim 3\%$ (60 K) at 2000 K, which is the minimum uncertainty to be expected from the single-shot temperature measurement. This is in good agreement with the observed experimental uncertainty of 4%, which indicates that the dye fluctuation is mainly responsible for the uncertainty in the CARS temperature measurement.

To test the accuracy of the CARS temperature measurement, a sodium-line-reversal experiment was conducted on the same flame under similar conditions. As mentioned earlier, the burner is equipped with a nebulizer which allows the inner flame region to be seeded for sodium-line-reversal measurements. The reversal arrangement used in this study was described in detail in Ref. 18. The results from individual measurements on this flame yielded a temperature

of $2201 \text{ K} \pm 30 \text{ K}$, in good agreement with the CARS measurement results.

A radial profile at two different axial locations was conducted on the propane flame and is shown in Fig. 6. As can be seen from these profiles, the temperature of the flame is fairly uniform over a broad region and drops sharply at the edges. As one probes higher in the flame, the high-temperature region becomes less broad due to the conical shape of the flame. This is demonstrated by the profile at the 55-mm axial position. The bars shown in this figure indicate one standard deviation of the single-shot data. At the edge of the flame, large deviations were encountered due to the interaction of the flame and the outer ambient air.

Simultaneous Number-Density and Temperature Determinations

Concentration measurements by the CARS technique have, in the past, been carried out by two methods. The first method consists of integrating the total CARS signal from the species of interest,⁴ and the second involves monitoring the interference of the resonant and nonresonant CARS signals.¹² In the latter method, the CARS bandspace contains the concentration information. Both methods require that the temperature be known before a concentration can be determined. In a nonturbulent, nonvarying flame, the average temperature will suffice for the concentration measurement. However, in a turbulent temperature-varying flame environment, the temperature and concentration must be measured simultaneously. This is possible from single-shot CARS data because the general shape of the Q -branch profile can be used to determine the temperature, while the integrated area of the Q branch can be used to determine the concentration. The integrated intensity can be an absolute or a relative measurement. The former, however, is extremely difficult. The latter is performed through the use of a ratioing technique in which the experimental parameters are canceled. The power-reference scheme found to yield the best results is shown in Fig. 3. It consists of retroreflecting $\sim 20\%$ of the pump and Stokes beams after the 50-cm focusing lens but before the beams are focused. The CARS signal generated in the reference is then isolated by a right-angle prism and routed to the spectrometer. The major advantage of this configuration is that the sample and reference paths are formed by the same lens and, because of the retroreflection, display the same spatial and temporal characteristics. With this arrangement, correlations between sample and reference intensities are consistently 94 to 97%.

The number density as determined from the integrated-CARS-intensity measurement for a major species (concentration $> 20\%$ by volume) in an atmospheric flame is given by (see the Appendix)

$$N_T = N_{300} \lambda (R_T \cdot P_T) / P_{300} \quad (8)$$

where N_T is the nitrogen number density at temperature T , N_{300} the nitrogen number density at 300 K, R_T the ratio of the integrated bandspace of the CARS spectrum at 300 K to the CARS spectrum at temperature T , P_T the experimentally measured integrated CARS power at temperature T , and P_{300} the experimentally measured integrated CARS power at 300 K. The ratio R_T takes into account the change in the Raman linewidths and population redistribution with temperature. The probable error in the measurement of N_T from probable errors in R_T , P_T , and P_{300} (assuming no intensity losses due to turbulence effects) is given by

$$\Delta N_T = \left| \left(\frac{\partial N_T}{\partial R_T} \right)_{P_T, P_{300}}^2 \Delta R_T^2 + \left(\frac{\partial N_T}{\partial P_{300}} \right)_{R_T, P_T}^2 \Delta P_{300}^2 + \left(\frac{\partial N_T}{\partial P_T} \right)_{R_T, P_{300}}^2 \Delta P_T^2 \right| \quad (9)$$

Combining Eqs. (8) and (9), performing the differentiation, and simplifying yields

$$E(N_T) = [1/4 E(R_T)^2 + 1/4 E(P_T)^2 + 1/4 E(P_{300})^2]^{1/2} \quad (10)$$

The uncertainty in the ratio R_T for a 4% temperature uncertainty is shown in Fig. 7. The uncertainty in R_T for a flame temperature of 2200 K is ~5%. The uncertainty in P_T and P_{300} without turbulence and assuming no problems from photon statistics (due to the large signal levels) is the correlation error observed between the sample and reference (~6%). Substituting the uncertainty in R_T and correlation error into Eq. (10) indicates that 5.1% uncertainty should be observed in the number-density measurement at 2200 K. The CARS signals during these experiments were maintained at a high intensity to avoid problems from photon statistical noise which would be added directly to the uncertainty of P_{300} and P_T . Turbulence compensation, if required, would necessitate an in situ reference scheme.^{19,20}

In order to check the error prediction given by Eq. (10), a series of 500 simultaneous measurements of temperature and N_2 concentration were made in the premixed propane burner. The fuel and air flows were adjusted to give an equivalence ratio of 1.2, as used in the earlier thermometry studies. The simultaneous data which were obtained are plotted in Fig. 8. Superimposed on these data are the results of an adiabatic flame calculation¹⁶ for a propane-air flame. The adiabatic equilibrium flame calculations are based upon the assumption that each homogeneous volume of gas within the flame

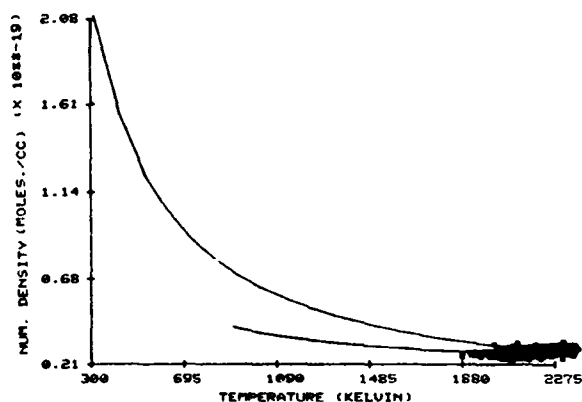


Fig. 8 Correlation plot of simultaneously determined temperature and N_2 concentration (dots) in premixed propane-air flame. Solid line represents results from adiabatic-equilibrium flame calculation.

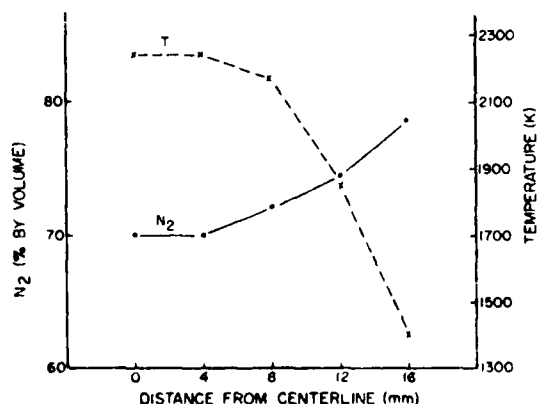


Fig. 9 Simultaneously determined temperature and N_2 concentration for radial profile of premixed propane-air flame.

consists of an equilibrium mixture of gases at adiabatic temperature. These calculations neglect radiative heat and mass transfer. The solid line in Fig. 8 is the adiabatic equilibrium calculation performed for fuel-to-air equivalence ratios between 0.1 and 3.0 using the computer code of Gordon and McBride.¹⁶ Most of the data are grouped very near the adiabatic flame curve, shown in this figure as a solid line. The upper curve corresponds to the fuel-lean case (excess air) and the lower curve corresponds to the fuel-rich case (excess fuel). The stoichiometric point (the point at which the fuel and air are mixed in such proportions that neither is in excess) is near the point where the two curves meet. The equivalence ratio of 1.2 indicates that the mixture was slightly fuel-rich, as demonstrated by the data which lie primarily on the lower fuel-rich curve near the stoichiometric point. The experimentally measured uncertainty in the concentration measurement (assuming the flame temperature and concentration to be constant) was 5.2%, which is in close agreement with the predicted uncertainty.

Figures 9 and 10 depict simultaneous measurement profiles which were made on the propane-fueled premixed burner. Figure 9 is a radial profile of the flame starting from the center 10 mm above the burner surface. As shown, the temperature drops as the edge of the flame is approached, while the percent volume of N_2 increases. An axial profile of the flame along the centerline is shown in Fig. 10. The figure indicates that the temperature drops off high in the flame, while the percent volume of N_2 increases.

Next, a study was conducted to determine whether the CARS instrument with its simultaneous measurement capability could follow the variation of the temperature and N_2 number density as a function of the fuel-air ratio of the premixed burner. To demonstrate this point, the propane fuel flow was varied to give fuel-to-air ratios ranging from 0.0614 (fuel lean) to 0.1074 (fuel rich). The temperature and N_2 number density were determined for 100 shots for each flow

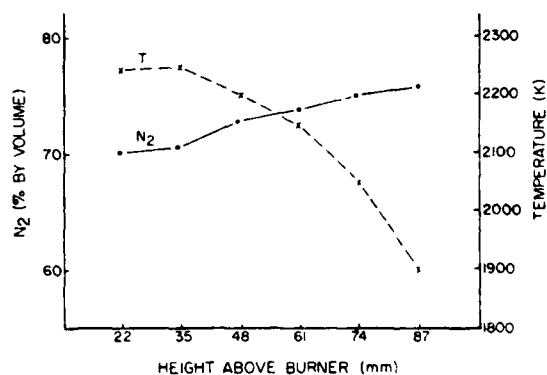


Fig. 10 Simultaneously determined temperature and N_2 concentration for axial profile of premixed propane-air flame.

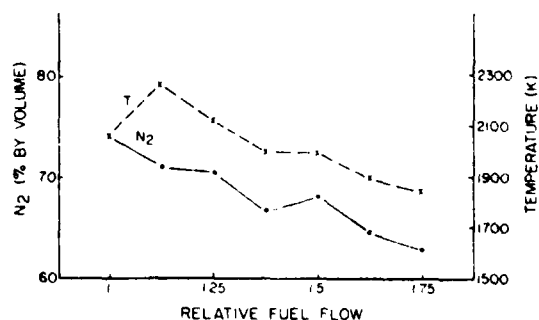


Fig. 11 Variation of simultaneously obtained temperature and N_2 concentration with relative fuel flow.

Table 1 Comparison of temperatures and number densities obtained from CARS measurements with those predicted by ideal flame calculations from the measured fuel-air ratios ($m = \text{CARS measurement}; f = \text{flow}$)

T_m	T_f	$(\%N_2)_m$	$(\%N_2)_f$
2165	2209.5	74.0 ± 4.3	72.8
2300	2269.4	71.0 ± 6.5	71.0
2122	2195.6	70.5 ± 7.0	69.1
2000	2110.7	66.7 ± 10	67.2
2006	2011.1	68.3 ± 5	65.3
1901	1930.0	64.4 ± 4	63.4
1853	1844.5	62.7 ± 9	61.8

condition. The data from this experiment are plotted in Fig. 11. These data indicate that a temperature maximum occurs at a near-stoichiometric fuel-to-air ratio and decreases as the fuel flow is increased or decreased relative to this point. The N_2 concentration shows a steady decline with an increase in fuel flow. The comparison with the predicted temperature and number densities based upon the fuel and air flows is given in Table 1. The results agree quite well with the predicted values based upon the equilibrium flame calculations.

Conclusions

Results of single-shot thermometry studies on a near-stoichiometric premixed propane-air flame show good agreement with results for sodium-line-reversal measurements. The experimentally measured temperature uncertainty was determined to be $\sim 4\%$. The uncertainty which was observed in these measurements can be related almost entirely to the nonuniformity from pulse to pulse of the broadband dye laser.

A retroreflection power-reference scheme has been developed which allows simultaneous temperature and N_2 -concentration measurements to be made in the propane-fueled flame. An error analysis of the concentration uncertainty was conducted, and the results closely follow the measured uncertainties in the propane-air flame ($\sim 5\%$). Results from profiling the propane-air flame and variation of the fuel-to-air ratios are reported. The measured temperature and N_2 -species concentration show good agreement with those predicted from adiabatic-equilibrium flame calculations.

Appendix: Derivation of Number-Density Equation

The third-order susceptibility can be rewritten to show its explicit dependence upon the number density

$$\chi^{(3)} = N\chi' \quad (A1)$$

where

$$\chi' = \frac{\chi_{nr}}{N} + \frac{2c^2}{\hbar\omega_2} \sum_{v,J} \frac{\Delta(v,J)}{\omega_r - \delta - i\Gamma} \frac{d\sigma}{d\Omega} \quad (A2)$$

Equation (A2) suggests that if the nonresonant susceptibility is too large to be neglected, the number density must be known before the CARS spectrum can be calculated and used to fit the temperature. However, without a temperature, the number density cannot be determined. To circumvent this dilemma, the N_2 number density is assumed to scale as the adiabatic flame calculations suggest, and these values are used to calculate and scale the nonresonant-susceptibility ratio given in Eq. (A2). This allows the CARS spectra to be calculated and the temperature to be fit, which, in turn, permits a nitrogen number density to be determined from the integrated CARS intensity. The experimentally measured integrated intensity is given by

$$\Sigma = 2\pi Q I_n A \tau / \sqrt{3} \hbar \omega_1 = K I_n \quad (A3)$$

where Q represents the monochromator and detector efficiency; A is the cross-sectional area of the focused laser beams; τ is the temporal pulse width of the Gaussian pump and probe lasers; and I_n is defined by

$$I_n(T) = \int I_i(\omega_i) d\omega_i \\ = I_1^m I_2 N_2^2 \int f_i(\omega_i - \delta) |\chi_i'(\delta)|^2 d\delta d\omega_i \quad (A4)$$

To account for the variation in the Stokes and pump lasers, a measurement is made simultaneously in the flame and the reference path. In this set of studies, the reference contained ambient air. Ratioing results in

$$\frac{\Sigma_{\text{flame}}}{\Sigma_{\text{ref}}} = \frac{k I_n(T)}{k' I_n(300)} = \frac{k I_1 I_2 N_2^2 \int f_i(\omega_i - \delta) |\chi_i'(\delta)|^2 d\delta d\omega_i}{k' I_1 I_2 N_{300}^2 \int f_i(\omega_i - \delta) |\chi_i'(\delta)|^2 d\delta d\omega_i} \quad (A5)$$

which reduces to

$$\Sigma_{\text{flame}} / \Sigma_{\text{ref}} = k N_2^2 / k' N_{300}^2 R_T \quad (A6)$$

where R_T is the ratio of the integrated CARS bandshapes. To cancel the experimental constants k and k' , a second measurement is made with ambient air in the sample. Ratioing these measurements yields

$$\frac{\Sigma_{\text{flame}} / \Sigma_{\text{ref}}}{\Sigma_{\text{no flame}} / \Sigma_{\text{ref}}} = \frac{k N_2^2 / k' N_{300}^2 R_T}{k / k'} = \frac{N_2^2}{N_{300}^2} \quad (A7)$$

Rearranging Eq. (A7) to solve for number-density results in Eq. (8).

Acknowledgment

This work was conducted, in part, under Contract F33615-80-C-2054 with the AFWAL Aero Propulsion Laboratory at Wright-Patterson Air Force Base, Ohio.

References

- Eckbreth, A.C., Hall, R.J., and Shirley, J.A., "Investigations of Coherent Anti-Stokes Raman Spectroscopy (CARS) for Combustion Diagnostics," AIAA Paper 79-0083, New Orleans, La., June 1979.
- Moya, F., Druet, S.A.J., and Taran, J.P.E., "Gas Spectroscopy and Temperature Measurement by Coherent Raman Anti-Stokes Scattering," *Optics Communications*, Vol. 13, 1975, pp. 169-174.
- Eckbreth, A.C. and Hall, R.J., "CARS Thermometry in a Sooting Flame," *Combustion and Flame*, Vol. 36, 1979, pp. 87-98.
- Roh, W.B., "Coherent Anti-Stokes Raman Scattering of Molecular Gases," Air Force Aero Propulsion Laboratory, Wright-Patterson Air Force Base, Ohio, AFAPL-TR-77-47, Aug. 1977.
- Switzer, G.L., Roquemore, W.M., Bradley, R.P., Schreiber, P.W., and Roh, W.B., "CARS Measurements in a Bluff-Body-Stabilized Diffusion Flame," *Applied Optics*, Vol. 18, 1979, pp. 2343-2345.
- Switzer, G.L., Goss, L.P., Roquemore, W.M., Bradley, R.P., Schreiber, P.W., and Roh, W.B., "Application of CARS to Simulated Practical Combustion Systems," *Journal of Energy*, Vol. 4, Sept.-Oct. 1980, pp. 209-215.
- Taran, J.P.E., "CARS Flame Diagnostics," Paper presented at the CARS Meeting of the Institute of Physics, AERE Harwell, March 1979.
- Eckbreth, A.C., "CARS Thermometry in Practical Combustors," *Combustion and Flame*, Vol. 39, 1980, p. 137.
- Stenhouse, I.A., Williams, D.R., Cole, J.B., and Swords, M.D., "CARS Measurements in an Internal Combustion Engine," *Applied Optics*, Vol. 18, 1979, pp. 3819-3825.
- Hall, R.J., Verdick, J.F., and Eckbreth, A.C., "Pressure Induced Narrowing of the CARS Spectrum of N_2 ," *Optic Communications*, Vol. 35, 1980, p. 69.
- Hall, R.J., "CARS Spectra of Combustion Gases," *Combustion and Flame*, Vol. 35, 1979, pp. 47-60.
- Eckbreth, A.C. and Hall, R.J., "CARS Concentration Sensitivity with and without Nonresonant Background Suppression,"

United Technologies Research Center, East Hartford, Conn., R80-354628-1, Final Report on ONR Contract N00014-79-C-0351, 1980.

¹³Hall, R.J., "Pressure-Broadened Linewidths for N₂ Coherent Anti-Stokes Raman Spectroscopy Thermometry," *Applied Spectroscopy*, Vol. 34, 1980, p. 700.

¹⁴Kim, A., "Computer Programming in Physical Chemistry Laboratory: Least Squares Analysis," *Journal of Chemical Education*, Vol. 47, 1970, pp. 120-122.

¹⁵Eckbreth, A.C., "BOXCARS: Cross-Beam Phase-Matched CARS Generation in Gases," *Applied Physics Letters*, Vol. 32, 1978, p. 421.

¹⁶Gordon, S. and McBride, B.J., "Computer Program for Calculation of Complex Equilibrium Composition Rocket Performances, Incident and Reflected Shocks, and Chapman-Jouguet Detonations," NASA SP273, May 1971; see also, NTIS N78-17724, March 1976.

¹⁷Tolles, W.M. and Turner, R.D., "A Comparative Analysis of the Analytical Capabilities of Coherent Anti-Stokes Raman Spectroscopy (CARS) Relative to Raman Scattering and Absorption Spectroscopy," *Applied Spectroscopy*, Vol. 31, 1977, p. 96.

¹⁸Goss, L.P. and Switzer, G.L., "Application of Coherent Anti-Stokes Raman Scattering to Combustion Media," Air Force Wright Aeronautical Laboratories, Wright-Patterson Air Force Base, Ohio, AFWAL-TR-80-2122, Feb. 1981.

¹⁹Goss, L.P. and Schreiber, P.W., "Assessment of the Application of CARS to Combustion Diagnostics," *Proceedings of the 1980 International Conference on Lasers*, New Orleans, La., July 1980, pp. 220-235.

²⁰Shirley, J.A., Hall, R.J., Verdick, J.F., and Eckbreth, A.C., "New Directions in CARS Diagnostics for Combustion," AIAA Paper 80-1542, Snowmass, Colo., July 1980.

Temperature and Species-Concentration Measurements in Turbulent Flames by the CARS Technique

L.P. Goss,* G.L. Switzer,† and D.D. Trump‡
Systems Research Laboratories, Inc., Dayton, Ohio
and

P.W. Schreiber§
Air Force Wright Aeronautical Laboratories, Wright-Patterson Air Force Base, Ohio

Simultaneous temperature and N_2 -concentration data have been obtained employing a 10-Hz coherent anti-Stokes Raman spectroscopy system on two propane-air turbulent-jet diffusion flames with Reynolds numbers of 2000 and 6000. Average values, probability density functions, and correlation plots show reasonable trends for both centerline and radial profiles of the turbulent flames.

Introduction

THE study of turbulent combustion on a fundamental level requires detailed spatially resolved information of the instantaneous values (acquired simultaneously) of a large number of scalar quantities such as temperature, species concentration, velocity, and pressure. It is important to measure such scalar quantities in order to produce the single and joint moments required by various modeling theories. The goal of the present study was to experimentally measure these quantities [single and joint probability density functions (pdf)] using nonperturbing experimental techniques in relatively simple turbulent flames. The experimental data can be compared with simple theories¹ (i.e., adiabatic flame calculations) and can be used to test and/or develop more complex theoretical models.²

Coherent anti-Stokes Raman spectroscopy (CARS)^{3,4} is an attractive experimental technique for this purpose because it can provide time-resolved (~ 10 ns) and spatially resolved (~ 0.1 mm³) (Ref. 5) measurements of temperature⁶⁻¹⁰ and major flame species simultaneously,¹¹⁻¹³ without appreciably perturbing the flame. This paper presents results obtained on propane-air turbulent-jet diffusion flames at moderate Reynolds numbers (Re , ~ 2000 -6000, based upon the cold airflow). These results are presented in the form of average values, scalar pdf's, and correlation plots of species concentration vs temperature. Comparisons with adiabatic flame calculations show good agreement with the simple model.

Experimental Methods

The CARS experimental setup, shown in Fig. 1, consists of a Quanta-Ray Nd:YAG laser whose frequency-doubled output is used to pump an oscillator-amplifier dye laser and to form the pump beams in a BOXCAR⁵ arrangement. The pump and probe beams are crossed and focused by a 50-cm-focal-length lens having a BOXCAR half-angle of 3 deg, which translates into a measured interaction length of ~ 1 mm. A retroreflection beam splitter is positioned after the focusing lens, and the split beam is used to form the reference path. The resulting CARS signals from both the sample and reference paths are predispersed by Pellin-Broca prisms and coupled into a Spex 1702 monochromator. The sample signal

is coupled to the monochromator by a series of splitters whose purpose will be discussed later. The experimentally measured resolution was 4.0 cm⁻¹ half-width, half-maximum (HWHM).

A Tracor-Northern TN1710 DARSS Reticon is used as the detector for the CARS system. The DARSS consists of an intensified, gated (photocathode microchannel plate) unit coupled with a linear (one-dimensional) diode array (Reticon). The major advantages of this detector over vidicon units are the large linear dynamic range and the smaller blooming and cross-talk between channels. To circumvent the single dimensionality of the detector, the entrance slit of the monochromator is rotated 90 deg from its usual vertical position to a horizontal position. This allows the various CARS signals to be aligned side by side on different regions of the detector.¹² The experimentally measured dispersion of the monochromator-detector system was 2.4 cm⁻¹/channel of the Reticon. The CARS signals are recorded simultaneously by the DARSS for analysis at a later date. The analysis includes both temperature and species-concentration fitting^{11,12} of the experimental spectrum. This experimental configuration allows simultaneous determination of temperature and species concentration. Unless otherwise reported, the temperatures and N_2 concentrations reported for the turbulent flames were determined from 500 single-shot measurements. The reported uncertainties correspond to one standard deviation.

The burner employed for these studies consists of a Perkin-Elmer assembly (No. 290-0107) with an adjustable nebulizer (No. 303-0352) for seeding.¹² The burner assembly consists of a concentric tube arrangement which can be operated independently for either a premix flame or a turbulent diffusion flame.

System Calibration

To determine a temperature from the Q-branch spectrum of N_2 , only the bandshape describing the populational distribution of the molecules is required; however, if number

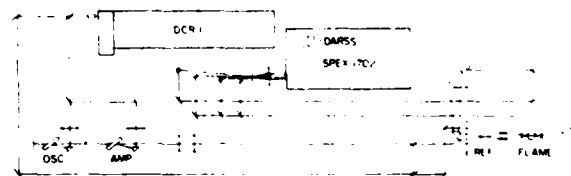


Fig. 1 Experimental CARS arrangement used for turbulent-flame studies.

Presented as Paper 82-0240 at the AIAA 20th Aerospace Sciences Meeting, Orlando, Fla., Jan. 11-14, 1982; submitted March 24, 1982; revision received Nov. 8, 1982. This paper is declared a work of the U.S. Government and, therefore, is in the public domain.

*Senior Chemist.

†Research Engineer.

‡Associate Engineer.

§Research Physicist, Aero Propulsion Laboratory, Member AIAA.

densities are desired, either an absolute or a relative measurement of the integrated CARS intensity of the Raman transition must be made. The former is extremely difficult, if not impossible, in most cases. The latter is performed through the use of a ratioing technique in which most of the experimental parameters are canceled. The power reference scheme found to yield the best results is shown in Fig. 1. It consists of retroreflecting ~20% of the sample, pump, and probe beams after the 50-cm focusing lens but before the beams are focused. The reference beams are then focused and crossed before the 50-cm lens and allowed to pass back through the lens. The CARS signal generated in the reference is then isolated by a right-angle prism and routed to the spectrometer. The major advantage achievable by this arrangement is that the sample and reference paths are formed by the same lens and, because of the retroreflection, display the same spatial and temporal characteristics. With this arrangement sample and reference intensity correlations are consistently between 94% and 97%.

If index-of-refraction gradients should become a problem in turbulent diffusion flames, the referencing scheme shown in Fig. 1 would have to be replaced with an in situ referencing scheme.^{14,15} These schemes are based upon monitoring the third-order nonresonant susceptibility which is produced simultaneously with the nonresonant Q-branch CARS signal. Since this nonresonant signal is produced along the same path as the resonant signal and experiences the same turbulence, it can be used to normalize the signal degradation induced by the turbulence. In the present study, the flame size and turbulence strength were such that they posed no serious index-of-refraction gradient problems.

The number density as determined by a CARS measurement for a major species at 1 atm pressure (concentration > 20% by volume) is given by¹²

$$N_T = N_{300} \sqrt{(R_T \times P_T) / P_{300}} \quad (1)$$

where N_T is the nitrogen number density at temperature T ; N_{300} is the nitrogen number density at 300 K; $R_T = \{P_{300} d\nu / \{P_T d\nu\}$ is the ratio of the calculated integrated powers of the CARS signal at 300 K to the CARS signal at temperature T ; P_T is the experimentally measured integrated CARS power at temperature T ; and P_{300} is the experimentally measured integrated CARS power at 300 K.

The ratio R_T takes into account the change in the Raman linewidths and population redistribution with temperature. The probable error in the measurement of N_T from probable errors in R_T , P_T , and P_{300} (assuming no intensity losses due to turbulence effects) is given by

$$\Delta N_T = \left[\left(\frac{\partial N_T}{\partial R_T} \right)^2_{R_T, P_{300}} \Delta R_T^2 + \left(\frac{\partial N_T}{\partial P_{300}} \right)^2_{R_T, P_T} \Delta P_{300}^2 + \left(\frac{\partial N_T}{\partial P_T} \right)^2_{R_T, P_{300}} \Delta P_T^2 \right]^{1/2} \quad (2)$$

Combining Eqs. (1) and (2), performing the differentiation, and simplifying yields

$$E(N_T) = [1/4 E(R_T)^2 + 1/4 E(P_T)^2 + 1/4 E(P_{300})^2]^{1/2} \quad (3)$$

The uncertainty in the ratio R_T in the 1200-2200 K range is essentially equal to the uncertainty in the temperature measurement. The uncertainty in P_T and P_{300} without turbulence and assuming no problems from photon statistics (due to the large signal levels) is the correlation error observed between the sample and reference. The uncertainty with the single-shot temperature measurement has been determined to be ~4% (Ref. 12). Substituting the temperature uncertainty and correlation errors into Eq. (3) indicates that a 4.7% uncertainty should be observed in the number-density

measurement. Photon statistical noise would be added directly to the uncertainty of P_{300} and P_T if the signal levels were to become small. Turbulence compensation, if required, would necessitate an in situ reference scheme.^{14,15}

To calibrate the 10-Hz CARS system in a known flame environment, a premixed near-stoichiometric mixture of propane and air was burned in the concentric tube burner. This flame has been studied extensively by two-line fluorescence and sodium-line reversal¹² and is known to have a steady, flat temperature distribution across its profile. The burner was operated at an airflow of 1.75 standard liters/min of air and 0.082 standard liters/min of propane. This corresponds to a fuel-to-air ratio of 0.0767 and an equivalence ratio of 1.20. Adiabatic flame calculations for a propane-air mixture predict an average temperature of 2200 K and an N_2 concentration of 2.54×10^{18} molecules/cm³. The average temperature measured by the CARS technique was 2170 ± 90 K, with an N_2 concentration of $(2.64 \pm 0.14) \times 10^{18}$ molecules/cm³. The experimentally measured concentration uncertainty is 5.3%, which is in close agreement with the predicted value of 4.7%. The average temperature and N_2 concentrations indicate quite good agreement between measured and predicted results.

The temperature histogram of 500 single CARS shots is shown in Fig. 2a. The bin size for the temperature and concentration pdf's was 100 K and 1.0×10^{18} molecules/cm³, respectively. The concentration histogram is shown in Fig. 2b, and the correlation of the two measured parameters is shown in Fig. 2c. Most of the data are grouped very near the adiabatic flame curve, shown in this figure as a solid line. The adiabatic equilibrium flame calculations are based upon the assumption that each homogeneous volume of gas within a turbulent flame consists of an equilibrium mixture of gases at adiabatic temperature. These calculations neglect radiative heat and mass transfer. The solid line in Fig. 2c is the adiabatic equilibrium calculation performed for fuel/air equivalence ratios between 0.1 and 3.0 using the computer code of Gordon and McBride.¹⁶ Initially the fuel and air were at atmospheric pressure (750 Torr) and 298 K. The equivalence ratio of 1.2 indicates a slightly fuel-rich mixture, as demonstrated by the data which lie primarily on the lower fuel-rich curve.

Turbulent-Flame Studies

A problem associated with multichannel-analyzer devices is the limitation in the linear dynamic range in single-shot operation. An estimate of the dynamic range which is required for studying a turbulent flame can be gained from consideration of the change in the intensity of the CARS signal with a temperature variation of 300 to 2200 K. The change in the intensity of the fundamental band of the Q branch of N_2 is ~240 for this temperature range. However, in determining a temperature from the Q-branch spectrum above 1200 K, a measurement must also be made of the hotband intensity. At 2200 K this intensity is one-fifth that of the fundamental. Because of the background variation of the OMA detectors, a signal of at least 20 counts must be maintained if the hotband is to be used for temperature determination. Thus a dynamic range of 1200 to 1 must be maintained by the OMA detector. Figure 3 demonstrates this limitation of the Tracor-Northern DARSS. The three single shots shown in this figure were taken in a turbulent propane diffusion flame. As indicated, the CARS spectra in the temperature range 1300-2300 K could be obtained, but cooler CARS signals saturated the detector. Most OMA devices, however, have only a 200-count dynamic range during single-shot operation. Since no OMA devices—either vidicon or Reticon—exist today which have the vast dynamic range required for the temperature regime 300-2300 K, an alternative approach must be pursued.

A solution to this problem is to incorporate a series of splitters, as shown in Fig. 1, into the CARS system and split

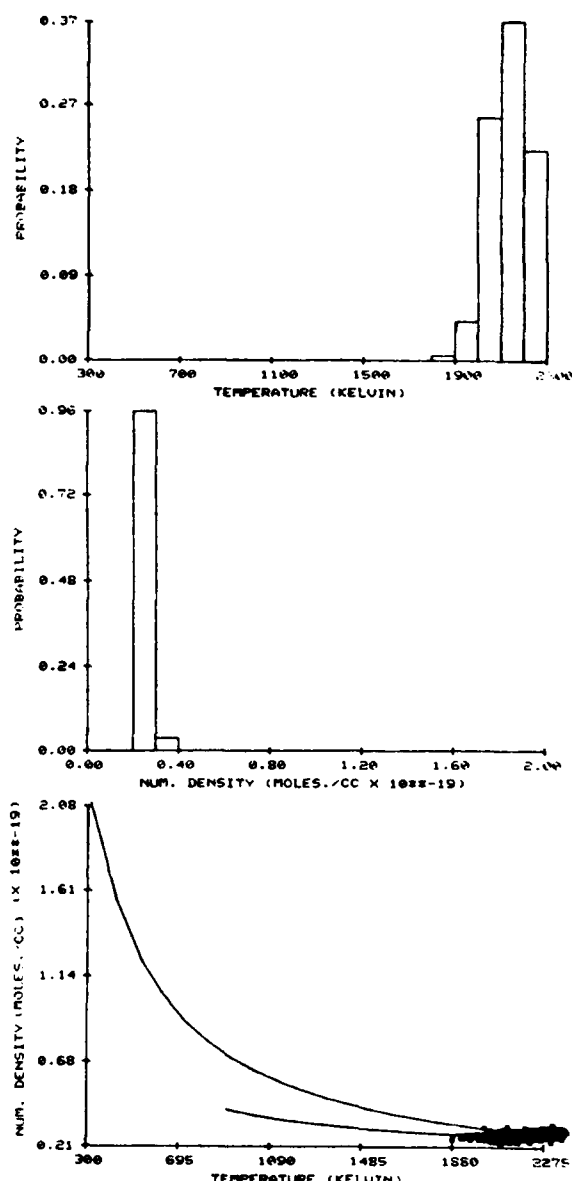


Fig. 2 Data obtained in the near-stoichiometric premixed flame. a) temperature pdf, b) concentration pdf, and c) correlation plot of temperature and concentration vs. adiabatic equilibrium calculation results (solid).

the Q-branch signal into several signals which differ in amplitude. By choosing the correct ratio of splitters, the effective dynamic range of the OMA can be increased from 200:1 to ~4000:1. In the arrangement shown in Fig. 1, a 4% reflection from a glass splitter along with a 20% dichroic reflector was used. This series of splitters was chosen because it allowed the entire temperature range 300-2300 K to be obtained on a single OMA detector. The high-temperature region, 2300-1500 K, was covered by the total reflector (the far-left peak in Fig. 3a). The medium temperature range, 1500-800 K, was covered by the 20% splitter (the center peak in Fig. 3b) and the low-temperature range, 800-300 K, by the 4% splitter (the far-right peak in Fig. 3c). By incorporation of a power reference into the system, simultaneous temperature and concentration measurements are obtained in highly turbulent flames.

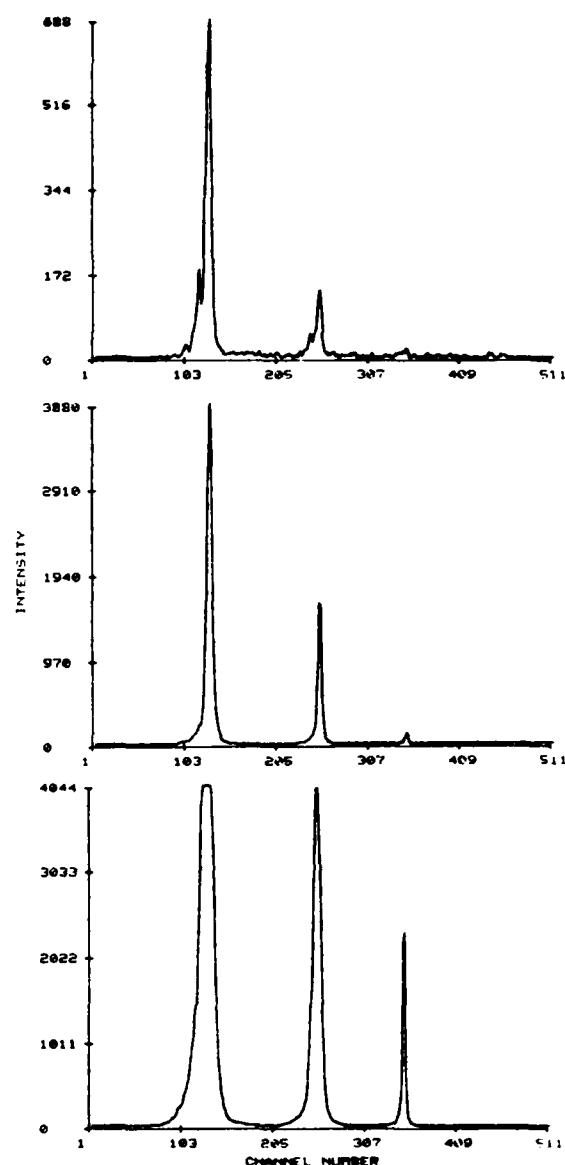


Fig. 3 Single-shot CARS spectra obtained with splitter arrangement depicting a) high-temperature leg (left peak, fitted temperature 2270 ± 40 K), b) medium-temperature leg (center peak, fitted temperature 1110 ± 35 K), and c) low-temperature leg (right peak, fitted temperature 500 ± 50 K).

The first turbulent flame studied by the 10-Hz CARS system is shown in Fig. 4. The burner conditions under which this flame was produced were a fuel flow of 1.9 liters/min of propane which was surrounded by an outer airflow of 17 liters/min, corresponding to a Reynolds number of 2000. The ratio of mass flows of air to fuel was ~6 to 1. The flame turbulence was thus dominated by the shear generated by the two mass flows. The flame displayed a high degree of large-scale turbulent structures and a length of 30 cm. The splitter technique was used to follow the temperature fluctuations. The retroreflection referencing scheme was employed for simultaneous concentration and temperature measurements. The measurements were made 16.5 cm above the fuel tube and directly on the centerline.

The data obtained from this study are shown in Fig. 5. The temperatures were observed to vary greatly from room

temperature to near stoichiometric in this flame. A pdf of the temperature data is shown in Fig. 5a. A 100-K bin size was used in this plot. The data seem to indicate a multimodal temperature distribution. This is primarily because the flame was highly susceptible to room-air currents and moved in and out of the probe volume. The low-temperature distribution is believed to be due primarily to the edge of the flame and outside air, while the higher temperatures are due to the central flame regions. The N_2 -concentration pdf for the N_2 -concentration data is shown in Fig. 5b. The bin size in this plot is 1.0×10^{18} molecules/cm³. The concentration shows a dominant peak at 3.0×10^{18} molecules/cm³, which corresponds to the hot-flame zones. The higher concentrations of N_2 are due to the lower-temperature regions. The cross-correlation between the simultaneous temperature and N_2 concentration is shown in Fig. 5c. Superimposed on these data are results from an adiabatic flame calculation for a propane-air flame. The upper line corresponds to a fuel-lean mixture and the lower, to a fuel-rich mixture. The turning point in the higher-temperature region corresponds to a stoichiometric mixture. As can be seen, the experimental data follow the general trends of the adiabatic flame calculations. The average temperature at this flame location was 1340 K, with a standard deviation of 520 K. The average concentration was 5.81×10^{18} molecules/cm³, with a standard deviation of 3.45×10^{18} molecules/cm³. Because of the low Reynolds number employed and the susceptibility of the flame to room-air currents in the laboratory, further profiling of the flame was not undertaken. Instead, the decision was made to increase the Reynolds number of the air flow to achieve a flame which was more turbulent and less susceptible to room-air currents.

The flame which was studied next is shown in Fig. 6. The flame length under the higher air flow conditions (40 liters/min air and 0.95 liters/min propane) was reduced to 145 mm. The air-to-fuel mass-flow ratio was ~ 28 to 1. This flame is characterized primarily by smaller-scale turbulence which is driven by the high airflow rates. A centerline profile of this turbulent flame was conducted with the 10-Hz CARS systems. The results are given in Table 1 and shown in Fig. 7. At the tip of the flame (position 145 mm), the average temperature is 868 K, with an average N_2 concentration of 9.63×10^{18}



Fig. 4 R_p - 2000 turbulent diffusion flame; film exposure - 100 ms.

molecules/cm³. The temperature pdf is strongly bimodal, which is characteristic of air entrapment in this region.¹⁷ The concentration pdf is also strongly bimodal. The agreement between the temperature and concentration data shown in the correlation plot for the 145-mm position and the simple adiabatic flame calculations is evident, even in this extremely turbulent region of the diffusion flame.

At the 105-mm centerline position, the average temperature has increased to 1350 K and the average concentration has decreased to 6.55×10^{18} molecules/cm³. The temperature pdf indicates that less air entrapment is occurring. The same result can be seen in the concentration pdf. The maximum average temperature is observed at the 75-mm position. The temperature and concentration pdf's are much sharper than those of the previous centerline positions, indicating that this region is predominantly hot burning gases with little or no cold fuel or air. The 75-mm position corresponds to the fuel-stagnation

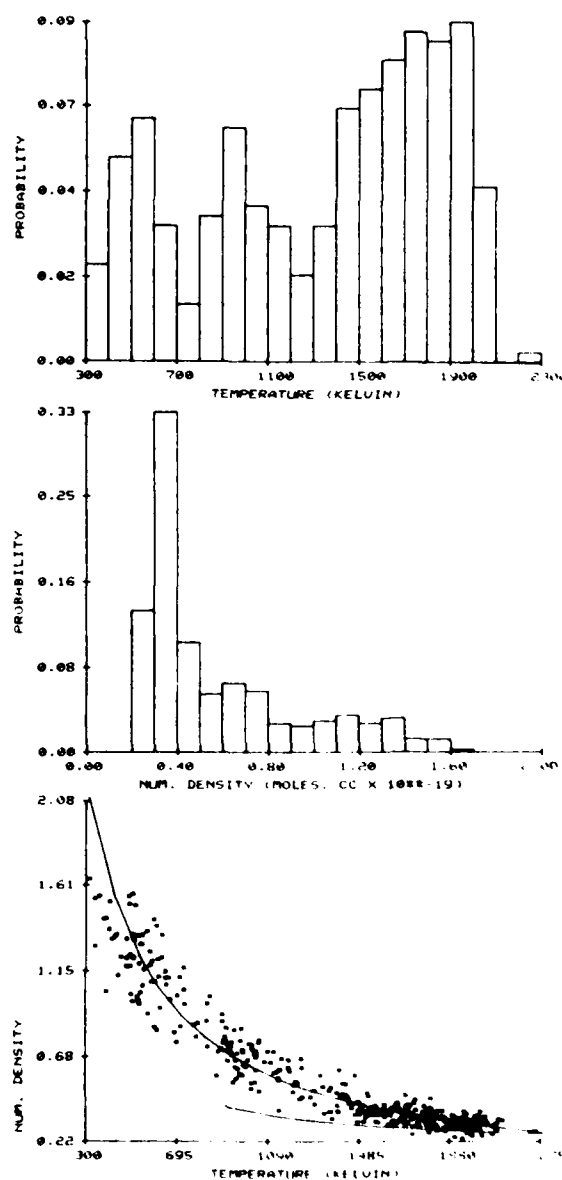


Fig. 5 R_p - 2000 turbulent flame. a) Temperature pdf, b) concentration pdf, and c) correlation plot of temperature and concentration vs. adiabatic equilibrium calculation results (solid).

point—the point at which the fuel jet becomes totally turbulent. This conclusion is justified by the fact that as the flame is probed lower on the centerline, the cold fuel jet can be seen in the CARS data. The fuel—because of its large nonresonant susceptibility—drastically increases the nonresonant background, distorting the observed CARS N_2 spectra. To obtain valid data in the fuel jet region, either the fuel composition must be measured simultaneously with the N_2 concentration and temperature or a background suppression technique must be employed.¹⁸ While no attempt was made to incorporate a background-cancellation scheme into the present CARS system to permit profiling of the fuel jet region, such a study will be conducted in the near future.

A radial profile of the reaction zone of the flame at a position 30 mm above the burner surface was conducted. In this study the position of the probe volume is reported as (x,y), where x is the radial distance from the center of the flame in millimeters and y is the vertical distance from the burner surface in millimeters. The flame in the 30-mm region consisted of a small blue flame sheath which marked the position at which the fuel and air were mixed in near-stoichiometric proportions. Table 2 gives the results of this profiling, and the pdf's and correlation plots are shown in Fig. 8. Only one edge of the flame was profiled in the study.

At position (-8.5, 30) (2 mm on the air side of the flame sheath), the average temperature is 1492 K. Since no burning gases exist in this region, the high temperature is due to thermal heat losses of the overall flame sheath.¹⁹ The temperature pdf indicates that a spread in temperature exists, but no bimodal character is evident. The correlation plot indicates that the data lie entirely on the fuel-lean curve, which is consistent with the probe measurement being located on the air side of the flame sheath. At position (-7.5, 30) the average temperature has increased to 1755 K. The temperature and concentration pdf's are not so broad as those at the (-8.5, 30) position. The correlation plot still indicates that this region is fuel lean, although more fuel-rich data are observed. At position (-6.5, 30), which corresponds to the

Table 1 Average temperature and N_2 -concentration results from a centerline profile of the turbulent propane diffusion flame. 500 data points were taken per centerline position (avg—average; SD—standard deviation)

Centerline position, mm	T_{avg} , K	T_{SD} , K	C_{avg} , molecules/cm ³ × 10 ⁻¹⁸	C_{SD} , molecules/cm ³ × 10 ⁻¹⁸
145	870	510	9.63	5.31
135	980	550	8.99	5.57
125	1110	580	7.77	5.27
115	1280	580	6.73	5.07
105	1350	590	6.55	5.18
95	1520	560	5.22	4.50
85	1610	470	4.93	4.56
75	1730	300	3.44	2.22
65	1650	220	3.80	1.01

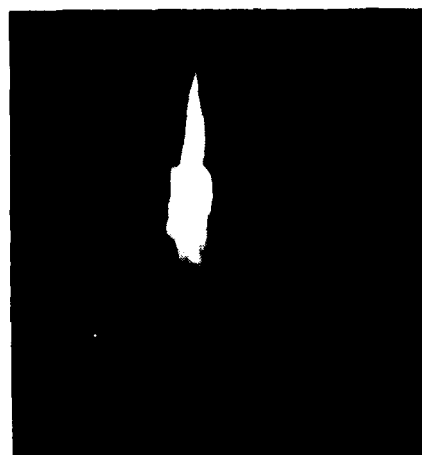


Fig. 6 $R_p \sim 6000$ turbulent diffusion flame; film exposure ~ 100 ms.

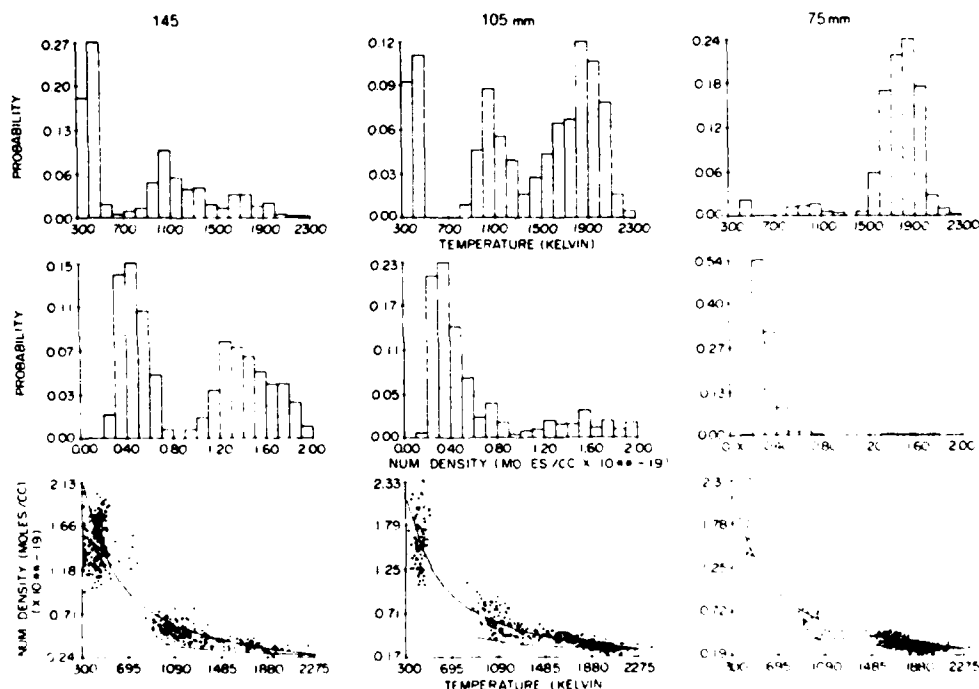


Fig. 7 Temperature-concentration pdf's and correlation plot of temperature and concentration vs adiabatic equilibrium calculation results obtained in $R_p \sim 6000$ turbulent diffusion flame at three centerline positions above the burner surface.

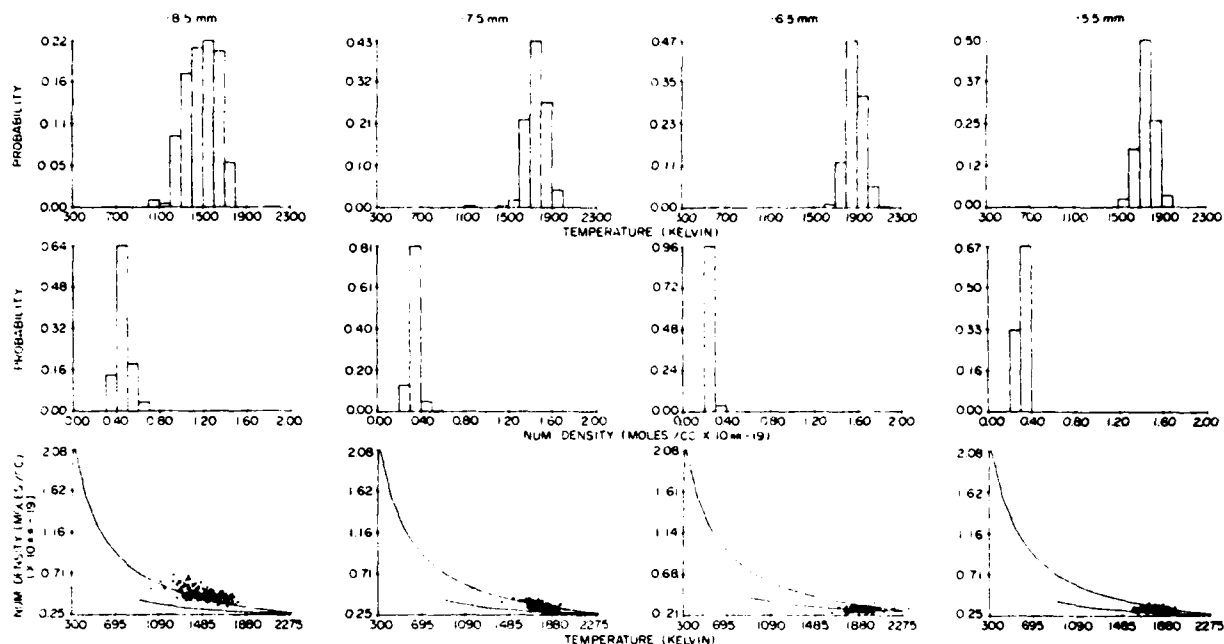


Fig. 8 Temperature concentration pdf's and correlation plot of temperature and concentration vs adiabatic equilibrium calculation results obtained in $R_p \sim 6000$ turbulent diffusion flame at four radial positions (about flame sheath) 30 cm above the burner surface.

Table 2 Results from a radial profile of the turbulent flame ($R_p \sim 6000$) taken at the centerline position, 30 mm. Radial position 0 mm corresponds to the center of the fuel jet. 500 data points were taken per position (avg—average; SD—standard deviation)

Radial position, mm	T_{avg} , K	T_{SD} , K	C_{avg} , molecules/cm ³ $\times 10^{-18}$	C_{SD} , molecules/cm ³ $\times 10^{-18}$
-8.5	1490	150	4.61	0.62
-7.5	1760	90	3.40	0.38
-6.5	1880	80	2.68	0.19
-5.5	1760	70	3.11	0.23

center of the flame sheath, the average temperature has reached a maximum of 1880 K. The temperature and concentration pdf's are quite narrow, and the correlation plot indicates a largely fuel-rich region. Moving 1 mm to the fuel side of the flame (~ 5.5 , 30) resulted in a lower average temperature of 1760 K. The temperature and concentration pdf's begin to broaden once more, and the correlation plot indicates that almost equal amounts of fuel-rich and fuel-lean data have been obtained. Beyond the 2-mm position on the fuel side (~ 4.5 , 30), the cold fuel jet again becomes a problem. While this study demonstrates that the spatial resolution was sufficient to obtain reasonable data in the flame-sheath region, higher spatial resolution would be required to obtain detailed information on this structure. A study of the sheath region employing a larger BOXCARs crossing angle will be conducted in the near future.

Conclusions

A 10-Hz CARS instrument capable of making simultaneous temperature and N_2 -concentration measurements has been built and used to study two propane-air turbulent-diffusion flames having Reynolds numbers of 2000 and 6000. Calibration of this instrument in a near-stoichiometric premixed flame indicates a temperature measurement uncertainty of 4% and an N_2 -concentration measurement uncertainty of 5%. Studies on the turbulent diffusion flames indicate that this instrument is capable of monitoring a temperature fluctuation in the range of 300-2300 K. Average

values, pdf's, and correlation plots show reasonable trends for centerline and radial profiles of the turbulent flame. The centerline profile of the $R_p \sim 6000$ flame indicates that the maximum temperature is observed just above the breakup point of the fuel jet. pdf's high in the turbulent flame indicate large amounts of air entrainment.

Future work will be directed toward reduction of measurement uncertainties and more extensive profiling of the $R_p \sim 6000$ flame utilizing background-canceling techniques for measurements in the fuel jet.

Acknowledgments

The authors gratefully acknowledge helpful discussions with Dr. M.L. Roquemore (APL) and the computer systems software contributions of T.E. Austin (SRL). This work was supported in part under Air Force Contract F33615-80-C-2054.

References

- Drake, M.C., Lapp, M., Penney, C.M., Warsaw, S., and Gerhold, B.W., "Measurements of Temperature and Concentration Fluctuations in Turbulent Diffusion Flames Using Pulsed Raman Spectroscopy," *Proceedings of the Eighteenth Symposium (International) on Combustion*, The Combustion Institute, University of Waterloo, Waterloo, Canada, 1981, pp. 1521-1531.
- Bilger, R.W., "Molecular Transport Effects in Turbulent Diffusion Flames at Moderate Reynolds Numbers," AIAA Paper 81-0104, 1981.
- Nibler, J.W., Shaub, W.M., McDonald, J.R., and Harvey, A.B., "Coherent Anti-Stokes Raman Spectroscopy," in *Vibrational Spectra and Structure*, Vol. 6, edited by J.R. Durig, Elsevier, Amsterdam, 1977, pp. 173-225.
- Eckbreth, A.C., Bonczak, P.A., and Verdieck, J.F., "Combustion Diagnostics by Laser Raman and Fluorescence Techniques," *Progress in Energy and Combustion Science*, Vol. 5, 1979, pp. 253-322.
- Eckbreth, A.C., "BOXCARs: Crossed-Beam-Phase-Matched CARS Generation in Gases," *Applied Physics Letters*, Vol. 32, 1978, pp. 421-423.
- Eckbreth, A.C., "CARS Thermometry in Practical Combustors," *Combustion and Flame*, Vol. 39, 1980, pp. 133-147.
- Stenhouse, I.A., Williams, D.R., Cole, J.B., and Swords, M.D., "CARS Measurements in an Internal Combustion Engine," *Applied Optics*, Vol. 18, 1979, pp. 3819-3825.

- ⁸Taran, J.P.E., "CARS Flame Diagnostics," Paper presented at the CARS Meeting of the Institute of Physics, AERE, Harwell, Great Britain, March 1979.
- ⁹Switzer, G.L., Roquemore, W.M., Bradley, R.P., Schreiber, P.W., and Roh, W.B., "CARS Measurements in a Bluff Body-Stabilized Diffusion Flame," *Applied Optics*, Vol. 18, 1979, pp. 2343-2345.
- ¹⁰Switzer, G.L., Goss, L.P., Roquemore, W.M., Bradley, R.P., Schreiber, P.W., and Roh, W.B., "Application of CARS to Simulated Practical Combustion Systems," *Journal of Energy*, Vol. 4, May 1980, pp. 209-215.
- ¹¹Goss, L.P., Switzer, G.L., and Schreiber, P.W., "Flame Studies with the Coherent Anti-Stokes Raman Spectroscopy Technique," AIAA Paper 80-1543, 1980.
- ¹²Goss, L.P. and Switzer, G.L., "Application of Coherent Anti-Stokes Raman Scattering to Combustion Media," AFWAL-TR-80-2122, Feb. 1981.
- ¹³Eckbreth, A.C. and Hall, R.J., "CARS Concentration Sensitivity With and Without Nonresonant Background Suppression," R80-354628-1, Final Report on ONR Contract N00014-79-C-0351, United Technologies Research Center, East Hartford, Conn., 1980.
- ¹⁴Goss, L.P. and Schreiber, P.W., "Assessment of the Application of CARS to Combustion Diagnostics," *Proceedings of the International Conference on Lasers '80*, edited by C.B. Collins, STS Press, McLean, Va., 1981, pp. 220-235.
- ¹⁵Shirley, J.A., Hall, R.J., Verdieck, J.L., and Eckbreth, A.C., "New Directions in CARS Diagnostics for Combustion," AIAA Paper 80-1542, 1980.
- ¹⁶Gordon, S. and McBride, B.J., "Computer Program for Calculation of Complex Equilibrium Composition Rocket Performances, Incident and Reflected Shocks, and Chapman-Jouquet Detonations," NASA SP-273, 1971.
- ¹⁷Lapp, M., *Laser Probes for Combustion Chemistry*, edited by D.R. Crosley, American Chemical Society Symposium Series 134, American Chemical Society, Washington, D.C., 1980, pp. 207-231.
- ¹⁸Rahn, L.A., Zych, L.J., and Mattern, P.L., "Background-Free CARS Studies of Carbon Monoxide in a Flame," *Optics Communications*, Vol. 30, No. 2, 1979, pp. 249-252.
- ¹⁹Gaydon, A.G. and Wolfhard, H.G., "The Structure of the Reaction Zone," in *Flames*, 3rd ed., Chapman and Hall, Ltd., London, 1970, pp. 85-128.

CARS Thermometry and N_2 Number-Density Measurements in a Turbulent Diffusion Flame

L. P. Goss,* D. D. Trump,† G. L. Switzer,‡ and B. G. MacDonald§
Systems Research Laboratories, Inc., Dayton, Ohio

Abstract

An extensive X-Y profiling of a turbulent propane diffusion flame has been conducted and the data analyzed to yield average temperature and temperature fluctuation contour maps. The average temperature contour resembles still photographs of the flame, while the temperature fluctuation contour shows the true nature of the turbulent flame as displayed by 500-frame/s cine photographs. Included in the data analysis is a discussion of the probability distribution functions (PDF) which were obtained throughout the flame. Both single and multimodal PDF's were obtained at various locations in the flame. In an attempt to explain the origin of the various modes of the PDF's, a conditional sampling technique was used to measure the CARS temperature in the presence and absence of visible flame emission. The results indicate that in the presence of visible flame, the same high-temperature distribution is observed regardless of flame location, while the temperature distribution in the absence of flame emission varies considerably with location and mixing.

Introduction

The study of turbulent combustion on a fundamental level requires spatially resolved information on the instantaneous values of a large number of scalar quantities such as temperature, species concentration, velocity, and pres-

Presented as Paper 83-1480 at AIAA 18th Thermophysics Conference, Montreal, Canada, June 1-3, 1983. Copyright © American Institute of Aeronautics and Astronautics, Inc., 1983. All rights reserved.

*Senior Chemist, Research Applications Division.

†Associate Engineer, Research Applications Division.

‡Research Engineer, Research Applications Division.

§Research Chemist, Research Applications Division.

Reprinted from Combustion Diagnostics by Nonintrusive Methods, edited by Jeffrey A. Roux and T. Dwayne McCay, Vol. 92 of Progress in Astronautics and Aeronautics, 1984.

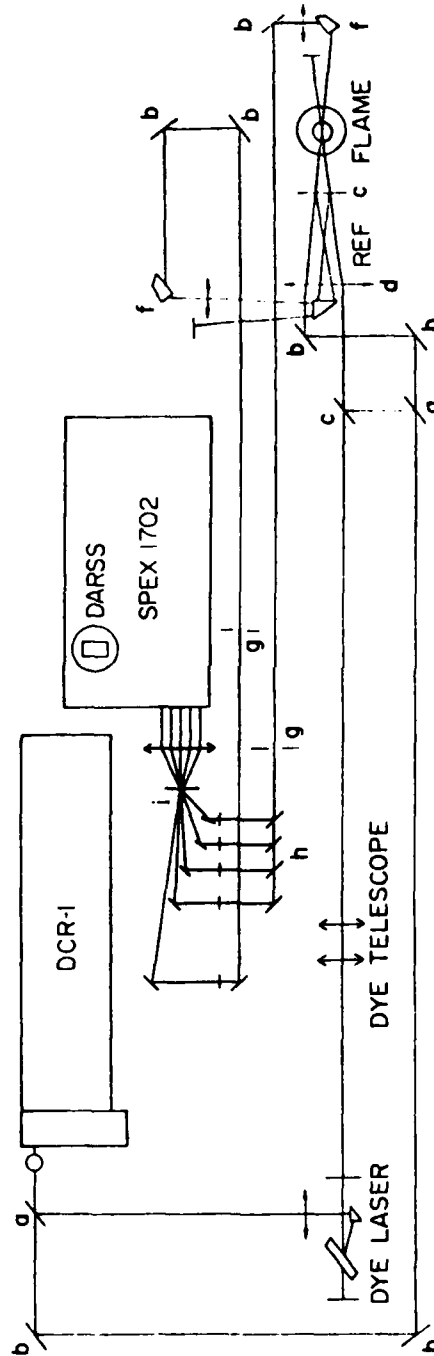


Fig. 1 CARS optical schematic. Arrows indicate lenses. a) 50% beamsplitter for 532 nm, b) total reflector, c) dichroic, green reflector, red transmitter, d) 50-cm lens, e) 50-cm lens, f) Pellin-Borca prism, g) iris, h) beamsplitter array (0.1%, 1%, 10%, and total reflector), i) 532-nm filter.

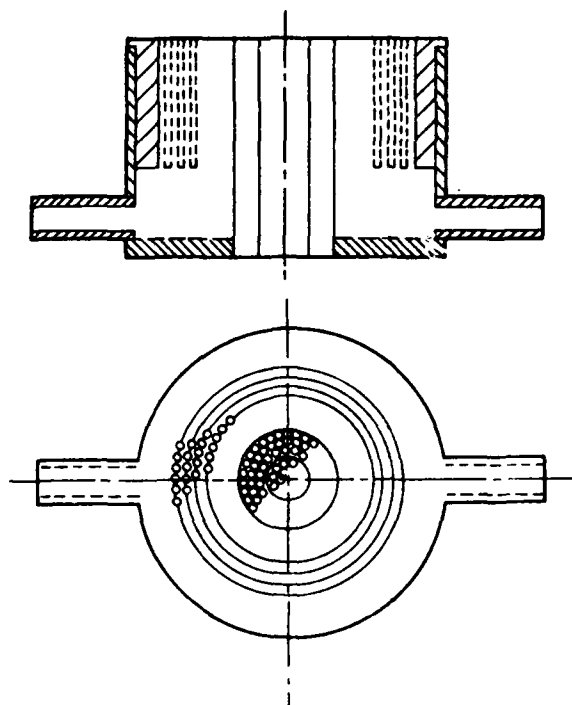


Fig. 2 Concentric tube burner assembly used for turbulent flame studies. Outer capillaries correspond to an argon sheath which was not employed in these studies.

sure. Coherent anti-Stokes Raman spectroscopy (CARS) has proven to be an attractive experimental technique for this purpose because it can provide time resolved (10 ns) and spatially resolved (0.1 mm^3) measurements of temperature and major flame species, without appreciably perturbing the flame under study. This paper presents results obtained on a propane-air turbulent diffusion flame at a Reynolds number of 6000 (based upon air flow). These results are presented in the form of average temperature and temperature fluctuation contour maps and species concentration PDF's. Conditional sampling has also been conducted on the turbulent flame in an attempt to explain the various contributions to the PDF's.

Experimental Methods

The CARS apparatus which was employed for these studies (see Fig. 1) is described in detail in Refs. 1 and 2 and, therefore, will be discussed only briefly here. The heart

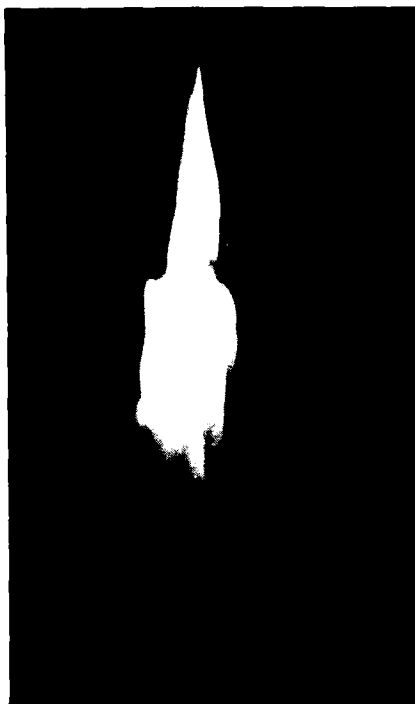


Fig. 3 Still photograph of the $Re \sim 6000$ turbulent propane diffusion flame. Exposure time was ~ 100 ms.

of the system is a Nd:YAG laser which is employed both in the CARS process and in pumping a broadband dye laser. A BOXCARS configuration is used to achieve a spatial resolution of 1 mm along the longest beam axis. A power reference is employed for concentration measurements along with a Reticon detector for single-shot temperature measurements. The system was especially designed to acquire CARS data at a 10-Hz rate, which required interfacing to a minicomputer for control of the data acquisition. Data reduction consists of fitting the observed N₂ CARS spectral bandshape to obtain the temperature and integrating the CARS signal to obtain the concentration. The temperature fit employs a nonlinear least-squares iterative routine requiring typically three cycles of the iteration for convergence.³ Once the temperature has been fit, the concentration can be determined from the integrated CARS signal. The N₂ number density is given by⁴

$$N_T = N_{300} \sqrt{R_T \cdot I_T / I_{300}} \quad (1)$$



Fig. 4 Sequence of shots taken from a 500-frame/s movie of the $Re \sim 6000$ turbulent propane flame.

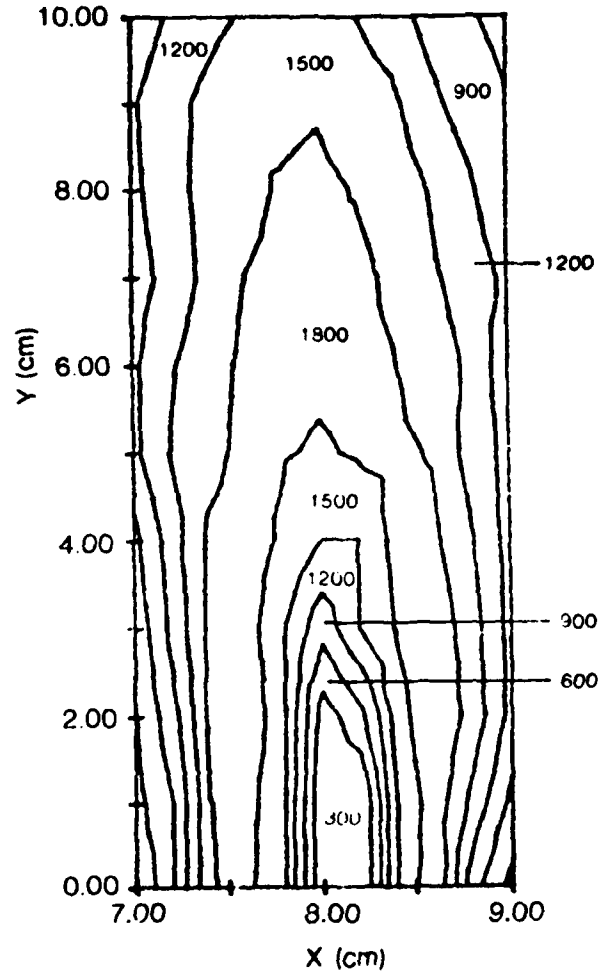


Fig. 5 Average-temperature contour of the $Re \sim 6000$ turbulent diffusion flame. Position 0.0 is 2 cm above burner surface.

where N_T is the N_2 number density at temperature T ; N_{300} is the N_2 number density at 300 K; R_T is the ratio of the band-shapes of the CARS spectrum at 300 K to that of the CARS spectrum at temperature T ; I_T is the experimentally measured integrated CARS intensity at temperature T ; and I_{300} is the experimentally measured integrated CARS intensity at 300 K. The ratio R_T takes into account the change in the Raman linewidths and population redistribution with temperature. Approximately 1 s of CPU time per spectrum is required for the data analysis discussed above.

The burner employed for these studies is a Perkin-Elmer assembly (No. 290-0107)^{5,6} consisting of a concentric-tube arrangement which can be operated independently for either a premixed flame or a turbulent diffusion flame. The burner surface consists of a capillary plate which is used to stabilize the flame under high-flow-rate conditions. The burner design is depicted in Fig. 2.

Contour Maps and PDF's

The flame that was employed for the turbulent flame studies is shown in Fig. 3. The burner conditions under which this flame was produced were an inner fuel flow of

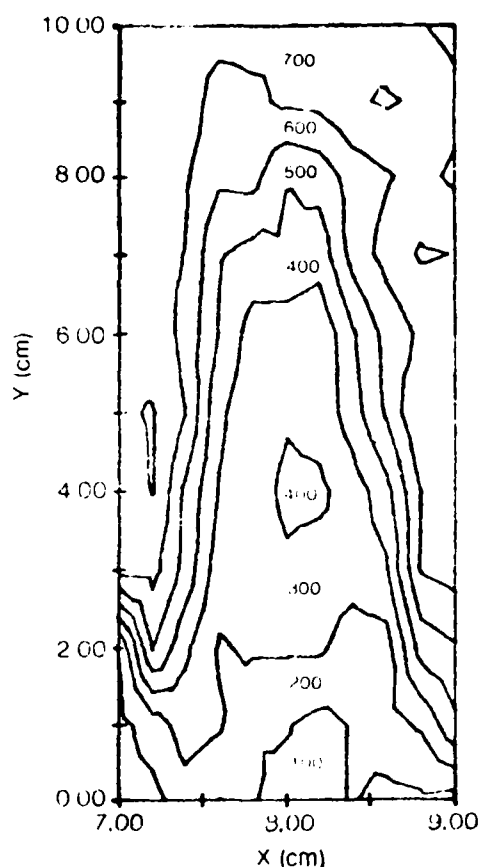


Fig. 6 Temperature-fluctuation contour of the $Re \sim 6000$ turbulent diffusion flame. Position 0.0 is 2 cm above burner surface.

0.95 μ /min of propane and an outer air flow of 40 μ /min. The flame height was 14.5 cm, while the air-to-fuel mass flow ratio was 28 to 1. The flame was characterized primarily by turbulence, driven by the shear produced between the two fluid flows. Fast cine photographs of the flame at 500 frames/s are shown in Fig. 4. At 2-ms intervals the effects of the shear of the flame can be observed.

A measurement grid consisting of an 11×11 matrix was superimposed on this turbulent flame. At each grid point 1500 single shots of data were taken and the data analyzed to obtain contour maps of the average values and their fluctuation and PDF's of the temperature and N_2 concentration.

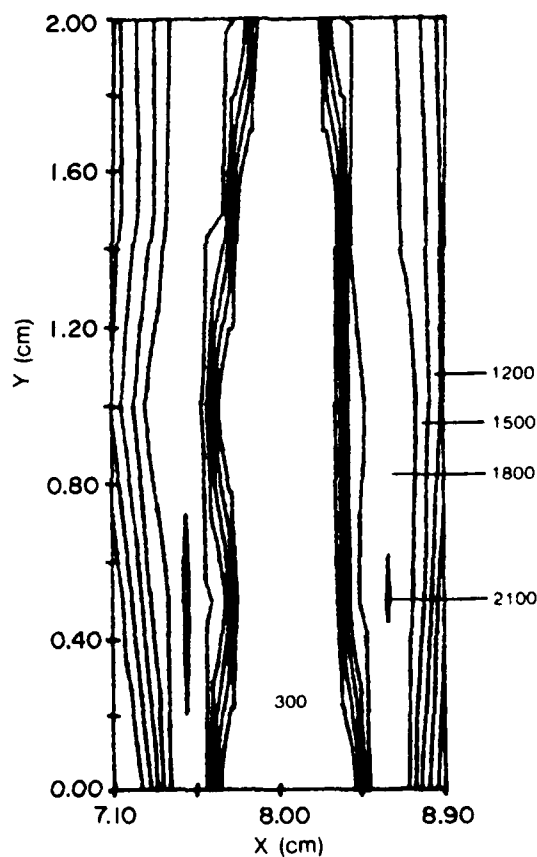


Fig. 7 Average-temperature contour of the flame-sheath region of the turbulent flame.

A contour plot of the average temperatures obtained in the turbulent flame is shown in Fig. 5. The isotherms of the contours cover a 300-K range and are individually labeled. The 0.0 position of the contour map is 2 cm above the burner surface. The propane fuel jet appears as a cold 300-K region in the bottom center of the flame. As one progresses up the centerline of the flame, the temperature rises to a maximum near $Y = 6$ cm and begins to fall off above $Y = 8$ cm. The maximum centerline temperature corresponds to the highly sooty central region displayed in Fig. 3. Near the base of the flame, the cold central fuel jet is surrounded by a blue flame sheath ~ 2 mm in diam.

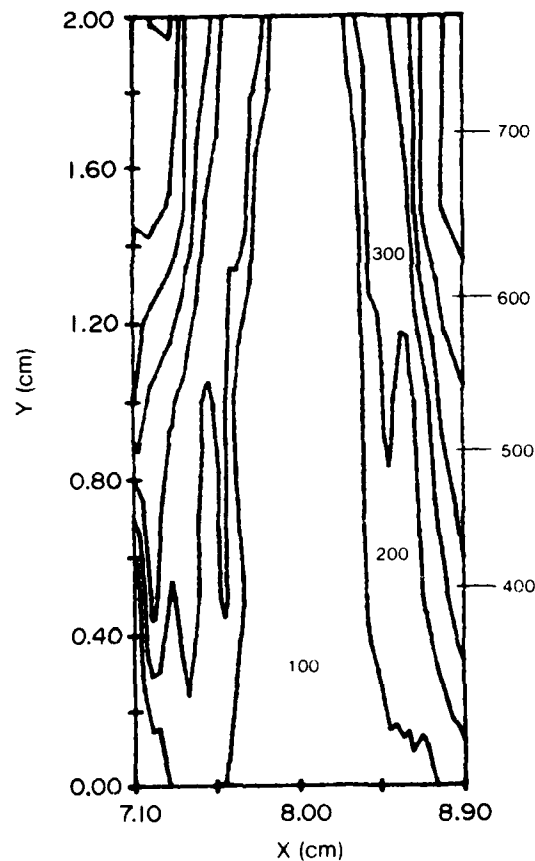


Fig. 8 RMS temperature contour of the flame-sheath region of the turbulent flame.

This sheath is extremely hot and will be discussed in more detail later. The overall picture of the flame given by the contour is one of a symmetric flame system in contrast to that indicated by the high-speed cine photographs. While the average temperature contour is useful for identifying average flame characteristics, the fluctuation contour shown in Fig. 6 displays the true turbulent nature of the flame. In this contour the isotherms represent a 100-K range. The fluctuations are small at a point low in the flame but increase drastically as more and more air becomes entrained into the central fuel jet. The turbulence becomes quite large in the upper regions of the flame as the shear generated by the two different air flows dominates the flame. Thus, while the average temperature gives a picture of the time averaged flame, the fluctuation contour gives insight into the true turbulent nature of the flame system.

As mentioned earlier, surrounding the fuel jet near the burner surface is a blue flame sheath which is ~ 2 mm in diam. In order to obtain a better understanding of this structure, a finer grid spacing was used for a profile. An 11×11 matrix was chosen to cover a 2×2 cm² region. The average temperature contour obtained in this region is shown in Fig. 7. The flame sheath, as indicated, is quite hot, reaching the near stoichiometric temperature of 2100 K, while the nearby fuel and air jets are cold. The flame sheath does not reach the stoichiometric temperature due to radiant heat loss of the small structure.⁷ The fluctuation contour of this structure is shown in Fig. 8. The contour lines tend to map the air entrainment which is occurring at this location. While this study of the sheath indicates that the spatial resolution of the instrument is sufficient to obtain reasonable data, higher spatial resolution would be required for a more detailed study of this small structure.

Figures 9-14 display the individual PDF's obtained during profiling of the turbulent flame. Each PDF is the result of 1500 single shot measurements at a given location. The coordinates are the same as those used for the contour maps discussed above. Figure 9 displays the PDF's obtained at the $Y = 0.0$ cm position across the flame. As shown in the still photograph (Fig. 3) and in the average temperature contour map (Fig. 5), the flame sheath is located in this region. The first PDF at $X = 7.3$ cm corresponds to a location 2 mm on the air side of the sheath. Although no visible flame exists in this region, the temperature is higher than that of the ambient air due to heat losses of the flame sheath. At $X = 7.4$ cm, the outer edge of the sheath is being probed, resulting in a high average temperature. The center of the sheath was observed at $X = 7.5$ cm,

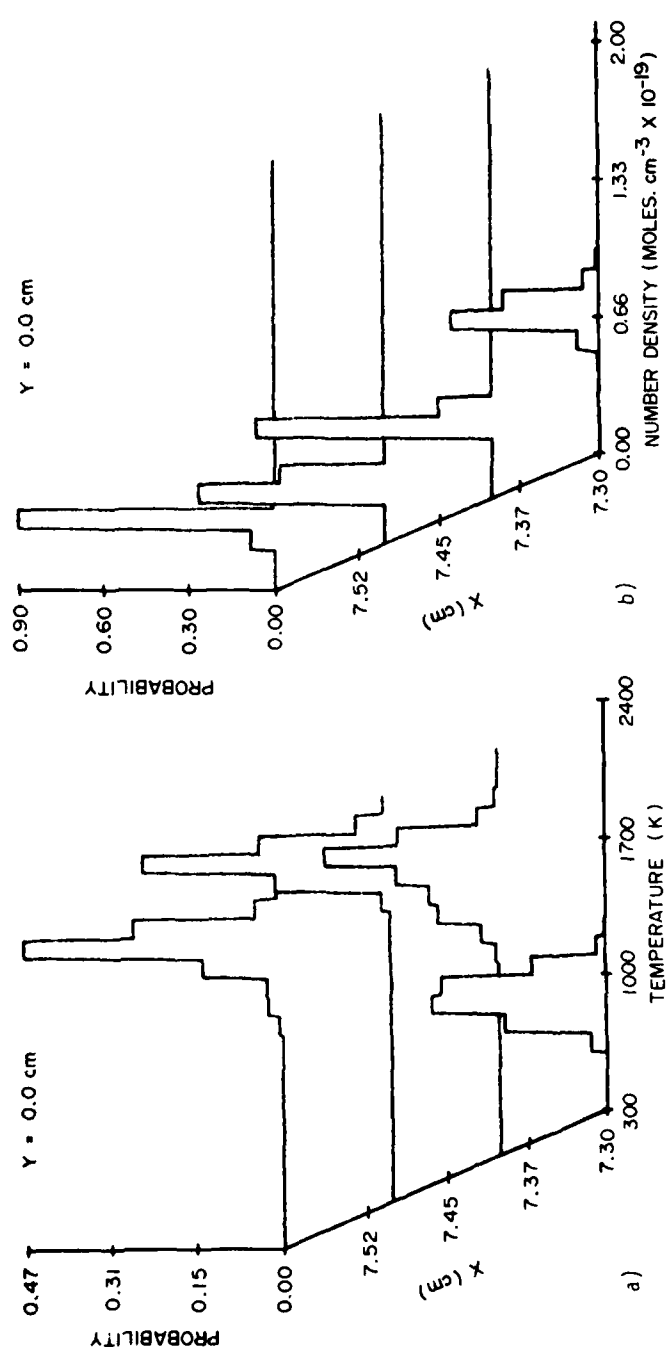


Fig. 9a) Temperature and b) N₂ concentration PDF's obtained at the $Y = 0$ cm position of the turbulent diffusion flame.

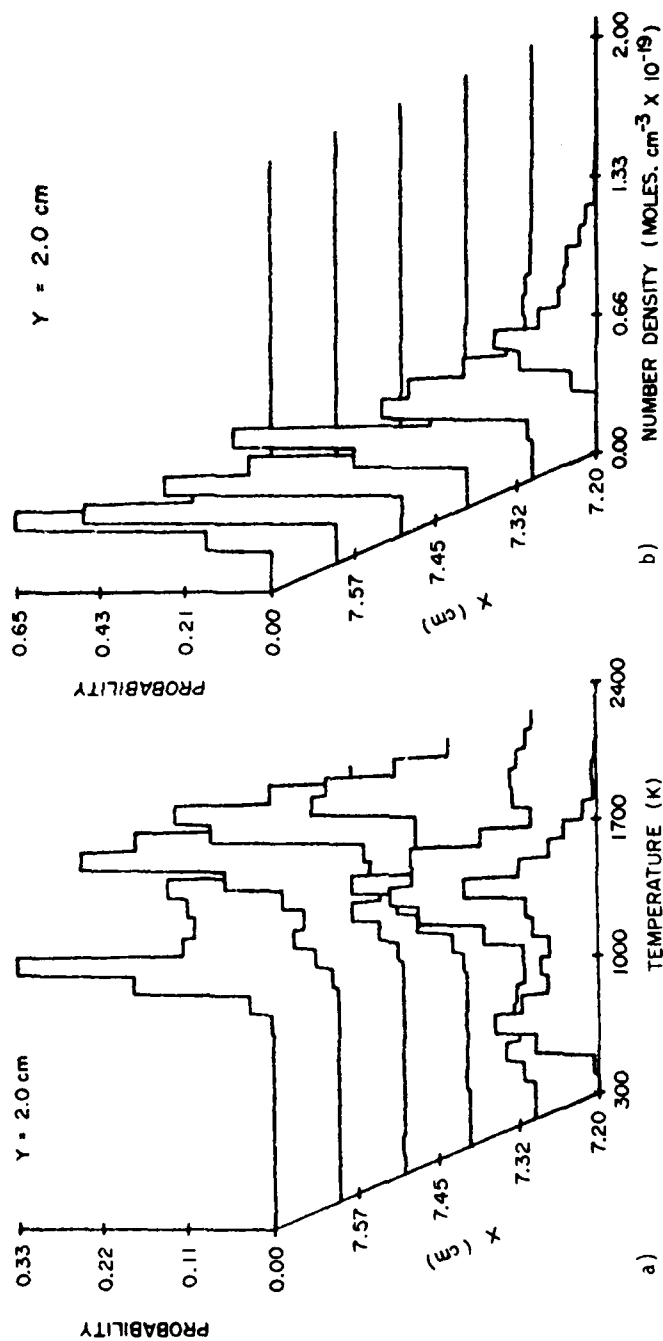


Fig. 10a) Temperature and b) N_2 concentration PDF's obtained at the $Y = 2$ cm position of the turbulent diffusion flame.

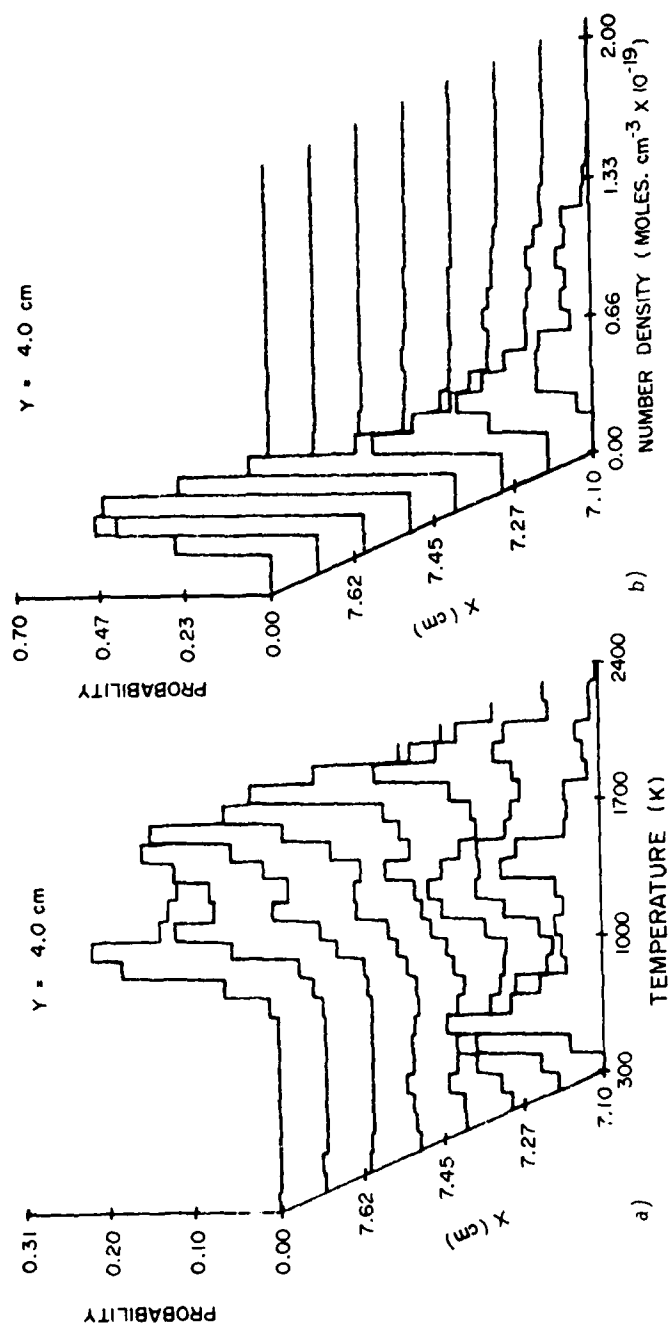


Fig. 11a) Temperature and b) N_2 concentration PDF's obtained at the $Y = 4$ cm position of the turbulent diffusion flame.

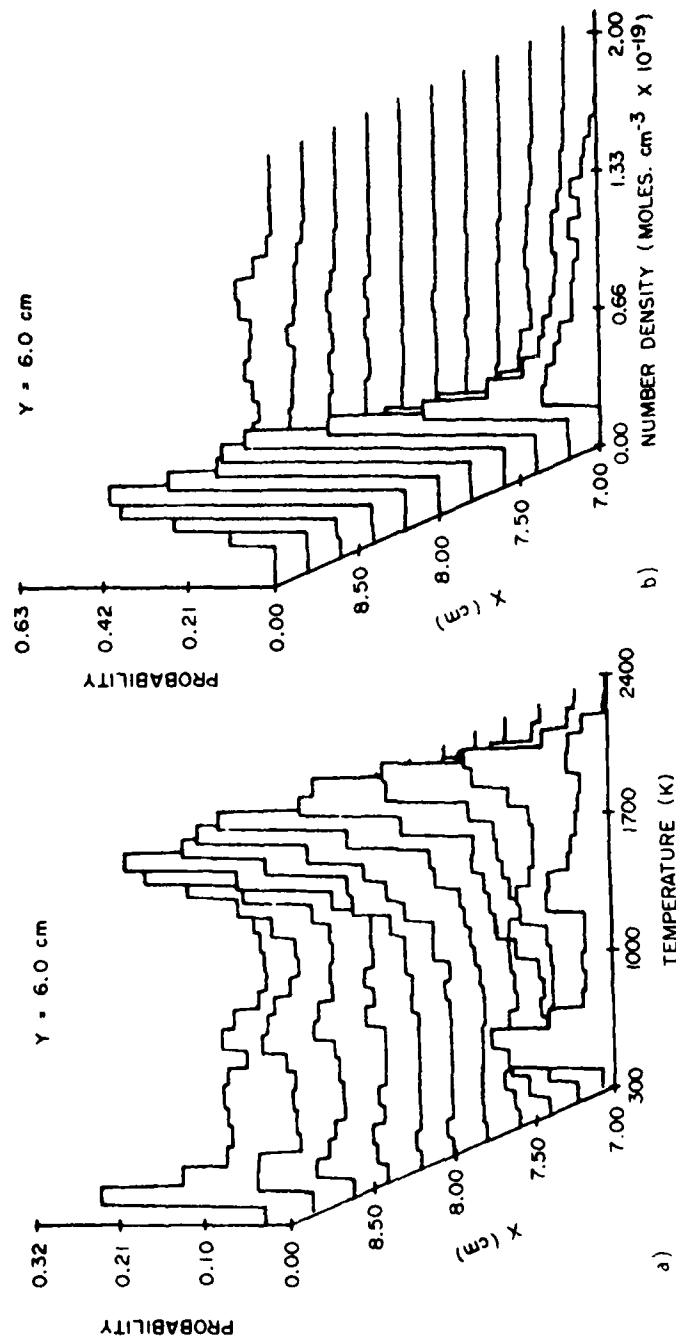


Fig. 12a) Temperature and b) N₂ concentration PDF's obtained at the $Y = 6$ cm position of the turbulent diffusion flame.

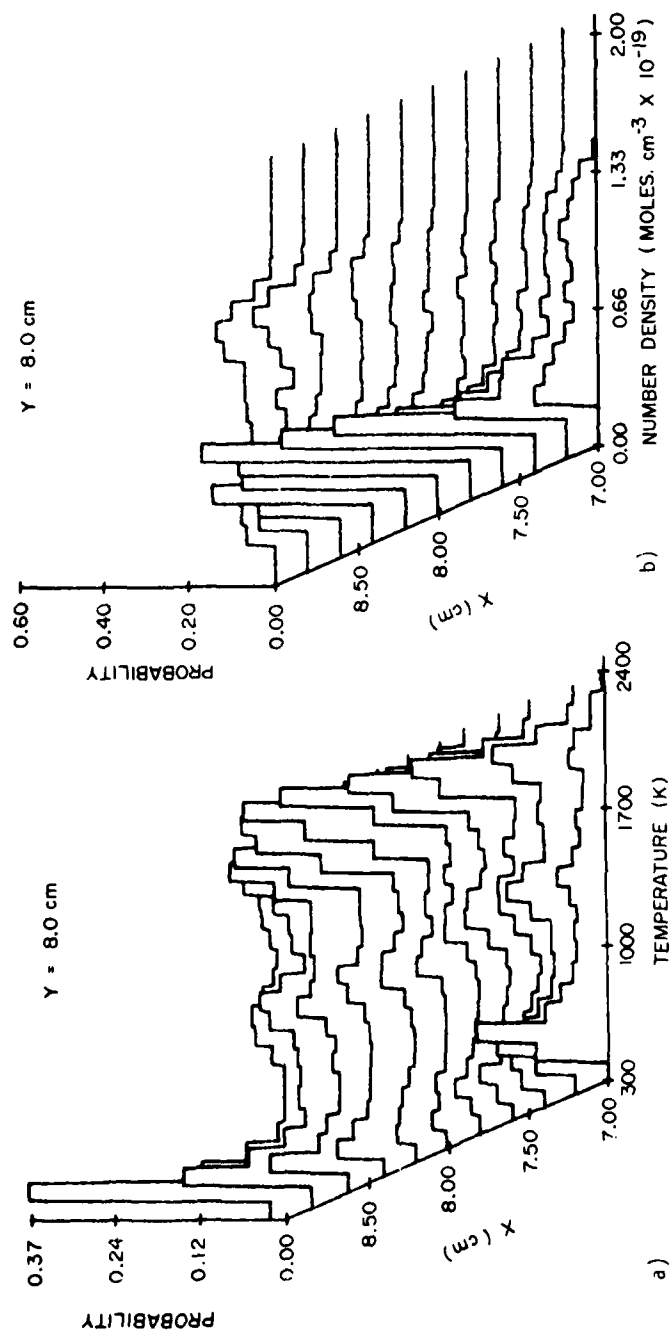


Fig. 13a) Temperature and b) N_2 concentration PDF's obtained at the $Y = 8$ cm position of the turbulent diffusion flame.

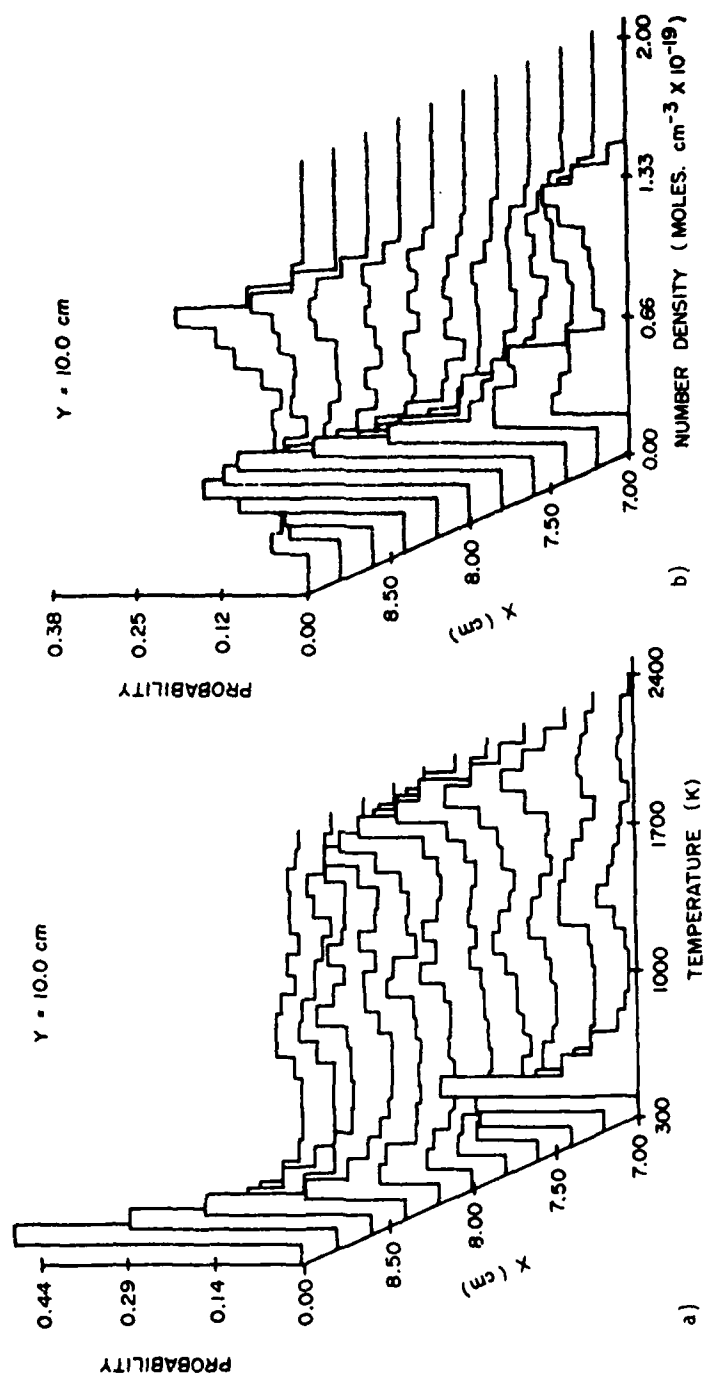


Fig. 14a) Temperature and b) N₂ concentration PDF's obtained at the Y = 10 cm position of the turbulent diffusion flame.

as indicated by the lower temperature at $X = 7.6$ cm. The N_2 concentration PDF's for this region are shown in Fig. 9b. Since an inverse relationship exists between the temperature and the N_2 concentration, the low N_2 number densities correspond to the hot temperature regions, which results in a narrow, low N_2 concentration mode for the PDF's in this region. As one proceeds higher up the sheath $Y = 2-4$ cm (Figs. 10-11), more high-temperature distributions are observed due to spreading of the sheath. The N_2 distributions display similar behavior. At the $Y = 6$ cm position (Fig. 12), the fuel jet is beginning to break up due to the dominance of the outer air jet. On centerline at this position, the maximum temperature outside the sheath area is observed. The fuel jet is no longer distinguishable, and a broadband sooty background dominates the flame emission. The PDF's of the outer edges of the flame at this location display a multimodal character, indicating intermittency due to the large air entrainment.⁸ The N_2 PDF's are correspondingly broadened for the outer flame locations. As one proceeds from the $Y = 6$ cm to the $Y = 10$ cm position (Figs. 12-14), the temperature modes of the respective PDF's remain the same; only their relative population varies with position. At the upper flame locations, more and more air entrainment is observed as the cold outer air is mixed with the hot inner flame mixtures. The average temperature drops in this region as well as the width of the flame. At the $Y = 8-10$ cm positions (Figs. 13-14), the flame is dominated by the cold outer air flow, the respective temperature and N_2 PDF's becoming quite broad.

Conditional Sampling Results

The temperature PDF which is obtained at a given flame location can be thought of as consisting of three different components--unburnt gases, burnt gases, and burning gases. It is the various contributions of each of these which determine the characteristics of the PDF. Unburnt gases would be expected to be cold, burnt gases relatively hot, and burning gases extremely hot. Mixtures of unburnt and burnt gases could cover the entire temperature range, which is evident in the PDF's obtained downstream in the flame.

Ideally, one would like to be able to determine the various contributions of the three gas components to the total PDF. One method of accomplishing this for the burning gases is to monitor the flame emissions simultaneously with the CARS measurement. By monitoring the chemiluminescent emission of the flame, the CARS temperature data can be divided into two groups--one in which no visible flame emission is present and the second in which

active combustion is occurring. Earlier work at this laboratory indicated that flame emission observed by a photomultiplier could be used to follow the dynamic behavior (flame turbules) of a turbulent propane flame⁹ and conditionally sample velocity data in a large-scale combustor.¹⁰ The emission system employed for the CARS study consisted of two orthogonally placed PMT's in which the image of the flame was projected (1 to 1) onto a 500- μ circular slit which defined the sample volume. Since the emission technique is a line-of-sight observation, two views were employed to confirm that the flame was actually present in the sample volume during the CARS measurement. The slits were aligned with the CARS sample volume by placing a card at the focus of the CARS beams, imaging the scattered light from the focus onto the slit, and aligning the slit with this image. This procedure was repeated for the second PMT to insure that both PMT's were monitoring the same position.

To determine which emission data were coincident with a laser shot, the Q-switch signal of the laser was monitored and used to set one bit of the 16-bit emission data word which was stored by the minicomputer. The most significant bit was chosen for this purpose since it indicates a negative value which could be easily distinguished. The two channels of emission data were transferred to the computer at a data rate of 20 kHz.

When combined with emission data, the temperature PDF can be divided into two conditionally sampled PDF's--one in the absence and one in the presence of visible flame emission. The cutoff point used to determine the absence of emission was 50 counts (out of 1000). The PDF plots obtained at three locations in the turbulent propane flame discussed above are shown in Figs. 15a-c. Position 1 corresponds to a centerline location 12 cm above the burner surface (position $Y = 10$ cm on the flame contour map). The temperature PDF for this location is shown in Fig. 15a. The average temperature was 1275 ± 605 K. The emission data taken simultaneously with the temperature data indicated that the flame was present only 29% of the time, which accounted for the low average temperature. The conditionally sampled PDF (shaded area of Fig. 15b) indicated that the visible flame is characterized by an average temperature of 1828 ± 170 K and a well-defined temperature distribution. The majority of the observed PDF is thus due to nonvisible gases (unburnt and burnt) having an average temperature of 1211 K.

At Position 2, located 10 cm above the burner surface (position $Y = 8$ cm on the flame contour map), the average temperature has increased to 1458 ± 455 K. The flame emission data indicated that the flame was present 43% of the

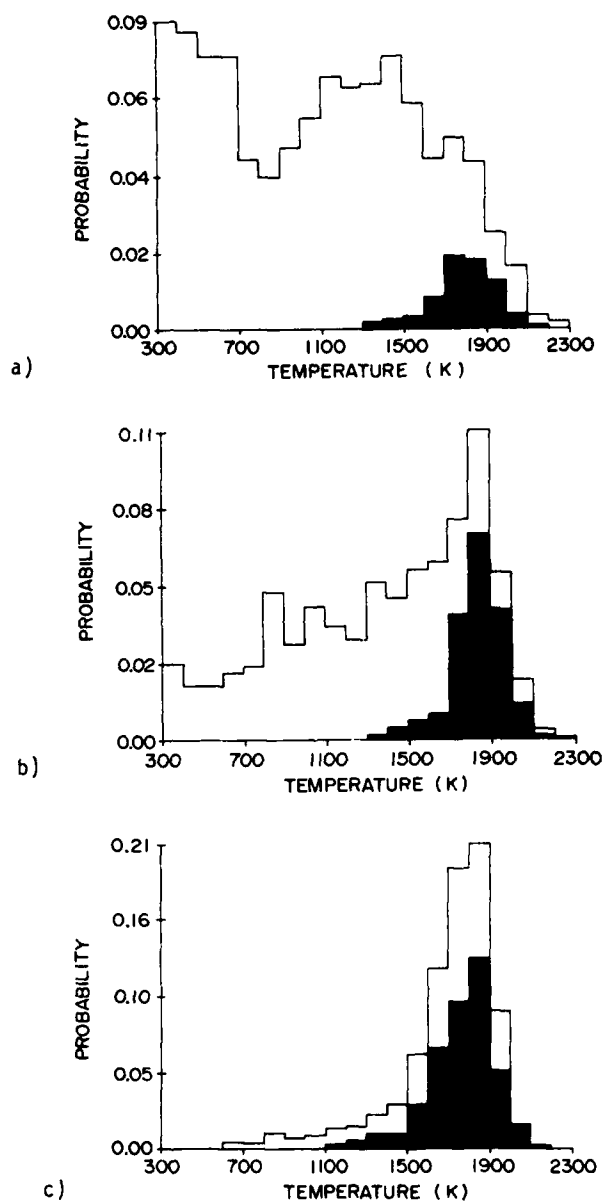


Fig. 15 Complete and conditionally sampled (black) temperature PDF's obtained on centerline a) 12 cm, b) 10 cm, and c) 8 cm above the burner surface.

time, which explains the higher temperature at this location. The temperature PDF for this location is shown in Fig. 15c. Notice that the general trends of the conditionally sampled data (flame present) are the same as those observed at Position 1, the major difference being that the flame is present more often at Position 2 (Fig. 15b). The average temperature (flame present) was 1801 ± 165 K.

At Position 3, 8 cm above the burner surface (position $Y = 6$ cm on the flame contour map), the average temperature has increased to 1704 ± 222 K. The emission data indicated that the flame was present 66% of the time. The region is thus dominated by the active combustion of the propane fuel. The conditionally sampled temperatures (flame present) display similar behavior to the other locations probed, with an average temperature of 1705 ± 185 K.

While the conditionally sampled data (flame present) displayed similar behavior regardless of the sampling position, the emission data (flame absent) exhibited widely varying behavior which was dependent on the mixing properties of the flame. The high temperatures in the absence of the flame are considered to be regions in which the flame turbules have just burned out but have not yet mixed with any cooler gases. The low-temperature regions consist of ambient air which is being entrained, and the intermediate temperature regions are the result of mixing of the burnt and unburnt gases. Presently 500-frame/s cine photography is being incorporated which will be synchronized to the laser firing; this will aid in determining whether the interpretation of the emission data is correct.

Conclusions

A 10-Hz CARS instrument capable of simultaneous temperature and N_2 number density measurements has been employed for extensive profiling of a turbulent propane diffusion flame. Contour maps and PDF's constructed from the CARS data allow a more detailed study of the flame than that possible with conventional probes. Conditional sampling of the CARS temperature data by flame-emission monitoring indicates that the portion of the temperature PDF due to active combusting gases is consistent regardless of flame location, while the portions of the PDF due to non-combusting gases (either unburnt or burnt) are complex and vary with flame location.

Acknowledgment

This work was supported by US Air Force Contract F33615-80-C-2054.

References

- ¹Goss, L. P., Trump, D. D., MacDonald, B. G., and Switzer, G. L., "10-Hz Coherent Anti-Stokes Raman Spectroscopy Apparatus for Turbulent Combustion Studies," Review of Scientific Instruments, Vol. 54, No. 5, May 1983, pp. 563-571.
- ²Goss, L. P., Switzer, G. L., Trump, D. D., and Schreiber, P. W., "Temperature and Species-Concentration Measurements in Turbulent Diffusion Flames by the CARS Technique," AIAA Paper 82-0240, AIAA 20th Aerospace Sciences Meeting, Orlando, Florida.
- ³Kim, A., "Computer Programming in Physical Chemistry Laboratory: Least Squares Analysis," Journal of Chemical Education, Vol. 47, February 1970, pp. 120-122.
- ⁴Goss, L. P., Switzer, G. L., and Schreiber, P. W., "Flame Studies with the Coherent Anti-Stokes Raman Spectroscopy Technique," AIAA Paper 80-1543, AIAA 15th Thermophysics Conference, Snowmass, Colorado.
- ⁵Goss, L. P., and Switzer, G. L., "Application of Coherent Anti-Stokes Raman Scattering to Combustion Media," Air Force Wright Aeronautical Laboratories, Wright Patterson Air Force Base, Ohio, AFWAL-TR-80-2122, Feb. 1981.
- ⁶Haraguchi H., and Winefordner, J. D., "Flame Diagnostics: Local Temperature Profiles and Atomic Fluorescence Intensity Profiles in Air-Acetylene Flames," Applied Spectroscopy, Vol. 31, November 1977, pp. 195-200.
- ⁷Gaydon, A. G., and Wolfhard, H. G., "The Structure of the Reaction Zone," Flames (3rd ed.), Chapman and Hall, Ltd., London, 1970.
- ⁸Lapp, M., Laser Probes for Combustion Chemistry, American Chemical Society Symposium Series, Vol. 134, edited by D. R. Crosley, American Chemical Society, Washington, D.C., 1980, Chap. 17.
- ⁹Roquemore, W. M., Britton, R. L., and Sandhu, S. S., "Investigation of the Dynamic Behavior of a Bluff Body Diffusion Flame Using Flame Emission," AIAA Paper 82-0178, AIAA 20th Aerospace Sciences Meeting, Orlando, Florida.
- ¹⁰Magill, P. D., Lightman, A. J., Orr, C. E., Bradley, R. P., and Roquemore, W. M., "Flowfield and Emission Studies in a Bluff Body Combustor," AIAA Paper 82-0883, AIAA/ASME 3rd Joint Thermophysics, Fluids, Plasma and Heat Transfer Conference, St. Louis, Missouri.

2.5 MULTIPLE-SPECIES MEASUREMENTS

One of the drawbacks of CARS as compared to ordinary Raman-scattering techniques is that each molecule of interest requires a separate dye laser for probing. In ordinary Raman scattering a single laser is used to monitor all species of interest. In the CARS technique the difference in frequency between the probe laser and the pump laser must be tuned to the energy level of the molecule of interest. This results in the need for multiple dye lasers in order to probe multiple species. There is strong interest in measuring the concentration of N_2 and O_2 in order to determine the local fuel-to-air ratio. To achieve this a second dye laser must be incorporated into the CARS arrangement. In the case of O_2 , it was necessary to use a narrow-band dye rather than a broadband to improve the CARS signal strength. The experimental setup used for the simultaneous-temperature, N_2 , and O_2 studies is shown in Fig. 8. A folded-BOXCAR arrangement was used to allow the spatial separation of the two probe beams and their resulting CARS signals.

To permit quantitative O_2 measurements, a reference cell was incorporated in which 1 atm. of N_2 and 3 atm. of O_2 were mixed for monitoring the power variation. Because of the size of the cell which was used for this study, a different referencing scheme was employed for this purpose. This scheme is shown in Fig. 9. The reference beams are picked off at 90 deg. instead of being retroreflected in the usual manner.

To ensure that the focal volumes would be identical, a compensator was inserted into the reference leg to make the sample and reference paths equivalent. This arrangement allows the high-pressure cell to be inserted into the

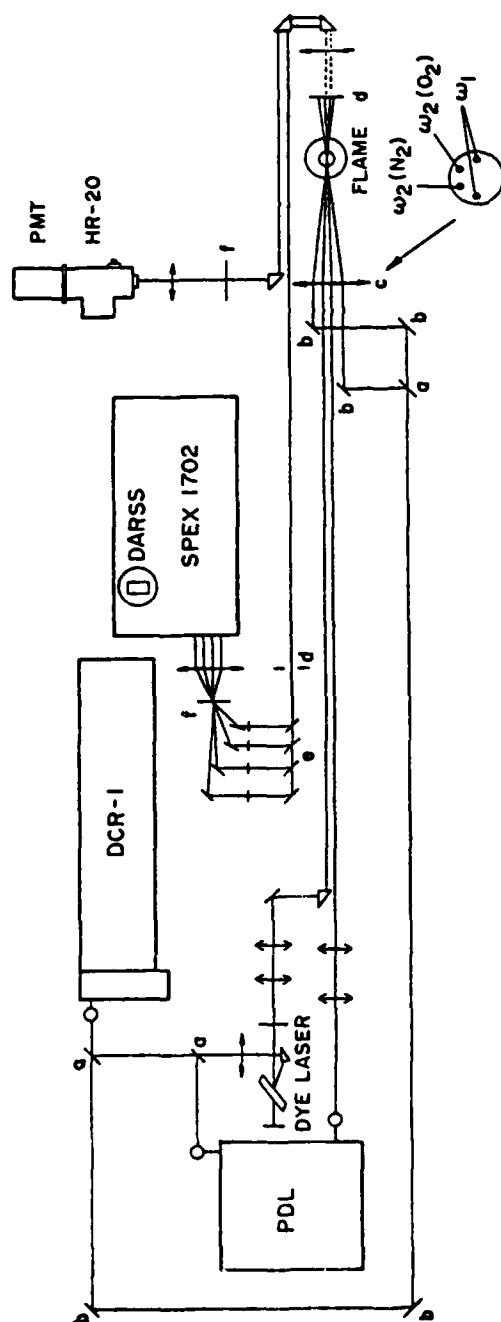


Figure 8. Optical Schematic of CARS Setup for Simultaneous Temperature- N_2 and Relative- O_2 Concentration Measurements.

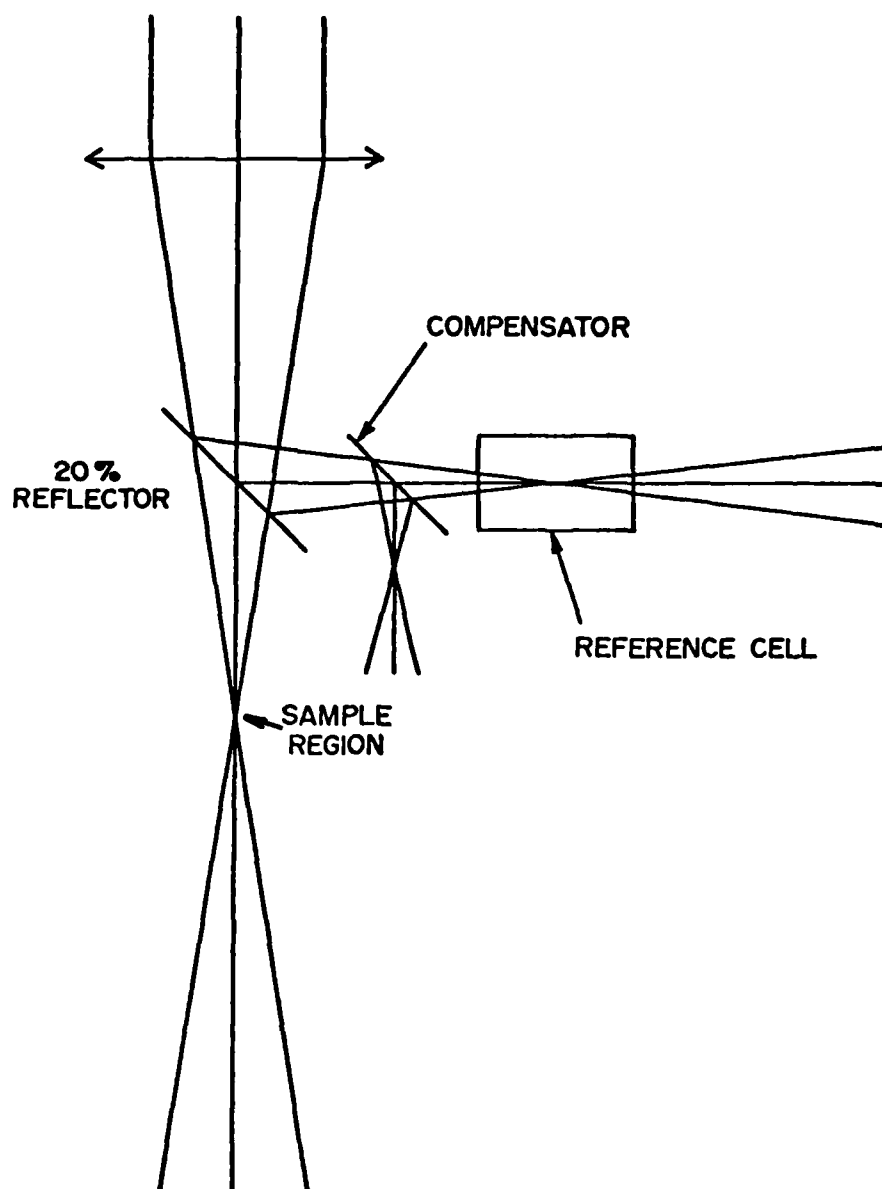


Figure 9. Right-Angle Reference Scheme Employed for O_2-N_2 Studies.

reference path without interfering with the sample path. The O_2 reference signal, just as the O_2 sample signal, is filtered by an HR20 spectrometer and detector by an S-20 pmt. The pmt signals are digitized and stored with the DARSS data in the SDM of the TN 1710 and subsequently sent to the ModComp computer for analysis.

For analysis of the oxygen data, a software program capable of calculating the O_2 spectrum as a function of temperature is required. The program is based upon the diatomic N_2 -spectral-calculation program which has been extensively used in the past. The N_2 program was modified for O_2 by changing the spectral constants and excluding the even rotational lines which are missing in the O_2 spectra due to nuclear spin. The spectral constants which were employed were taken from Hertzberg.⁶ The Raman linewidths are assumed to vary with the inverse square root of the temperature with, no J dependence. The O_2 concentration is assumed to vary as predicted by adiabatic flame calculations.⁷ A power-series equation was fit for the variation of the O_2 concentration with temperature and is given below:

$$C(O_2) = 2.687 \times 10^{19} \left(\frac{2.73}{T} \right) [23.108 - 6.74 \times 10^{-3} T - 1.604 \times 10^{-6} T^2 + 4.217 \times 10^{-10} T^3 - 1.45 \times 10^{-13} T^4] \quad (8)$$

The nonresonant-susceptibility variation with temperature is based upon adiabatic calculations of the major species of the flame. Unlike N_2 , the concentration of O_2 varies greatly with temperature in a flame due to consumption. As the flame temperature approaches the stoichiometric temperature, the O_2 concentration decreases rapidly. Because of the formulation used for determination of the number density, this presents a problem with the calculations

at high temperatures. The reason for this is as follows. In the derivation for the number-density equation, the explicit dependence of the third-order susceptibility on number density was given by⁸

$$\chi^{(3)} = N\chi' \quad (9)$$

where

$$\chi' = \frac{\chi_{nr}}{N} + \frac{2c^4}{\hbar\omega_2} \sum_{v,J} \frac{\Delta(v,J) \left(\frac{d\sigma}{d\Omega}\right)_{v,J}}{\omega_r - \delta - i\Gamma(v,J)} \quad (10)$$

In Eq. (10) χ_{nr} is the nonresonant susceptibility, $\Delta(v,J)$ the populational difference term, and $\left(\frac{d\sigma}{d\Omega}\right)$ the Raman-scattering cross section. The expression for χ' given in Eq. (10), however, becomes artificially large in the case of O_2 at high temperatures because of the low O_2 number density

$$\left(\frac{\chi_{nr}}{N} \rightarrow \infty\right) \text{ as } N \rightarrow 0$$

Thus, a new approach must be taken in order to determine the O_2 density. The experimentally measured integrated CARS intensity is given by

$$\Sigma = \frac{2\pi Q I_n A \tau}{\sqrt{3\hbar\omega_3}} = k I_n \quad (11)$$

where Q represents the monochromator and detector efficiency, A is the cross sectional area of the focused laser beams, τ is the temporal pulse width of the Gaussian pump and probe lasers, and I_n is defined by

$$I_n(T) = \int I_3(\omega_3) d\omega_3 \equiv I_1^{Tot} I_2 \int \hat{I}_1(\omega_3 - \delta) |\chi^{(3)}(\delta)|_T^2 d\delta d\omega_3 \quad (12)$$

To simplify the derivation, the following relationship is used:

$$\int \hat{I}_1(\omega_3 - \delta) |x^{(3)}(\delta)|_T^2 d\delta d\omega_3 = k \int |x^{(3)}(\delta)|_T^2 d\delta \quad (13)$$

Thus,

$$I_n(T) = I_1^{\text{Tot}} I_2 k \int |x^{(3)}(\delta)|_T^2 d\delta \quad (14)$$

Ratioing the integrated sample and reference intensities yields

$$\frac{\Sigma_{\text{flame}}}{\Sigma_{\text{ref}}} = \frac{k I_n(T)}{k' I_n(300)} = \frac{k \int |x^{(3)}(\delta)|_T^2 d\delta}{k' \int |x^{(3)}(\delta)|_{300}^2 d\delta} \quad (15)$$

Ratioing to room air for system calibration yields

$$\frac{I_f}{I_a} = \frac{\frac{\Sigma_{\text{flame}}}{\Sigma_{\text{ref}}}}{\frac{\Sigma_{\text{air}}}{\Sigma_{\text{ref}}}} = \frac{\int |x^{(3)}(\delta)|_T^2 d\delta}{\int |x^{(3)}(\delta)|_{300}^2 d\delta} \quad (16)$$

Expanding $|x^{(3)}(\delta)|_T^2$ gives

$$\begin{aligned} \int |x^{(3)}(\delta)|_T^2 d\delta &= \int |x_{nr}^{(3)}|_T^2 d\delta + \frac{2x_{nr}c^4}{\hbar\omega_2} N_T \int \Sigma_{v,J} \frac{R(v,J)(\omega_r - \delta)}{(\omega_r - \delta)^2 + \Gamma^2} d\delta \\ &+ \frac{4c^8 N_T^2}{\hbar^2 \omega_2^2} \int \Sigma_{v,J} \frac{R(v,J)}{(\omega_r - \delta) - i\Gamma} \Sigma_{v,J} \frac{R(v,J)}{(\omega_r - \delta) + i\Gamma} d\delta \end{aligned} \quad (17)$$

where $R(v,J) = \Delta(v,J) \left(\frac{d\sigma}{d\Omega} \right)_{v,J}$.

Substituting back into Eq. (16) and rearranging yields

$$\begin{aligned} \frac{I_f \int |x^{(3)}(\delta)|_{300}^2 d\delta}{I_a} &= |x_{nr}^{(3)}|_T^2 \int d\delta + \frac{2x_{nr}c^4 N_T}{\hbar\omega_2^4} \int \sum_{v,J} \frac{R(v,J)(\omega_r - \delta)}{(\omega_r - \delta)^2 + \Gamma^2} d\delta \\ &+ \frac{4c^8 N_T^2}{\hbar^2 \omega_2^8} \int \sum_{v,J} \frac{R(v,J)}{(\omega_r - \delta) + i\Gamma} \sum_{v,J} \frac{R(v,J)}{(\omega_r - \delta) - i\Gamma} d\delta \end{aligned} \quad (18)$$

The RHS of Eq. (18) is simply a quadratic equation in N_T . Solving the quadratic equation for N_T results in

$$N_T = \frac{-B \pm \sqrt{B^2 - 4AC}}{2A} \quad (19)$$

where

$$\begin{aligned} A &= \frac{4c^8}{\hbar^2 \omega_2^8} \int \sum_{v,J} \frac{R(v,J)}{(\omega_r - \delta) - i\Gamma} \sum_{v,J} \frac{R(v,J)}{(\omega_r - \delta) + i\Gamma} d\delta \\ B &= \frac{2x_{nr}c^4}{\hbar\omega_2^4} \int \sum_{v,J} \frac{R(v,J)(\omega_r - \delta)}{(\omega_r - \delta)^2 + \Gamma^2} d\delta \\ C &= |x_{nr}^{(3)}|_T^2 \int d\delta - \frac{I_f \int |x^{(3)}(\delta)|_{300}^2 d\delta}{I_a} \end{aligned} \quad (20)$$

This equation has been incorporated into the N_2 temperature-fitting routine and used for the analysis of the simultaneous temperature, N_2 , and O_2 work.

The decrease in the O_2 concentration in the flame results in a relatively large nonresonant contribution at high temperatures. This can lead to a large concentration uncertainty due to the decrease in the relative strength of the resonant-to-nonresonant CARS-signal component. The uncertainty in the measurement of the total CARS signal is typically 6-10%. As the resonant component becomes small with respect to the nonresonant, the uncertainties in the total CARS signal may be on the order of the value of the resonant components, resulting in large number-density errors. The number-density error can be expressed as⁹

$$E(N.D.) = \{1/4 E[I(T)]^2 + 1/4 E[I(300)]^2 + 1/4 E(R_T)^2\}^{1/2} \quad (21)$$

The error in the temperature measurement is typically 4%, while the uncertainty in the room-temperature intensity measurement is $\sim 6\%$. The uncertainty in the resonant component $I(T)$ is given by

$$E[I(T)] = E(I) \left[\frac{I_N}{I_R} \right] \quad (22)$$

where $E(I)$ is the measured uncertainty in the total intensity, $\sim 6\%$, and I_N/I_R is the ratio of the nonresonant-to-resonant component defined by

$$\frac{I_N}{I_R} = \frac{|x_{nr}|^2 \int d\delta}{\frac{2x_{nr}c^4}{\hbar\omega_2} \int \sum_{v,J} \frac{R(v,J)(\omega_\theta - \delta)}{(\omega_r - \delta)^2 + \Gamma^2} d\delta + \frac{4c^8}{\hbar^2\omega_2} \int \sum_{v,J} \frac{R(v,J)}{(\omega_r - \delta) - i\Gamma} \sum_{v,J} \frac{R(v,J)}{(\omega_r - \delta) + i\Gamma} d\delta} \quad (23)$$

A plot of $E(N.D.)$ is shown in Fig. 10. At 1800 K the error is 24%, while at 2100 K it is 177%. Thus, the method of determining the number density of O_2

02

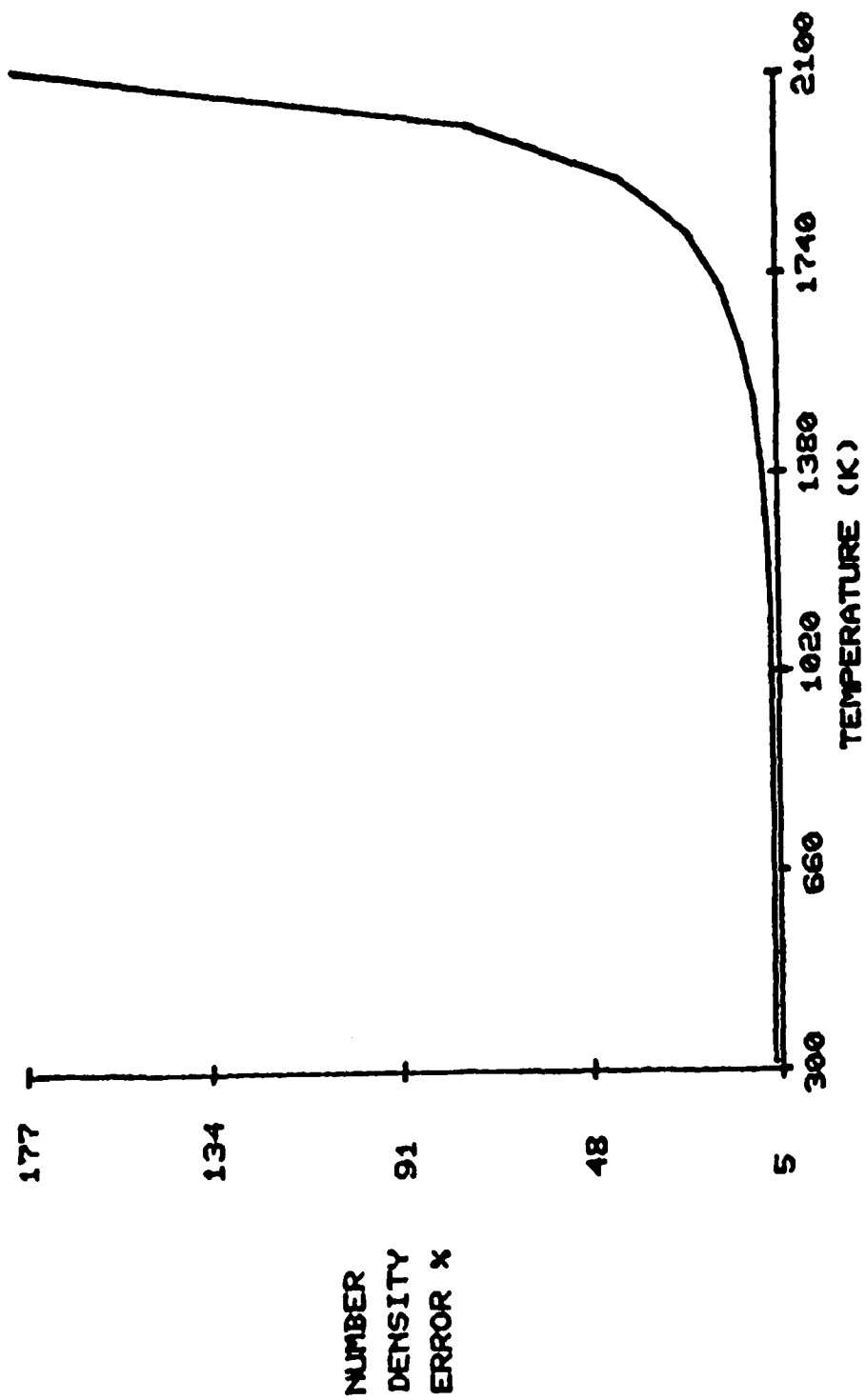


Figure 10. Relative O₂-Number Density Error Versus Temperature for Integration Method of Number-Density Determinations.

from integrated CARS measurements above 1800 K is not very accurate. However, below this temperature the errors are comparable to those of N_2 density measurements. To obtain data above 1800 K, either the background must be canceled by polarization selection¹⁰ or the O_2 lineshape used to determine the number density.¹¹

Preliminary results of data obtained on a turbulent diffusion flame are shown in Fig. 11-14. The data consist of temperature, N_2 , and O_2 histograms and N_2 - O_2 correlations. As discussed in the previous section, above 1800 K the O_2 concentrations are not accurate and deviate from the adiabatic predictions. The O_2 - N_2 correlations follow the adiabatic calculations below 1800 K.

2.6 ALTERNATE CARS TEMPERATURE METHODS

As mentioned in previous work,⁴ to obtain a temperature from a CARS spectrum, a least-squares fit of the data is necessary. This process usually requires ~ 3 sec. per experimental spectrum. In certain cases, however, it would be advantageous to have a real-time display of the temperature, even though the accuracy would be somewhat compromised. Two different temperature methods have been developed for this purpose. These methods are outlined below, along with an analysis of the uncertainties in each.

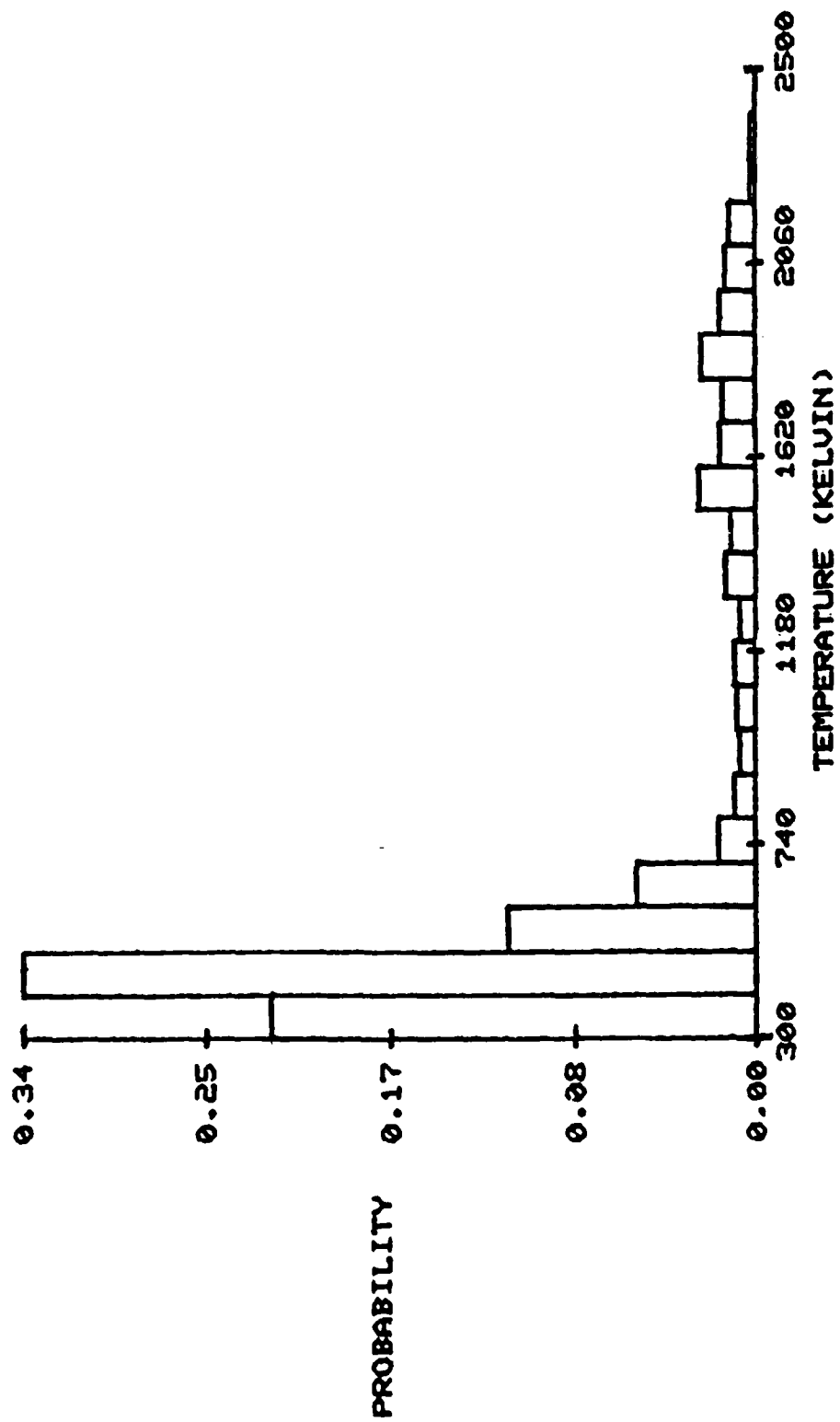


Figure 11. Temperature Histogram Obtained at Location 9.5 cm above Burner Surface.

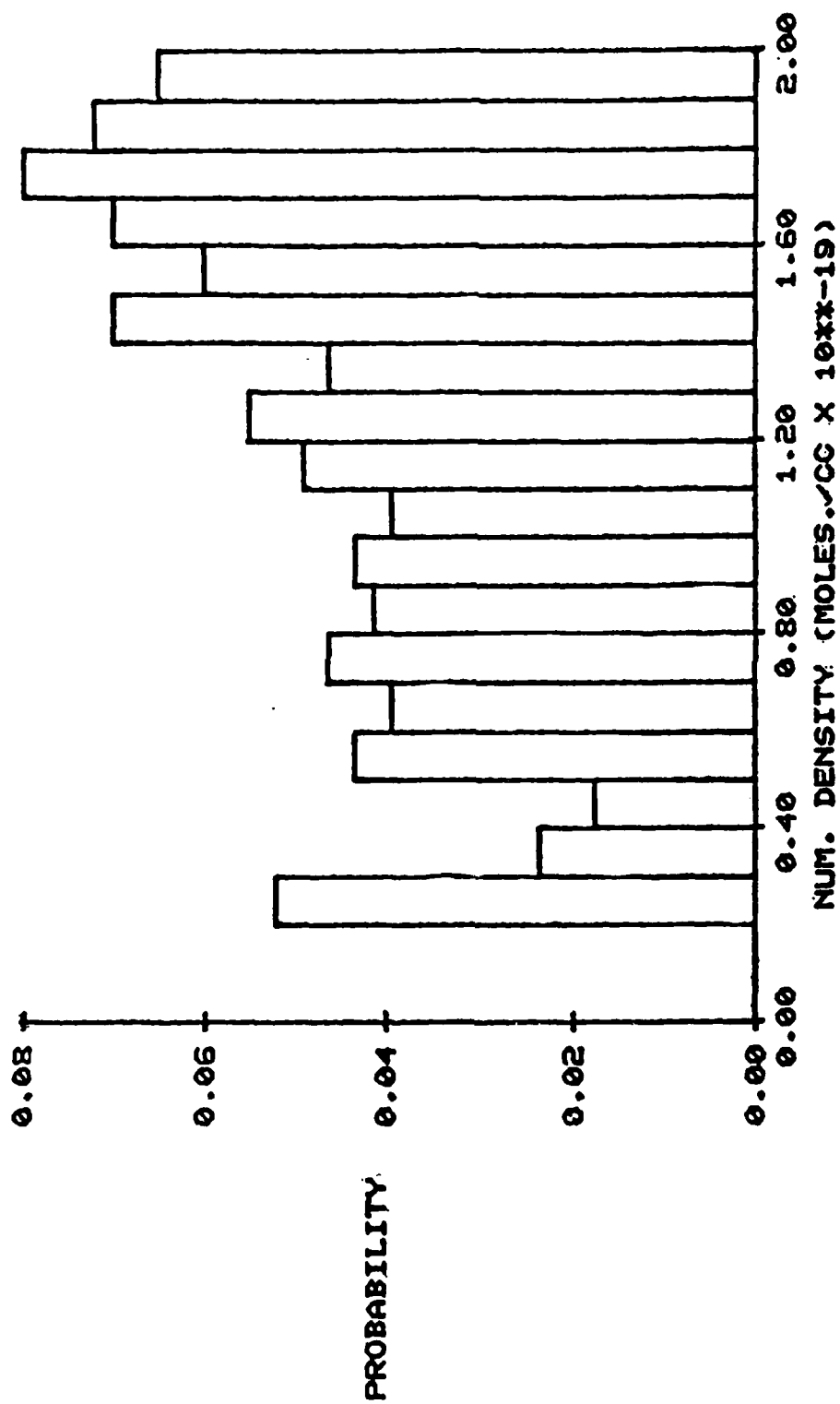


Figure 12. N₂-Number-Density Histogram Obtained at Location 9.5 cm above Burner Surface.

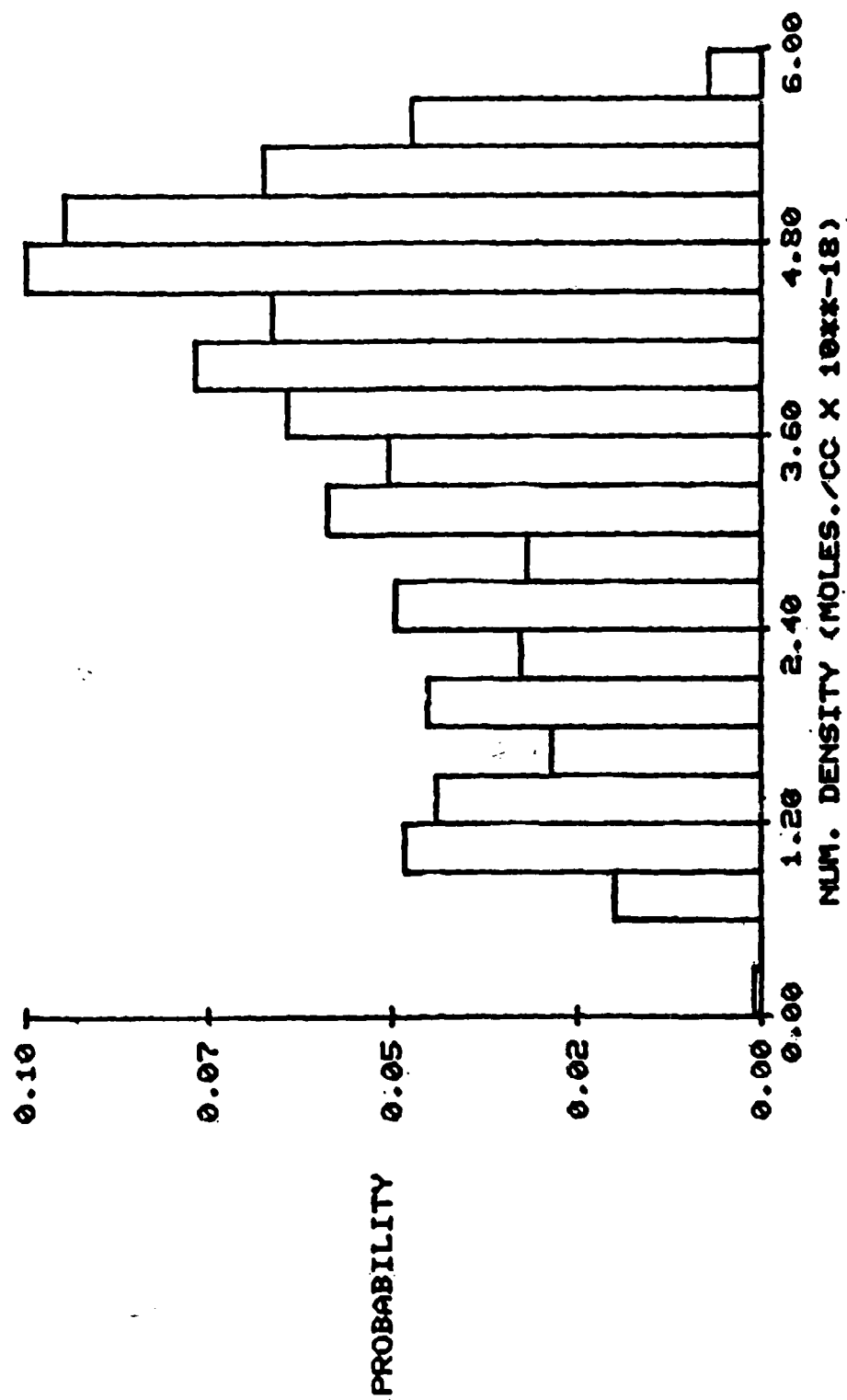


Figure 13. O₂-Number-Density Histogram Obtained at Location 9.5 cm above Burner Surface.

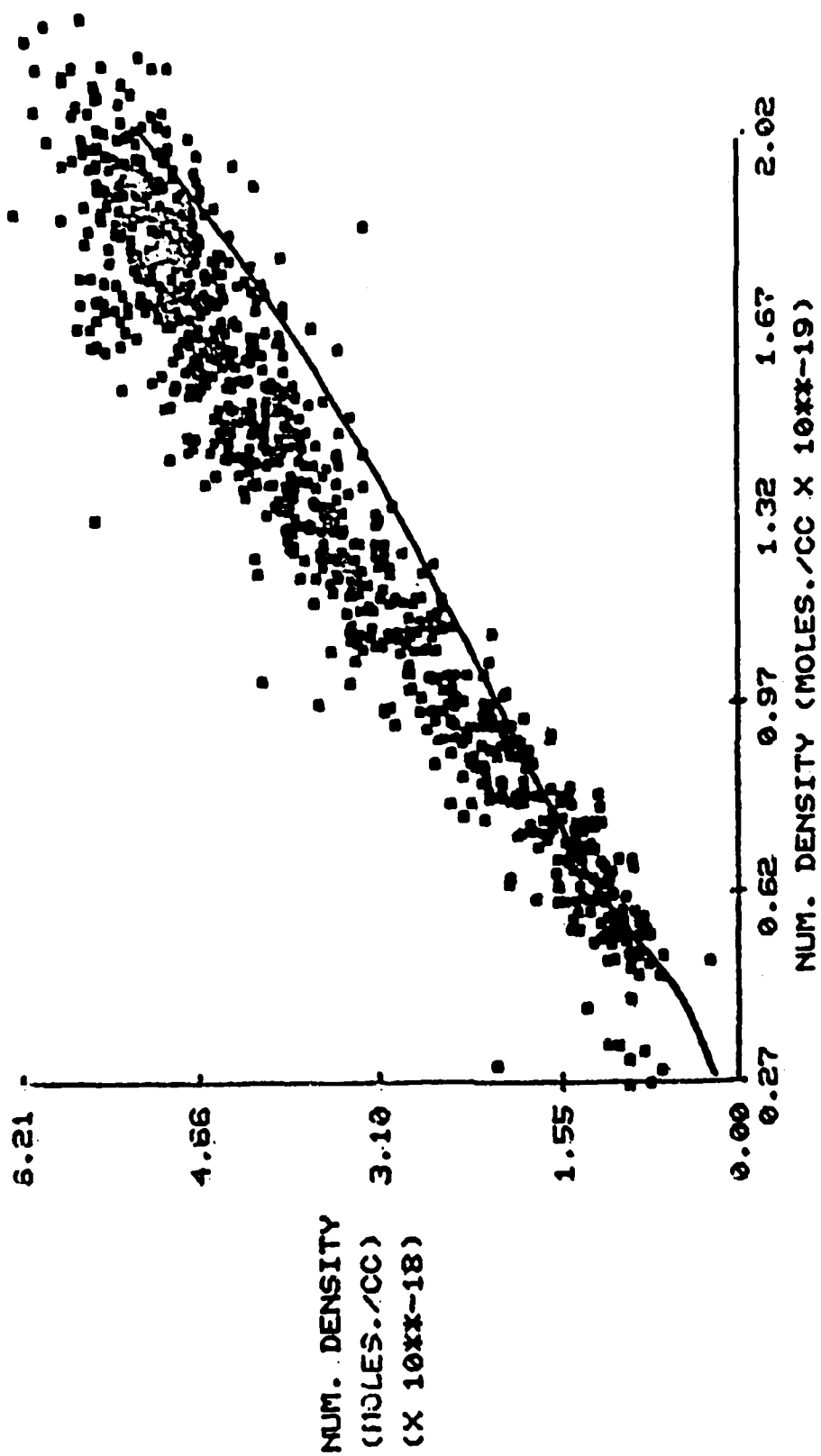


Figure 14. Correlation Plot of O₂-N₂ Versus Adiabatic Calculations (Solid)
Obtained at Location 9.5 cm above Burner Surface.

Nonresonant Temperature Method

As discussed in Refs. 12 and 13, the local flame temperature can be determined from a measure of the third-order nonresonant susceptibility. The signal obtained from the nonresonant susceptibility is given by

$$P_{\omega_3} = k \left(\frac{1}{T} \right)^2 |x_n^{(3)}|^2 P_{\omega_1}^2 P_{\omega_2} \quad (24)$$

where k is an experimental constant which takes into account the detector-monochromator efficiency; T is the temperature; $x_n^{(3)}$ is the nonresonant susceptibility at temperature T ; and P_{ω_i} is the power in the beam at frequency ω_i . As in the resonant concentration method, the signal variation due to the power fluctuation of the laser sources is monitored by ratioing to a reference leg. The ratio of sample to reference signal is given by

$$\frac{P_S}{P_R} = \frac{k' \left(\frac{1}{T_S} \right)^2 |x_n^{(3)}|_S^2 P_{\omega_1}^2 P_{\omega_2}}{k \left(\frac{1}{300} \right)^2 |x_n^{(3)}|_{300}^2 P_{\omega_1}^2 P_{\omega_2}} = \frac{k' \left(\frac{1}{T_S} \right)^2 |x_n^{(3)}|_S^2}{k \left(\frac{1}{300} \right)^2 |x_n^{(3)}|_{300}^2} \quad (25)$$

The experimental constants are determined from calibration of the sample and reference path by a calibrated gas, usually ambient air where the temperature and the magnitude of the nonresonant susceptibility are known. The calibration results in

$$\frac{P_{\text{flame}}}{P_{\text{no flame}}} = \frac{\frac{P_S}{P_R}}{\frac{P_S}{P_R}} = \frac{\frac{k' \left(\frac{1}{T_S} \right)^2 |x_n^{(3)}|_S^2}{k \left(\frac{1}{300} \right)^2 |x_n^{(3)}|_{300}^2}}{\frac{k' \left(\frac{1}{300} \right)^2 |x_n^{(3)}|_{300}^2}{k \left(\frac{1}{300} \right)^2 |x_n^{(3)}|_{300}^2}} = \frac{(300)^2 |x_n^{(3)}|_S^2}{(T_S)^2 |x_n^{(3)}|_{300}^2} \quad (26)$$

Solving for T results in

$$T_S = 300 \frac{|x_n^{(3)}|_S}{|x_n^{(3)}|_{300}} \sqrt{\frac{P_{\text{no flame}}}{P_{\text{flame}}}} \quad (27)$$

Assuming that the flame composition varies as predicted by the equilibrium flame calculations,¹⁴ the nonresonant susceptibilities are shown in Fig. 15. The nonresonant values of Rado were employed for the individual flame constituents. Notice that for a given temperature, two different susceptibility values are possible, depending upon whether there is an excess of fuel or air. To circumvent the problem, the average between the lean and rich values is used as the flame susceptibility. From Eq. (27) an analytical expression for the temperature uncertainty can be developed. The uncertainty is given by

$$E(T) = [E(x_n^{(3)})_S^2 + \frac{1}{4}E(P_{\text{flame}})^2 + \frac{1}{4}E(P_{\text{no flame}})^2]^{1/2} \quad (28)$$

The maximum uncertainty in the $x_n^{(3)}$ with temperature is the difference between the average value and the fuel-lean or -rich curve. At 2000 K this uncertainty is $\sim 2\%$. The uncertainty in the measured intensity is the correlation uncertainty between the sample and the reference which is measured to be $\sim 6\%$. Substituting these values into Eq. (28) yields

$$E(T) = [\frac{1}{4}(0.06)^2 + \frac{1}{4}(0.06)^2 + (0.02)^2]^{1/2} = 4.6\%$$

which translates into a 94-K uncertainty in the temperature at 2000 K. This is comparable to the uncertainty of the full Q-branch measurement at this temperature.

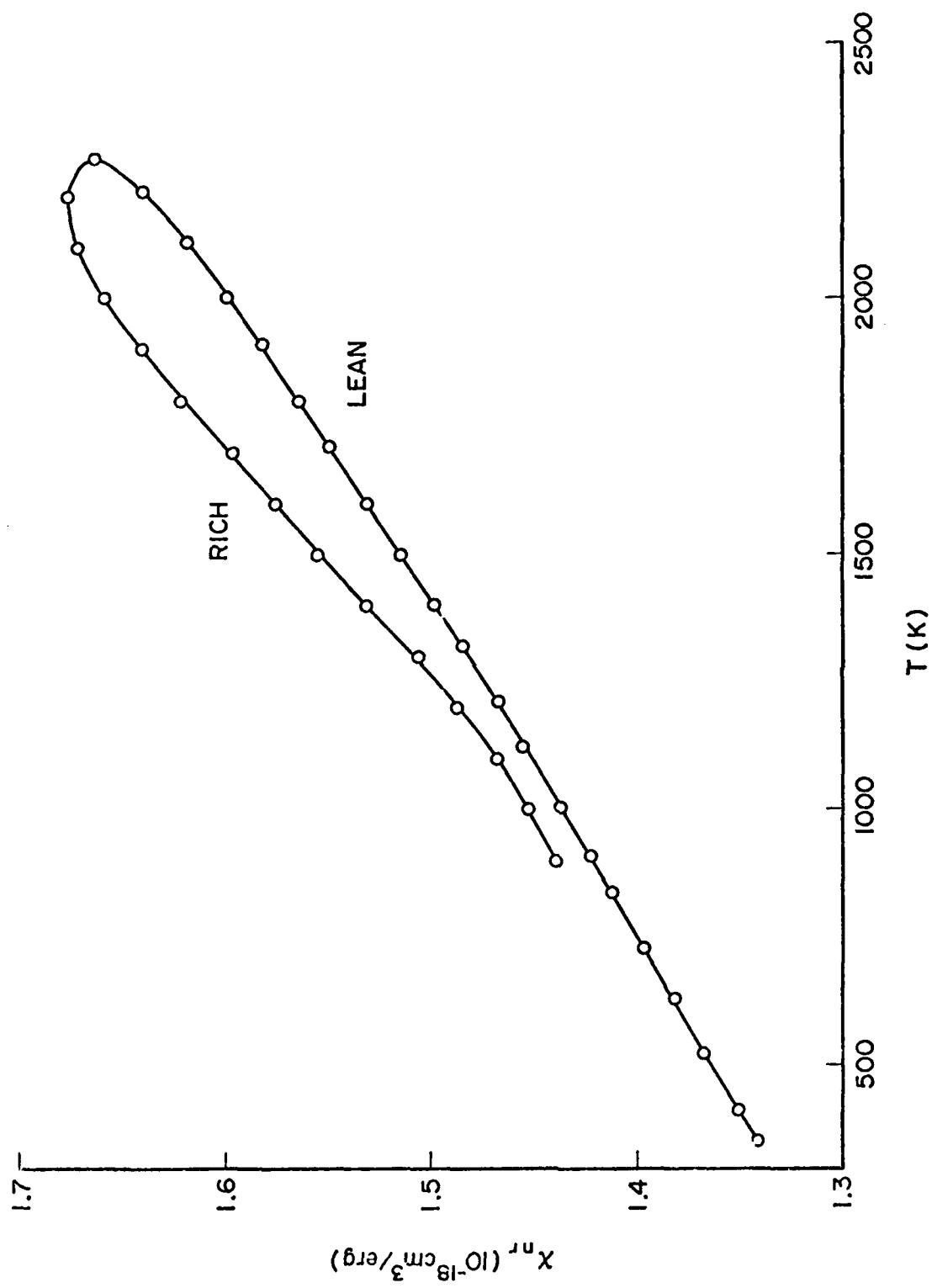


Figure 15. Variation in Nonresonant Susceptibility (χ_{nr}) as Function of Temperature.

Intensity Temperature Methods

Both the peak and integrated intensities of the Q-branch of N_2 are sensitive functions of the temperature, as shown in Fig. 16. The change in the CARS signal with temperature is predominantly due to the change in the number density with temperature. If the flame of interest can be modeled such that the composition of the main constituents are known as a function of temperature, then the variation in intensity alone can be used to determine the temperature. For the propane-air flame previously described, the adiabatic flame model of Gordon and McBride¹⁴ has been used.

Figure 17 is a plot of the temperature as a function of χ , the log of the intensity; the fit of this curve to a power series in χ is given by

$$T = A + B\chi + C\chi^2 + D\chi^3 + E\chi^4 \quad (29)$$

where $\chi = \log(I)$ and

$$A = 299.71$$

$$B = -504.72$$

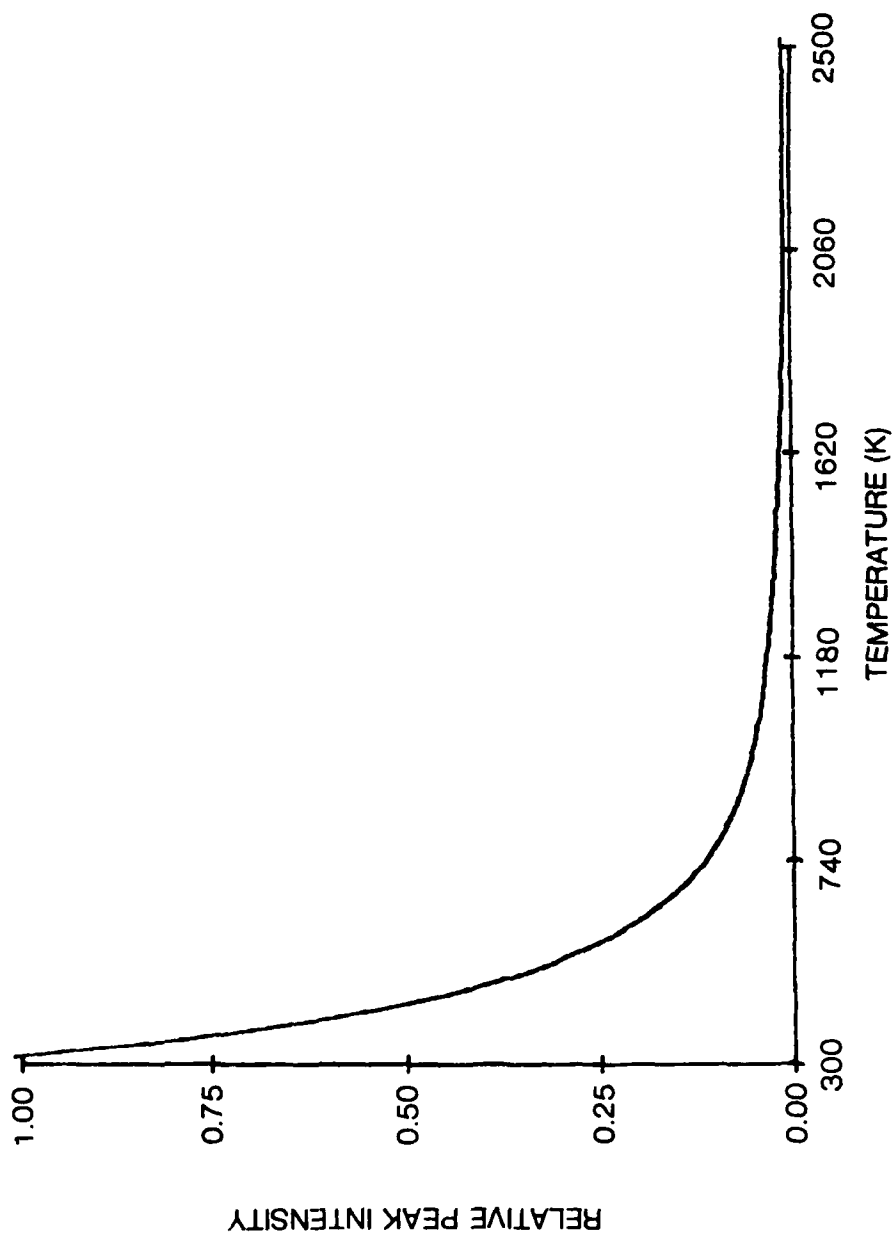
$$C = -401.43$$

$$D = -520.65$$

$$E = -123.32$$

By measuring the CARS intensity in the same manner as that required for the concentration measurement or nonresonant temperature measurement, the temperature can be determined from Eq. (29).

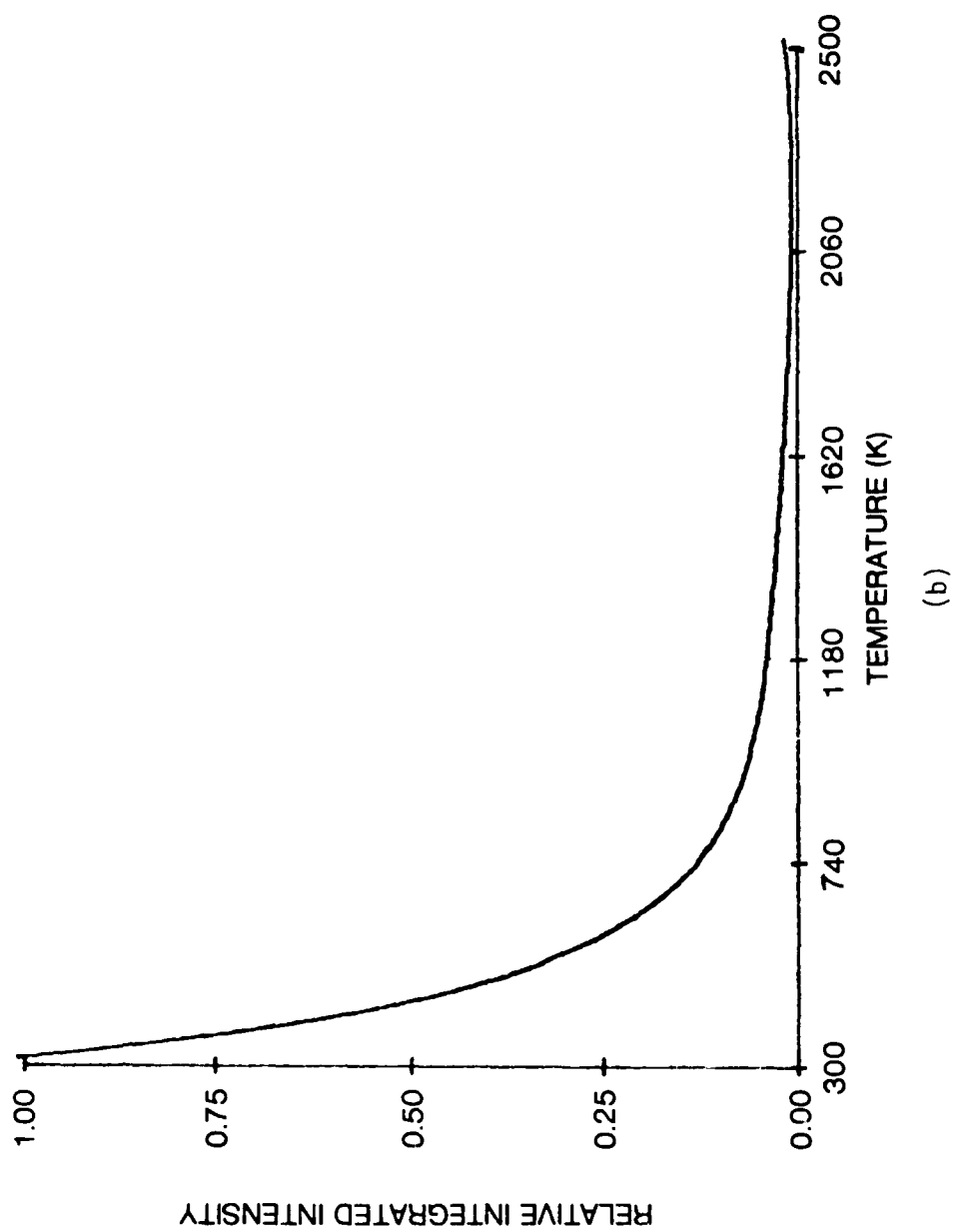
N₂ Q-BRANCH



(a)

Figure 16. Variation of (a) Peak and (b) Integrated CARS Intensity of Q-Branch of N₂ with Temperature.

N₂ Q-BRANCH



(b)

Figure 16. Continued.

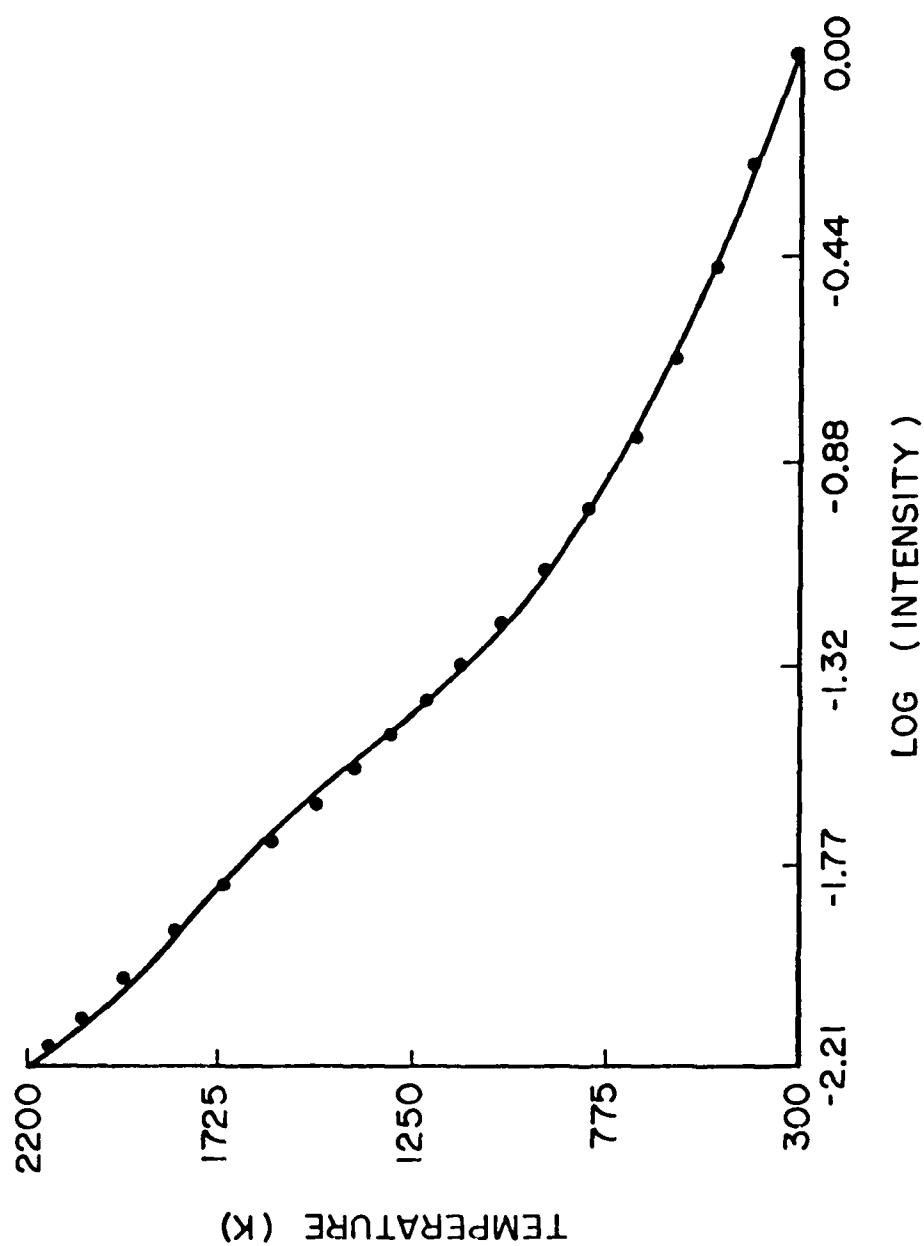


Figure 17. Plot of Variation of Temperature with Log of Integrated CARS Signal of Q-Branch of N_2 .

The uncertainty in the temperature determination, assuming the flame model to be valid, is given by

$$\frac{1}{\sigma_T^2} = \frac{1}{\sigma_m^2} \sum_i \left(\frac{dI_i}{dT} \right)^2 \quad (30)$$

Assuming an intensity uncertainty of 10% in the intensity measurement, the resulting temperature uncertainty as a function of temperature is shown in Fig. 18. The temperature uncertainty is quite low, except when the flame temperature becomes higher than ~ 2100 K. This is due to the fact that the derivative $(dI_i/dT) \rightarrow 0$ as $T \rightarrow 2200$ K, thus indicating that the method is not well suited for this region. However, below 2100 K and especially at low temperatures where there is no hot band for the full Q-branch temperature determination, the integrated-intensity method is quite attractive. Since the information required for the temperature measurement is normally obtained for the full Q-branch measurement, this method can be used to obtain a first estimate of the flame temperature in real time.

2.7 DETERMINATION OF RAMAN LINEWIDTHS FROM CARS SPECTRA

The sensitivity of the CARS spectrum to the linewidths of the Raman transition allows determination of the linewidth in certain cases. One such case is the hydrogen-fluoride (HF) molecule. In conjunction with AFIT thesis student R. A. Cleis and AFIT Prof. W. B. Roh, a study of the Raman linewidths of HF was undertaken and reported in the paper entitled, "Raman Linewidths of Hydrogen Fluoride Determined by Using Low-Resolution Coherent Anti-Stokes Raman Spectroscopy," which appears on the following pages.

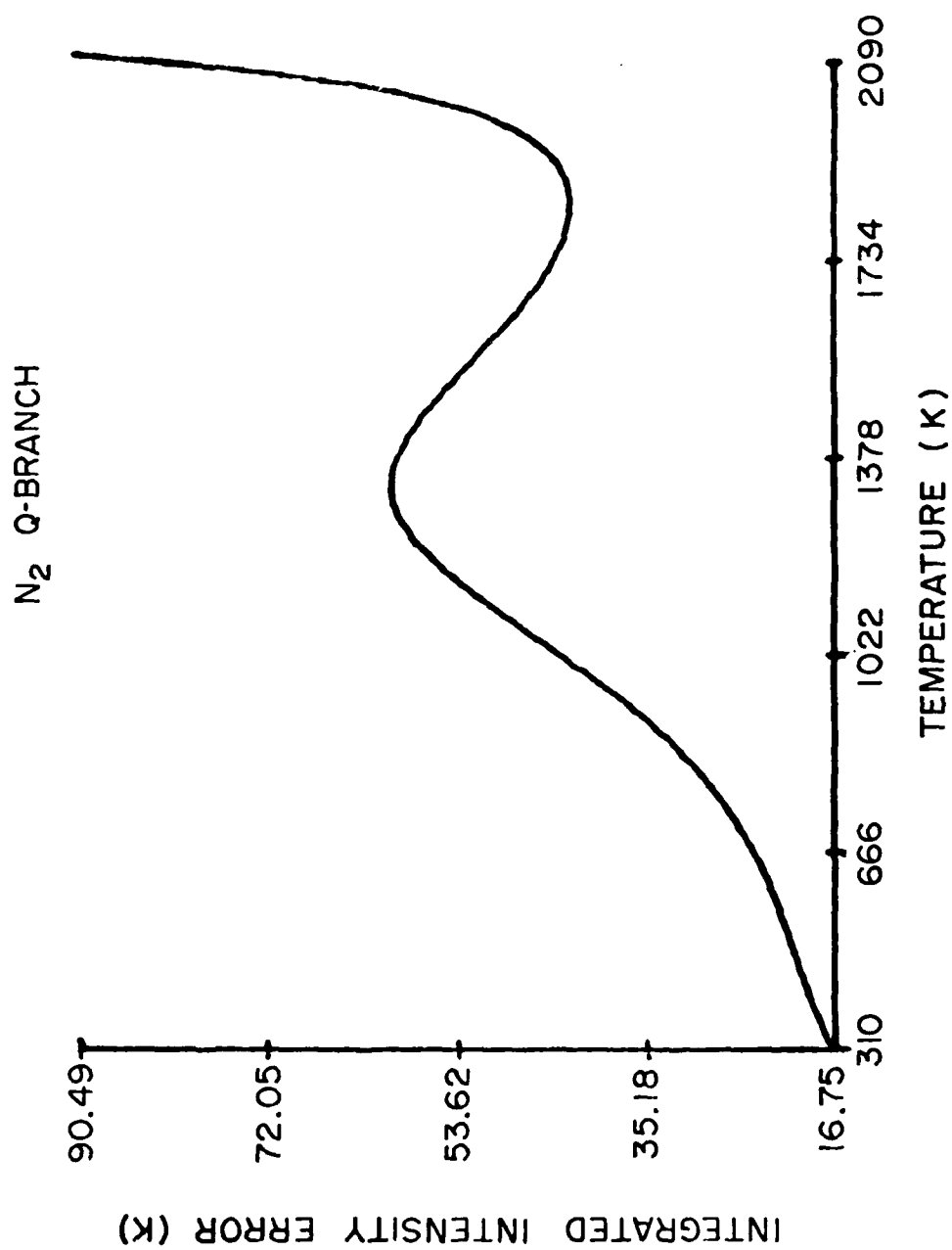


Figure 18. Uncertainty of Temperature Determined by Integrated CARS Intensity as Function of Temperature.

Raman linewidths of hydrogen fluoride determined by using low-resolution coherent anti-Stokes Raman spectroscopy

Richard A. Cleis* and Won B. Roh

Department of Engineering Physics, Air Force Institute of Technology, Wright-Patterson Air Force Base, Ohio 45433

Larry P. Goss

Systems Research Laboratories, Inc., 2800 Indian Ripple Road, Dayton, Ohio 45440-3696

Received May 14, 1984; accepted July 31, 1984

The *Q*-branch linewidths of hydrogen fluoride were measured by using coherent anti-Stokes Raman spectroscopy (CARS). The first seven transitions were excited by a broadband CARS system, and low-resolution spectra were recorded on an optical multichannel analyzer at pressures from 50 to 700 Torr in 50-Torr increments. A nonlinear least-squares program was employed to fit calculated spectra to experimental spectra by adjusting the linewidths. All lines displayed pressure broadening over the pressure region investigated, with relative magnitudes being consistent with theory and available infrared data. Although the *Q*-branch lines of the observed spectra were partially blended, the CARS data and calculations permitted consistent linewidth measurements over the pressure range of the experiment.

INTRODUCTION

Coherent anti-Stokes Raman spectroscopy (CARS) has become one of the more effective diagnostic tools for combustion and plasma media.¹ With this technique, parameters such as species concentration and temperature can be determined without introducing sensors into the medium under investigation. Typically, for these specific parameters, experimental CARS spectra of a given species, say, hydrogen fluoride (HF) are recorded and then analyzed in accordance with a theoretical model appropriate for that species.

One of the most important experimental parameters that enter into the theoretical model is the linewidths of the Raman transitions. The linewidth affects the CARS spectral profile in two ways: first, through an inverse-square (Γ^{-2}) dependence of the peak intensity of individual lines on linewidth, and second, through the interference among adjacent rotational Raman lines. Therefore Raman-linewidth data on relevant molecular species are essential for the development of the CARS technique into a practical diagnostic tool. Through high-resolution CARS or stimulated-Raman-gain experiments, such data have become available in recent years for certain molecules that are of interest to combustion diagnostics, such as nitrogen,² methane,^{3,4} hydrogen,⁴ deuterium,^{4,5} and acetylene.⁶ However, for many other relevant molecules, data are not yet available.

The HF molecule is of interest because of its importance in high-energy-laser applications. It is also an interesting molecule from a basic-spectroscopy standpoint in that the linewidths of the vibrational-rotational transitions are highly dependent on the rotational quantum number (*J*) of the states involved. Although this dependence is observed in other molecules as well, the variation in linewidth is not large and, consequently, the dependence can often be neglected in practice. The *J* dependence of linewidth for HF, while in-

teresting in its own right, is a source of error in CARS diagnostics if not properly taken into account in the theoretical model. In fact, in an earlier experiment, it was observed that this oversight resulted in an erroneous temperature estimate of 415 K from a spectrum of HF recorded at room temperature.⁷

In this paper, HF Raman linewidths are reported that were measured by using a low-resolution CARS system. In particular, the pressure-broadening coefficient (self-broadening) for each of the first seven vibrational-rotational *Q*-branch lines has been determined based on experimental CARS spectra in the pressure range 50–700 Torr of pure HF gas. The results obtained compare favorably with IR-absorption data available in the open literature. It is important to note that, in this research, the linewidth measurements were made by using a low-resolution CARS systems and that even the linewidth of the weak *Q*(0) line, which is almost always blended completely into the stronger *Q*(1) line, was determined.

THEORETICAL CONSIDERATIONS

The third-order susceptibility that governs CARS can be expressed in abbreviated form as

$$\chi^{(3)} = \chi_n + \chi_r, \quad (1)$$

where χ_n is the nonresonant contribution and χ_r is the Raman resonant contribution to the third-order susceptibility. χ_r , far from electronic resonance, is given by

$$\chi_r = \frac{2c^4}{h\omega_s^4} N \sum_{v,J} \frac{\Delta(v,J)(d\sigma/d\Omega)_{v,J}}{\omega_r - \delta - i\Gamma(v,J)}, \quad (2)$$

where *N* is the total number density of the species being probed, $\Delta(v,J)$ is the population difference between the states involved in the Raman transition, ω_r is the frequency of the

Raman transition, δ is the frequency difference between the pump ω_1 and the probe ω_2 , $\Gamma(\nu, J)$ is the HWHM of the Raman transition, and $(d\sigma/d\Omega)_{\nu, J}$ is the Raman-scattering cross section.

The CARS intensity distribution is given by⁸

$$I_3(\omega_3) \sim \int d\omega_3' T(\omega_3 - \omega_3') \int d\omega_1 I_1(\omega_1) \times \int d\omega_2 I_2(\omega_3' - \omega_1 + \omega_2) | \chi_3(\omega_1 - \omega_2) |^2, \quad (3)$$

where T is the slit function and I_1 and I_2 are the spectral densities of the pump and Stokes sources, respectively. In broadband CARS, the Stokes bandwidth normally is sufficiently large that I_2 can be taken outside the integrals; expression (3) is then expressible as

$$I_3(\omega_3) \sim I_1^{\text{tot}} I_2 \int I_1(\omega_3 - \delta) | \chi_3(\delta) |^2 d\delta, \quad (4)$$

where I_1^{tot} is the total pump intensity (integrated over all frequencies), I_2 is the Stokes intensity per unit frequency interval, I_1 is the pump intensity distribution convolved over the slit function, and the variable of integration δ varies over all values of the detuning $\omega_1 - \omega_2$.

For calculation of a CARS HF spectrum, the third-order susceptibility is generated according to Eqs. (1) and (2) and subsequently convolved over the pump-laser linewidths and the appropriate slit function as dictated by expression (4).

A nonlinear least-squares (NLLS) program has been developed for determining the Raman linewidths from the observed experimental spectrum. The program is based on the matrix equation^{9,10}

$$\Delta \Gamma = (J^+ J)^{-1} J^+ \Delta \phi, \quad (5)$$

where J is the Jacobian matrix whose elements are defined by $J_{im} = dI_i/d\Gamma_m$ (I_i being the i th intensity and Γ_m the m th Raman linewidth), J^+ is the transpose of the J matrix, $\Delta \phi$ is the matrix with elements $\Delta \phi_i = I_{i\text{obs}} - I_{i\text{cal}}$ (where $I_{i\text{obs}}$ is the i th observed experimental intensity and $I_{i\text{cal}}$ the i th calculated intensity), and $\Delta \Gamma$ is the matrix whose elements are corrections to be made to the Raman linewidths.

The iteration given in Eq. (5) was used to best fit the Raman linewidths, as a function of pressure. The pressure-broadening coefficients (a_J) were then determined with the aid of a linear-regression routine.

EXPERIMENT

The experimental system employed in these experiments was similar to that in Ref. 11 and is shown in Fig. 1. A Q-switched Quanta Ray Nd:YAG laser with an amplifier stage is frequency doubled and filtered through a prism harmonic separator. The resulting 532-nm beam (HWHM 0.5 cm⁻¹) is split into four beams of equal intensity.

Three of the beams are used to pump a three-stage dye laser, while the remaining beam is focused in the sample cell (along with the dye beam) to generate the CARS signal.

The dye-laser beam is generated from an oscillator stage and two amplifier stages. Each stage is optically pumped by one of the equal-intensity portions of the 532-nm beam. A single mechanical pump circulates the dye fluid for all three stages.

A collinear focusing arrangement is incorporated by first collimating the dye beam with a simple telescope and then

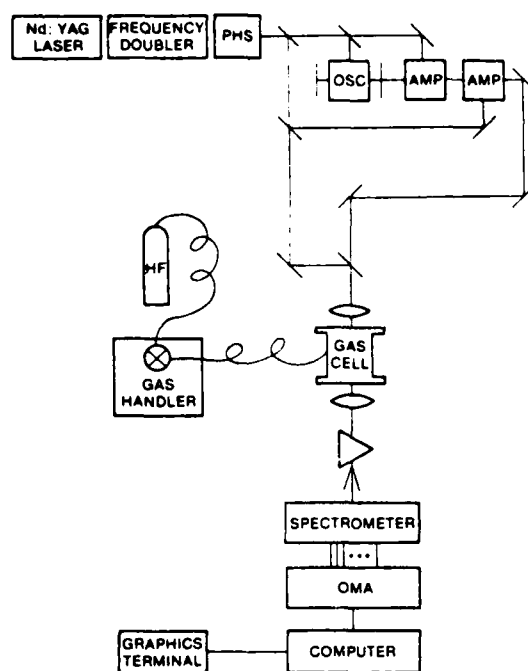


Fig. 1. Schematic diagram of experimental system: PHS, prism harmonic separator; OSC, dye oscillator.

combining it through a dichroic mirror with the 532-nm beam. The combined beams are focused through a 30-cm lens into a gas cell fitted with sapphire windows, which are impervious to the highly corrosive HF gas. A gas-handling system transfers the gas to the cell through stainless-steel tubing and polyethylene hoses. Pressure is monitored with a capacitance manometer built into the gas-handling system.

The two beams and the generated CARS signal leaving the gas cell are collimated with a second 30-cm lens. Separation of the CARS signal from the dye beam and the 532-nm beam is achieved with a Pellin-Broca prism and an aperture. The signal is then focused into a Spex 0.75-m monochromator.

The monochromator was fitted with a 512-channel intensified diode-array rapid-scanning-spectrometer detector head compatible with a Tracor-Northern Model TN-1710 optical multichannel analyzer (OMA). With this arrangement, data could be taken during the laser pulse and then converted and read by the OMA before the next pulse. A 632-nm-groove/mm grating with a blaze angle of 49° produced dispersion equivalent to 0.875 cm⁻¹/channel of the detector. The individual diodes were separated by 50-μm centers.

CARS data could be acquired by the OMA and sent to a ModComp 7840 Classic 16-bit minicomputer for storage on tape for future analysis. The system was capable of producing and recording CARS data at a 10-Hz rate; therefore it was possible to record 1000 pulses of CARS data at 14 different sample pressures in one afternoon.

The experimental data stored on tape consisted of CARS sample and background spectra. Background data were recorded by blocking the dye beam to eliminate the CARS signal and then measuring the intensity of the scattered 532-nm beam. The spectral profile of the dye laser was also recorded by generating a nonresonant CARS signal in propane gas. This profile was used to normalize the HF CARS signal with

respect to nonuniform excitation of the broadband Stokes beam.

CARS data (1000 pulses) and background data (200 pulses) were recorded at 50-Torr increments between 50 and 700 Torr. At each pressure, CARS and background data were individually averaged, and then the background was subtracted from the CARS intensity recorded by each channel.

RESULTS AND DISCUSSION

The pressure-broadening coefficients (a_J) of the first seven vibrational-rotational transitions of HF were determined as follows: First, the Raman linewidths at each experimental pressure were obtained by fitting the experimental data with the NLLS iteration [Eq. (5)], and second, the pressure-broadening coefficients were calculated from the slopes of the linewidth-pressure relationship. The most important concept is the dependence of the peak intensity in the observed spectra on the linewidths (Γ_J) of the corresponding Raman transitions. At a given pressure, the Raman linewidths can be used for partial determination of both the magnitudes and the widths of the peaks of the observed spectrum. However, the range of Raman linewidths encountered in the experiment was small compared with the resolution of the experimental system; therefore the analytical procedure was dependent primarily on the information contained in the peak intensities.

The first step in the analysis was the reduction of the raw experimental spectra to correct for the slowly varying baseline shift that was due to background noise, nonresonant contributions, etc. The background-corrected CARS spectra were then normalized according to a nonresonant spectrum obtained in propane gas. This step compensates for the non-uniform intensity distribution of the Stokes beam. An example of a background-corrected, normalized CARS spectrum is shown in Fig. 2. The spectra recorded at each pressure are fitted to a calculated spectrum using the effective slit function estimated initially from the spectrum recorded at the lowest pressure (50 Torr).

Computer calculation of the CARS spectrum was performed by first evaluating the nonlinear susceptibility [Eqs. (1) and (2)] and then the spectral intensity of the anti-Stokes radiation generated [expression (4)]. The effect of the finite

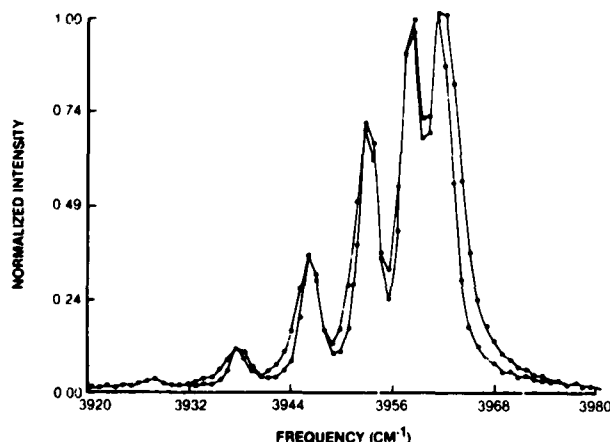


Fig. 2. Superimposed spectra of 50- and 700-Torr HF. The maximum intensity of each spectrum was normalized to 1.

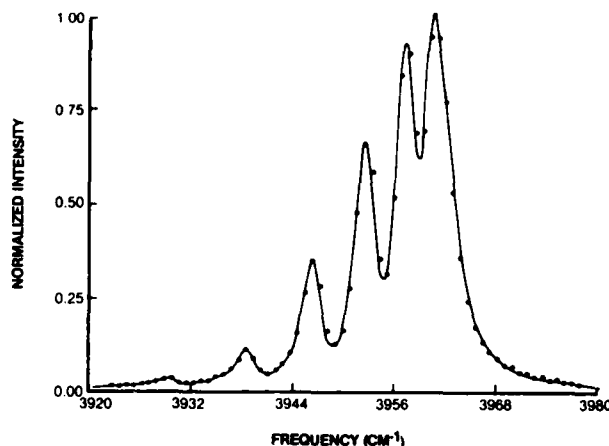


Fig. 3. NLLS fit of CARS spectrum of 700-Torr HF.

laser linewidth (a Gaussian with 0.5-cm^{-1} HWHM for the pump laser) is incorporated in this step. The anti-Stokes spectral power density is convolved with the effective slit function of the detection system (monochromator and OMA), which yields the final calculated spectrum.

Details of the NLLS fitting routine (which makes use of a form of area normalization to match the amplitude of the data to calculations) were given previously.¹⁰ The dependent variables in the fitting routine are the seven linewidths of the HF Raman lines (Γ_J , $J = 0-6$). Shown in Fig. 3 is a representative experimental spectrum fitted to a calculated spectrum.

It is important to note that the fitting routine does not depend on the existence of a known linewidth for any of the Raman lines observed in the spectrum for calibration purposes. This would seem implausible in view of the fact that only the relative signal strengths are used in the fitting process. However, thanks to the interference effect that one observes in CARS spectra among adjacent Raman resonances (especially when the lines are within a linewidth or so of each other), the absolute magnitude of Raman linewidths affects the shape as well as the magnitude of the CARS signal. Thus the fitting routine is able to extract the linewidths of all Raman lines without the aid of an external calibration source. This particular technique is applicable to all molecular species with the possible exception of H_2 at low pressure.

The NLLS-fitting-routine results were dependent on the experimental slit width Γ_c . An overestimated Γ_c causes the routine to converge to smaller values of Γ_J , since the total contribution of Γ_c , Γ_J , and the width of the spectral profile of the pump beam must best fit the widths of the peaks in the experimental spectra. Since the results are sensitive to errors in Γ_c , accurate determination of Γ_c is critical. Once the linewidth at each of the 14 experimental pressures was determined through the nonlinear-estimation routine, these linewidths were used for determining the pressure-broadening coefficients with the aid of a linear-regression routine. Figure 4 shows a typical pressure dependence of the Raman linewidth, and Table 1 lists the pressure-broadening coefficients (a_J) and deviation of the coefficients as determined by the regression analysis for all lines measured.

The validity of the Γ_c value used in the nonlinear fitting procedure can be tested by investigating the y intercepts of

the regression line computed for Γ_J versus pressure. Although pressure broadening does not occur at low pressures, the extrapolated regression lines should pass through the Doppler-broadened linewidth, which, at the very small value of 0.0055 cm^{-1} HWHM, is for all practical purposes at the origin. The y intercepts of the $Q(1)$ – $Q(5)$ transitions are near the origin, and the y intercepts of the $Q(0)$ and $Q(6)$ transitions are good, considering that the former is not resolved and

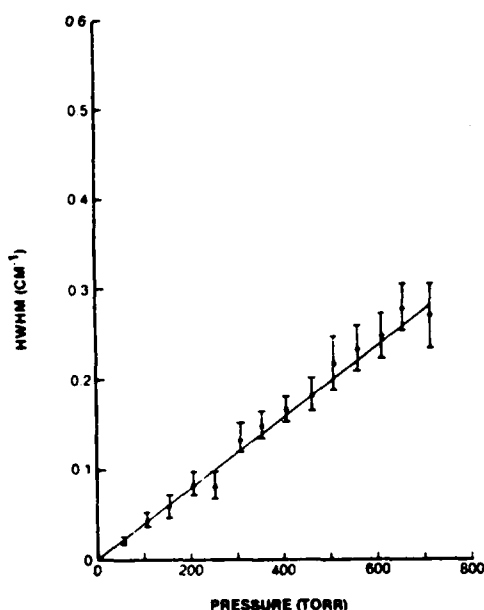


Fig. 4. Pressure dependence of Raman linewidth of $Q(5)$ line.

Table 1. Experimentally Obtained Pressure-Broadening Coefficients of HF and Their Standard Deviation^a

J	a_J ($\text{cm}^{-1}/\text{Torr}$)	$\sigma(a_J)$ ($\text{cm}^{-1}/\text{Torr}$)	Y intercept (cm^{-1})
0	0.5646×10^{-3}	0.027×10^{-3}	-0.0307
1	0.6376×10^{-3}	0.037×10^{-3}	0.0045
2	0.7310×10^{-3}	0.042×10^{-3}	0.0035
3	0.6481×10^{-3}	0.033×10^{-3}	0.0006
4	0.4796×10^{-3}	0.019×10^{-3}	0.0005
5	0.4102×10^{-3}	0.014×10^{-3}	0.0010
6	0.2888×10^{-3}	0.026×10^{-3}	0.0300

^a HWHM of instrument slit function = 0.767 cm^{-1} .

Table 2. Variation of y Intercept with Instrument Slit Function

J	Width of Slit Function (cm^{-1} HWHM)		
	0.700	0.767	0.900
0	-0.0528	-0.0307	-0.0023
1	0.1460	0.0045	-0.0060
2	0.0223	0.0035	-0.0120
3	0.0173	0.0006	-0.0118
4	0.0131	0.0005	-0.0074
5	0.0109	0.0010	-0.0040
6	0.0451	0.0300	-0.0193

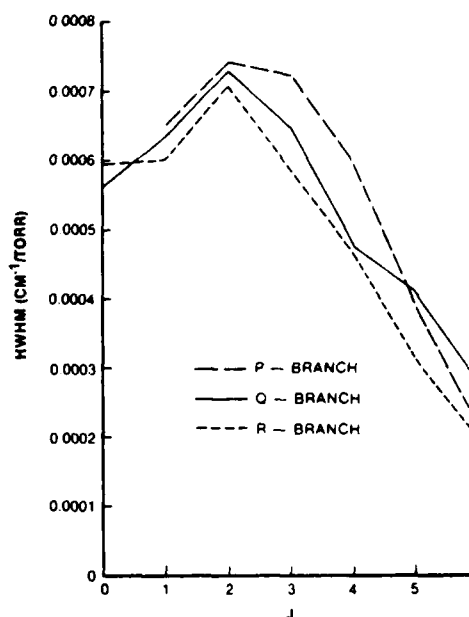


Fig. 5. Comparison of pressure-broadening coefficients of the P , Q , and R branches of HF.

the latter produced low-intensity signals during the experiment (Table 2).

Since the only independent variable in the NLLS fitting routine was Γ_e , the sensitivity of the y intercepts to Γ_e was analyzed. The pressure-broadening coefficients and y intercepts were determined for six different values of Γ_e ranging from 0.70 to 0.90 cm^{-1} . Table 2 gives the resulting y intercepts for the two extreme values as well as the optimum value of Γ_e determined earlier. The overestimate of Γ_e results in negative intercepts, and the underestimate results in positive intercepts. The negative intercepts obtained with $\Gamma_e = 0.9 \text{ cm}^{-1}$ HWHM are not large, since the fitting routine does not permit negative solutions to the linewidths. When Γ_e is overestimated, the solutions for Γ_J becomes smaller, but the values of Γ_J at the lowest pressures can only approach zero. This affects the solutions at the lower and higher pressures, since the relative magnitudes of the peaks in the experimental spectra are determined by the relative magnitudes of Γ_J . Underestimates of Γ_e , on the other hand, cause the y intercepts to rise more rapidly, since the solutions to the linewidths can increase without bound. The main point here is that, by selecting a value of Γ_e that yields vanishingly small y intercepts for all Raman lines, one can refine and optimize the value of Γ_e and thereby the values of the pressure-broadening coefficients estimated in the analysis.

The pressure-broadening coefficients for Q -branch lines obtained in the present analysis are displayed in Fig. 5, along with those for P - and R -branch lines obtained from IR absorption data available in the open literature.¹² Note that the Q -branch broadening coefficients lie, for the most part, between those of the P and R branches. This observation is gratifying for the following reasons: Since Q -branch lines and P - and R -branch lines are exclusively observed in Raman and the IR, respectively, direct comparison between the two sets of data does not appear to be meaningful. However, in view of the fact that $Q(J)$, $P(J)$, and $R(J)$ lines have a common lower level and that the upper level of the $Q(J)$ line is sand-

Table 3. Q(3) Pressure-Broadening Coefficient Estimated from IR Data^a

Transition	Coefficient	Remark
R(3)	0.587	Average of R(3) and P(3)
P(3)	0.725	
Q(3)	0.656	
R(2)	0.707	Average of R(2) and P(4)
P(4)	0.596	
Q(3)	0.651	

^a Data calculated from linewidths given in Ref. 12.

wiched in energy between $P(J)$ and $R(J)$, it is reasonable to expect, on the basis of lifetime and dephasing time of the levels, that the linewidth of the $Q(J)$ line lies between those of the $P(J)$ and $R(J)$ lines. By the same token, it is reasonable to expect a similar relationship among $Q(J)$, $R(J-1)$, and $P(J+1)$.

In the pressure-broadened region, the linewidths are directly proportional to pressure. Thus the relationships among linewidths hold for the pressure-broadening coefficients as well. For example, the pressure-broadening coefficient a_3 of the $Q(3)$ line can be calculated by averaging the coefficients of $P(3)$ and $R(3)$ lines and of $P(4)$ and $R(2)$. Table 3 shows the results obtained from the data in Ref. 12. The pressure-broadening coefficient of the $R(3)$ transition is smaller than that of the $P(3)$ transition, and the pressure-broadening coefficient of the $R(2)$ transition is larger than that of the $P(4)$ transition. Also note that the average of the pressure-broadening coefficients of the $P(3)$ and $R(3)$ transitions is remarkably close to the average of the pressure-broadening coefficients of the $P(4)$ and $R(2)$ transitions. These observations are consistent and tend to substantiate the assumption that the Q -branch linewidths are approximately equal to the average of those of the corresponding P - and R -branch lines. At the same time, the observation lends credence to the linewidth-measurement technique described in this paper for the determination of Raman lines and their pressure-broadening coefficients for HF and other molecules. The IR data used in Fig. 5 for comparison purposes were obtained from a gas sample at an elevated temperature (373 K), as compared with room temperature (298 K) for the present research. However, the effect of a temperature variation of 75 K on the linewidths has been shown to be minimal for $R(2)$, $R(3)$, $P(3)$, and $P(4)$ lines.¹³ Thus the conclusions drawn in the preceding paragraph should be valid. Although an IR-absorption measurement has been made at room temperature,¹⁴ the data cover only R -branch lines and not P -branch lines. As a result, these data were not applicable for the present analysis. In addition, the measured linewidths of the R -branch lines were unreasonably larger than those determined from other IR data,^{12,14} even when temperature effects were taken into account. Consequently, the data were discarded in the present analysis. High-resolution measurements will ultimately provide validation of the technique and the results discussed here. To that end, research is now in progress to make cw CARS measurements of HF linewidths by using a single-mode laser system.

In summary, a low-resolution, broadband CARS system was used to measure the linewidths of the first seven vibrational-rotational Raman transitions of HF. A NLLS routine was used to fit the calculated experimental spectra by adjusting the linewidths. Although some of the observed lines in the spectra are at least partially blended, the analysis described herein permits consistent linewidth measurements. In fact, the analysis takes advantage of the overlap in determining the linewidth without relying on external references. The pressure-broadening coefficients determined from the measured linewidths are found to be consistent with the results obtained using the available IR data.

ACKNOWLEDGMENT

The research for this paper was supported in part by U.S. Air Force contract F33615-80-C-2054.

* Present address, Air Force Weapons Laboratory (AFWL/ARBA), Kirtland Air Force Base, New Mexico 87117.

REFERENCES

1. See, for example, A. C. Eckbreth and P. W. Schreiber, "Coherent anti-Stokes Raman spectroscopy (CARS): application to combustion and gas-phase diagnostics," in *Chemical Application of Nonlinear Raman Spectroscopy*, A. B. Harvey, ed. (Academic, New York, 1981).
2. A. Owyong, "High resolution coherent Raman spectroscopy of gases," in *Laser Spectroscopy IV*, H. Walther and K. W. Roche, eds. (Springer-Verlag, New York, 1979).
3. A. Owyong, C. W. Patterson, and R. S. McDowell, "Cw simulated Raman gain spectroscopy of the ν_1 fundamental of methane," *Chem. Phys. Lett.* **59**, 156-162 (1978); erratum **61**, 636 (1979).
4. M. A. Hennesian, L. Kulevskii, and R. L. Byer, "Cw high resolution CARS spectroscopy of H_2 , D_2 , and CH_4 ," *Opt. Commun.* **18**, 225-226 (1976).
5. B. B. Krynetsky, L. A. Kulevsky, V. A. Mishin, A. M. Prokhorov, A. D. Savelev, and V. V. Smirnov, "High resolution cw CARS spectroscopy in D_2 gas," *Opt. Commun.* **21**, 225-228 (1977).
6. V. I. Fabelinsky, B. B. Krynetsky, L. A. Kulevsky, V. A. Mishin, A. M. Prokhorov, A. D. Savelev, and V. V. Smirnov, "High resolution cw CARS spectroscopy of the Q -branch of the ν_2 band in C_2H_2 ," *Opt. Commun.* **20**, 389-391 (1977).
7. W. B. Roh, "Coherent anti-Stokes Raman scattering of molecular gases," Tech. Rep. AFAPL-TR-77-47 (Air Force Aero Propulsion Laboratory, Wright-Patterson AFB, Ohio, August 1977).
8. R. J. Hall, J. F. Verdick, and A. C. Eckbreth, "Pressure induced narrowing of the CARS spectrum of N_2 ," *Opt. Commun.* **35**, 69-71 (1980).
9. L. P. Goss, G. L. Switzer, and P. W. Schreiber, "Flame studies with the coherent anti-Stokes Raman spectroscopy technique," *J. Energy* **7**, 389-394 (1983).
10. A. Kim, "Computer programming in physical chemistry laboratory: least-squares analysis," *J. Chem. Educ.* **47**(2), 120-122 (1970).
11. L. P. Goss, D. D. Trump, B. G. MacDonald, and G. L. Switzer, "10-Hz coherent anti-Stokes Raman spectroscopy apparatus for turbulent combustion studies," *Rev. Sci. Instrum.* **54**, 563-571 (1983).
12. R. J. Lovell and W. F. Herget, "Lorentz parameters and vibration-rotation interaction constants for the fundamental bands of HF," *J. Opt. Soc. Am.* **52**, 1374-1376 (1962).
13. W. S. Benedict and R. Herman, "The calculation of self-broadened line widths in linear molecules," *J. Quant. Spectrosc. Radiat. Transfer* **3**, 265-278 (1963).
14. R. Beigang, G. Litfin, and R. Schneider, "Line shapes and half widths of pure- and foreign-gas-broadened 2.5- μ m HF absorption spectra," *Phys. Rev. A* **20**, 229-232 (1979).

2.8 BLACKBODY THERMOMETRIC PROBE

The construction of a blackbody thermometric probe based upon a high-temperature optical-fiber thermometer made from a single-crystal sapphire initially developed at the National Bureau of Standards (NBS) was undertaken.¹⁵⁻¹⁷ Present interest in this area stems from the possible extension of the high-frequency thermometric capabilities of the probe to turbulent flame studies.

The original probe developed by Dils¹⁵ is shown in Fig. 19. It consists of three basic elements--a signal generator, one or more transmitting optical fibers, and an optical detector. Any effective blackbody configuration may be used for the signal generator at the tip of the high-temperature fiber. A single blackbody cavity can be created by sputtering a thin metallic coating onto the surface of the fiber. In his initial experiments, Dils used platinum films. The equations describing the blackbody emission from this cavity are well established. The Planck equation which describes the spectral distribution of radiance or an ideal blackbody is used in conjunction with the Gouffé equation which describes the apparent emittance at the exit of the cavity to determine the total spectral flux entering the fiber

$$L(\lambda_o) = \frac{a \epsilon_o c_1}{\lambda^5 [\exp(c_2/\lambda_o T) - 1]} \text{ [W/m]} \quad (31)$$

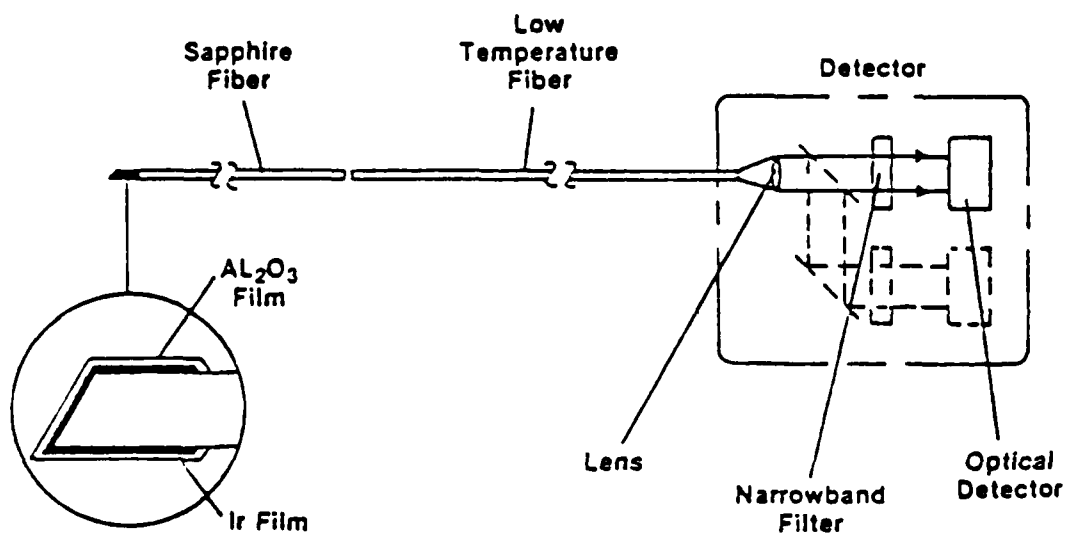


Figure 19. High-Temperature Blackbody Probe.

where

a = area of the cavity exit (m^2)

ϵ_o = apparent emittance of the cavity

c_1 = first radiation constant ($3.7418 \times 10^{-16} \text{ W m}^2$)

c_2 = second radiation constant ($1.43879 \times 10^{-2} \text{ m.K}$)

λ_o = wavelength in vacuum (m)

T = temperature (K)

A wavelength, λ_o , is selected which will provide maximum sensitivity to temperature changes and low absorption in sapphire at elevated temperatures.

The second element of the thermometer consists of both high- and low-temperature optical fibers which transmit the blackbody signal to the detector. The third element is the detector system which can be constructed from a wide range of conventional components. The principal components are a light-gathering lens, a narrow-band filter, and a photomultiplier or silicon detector. Optical density filters can be included to control the light density at the detector.

The optical-fiber probe, as demonstrated by Dils, is an extremely accurate means of measuring the average temperature in the range of 600 - 2000°C. The primary interests of the present effort are the possible high-frequency applications of such a thermometer and the possibility of extending the temperature-measurement range. Thus, the thrust of this work was the modification of the third stage or detection scheme for the thermometric probe. Assuming, for the moment, that the probe has high-frequency-response

capability, the major alteration to the present detection scheme involves the incorporation of a fast detector along with a fast, high-resolution (15 - 16 bit) ADC. The second goal of extending the temperature-measurement range of the probe is the more difficult, as pointed out below.

The problem surrounding extension of the measurement range at high frequency concerns the blackbody emission. Figure 20 displays the variation of a blackbody emitter with temperature. The wavelengths chosen in the past for temperature measurements with this probe were 600 and 800 nm. At these wavelengths dynamic-range measurement capabilities of 10^{16} and 10^{13} , respectively, would be needed to measure the full range of temperatures in a turbulent flame (300 to 2300 K). No detector exists today which possesses such a large dynamic-range capability. Thus, while the nonlinearity of the blackbody probe is ideal for high sensitivity, it is troublesome when one is attempting to cover a wide temperature range.

The approach which has been taken in attempts to overcome the dynamic-range problem is optical multiplexing of the blackbody signal which involves splitting the signal into multiple signals, each covering a $10^3 - 10^4$ dynamic-range region.¹⁸ The extent of the region covered is determined by the capability of the detector used, typically 10^4 for PMTs or diodes. Thus, potentially a 10^{12} dynamic range could be covered by a three/split-three detector combination. However, a problem arises concerning protection of the most sensitive detector leg when the range becomes wider than 10^8 . A 10^8 dynamic range appears to be the limiting range. At 800 nm this corresponds to a temperature range of 700 - 1700 K. To further extend the temperature range, a shift to longer wavelengths is required; this lowers the temperature sensitivity and compresses

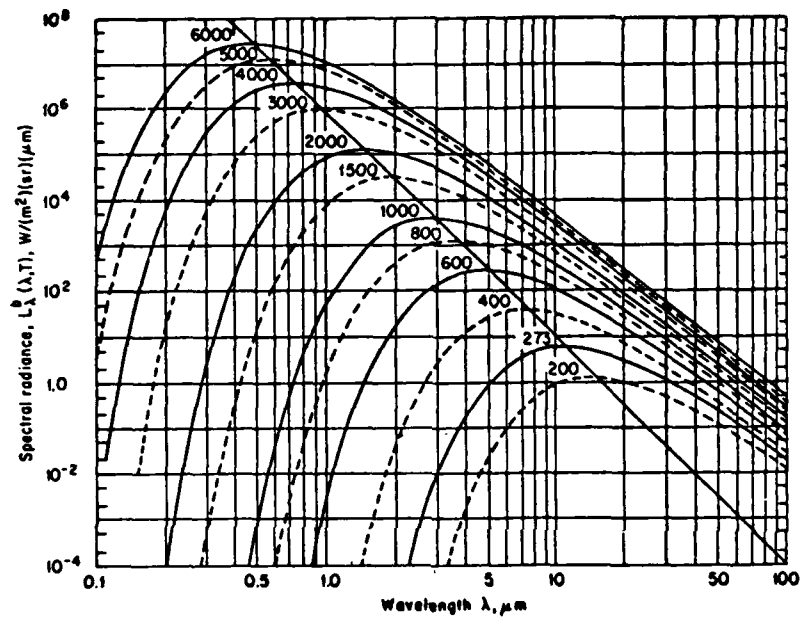


Figure 20. Spectral Radiance of Blackbody at Various Temperatures (K).

the dynamic-range requirements. However, the extent to which one can shift to the red is limited due to the low-temperature fiber-transmission characteristics. The low-temperature quartz-fiber transmission is shown in Fig. 21. The ideal wavelength, considering the fiber transmission and the availability of adequate detectors, is $1.6 \mu\text{m}$. At $1.6 \mu\text{m}$ a dynamic range of 10^8 will cover a temperature range of 500 - 2300 K, which results in reasonable coverage of the turbulent flame.

The instrument design is shown in Fig. 22. The output from the low-temperature quartz fiber is collimated by a 2.5-cm-focal-length lens and passed through a $1.6\text{-}\mu\text{m}$ filter. The filter light is then focused by a 25-cm-focal-length lens. Prior to the focus, the light is split into two portions by a pellicle. The reflected portion of the pellicle is the high-temperature leg, while the transmitted portion is the more sensitive low-temperature leg. The light intensity in each leg is adjusted by optical-density filters to give a 10^4 to 1 split. The detector employed in this instrument is an InGaAs photodiode, made especially for detection of radiation between 0.9 and $1.7 \mu\text{m}$. The spectral response of this detector is shown in Fig. 23. The InGaAs detector is used in the photovoltaic rather than the photoconductive mode of detection. Although this reduces the noise-related leakage current of the detector, unfortunately, it also reduces the overall response of the diode. The reduction of the frequency response can be calculated in a straightforward manner. The frequency response in the voltaic mode is area dependent and, for this detector, is equal to 0.10 MHz/cm^2 . Thus, for a $500\text{-}\mu\text{m}$ -diam. diode (circular), the cutoff frequency with no bias current is $\sim 78 \text{ kHz}$. Since the maximum frequency requirement for a turbulent flame is 10 kHz , which requires a sampling rate of 20 kHz , the response of the diode is more than adequate.

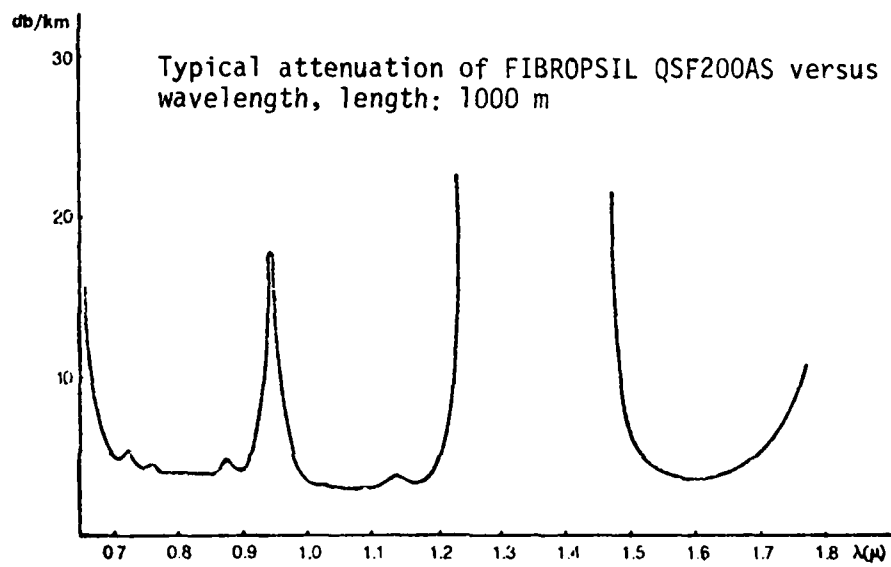
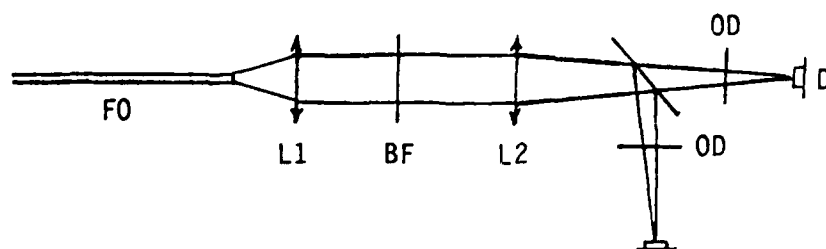
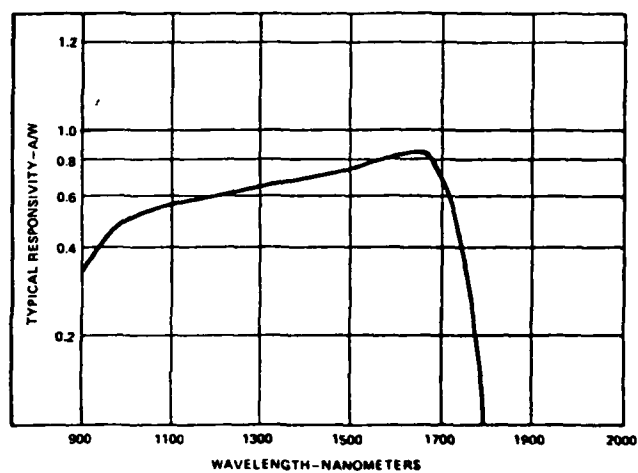


Figure 21. Transmission Attenuation of Quartz Fiber.



F0 - Fiber Optic
 L1 - 2.5-cm-Focal-Length Lens
 L2 - 25-cm-Focal-Length Lens
 BF - Bandpass Filter
 OD - Optical Density Filter
 D - InGaAs Detector

Figure 22. Schematic Diagram of Receiver Optics.



LS-6644

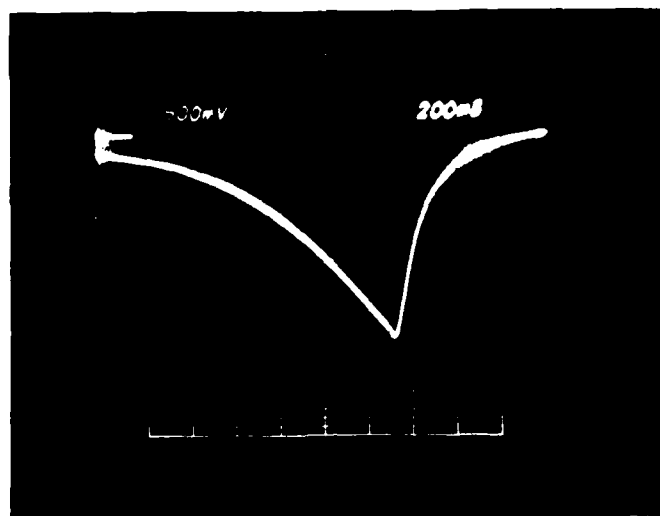
Figure 23. Spectral Response of InGaAs Detector.

The above experimental design thus offers extended temperature and frequency response for turbulent flame studies.

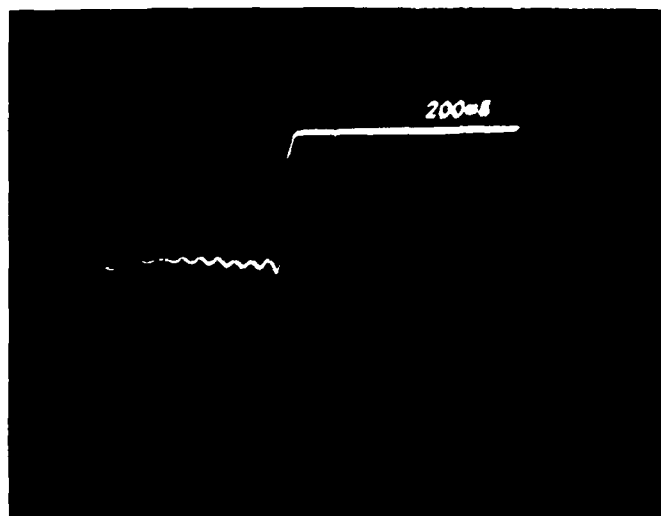
Probe Frequency Response

For determining the frequency response of the optical probe, a simple heating-cooling experiment was conducted. The experiment consisted of heating the probe to a relative high temperature and then quickly removing the heat source. The blackbody emission of the probe was monitored by an S-20 PMT. The results of the experiment are depicted in Fig. 24. While the response times were expected to be better than 200 μ sec., the observed response was less than 250 msec. Figure 24(a) shows the slow cooling which was observed, while 24(b) displays the speed with which the heat source was removed, indicating that the probe indeed is slow in responding to changes in temperature. After a discussion with Dils, it was realized that in order to achieve the high-frequency responses noted in his publications, it would be necessary to compensate for the slow response of the probe.

The response time of the optical probe to changes in the surrounding gas temperature is controlled by heat transfer from the gas to the thin-film radiator. For describing such a system, the transfer function, which is defined as being the Fourier transform of the response to an impulse change in temperature, must be determined. The transfer function for this probe has been modeled by Dils and Tichenor and is displayed in Fig. 25.¹⁷ Two regions are important in the probe response--the first is at relatively low frequencies where the thermal wavelength, defined below, is large compared to the dimensions of the optical probe,



(a)



(b)

Figure 24. (a) Response of Blackbody Probe to Change in Temperature
(b) Photograph Depicting Speed at Which Heat Source Was Removed from Probe.

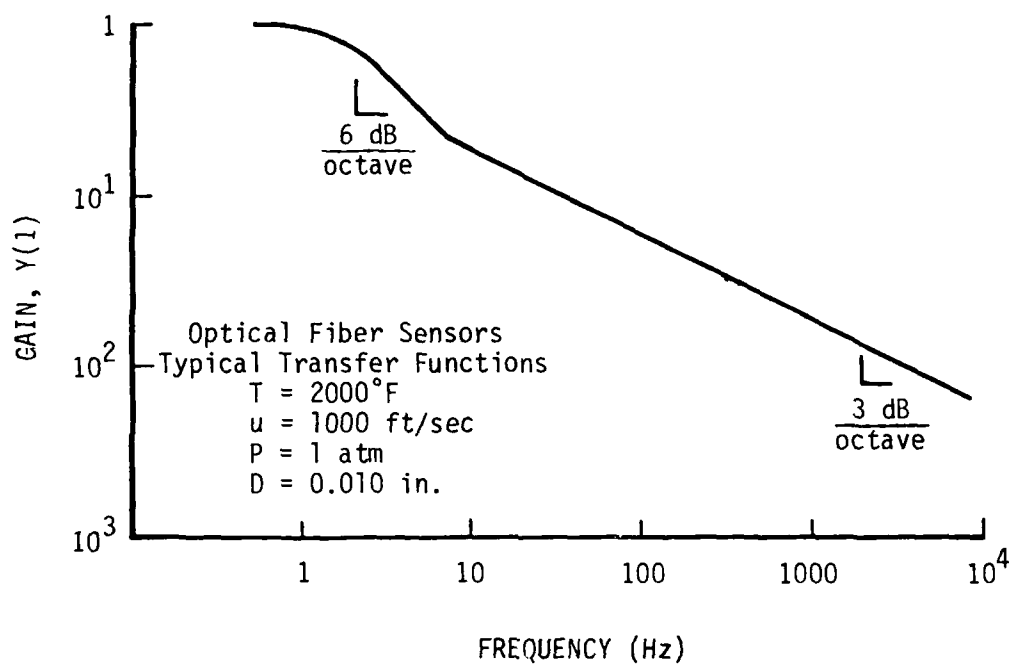


Figure 25. Transfer Function of Blackbody Probe.

$$\lambda_T = \sqrt{\frac{K_f}{2\rho_f C_f \pi^2 \omega}} \quad (32)$$

where

K_f = fiber thermal conductivity

ρ_f = fiber density

C_f = fiber specific heat

ω = frequency of heat change

In the low-frequency case, the response of the probe is similar to that of a thin wire thermocouple,¹⁹ given by

$$y(\omega) = \frac{6h}{\omega d_f \rho_f C_f} \quad (33)$$

where h = convective heat-transfer coefficient. In this case the probe displays a 6-dB/octave rolloff, as depicted in Fig. 25.

In the second region of interest, the thermal wavelength becomes small with respect to the physical dimensions of the optical probe; this occurs at frequencies in excess of 50 Hz. In this case the temperatures within the probe obey the quasi-steady solution to a semi-infinite solid subjected to sinusoidal oscillations in gas temperature.²⁰ Since the thermal radiator is very thin compared to the thermal wavelength, the radiation captured by the optical fiber depends only on the surface temperature. The transfer function relating probe temperature to gas temperature is given by

$$y(\omega) = \frac{h}{\sqrt{K_f \rho_f C_f \omega}} \quad (34)$$

This transfer function is plotted in Fig. 25 and displays a 3-dB/octave roll-off with frequency. The transfer function of the optical probe is considerably more complex than that of a thin wire thermocouple.

At this point three possible options are recognized. The first involves using the probe as it is presently configured and attempting to devise a compensation scheme that could account for the transfer function of the probe. At the very least an experimental measurement of the transfer function under actual conditions of use is required. This could possibly be undertaken by employing a chopped cw CO₂ laser beam and monitoring the response of the probe as a function of the chopper frequency. This experiment will be conducted in the near future.

The second and third options involve physical modifications to the probe which would either eliminate the complex transfer function or simplify it considerably. The simplest option to implement is to increase the probe diameter considerably, thereby minimizing the low-frequency thermal wavelength penetration region. This will eliminate the 6-dB/octave rolloff portion of the response curve, reducing the need to know where the 6-dB region transforms into 3-dB region. The third option involves attempts to eliminate any rolloff in response of the probe; this would require redesign of the probe itself. The large bulk of the sapphire fiber must be reduced before the frequency response of the probe can be improved.

The effect of the probe diameter on the transfer function is given by the convective heat-transfer coefficient:

$$h = \frac{0.48 R_e^{0.51} K_g}{d} \quad (35)$$

where

R_e = the Reynolds number of the flow

d = the diameter of the optical fiber

K_g = the thermal conductivity of the gas

Substituting the above expression into Eq. (31) indicates that if the size reduction is relatively small--such that the thermal wavelength at high frequencies becomes smaller than the physical dimensions of the probe--then the response will increase linearly with a decrease in fiber diameter. If, however, the fiber size is made extremely small and the thermal wavelength does not become small with respect to the size of the fiber, then Eq. (33) determines the response of the probe. In this case a reduction in the probe diameter will quadratically increase the response of the probe. In order to obtain some idea of how small the fiber should be to give a response of 1000 Hz, the thermal wavelength in the sapphire was calculated from Eq. (32) to be 1 mil. Thus, a 25- μ m sapphire fiber would be required to achieve a 1000-Hz response without compensation.

2.9 THERMOMETRY AND SPECIES-CONCENTRATION MEASUREMENTS BY LASER-DEFLECTION TECHNIQUES

The availability of tunable high-peak-power laser sources has stimulated research in the area of combustion diagnostics, with the goal being to understand the basic fluid and chemical properties of combustion. Thermometry is usually conducted and majority species detected by means of the CARS technique, while radical intermediates at much lower concentrations are often probed using laser-induced fluorescence (LIF). CARS, however, is typically insensitive to trace species; and LIF techniques often suffer from collisional quenching of the fluorescence in high-pressure environments. As a result emphasis has recently been placed on the development and application of techniques which are not only sensitive to minor flames species but also free from uncertainties due to collisional quenching. Newly developed techniques include optoacoustic laser deflection (OLD) and photothermal deflection spectroscopy (PTDS). These techniques not only complement CARS and LIF but also extend the applicability of laser diagnostics in the area of combustion studies.

These techniques are discussed in the three papers which follow. The first entitled, "Hydroxyl (OH) Distributions and Temperature Profiles in a Premixed Propane Flame Obtained by Laser-Deflection Techniques," demonstrates the ability of PTDS in the measurement of the OH radical in a premixed flame. The OLD technique was utilized for thermometry. Both average-temperature profiles and probability distribution functions were obtained on a premixed flame by this technique. The second paper entitled, "Time-Resolved Temperature Measurements in a Laboratory Flame Using the Optoacoustic Beam-Deflection Method," demonstrates the high-repetition-rate capability of the OLD technique

for thermometry measurements in a premixed flame. The third paper entitled, "Time-Resolved Temperature Measurements in a Premixed Flame Using the Opto-acoustic Beam-Deflection Technique," discusses in detail the generation of the acoustic pulse, the temperature dependence of the sound velocity, the deflection of the probe beam by the sound wave, and measurements at 100 and 1200 Hz in the reaction zone of a premixed flame. The results of this work indicate that a high-frequency copper-vapor laser could be utilized for thermometry at 5 kHz. The sound production on solid surfaces was investigated in conjunction with an AFIT thesis student, Maj. Haksoo Yoon.

Hydroxyl (OH) distributions and temperature profiles in a premixed propane flame obtained by laser deflection techniques

Sigmund W. Kizirnis, Robert J. Brecha, Biswa N. Ganguly, Larry P. Goss, and Rajendra Gupta

OH-concentration distributions and temperature profiles have been measured on a premixed propane-air flame by laser deflection techniques. Photothermal deflection spectroscopy has been utilized for the measurement of the OH radical. Both a low-spatial-resolution (near collinear) and high-spatial-resolution (crossed-beam) scheme were used to profile the premixed flame. An optoacoustic deflection technique was utilized for thermometry. Both average-temperature profiles and probability distribution functions were determined by this technique. A comparison with data obtained by the CARS technique demonstrated that no significant flame perturbation was occurring.

1. Introduction

The availability of tunable high-peak-power laser sources has stimulated research in the area of combustion diagnostics, with the goal being to understand the basic fluid and chemical properties of combustion. Thermometry and majority species are usually detected by means of Raman techniques,^{1,2} while radical intermediates in a much lower concentration are often probed using laser-induced fluorescence (LIF).³⁻⁵ Raman methods, however (with the exception of electronically enhanced Raman techniques),^{6,7} are insensitive to trace species; and LIF techniques often suffer from collisional quenching of the fluorescence in high-pressure combustion environments.⁵ As a result emphasis has recently been placed on the development and application of techniques which are not only sensitive to minor flame species but also free from uncertainties due to collisional quenching. Newly developed techniques include optoacoustic spectroscopy,^{8,9} photoacoustic deflection spectroscopy (PADS)^{10,11} and photothermal deflection spectroscopy (PTDS).^{10,12,13} These techniques not only complement the well-established Raman and LIF techniques but also widen the

applicability of laser diagnostics in the area of combustion studies.

Photothermal deflection spectroscopy (PTDS), as pioneered by Amer and co-workers,¹³ has been shown recently to have excellent potential for minority-species concentration measurements,¹² as demonstrated by observation of the PTDS signal from NO₂ produced in a methane-air premixed flame. It was further demonstrated that the OH radical could be observed in a premixed methane-air flame by the PTDS technique.¹⁰ In this technique two laser beams, a dye laser (pump) beam and a He-Ne (probe) beam, intersect in the region where the molecules of interest are to be detected. The pump beam is tuned to an absorption line of the molecules of interest, and the laser energy absorbed by these molecules is lost through quenching collisions with other flame molecules, resulting in the heating of the flame gases. Due to the spatial profile of the laser (generally assumed to be Gaussian) and thermal diffusion of heat, a refractive-index gradient is produced. The probe beam is deflected due to this gradient which is observed by a position-sensitive optical detector. The amplitude of the signal is proportional to the concentration of the probed molecules. The technique has high sensitivity,^{10,12} which is appropriate for minority species, and displays good spatial resolution if the two beams intersect at approximate right angles. Temporal resolution can be achieved by using a pulsed laser. The technique is nonperturbing, a typical temperature change produced by the absorption of laser energy being of the order of 1 K.

Another technique which has been shown to have high potential for the measurement of very low concentrations in combustion environments is the opto-

Rajendra Gupta is with University of Arkansas, Physics Department, Fayetteville, Arkansas 72701; L. P. Goss is with Systems Research Laboratories, Inc., 2800 Indian Ripple Road, Dayton, Ohio 45440; the other authors are with AFWAL Aero Propulsion Laboratory, Wright-Patterson AFB, Ohio 45433.

Received 29 March 1984.

0003-6935/84/213873-09\$02.00/0.

© 1984 Optical Society of America.

acoustic (photoacoustic) technique. Parts-per-million sensitivity has been obtained with NO_2 molecules,⁹ and higher sensitivity can be achieved for strongly absorbing OH molecules.¹⁴ Crosley¹⁵ recently demonstrated that OH, NH_2 , CO_2 , and H_2O could be monitored by means of this technique. Achievement of spatial resolution through the use of a microphone as the acoustic detector, however, is difficult. A detection method employing laser beam deflection (PADS) has been used in an attempt to improve the spatial resolution of this technique.^{10,11} PADS has some advantages over PTDS, although its sensitivity is lower.¹¹

One interesting application of the optoacoustic technique which was demonstrated by Tam¹⁰ involved determination of flame temperature by measurement of the sound velocity between two probe beams. In this method an intense sound pulse was generated by a plasma spark created by focusing an intense 1064-nm 10-nsec Nd:YAG laser. Two probe beams were employed to monitor the speed of the sound pulse over a distance defined by the probe-beam separation. Since the velocity of sound varies with the square root of the temperature, the temperature can be determined from the sound transit time. However, the spark as well as the blast wave generated by the gas breakdown can greatly disrupt the flow and, in the case of unburnt fuel and air mixtures, even cause ignition of the gases. In the present study a small wire was employed for the target of the pump laser for sound production, which reduced the perturbation of the flame and the requirements for high peak powers. The sound pulse produced with a wire target is of sufficient amplitude to permit thermometry with laser powers as low as 2 mJ/pulse.

Studies with both the optoacoustic and the PTDS techniques on a premixed propane-air flame are reported in this paper. The PTDS technique was employed to determine OH distributions, while the optoacoustic technique was used to determine the temperature profile.

II. Apparatus

The experimental setup for the PTDS studies is shown schematically in Fig. 1. A Quanta-Ray model PDL dye laser was pumped by a frequency-doubled Quanta-Ray Nd:YAG laser. The DCM dye employed typically delivered 7 mJ of energy in a pulse length of 10 nsec at 6200 Å. The dye laser output at 6200 Å was frequency doubled by an Inrad autotracking harmonic generator assembly. The typical UV output at 3100 Å was $\sim 200 \mu\text{J}/\text{pulse}$ in a spectral width of $\sim 18 \text{ GHz}$. The frequency-doubled UV output was tuned to one of the main branch transitions of the OH molecule and allowed to pass through a propane-air flame. Radiation from a Spectra-Physics model 233 He-Ne laser intersected the dye-laser beam inside the flame. These beams were focused in the flame using long-focal-length lenses ($\sim 50 \text{ cm}$). The beam diameter near the focal point was $\sim 1 \text{ mm}$. Both a low-spatial-resolution near-collinear and a high-spatial-resolution 12° crossed-beam configuration were used to profile the premixed flame. Most of

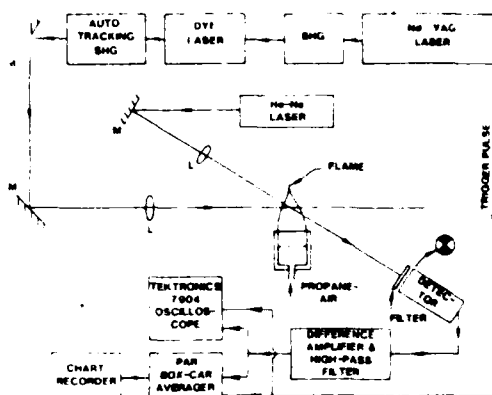


Fig. 1. Schematic illustration of the PTDS experimental arrangement.

the dye-laser energy absorbed by the OH molecules eventually appeared as heat in the irradiated region due to collisional de-excitation. Refractive-index gradients were produced in the medium due to the spatial profile of the pump-laser beam, which causes the overlapped probe beam to be deflected. This deflection was monitored by a Silicon Detector Corp. model SD-380-23-21 position-sensitive detector having four quadrants; the two quadrants oriented in the direction of the deflection were used in the present experiment. The signals from the individual quadrants were passed through a current-to-voltage amplifier and fed into a difference amplifier which was used to gain the difference signal. The output of the difference amplifier was filtered by a high-bandpass filter (3-dB point at 10 kHz) to reduce low-frequency signal fluctuations due to the He-Ne instabilities and the index-of-refraction gradients in the flame. The signal shape was observed on a Tektronix model 7904 oscilloscope equipped with a programmable digitizer (model 7D20) and triggered by the Q-switch pulse from the Nd:YAG laser. The signal was measured by a PAR model boxcar integrator which was also triggered by the Nd:YAG laser. The boxcar gate was set at 20 μsec to envelop most of the PTDS signal, and the output of the boxcar was recorded on a chart recorder.

Before measurements were made, the He-Ne quiescent position was adjusted to give a zero difference signal. This insured that the maximum deflection was observed and aided in minimizing the high-frequency noise of the probe laser. A deflection of the probe laser would result in an imbalance between the two quadrants and produce a difference signal.

The arrangement for the optoacoustic experiment is shown in Fig. 2. The frequency-doubled output from the Quanta-Ray Nd:YAG laser was mildly focused (50-cm focal length) on a small 500- μm wire. Two He-Ne lasers were used for the probe beams; each beam was imaged onto a separate PIN diode detector. The electronics for the PIN diodes were similar to those of the quadrant detector, except that no difference-amplifier stage was employed. The probe beams were located 2 cm upstream of the wire sound source to mini-

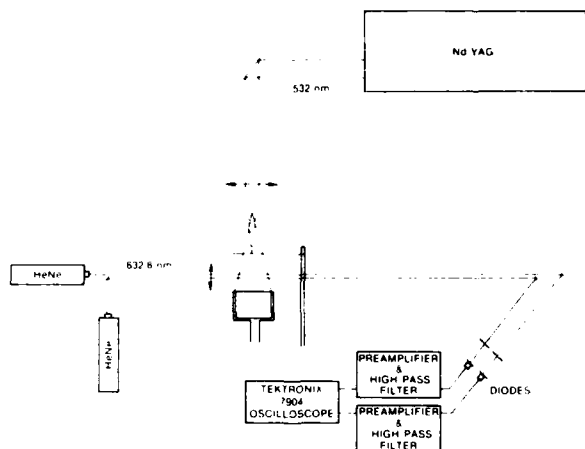


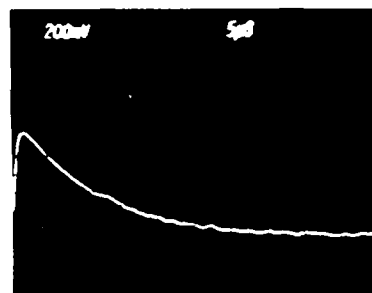
Fig. 2. Schematic illustration of the optoacoustic experimental arrangement.

mize flow disturbances within the probe region. The probe beams were placed 2 mm apart, resulting in an estimated spatial resolution of 0.5 mm^3 . A 2-mJ 532-nm laser pulse, mildly focused in ambient air, resulted in a deflection signal of 0.2 V.

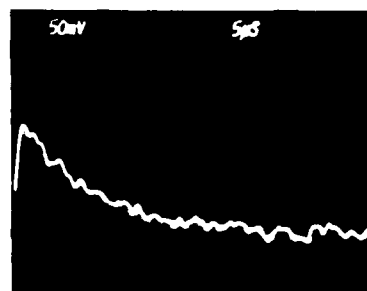
The burner was fabricated from stainless steel and is $\sim 7.6 \text{ cm}$ ($\sim 3 \text{ in.}$) in diameter. A fuel-rich mixture of propane and air with an equivalence ratio of 1.48 was used. The flame extends $\sim 18 \text{ cm}$ ($\sim 7 \text{ in.}$) above the burner head. A chimney, which was used to help stabilize the flame, greatly limited the accessibility of the upper part of the flame for optical measurements. Some of the experiments were conducted without the chimney, and the flame in these conditions was unstable. The burner was mounted on a motor-driven X-Y translator to permit horizontal and vertical movements.

III. OH Measurements

A typical single-shot OH photothermal signal deflection is shown in Fig. 3(a). The frequency-doubled dye laser was tuned to the $Q_1(7)$ absorption line of the $v'' = 0$ to $v' = 0$ band of the $X^2\Pi - A^2\Sigma^+$ electronic transition of OH at 3089.6 \AA . The pump and probe beams were arranged in the near-collinear configuration, resulting in low spatial resolution. At the instant of laser firing, the probe beam was deflected due to refractive-index gradients produced by the adsorption of laser energy by the OH molecules and subsequent heating of the irradiated region due to quenching collisions. The deflection of the probe beam gave rise to a difference signal at the quadrant detector. The probe beam returned to its original position on the time scale of the thermal diffusion. The deflection of the probe due to absorption of the OH molecules can be distinguished from refractive-index gradients produced by the flame (even in the case of high turbulence) in two ways. First, as seen in Fig. 3, the frequency of the PTDS signal is of the order of 15–50 kHz, while the maximum fluctuations in a turbulent flame are 10 kHz (typically 1–2 kHz). Thus, electronic filtering, as em-



(a)



(b)

Fig. 3. Typical single-shot photothermal signal from OH molecules in propane-air flame with probe and pump beams (a) near-collinear and (b) 12° crossed. Pump laser tuned to $Q_1(7)$ of OH at 3089.6 \AA .

ployed, can remove turbulence-induced refractive indices. Second, the PTDS signal occurs immediately after the laser pulse, thus allowing for a narrow window to minimize laser and detector noise.

By routing the amplified and filtered difference output of the quadrant detector into a boxcar integrator, the relative signal strength of the photothermal deflection could be recorded and plotted on a strip-chart recorder as the flame was traversed. This allowed the OH profiles shown in Fig. 4 to be measured. The boxcar integrator gate was set at $20 \mu\text{sec}$ with a 1-msec integration time constant. The zero of the abscissa of Fig. 4 corresponds approximately to the center of the flame. These measurements were repeated at different heights above the burner head, as indicated in the diagram. Since the beam configuration was not changed and only the flame was moved through the beams, the photothermal signal strength was directly proportional to the OH density (neglecting any corrections for the temperature nonuniformity across the flame). Note that the OH density is highest near the edges of the flame. The asymmetric OH density was reproducible and consistent from run to run and believed to be characteristic of the burner employed. Due to the presence of the chimney, measurements at heights $> 35 \text{ mm}$ above the burner head could not be made. The observed profiles are quite similar to OH profiles obtained by

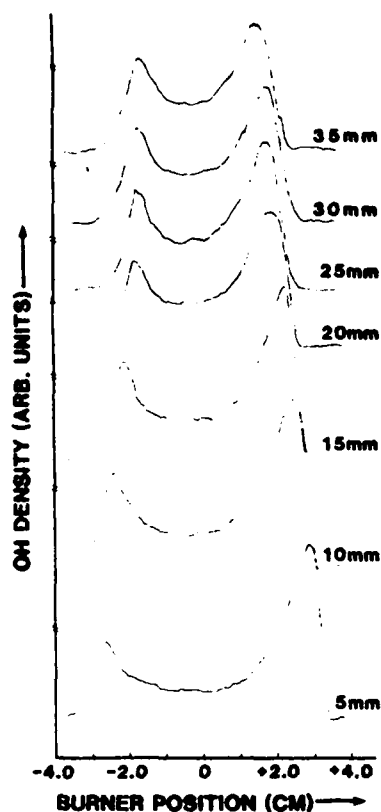


Fig. 4. OH concentration profiles in propane-air flame at various heights above burner head. Probe and pump beams were near-collinear, giving low spatial resolution. Zero of abscissa represents center of burner.

Alden *et al.*¹⁷ and Dyer and Crosley¹⁸ on premixed hydrocarbon-air flames.

To facilitate measurements at heights >35 mm above the burner head, the stabilizing chimney was removed and the flame flickered at the rate of a few hertz. Figure 5 shows the OH profiles at various heights above the burner in the nonsteady flame. The OH concentration at the edges appears to be reversed; however, it was the direction of scan which was reversed. The periodic oscillations in the signal are believed to be due solely to flicker of the flame and do not represent laser perturbations or detector noise. If laser perturbations were indeed occurring, they would also have been displayed in Fig. 4. The likelihood of laser perturbations of this flame is small due to the low powers used for the measurements and the large size of the burner. Small jets, however, are very sensitive to acoustic perturbations, and care must be taken with these systems when measurements are made close to the jet nozzle.¹⁹ The flame flicker in our experiment can be avoided by using a transparent quartz chimney.

While the measurements made with the collinear arrangement displayed strong signals, indicating good detectivities of OH in the flame, the spatial resolution of the measurements greatly limits the usefulness of the data—especially in the area of combustion-model

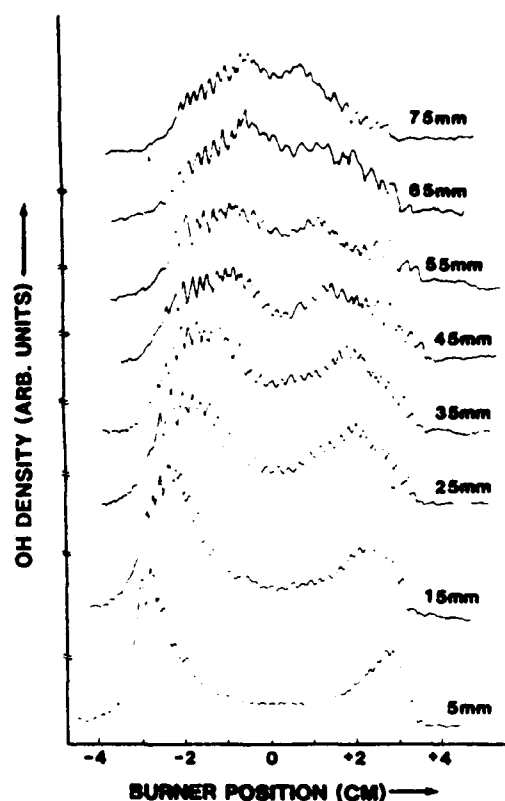


Fig. 5. Results similar to those of Fig. 4, with the flame being operated without a chimney. In these conditions, the flame was flickering at the rate of a few hertz; small oscillations in the figure represent the effect of flicker on OH density. OH peaks are reversed compared with those in Fig. 4, since the direction of the flame scan was reversed.

evaluation where high spatial resolution is required and a cross-beam configuration must be employed. To demonstrate that the signal-to-noise ratio was sufficiently large—even with a small overlap between the pump and probe beams—a crossing angle of 12° was chosen as a test case. In the near-collinear configuration case, the interaction zone over which the measurement was made consisted of a substantial part of the 8-cm flame width. With a 12° crossed-beam configuration, the interaction length is ~ 3 mm (3 mm^3 vol). The observed signal drop shown in Fig. 3(b) on changing from the near-collinear to the 12° crossed-beam configuration was a factor of 4.

The spatially resolved OH distribution in the premixed flame, as measured by the crossed-beam technique, is shown in Figs. 6 and 7. In Fig. 6 the chimney was replaced on the burner to permit a relatively stable flame to be profiled. Several points should be noted in Fig. 6 relative to the low-resolution profile shown in Fig. 4. The two peaks in OH concentration near the edge of the burner are much sharper in the crossed-beam case than in the collinear case, while the central regions of the flame, <35 mm high, show a much lower OH number density. This is due to the large interaction region in the low-resolution case which acts to smear and broaden the observed profiles.

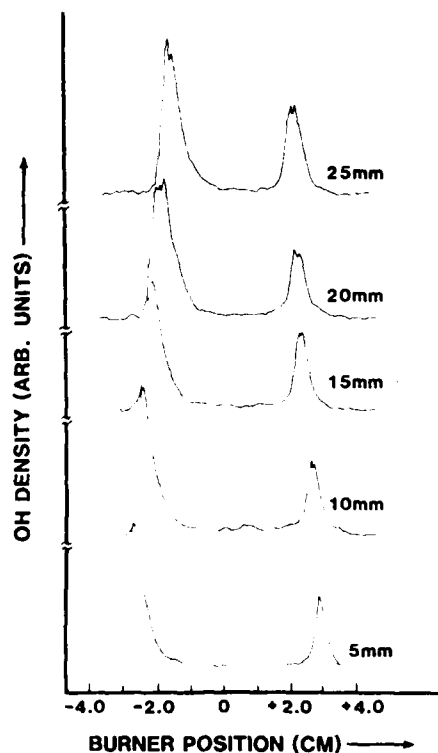


Fig. 6. OH density profile of flame with higher spatial resolution (3 mm^3). Note that OH density is lower in the center of the flame and OH density peaks at the edges are sharper than low-resolution data indicate.

Figure 7 shows the effect of the flame flicker when the chimney is removed. Note that the OH profile breaks up into four peaks at about the midpoint of the flame. This is most evident in the 65–85-mm range in Fig. 7. The four peaks are believed to be an artifact of the synchronization of the low-frequency flame flicker with the 10-Hz data acquisition. As one moves higher up the flame, the four peaks collapse into one. Most of the low-frequency noise at heights above 25 mm in Fig. 7 is caused by flame instability. This breakup of the OH distribution was not observed in Fig. 5 due to the spatial averaging that was occurring with the small-angle beam overlap.

To put the OH concentration measurements on an absolute scale, the absolute OH density was determined at one place in the flame by absorption measurements. The laser was tuned to the $Q_1(7)$ line of OH molecules at 3089.6 \AA , and absorption of the laser energy was measured by a Scientec power meter. The absorption was measured to be 8.6% at a height of 5 mm above the burner head which corresponds to an OH density of $\sim 5 \times 10^{14} \text{ molecules/cm}^3$ at the edge of the flame. The flame in the present study was used in fuel-rich conditions (equivalence ratio = 1.48).

In Fig. 8 the photothermal deflection spectrum of OH molecules is shown. The PTDS signal was recorded using a boxcar averager, as above, at a fixed point in the flame while scanning the frequency of the dye-laser

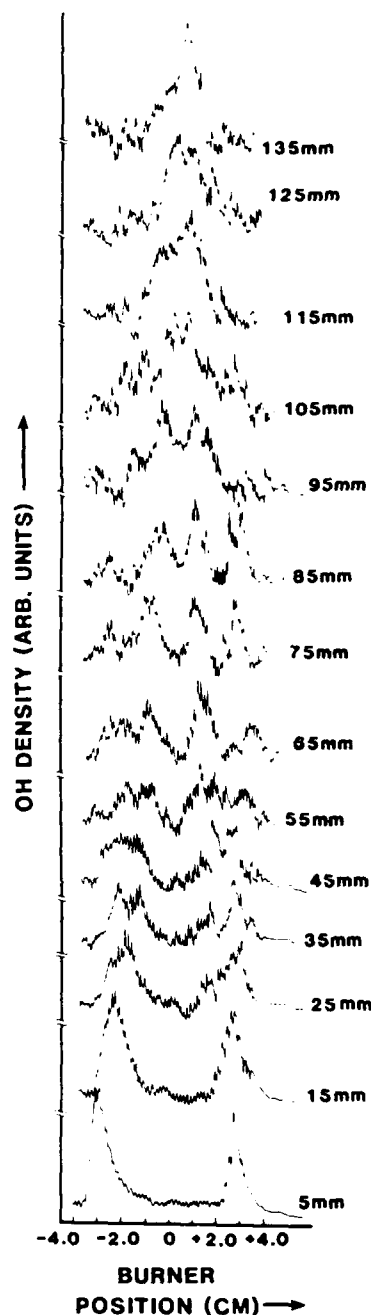


Fig. 7. Data similar to that of Fig. 6 with chimney removed. The flame, in this case, was flickering and wandered near the top.

beam. The autotracker rotated the second harmonic crystal for optimum UV output as the dye-laser frequency was scanned, giving a smooth UV output as a function of frequency. The features in Fig. 8 can be identified with known transitions in the OH spectrum. These results demonstrate that PTDS can be used as a sensitive spectroscopic technique for atomic and molecular species.

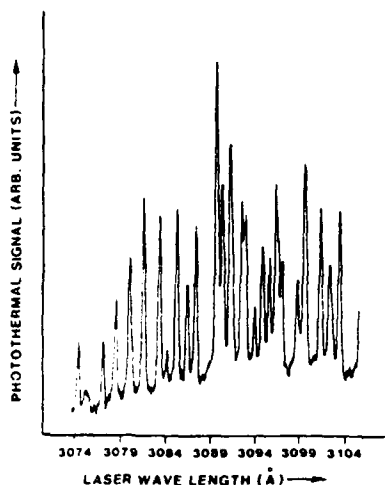


Fig. 8. Absorption spectrum of OH molecules. Photothermal signal strength was plotted as the pump laser frequency was scanned.

IV. Thermometry

As mentioned previously, the velocity of an acoustic wave which is propagating through a flame is dependent on the temperature of the flame. The relationship between the temperature and the acoustic-wave-propagation velocity is given by

$$T = \frac{V_0^2 \bar{m}}{R \left[1 + \frac{R}{C_v(T)} \right]}, \quad (1)$$

where \bar{m} is the average molecular weight of the gases in the flame, R is the universal gas constant, V_0 is the sound velocity, and $C_v(T)$ is the temperature-dependent average molar specific heat at constant volume in the flame.

The solution of Eq. (1) for temperature T requires that \bar{m} and $C_v(T)$ be known. In a premixed propane-air flame in the experimental conditions of the present study, the main gaseous component is N_2 , with the other major components being CO_2 and H_2O . An adiabatic flame code²⁰ can be used to yield the gaseous composition of the flame as a function of temperature from which \bar{m} and $C_v(T)$ can be calculated and used to extract a temperature from a sound-velocity measurement. In the most accurate case, this is the approach of choice. However, to a first approximation the composition can be assumed to be constant with temperature; and by simply ratioing the velocity measured by ambient conditions to that in the flame, a temperature can be determined,

$$\frac{T_f}{T_a} = \left(\frac{V_f}{V_a} \right)^2. \quad (2)$$

If the gas velocity is small compared to the speed of sound, Eq. (2) can be simply written as

$$\frac{T_f}{T_a} = \left(\frac{\Delta t_a}{\Delta t_f} \right)^2, \quad (3)$$

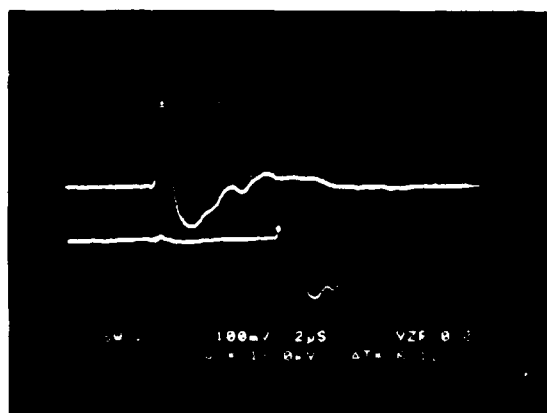
where Δt_a and Δt_f are the measured times required for the acoustic pulse to travel between the two probe

beams with and without the flame. Equation (3) is found to give only a small underestimate of the correct T value (in the present flame conditions) compared with Eq. (1) which uses the appropriate \bar{m} and $C_v(T)$ values as well as takes into account the gas velocities of the flame. In general, this will not be the case in a turbulent diffusion flame where \bar{m} can vary greatly, and thus, Eq. (1) must be employed.

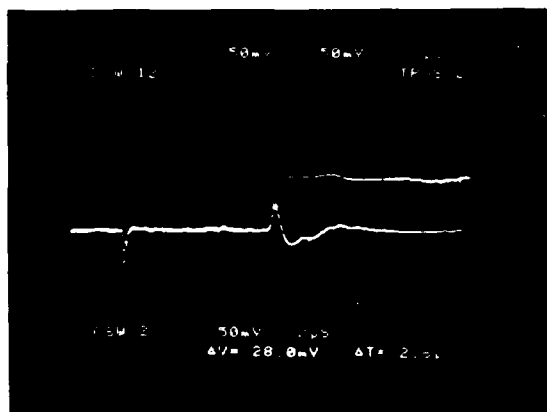
The basic experiment is to measure the velocity of an acoustic pulse as it travels through the flame. A small wire which was pulsed with a low-power, <2 mJ/pulse, mildly focused frequency-doubled Nd:YAG laser was used as the acoustic source (see Fig. 2). Absorption of the pump beam by the wire produces a localized heating of the wire which acts to heat the surrounding gases, giving rise to a pressure increase. This acoustic pulse travels outward, causing a change in the refractive index of the medium. The arrival of the acoustic pulse at a beam was measured by an observation of the deflection of that beam. Two probe beams separated by 2 mm were used to monitor the sound velocity. The probe beams were arranged upstream of the wire in order that no significant perturbation of the flame would be produced by the wire at the position of the probe beams.

The photoacoustic deflection signals in the absence and presence of the flame are shown in Fig. 9. Note the drop in amplitude of the acoustic signal with temperature. This effect is due to the lower number density at the elevated temperature. The width of the acoustic deflection is primarily determined by the transit time of the sound pulse across the He-Ne probe beam. The probe beams were focused to decrease their size and increase the time resolution (spatial resolution) of the acoustic measurement. The acoustic deflection signals were recorded on a transient digitizer which allowed the acoustic transit time to be determined. Both single-shot and averaged transit times were recorded and compared. The temperature profiles shown in Fig. 10 were determined in this manner. Note that the temperature profile across the premixed flame was essentially constant, with a slight drop in temperature at the center. As the flame is profiled at different heights above the burner, the temperature results clearly reveal the narrowing of the flame along with a gradual drop in temperature. Similar results have been obtained with the CARS technique on a propane-air premixed flame.²¹

To demonstrate that the beam steering of the flame did not adversely affect the temperature measurements, the stabilizing chimney was removed from the burner and three sets of 100 single-shot temperatures were taken above the flickering flame. The resulting temperature probability distribution functions (pdfs) are shown in Fig. 11. Low in the flame (4 cm above burner surface), a single-mode pdf is observed with an average temperature of $1831 \text{ K} \pm 67 \text{ K}$. At a position 7 cm above the burner, the pdf begins to show signs of a bimodal distribution. The average temperature has dropped to 1525 K. At the 11-cm position, a distinctive bimodal distribution is observed with an average temperature of 1196 K. The index-of-refraction gradients



(a)



(b)

Fig. 9. Optoacoustic deflection signals (a) in room air and (b) in a propane-air flame.

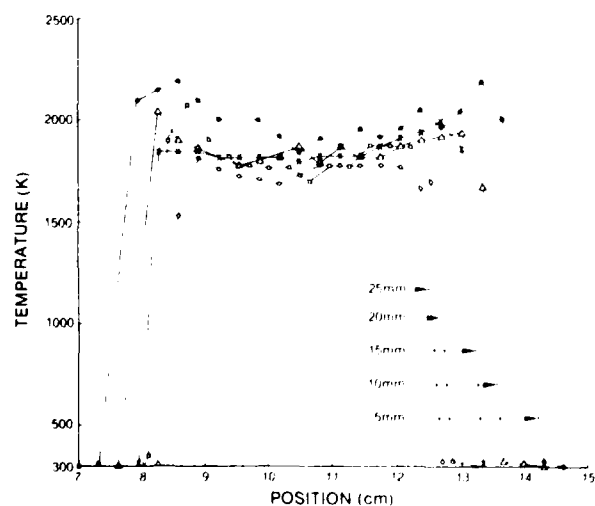


Fig. 10. Average-temperature profiles taken in a propane-air flame by the optoacoustic technique.

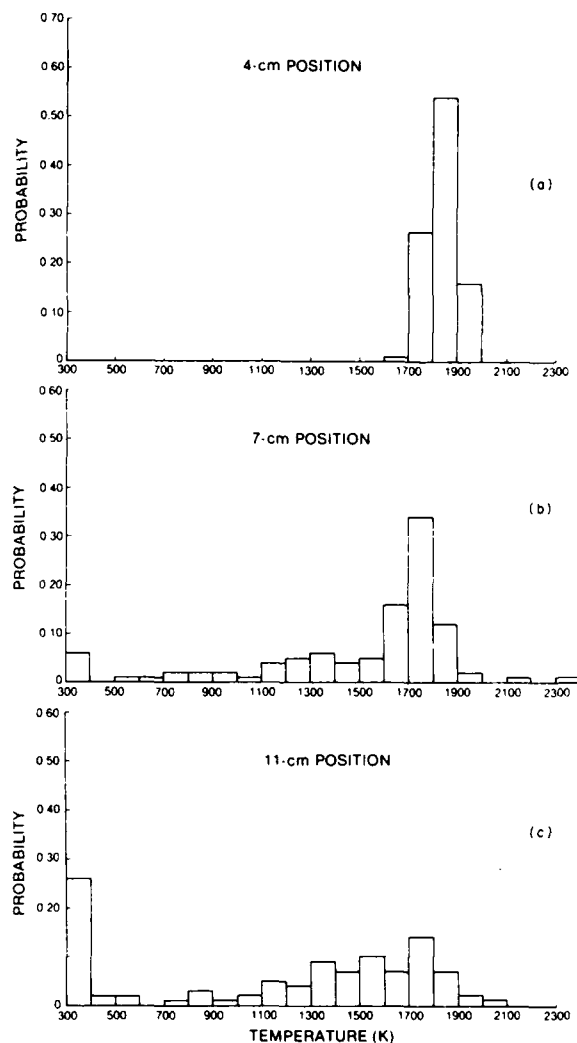


Fig. 11. Probability distribution functions obtained at flame locations (a) 4 cm, (b) 7 cm, and (c) 11 cm above the burner surface.

in the upper part of the flame are severe due to the large temperature variation which occurs there. However, electronic filtering of the signal which blocked the low-frequency fluctuations below 10 kHz and passed the higher frequencies associated with the acoustic signal (500 kHz) allowed the acoustic signals to be measured without interference from the flame turbulence. The observed pdf's in this flame are very similar to reported results on a turbulent flame obtained by the CARS technique.^{22,23}

This method of temperature measurement was compared with CARS, which is an established technique for temperature measurements. The optoacoustic technique indicated a temperature of 1950 K, at a position 5 mm above the burner surface, while the CARS technique indicated 1970 K. Both methods yielded consistent results, proving the reliability of this technique. Also, for the stoichiometry of the flame, both methods yielded results in agreement with theoretical predictions²⁰ (equivalence ratio = 1.48, $T = 1968$ K),

proving that the presence of the thin wire caused no significant perturbation of the flame at the site of measurement (region between the two probe beams).

This technique of temperature measurement is closely related to photoacoustic deflection spectroscopy (PADS)¹¹ and to optoacoustic laser deflection (OLD).¹⁶ In PADS the acoustic signal is generated by the absorption of the pump-laser energy by the flame molecules themselves (the pump laser being tuned to a transition of the molecules). The PADS technique was not utilized as the sound source in these experiments due to the limited distribution of the OH molecules. However, with a more uniformly distributed absorbing species, the PADS technique could be employed. The OLD technique was not employed because of the perturbation to the flame caused by optical breakdown, as discussed earlier.

V. Conclusions

It has been demonstrated that PTDS can be used to measure concentration profiles of a minority combustion species. In particular, OH concentration profiles have been measured in a propane-air flame. The technique is nonperturbing and possesses both spatial and temporal resolution. The temporal capabilities of this technique have not been exploited in this particular experiment. However, an examination of Fig. 3 shows that complete concentration information at a point in the flame can be obtained in $\sim 40 \mu\text{sec}$. Therefore, data can be acquired at a 10-kHz rate if a suitable laser is available. Local temperatures of the flame can be deduced from a measure of the thermal diffusion times. PTDS was not used for this purpose in the present study because of the lack of a quantitative theoretical model. By using several probe beams at right angles to the pump beam along the length of the pump beam, one can, in principle, measure concentration and temperature simultaneously at several points along a line in the flame. Moreover, a theoretical model of the PTDS is being developed which will permit absolute temperature and concentration measurements of OH without the need for calibration by absorption measurements.

It has also been demonstrated that the optoacoustic deflection technique can be employed for thermometry, in both a laminar and a turbulent flame environment. The advantages of acoustic deflection thermometry over other thermometry techniques are that it is relatively simple to implement, it does not require the high-peak-power pulsed laser necessary for nonlinear Raman techniques, and it potentially can be extended to the analysis of high-frequency temperature fluctuations if a suitable laser is utilized for the sound production. However, because of the dependence of the sound velocity on \bar{m} , a knowledge of the flame composition—especially in the case of a turbulent-diffusion flame—is necessary. It is in the high-frequency-thermometry area that the acoustic deflection technique will be extended in the near future.

The authors would like to thank D. Linder for his excellent technical help and K. Herren for his generous

loan of several instruments. R. Gupta would like to thank the Plasma Physics Group of the Air Force Wright Aeronautical Laboratories/Aero Propulsion Laboratory for their kind hospitality while this work was being performed. This work was entirely supported by and performed at the Aero Propulsion Laboratory at Wright-Patterson AFB, Ohio.

References

1. M. D. Drake, M. Lapp, C. M. Penney, S. Warshaw, and B. W. Gerhold, "Measurements of Temperature and Concentration Fluctuations in Turbulent Diffusion Flames Using Pulsed Raman Spectroscopy," in *Proceedings, Eighteenth Symposium (International) on Combustion* (Combustion Institute, Pittsburgh, Pa., 1981), p. 1521.
2. A. C. Eckbreth and R. J. Hall, "CARS Concentration Sensitivity With and Without Nonresonant Background Suppression," *Combust. Sci. Technol.* **25**, 175 (1981).
3. J. W. Daily, "Saturation Effects in Laser Induced Fluorescence Spectroscopy," *Appl. Opt.* **16**, 568 (1977).
4. R. P. Lucht, D. W. Sweeney, and N. M. Laurendeau, "Saturated-Fluorescence Measurements of the Hydroxyl Radical," in *Laser Probes for Combustion Chemistry*, D. R. Crosley, Ed. (American Chemical Society, Washington, D.C., 1980), Vol. 134, p. 145.
5. D. R. Crosley, "Collisional Effects on Laser-Induced Fluorescence Flame Measurements," *Opt. Eng.* **20**, 511 (1981).
6. B. Attal, K. Muller-Dethlefs, D. Debarre, and J. P. E. Taran, "Resonant CARS Spectroscopy of C_2 ," *Appl. Phys. B* **28**, 121 (1982).
7. B. Attal, D. Debarre, K. Muller-Dethlefs, and J. P. E. Taran, *Rev. Phys. Appl.* **18**, 39 (1983).
8. J. E. Allen, Jr., W. R. Anderson, and D. R. Crosley, "Optoacoustic Pulses in a Flame," *Opt. Lett.* **1**, 118 (1977).
9. K. Tennal, G. J. Salamo, and R. Gupta, "Minority Species Concentration Measurements in Flames by the Photoacoustic Techniques," *Appl. Opt.* **21**, 2133 (1982).
10. A. Rose, J. D. Pyrum, G. J. Salamo, and R. Gupta, in *Proceedings, International Conference on Lasers '82*, R. C. Powell, Ed. (STS Press, McLean, Va., 1983).
11. A. Rose, G. J. Salamo, and R. Gupta, "Photoacoustic Deflection Spectroscopy: A New Species-Specific Method for Combustion Diagnostics," *Appl. Opt.* **23**, 781 (1984).
12. A. Rose, J. D. Pyrum, C. Muzny, G. J. Salamo, and R. Gupta, "Application of the Photothermal Deflection Technique to Combustion Diagnostics," *Appl. Opt.* **21**, 2663 (1982).
13. W. B. Jackson, N. M. Amer, A. C. Boccara, and D. Fournier, "Photothermal Deflection Spectroscopy and Detection," *Appl. Opt.* **20**, 1333 (1981).
14. A. Rose, J. D. Pyrum, G. J. Salamo, and R. Gupta, "Photoacoustic Detection of OH Molecules in a Methane-Air Flame," *Appl. Opt.* **23**, 1573 (1984).
15. G. P. Smith, M. J. Dyer, and D. R. Crosley, "Pulsed Laser Optoacoustic Detection of Flame Species," *Appl. Opt.* **22**, 3995 (1983).
16. W. Zapka, P. Pokrowsky, and A. C. Tam, "Noncontact Optoacoustic Monitoring of Flame Temperature Profiles," *Opt. Lett.* **7**, 477 (1982).
17. M. Alden, H. Etner, G. Holmstedt, S. Svanberg, and T. Hogberg, "Single-Pulse Laser-Induced OH Fluorescence in an Atmospheric Flame, Spatially Resolved with a Diode Array Detector," *Appl. Opt.* **21**, 1236 (1982).
18. D. J. Dyer and D. R. Crosley, "Two-Dimensional Imaging of OH Laser-Induced Fluorescence in a Flame," *Opt. Lett.* **7**, 382 (1982).

19. See, for example, D. C. Fourquette and M. B. Long, "Highly Localized Pressure Perturbations Induced by Laser Absorptive Heating in the Shear Layer of a Gas Jet," *Opt. Lett.* 8, 605 (1983), and references therein.
 20. S. Gordon and B. J. McBride, "Computer Program for Calculation of Complex Equilibrium Composition Rocket Performances, Incident and Reflected Shocks, and Chapman-Jugnet Detonations," NASA SP-273-1971, NTIS N71-37775 (NTIS, Springfield, Va., 1971).
 21. L. P. Goss, G. L. Switzer, and P. W. Schreiber, "Flame Studies with the Coherent Anti-Stokes Raman Spectroscopy Technique," *J. Energy* 7, 389 (1983).
 22. L. P. Goss, G. L. Switzer, D. D. Trump, and P. W. Schreiber, "Temperature and Species-Concentration Measurements in Turbulent Flames by the CARS Techniques," *J. Energy* 7, 403 (1983).
 23. L. P. Goss, B. G. MacDonald, D. D. Trump, and G. L. Switzer, "10-Hz Coherent Anti-Stokes Raman Spectroscopy Apparatus for Turbulent Combustion Studies," Paper No. AIAA-83-1480 presented at the AIAA Eighteenth Thermophysics Conference, June 1983, Montreal, Canada.
-

Time-resolved temperature measurements in a laboratory flame using the optoacoustic laser-beam-deflection method

Dennis F. Grosjean, Benjamin Sarka, and Larry P. Goss

Systems Research Laboratories, Inc., 2800 Indian Ripple Road, Dayton, Ohio 45440-3696

Received December 26, 1984; accepted April 19, 1985

A method of obtaining time-resolved measurements of gas temperatures in a combustion environment is described. The noncontact optical laser-beam deflection technique utilizes rapid heating at a gas-solid interface as an acoustic source and is capable of acquiring localized temperature values at a repetition rate of >1 kHz. Measurements taken on a premixed propane-air laboratory flame show a 12.5-Hz thermal oscillation at the flame edge and no significant oscillation at the center.

The combustion-diagnostics area has undergone rapid growth over the past several years owing to the availability of tunable high-peak-power laser sources. Such techniques as Raman, nonlinear Raman [coherent anti-Stokes Raman spectroscopy (CARS), stimulated Raman gain], and laser-induced fluorescence have been widely applied for thermometry and major-minor species measurements to the study of reacting-flow systems.¹⁻⁵ The extension of these techniques to high frequencies—essential to an understanding of turbulence phenomena—has suffered from the lack of high-repetition-rate, high-peak-power laser sources. High-frequency thermometry has, to date, been carried out using fine-wire thermocouples or Rayleigh scattering. Both methods are extremely difficult to apply to a practical flame system.

The work of Zapka *et al.*⁶ was the first demonstration of the optoacoustic laser-beam deflection (OLD) method. These authors utilized the focused beam of a 200-mJ Nd:YAG laser to effect a gas breakdown. Propagation of the resulting acoustic pulse was detected upstream in the gas flow of a burner by observation of the deflections of two He-Ne laser beams separated by 1 cm. A basic limitation of the original work resulted from the method of sound-pulse generation. The required gas breakdown dictates the use of a high-power laser, limiting the choice of excitation sources.

Recent work by Kizirnis *et al.*⁷ has shown that a suitable acoustic pulse can be generated without the occurrence of a gas breakdown. In this case local heating at a gas-solid interface (thin tungsten wire) caused by a mildly focused, low-power pulsed laser served as the acoustic source.

Since optical absorption at a gas-solid interface covers a broad spectral range, wavelength requirements of the pump laser are greatly relaxed. Also, the necessary optical power appears to be within the range of several commercially available high-repetition-rate lasers, including the copper-vapor and rare-gas-halide systems. Consequently, a 1.5-kHz XeCl laser has been utilized in the present experiment to demonstrate the efficacy of the OLD technique to produce time-resolved measurements of temperature fluctuations within a propane-air premixed flame.

The experimental setup is shown in Fig. 1. The pump laser provides a 6-mJ, ~ 30 -nsec-wide pulse at 308 nm. Although this laser—built for the U.S. Air Force Aero Propulsion Laboratory⁸—is not a commercial product, suitable 200-Hz systems are readily available. It is anticipated that the visible output of available copper-vapor lasers that are capable of operation at ~ 5 kHz will also serve as an acceptable pump source. The main requirements of the pump source are a short pulse of $\lesssim 100$ -nsec duration at an energy of $\gtrsim 5$ mJ and a wavelength range within the absorption band of the solid surface.

In a recent study⁹ of 15 potentially useful target materials, tungsten received a high rating at room temperature, but the amplitude of the acoustic impulse in the presence of a flame dropped rapidly as a function of the number of pulses. Titanium was found to be the most acceptable material for use with the laboratory flame of interest here. The acoustic-pulse amplitude was essentially independent of the number of pulses, making it ideal for high-repetition-rate operation.

For maximum spatial resolution the rectangular-shaped output of the XeCl laser was focused onto the target in such a way that the long dimension was along the axis of the target (perpendicular to the direction of gas flow). This orientation resulted in minimal spreading of the cylindrically shaped acoustic wave as

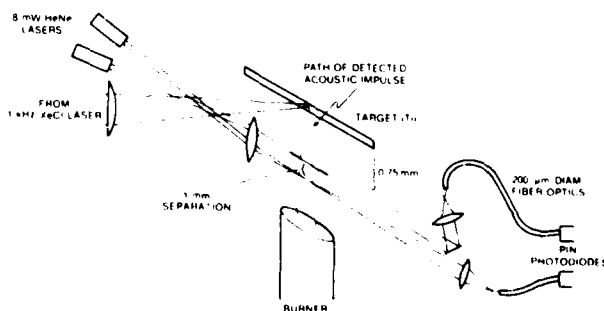


Fig. 1. Optical setup for high-repetition-rate temperature measurements utilizing the optoacoustic laser-beam deflection technique.

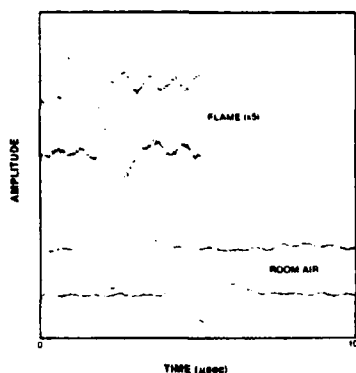


Fig. 2. Typical optoacoustic beam-deflection signals in flame and in room-temperature air.

it traveled upstream (downward in Fig. 1). The use of a sliding acoustic mask showed the spatial resolution along the probe beams to be ~ 2 – 3 mm for the probe beams located 0.75 cm from the target. At 1 cm from the target, a resolution of ~ 3 – 4 mm was obtained.

The sources of the probe beams were two independent 8-mW He-Ne lasers. Although low-frequency fluctuations owing to flame turbulence (and resultant probe-beam wander) and extraneous acoustic noise can be easily eliminated by electronic high-pass filters, general-purpose He-Ne lasers exhibit amplitude oscillations at ~ 1 MHz. In addition, this noise is polarization dependent in that the use of polarizing elements, such as beam splitters, will cause an increase in the observed noise level. Unpolarized low-noise lasers were used in the present study.

In the ideal case the beam waist in the detection region would be smaller than the acoustic wavelength. Assuming that this wavelength is determined by the pump-laser pulse width¹⁰ (~ 30 nsec for the XeCl source used here), the probe beams should be limited to a diameter of ~ 40 μ m at gas temperatures of ~ 2000 K and ~ 15 μ m at room temperature. From observed pulse widths the present setup has a beam diameter of ~ 200 μ m. This has proved to be acceptable for measurement precision of better than ± 100 K.

The entrances of the fiber optics shown in Fig. 1 serve as the motion-detection points of the deflected probe beams; the output ends are incident upon commercial fast photodiodes. The fiber optics may be eliminated and the probe beams set incident upon the edge of the active detector region. The 200- μ m-diameter fibers, however, provided a high degree of alignment flexibility in this experiment.

The signal currents of the fast optical diodes of Fig. 1 were routed through current-to-voltage converters, filtered for removal of low-frequency components (3-dB point = 75 kHz), buffered into high-speed amplifiers, and terminated at high-speed analog-to-digital converters (LeCroy 6102 amplifier and MM8818 transient recorders). The 8-bit digitized outputs were stored in real time in a cache memory (98 Kbytes maximum per channel) and later processed in a microcomputer.

Figure 2 shows typical signals acquired in room-temperature air and in a premixed propane-air flame.

The 2.59- μ sec separation of the probe signals at room temperature indicates an effective beam separation of 1.00 mm. The drop in signal amplitude at high temperatures is primarily due to the decreased gas number density. This amplitude decrease causes difficulty in determining the positions of the peaks since the signal-to-noise ratio is quite small. This situation is aggravated by the fact that the effective frequency of the signal is very close to the noise frequency. It was found necessary to use a fourth-order, bandpass digital filter in processing the data for separation of the acoustic pulse signals from the high-frequency noise of the He-Ne probe lasers. However, the optical setup has not yet been optimized; improvements subsequent to the

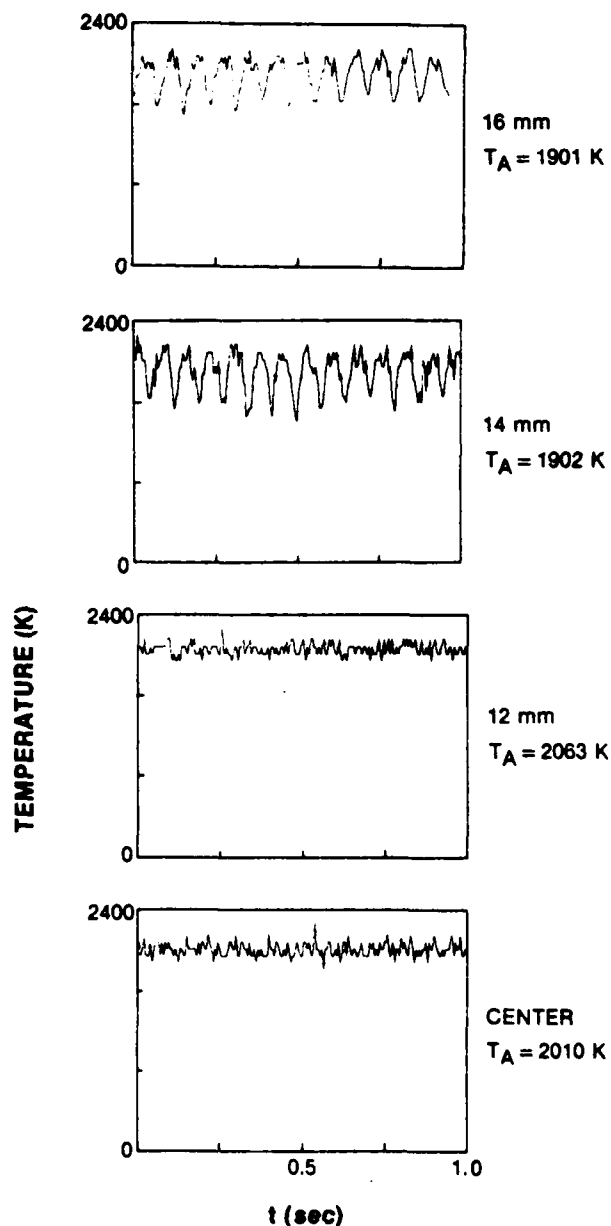


Fig. 3. Plots of temperature versus time in premixed propane-air flame at various radial distances 3 cm above burner surface.

work reported herein have shown enhancements in signal-to-noise ratio.

After filtering of the acquired signals, a correlation operation was performed in order to determine the time difference of the positive peaks of the recorded signals. The temperature (T) is related to the acoustic-wave-propagation velocity (v) by^{6,7}

$$T = v^2 \bar{m} / R \left[1 + \frac{R}{C_V(T)} \right], \quad (1)$$

where \bar{m} is the average molecular weight of the gases, R is the universal gas constant, and $C_V(T)$ is the temperature-dependent average molar specific heat at constant volume. The ratio of the temperature in a flame (T_f) to a reference temperature (T_r) at a measurement point, then, is

$$\frac{T_f}{T_r} = \left(\frac{\Delta t_r}{\Delta t_f} \right)^2 \frac{\bar{m}_f \left[1 + \frac{R}{C_V(T_r)} \right]}{\bar{m}_r \left[1 + \frac{R}{C_V(T_f)} \right]}, \quad (2)$$

where \bar{m}_f and \bar{m}_r refer to the average molecular weights at the measurement point in the flame and at reference conditions, respectively. Here, the velocity ratio is represented by the ratio of the measured acoustic travel time (Δt_r) at T_r to the travel time (Δt_f) at T_f since the probe-beam separation distance is constant. Room-temperature air was typically used as the reference point.

If the chemical composition of the flame is known, the uncertainty in Eq. (2) is determined by the uncertainty in the measurement of the acoustic travel times, as discussed above; statistical sampling will improve this. For unknown stoichiometry the range of error introduced by \bar{m}_f and $C_V(T_f)$ can be bounded by the composition limits. For the unconfined flame of interest here, an adiabatic model for a propane-air flame¹¹ was combined with tabulated values¹² of $C_V(T)$, with lean and rich fuel-air ratios setting the temperature boundaries. The mean values of the limits calculated as a function of $\Delta t_r/\Delta t_f$ represent the values reported here. The error range is small at high temperatures ($\pm 2.3\%$ at ~ 2200 K) and increases to $\pm 10\%$ at ~ 1750 K.

Typical results obtained on a premixed propane-air flame are shown in Fig. 3. The flame source was a 3.5-cm-diameter Meker-type laboratory burner. Measurements were made 3 cm above the surface. A low-frequency oscillation of 12.5 Hz is clearly developed at the edge of the flame (16-mm radial point). At 14 mm the oscillation is distorted; by 12 mm, it completely disappears. The low-frequency oscillations observed in this type of flame were also observed by Hanson *et al.*¹³ while recording OH profiles by means of a digital camera system. The value of the maximum average temperature of Fig. 3 peaks at the 12-mm point and then decreases as the radial distance decreases. The data shown were acquired at a repetition rate of 200 Hz. Scans at 1 kHz failed to reveal any significant higher-frequency thermal oscillations.

The accuracy and precision of the technique were examined at the center of the flame. The high-repetition-rate OLD method yielded a temperature of 2010

± 73 K for a sample size of 384 (maximum memory utilized). The uncertainty here is defined as one standard deviation (probability distribution function is approximately Gaussian); the greatest recorded error was 265 K. The CARS technique was used at the same position under similar burner conditions, yielding a temperature value of 2030 ± 110 K for 1500 samples. This substantiates the earlier work of Kizirnis *et al.*,⁷ although the present data were collected at a 200-Hz repetition rate.

The high-repetition-rate application of the opto-acoustic laser-beam deflection technique described here is the first reported demonstration of nonintrusive time-resolved temperature measurements in a flame. The relative ease of implementation and the ready availability of suitable pump sources results in this method's having wide applicability in combustion diagnostics and modeling.

This research was supported through the San Jose State University Foundation by U.S. Air Force contract F33615-81-C-2013. The authors wish to thank D. Trump for his assistance with the signal-detection electronics and B. Ganguly and S. Kizirnis for helpful discussions.

References

1. M. D. Drake, M. Lapp, C. M. Penney, S. Warshaw, and B. W. Gerhold, in *Proceedings, Eighteenth Symposium (International) on Combustion* (Combustion Institute, Pittsburgh, Pa., 1981), p. 1521.
2. A. C. Eckbreth and R. J. Hall, *Combust. Sci. Technol.* **25**, 175 (1981).
3. J. W. Daily, *Appl. Opt.* **16**, 568 (1977).
4. R. P. Lucht, D. W. Sweeney, and N. M. Laurendeau, in *Laser Probes for Combustion Chemistry*, D. R. Crosley, ed. (American Chemical Society, Washington, D.C., 1980), Vol. 134, p. 145.
5. D. R. Crosley, *Opt. Eng.* **20**, 511 (1981).
6. W. Zapka, P. Pokrowsky, and A. C. Tam, *Opt. Lett.* **7**, 477 (1982).
7. S. W. Kizirnis, R. J. Brecha, B. N. Ganguly, L. P. Goss, and R. Gupta, *Appl. Opt.* **23**, 3873 (1984).
8. D. F. Grosjean, "Electric discharge excitation and energy source integration," Rep. AFWAL-TR-84-2074 (Air Force Wright Aeronautical Laboratories, Wright-Patterson Air Force Base, Ohio, January 1985).
9. H. Yoon, "Experimental investigation of the pulsed photoacoustic effect produced on a solid surface," master's thesis (Air Force Institute of Technology, Wright-Patterson Air Force Base, Ohio, December 1984).
10. C. K. N. Patel and A. C. Tam, *Rev. Mod. Phys.* **53**, 517 (1981).
11. S. Gordon and B. J. McBride, "Computer program for calculation of complex equilibrium composition rocket performances, incident and reflected shocks, and Chapman-Jouguet detonations," NASA Rep. SP273, May 1971; NTIS Rep. N78-17724 (National Technical Information Service, Springfield, Va., 1976).
12. K. Raznjevic, *Handbook of Thermodynamic Tables and Charts* (Hemisphere, Washington, D.C., 1976).
13. R. K. Hanson, B. Hiller, E. C. Rea, J. Seitzman, G. Ky-chakoff, and R. D. Howe, "Laser-based diagnostics for flowfield measurements," presented at the Winter Annual Meeting of the American Society of Mechanical Engineers, New Orleans, La., December 9-14, 1984.

AIAA'85

AIAA-85-1445

**Time-Resolved Temperature Measurements in a
Premixed Flame Using the Optoacoustic Beam-
Deflection Technique**

L. P. Goss, D. F. Grosjean, and B. Sarka, Systems
Research Laboratories, Inc., Dayton, OH 45440-3696;
S. W. Kizirnis, AFWAL Aero Propulsion Laboratory,
Wright-Patterson AFB, OH 45433-6503

**AIAA/SAE/ASME/ASEE 21st Joint
Propulsion Conference**

July 8-10, 1985 / Monterey California

For permission to copy or republish, contact the American Institute of Aeronautics and Astronautics
1633 Broadway, New York, NY 10019

TIME-RESOLVED TEMPERATURE MEASUREMENTS IN A PREMIXED FLAME USING THE OPTOACOUSTIC BEAM-DEFLECTION TECHNIQUE*

L. P. Goss,** D. F. Grosjean, and B. Sarka
Systems Research Laboratories, Inc.
Dayton, OH 45440-3696

S. W. Kizirnis
AFWAL Aero Propulsion Laboratory
Wright-Patterson Air Force Base, OH 45433-6503

Abstract

A method of obtaining time-resolved measurements of gas temperatures in a combustion environment is described. The noncontact optical laser-beam deflection technique utilizes rapid heating at a gas/solid interface as an acoustic source and is capable of acquiring localized temperature values at a repetition rate of > 1 kHz. Generation of the photoacoustic signal at the target surface, deflection of the laser probe, and the relationship between the deflection and the detector voltage are discussed in detail. Measurements taken on a Meker-type pre-mixed propane-air laboratory flame show a 12.5-Hz thermal oscillation at the flame edge and no significant oscillation at the center. Measurements through the reaction zone of a Bunsen burner-type flame display a high degree of fluctuation, varying from room temperature to stoichiometric temperature for the fuel-to-air mixture.

Introduction

The combustion-diagnostics area has undergone rapid growth over the past several years due to the availability of tunable high-peak-power laser sources. Such techniques as Raman, nonlinear Raman (CARS, SRG), and laser-induced fluorescence (LIF) have been widely applied for thermometry and major-minor species measurements to the study of reacting flow systems.¹⁻⁵ The extension of these techniques to high frequencies--essential to an understanding of turbulence phenomena--has suffered from the lack of high-repetition-rate, high-peak-power laser sources. High-frequency thermometry has, to date, been carried out using fine-wire thermocouples or Rayleigh scattering. Both methods are extremely difficult to apply to a practical flame system.

This paper describes a high-frequency demonstration of the optoacoustic laser deflection (OLD) thermometric technique which can be applied to diverse, practical flame environments. The technique involves measurement of the propagation velocity of an acoustic impulse between two measurement points defined by monochromatic beams. The method is nonintrusive at the point of measurement, does not require focus coincidence of multiple beams, and can be used with a number of commercially available high-repetition-rate lasers.

The work of Zapka, Pokrowsky, and Tam⁶ was the first demonstration of the OLD method. These authors utilized the focused beam of a 200-mJ Nd:YAG laser to effect a gas breakdown. Propagation

of the resulting acoustic pulse was detected upstream in the gas flow of a burner by observation of the deflections of two He-Ne laser beams separated by 1 cm. The time between deflections represented the difference in arrival time of the acoustic pulse; after correction for the gas-flow velocity, the acoustic velocity was determined and the average temperature within the measurement area extracted.

A basic limitation of the original work resulted from the method of sound-pulse generation. The required gas breakdown dictates the use of a high-power laser, limiting the choice of excitation sources. In addition, a blast wave resulting from the breakdown may perturb the measurement region and produce erroneous results.

Recent work by Kizirnis, et al.,⁷ has shown that a suitable acoustic pulse can be generated without the occurrence of a gas breakdown. In this case local heating at a gas/solid interface (thin tungsten wire) caused by a mildly focused, low-power pulsed laser served as the acoustic source. Results obtained on a propane-air premixed flame were similar to those from measurements made using the CARS technique.

Since optical absorption at a gas-solid interface covers a broad spectral range, wavelength requirements of the pump laser are greatly relaxed. Also, the necessary optical power appears to be within the range of several commercially available high-repetition-rate lasers, including the copper-vapor and rare-gas-halide systems. Consequently, a 1.4-kHz XeCl laser has been utilized in the present experiment to demonstrate the efficacy of the OLD technique to produce time-resolved measurements of temperature fluctuations within a propane-air premixed flame.

Theoretical

To obtain an understanding of the OLD technique, it is important to review the temperature dependence of the acoustic velocity, the photoacoustic generation of the sound pulse, the detection of the sound pulse by deflection of the probe laser, and the relationship of the observed electronic signal to the sound intensity.

Temperature Dependence of Sound Velocity

The relationship between the speed of sound in a gas mixture and the temperature is given by⁸

$$T = \frac{v_0^2 \bar{m}}{R \left[1 + \frac{R}{C_v(T)} \right]} \quad (1)$$

where \bar{m} is the average molecular weight of the gases

*Work supported in part through the San Jose State University Foundation by USAF Contract F33615-81-C-2103 and in part through the AFWAL Aero Propulsion Laboratory by USAF Contract F33615-80-C-2054.

**Member AIAA

This paper is declared a work of the U.S. Government and therefore is in the public domain.

in the flame, R the universal gas constant, v_0 the sound velocity, and $\bar{C}_v(T)$ the temperature-dependent average molar specific heat at constant volume in the flame. Ratioing the velocity data from measurements under ambient conditions (subscript a) to those in the flame (subscript f) gives

$$\frac{T_f}{T_a} = \left(\frac{v_f}{v_a}\right)^2 \frac{K_f}{K_a} \quad (2)$$

where the constant K incorporates the gas constant, molecular weight, and specific heat. In the case of most flames encountered in the laboratory with slow gas flows (less than 20 m/s), the time for transit of the sound pulse can be used directly, yielding

$$\frac{T_f}{T_a} = \left(\frac{\Delta t_a}{\Delta t_f}\right)^2 \frac{K_f}{K_a} \quad (3)$$

Equation (3) is the basic equation used for data analysis in this work. The dependence of the sound velocity upon average molecular weight and specific heat must be taken into account to ensure accurate temperature measurements. For small hydrocarbon fuels, however, neglecting the composition (temperature) effect of these variables results in relatively small temperature errors (especially in the case of lean fuel-to-air mixtures).

Production of Acoustic Pulse

The generation of the photoacoustic pulse from a target material resulting from photon absorption from a laser relies upon the conversion of the absorbed optical radiation into heat by nonradiative relaxation processes. It is assumed that non-radiative relaxation predominates in the medium, where the thermal energy E_{th} is given by

$$E_{th} = E_{abs} = E_0 \alpha l \quad (4)$$

Knowing the specific heat at constant pressure C_p , the temperature rise ΔT of the illuminated volume can be evaluated from

$$E_{th} = C_p V \Delta T \quad (5)$$

where V is the illuminated volume and ρ is the mass density of the medium. Since

$$V = \pi R^2 l \quad (6)$$

the temperature rise is

$$\Delta T = \frac{E_0 \alpha}{\pi R^2 C_p \rho} \quad (7)$$

Now if one assumes adiabatic, isobaric expansion, the new volume of the illuminated region can be calculated. With ΔR being the increase in the radius of the illuminated volume,

$$\pi R^2 l = \pi (R + \Delta R)^2 l = \beta V \Delta T \quad (8)$$

where β is the volumetric expansion coefficient. If $\Delta R \ll R$, the increased radius is

$$\Delta R \sim \frac{1}{2} R \beta \Delta T \quad (9)$$

Inserting ΔT from Eq. (7),

$$\Delta R = \frac{E_0 \alpha \beta}{2 \pi R C_p \rho} \quad (10)$$

This expansion creates a pressure wave which travels radially outward from the illuminated cylinder at the velocity of sound. The change in pressure P created at a point is related to the frequency of the sound wave f_a and the displacement Δx through

$$P = 2 \pi f_a v_a \Delta x \quad (11)$$

But Δx is proportional to ΔR evaluated in Eq. (9). Thus, $\Delta x = \text{const} \times \Delta R$ and

$$P = \text{const.} \frac{f_a}{R} \frac{\beta v_a}{C_p} E_0 \alpha \quad (12)$$

For a fixed geometry of laser illumination and properties, f_a and R are constant. Therefore,

$$P = \text{const.} \frac{\beta v_a}{C_p} E_0 \alpha \quad (13)$$

Equation (13) contains most of the important parameters necessary for practical applications of photoacoustic spectroscopy, but it does not provide information regarding the temporal or spatial distribution of the photoacoustic output pulse.

For a cylindrical excitation source, the pressure amplitude of the photoacoustic signal is given by⁸

$$P(r, t_z) \sim \frac{\beta \alpha E_0}{\pi C_p \tau^2} \left(\frac{v_a \tau}{2 \pi r} \right)^{1/2} \quad (14)$$

Several interesting observations are possible with the pressure amplitude predicted in Eq. (14). First, the compression pulse at time t_- is followed by a rarefaction pulse (of nearly equal magnitude) at time t_+ , with the time interval between the compression and rarefaction being approximately the laser pulse width. This has been confirmed by several investigators, for example, Bunkin and Komissarov,⁹ Lyamshev and Naugol'nykh,¹⁰ and Naugol'nykh.¹¹ Secondly, the pressure amplitude $P(r, t)$ decreases with distance as $r^{-1/2}$, in accordance with the conservation of energy in cylindrical symmetry, as noted by Landau and Lifshitz.¹² When the source is a point, the pressure amplitude

decreases with distance as $1/r$, in accordance with the conservation of energy.

This behavior is depicted in Figs. 1 and 2 and is in good agreement with Eq. (13). According to

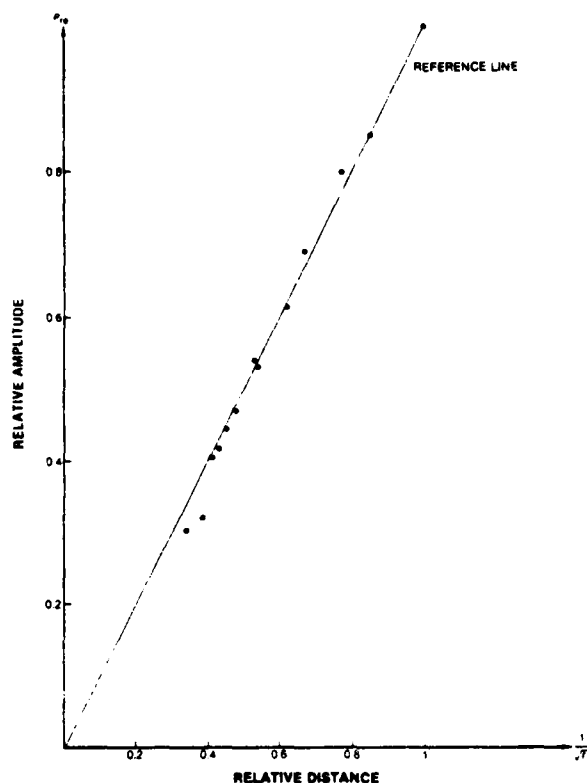


Figure 1. Cylindrical Propagation of Optoacoustic Signal.

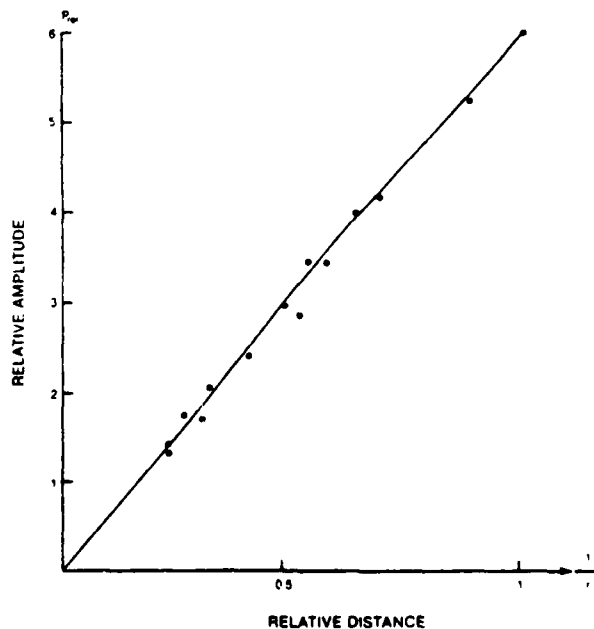


Figure 2. Radial-Distance Relation of Optoacoustic Signal from Point Source.

Eq. (14) the amplitude of the pressure pulse is linearly dependent upon the absorption coefficient of the material, dependent upon the inverse of the specific heat (heat capacity of the material), linearly dependent upon the laser power, and inversely dependent upon the pulse width of the laser. The latter dependence dictates the use of a short-pulse laser. The power dependence of the laser source is shown in Fig. 3.

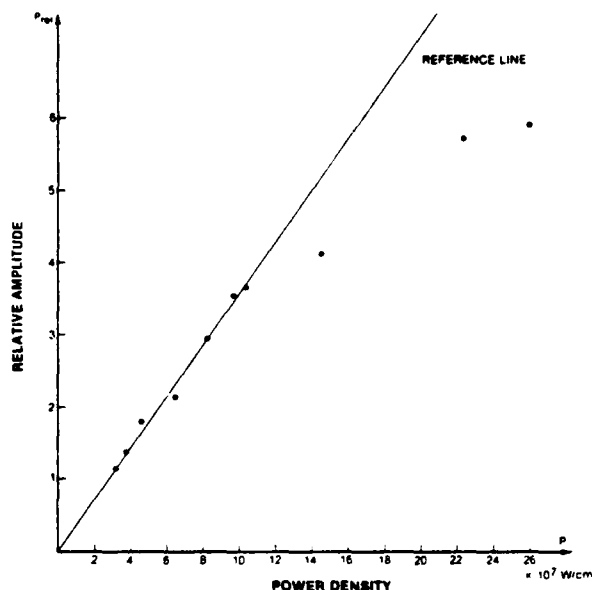


Figure 3. Relative Sound Amplitude vs. Laser Power Density for Optoacoustic Signal.

While the signal does display linear behavior, power densities above 100 MW/cm^2 result in non-linear saturation behavior, primarily due to the onset of plasma formation at the surface which absorbs the laser pulse.

According to Eq. (14) the properties of the target material which affect the acoustic signal are 1) the absorption coefficient, 2) the heat capacity, and 3) the volumetric expansion coefficient of the surrounding gas.

The results of a study of various materials is shown in Fig. 4. Titanium was found to be the prime candidate for the target material.

Probe Beam Deflection by PA Signals

Jackson and coworkers derived the equation for probe beam deflection as a function of the index of refraction.¹³ They used the index of refraction as a function of temperature and neglected the pressure contribution since, under the conditions of their study, it was very small compared to the temperature contribution. They noted, however, that the pressure contribution to the index of refraction has experimental importance at high frequencies, large probe beam offsets, and/or high pump beam peak powers, which is the case in the present study. Their derivation is followed here.

The index of refraction as a function of pressure is

$$n(r,t) = n_0 + \Delta n(r,t) = n_0 + \left. \frac{\partial n}{\partial P} \right|_{P_{\text{ambient}}} P(r,t) \quad (15)$$

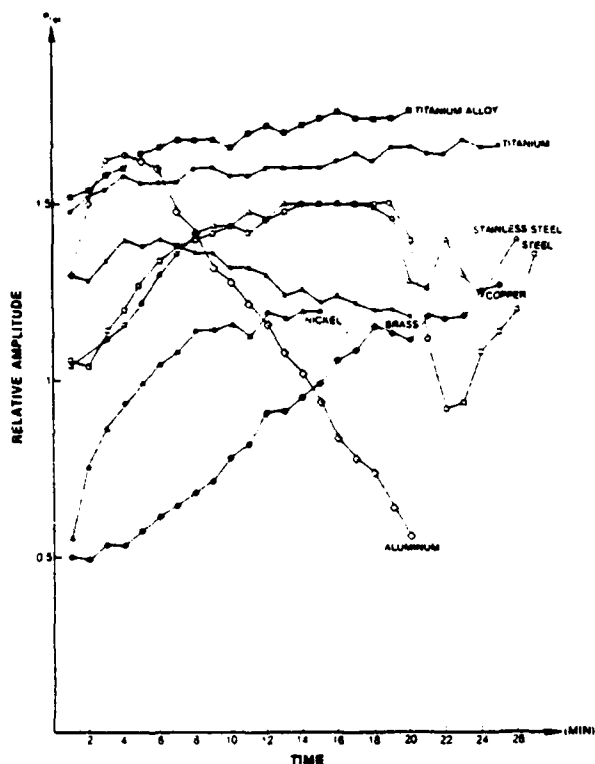


Figure 4. Relative Sound-Amplitude Variation for Different Target Materials.

The propagation of the Gaussian probe beam through the spatially varying index of refraction is given by⁴

$$\frac{d}{ds} \left(n_0 \frac{dr_0}{ds} \right) = \nabla_{\perp} n(r,t) \quad (16)$$

where r_0 is the perpendicular displacement of the beam from its original direction, n_0 is the uniform index of refraction, and $\nabla_{\perp} n(r,t)$ is the gradient of the index of refraction perpendicular to S_r (the ray path) (Fig. 5). Integrating Eq. (16) over S_r gives

$$\frac{dr_0}{ds} = \frac{1}{n_0} \int_{\text{path}} \nabla_{\perp} n(r,t) dS_r \quad (17)$$

$$= \frac{1}{n_0} \frac{\partial n}{\partial P} \int_{\text{path}} \nabla_{\perp} P(r,t) dS_r \quad (18)$$

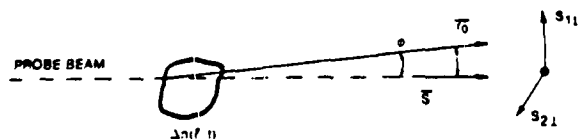


Figure 5. Scattering Geometry. Scattering region may focus the beam differently in the S_{11} and S_{21} directions (elliptical Gaussian beams).

For gases ($n \sim 1$), the index of refraction can be expressed as

$$n - 1 = K_{GD} \rho_{\text{gas}} \quad (19)$$

where K_{GD} is the Gladstone-Dale constant and ρ_{gas} is the density of the gas. Equation (19) is known as the simpler Gladstone-Dale law.¹⁵ Since ρ_{gas} is linearly proportional to the pressure of the gas, Eq. (19) becomes

$$n - 1 = KP \quad (20)$$

Therefore,

$$\frac{\partial n}{\partial P} = K \quad (21)$$

From Eq. (19),

$$\frac{dr_0}{ds} = K \int_{\text{path}} \nabla_{\perp} P(r,t) dS_r \quad (22)$$

since n_0 and $\partial n / \partial P$ are constant. When the path is the same for all measurements,

$$\frac{dr_0}{ds} = K^* P(r,t) \quad (23)$$

Equation (23) indicates that the displacement of the probe beam from its original direction is linearly proportional to the sound pressure.

Detector Response

Deflection of the probe beam due to a change in the index of refraction is detected by a position-sensitive detector which converts the deflection into an output voltage. The change in the signal ΔV_{det} above the dc level V_{det} is demonstrated in Fig. 6. Assuming a Gaussian probe beam,

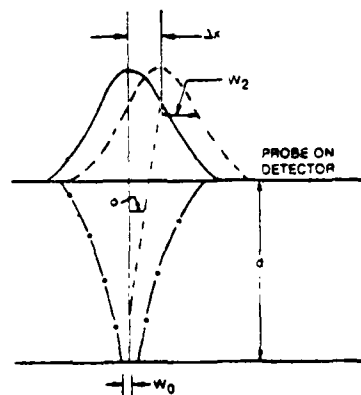


Figure 6. Probe Spot on Detector.

$$\begin{aligned} \frac{\Delta V_{\text{det}}}{V_{\text{det}}} &= \frac{\Delta I}{I_0} = 4\Delta x \int_0^{\infty} \frac{2}{\pi w_2^2} \exp(-2r^2/w_2^2) dr \\ &= \left(\frac{4}{\sqrt{2\pi}} \right) \frac{\Delta x}{w_2} \end{aligned} \quad (24)$$

where $\Delta x = \phi d$, d is the distance from the focal spot to the detector, I_0 is the probe-beam intensity, and w_2 is the spot radius on the detector. Since d is large,

$$w_2 \sim (\lambda d) / (\pi w_1 n_0) \quad (25)$$

where w_1 is the probe beam radius at the focal spot, λ is the probe beam wavelength, and n_0 is the index of refraction of the air. Hence,

$$\Delta V_{\text{det}} = \frac{4}{\sqrt{2\pi}} \frac{\phi \pi w_1 n_0}{\lambda} V_{\text{det}} \quad (26)$$

However, $\phi \sim dr_0/ds_r$, since the deflection is very small. Therefore,

$$\begin{aligned} \Delta V_{\text{det}} &\sim \frac{4}{\sqrt{2\pi}} \frac{\pi w_1 n_0}{\lambda} \frac{dr_0}{ds_r} V_{\text{det}} \\ &= K \frac{dr_0}{ds_r} \end{aligned} \quad (27)$$

since w_1 , n_0 , λ , and V_{det} are constant. When the probe beam is not focused, which is the case in the present study, d is the deflected spot distance from the detector and w_1 is the probe beam radius at the deflected spot. When the deflected spot is limited to one position, d and w_1 remain constant; therefore, the voltage change is still a linear function of displacement of the probe beam at the detector.

Experimental

The experimental setup is shown in Fig. 7. The pump laser provides a 6-mJ, ~ 30 -nsec-wide pulse at 308 nm. Although this laser--built for the Air Force Aero Propulsion Laboratory¹⁰--is not a commercial product, suitable 200-Hz systems are readily available. It is anticipated that the visible output of available Cu-vapor lasers which are capable of operation at ~ 5 kHz will also serve as an acceptable pump source. The main requirements of the pump source are (1) a short pulse of ≤ 100 nsec duration at an energy of ≥ 5 mJ, and (2) a wavelength range within the absorption band of the solid surface.

For maximum spatial resolution the rectangular-shaped output of the XeCl laser was focused onto

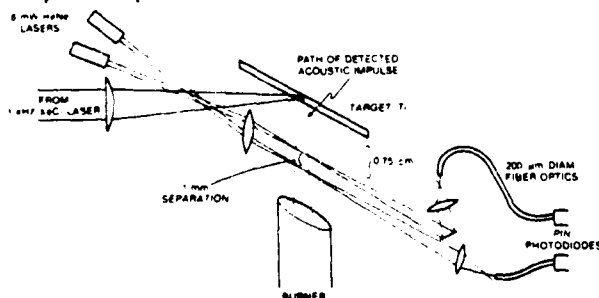


Figure 7. Optical Setup for High-Repetition-Rate Temperature Measurements Utilizing the Optoacoustic Laser-Beam Deflection Technique.

the target in such a way that the long dimension was along the axes of the target (perpendicular to the direction of gas flow). This orientation resulted in minimal spreading of the cylindrically shaped acoustic wave. Figure 8 shows the result of scanning with a 1-mm-wide slot through the path of the acoustic pulse. The mask was oriented perpendicular to, and located ~ 1 mm above, a HeNe probe beam; the figure shows the waveshape of the detector output. Also the signal with the mask removed is shown. From these data the spatial resolution along the probe beams was estimated to be 2-3 mm for the probe beams located 0.75 cm from the target.

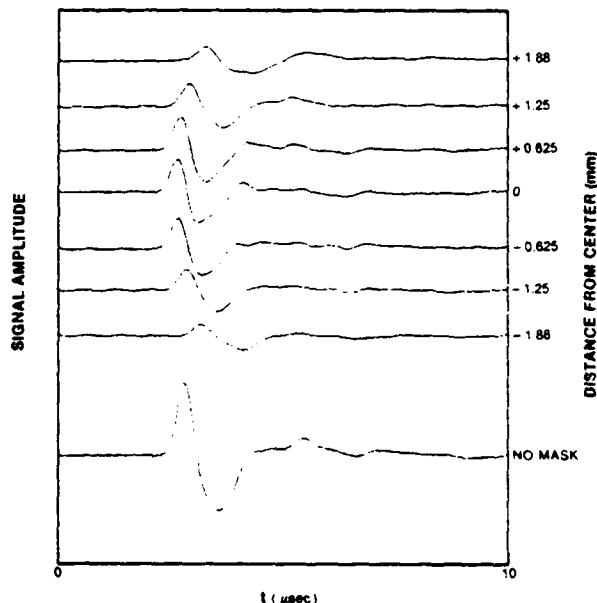


Figure 8. Optoacoustic Deflection Signals Resulting from Scan of 1-mm-Wide Mask Located 1 mm above Probe Beam. Target-to-beam distance = 0.75 cm. Mask oriented perpendicular to probe beam.

The sources of the probe beams were two independent 8-mW HeNe lasers. Many other cw sources may be used since the wavelength is not critical. The main requirements are (1) sufficient power such that a high-speed transient is detectable, (2) sufficiently low noise in the frequency range of the transient, and (3) sufficiently small beam waist in the detection region to define the location of the deflections and, consequently, the separation of the measurement points. Points 2 and 3 are the most difficult to achieve.

Although low-frequency fluctuations due to flame turbulence and extraneous acoustic noise can be easily eliminated by electronic high-pass filters, general-purpose HeNe lasers exhibit amplitude oscillations at ~ 1 MHz. In addition, this noise is polarization dependent in that the use of polarizing elements, such as beam splitters, will cause an increase in the observed noise level. Unpolarized low-noise lasers were used in the present study, although the signal-to-noise ratio was marginally acceptable at times.

In the ideal case the beam waist in the detection region would be smaller than the acoustic wavelength. Assuming that this wavelength is determined

by the pump-laser pulse width¹⁷ (~ 30 nsec for the XeCl source used here), the probe beams should be limited to a diameter of ~ 40 μm at gas temperatures of ~ 2000 K and ~ 15 μm at room temperature. From the pulse width of Fig. 8, the present setup has a beam diameter of ~ 200 μm . This has proven to be acceptable for measurement precision of better than ± 100 K.

The entrances of the fiber optics shown in Fig. 7 serve as the motion-detection points of the deflected probe beams; the output ends are incident upon a commercial fast pin photodiode. The fiber optics may be eliminated and the probe beams set incident on the edge of the active detector region. The 200- μm -diam. fibers, however, provided a high degree of alignment flexibility in this experiment.

A block diagram of the processing electronics is shown in Fig. 9. The signal current of the fast optical diode was routed through a current-to-voltage converter, filtered for removal of low-frequency components (3-dB point = 75 kHz), buffered into high-speed amplifiers, and terminated at high-speed analog-to-digital converters (LeCroy 6102 amplifier and MM 8818 transient recorders). The 8-bit digitized output was stored in real time in a cache memory (98 Kbytes maximum per channel). After completion of a scan, the data were read into a microcomputer (HP 9836) and processed. The timing of the transient recorders was controlled in the following manner. A delayed trigger pulse from the pump laser effected a pulse train of 256 or 512 bytes (selectable) simultaneously to the digitizers at a 50-MHz clock rate. This insured time synchronization between the signals of the two probe-laser beams. Data acquisition was terminated when a selected portion of the cache memory was filled.

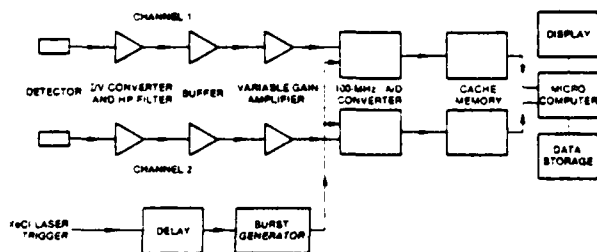


Figure 9. Block Diagram of Detection and Processing Electronics for Optoacoustic Technique.

Figure 10 shows typical signals acquired in room-temperature air and in a pre-mixed propane-air flame. The 2.59- μsec separation of the probe signals at room temperature indicates an effective beam separation of 1.00 mm. The drop in signal amplitude at high temperatures is primarily due to the decreased gas number density.

Data analysis consists of first filtering the optoacoustic signal to remove low- and high-frequency HeNe probe laser noise. After filtering, a correlation operation is performed in order to determine the time difference of the positive peaks of the recorded signals, and Eq. (3) is applied. If the chemical composition of the flame is known, the uncertainty in the resulting temperature is determined by the uncertainty in the measurement of

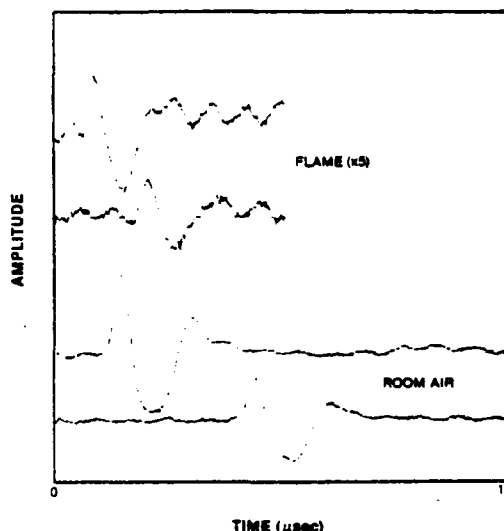


Figure 10. Typical Optoacoustic Beam Deflection Signals in Flame and in Room Temperature Air.

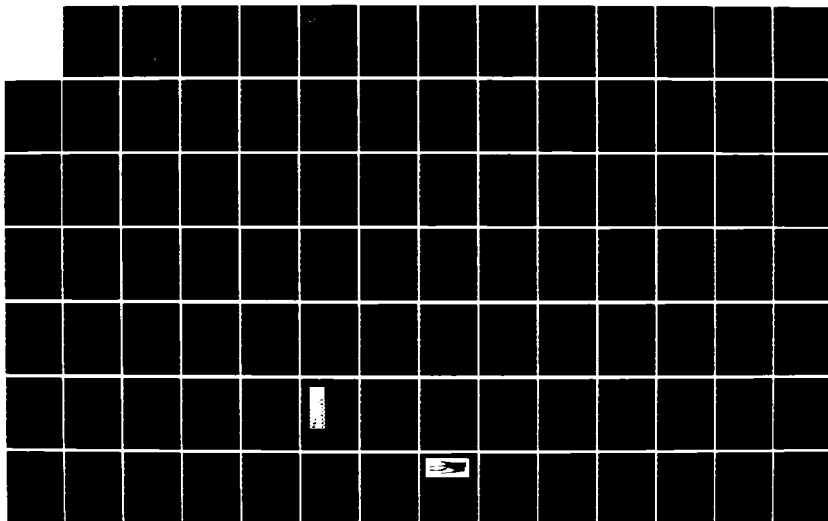
the acoustic travel times; statistical sampling will improve this. For unknown stoichiometry the range of error introduced by \bar{m} and $C_p(T_f)$ can be bounded by the composition limits. For the Meker-type unconfined flame, an adiabatic model for a propane-air flame¹⁸ was combined with tabulated values of $C_p(T)$, with lean and rich fuel-air ratios setting the temperature boundaries. The mean values of the limits calculated as a function of $\Delta T_f/\Delta T_r$ represent the values reported here. The error range is small at high temperatures ($\pm 2.3\%$ at ~ 2200 K) and increases to $\pm 10\%$ at ~ 1750 K.

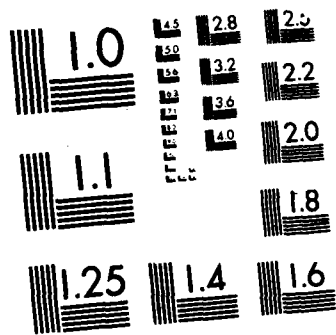
Results and Discussion

Typical results obtained on a pre-mixed, propane air flame are shown in Fig. 11. The flame source was a 3.5-cm-diam. Meker-type laboratory burner. Measurements were made 3 cm above the surface. A low-frequency oscillation of 12.5 Hz is clearly developed at the edge of the flame (16-mm radial point). At 14 mm the oscillation is distorted; by 12 mm, it completely disappears. The low-frequency oscillations observed in this type of flame were also observed by Hanson, et al.,¹⁹ while recording OH profiles by means of a digital camera system. The value of the maximum average temperature of Fig. 11 peaks at the 12-mm point and then decreases as the radial distance decreases. The data shown were acquired at a rep rate of 200 Hz. Scans at 1 kHz failed to reveal any significant higher-frequency thermal oscillations.

The temperature probability distribution function (PDF) of the data acquired at the flame center is shown in Fig. 12. The RMS error was calculated to be ± 73 K. A CARS measurement made on the same burner under similar conditions yielded a temperature value of 2030 ± 110 K. The excellent agreement with the CARS technique indicates the precision of the high-rep-rate optoacoustic laser-beam deflection method of temperature measurement. The lower RMS values of the new technique are encouraging, especially since the accuracy of this technique increases at lower temperatures. As the gas temperature decreases, the acoustic velocity decreases

AD-A173 414 LASER OPTICS/COMBUSTION DIAGNOSTICS(U) SYSTEMS RESEARCH 3/3
LABS INC DAYTON OH RESEARCH APPLICATIONS DIV
L P GOSS ET AL JUL 86 SRL-6603 AFMAL-TR-86-2023
UNCLASSIFIED F33615-80-C-2054 F/G 21/2 NL





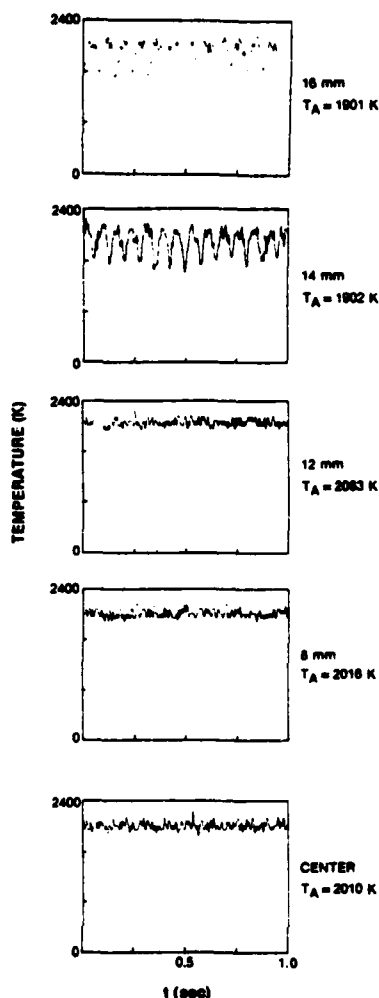


Figure 11. Plots of Temperature vs. Time in Pre-mixed Propane-Air Flame at Various Radial Distances at Position 3 cm above Burner Surface.

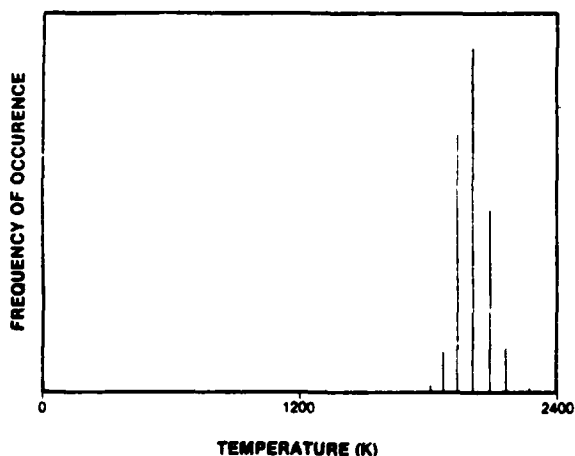


Figure 12. Probability Distribution Function of Measured Temperatures Corresponding to Center Position of Fig. 11.

and the gas density increases. These characteristics result in higher time resolution and higher signal-to-noise ratios. Accuracy in determining the transit time of the acoustic pulse is, thus, increased and a lower RMS error at low temperatures is obtained. This makes the OLD technique very useful when large temperature fluctuations are encountered.

Figure 13 displays results on a Bunsen-burner-type flame in which higher-frequency-component temperature fluctuations were observed. Note the large temperature fluctuations observed in the vicinity of the reaction zone. These measurements were made at 100 Hz, except for the location high in the reaction zone where they were made at 1000 Hz also [Fig. 13(b)]. This figure indicates that 1000 Hz is not a

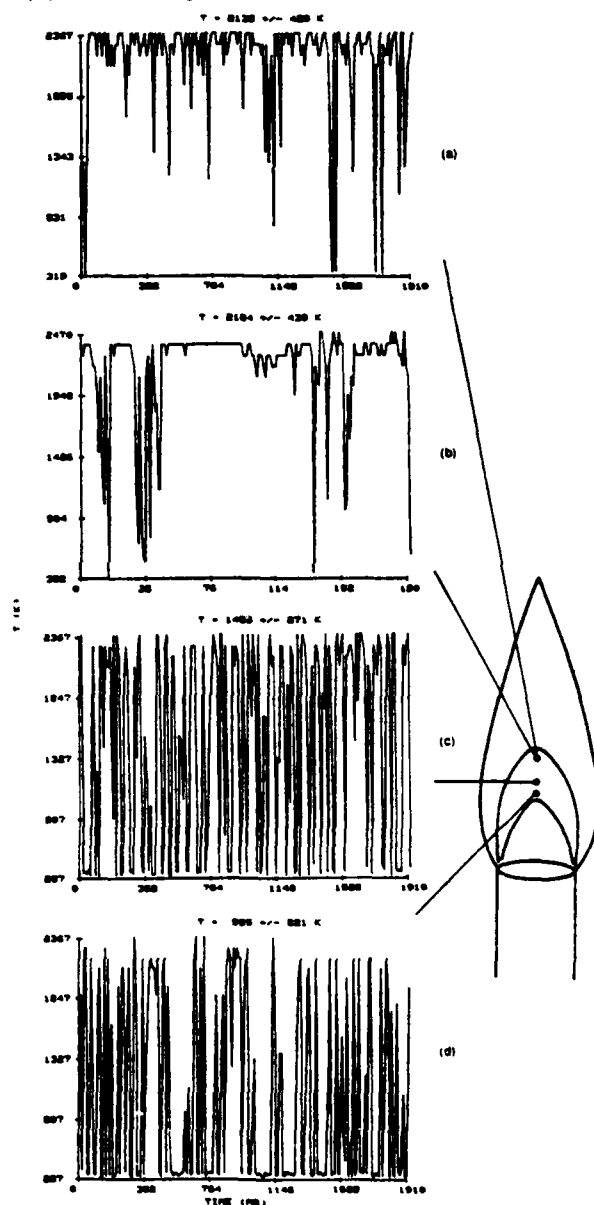


Figure 13. Temporal-Spatial Profile of Bunsen-Burner-Type Flame at 100 Hz. (a) High in Reaction Zone, (b) Same Location as (a) but at 1000 Hz, (c) Middle of Reaction Zone, and (d) Low in Reaction Zone.

sufficiently fast rate for following the temperature fluctuations completely. To adequately follow the high-frequency temperature fluctuations that can exist in turbulent flames, a 5-kHz laser such as a Cu-vapor laser will be required.

Conclusions

In conclusion, the feasibility of using the OLD technique for high-frequency thermometric studies has been demonstrated in two premixed propane-air flames. The results indicate that the technique is capable of frequencies as high as those of the pulsed laser source. For known stoichiometry, the precision of the technique is comparable to that of CARS at high temperatures (± 75 K) but is superior to CARS at low temperatures (± 1 K). Measurements in the reaction zone of a Bunsen-burner-type flame displayed high-frequency components (> 1000 Hz). This technique promises to be a valuable tool for high-frequency thermometric studies of flames.

References

1. M. D. Drake, M. Lapp, C. M. Penney, S. Warshaw, and B. W. Gerhold, "Measurements of Temperature and Concentration Fluctuations in Turbulent Diffusion Flames Using Pulsed Raman Spectroscopy, Eighteenth Symposium (International) on Combustion (Combustion Institute, Pittsburgh, PA, 1981), p. 1521.
2. A. C. Eckbreth and R. J. Hall, *Combust. Sci. Technol.* **25**, 175 (1981).
3. J. W. Daily, *Appl. Opt.* **16**, 568 (1977).
4. R. P. Lucht, D. W. Sweeney, and N. M. Laurendeau, "Saturated Fluorescence Measurements of the Hydroxyl Radical," in *Laser Laser Probes for Combustion Chemistry*, D. R. Crosley, Ed. (American Chemical Society, Washington, D. C., 1980), Vol. 134, p. 145.
5. D. R. Crosley, *Opt. Eng.* **20**, 511 (1981).
6. W. Zapka, P. Pokrowsky, and A. C. Tam, *Opt. Lett.* **7**, 477 (1982).
7. S. W. Kizirnis, R. J. Brecha, B. N. Ganguly, L. P. Goss, and R. Gupta, *Appl. Opt.* **23**, 3873 (1984).
8. A. C. Tam, "Photoacoustics: Spectroscopy and Other Applications," Chapter 1 in *Ultrasensitive Laser Spectroscopy*, D. S. Klinger, Ed. (Academic Press, NY, 1983).
9. F. V. Bunkin and V. M. Komissarov, *Sov. Phys. (Acoustics)* **19**, 203 (1973).
10. L. M. Lyamshev and K. A. Naugol'nykh, *Sov. Phys. (Acoustics)* **22**, 354 (1976).
11. K. A. Naugol'nykh, *Sov. Phys. (Acoustics)* **23**, 98 (1977).
12. L. D. Landau and E. M. Lifshitz, *Fluid Mechanics* (Translated from Russian by J. B. Sykes and W. H. Reed) (Addison-Wesley, Reading MA, 1959).
13. W. B. Jackson, N. M. Amer, A. C. Boccara, and D. Fournier, *Appl. Opt.* **20**, 1333 (1981).
14. L. W. Casperson, *Appl. Opt.* **12**, 2434 (1973).
15. W. L. Wolfe and G. J. Zissis, *Infrared Handbook* (Department of the Navy, Washington, D. C., 1978).
16. D. F. Grosjean, "Electric Discharge Excitation and Energy Source Integration," AFMAL-TR-84-2074 (Air Force Wright Aeronautical Laboratories, Wright-Patterson Air Force Base, OH, January 1985).
17. C. K. N. Patel and A. C. Tam, *Rev. Mod. Phys.* **53**, 517 (1981).
18. S. Gordon and B. J. McBride, "Computer Program for Calculation of Complex Equilibrium Composition Rocket Performances, Incident and Reflected Shocks, and Chapman-Jouguet Detonations," NASA SP273, May 1971; see also NTIS N78-17724, March 1976.
19. R. K. Hanson, B. Hiller, E. C. Rea, J. Seitzman, G. Kychakoff, and R. D. Howe, "Laser-Based Diagnostics for Flowfield Measurements," Presented at the Winter Annual Meeting of ASME, New Orleans, LA, December 9-14, 1984.

2.10 COMBINED CARS-LDA INSTRUMENT

A combined CARS-LDA instrument capable of simultaneous thermometry and velocity measurements has been constructed and tested on a laboratory-scale propane-air Bunsen burner. The design, construction, and testing of this instrument are discussed in the three following papers entitled, "Simultaneous CARS and LDA Measurements in a Turbulent Flame," "An Investigation of Temperature and Velocity Correlations in Turbulent Flames," and "Combined CARS/LDA Instrument for Simultaneous Temperature and Velocity Measurements."

AIAA'84

AIAA-84-1458

**Simultaneous CARS and LDA Measurements
in a Turbulent Flame**

L. P. Goss and D. D. Trump, Systems Research
Labs., Inc., Dayton, OH; W. M. Roquemore,
Aero Propulsion Laboratory (AFWAL/POSF),
Wright-Patterson AFB, OH 45433

AIAA/SAE/ASME
20th Joint Propulsion Conference
June 11-13, 1984/Cincinnati, Ohio

For permission to copy or republish, contact the American Institute of Aeronautics and Astronautics
1633 Broadway, New York, NY 10019

SIMULTANEOUS CARS AND LDA MEASUREMENTS IN A TURBULENT FLAME*

L. P. Goss and D. D. Trump
Systems Research Laboratories, Inc.
Dayton, Ohio 45440-3696

W. M. Roquemore
Aero Propulsion Laboratory (AFWL/POSF)
Wright-Patterson Air Force Base, Ohio 45433

Abstract

A combined CARS-LDA instrument capable of making simultaneous thermometry and velocity measurements has been constructed and tested on a laboratory propane-air burner. Three different approaches on interfacing the instruments are discussed; two of these actually were implemented and tested. The coincidence time between measurements was determined to be 250 μ s with Method II and 4 μ s with Method III. The difference between these methods is primarily in the firing sequence of the Nd:YAG (CARS system) and the LDA acceptance window. Simultaneous thermometry and velocity measurements have been made at three locations in a turbulent propane diffusion flame for both methods, and the results are discussed. The results of this study indicate that the coincidence time of the two measurements can be as close as ~ 4 μ s--but only at the cost of reducing the data-acquisition rates.

Introduction

The transport rates of heat, mass, and momentum associated with the turbulent motion of fluids are several orders of magnitude greater than the molecular rates occurring in nonturbulent flows. These high rates of transport are a consequence of the correlation between the fluctuating components of velocity and state scalar variables. Models for predicting these correlations in turbulent flow are essential ingredients for the prediction of turbulent-flow behavior--presently an area of high interest in turbulence research.

For testing these models, an expanded and improved experimental data base--in particular, data on velocity and scalar correlations--is badly needed. Measurement of velocity and scalar correlations requires simultaneous measurement of the velocity and another state variable such as temperature or species concentration. Since measurement of any state variable can be difficult at best, it is not surprising that relatively few joint measurements have been made. Laser Doppler velocimetry (LDV) has been combined with thermocouple,¹⁻³ pulsed Raman,⁴⁻⁶ cw Rayleigh,⁷ Mie scattering,⁸ and fluorescence⁹ techniques in attempts to determine the various correlations between velocity and temperature or species concentration.

This paper describes the first attempt to make simultaneous velocity and temperature measurements by means of a combined LDA-CARS instrument. Another group has reported making CARS and LDA measurements; however, no attempt has been made to make the simultaneous, coincident measurements of the instantaneous velocity and temperature which are needed for evaluating the correlations between the scalars.¹⁰

*Work supported in part by USAF Contract F33615-80-C-2054.

This paper is declared a work of the U.S. Government and therefore is in the public domain.

Experimental

CARS Instrument

The design of the CARS instrument was discussed in detail previously and will be mentioned here only briefly. The CARS system shown in Fig. 1 was built by SRL under Contract F33615-80-C-2054 and is essentially the same as that reported in Ref. 11, except for the replacement of the TN1223-2GI with a new TN6132 diode-array detector. Because the new detector--when directly compared with the old--displayed less cross-talk, a larger dynamic range, and little (if any) memory retention, the splitter arrangement as well as the data-acquisition software of the previous CARS system was modified.¹² The dynamic range of the new detector was measured to be greater than 100 to 1 and was independent of the focusing characteristics of the beam.¹³ The number of splits necessary to cover the 1000-to-1 range needed to follow the CARS signal variation in a turbulent flame was thus reduced from 4 to 2. A 33-to-1 splitter arrangement was implemented to replace the previous 10-to-1 splits. Also, because the new detector did not display the memory retention of the TN1223, the cleansing scans employed to reduce the memory retention were eliminated from the data-acquisition cycle.

To ensure that the splitter arrangement and data-acquisition software of the new detector would measure the temperature accurately, a furnace study was conducted using a platinum coil furnace capable of reaching temperatures as high as 1700 K. A chromel-alumel thermocouple was used to measure the temperature of the furnace to ensure the stability of the temperature during the CARS measurement and to record the temperature for comparison purposes. Figure 2 displays the CARS-vs-thermocouple temperature data obtained in this study. The error bars indicate the spread of the data observed for 1500 CARS samples. Notice that the average temperatures (represented by the dots) are in good agreement with the thermocouple temperatures. The spread in the data is indicative of the shot-to-shot uncertainty caused by fluctuations in the dye laser. No gaps are evident in the temperature data, indicating good overlap with the 33-to-1 split. The overlap of the peaks occurs at ~ 800 K. These data indicate that the split is more than adequate to cover the 300-2300 K temperature range encountered in turbulent combustion flows.

Since only temperature data were used for this study, no power reference was employed. The data-reduction software is the same as reported in Ref. 11.

LDA Instrument

The LDA system shown in Fig. 1 was built by LORI under Air Force Contract F33615-78-C-2005¹⁴ and is a two-velocity-component, real-fringe system

based on polarization separation of the velocity components. The 488-nm line from a Spectra-Physics argon-ion laser was used as the light source, with TiO_2 particles of nominal 1- μ size being used as the scattering particles. The scattered light was collected in the forward direction slightly off-axis (12 deg.) by a parabolic mirror which collimated and reflected the light to the collection optics. The collection optics consisted of a focusing lens, a Glan Thompson polarization beam-splitter to separate the various polarization components, and two optical fibers. The fiber optics allowed the processing electronics to be remotely located from the flame environment. The processor electronics consisted of two 1990 TSI burst-counter processors modified to permit coincident velocity as well as CARS data to be obtained. A computer interface allowed data rates in excess of 30,000 velocities/sec. to be transferred and stored on a ModComp computer. A 40-MHz Bragg shifter was used to shift the Doppler signal to remove direction ambiguities.

The two velocity components to be measured by the LDA system were oriented orthogonal to each other and set at a 45-deg. angle to the laboratory frame of reference. This was done to ensure high data rates in both velocity components. The velocities in the laboratory frame of reference were determined by mathematical rotation of the frame of reference during data analysis. The data-analysis routines are discussed in detail in Ref. 14.

Burner System

The laboratory burner system used in these studies was the same as that reported in Ref. 15, with the exception that it was modified to permit seeding with TiO_2 particles. Both the inner and outer tube flows were seeded to minimize biasing problems with the LDA measurements. In the single-component studies conducted with Method III, the burner was rotated 45 deg. in order that the measured velocity component would correspond to the axial-flow component of the flame.

Interfacing Instruments

Several problems arose while interfacing the LDA and CARS instruments. The main problem involved designing the appropriate interface to ensure that both types of measurements would be made simultaneously (or as nearly as possible). The actual time coincidence required to ensure that no change in the flame sample position will take place between the two measurements is dictated by the fluid dynamics of the flame system under study. With relatively low velocity flows such as those encountered in the laboratory flame (0 - 3 m/s), the time difference of the measurements must be on the order of hundreds of microseconds to ensure that the sample area of the flame does not move significantly. At higher flow rates, such as those encountered in gas-turbine systems, the coincidence time must be on the order of tens of microseconds.

The requirements for a coincidence on the order of a few hundred microseconds can be readily met with the Nd:YAG laser system being employed for the present experiments. However, time requirements at higher flow rates are more difficult to obtain and result in a significant drop in data-acquisition rates, as will be discussed in the following paragraphs.

The Nd:YAG laser (Quanta-Ray) used in the CARS experiment was designed to operate at a 10-Hz rate, while the LDA instrument processes velocities at a rate which is related to the passage of the TiO_2 seed particles through the fringe pattern. Since particle arrival is random in nature, the coupling of the two instruments requires that a random event be coupled to a 10-Hz repetitive event.

Three separate approaches were considered for interfacing the two instruments; only two were actually implemented and tested. In Method I the two instruments are allowed to free run, with a common high-resolution clock being used to tag the individual CARS and LDA events. The major drawback of such an approach is the massive amount of non-coincident data which must be taken and stored to ensure that the amount of coincident data acquired is adequate. Since at high velocities, less than one shot in 50 would be coincident data, it was decided to examine approaches that would permit collection of coincident data only.

The second approach (Method II) was to create a 10-ms window during every 100-ms interval (time corresponding to the 10-Hz Nd:YAG firing); if an LDA velocity realization occurred during this window, then the CARS laser system would be fired. The function of this window was to limit the amount of LDA data obtained to that necessary to ensure adequate sampling. If no velocity realization occurred during the window, the Nd:YAG laser flashlamps would be discharged to ensure a constant thermal loading. The laser firing for the Nd:YAG consisted of first discharging the flashlamps to obtain a population inversion and then pulsing the Q-switch to depopulate the upper laser levels and thereby obtain a giant laser pulse. The time separation between the flashlamp discharge and the Q-switch pulsing is ~ 250 μ s. This was a fixed time separation and, thus, represented the nearest coincidence between the velocity and CARS events in this scheme. Thus, Method II is only adequate for low-velocity flows. The laboratory burner employed for testing of the instruments in this method displayed a maximum flow rate of ~ 3 m/s. At this velocity the 250- μ s delay between events allows the flame sample volume being measured to move only 750 μ m. At the high-velocity flow normally encountered in practical systems, this delay is inadequate, allowing the sampled volume to move ~ 1.25 cm with a fluid flow of 50 m/s.

The third approach (Method III) involved windowing the LDA events as in Method II, except that instead of the flashlamp of the Nd:YAG laser being fired after the LDA velocity occurrence, it would be fired at a 10-Hz rate, regardless of the LDA event. A second window centered about the optimum time delay for the Q-switch was employed; and if an LDA event occurred in this 100- μ s window, the Q-switch was allowed to fire, resulting in a CARS event. The 100- μ s window was determined experimentally by varying the time delay between the lamp firing and the Q-switching. When the window is centered on the optimum delay (250 μ s), firing the Nd:YAG laser 50 μ s on either side of center corresponded to a $\sim 25\%$ drop in laser power. The net result of such an approach is that the coincidence time is determined by the time required by the burst-counter processor to determine the velocity from a Doppler burst (4 μ s) and the time required by the laser to lase after the Q-switch

pulse has occurred (50 ns). With this method a 50-m/s gas pocket would move only 200- μ m in the 4 μ s between velocity and temperature measurements.

The drawback of such an approach is the narrow window over which the LDA event is accepted, resulting in a substantially reduced data-acquisition rate. With the LDA in the free-run mode, ~ 200 velocity realizations/s are observed in the flame. With Method I all of the data would be taken with only a few coincidences occurring (one every 50 shots at 50 m/s). With Method II the total time per second during which the LDA processors are allowed to search for an event is 100 ms (10 ms/shot \times 10 shots). Thus, on the average, 20 velocities could be recorded by the LDA system during this time period, allowing for a nominal 10-Hz data rate in combination with the CARS instrument. With Method III the window is 100 μ s instead of 10 ms, allowing for a total sampling time per second of 1 ms (100 μ s/shot \times 10 shots). This allows, on the average, ~ 2 velocities per 10-s interval to be obtained. Thus, the more stringent the time coincidence imposed by the experimental conditions, the lower the overall data rates.

The experimental arrangement of the combined instruments is displayed in Fig. 1. For minimizing the optical rearrangement of both systems, a counter-propagating arrangement was used in which the CARS and LDA instruments were on separate optical tables. The collimating lens and turning mirrors of the CARS system were rearranged on the LDA optics table, while the parabolic forward-scattering collection mirror of the LDA system was placed on the CARS table. This caused no major problems for either system and also minimized the number of optical changes necessary. To ensure that both measurement sample volumes overlapped, a 100- μ m circular aperture was used to locate and align both foci at a common point.

One problem encountered during the experiments was optical breakdown caused by the seed particles under heavy seeding conditions at room temperature. To minimize this effect, the foci of the CARS pump and probe beams were reduced by changing from a 50- to an 80-cm-focal-length lens. This lowered the spatial resolution to ~ 1.5 mm in the longest dimension but substantially reduced the occurrence of optical breakdown. No such problem was encountered in the flame due to the reduced seed densities associated with the elevated temperatures.

The timing sequence for both Methods II and III is shown in Fig. 3. The CARS shot gate is issued by a machine-code software program from the TN1710 controller (LSI 11/03 microprocessor). If a velocity realization occurs during the gate, the velocity data are transferred under direct-memory-access (DMA) control to the 7840 ModComp computer for storage on a 20-Mbyte disc system. The data-ready signal from the TSI 1990 Burst-Counter Processor is sent to the TN1710 unit which, upon receipt, sends the fire Q-switch command signal to the Nd:YAG laser. The TN6132 multichannel detector transfers the CARS data to the spectral-data memory (SDM) of the TN1710 from which the data are transferred under DMA control to the 7840 computer. Before the transfer takes place, the last ten channels of the 1024 channel CARS data are overwritten with the shot count for that particular laser firing. This shot count corresponds to the number of laser pulses which have occurred since

the program start and is equal to the number of gate pulses sent to the TSI 1990 Burst-Counter Interface. The shot count is used for bookkeeping by analysis programs which convert the raw LDA periods to velocities.

Results and Discussion

Experimentally Methods II and III were tested on the laboratory propane burner.¹⁵ Method II was employed first because it allowed high data rates (10 Hz) and both velocity components to be obtained. Figure 4 displays the velocity-temperature correlation plots obtained at three centerline locations. The three locations correspond to 6, 8, and 10 cm above the burner surface. The average temperature, rms temperature, average velocity, rms velocity, and cross-correlation coefficients are listed in Table 1 for all three positions. The temperature pdf's obtained at these locations are very similar to results obtained earlier on this burner which displayed a distinct single peak at 6 cm but bimodal peaks at locations 8 and 10 cm¹⁵ above the burner. The burner was operated as a turbulent diffusion flame, with a central fuel jet surrounded by annular air flow.¹⁵ The U velocity corresponds to the axial flame velocity, while the V corresponds to the radial. The major velocity component, as expected, was the axial component and slowly decreases with downstream axial location. The radial-velocity components are small on the average but display variations as large as the axial, which indicates a large degree of turbulence. The correlation plots U vs. T and V vs. T (Fig. 4) indicate that very little correlation was observed between velocity and temperature. The cross-correlation coefficients are listed in Table 1 and defined as

$$R_{u-t} = u\bar{u}/u'\bar{u}', \quad R_{v-t} = v\bar{v}/v'\bar{v}'$$

where $u = U - \bar{U}$, $v = V - \bar{V}$, $\bar{u} = T - \bar{T}$, u' is the rms of u , and v' is the rms of v . The cross-correlation coefficients indicate--as does the correlation plots--that the correlation between velocity and temperature was small at the locations probed.

Table 1 Comparison of Methods II and III. Correlation coefficients are small in both cases, indicating little correlation between velocity and temperature at these locations.

Method II

X (cm)	T (K)	U (m/s)	V (m/s)	R_{u-t}	R_{v-t}
6	1516 \pm 432	-2.85 \pm 3.18	-0.45 \pm 3.13	-0.037	0.037
8	1322 \pm 499	-2.63 \pm 3.23	-0.28 \pm 3.19	0.080	0.028
10	1026 \pm 529	-2.39 \pm 3.42	-0.38 \pm 3.39	0.037	-0.021

Method III

X (cm)	T (K)	U (m/s)	R_{u-t}
6	1530 \pm 440	-2.91 \pm 3.20	-0.04
8	1327 \pm 505	-2.65 \pm 3.30	-0.02
10	1047 \pm 525	-2.42 \pm 3.08	-0.05

Initially it was not known whether the lack of correlation was due to the low time coincidence of Method II or was simply a characteristic of the unconfined turbulent flame. Method III was thus employed to reduce the time delay between the CARS and LDA measurements. It was discovered during studies with Method III that one of the burst-counter processors exhibited a significantly lower data-throughput rate (approximately a factor of 3). Because of the already low data rates associated with this method, the decision was made to switch to a single-component velocity measurement and use the faster processor. Because the velocity component measured by the LDA system is oriented 45 deg. with respect to the laboratory frame of reference, the decision was made to rotate the burner 45 deg. in order that the LDA and laboratory frames of reference would be identical; thus, the axial component of velocity was measured directly. It was decided to use this approach rather than change the LDA optical train which would have required a massive rearrangement. Converting to a single-velocity-component system improved the data rates to ~ 0.3 Hz. Table 1 shows a comparison of the two methods tested. The correlation plots at the three different locations are displayed in Fig. 5. The cross-correlation coefficients are confirmed to be quite small in the flame at the indicated centerline positions. Because of the low data rates with Method II, only 200 coincident measurements were obtained at each location, as compared to 1500 with Method III. The 200 samples required ~ 12 min. per measurement point.

The potential for biasing was clearly demonstrated with Method III. Because of the temperature effect on seed densities, the higher temperatures are expected to have lower seed densities. This can result in a situation where biasing toward lower temperatures occurs. Since the CARS laser firing depends on the presence of a seed particle during a 100- μ s window every 100 ms and since the probability of the seed being present is greater at low temperatures than a preferential sampling of low temperatures is likely to occur. This effect is actually enhanced by Method III because of the small sampling window employed for coincidence. This is demonstrated in Fig. 6. Figure 6(a) displays a 1500-shot temperature pdf obtained at a 10-Hz rate independent of the LDA measurements. Figure 6(b) displays a 200-shot pdf obtained by Method III coincidentally with the LDA measurements. Clearly the average temperature in the coincident case is lower than that for the non-coincident 1500-sample pdf. This biasing can be reduced by increasing the seed levels of the fuel tube. However, it is clear that the average temperature, rms of temperature, and pdf's should be measured independently of the LDA to minimize particle-biasing effects.

Future plans with this system include examining various burner configurations from which temperature-velocity correlations have been reported. Attempts will be made to increase the data rates of Method III in order that two-component velocity measurements can be made. This will include examining closely the burst-counter processor performance and methods of increasing the seed densities.

References

1. I. G. Shepherd and J. B. Moss, "Characteristic Scales for Density Fluctuations in a Turbulent Premixed Flame," *Comb. Sci. Tech.* **25**, 127 (1981).
2. I. G. Shepherd, J. B. Moss, and K. N. C. Bray, "Turbulent Transport in a Confined Premixed Flame," in *19th Symposium (International) on Combustion* (The Combustion Institute, Pittsburgh, PA, 1982), p. 423.
3. H. Tanaka and T. Yanagi, "Cross-Correlation of Velocity and Temperature in a Premixed Turbulent Flame," *Combust. Flame* **51**, 183 (1983).
4. S. Warshaw, M. Lapp, C. M. Penny, and M. C. Drake, "Temperature-Velocity Correlation Measurements for Turbulent Diffusion Flames from Vibrations Raman-Scattering Data," in *Laser Probes for Combustion Chemistry*, D. R. Crosely, Ed. (American Chemical Society, Washington, D.C., 1981).
5. S. Lederman and C. Posillico, "Unified Spontaneous Raman and CARS System," *AIAA J.* **19**(6), 824 (1981).
6. R. M. Dibble, W. Kollmann, and R. W. Schefer, "Conserved Scalar Fluxes Measured in a Turbulent Nonpremixed Flame by Combined Laser Doppler Velocimetry and Laser Raman Scattering," *Combust. Flame* **55**, 307 (1984).
7. R. W. Dibble, G. D. Rambach, R. E. Hollenbach, and J. T. Ringland, "Simultaneous Measurements of Velocity and Temperature in Flames Using LDV and CW Laser Rayleigh Thermometry," Paper No. WSS/CI 81-84, Presented at 1981 Fall Meeting of the Western States Section of the Combustion Institute, Tempe, AZ, October 1981.
8. S. H. Starnner and R. W. Bilger, "Measurements of Scalar-Velocity Correlations in a Turbulent Diffusion Flame," Paper No. 89 in *Eighteenth Symposium (International) on Combustion* (The Combustion Institute, Pittsburgh, PA, 1980).
9. F. K. Owen, "Simultaneous Laser Velocimetry and Laser Induced Photoluminescence Measurements of Instantaneous Velocity and Concentration in Complex Mixing Flows," *AIAA Paper No. 76-35*, 1976.
10. S. Fujii, M. Gomi, and K. Eguchi, "A Remote Laser-Probe System for Velocity and Temperature Measurements," *J. Fluids Engin.* **105**, 129 (1983).
11. L. P. Goss, D. D. Trump, B. G. MacDonald, and G. L. Switzer, "10-Hz Coherent Anti-Stokes Raman Spectroscopy Apparatus for Turbulent Combustion Studies," *Rev. Sci. Instrum.* **54**, 563 (1983).
12. L. P. Goss, D. D. Trump, and G. L. Switzer, "Laser Optics/Combustion Diagnostics," Quarterly Status Report 6603-13 under Contract F33615-80-C-2054, Covering the period 3 September - 2 December 1983 (Systems Research Laboratories, Inc., Dayton, OH, 16 March 1984).

13. R. R. Antcliff, M. E. Hillard, and O. Jarrett, Jr., "Intensified Silicon Photodiode Array Detector Linearity Application to Coherent Anti-Stokes Raman Spectroscopy," Submitted to Appl. Opt.
14. A. Lightman, R. D. Magill, and R. J. Andrews, "Laser Diagnostic Development and Measurement and Modeling of Turbulent Flowfields of Jets and Wakes - Part I," AFWAL-TR-83-2044 (University of Dayton Research Institute, Dayton, OH, June 1983).
15. L. P. Goss, B. G. MacDonald, D. D. Trump, and G. L. Switzer, "CARS Thermometry and N_2 Number Density Measurements in a Turbulent Diffusion Flame," AIAA Paper No. 83-1480, 1983.

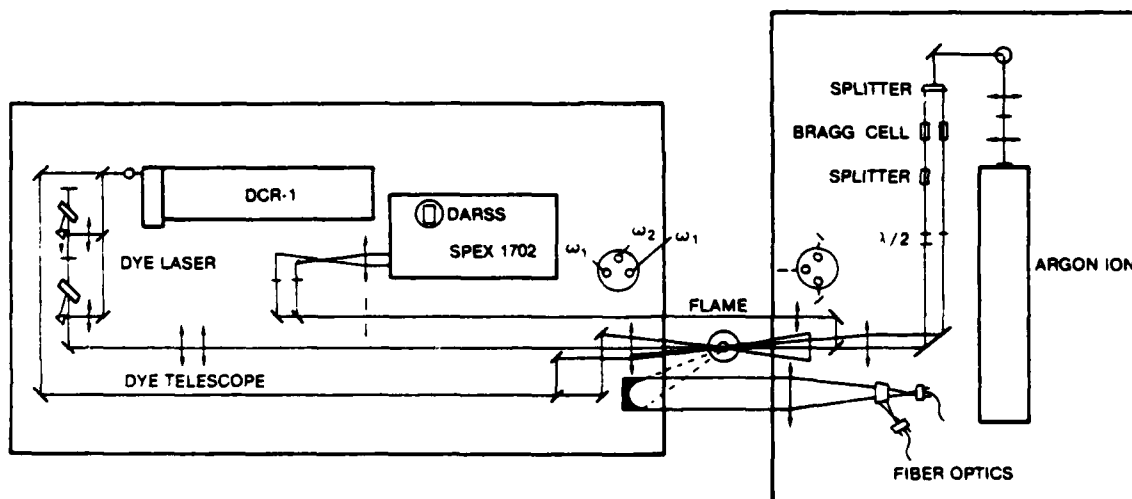


Figure 1. Optical Layout of Combined CARS-LDA Instrument.

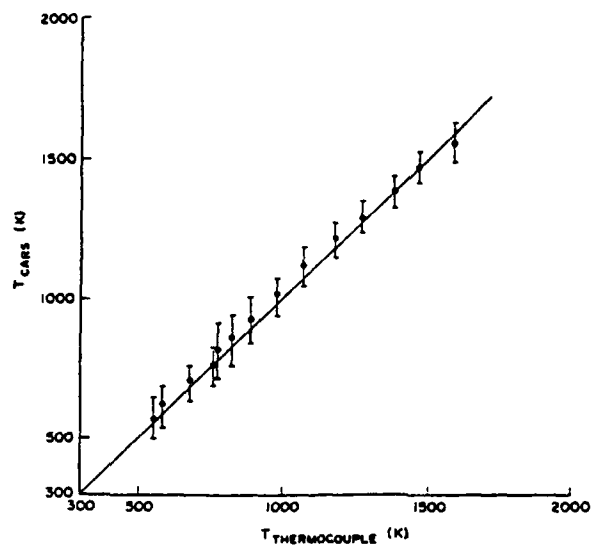
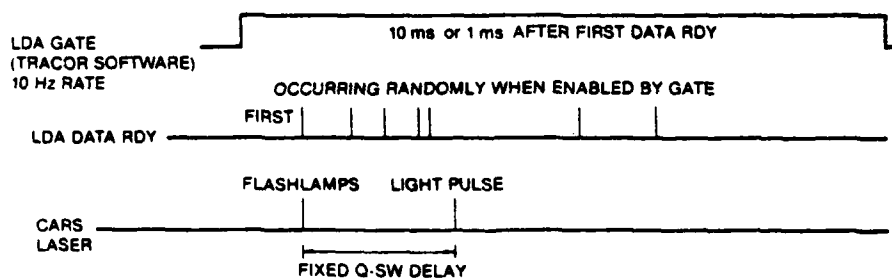


Figure 2. Calibration of Two-Split CARS System with Electric Furnace.

METHOD II



METHOD III

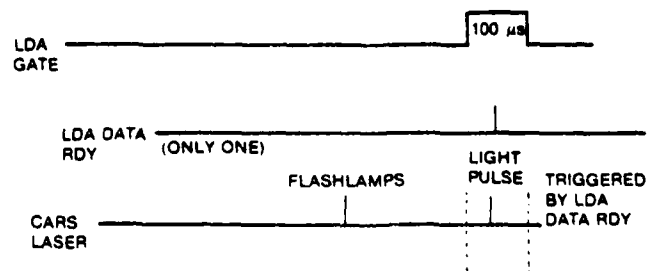
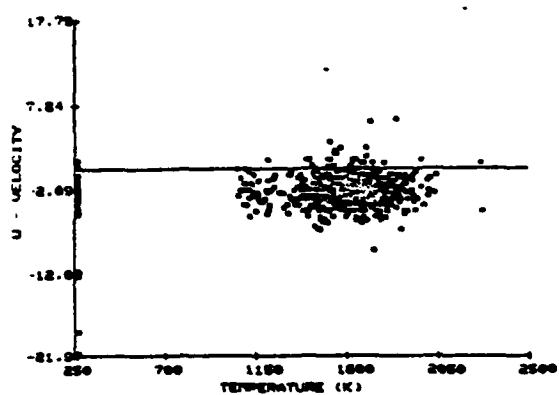
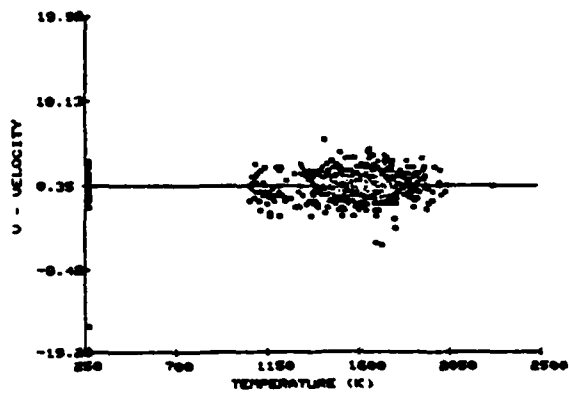


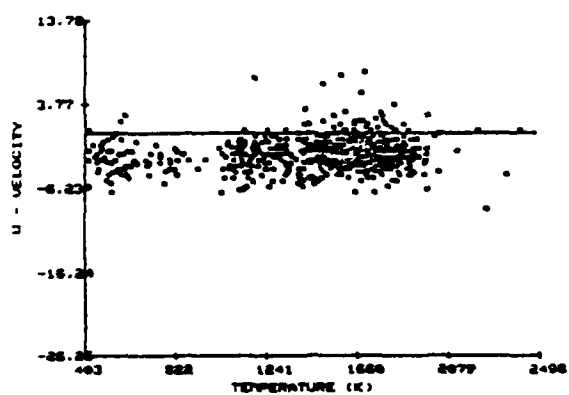
Figure 3. Critical Timing Schemes for Methods II and III.



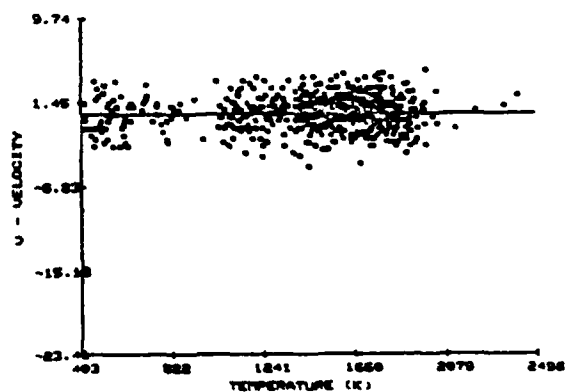
(a)



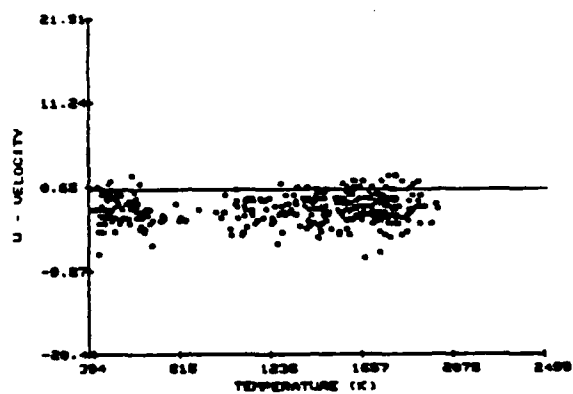
(b)



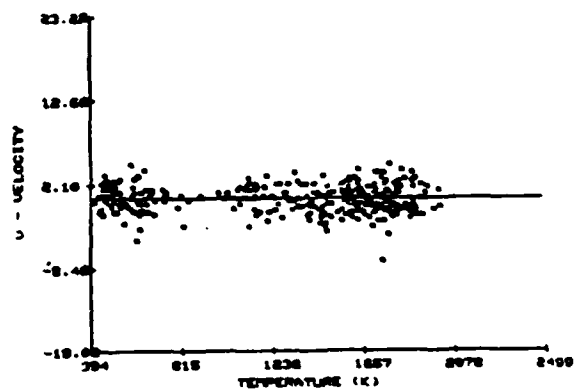
(c)



(d)

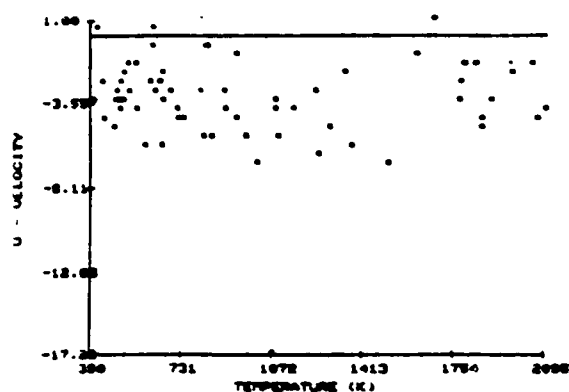


(e)

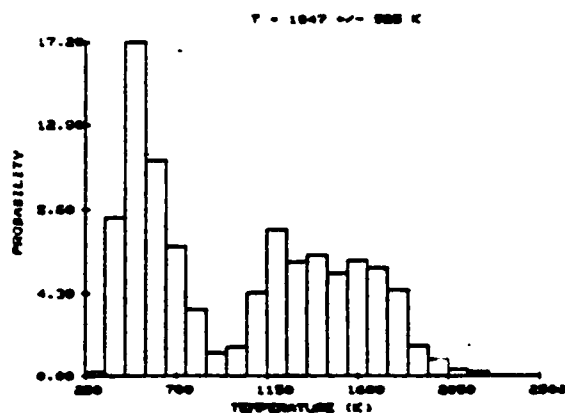


(f)

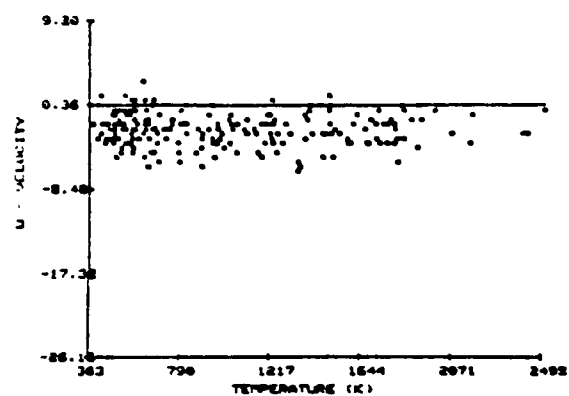
Figure 4. Correlation Plots of U-T and V-T Obtained with Method II at Positions a,b) 6 cm, c,d) 8 cm, and e,f) 10 cm above Burner Surface.



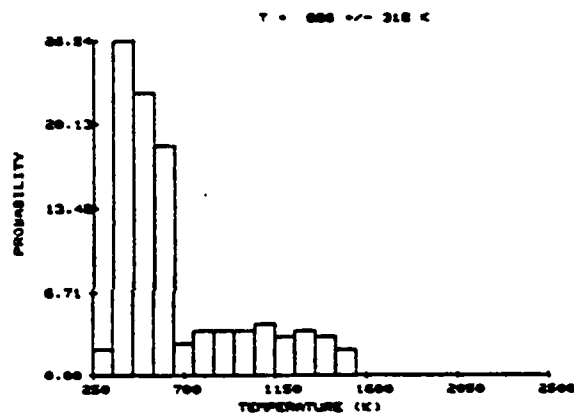
(a)



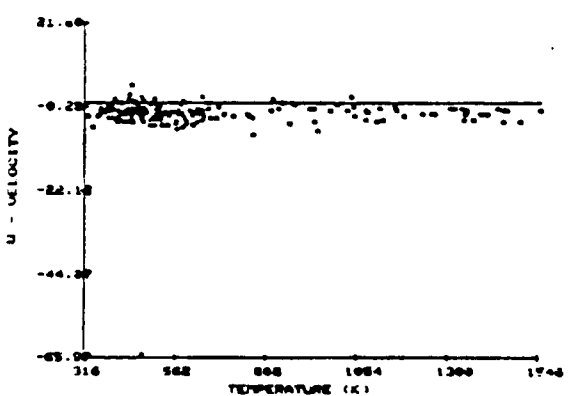
(a)



(b)



(b)



(c)

Figure 6. PDF's Depicting the Biasing Effects of the Narrow Window of Method III
a) 1500-Shot pdf, b) Biased pdf Obtained

Figure 5. Correlation Plots of U-T Obtained with Method III at Positions a) 6 cm, b) 8 cm, and c) 10 cm above Burner Surface.

Published in Experimental Measurements and Techniques in Turbulent Reactive and Non-Reactive Flows (Selected Papers from Winter Annual Meeting of ASME, New Orleans, LA, Dec. 9-14, 1984), AMD-Vol. 66, R. M. C. So, J. H. Whitelaw, and M. Lapp, eds. (American Society of Mechanical Engineers, New York, 1984), pp. 215-221.

AN INVESTIGATION OF TEMPERATURE AND VELOCITY CORRELATIONS IN TURBULENT FLAMES

L. P. Goss and D. D. Trump
Systems Research Laboratories Inc.
Dayton, Ohio

W. M. Roquemore
Aero Propulsion Laboratory (AFWAL/POSF)
Wright-Patterson Air Force Base, Ohio

ABSTRACT

A combined CARS-LDA instrument capable of making simultaneous temperature and velocity measurements has been constructed and tested on a laboratory propane-air burner. The coincidence time between velocity and temperature measurements was determined to be 4 μ s with this instrument. Simultaneous thermometry and velocity measurements have been made in a turbulent propane diffusion flame and a premixed propane-air flame. No significant correlations were obtained in the diffusion flame; however, the premixed flame displayed distinctive correlations near the reaction zone.

INTRODUCTION

The transport rates of heat, mass, and momentum associated with the turbulent motion of fluids are several orders of magnitude greater than the molecular rates occurring in nonturbulent flows. These high rates of transport are a consequence of the correlation between the fluctuating components of velocity and state scalar variables. Models for predicting these correlations in turbulent flow are essential ingredients for the prediction of turbulent-flow behavior--presently an area of high interest in turbulence research.

For testing these models, an expanded and improved experimental data base--in particular, data on velocity and scalar correlations--is badly needed. Measurement of velocity and scalar correlations requires simultaneous measurement of the velocity and another state variable such as temperature or species concentration. Since measurement of any state variable can be difficult at best, it is not surprising that relatively few joint measurements have been made. Laser Doppler Velocimetry (LDV) has been combined with thermocouple,¹⁻⁴ pulsed Raman,⁵⁻⁷ cw Rayleigh,⁸ Mie scattering,⁹ fluorescence,¹⁰ and CARS^{11,12} techniques in attempts to determine the various correlations between velocity and temperature or species concentration.

This paper describes studies of simultaneous velocity and temperature measurements which were made using a combined LDA-CARS instrument on two propane-air flames.

*Work supported in part by USAF Contract F33615-80-C-2054.

INSTRUMENTATION

Combined CARS-LDA Instrument

The individual CARS and LDA instruments have been described in Refs. 13 and 14, respectively, and only details concerning the combination of the two instruments will be discussed here. The different approaches to interfacing the two instruments were discussed in Ref. 10. The method which yielded the highest temporal coincidence was adopted for this work. This method involved firing the CARS laser flashlamps at a 10-Hz rate and windowing the CARS Q-switch firing (100- μ s window centered at a 250- μ s delay from the flashlamp firing). If a velocity realization from the two velocity processors occurs during this window, the Q-switch is allowed to fire and the laser pulse occurs within several hundred nanoseconds. The coincidence time between the temperature and velocity measurements is determined by the amount of time required by the burst-counter processors to determine the velocity from a Doppler burst of ~ 4 μ s.

The drawback of such an approach is the narrow window over which the LDA event is accepted, resulting in a substantially reduced data-acquisition rate. With the LDA in the free-run mode, ~ 400 velocity realizations per second are observed in the flame. With this method the window is 100 μ s allowing for a total sampling time per second of 1 ms (100 μ s/shot \times 10 shots). This allows, on the average, ~ 4 velocities per 10-s interval to be obtained. Thus, the stringent time coincidence imposed by the experimental conditions lowers the overall data rates substantially.

The experimental arrangement of the combined instruments is displayed in Fig. 1. For minimizing the optical rearrangement of both systems, a counter-propagating arrangement was used in which the CARS and LDA instruments were on separate optical tables. The collimating lens and turning mirrors of the CARS system were rearranged on the LDA optics table, while the parabolic forward-scattering collection mirror of the LDA system was placed on the CARS table. This caused no major problems for either system and also minimized the number of optical changes necessary. To ensure that both measurement sample volumes overlapped, a 100- μ m circular aperture was used to locate and align both foci at a common point.

One problem encountered during the experiments was optical breakdown caused by the seed particles under heavy seeding conditions at room temperature. To minimize this effect, the foci of the CARS pump and probe beams were reduced by changing from a 50- to an 80-cm-focal-length lens. This lowered the spatial resolution to ~ 1.5 mm in the longest dimension but substantially reduced the occurrence of optical breakdown. No such problem was encountered in the flame due to the reduced seed densities associated with the elevated temperatures.

The timing sequence for the combined instrument is shown in Fig. 2. The CARS shot gate is issued by a machine-code software program from the TN1710 controller (LSI 11/03 microprocessor). If a velocity realization occurs during the gate, the velocity data are transferred under direct-memory-access (DMA) control to the 7840 ModComp computer for storage on a 20-Mbyte disc system. The data-ready signal from the TSI 1990 Burst-Counter Processor is sent to the TN1710 unit which, upon receipt, sends the fire Q-switch command signal to the Nd:YAG laser. The TN6132 multichannel detector transfers the CARS data to the spectral-data memory (SDM) of the TN1710 from which the data are transferred under DMA control to the 7840 computer. Before the transfer takes place, the last ten channels of the 1024 channel CARS data are overwritten with the shot count for that particular laser firing. This shot count corresponds to the number of laser pulses which has occurred since the program start and is equal to the number of gate pulses sent to the TSI 1990 Burst-Counter Interface. The shot count is used for bookkeeping by analysis programs which convert the raw LDA periods to velocities.

Burner System

The laboratory burner system used in these studies was the same as that reported in Ref. 15, with the exception that it was modified to permit seeding with TiO_2 particles. Both the inner and outer tube flows were seeded to minimize biasing problems with the LDA measurements.

RESULTS AND DISCUSSION

To evaluate whether the combined instrument could indeed measure correlations between the velocity and temperature of a flame, the following experiment was conducted. First, the burner was operated with a low air flow with no propane fuel. To produce a different temperature and velocity, a hand-held propane torch at a significantly higher temperature and velocity was inserted into the probe region of the CARS-LDA instrument. Measurements were then made while the torch was moved in and out of the probe region. The results of the study are shown in Fig. 3. The correlation plot shown in Fig. 3(a) indicates a very strong degree of correlation, as evidenced by the correlation coefficient of 0.86. Histogram plots of the velocity and temperature are shown in Figs. 3(b) and (c), respectively. In both cases notice the bimodal behavior. These results indicate that the combined instrument is capable of measuring correlations between velocity and temperature.

It was discovered during studies with the turbulent flame that one of the burst-counter processors exhibited a significantly lower data-throughput rate (approximately a factor of 3). Because of the already low data rates associated with this method, the decision was made to switch to a single-component velocity measurement and use the faster processor. Because the velocity component measured by the LDA system is oriented 45 deg. with respect to the laboratory frame of reference, the decision was made to rotate the burner 45 deg. in order that the LDA and laboratory frames of reference would be identical; thus, the axial component of velocity was measured directly. It was decided to use this approach rather than change the LDA optical train which would have required a massive rearrangement. Because of the low data rates, only 200 measurements were obtained at each location. The 200 samples required ~ 12 min. per measurement point. The velocity-temperature correlations were obtained at three different centerline locations in a turbulent diffusion flame (6, 8, and 10 cm above the burner surface). The average temperature, rms temperature, average velocity, rms velocity, and cross-correlation coefficients are listed in Table 1 for all three positions. The temperature pdf's obtained at these locations are very similar to results obtained earlier on this burner which displayed a distinct single peak at 6 cm but bimodal peaks at locations 8 and 10 cm above the burner. The burner was operated as a turbulent diffusion flame, with a central fuel jet surrounded by annular air flow.¹⁵ The U velocity corresponds to the axial flame velocity, which was observed to decrease slowly with downstream axial location. A correlation plot of U vs. T at 8 cm (Fig. 4) indicates that very little correlation was observed between velocity and temperature. The cross-correlation coefficients are listed in Table 1 and defined as

$$R_{u-t} = u\theta / u'\theta', \quad R_{v-t} = v\theta / v'\theta'$$

where $u = U - \bar{U}$, $v = V - \bar{V}$, $\theta = T - \bar{T}$, u' is the rms of u , and v' is the rms of v . The cross-correlation coefficients indicate--as do the correlation plots--that the correlation between velocity and temperature was small at the locations probed in the diffusion flame.

Table 1 Temperatures, Velocities, and Correlation Coefficients at Three Centerline Positions in the Turbulent Diffusion Flame.

X (cm)	T (K)	U (m/s)	R_{u-t}
6	1530 ± 440	2.91 ± 3.20	0.04
8	1327 ± 505	2.65 ± 3.30	0.02
10	1047 ± 525	2.42 ± 3.08	0.05

A premixed propane-air flame under high flow rates was examined next because of the reported velocity-temperature correlations in similar flames.^{3,4} A trend for the correlation coefficient to be negative inside the flame front and positive outside has been reported.^{3,4} A new burst-counter processor was installed prior to the premixed propane-air flame studies and, thus, two velocity components were measured in this flame. The results of this study are listed in Table 2 and depicted in Figs. 5(a) and (b). A noticeable negative correlation inside the flame front and positive correlation outside was observed, as indicated in Table 2. The values of the correlations are qualitatively in agreement with Ref. 12. The uncertainty of each correlation, however, is ~ 30% due to the small number of samples taken. Improved seeding techniques should allow a more accurate determination of correlation coefficients and a more extensive survey of the premixed flame.

Table 2 Temperatures, Velocities, and Correlation Coefficients at Three Radial Positions in the Premixed Flame (Axial Position 3.5 cm above Burner Surface).

<u>Y</u> (mm)	<u>T</u> (K)	<u>U</u> (m/s)	<u>V</u> (m/s)	<u>R_{u-t}</u>	<u>R_{v-t}</u>
0	650 ± 250	9.58 ± 2.4	0.19 ± 3.1	-0.10	-0.048
3.5	660 ± 190	9.46 ± 2.9	0.26 ± 3.6	-0.20	-0.095
4.5	1730 ± 100	9.52 ± 3.7	2.12 ± 3.7	0.28	0.028

REFERENCES

1. I. G. Shepherd and J. B. Moss, "Characteristic Scales for Density Fluctuations in a Turbulent Premixed Flame," *Comb. Sci. Tech.* **25**, 127 (1981).
2. I. G. Shepherd, J. B. Moss, and K. N. C. Bray, "Turbulent Transport in a Confined Premixed Flame," in *19th Symposium (International) on Combustion* (The Combustion Institute, Pittsburgh, PA, 1982), p. 423.
3. H. Tanaka and T. Yanagi, "Cross-Correlation of Velocity and Temperature in a Premixed Turbulent Flame," *Combust. Flame* **51**, 183 (1983).
4. T. Yanagi and Y. Mimura, "Velocity Temperature Correlation in Premixed Flame," in *18th Symposium (International) on Combustion* (The Combustion Institute, Pittsburgh, PA, 1981), p. 1031.
5. S. Warshaw, M. Lapp, C. M. Penny, and M. C. Drake, "Temperature-Velocity Correlation Measurements for Turbulent Diffusion Flames from Vibrational Raman Scattering Data," in *Laser Probes for Combustion Chemistry*, D. R. Crosely, Ed. (American Chemical Society, Washington, D.C., 1981), p. 239.
6. S. Lederman and C. Posillico, "Unified Spontaneous Raman and CARS System," *AIAA J.* **19**(6), 824 (1981).
7. R. M. Dibble, W. Kollmann, and R. W. Schefer, "Conserved Scalar Fluxes Measured in a Turbulent Nonpremixed Flame by Combined Laser Doppler Velocimetry and Laser Raman Scattering," *Combust. Flame* **55**, 307 (1984).
8. R. W. Dibble, G. D. Rambach, R. E. Hollenbach, and J. T. Ringland, "Simultaneous Measurements of Velocity and Temperature in Flames Using LDV and CW Laser Rayleigh Thermometry," Paper No. WSS/CI 81-84, Presented at 1981 Fall Meeting of the Western States Section of the Combustion Institute, Tempe, AZ, October 1981.
9. S. H. Starner and R. W. Bilger, "Measurements of Scalar-Velocity Correlations in a Turbulent Diffusion Flame," Paper No. 89 in *18th Symposium (International) on Combustion* (The Combustion Institute, Pittsburgh, PA, 1980), p. 921.

10. F. K. Owen, "Simultaneous Laser Velocimetry and Laser Induced Photoluminescence Measurements of Instantaneous Velocity and Concentration in Complex Mixing Flows," AIAA Paper No. 76-35, 1976.
11. L. P. Goss, D. D. Trump, and W. M. Roquemore, "Simultaneous CARS and LDA Measurements in a Turbulent Flame," AIAA Paper No. 84-1458, 1984.
12. S. Fujii, M. Gomi, and K. Eguchi, "A Remote Laser-Probe System for Velocity and Temperature Measurements," J. Fluids Engin. 105, 129 (1983).
13. L. P. Goss, D. D. Trump, B. G. MacDonald, and G. L. Switzer, "10-Hz Coherent Anti-Stokes Raman Spectroscopy Apparatus for Turbulent Combustion Studies," Rev. Sci. Instrum. 54, 563 (1983).
14. A. Lightman, R. D. Magill, and R. J. Andrews, "Laser Diagnostic Development and Measurement and Modeling of Turbulent Flowfields of Jets and Wakes - Part I," AFWAL-TR-83-2044 (University of Dayton Research Institute, Dayton, OH, June 1983).
15. L. P. Goss, B. G. MacDonald, D. D. Trump, and G. L. Switzer, "CARS Thermometry and N_2 Number Density Measurements in a Turbulent Diffusion Flame," AIAA Paper No. 83-1480, 1983.

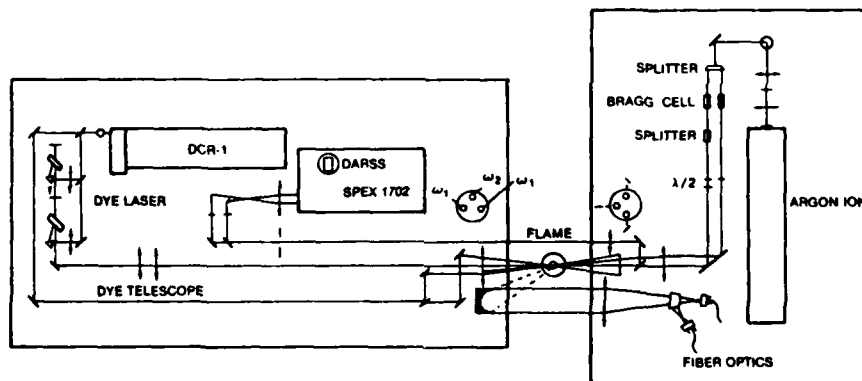


Figure 1. Optical Layout of Combined CARS-LDA Instrument.

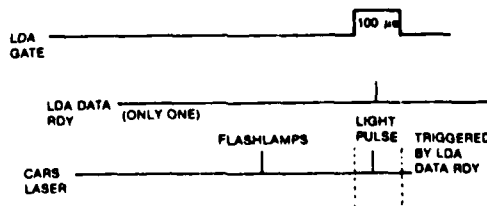


Figure 2. Timing Scheme for Combined CARS-LDA Instrument.

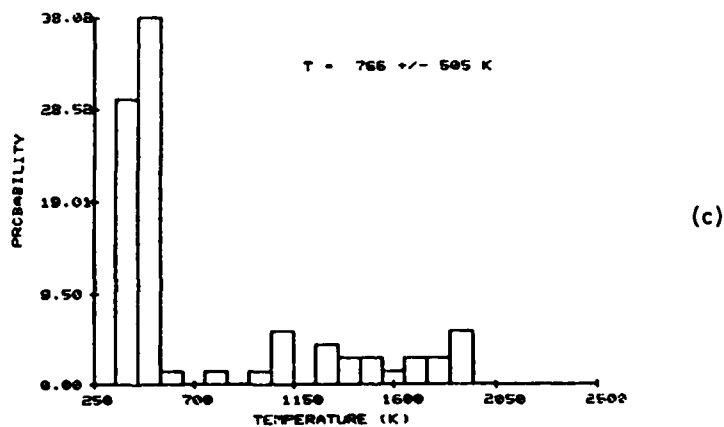
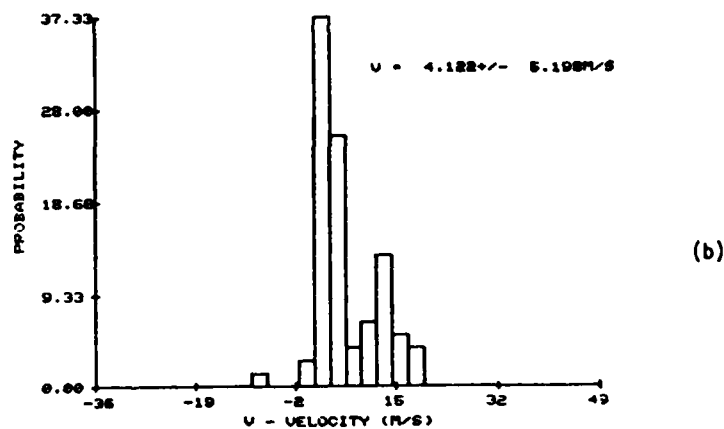
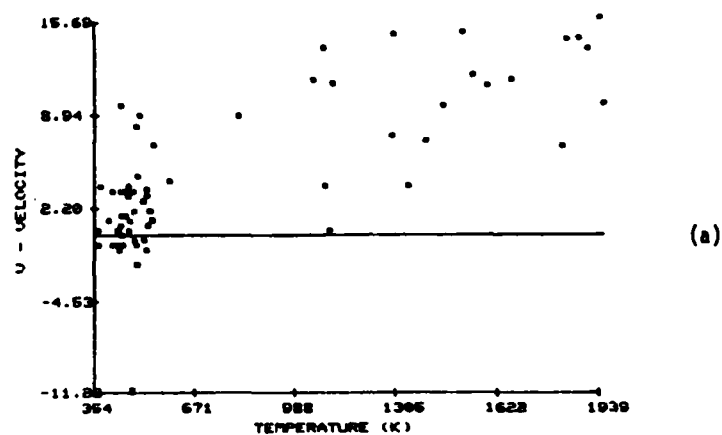


Figure 3. (a) Correlation Plot of V-T, (b) Velocity Histogram, and (c) Temperature Histogram Obtained in Torch-Burner Study.

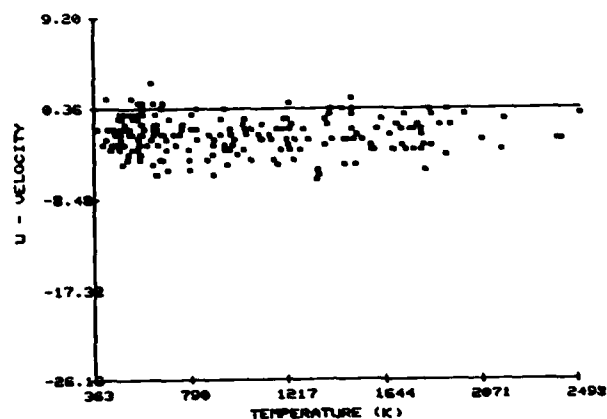
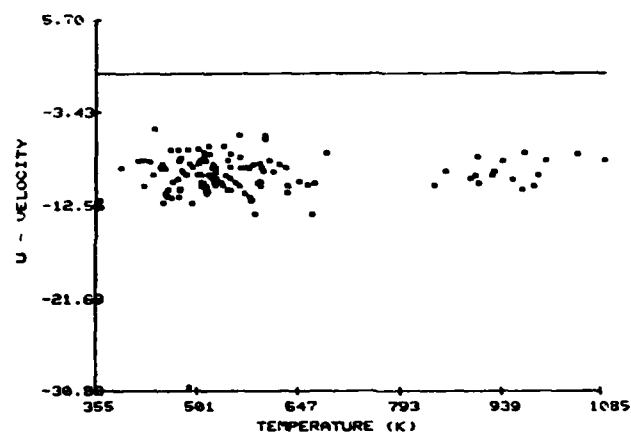
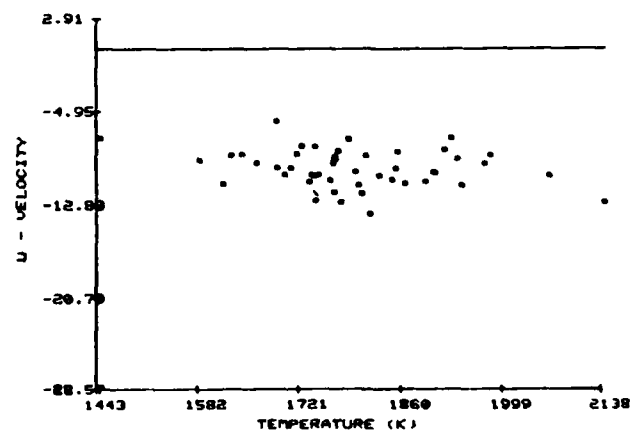


Figure 4. Correlation Plot of U-T Obtained at Position 8 cm above Burner Surface in Turbulent Diffusion Flame.



(a)



(b)

Figure 5. Correlation Plots of U-T Obtained at Radial Positions (a) 3.5 mm and (b) 4.5 mm from Centerline and 3.5 cm above Burner Surface in Premixed Propane-Air Flame.

COMBINED CARS/LDA INSTRUMENT FOR
SIMULTANEOUS TEMPERATURE AND VELOCITY MEASUREMENTS*

L. P. Goss and D. D. Trump
Systems Research Laboratories, Inc.
2800 Indian Ripple Road
Dayton, Ohio 45440-3696

W. M. Roquemore
Air Force Wright Aeronautical Laboratories
Aero Propulsion Laboratory (AFWAL/POSF)
Wright-Patterson Air Force Base, Ohio 45433-6503

*Accepted for publication in Experiments in Fluids.

Abstract

The performance of a combined CARS/LDA instrument capable of measuring temperature and two velocity components with a time coincidence of about 4 μ s is evaluated in a turbulent premixed propane-air Bunsen-burner flame. Measurements near the base of the flame exhibit negative axial correlations, indicative of normal gradient transport; those near the flame tip show strong positive axial correlations, indicative of counter-gradient transport. The radial correlations are positive both in the reaction zone and in the plume. Conditional-sampling measurements strongly indicate that the CARS/LDA instrument provides a Favre average of velocity, temperature, and velocity-temperature correlation due to the density weighting of Al_2O_3 seed particles in the flame.

1 Introduction

The possibility of using combustion models to improve the design methodology for practical combustors has stimulated new interest in the study of turbulent transport processes. Turbulent transport rates of heat, mass, and momentum are orders of magnitude larger than molecular transport rates in nonturbulent flows. These high transport rates are primarily due to the correlation between the fluctuating components of velocity and state (scalar) variables. Turbulence models, which must predict these correlations, are believed to be a major source of error in the design models. The need for development and evaluation of improved turbulence models has reinforced efforts to expand and improve the experimental turbulent-transport data base.

Experimental studies of turbulent transport processes are very difficult because simultaneous measurement of velocity and a state variable such as temperature or species concentration is required at a common point. The development of laser Doppler anemometry (LDA) has provided the means for measuring velocities in combusting flows. Reliable scalar measurements in adverse flame environments have proven to be much more difficult, and it is not surprising that relatively few combined measurements have been made. Shepherd and Moss (1981), Shepherd et al. (1982), Tanaka and Yanagi (1983), Yanagi and Mimura (1981), and Heitor et al. (1984) combined LDA with a thermocouple to make simultaneous temperature and velocity measurements in premixed flames. Brum et al. (1983) used LDA and a thermocouple to study a complex diffusion flame. Pulsed Raman and LDA were combined in studies conducted by Warshaw et al. (1981), Lederman and Posillico (1981), and Dibble et al. (1984). Simultaneous

density and velocity measurements were made by Dibble et al. (1981) using Rayleigh scattering and LDA. Mie scattering and LDA were used by Starner and Bilger (1980) to obtain concentration and velocity correlations. Coherent anti-Stokes Raman spectroscopy (CARS) and LDA have been used by Fujii et al. (1983), Fujii et al. (1984), and Goss et al. (1984) to obtain velocity-temperature correlations.

Problems arise in the use of any of these techniques in environments similar to those encountered by practical combustors. For example, the measurements of Yanagi and Mimura (1981) and Heitor et al. (1984) were restricted to a few minutes because seed particles coated the thermocouple. A more serious problem occurs in highly sooting flames because the soot coats the thermocouple. Heitor et al. (1984) also discuss the need for and difficulties and unknowns associated with determining the thermocouple time constant in the measurement environment. Mie scattering has been used by Starner and Bilger (1980) as a measure of gas density; however, uncertainties were associated with correcting for fluctuations in the inlet seeding densities. Pulsed Raman and Rayleigh scattering are established techniques, but their use is confined to clean flames. CARS is an expensive and complicated optical technique; however, Eckbreth (1980), Taran and Pealat (1982), and Switzer et al. (1980) have demonstrated that it can be used in simulated practical combustors. Thus, CARS/LDA has the potential of becoming a tool for studying the transport properties of turbulent combusting flows which are similar to those in practical combustors.

A combined CARS/LDA instrument designed for simultaneous measurements of velocity and temperature in reacting flows is described herein. This

instrument has been developed to minimize the time difference between velocity and temperature measurements. The advantages of combining the LDA and CARS instrument are: (1) the demonstrated ability of CARS to obtain temperatures in diverse flame environments, (2) the nonintrusive nature of the measurements, and (3) the ability to examine the effects of seed biasing. The last advantage is quite significant in demonstrating the heavy-density-weighted biasing (Favre averaging) that occurs with the LDA measurement. The density bias affects not only the average temperature and velocity measurements obtained simultaneously but also the magnitude of the correlations between the velocity and temperature, as will be discussed in detail in this paper.

2 Burner Description

After a survey of the literature, it was decided that a simple premixed propane-air Bunsen-burner flame would be a good candidate for study since it has been shown by several investigators to display a high degree of velocity-temperature correlation in and around the reaction zone. The burner employed in these studies was a standard Bunsen burner, except that the air-inlet holes were covered and the needle valve replaced to permit use of a controlled premixed propane-air mixture. The equivalence ratio of the gas mixture used in these studies was 1.3.

3 CARS Instrument

The design and the data-reduction routines of the CARS instrument (shown in Fig. 1) have been discussed in detail by Goss et al. (1983), and only the salient features will be mentioned here. The frequency-doubled output from a Quanta-Ray DCR-2 Nd:YAG laser was used to pump a broadband dye laser (oscillator-amplifier combination) and also used as the pump frequency in the CARS process. A folded BOXCARS configuration was used to achieve a spatial resolution of 2 mm along the major beam axis. This system was designed to acquire CARS data at a 10-Hz rate which required interfacing to a minicomputer for control of the data acquisition. Data reduction consisted of fitting the observed N_2 CARS spectral bandshape by means of a nonlinear least-squares iterative routine.

The primary differences between the CARS system described by Goss et al. (1983) and the system used in this study are associated with a change in the photodiode-array detector. The previously used TN1223 detector was replaced with a TN6132 1024-element detector. The latter detector, when directly compared with the former, displayed less cross-talk, a larger dynamic range, and little--if any--memory retention. As a result, the splitter arrangement as well as the data-acquisition software of the previous system could be simplified. Calibration of the new detector has been described by Goss et al. (1983). This CARS system displayed 80-K precision for repeated single-shot temperature measurements and 10-K accuracy in time-averaged mean measurements, as compared to a chromel-alumel thermocouple.

4 LDA Instrument

The LDA system shown in Fig. 3 was built by Lightman et al. (1983) and is a two-velocity-component, real-fringe system based on polarization separation of the velocity components. The 488-nm line from a Spectra-Physics argon-ion laser was used as the light source, with $\sim 1\text{-}\mu\text{m}$ -dia. alumina particles (Al_2O_3) being used as the scattering medium. The scattered light was collected in the forward direction slightly off-axis (12 deg.) by a parabolic mirror which collimated and reflected the light to the collection optics. The collection optics consisted of a focusing lens, a Glan Thompson polarization beam splitter to separate the various polarization components, and two optical fibers. The optical fibers allowed the processing electronics to be remotely located from the flame environment. The processor electronics consisted of two 1990 TSI burst-counter processors which were modified to permit coincident velocity as well as CARS data to be obtained. A computer interface allows data rates in excess of 30,000 velocities/s to be transferred and stored on a Modcomp computer. A 40-MHz Bragg shifter was used to shift the Doppler signal in order to remove direction ambiguities in the experiments reported by Goss et al. (1984). This, however, resulted in a relatively coarse velocity resolution (0.5 m/s) due to the bit resolution of the 1990 processors. To circumvent this problem, the 40-MHz signal was mixed with a 35-MHz signal, resulting in a 5-MHz Doppler signal with a velocity resolution of 0.006 m/s which is better suited for the low-velocity flames under study.

In the earlier studies conducted by Goss et al. (1984) with the combined CARS/LDA instrument, TiO_2 particles were used exclusively as the seed.

It was observed in the present work that TiO_2 displays a higher-than-expected dropout rate at high temperatures. The velocity-realization rate is expected to decrease at higher temperatures due to the density weighting of the LDA measurement (high temperatures, low seed density). However, the dropout rate for TiO_2 was two to three times higher than could be explained by a density-weighting mechanism. Several suggestions have been made by Moss (1979) and Ebrahimi and Kleine (1977) to explain this phenomenon. For example, it was suggested that TiO_2 may undergo a phase transition at high temperatures which results in a smaller scattering cross section and reduced signal strengths. It has also been suggested that the TiO_2 particle may break up to form smaller particles at high temperatures, thus reducing the scattering cross section. A systematic study of this phenomenon was not conducted in the present investigation. Rather, it was decided to use alumina particles as the seed. These particles, when tested under flame conditions similar to those used with the Al_2O_3 , displayed close agreement with expected density-weighted dropout rates. Thus, alumina seed particles were used for the experiments reported in this paper, unless otherwise stated. The density-weighted biasing will be discussed in more detail in a later section.

5 Combined CARS/LDA System

Several problems arose while interfacing the LDA and CARS instruments. The main problem involved designing the appropriate interface to ensure that the CARS and LDA measurements would be as simultaneous as possible. The time coincidence required to ensure that the conditions at the

measurement point will be the same as those during the time interval between the two measurements is dictated by the fluid dynamics of the flame under study. To ensure that temperature and velocity measurements, from a practical viewpoint, are simultaneous in the low-velocity Bunsen-burner flame (0 to 5 m/s), the time difference between the measurements must be on the order of hundreds of microseconds. At higher flow rates such as those encountered in gas-turbine systems, the coincidence time must be on the order of tens of microseconds.

The Nd:YAG laser used in the CARS experiment was designed to operate at a 10-Hz rate; the LDA instrument processes velocities at a rate which is related to the passage of the seed particles through the fringe pattern. Since particle arrival is random in nature, the coupling of the two instruments requires that random events be coupled to a 10-Hz repetitive event.

The approach followed in combining these two instruments involved creating a 100- μ s window during every 100-ms firing interval of the Nd:YAG laser. If an LDA realization should occur during this window, the CARS laser would be allowed to Q-switch. The firing sequence of the Nd:YAG laser consists of first discharging the flashlamps to obtain a population inversion and then pulsing the Q-switch to depopulate the upper laser levels and, thereby, obtain a giant laser pulse. The time separation between the flashlamp discharge and the Q-switch pulsing is 250 μ s. The 100- μ s LDA window is centered about the optimum 250- μ s delay after the flashlamp firing. The width of the 100- μ s window was determined experimentally by varying the time delay between the lamp firing and the

Q-switching. When the window is centered on the optimum delay, firing the Nd:YAG laser 50 μ s on either side of center corresponds to a 25% drop in laser power. The net result of such an approach is that the coincidence time is determined by: (1) the time required by the burst-counter processor to determine the velocity from a Doppler burst (4 μ s) and (2) the time required for the laser to lase after the Q-switch pulse has occurred (50 ns). With this method a 50-m/s fluid element would move only 200 μ m in the 4- μ s interval between velocity and temperature measurements.

The drawbacks of such an approach are that the narrow window over which the LDA event is accepted results in a substantially reduced data-acquisition rate. With the LDA in the free-run mode, 500 velocity realizations per second are observed in the flame. With a 100- μ s window every 100 ms, the total sampling time per second is 1 ms. This allows, on the average, only 1.0 simultaneous velocity-temperature measurement every two seconds.

The experimental arrangement of the combined CARS/LDA instrument is displayed in Fig. 1. In order to minimize the changes in optical configuration of the separate systems, a counter-propagating arrangement was used in which the instruments were on separate optical tables. The collimating lens and turning mirrors of the CARS system were rearranged on the LDA optics table, while the parabolic forward-scattering collection mirror of the LDA system was placed on the CARS table. This caused no major problem for either system and also minimized the number of optical changes necessary. To ensure overlapping of the measurement volumes for

the two systems, a 100- μ m circular aperture was used to locate and align the foci at a common point.

The timing sequence for data acquisition is shown in Fig. 4. The CARS shot gate is initiated by a machine-code software program from the TN1710 controller (LSI 11/02 microprocessor). If a velocity realization occurs during the gate, data are transferred under direct-memory-access (DMA) control to the 7840 Modcomp computer for storage on a 20-Mbyte disc system. The data-ready signal from the TSI 1990 burst-counter processor is sent to the TN1710 unit which, in turn, sends the fire Q-switch command signal to the Nd:YAG laser. The TN6132 multichannel detector transfers the CARS data to the spectral-data memory (SDM) of the TN1710 from which the data are transferred under DMA control to the 7840 computer. Before the data are transferred to the 7840 computer, the last ten channels of the 1024-channel CARS data are overwritten with the shot count for that particular laser firing. The shot count is used for bookkeeping by analysis programs.

One problem encountered during checkout experiments at room temperature was optical breakdown caused by the seeding conditions. To minimize this effect, the energy density at the foci of the CARS pump and probe beams was reduced by changing from a 50- to an 80-cm-focal-length lens. This lowered the spatial resolution to 2 - 3 mm in the longest dimension but substantially reduced the occurrence of optical breakdown. No such problem was encountered in the flame due to the reduced seed densities associated with the elevated temperatures. The 80 cm-focal-length lens was used in the experiments reported herein.

For low-velocity flows the seed particle has insufficient time to clear the sample volume before the CARS laser fires; thus, potential problems related to the presence of the seed during the CARS measurement must be addressed. Possible problems include: (1) optical breakdown, which is addressed in the above paragraph, (2) a contribution to the overall non-resonant susceptibility produced by the particles, which would effectively increase the measured CARS temperature, and (3) a reduction in the temperature of the flame due to heat loss in the form of blackbody emission by the seed. To determine whether the presence of the seed particle affects the CARS measurement, an experiment was conducted in which the plume region of the premixed flame was measured with and without seed particles. The result was that the two measured mean temperatures always agreed to within 10 K. The 10-K difference is well within the reproducibility of the burner experiments; thus, no major effects were observed due to the presence of the seed particle in the measurement volume.

6 Results and Discussion

6.1 Flame Characteristics

A turbulent Bunsen-burner flame was chosen for this study because experiments have demonstrated that large velocity-temperature correlations exist in and around the reaction zone. The detection of similar correlations with the combined CARS/LDA system would indicate that the system was functioning properly. Yanagi and Mimura (1981) and Tanaka and Yanagi (1983) observed both positive and negative correlations in different regions of a premixed propane-air flame. Extensive mapping of

the velocity-temperature correlations was carried out in the Tanaka and Yanagi (1983) study using a two-component LDA system and a fine-wire thermocouple. Although significant differences exist between that experiment and the present one, in general, the qualitative trends of the time-averaged flame characteristics and the velocity-temperature correlations are very similar. These similarities and differences will be discussed in this section.

The Bunsen burner employed by Tanaka and Yanagi (1983) made use of screens to generate turbulence, and the flame was stabilized by a pilot flame surrounding the burner port. It was found in the present investigation that the seed particles clogged the screen when such a burner was operated for long periods of time. Since the low data rates being employed here made it essential that the burner operate stably for long time periods, this approach was abandoned. For the burner in the present study, turbulence and flame stabilization were achieved by intrusions into the exit tube. Tanaka and Yanagi (1983) used a natural gas-air mixture with an equivalence ratio of 0.6; whereas, a propane-air mixture with an equivalence ratio of 1.3 was used here.

The tip of the visible flame here was 23 mm (2.1 D); whereas, the flame used by Tanaka and Yanagi (1983) had a visible length of 6.2 D. In a comparison of the results of these two studies, it is assumed that the processes occurring in the respective reaction zones should be similar if scaled by the respective lengths of the visible reaction zone.

The average and rms temperature, axial velocity, and radial velocity at two axial positions are plotted in Figs. 3 - 5. These data were

collected with the CARS and LDA systems operating independently. Superimposed on these plots is a time-averaged display of the premixed flame obtained from a long-exposure flame photograph. At an axial position 15 mm just inside the visible flame region, the temperature profile in Fig. 3 shows a large dip in the central region of the reaction zone and a peak in the surrounding plume; whereas, the rms fluctuations peak at the center and decrease sharply in the plume region. The axial velocity and corresponding fluctuation are relatively flat at this axial location, as noted in Fig. 4. The radial velocity profile at 15 mm shown in Fig. 5 is similar to the temperature profile, with a peak value occurring just outside the flame zone very near the edge of the burner and the fluctuations being nearly flat. One of the intrusions used to stabilize the flame was inadvertently located in the measurement plane to the right of the centerline; no intrusion occurred to the left of the centerline. This is believed to be the cause of the asymmetry noted in Figs. 3 - 5. Disregarding the asymmetry, the observed trends for the mean and fluctuations at the 15-mm position are similar to those observed by Tanaka and Yanagi (1983) near the bottom of the visible flame.

At the 1.5-mm axial position, the flame is quite stable and displays little temperature fluctuation, as noted in Fig. 3. The mean temperature and radial velocity maximize at the plume-reaction zone interface and decrease on either side due to the narrow width of the flame in this area. This observation is different from that of Tanaka and Yanagi (1983); the peak temperature occurred at the edge of their pilot burner. Nevertheless, the time-averaged characteristics of their flame and ours are quite similar if scaled by the visible flame length.

6.2 Bias Errors

Direct evaluation of the performance of the combined CARS/LDA system in a turbulent flame is difficult since no other technique exists for checking the velocity results--much less an established technique for providing simultaneous temperature and velocity correlations. Therefore, one normally relies on checks of the individual instruments under test conditions where other techniques are known to provide reliable data. Lightman et al. (1983) performed such checkout tests with the LDA system used in this study and found that for cold-flow environments, data from hot-film and Pitot-static probe measurements compared favorably with the LDA results. Also, Goss et al. (1983) demonstrated the performance of the CARS system in comparative studies with thermocouples in furnace and flame environments. Indeed, the mean and rms data presented in the previous section indicate that the individual CARS and LDA systems are performing properly in the Bunsen-burner flame. Since the combined CARS/LDA system is extremely complex, checks of the individual instruments are not sufficient to assure the performance of the combined instrument.

The individual CARS/LDA measurements can be used with conditional sampling techniques to determine whether bias errors are present in the combined CARS/LDA system. A CARS/LDA measurement is initiated by the presence of a seed particle in the measurement volume during the time interval (window) when the CARS laser is ready to fire. Since the distribution of seed particles in the flow determines the measurement sampling statistics, bias errors due to seeding may occur. The presence and magnitude of seed biasing errors are very difficult to assess

because an accurate unbiased measurement is also required. A CARS temperature measurement made simultaneously with an LDA measurement is a conditional measurement since it depends on the presence of seed. However, unconditional CARS temperatures can be measured independently at a constant rate. These unconditional measurements will also be unbiased as long as the measurement frequency is not locked to an instability frequency in the flow. By comparing the mean and probability distribution functions (pdf's) for conditional and unconditional temperature measurements, biasing errors can be examined for different test conditions.

Three different seed bias errors are known to occur in LDA measurements in cold flows. First, if the seed particles are too large to follow the flow field, then the velocity measurements will be biased toward the low velocities. It is generally accepted that such errors do not exist in turbulent flows when the particles are $\sim 1 \mu\text{m}$ in diameter. The second type of error is due to a variation of seed density which results from nonuniform seeding. This error can occur even when only one flow stream is present. For example, a uniformly seeded jet ejected into still room air will entrain unseeded air into the plume. This can cause the velocities in the shear layer to be biased toward the higher values since the higher velocities from the inner region of the jet are most likely to be measured. Errors due to nonuniform seeding have been discussed by Durst (1974) and Yule et al. (1980). The third type of error was first considered by McLaughlin and Tiederman (1973) and more recently by Edwards and Baratici (1984) and Chen and Lightman (1985). A

bias error in a uniformly seeded flow may result because there is a higher probability that a seed particle is present in the faster-moving than in the slower-moving fluid elements. This causes the velocity pdf's and the average velocity to be biased toward the higher values. Although these errors are known to occur in cold flows, they can also occur in combustion flows.

Additional errors can occur as a result of combustion. High flame temperatures can cause a reduction in the effective scattering cross sections of certain seed materials which results in a higher probability of sampling low-temperature fluid elements. As mentioned earlier, Ebrahimi and Kleine (1977) observed such an effect for TiO_2 . Figure 6 demonstrates that the CARS/LDA system through the use of conditional sampling can detect this effect. Each pdf contains about 1500 individual measurements. The conditional pdf's in column \bar{T}_C , as compared to the unconditioned pdf's in column \bar{T}_U , are strongly weighted toward the lower temperatures. For example, the high-temperature peak shown in the unconditional measurements at $r = 0$ is extremely weak in the conditional pdf. Biasing of the conditional measurements toward low temperatures is also very evident in the mean temperatures shown in Fig. 6. However, the bias in the width (rms value) of the distribution depends on the actual shape of the unconditional pdf.

Another bias error that may occur in flames is due to a variation in gas density. The seed density is expected to be proportional to the gas density. This will result in a higher probability of measuring low-temperature, high-density fluid elements if the samples are not collected at a constant rate. This bias error might be somewhat offset by

the McLaughlin-Tiederman high-velocity bias if the lower-density fluid elements are moving faster than the high-density elements. However, the two bias errors need not cancel out. A gas-density bias error was suggested by Magill et al. (1982) to explain a bias toward low-velocity, low-temperature fluid elements when high-velocity, high-temperature fluid elements were known to be present more than 60% of the time. Recently, Heitor et al. (1984) computed a Favre-averaged pdf from unconditional (constant-sampling-rate) thermocouple measurements and compared the results with a pdf obtained from conditionally sampled simultaneous LDA and thermocouple measurements. Although their data samples were not sufficiently large to rule out sampling errors, the Favre-averaged and conditional pdf's were similar.

The low-temperature bias error noted in Fig. 6 may be due, in part, to gas-density variations. To determine whether this is the case, the unconditional pdf's were density weighted using Eqs. (1) and (2)

$$B_{Fi} = \frac{\tilde{T}_F B_{Ui}}{T_i} \quad (1)$$

$$\tilde{T}_F = \frac{1}{\left(\frac{1}{T_u}\right)} \quad (2)$$

where B_{Fi} is the density-weighted probability of measuring a temperature T_i , \tilde{T}_F the Favre-averaged or density-weighted temperature, T_u the unconditional temperature, and B_{Ui} the unconditioned probability of measuring temperature T_i . A comparison of the pdf's in Columns \tilde{T}_C and \tilde{T}_F in Fig. 6 reveals that the low temperatures are more pronounced than would be

expected as a result of density weighting. Indeed, the drop-out rate of the LDA data taken with TiO_2 was almost a factor of three higher than expected from assuming that the seed-particle density varies as the gas density. The data in Fig. 6 indicate that TiO_2 is not a good seed particle for combustng flows.

Figure 7 illustrates the density bias error which may result from the use of Al_2O_3 seed particles. This figure contains unconditional and conditional temperature pdf's measured at an axial location of 15 mm and at three radial locations. The average conditional temperatures are more than 270 K lower than the unconditional ones, and the pdf's are weighted toward the low-temperature, high-density values. Comparison of the shapes of the density-weighted pdf's (Column \bar{T}_F) with those of the conditional pdf's (Column \bar{T}_C) gives strong support to the proposition that the measurements conditioned by the presence of seed particles are density weighted. Therefore, Al_2O_3 seed particles were used in the remainder of this study.

Table 1 shows a more detailed comparison of the mean and rms temperatures at different radial locations in the flame. The error between \bar{T}_F and \bar{T}_C is typically 4.6%, whereas the error in the rms values is typically 17.3%. Although these errors are considerably smaller than those of the unconditional and conditional data, they are, nevertheless, much larger than would be expected from the precision of the individual CARS measurements. The relative disagreement between the rms values of \bar{T}_F and \bar{T}_C suggests the possibility of a sampling error. It appears that a larger sample is required for conditional CARS/LDA measurements to permit accurate determination of the rms values. Even with a sampling

error, the conditional measurements appear to be strongly density weighted.

The possibility exists that the combined CARS/LDA measurements may be biased to a greater extent than expected from density weighting alone. The simultaneous measurements depend not only on the presence of seed particles but also on the window during which the CARS laser fires. It is conceivable that an additional bias error could result due to the window width. For example, Nejad and Craig (1985) observed bias errors in 2D LDA measurements in cold flows due to the window width when data were obtained at a uniform rate. The possibility of a window bias for the CARS/LDA measurement was examined in the present investigation by comparing axial velocity pdf's obtained simultaneously with and independently of the CARS measurements. The results indicate that such a bias would be less than 1% of the mean velocity value.

6.3 Temperature/Velocity Correlations

As discussed in Section 6.2, the velocity measurements appear to be density weighted with alumina seed particles and, thus, are Favre averaged. However, since the temperature is determined simultaneously with the velocity, the Reynolds-averaged correlations can be determined by correcting the individual measurement using

$$\overline{u\theta} = \frac{\sum_{i=1}^N T_{Fi} u'_{Fi} \theta_{Fi}}{\sum_{i=1}^N T_{Fi}} \quad (3)$$

where u'_{Fi} is the axial velocity fluctuation about the Favre average of the i^{th} measurement. T_{Fi} is the density-weighted i^{th} measured temperature, θ'_{Fi} the i^{th} measured temperature fluctuation about the Favre average, and N the total number of measurements. This allows a direct comparison between the Reynolds- and Favre-averaged correlations.

The axial and radial velocity correlations with temperature near the base of the burner in Figs. 8 and 9 show the same trends as those observed by Tanaka and Yanagi (1983). They found a negative correlation between axial velocity and temperature at the interface of the reaction zone and the burnt mixture and a positive correlation between radial velocity and temperature very near the same radial location. The same trends can be observed in the 1.5-mm profiles shown in Figs. 8 and 9.

Figures 8 and 9 also show velocity-temperature correlation profiles at the 15-mm position near the tip of the reaction zone. The axial velocity-temperature correlation has a minimum at the centerline where the average temperature is a minimum and peaks near the plume-reaction zone interface. A peak of 81 is observed, indicating strong positive correlation (high temperature, high velocity) in this region. Since the mean temperature gradient is also positive at this location (See Fig. 3), counter-gradient transport is occurring.

The large fluctuations in the reaction-zone area are due to the penetration of the unburnt gases into this region, as demonstrated by the pdf's shown in Fig. 7. Disregarding the conditionally sampled pdf's in this figure, the unconditionally sampled pdf (sampled without the LDA) displayed bimodal peaks in the central region of the flame ($r = 0$). Notice

the strong low-temperature peak indicative of the penetration of unburnt gases. In the plume region ($r \approx 6$), the pdf becomes single mode, indicating primarily burnt gases.

In general, the magnitude of the correlations is lower in the biased case, with the maxima shifted from just inside the reaction-zone plume interface to the right of the interface. The difference in the magnitude of the correlations due to density weighting can vary as much as a factor of 2. The observed shift in the maxima is on the order of 1 mm.

The effect on the radial correlations shown in Fig. 9 is quite similar to that on the axial correlations. Both an amplitude and a spatial difference are observed between the density-biased and corrected radial correlations. The amplitude difference in the radial-correlation case is somewhat smaller, ≈ 1.4 ; but the spatial shift of the maxima is approximately the same, 1 mm. Thus, while the general features of the density-biased correlations are the same as those of the corrected correlations, the amplitudes as well as the spatial locations of the maxima are different and must be taken into account if an accurate determination of the correlations is to be made.

7 Summary and Conclusions

The ability of a combined CARS/LDA instrument to make temperature and two-velocity-component measurements nearly simultaneously (within 4 μ s) at a common point in a flame has been demonstrated. A turbulent pre-mixed propane-air Bunsen-burner flame was chosen for this study because

of the characteristics: 1) positive radial velocity and temperature correlations in the turbulent reaction zone where the temperature gradient is positive, 2) negative axial velocity and temperature correlations near the burner base, and 3) positive correlations near the tip of the reaction zone. The CARS/LDA measurements confirmed these characteristics for the Bunsen-burner flame. These results are viewed as a necessary condition for demonstrating the performance of the CARS/LDA system.

The ability of the CARS/LDA system to examine bias errors due to the presence of seed particles has been demonstrated. Simultaneous CARS temperature and LDA velocity measurements are conditioned by the probability that there is a seed particle in the measurement volume during the 100- μ s time interval in which the CARS laser is ready to fire. Comparisons of CARS temperature pdf's obtained independently (unconditional) and simultaneously (conditional) with the LDA using Al_2O_3 seed particles show a strong weighting toward low temperatures (high densities). Density-weighted temperature pdf's were computed using the unconditioned pdf data. The density-weighted pdf's compared favorably with the conditioned pdf's, which strongly suggests that the CARS/LDA system provides Favre-averaged data. When TiO_2 is used as a seeding material, a bias occurs due to a change in the TiO_2 particle-scattering cross section at high flame temperatures; this was demonstrated by comparing conditional and unconditional temperature pdf's.

A major problem with the CARS/LDA system involved low sampling rates ($< 0.5/s$) requiring very long data-collection times and resulting in the possibility that some of the data might be under-sampled. Low sampling

rates were caused by the narrow 100- μ s window used in obtaining the 4- μ s coincidence between the velocity and temperature and the low seeding rates which normally occur in flames.

In order for the CARS/LDA system to become a practical tool for studying turbulent flames, increased data-acquisition rates which approach the speed of the CARS laser firing are essential. Increased rates can be achieved by improving seeding techniques. The development of a high-constant-output seeder is important for future transport studies in turbulent flames. Another improvement to the CARS/LDA system which should result in increased data rates is to eliminate the 100- μ s window and fire the CARS laser at a constant rate of 10 Hz while free running the LDA. Coincidence would be achieved by interpolation of the LDA data to obtain the two velocity components at the time of the CARS laser firing. The accuracy of the assigned velocities and the uncertainty in the velocity-temperature correlations could be estimated using the LDA data collected before and after the CARS laser firing. This procedure should improve the data-collection rate without seriously reducing the coincidence time. This approach will be investigated in future studies.

References

- Brum, R. D.; Seiler, E. T.; LaRue, J. C.; Samuelsen, G. S. 1983: Instantaneous two-component laser anemometry and temperature measurements in a complex flow model combustor, AIAA-83-0334.
- Chen, T.-H.; Lightman, A. J. 1986: Effects of particle arrival statistics on laser anemometer measurements. Presented at the ASME 1985 Winter Annual Meeting. To be published in International Symposium on Laser Anemometry.
- Dibble, R. M.; Kollmann, W.; Schefer, R. W. 1984: Conserved scalar fluxes measured in a turbulent nonpremixed flame by combined laser Doppler velocimetry and laser Raman scattering, Comb. Flame 55, 307.
- Dibble, R. M.; Rambach, G. D.; Hollenbach, R. E.; Ringland, J. T. 1981: Simultaneous measurements of velocity and temperature in flames using LDV and CW laser Rayleigh thermometry. Presented at Fall Meeting of the Western State Section of the Combustion Institute, WSS/C1 81-84, October.
- Durst, F. 1973: In: Second International Workshop on Laser Velocimetry, Vol. 2, 471-467.
- Ebrahimi, I; Kline, R. 1977: The nozzle flow concentration fluctuation field in round turbulent free jets and jet diffusion flames. In: Sixteenth (International) Symposium on Combustion, 1711.
- Edwards, R. V.; Baratuci, W. 1984: Simulation of particle measurement statistics for laser anemometers. Presented at the Ninth Turbulence Symposium, Rolla, Missouri.
- Fujii, S.; Gomi, M.; Eguchi, K. 1983: A remote laser-probe system for velocity and temperature measurements. J. Fluids Eng. 105, 129.

- Fujii, S; Gomi, M.; Eguchi, K.; Yamayuchi, S.; Jin L. 1984: Time resolved LDV and CARS measurements in a premixed reacting flow. Comb. Sci. Tech. 36, 211.
- Goss, L. P.; Trump, D. D.; MacDonald, B. G.; Switzer, G. L. 1983: 10-Hz coherent anti-Stokes Raman spectroscopy apparatus for turbulent combustion studies. Rev. Sci. Instrum. 54, 563.
- Goss, L. P.; Trump, D. D.; Roquemore, W. M. June 1984: Simultaneous CARS and LDA measurements in a turbulent flame. AIAA 84-1458.
- Goss, L. P.; Trump, D. D.; Roquemore, W. M. 1984: An investigation of temperature and velocity correlations in turbulent flames. In: Experimental Measurements and Techniques in Turbulent Reactive and Non-Reactive Flows, p. 215. (eds. So, R. M.; Whitelaw, J. H.; Lapp, M.), New York: The American Society of Mechanical Engineers.
- Goss, L. P.; Trump, D. D.; Switzer, G. L. 1983: Laser Optics/Combustion Diagnostics. Quarterly Status Report 6603-13 Under U. S. Air Force Contract F33615-80-C-2054, covering the period September to December, Dayton: Systems Research Laboratories, Inc.
- Heitor, M. V.; Taylor, A. M. K. P.; Whitelaw, J. H. 1984: Simultaneous velocity and temperature measurements in a premixed flame. In: Experimental Measurements and Techniques in Turbulent Reactive and Non-Reactive Flows, p. 243. (eds. So, R.M.; Whitelaw, J. H.; Lapp, M.), New York: The American Society of Mechanical Engineers.
- Lederman, S.; Posillico, C. 1981: Unified spontaneous Raman and CARS system. AIAA J. 19, 824.
- Lightman, A.; Magill, R. D.; Anderson, R. J. 1983: Laser diagnostic development and measurement and modeling of turbulent flowfields of jets and wakes. Part 1, AFWAL-TR-83-2044.

- Magill, P. D.; Lightman, A.; Orr, C. E.; Bradley, R. P.; Roquemore, W. M. 1982: Simultaneous velocity and emission measurements in a bluff-body combustor. AIAA 82-0883.
- McLaughlin, D. K.; Tiederman, W. G. 1973: Biasing correction for individual realization of laser anemometer measurements in turbulent flows. *Phys. Fluids*, 16, 2082.
- Moss, J. B. 1980: Simultaneous measurements of concentration and velocity in an open premixed turbulent flame. *Comb. Sci. Tech.* 22, 119.
- Nejad, A. S.; Craig, R. R. 1986: Biasing in 2d individual realization LDV systems. To Be Published.
- Shepherd, I. G.; Moss, J. M. 1981: Characteristic scales for density fluctuations in a turbulent premixed flame. *Comb. Sci. Tech.* 25, 127.
- Shepherd, I. G.; Moss, J. M.; Bray, K. N. C. 1982: Turbulent transport in a confined premixed flame. In: 19th Symposium (International) on Combustion, p. 423. Pittsburgh: The Combustion Institute.
- Starner, S. H.; Bilger, R. W. 1980: Measurements of scalar-velocity correlations in a turbulent diffusion flame. In: 18th Symposium (International) on Combustion, p. 921. Pittsburgh: The Combustion Institute.
- Tanaka, H.; Yanagi, T. 1983: Cross-correlation of velocity and temperature in a premixed turbulent flame, *Comb. Flame* 51, 183.
- Warshaw, S.; Lapp, M.; Penny, C. M.; Drake, M. C. 1981: Temperature-velocity correlation measurements for turbulent diffusion flames from vibrational Raman scattering data. In: *Laser Probes for Combustion Chemistry*, p. 239. (ed. Crosely, D. R.), Washington, D. C.: The American Chemical Society.

- Yanagi, T.; Mimura, Y. 1981: Velocity temperature correlation in pre-mixed flame. In: 18th Symposium (International) on Combustion, p. 1031, Pittsburgh: The Combustion Institute.
- Yule, A. J.; Chigier, N. A.; Boulderston, R.; Ventura, J. 1980: Combustion-transition interaction in a jet flame. AIAA J. 19, 752.

List of Figures

- Fig. 1. Optical layout of the combined CARS/LDA instrument.
- Fig. 2. Timing sequence for data-acquisition for the combined CARS/LDA instrument.
- Fig. 3. The time-averaged (\bar{T}) and rms (θ) temperature profiles at axial locations of 1.5 and 15 mm. CARS temperature measurements were made independently of the LDA measurements at a rate of 10 Hz.
- Fig. 4. Time-averaged (\bar{U}) and rms (u') axial velocity profiles at axial locations of 1.5 and 15 mm. LDA measurements were made independently of CARS measurements at an average rate of 500 realizations/s.
- Fig. 5. Time-averaged (\bar{V}) and rms (v') radial velocity profiles at axial locations of 1.5 and 15 mm. LDA measurements were made independently of the CARS measurements at an average rate of 500 realizations/s.
- Fig. 6. CARS temperature pdf's obtained at an axial location 21.5 mm and radial locations of 9, 4, and 6 mm. \bar{T}_U represents the CARS temperatures measured independently of LDA velocities (unconditional). \hat{T}_F represents the Favre average of the \bar{T}_U temperature pdf's, and \bar{T}_C represents the CARS temperatures measured simultaneously with LDA velocities using TiO_2 seed particles (conditional).

Fig. 7. CARS temperature pdf's obtained at an axial location of 15 mm and radial locations of 0, 4, and 6 mm. \bar{T}_U represents the CARS temperature measurements made independently of the LDA measurements (unconditional). \bar{T}_F represents the Favre average of the \bar{T}_U temperature pdf's, and \bar{T}_C represents the CARS temperature measurements made simultaneously with LDA measurements using Al_2O_3 seed particles (conditional).

Fig. 8. Favre- and Reynolds-averaged axial velocity/temperature correlations about the mean at axial locations of 1.5 and 15 mm. Al_2O_3 particles were used to seed the flow.

Fig. 9. Favre- and Reynolds-averaged radial velocity/temperature correlations about the mean at axial locations of 1.5 and 15 mm. The LDA measurements were made using Al_2O_3 particles.

Table 1. Comparison of mean \bar{T} and fluctuating θ temperatures at an axial location of 15 mm and various radial locations: unconditioned (U), Favre averaged (F), and seed conditioned (C)

r (mm)	Average temperature (K)				Root-mean-square temperature (K)			
	\bar{T}_U	\bar{T}_F	\bar{T}_C	$\frac{\bar{T}_F - \bar{T}_C}{\bar{T}_F}$	θ_U	θ_F	θ_C	$\frac{\theta_F - \theta_C}{\theta_C}$
	(K)	(K)	(K)	(%)	(K)	(K)	(K)	(%)
0.0	883	678	582	14.0	531	393	289	26.5
1.0	1002	742	722	2.7	547	439	378	13.8
2.0	1040	782	774	1.0	541	449	391	12.9
3.0	1342	1029	994	3.4	568	566	472	16.6
4.0	1655	1426	1368	4.1	464	572	525	8.2
5.0	1885	1816	1744	4.0	285	356	384	7.9
6.0	1878	1656	1607	3.0	263	255	278	8.3
7.0	1806	1783	1741	2.4	190	199	263	32.2
8.0	1759	1733	1611	7.0	203	211	273	29.4

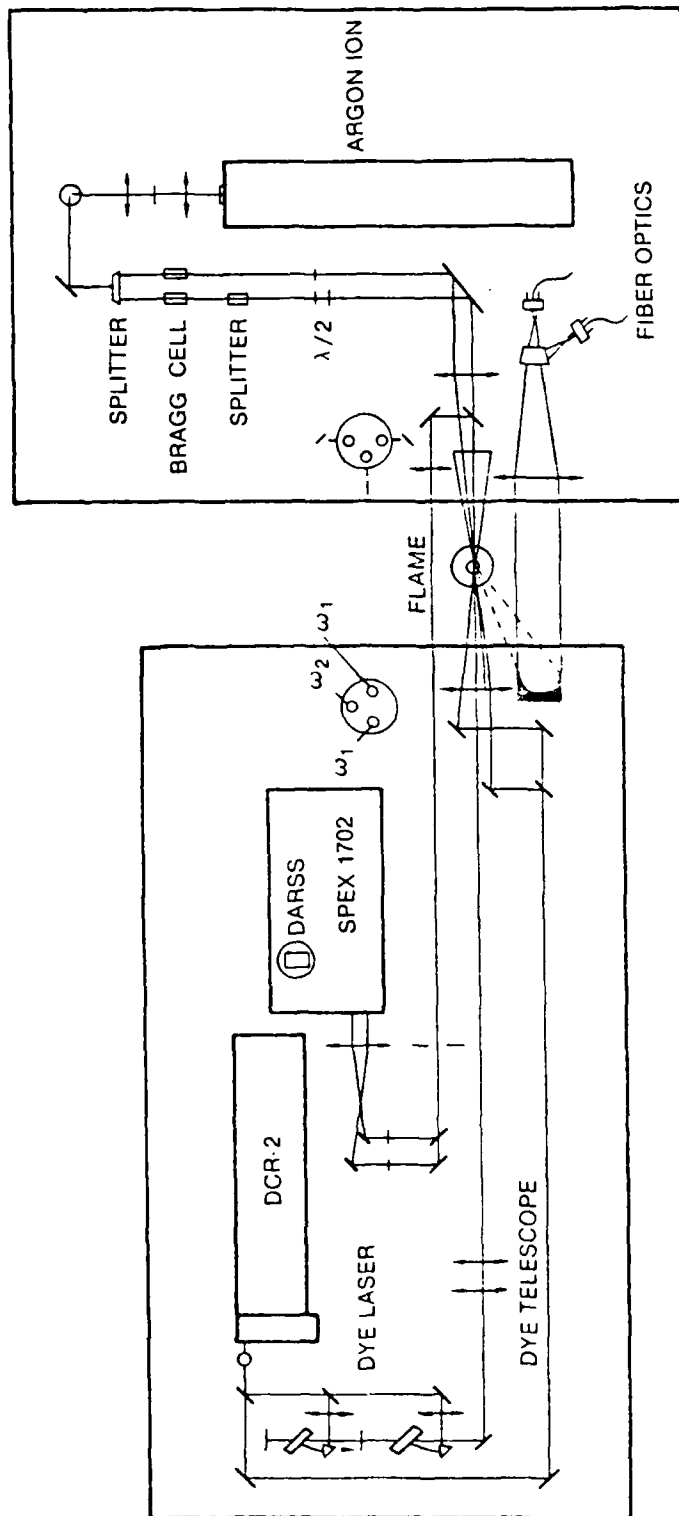


Figure 1

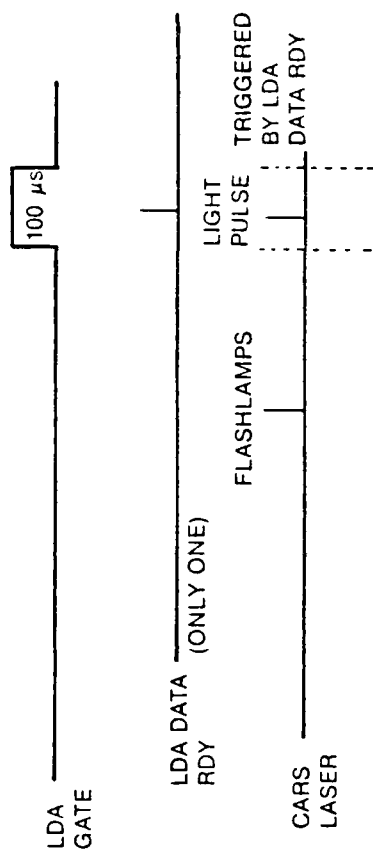


Figure 2

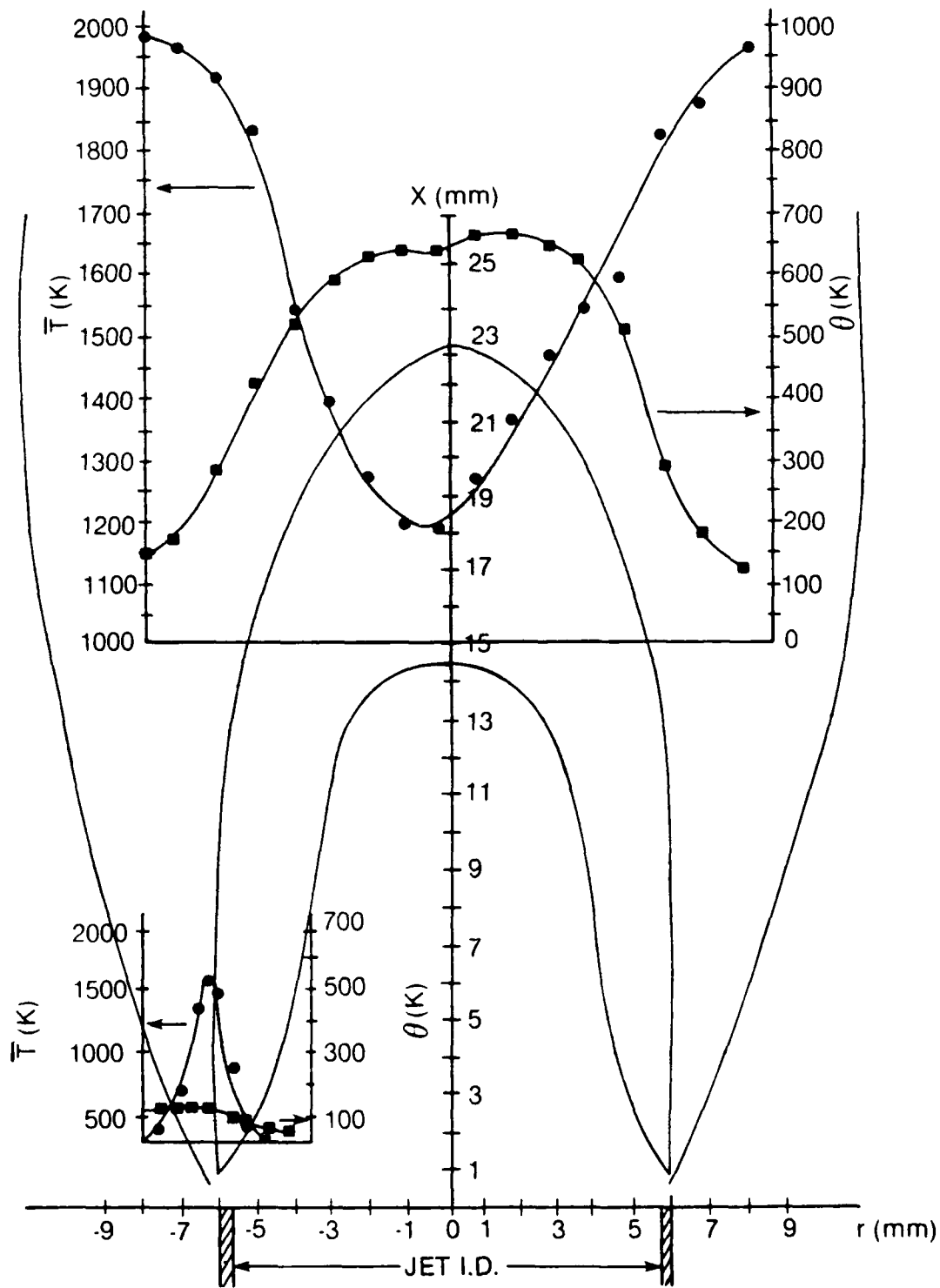


Figure 3

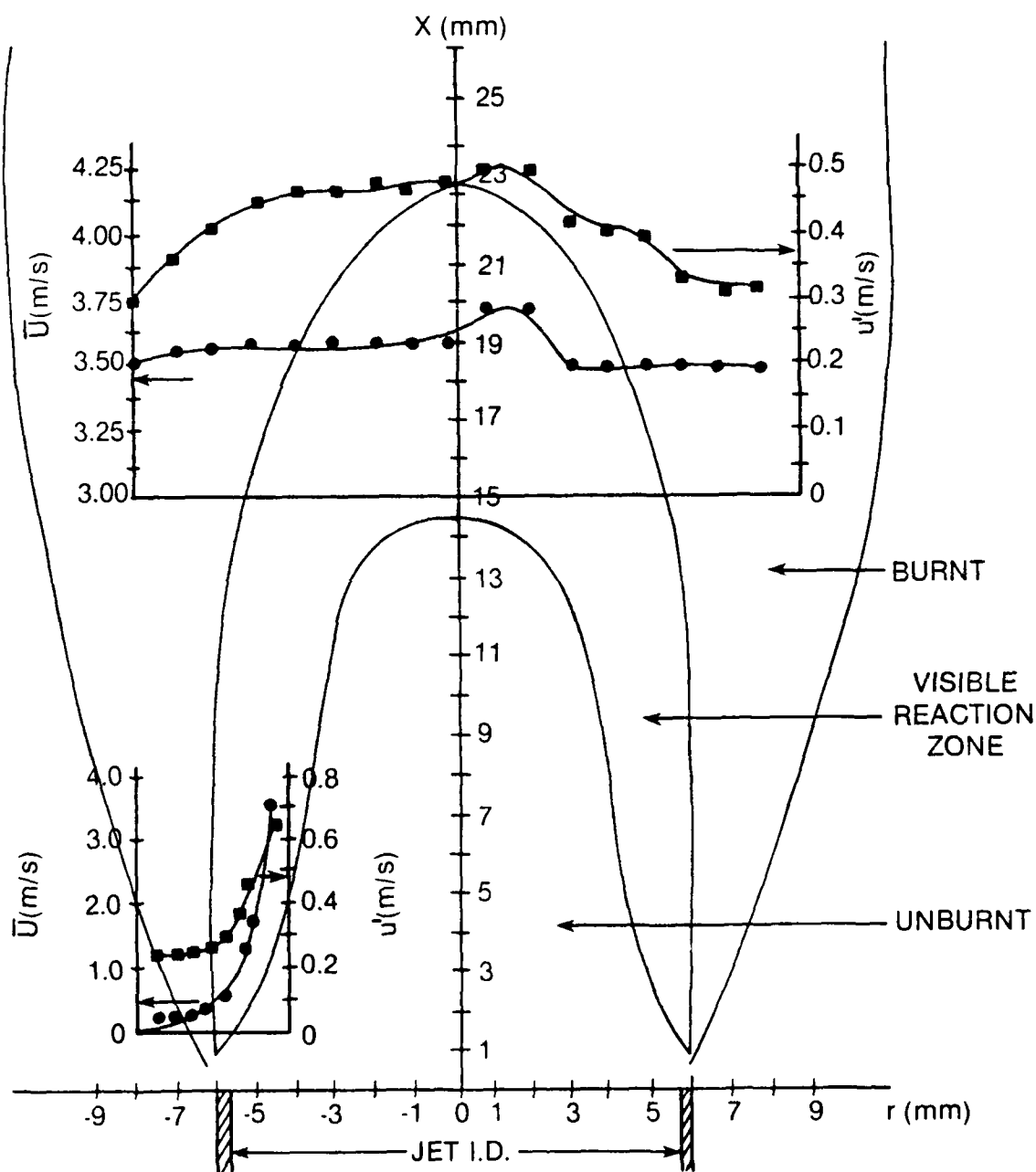


Figure 4

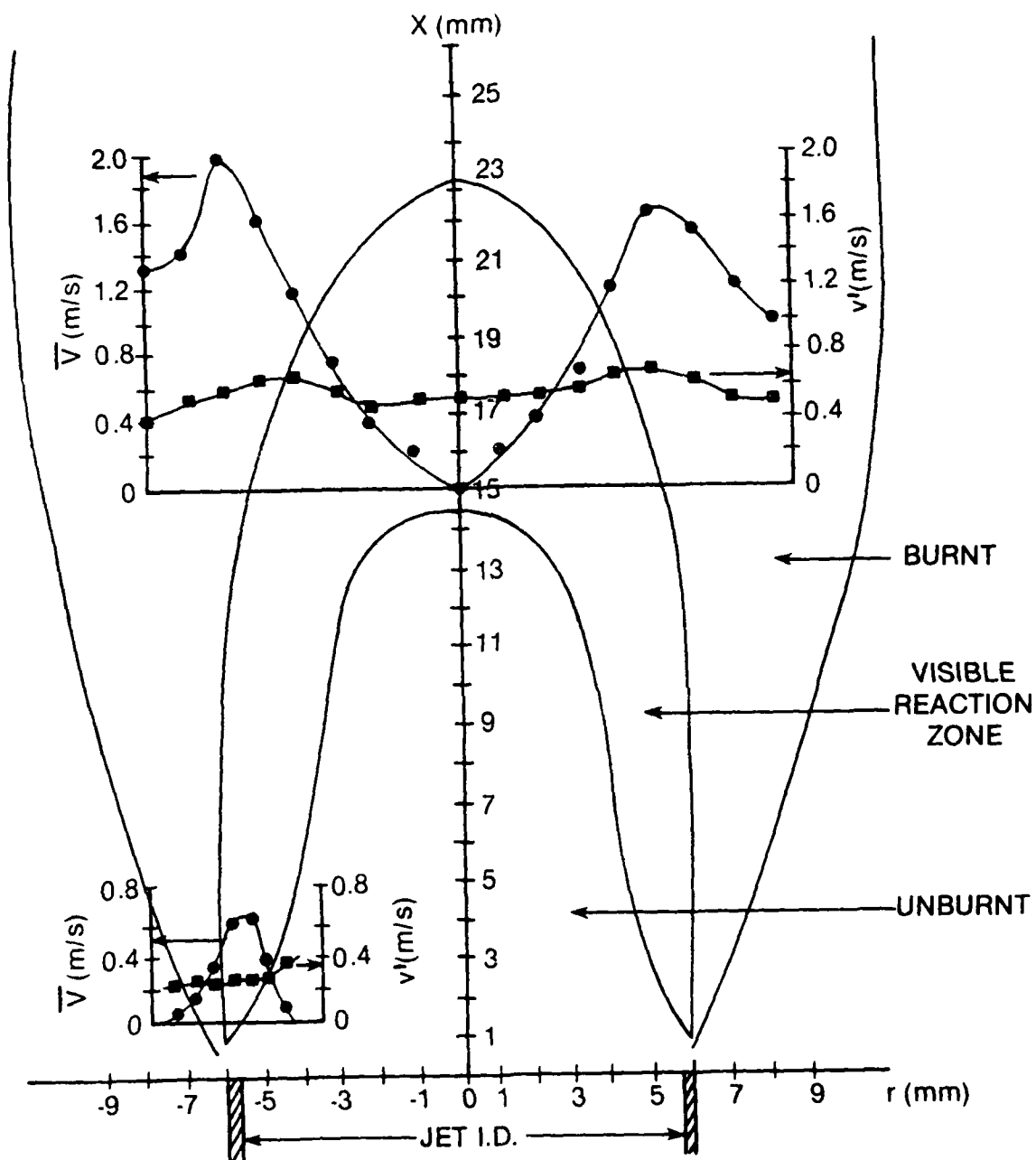


Figure 5

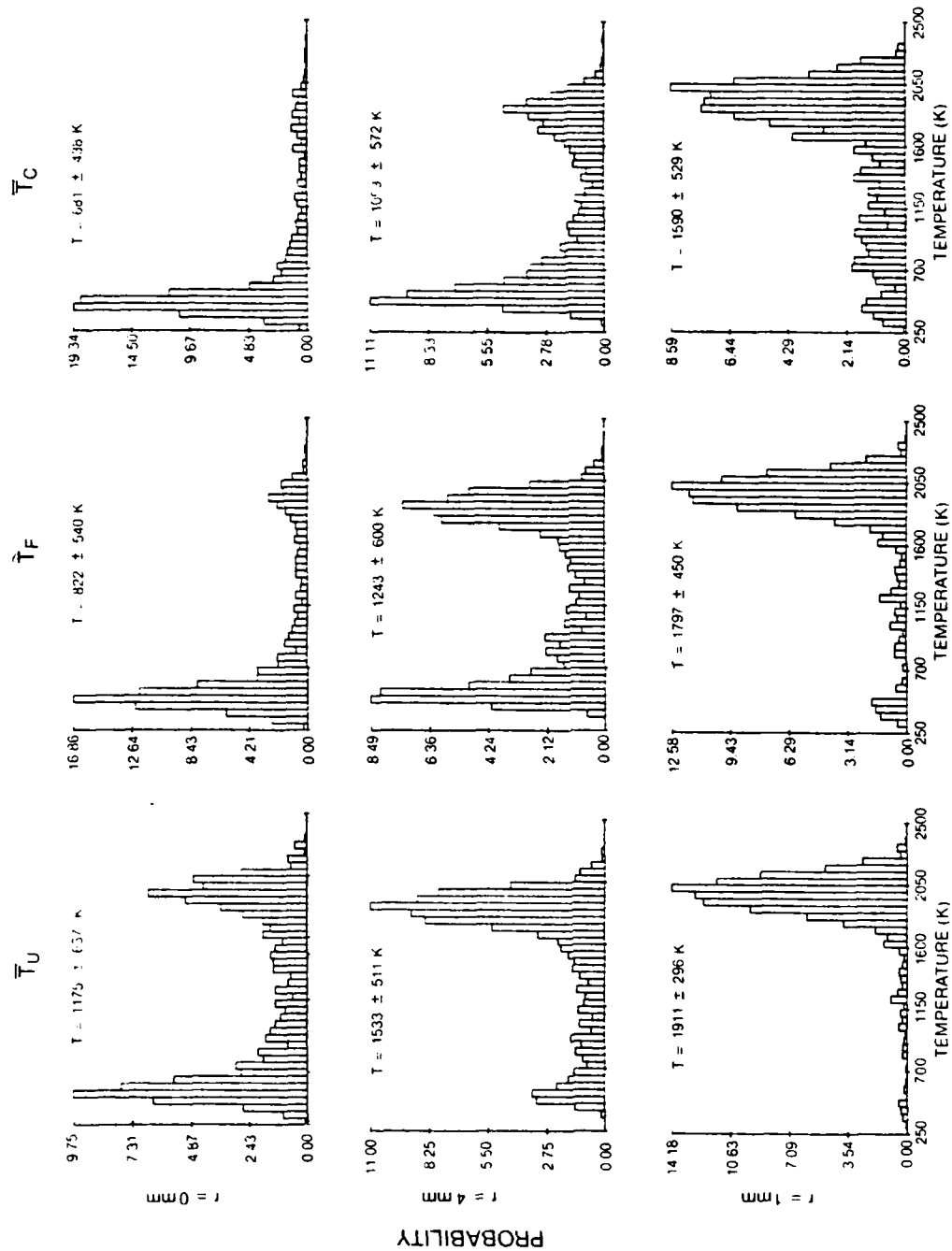


Figure 6

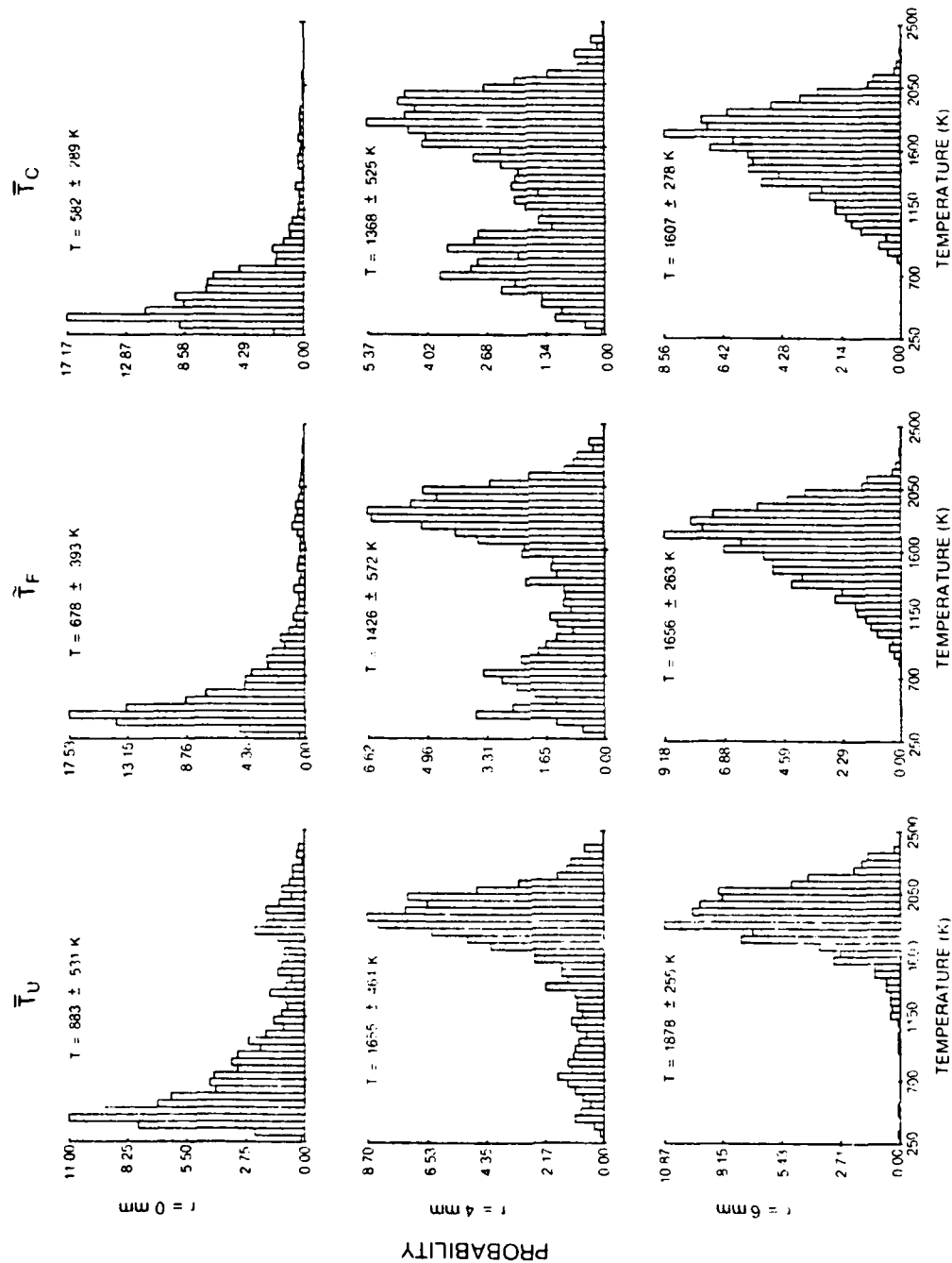


Figure 7

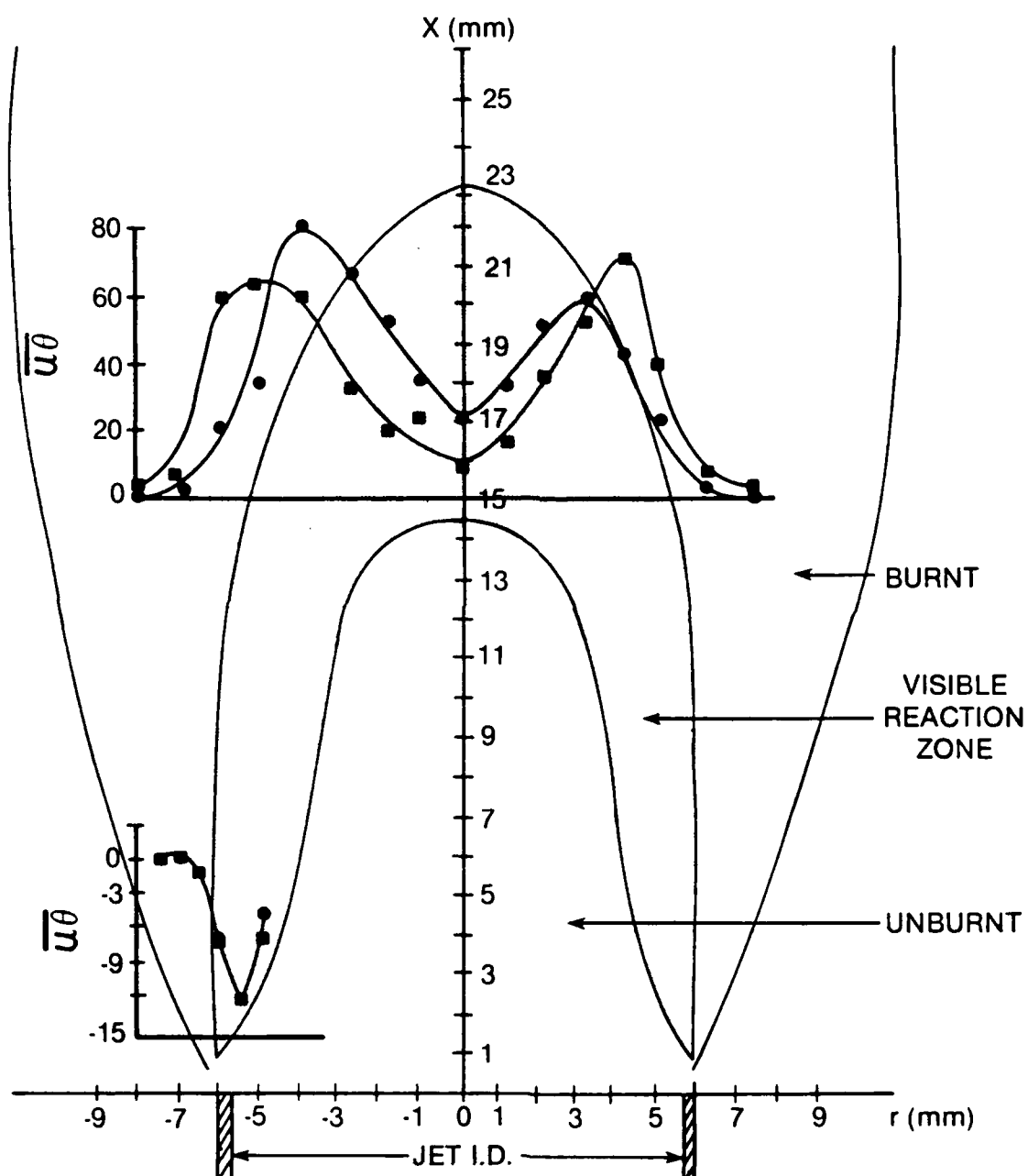


Figure 8

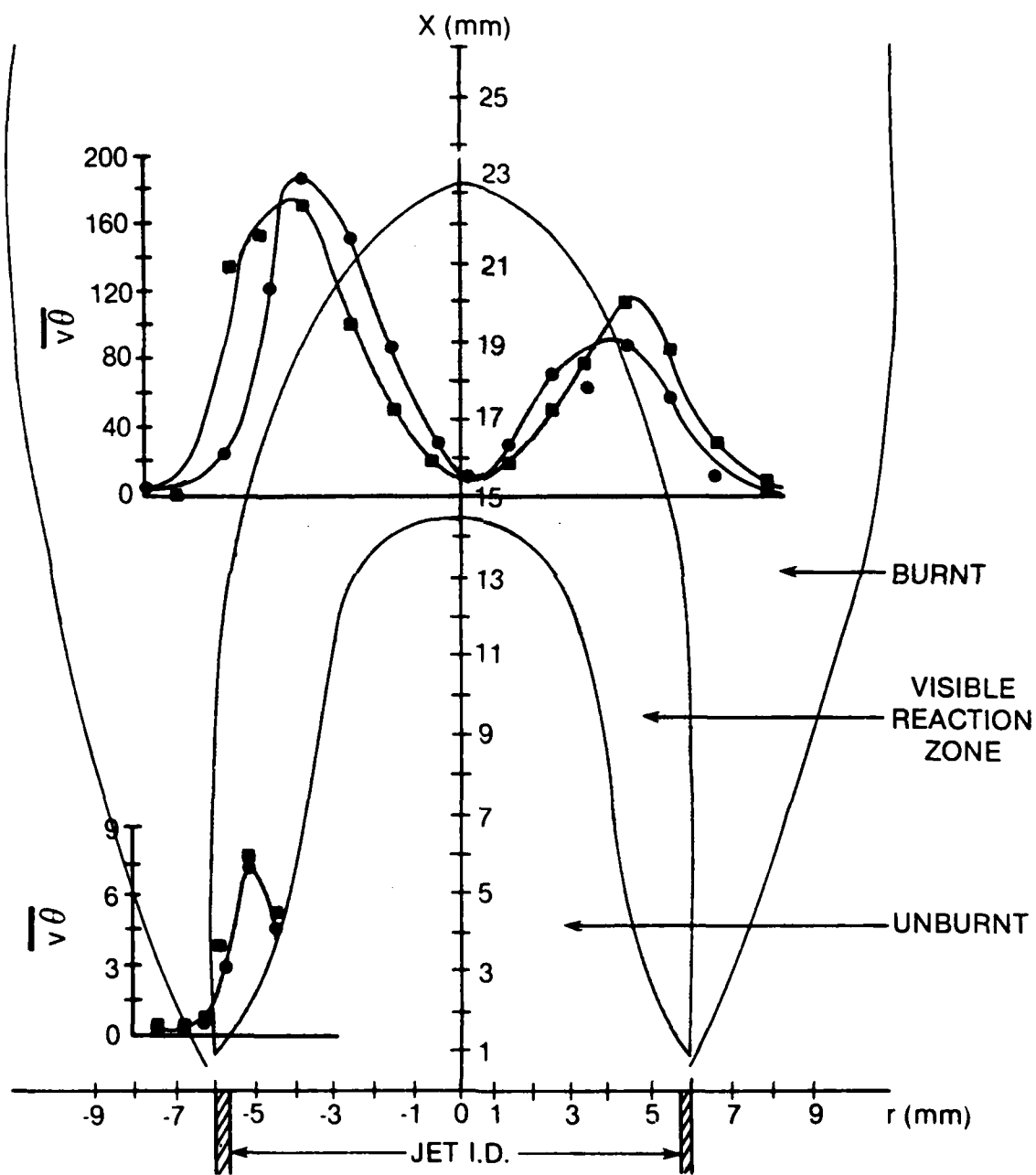


Figure 9

Section 3

HARDENED-CARS-SYSTEM DEVELOPMENT

A hardened CARS system was designed and constructed to perform diagnostics in the AFWAL Room 20 Combustor Test Facility. The initial system was designed to perform temperature and species-concentration measurements on a single molecular species. A complete description of this system and its characterization is contained in a paper entitled, "A Hardened CARS System for Temperature and Species Concentration Measurements in Practical Combustion Environments," which follows.

The capability of the original hardened system was greatly expanded by the replacement of the original dye amplifier by a second dye laser. This provided the capability of simultaneous determination of two species concentrations, in particular, nitrogen and oxygen. The system was further modified to incorporate a dynamic-range-enhancement scheme.²¹ This modification extended the limited linear operating range of the DARSS detector sufficiently to accommodate the intensity fluctuations found in turbulent combustion environments.

After initial checkout and calibration of the basic system, an extensive software development effort was initiated. The most fundamental routines developed for the acquisition and maintenance of the hardened-system data are listed in Table II.

TABLE II

HARDENED-CARS-SYSTEM SOFTWARE

PROGRAM NAME	DESCRIPTION
SPCGEN	"SPC Generate" generates a library of calculated spectral data and stores this information on disk partition SPC.
SPCRED	"SPC Read" reads and displays calculated spectral data.
SPCSUM	"SPC Summary" prints a summary of several important parameters calculated by SPCGEN.
DATAKE	"Data Take" acquires experimental data and stores on either tape or disk.
REDUCE	"Reduce" reduces experimental data to temperatures and concentrations and creates a library of reduced data on disk.
REDATA	"Read Data" reads and prints either experimental or reduced data.
LIBXFR	"Library Transfer" transfers the reduced data library created on disk to permanent storage on magnetic tape.

TABLE II (Continued)

PROGRAM NAME	DESCRIPTION
LIBPLT	"Library Plot" searches library data on either disk or tape for date, time, and position and plots the PDF's and profiles of temperature and N ₂ and O ₂ concentrations.
PMTDTA	"Photomultiplier Data" provides set-up displays for integrated-intensity measurements and also provides quick-look temperature and concentration determinations.
SPCELM	"SPC Elements" generates a library of spectral elements from which spectra can be created to provide compensation for nonresonant background contributions.
REDELM	"Read Elements" reads and displays spectra stored by SPCELM.
REDUSE	"Reduce" reduces experimental data to temperatures and concentrations through the use of the spectral elements of SPCELM to compensate for nonresonant background effects.

A hardened CARS system for temperature and species-concentration measurements in practical combustion environments^a

G. L. Switzer and L. P. Goss

Systems Research Laboratories, Incorporated, 2800 Indian Ripple Road, Dayton, Ohio 45440-3696

A system employing the technique of Coherent Anti-Stokes Raman Spectroscopy (CARS) has been constructed to permit non-intrusive combustion diagnostics in the harsh environment of practical combustion systems. Features incorporated in the system design include the capability of obtaining simultaneous temperature and concentration information on multiple gas species, temporally resolved true time-averaged data at rates of up to 20 Hz, and high spatial resolution within the sampled volume. In order to handle the potentially large number of CARS optical signals economically, optical fibers are employed to accomplish a parallel-to-serial conversion of the light pulses between the hardened optical system and a remotely situated spectrometer/detector combination. A description of the system and its capabilities is presented along with a quantitative description of such parameters as measurement accuracy, precision, and spatial resolution.

INTRODUCTION

The potential of the coherent anti-Stokes Raman spectroscopy (CARS) technique for non-perturbing optical diagnostics in practical combustion media has continued to develop over the past few years.¹⁻⁴ At the Air Force Wright Aeronautical Laboratories/Aero Propulsion Laboratory, a program contributing to this development has been directed toward employing the CARS technique to obtain temperature and number-density information in the harsh environment produced by simulated practical combustors. Experiments conducted early in this program with a ruby-laser-based collinear optical system operating at 1 Hz⁵ demonstrated the ability of a CARS system to perform reliably in such hostile environments. Data from these initial experiments indicated that improvements in the CARS-diagnostic-system capabilities were needed. For these improvements a system capable of high spatial resolution was required to provide more spatially precise single-shot simultaneous temperature and number-density data as well as higher repetition rates. With higher repetition rates, sufficient data could be obtained in a short period of time to allow true time-averaged measurements of these quantities to be developed from their probability distribution functions (pdf's).

This paper contains a description of an environmentally hardened CARS system constructed to incorporate those improvements which were suggested by earlier experimentation. Among other improvements to system performance, the system design has been extended to include the capability of performing temperature and number-density measurements simultaneously on more than one gas species. The results of measurements performed during the initial check-out of this system in the laboratory are presented to give an indication of the precision and accuracy of which the system is presently capable.

OPTICAL-SYSTEM CONFIGURATION

The hardened CARS system is based upon a Quanta-Ray DCRIA frequency-doubled neodymium-YAG laser (which has a maximum repetition rate of 20 Hz) and a folded BOXCAR⁶⁻⁷ optical configuration which permits very high spatial resolution. The optical layout of the system is shown schematically in Fig. 1 and can be traced as follows. The Quanta-Ray laser is supported above a 1.2 m x 1.83 m Newport Research Corp. breadboard table top. Its 532-nm (green) output is folded down by periscope P1 to an optic plane 7.6 cm above the table. Approximately 50% of the nominally 185 mJ of green output is passed through beam splitter BS1 and focused by lens DL1. This focused beam is split in half by beam splitter BS2. The portion reflected from BS2 is used

for optical pumping of dye cell DC1 which, combined with mirrors DM1 and DM2, forms a broad-band (150 cm⁻¹), concentration-tuned dye-laser oscillator. The remaining green pump energy transmitted through BS2 is used to pump dye cell DC2 for dye-laser amplification (optionally, the energy used to pump the amplifier can be diverted and used to drive a second-frequency dye oscillator for multiple-species operation). The Stokes-radiation beam thus produced passes through a beam-expander telescope formed by dye lenses DL2 and DL3 in order that its divergence may be adjusted to produce a coincident focus of the dye and green beams in the sample volume.

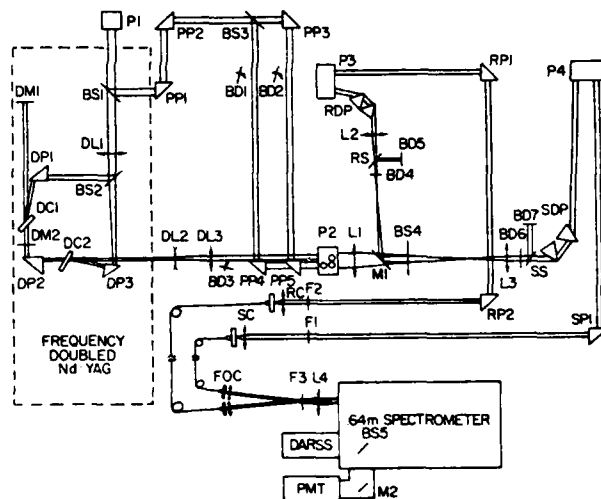


FIG. 1. CARS-Optical-System Schematic.

The remaining green beam, formed from the 50% of the input energy reflected from beam splitter BS1, is split in half by beam splitter BS3 after passing through a delay-equalization path formed by pump prisms PP1 and PP2 to compensate for a delay experienced in the dye-laser geometry. The beam reflected at BS3 is passed parallel to the table toward pump prism PP4. The transmitted portion reflected by PP3 is inclined such that as it leaves prism PP5, it is vertically aligned with--but displaced 2.5 cm below--the green beam leaving PP4. It is this separation of the two green "pump" beams which forms the basis for the

BOXCARS⁸ configuration. The dye-laser beam is made parallel and coplanar with the pump beam from prism PP4 but separated horizontally by 1 cm, causing the formation of the folded BOXCARS geometry.

The three-beam configuration thus formed is elevated to a height of 38 cm by periscope P2 which consists of a 50-mm right-angle prism on the bottom and two 25-mm prisms on the top. One of the upper prisms controls the pointing of the pump and dye pair, while the other directs the single pump beam toward a 10-cm-diam., 50-cm-focal-length lens L1. Since the upper two prisms on periscope P2 are independently adjustable in their vertical separation, the CARS geometry is continuously adjustable from collinear (with properly reconfigured dye placement) to BOXCARS with a maximum crossing full angle of ≈ 10 deg. The three beams converge from L1 through beam splitter BS4 toward a sample volume located midway between BS4 and a 7.6-cm-diam., 40-cm-focal-length collimating lens L3. The spacing of the components BS4 and L3 is such that the sampled volume can be scanned ± 1 cm about the center of a 47-cm-diam. combustion tunnel. After collimation at L3, most of the green and dye energies are absorbed in beam dumps BD6 and BD7. The anti-Stokes signals generated in the sample volume are spatially separated from any remaining green light by passing them through sample-dispersing prisms SDP. After dispersion, separation of spectral components takes place over a 3-m path traversing periscope P4, sample prism SP1, and neutral-density filter F1; and, finally, the anti-Stokes energy is focused onto a 200- μ m-diam. fused-silica fiber-optic waveguide by the numerical-aperture-matching sample-collection optic SC.

In order to compensate for fluctuation in the CARS signals caused by laser-power fluctuations or slight beam misalignments, a parallel referencing scheme is employed. The medium in which the reference signal is generated is controlled to produce either a resonant or a nonresonant CARS signal, depending upon whether integrated intensity or spectral normalization of the sample signal is desired. This reference leg begins with the 15% energy reflection from beam splitter BS4. A description similar to that given for the operations performed in the sample beam path can be given for the reference leg ending with the signal being focused into a reference fiber by the collection optic RC.

The lengths of the sample and reference fiber-optic waveguides are critical to overall system operation and are determined using two criteria. First, in order to minimize environmental effects found in practical combustion situations upon the sensitive optical detectors, the spectrometer and detectors are separated from the optical system and operated in a controlled environment. To accomplish this separation, a minimum of 20 m of fiber optics is presently required. Second, for reasons to be discussed in conjunction with the data-collection electronics, the reference fiber optic is made 20 m (≈ 100 -ns optical transit time) longer than the sample. The diameter of these fibers (200 μ m) also has an impact upon system performance. Since the CARS signals transmitted through the fibers lose their spatial coherence, the degree to which these signals can be refocused upon the detectors is limited to a minimum which is the fiber diameter, resulting in lowered system spectral resolution.

Upon exiting the optical fibers, the sample and reference beams are collected by fiber-optic collimators FOC, pass through band-pass filter F3, and are focused in a horizontal plane by the f-number (F/5.2) matching lens L4. The parallel beams pass through the horizontal entrance slit of an Instruments SA HR-640 spectrometer, and their spectral contents are imaged at separate locations upon a Tracor Northern TN-1710 DARSS system detector head. Beam splitter BS5 directs 30% of the CARS signals into an EMI D551 photomultiplier tube which is employed for performing integrated intensity measurements.

The input-optics platform to the spectrometer which contains the fiber-optic collimators FOC, filter F3, and lens L4 also contains a system feature which

greatly improves the available dynamic range of the multichannel detection system. The usable, linear dynamic range of the DARSS system for the short-pulsed optical phenomena being studied has been measured to be ≈ 20 . In order to extend this factor to the order of at least 300, which can be anticipated in a turbulent combustion environment, the sample CARS signal may be split after being collimated into two, three, or more different proportions. These beams are then displaced across the DARSS detector as described previously. The largest portion of the sample beam is monitored for the highest temperature indications, and the weakest split is adjusted to permit observation of the coolest temperatures present. Thus, with the proper selection of splitting ratios, one of the multiple signals will be located within the usable linear range of the DARSS at all available temperatures.

The optical system—with the exception of the spectrometer and detectors—is enclosed by a lightweight protective cover which provides isolation from acoustic vibrations, thermal gradients, and atmospheric dust. The NRC honeycomb table top is supported on pneumatic casters which allows the system to be easily transported.

DATA-COLLECTION ELECTRONICS

Once the sample and reference CARS optical signals have been converted by the detectors, the data are conditioned, collected, and stored for subsequent analysis by the data-collection electronics outlined in Fig. 2. The spectral information obtained by the Diode Array Rapid Scan Spectrometer (DARSS) is digitized by the Tracor Northern 1710 Multichannel Analyzer System. The 512 channels of data produced are then transferred via computer-interfacing circuitry to a Modular Computer Systems (MODCOMP) 7840 Classic Series Computer where permanent storage is provided on 10-MByte disks. Machine-language software has been developed for the PDP-11 based Tracor system which controls and synchronizes the firing of the laser, handshaking with the MODCOMP computer, and integrated as well as spectral-data transfer. The data transfer is accomplished within 15 msec, allowing ample time for DARSS signal integration during normal 10-Hz (100-msec) operation.

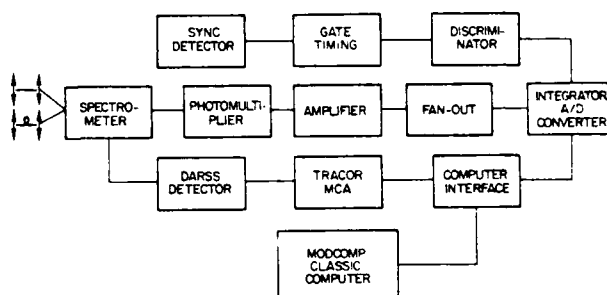


FIG. 2. Signal-Detection and Data-Collection Electronics Configuration.

All integrated intensity information is obtained by the common photomultiplier tube and is processed in a serial fashion. This feature is made possible by a parallel-to-serial conversion in the ≈ 10 -nsec FWHM CARS optical pulses arriving at the detector. That is, since the reference fiber optic is made 20 m longer than the sample, the reference signal arrives at the PMT ≈ 100 -nsec after the sample signal. The series of pulses thus formed can be amplified and is then duplicated by a LeCroy Research Systems Model 428F Linear FAN-OUT. The duplicated signal trains are applied to separate analog inputs of a LeCroy 2249SG 12-Channel Analog-to-Digital Converter (ADC). A PIN diode detector

sensing the green output of the laser synchronizes the generation of a series of properly timed and spaced gate signals which are applied to gate inputs on the ADC. Since each channel of the ADC must be gated into operation, the time of arrival of a gate pulse determines which signal of the analog input pulse train will be digitized in a given ADC channel. Once the integrated data have been digitized, they are passed via the computer interface to MODCOMP disc storage. For the six channels of data presently employed, the digitization-plus-transfer cycle is accomplished within 100 μ sec.

Although the system description to this point has been concerned with only two signals—one sample and one reference—the capability exists for up to six different optical inputs to be integrated and digitized in the manner described. Thus, optical inputs for up to three molecular species (three sample plus three reference signals) can be accommodated. The likelihood of performing simultaneous multiple-species measurements is increased due to the factor of ≈ 100 increase in sensitivity gained by use of photomultiplier rather than DARSS detection. Since it is only necessary to employ the DARSS detector in order to obtain spectral information on one species (e.g., nitrogen) for temperature determination, much weaker signals will suffice to furnish simultaneous multiple-species number-density information. Thus, the increased PMT sensitivity can be employed to offset the power requirements imposed on the additional Stokes lasers (and ultimately the Nd:YAG laser) which must be configured into the optical system.

SYSTEM-PERFORMANCE CHARACTERIZATION

A series of controlled experiments was conducted in order to characterize the CARS-system measurement capabilities. For this initial measurement program, the following system configuration and parameters were employed. Laser operation was at 10 Hz, with a 10-nsec FWHM pulse width. A single species (nitrogen) was observed to obtain simultaneous temperature and number-density information. A folded BOXCARS optical geometry defined by an 8.7-deg. full angle between the green beams and the dye beam which lies at 1.5 deg. to their plane was employed to obtain near-maximum spatial resolution. An ambient-air reference, producing resonant nitrogen CARS signals, was used for normalization of the integrated-intensity data only (i.e., no spectral normalization was employed). The spectral dispersion on the DARSS detector was measured to be 2.7 cm^{-1} /channel, contributing to an overall system spectral resolution of 7.2 cm^{-1} . Intensifier gating of the DARSS detector was employed for a period of 10 μ sec.

The following experiment was performed in order to characterize the spatial resolution of the system which can be expected at operational beam-energy densities. A "slab" of nitrogen gas was formed from a 3-cm-long nozzle having a rectangular cross section of 0.27 mm \times 10.9 mm. The tip of the nozzle was located 2.4 mm below the sample volume, and the slab was translated along the optic axis through the common foci of the CARS beams in such a way that the beams passed through the thinnest dimension of the slab. The effect of passing the pure nitrogen through the sample volume was enhanced by applying a continuous purge of helium to the focal area to remove the contribution of atmospheric nitrogen from the measurement. The result of this experiment is shown in Fig. 3. These data indicate that $> 97\%$ of the CARS signal is generated within a 2-mm path along the optic axis. A similar data set, obtained by rotating the nozzle 90 deg. and translating the thin dimension of the slab perpendicular to the optic axis through the common foci, indicated that $> 98\%$ of the signal generation is obtained within 0.8 mm. Assuming symmetry in the transverse dimensions, these numbers suggest a sample volume on the order of $\approx 1.3 \text{ mm}^3$. It is, however, important to note that these measured dimensions, which describe the spatial resolution of this geometry, were possibly affected by such factors

as the alignment of the slab to the optic axis or a thickening of the nitrogen slab beyond 0.27 mm as the gas exited the nozzle. For these reasons the indicated dimensions should be considered as maximum values only, until a more precise measurement scheme can be designed.

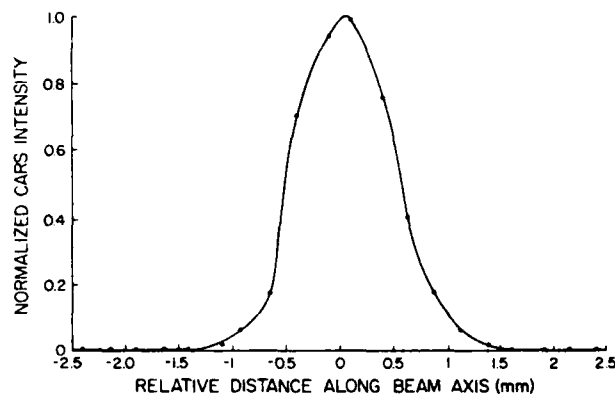


FIG. 3. Axial Distribution of CARS Generation through Sample Volume.

An indication of the CARS system capability to determine molecular concentration at room temperature is given in Table I. This table contains the results of nitrogen-concentration measurements (based upon integrated-intensity data and the Ideal Gas Law) performed on a sample cell filled to 1 atm. pressure at 294 K with the stated proportions of nitrogen in oxygen. The measured concentrations represent the average of up to 10 groups of 40 single-shot concentration determinations each. The precision of these measurements (defined by one standard deviation) reflects the $\approx 5\%$ shot-to-shot intensity fluctuations experienced in the CARS signals after normalization. Although the measured concentration values in Table I agree with the mixed values well within the stated margins of error, it is believed that the noticeable decrease in accuracy (defined by $1 - |\text{mixed-measured}|/\text{mixed}$) experienced in the 10% measurement is caused by the onset of background, non-resonant CARS contributions from oxygen. This effect could be reduced by employing a form of background reduction.⁹

TABLE I

AMBIENT-TEMPERATURE N_2 -CONCENTRATION MEASUREMENT ACCURACY

SAMPLE MIXTURE (N_2 IN $\text{O}_2 \pm 1.5\%$) (%)	MEASUREMENT		
	CONCENTRATION (%)	PRECISION (\pm) (%)	ACCURACY (%)
80	77.8	3.7	97
60	59.3	3.0	98
40	39.0	2.1	98
20	20.6	1.1	97
10	11.2	0.6	89

Although the folded BOXCARS configuration provides excellent spatial resolution, it has the disadvantage of being a less efficient CARS generator than planar BOXCARS. The effect of this geometry upon signal strength is quite pronounced at the large beam-crossing angles employed in this system. However, as indicated by the spectrum in Fig. 4 (a 2014-K spectrum with a ± 40 -K fitting error estimated from the degree to which a nonlinear least-squares fitting routine¹⁰ could match

calculated spectrum to the measured data obtained in a premixed propane flame), there is sufficient signal-generation capability to permit observation of the temperatures that can be expected from the combustion of most common fuels.

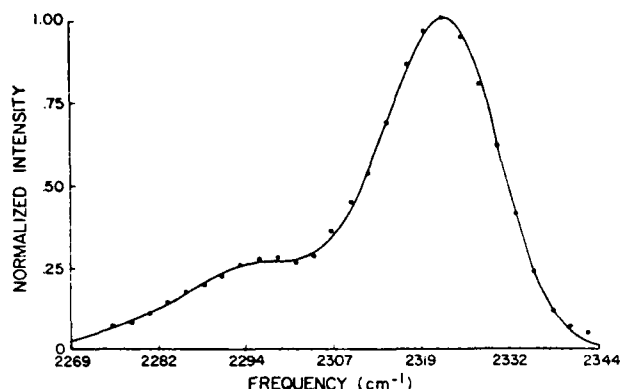


FIG. 4. Single-Shot N_2 Spectrum in Premixed Propane Flame, 2014 ± 40 K. Calculated (-), Experimental (·).

To obtain a measure of accuracy in simultaneous temperature and number-density determinations, a simple "hot-air" furnace was constructed. The furnace, consisting of a 2.5-cm-i.d. \times 20-cm-long stainless-steel tube, was supported above a 10-cm-long premixed propane flame and centered on the CARS sample volume. The ends of the tube extended sufficiently beyond the combustion region that no combustion products (or effects other than temperature) would influence the CARS signals produced. A chromel-alumel thermocouple placed within 2 mm of the sample volume indicated a furnace temperature of 965 K with drifts of ± 10 K. Based upon this average temperature and assuming only a $1/T$ density dependence, the nitrogen number density sampled would be $\approx 5.94 \times 10^{18}$ molecules/cm³. While the thermocouple was monitoring the furnace temperature, data for 1,000 single-shot CARS measurements were recorded. Figure 5 is an example of the single-shot spectra obtained during this experiment. The pdf's

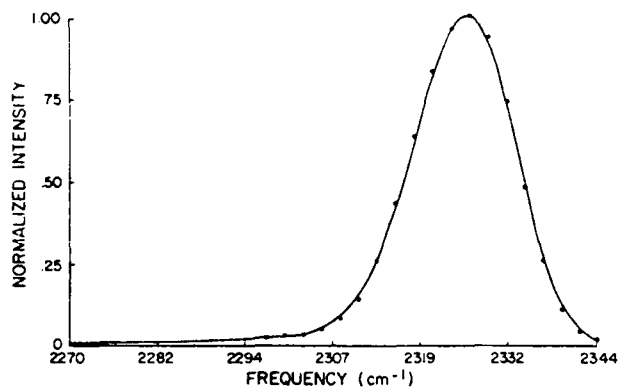


FIG. 5. N_2 Spectrum from Hot-Air Furnace, 980 ± 35 K. Calculated (-), Experimental (·).

developed from these 1,000 samples for furnace temperature and number density are shown in Figs. 6 and 7, respectively. They indicate a CARS-derived mean

temperature of 894 K with a standard deviation of ± 60.9 K ($\pm 7.5\%$) and a mean number density of 6.12×10^{18} molecules/cm³ with a standard deviation of $\pm 0.54 \times 10^{18}$ molecules/cm³ ($\pm 8.8\%$). The marginal agreement between the thermocouple and CARS temperatures suggests the possibility of systematic error in some measured parameter. It is believed that this error will be greatly reduced by refining the determination of such parameters as the system spectral resolution (which influences the shape of the calculated spectra); such refinements will come about through further testing and calibration. However, by comparing the averaged quantities of the thermocouple and CARS data, a measurement accuracy of $\approx 92.6\%$ for temperature and $\approx 97.1\%$ for number density was indicated in these preliminary measurements.

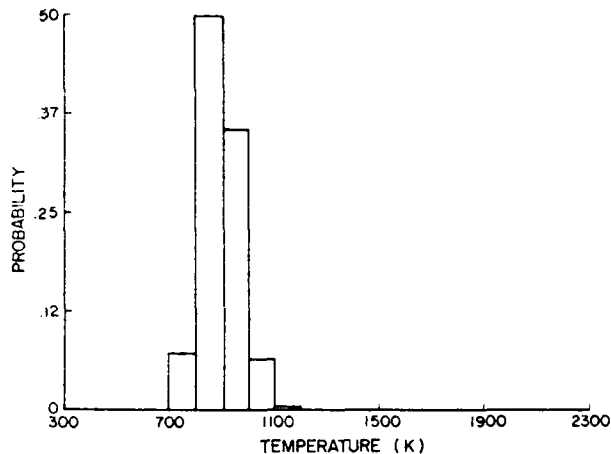


FIG. 6. Probability Distribution Function for Hot-Air-Furnace Temperature.

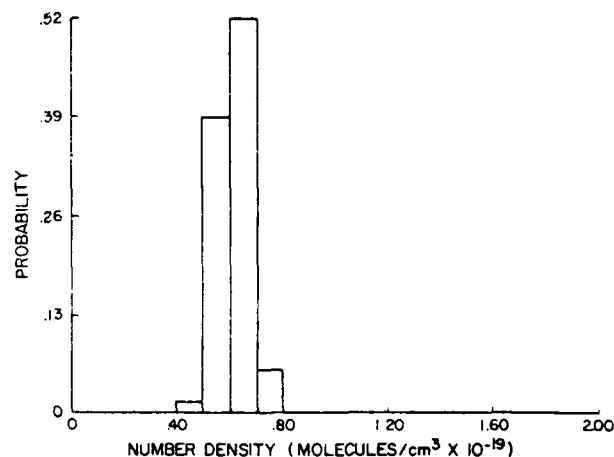


FIG. 7. Probability Distribution Function for Hot-Air-Furnace N_2 Density.

CONCLUSIONS

The ability of the hardened CARS optical diagnostic system described here to perform simultaneous temperature and number-density measurements on a single gas species with a high degree of spatial and temporal resolution has been demonstrated in the laboratory. System performance obtained during these measurements

indicates the capability of the system in obtaining simultaneous multiple-species CARS information in the environments presented by practical combustion systems. Implementation and demonstration of this and the additional system capabilities that have been described are planned.

Although the determinations of measurement accuracy and precision presented here were not intended to be rigorous or exhaustive, it is felt that they do support a high level of confidence in the ability of the CARS technique to provide valuable diagnostic information on combustion processes.

REFERENCES

- a) Work sponsored by Air Force Wright Aeronautical Laboratories Aero Propulsion Laboratory under Contract F33615-80-C-2054.
1. G. L. Switzer, W. M. Roquemore, R. B. Bradley, P. W. Schreiber, and W. B. Roh, "CARS Measurements in a Bluff-Body Stabilized Diffusion Flame," *Appl. Opt.* 18, 2343 (1979).
2. A. C. Eckbreth, "CARS Thermometry in Practical Combustors," *Comb. Flame* 39, 133 (1980).
3. B. Attal, M. Paelat, and J-P Taran, "CARS Diagnostics of Combustion," *J. Energy* 4, 135 (May-June 1980).
4. I. A. Stenhouse, D. R. Williams, J. E. Cole, and M. D. Swords, "CARS Measurements in an Internal Combustion Engine," *Appl. Opt.* 18, 3819 (1979).
5. G. L. Switzer, L. P. Goss, W. M. Roquemore, R. P. Bradley, P. W. Schreiber, and W. B. Roh, "Application of CARS to Simulated Practical Combustion Systems," *J. Energy* 4, 209 (1980).
6. Y. Prior, "Three-Dimensional Phase Matching in Four-Wave Mixing," *Appl. Opt.* 19, 1741 (1980).
7. J. A. Shirley, R. J. Hall, and A. C. Eckbreth, "Folded BOXCARS for Rotational Raman Studies," *Opt. Lett.* 5, 380 (1980).
8. A. C. Eckbreth, "BOXCARS: Crossed-Beam-Phase-Matched CARS Generation in Gases," *Appl. Phys. Lett.* 32, 421 (1978).
9. L. A. Rahn, L. J. Zych, and P. L. Mattern, "Background-Free CARS Studies of Carbon Monoxide in a Flame," *Opt. Comm.* 30, 249 (1979).
10. L. P. Goss, G. L. Switzer, and P. W. Schreiber, "Flame Studies with the Coherent Anti-Stokes Raman Spectroscopy Technique," Paper No. AIAA-80-1543 presented at the 15th AIAA Thermophysics Conference, Snowmass, CO, 14-16 July 1980.

The completed two-species hardened system was installed in the combustor test facility, and a checkout and measurement program was carried out. During system checkout in the tunnel, problems with thermally induced drifting in the Quanta-Ray Nd:YAG laser Q-switch and harmonic generator as well as with tunnel window damage caused by the high-power-density laser beams were encountered and corrected. After successful demonstration of system operation during the checkout phase, the hardened system was employed to profile the combustion environment at distances greater than 40 cm downstream of the bluff-body combustor. Although CARS temperature information obtained as a result of these measurements compared quite favorably with thermocouple data, the concentration data obtained with the CARS system were found to be unreliable.

The capability of obtaining flame luminosity data simultaneously with the CARS data was added to the hardened system, and another series of measurements was performed. The experiments performed during both of these programs and the results obtained are reported in a paper entitled, "Simultaneous CARS and Luminosity Measurements in a Bluff-Body Combustor," which follows.

AIAA'83

AIAA-83-1481

**Simultaneous CARS and Luminosity
Measurements in a Bluff-Body Combustor**

G.L. Switzer, D.D. Trump, and L.P. Goss,
Systems Research Laboratories, Inc., Dayton,
OH 45440-3696; and W.M. Roquemore,
R.P. Bradley, J.S. Stutrud, and C.M. Reeves,
Air Force Wright Aeronautical Labs,
Wright-Patterson AFB, OH 45433

AIAA 18th Thermophysics Conference

June 1-3, 1983
Montreal, Canada

For permission to copy or republish, contact the American Institute of Aeronautics and Astronautics
1290 Avenue of the Americas, New York, NY 10104

SIMULTANEOUS CARS AND LUMINOSITY MEASUREMENTS IN A BLUFF-BODY COMBUSTOR

G. L. Switzer, D. D. Trump, and L. P. Goss
Systems Research Laboratories, Inc.
Dayton, OH 45440-3696

W. M. Roquemore, R. P. Bradley, J. S. Stutrud, and C. M. Reeves
Air Force Wright Aeronautical Laboratories
Aero Propulsion Laboratory
Wright-Patterson AFB, OH 45433

Abstract

High-speed ciné pictures of a diffusion flame stabilized by an axisymmetric, ducted bluff-body research combustor show that large-scale flame structures are formed downstream of the recirculation zone. These flame structures, referred to as flame turbules, are separated axially by non-luminous regions. Results of simultaneous temperature and flame-luminosity measurements in the region of these flame turbules are reported. The coherent anti-Stokes Raman spectroscopy (CARS) technique was used to make time and spatially resolved temperature measurements. Flame luminosity, along the line of sight passing through the CARS sampling volume, was recorded for each CARS measurement and used as a condition for sampling the CARS data. The characteristics of the flame turbules are interpreted in terms of the temperature probability distribution function (pdf). Temperature pdf's obtained at different axial and radial locations downstream of the recirculating zone and for different air- and fuel-flow rates are also presented.

Introduction

The Air Force Wright Aeronautical Laboratories/Aero Propulsion Laboratory is sponsoring a research program directed toward experimental evaluation and theoretical development of combustion models.¹ As part of this program, a large-scale research combustor has been developed which has a simple geometry and clean inlet conditions for modeling, provides good measurement access to the combustion zones, and yet has some of the features of practical combustion devices. Both conventional probes and advanced laser techniques are being developed to study combustion processes in this combustor. Experiments conducted early in this program with a ruby-laser-based collinear optical system operating at 1 Hz demonstrated the ability of a CARS system to operate in the hostile environment of the research combustor.^{2,3} These initial experiments also demonstrated the need to improve the spatial resolution of the CARS system and to increase the repetition rate of the measurements. This paper reports the results of initial checkout tests in the research combustor of a second-generation CARS system which has both an improved spatial resolution and a higher repetition rate. The time-averaged results of instantaneous CARS temperature measurements are compared with results obtained with a thermocouple in a parabolic flow region which was believed to be unperturbed by the presence of the thermocouple.

The flame in the research combustor is stabilized by the recirculation zone established by the bluff-body face of the combustor. High-speed ciné pictures show that large flame structures occur

*Work supported in part by USAF Contract F3315-80-2054.

downstream of the recirculation zone.⁴ These structures, denoted as flame turbules, are islands of flame surrounded by noncombusting regions and are believed to be the result of vortex shedding from the bluff-body.⁵ Flame luminosity-vs-time records have been used for studying the dynamic characteristics of these turbules⁴ and as a condition for sampling velocity data collected with a laser Doppler anemometer (LDA).⁶ The conditionally sampled data show that the mean axial velocity is significantly higher in the flame turbules than in the nonluminous regions. Experiments conducted with a small laboratory Meeker burner have demonstrated a technique which employs flame luminosity for conditional sampling of CARS data.⁷ The feasibility of using flame luminosity as a condition for sampling CARS temperature data taken in the research combustor downstream of the recirculation zone is examined in this paper. Also, the temperature pdf's at different axial and radial locations downstream of the recirculation zone are presented along with pdf's obtained under different air- and fuel-flow conditions of the combustor.

Experimental Set-Up

Combustion-Tunnel Facility

A schematic diagram of the axisymmetric bluff-centerbody research combustor in the combustion tunnel is shown in Fig. 1. The centerbody is 79 cm long and has a diameter (D) of 14 cm. Gaseous

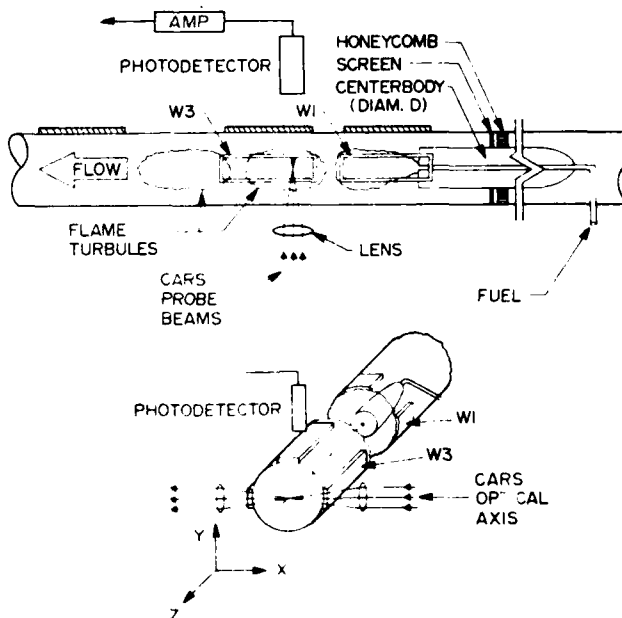


Figure 1. Schematic Diagram of the Combustor and the Optical Configuration Used to Make Simultaneous Flame-Luminosity and CARS-Temperature Measurements.

propane fuel is injected from the center of the bluff-body face through a 4.8-mm-diam. nozzle. The annular air is conditioned using a honeycomb flow straightener and screens. The centerbody is mounted in a 25.4-cm-diam. duct containing 30.5 by 7.6 cm viewing ports which provide optical and conventional probe access to combustion regions. Additional information on the combustion tunnel facility is given in Ref. 1.

Thermocouple Description

Average flame temperatures were measured by a shielded thermocouple probe for which the radiation losses (at the indicated temperatures) were assumed to be negligible. The thermocouple probe was mounted vertically through a special slide arrangement located on the top of the duct. This permitted access to axial regions covered by window W3 in Fig. 1 without causing significant disturbance in the flow. The probe housing is water cooled and has an outside diameter of 6.35 mm. The platinum sensing head of the probe is made in the form of a T which is rotated on its side, with the base of the T pointing upstream. A Type-R thermocouple is contained in a 4.76-mm-diam. shield that forms the base of the T. The shield is open on the upstream end, and bleed holes are provided downstream of the thermocouple junction to allow the gas to pass between the thermocouple and the shield. The T-shape design of the sensing head was adopted after experience showed that it tended to reduce the flow-interference effects of the probe. The Instrument Development Group at NASA Lewis Research Center designed and fabricated the probe using criteria derived from Ref. 8.

CARS System Description

Optical Configuration

The CARS system is based upon a frequency-doubled neodymium-YAG laser operating at a 10-Hz repetition rate and in a folded BOXCARS⁹ optical geometry. This combination allows high temporal [10-ns full width half maximum (FWHM)] and spatial (< 1 mm³) measurement resolution within the combustion medium. A detailed description of the basic optical configuration and design features of this system can be found elsewhere.¹⁰ Figure 2 is the optical schematic of the CARS system as configured

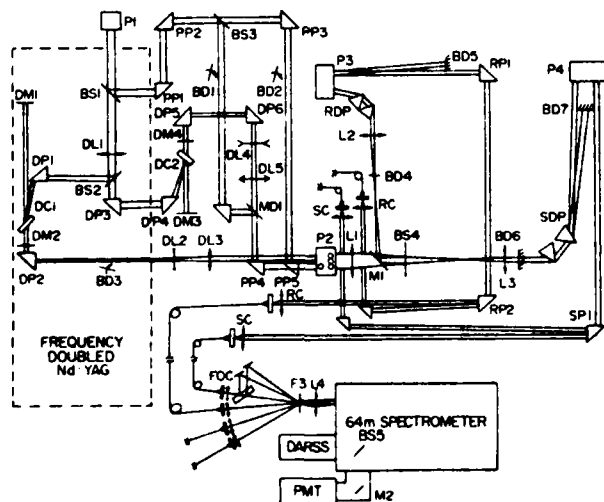


Figure 2. CARS Optical-System Schematic.

for these measurements to obtain simultaneous temperature and N₂- and O₂-concentration data. Two dye lasers, consisting of flowing dye cells DC1 and DC2 and their associated dichroic mirrors (DM1-4), produce the broadband (150 cm⁻¹ FWHM) Stokes radiation for N₂ and O₂, respectively. These two beams are combined with two equal-intensity beams of the 532-nm pump radiation, and the four beams are elevated via periscope P2. The CARS beams are then directed to form a folded BOXCARS geometry in which the pump beams converge at a full angle of ≈ 6 deg. and the N₂ and O₂ Stokes beams converge with full angles of 1.5 deg. and 0.5 deg., respectively, from the plane containing the pump beams. Anti-Stokes signals for both gas species are produced in the sample volume and also in a resonant CARS reference cell containing a mixture of N₂ and O₂. These reference signals are used for laser-power normalization. Sample and reference anti-Stokes signals are isolated by dispersing prisms SDP and RDP, respectively, and de-elevated by periscopes P4 and P3. The two pairs of signals are then focused into 200- μ m-diam. fiber-optic transmission lines by the sample- and reference-collection optics SC and RC.

The four CARS signals are transmitted through separate fiber-optic delay lines of varying lengths to a remotely situated spectrometer where each is detected and analyzed for spectral content by a diode array rapid scan spectrometer (DARSS) Reticon detector and for integrated intensity by a photomultiplier. In addition to the four beams transmitted by the fiber optics, two beams are generated as a result of splits of 1% and 10% of the N₂ sample beam before it enters the spectrometer. These two beams plus the remaining 89% of the N₂ sample CARS signal form the basis of a scheme to expand the dynamic range of the DARSS to the level necessary to accommodate the large signal fluctuation encountered in a dynamic environment.¹¹ The combined effects of the fiber-optic core diameter, the 1200 grooves/mm spectrometer grating, and the 50- μ m interchannel spacing of the DARSS construction contribute to a DARSS dispersion of 2.6 cm⁻¹/channel and an overall system resolution of 7.5 cm⁻¹ HWHM.

Data-Collection Electronics

Once the sample and reference CARS optical signals have been converted by the detectors, the data are collected and stored for subsequent analysis by the data-collection electronics outlined in Fig. 3. The spectral information obtained by the DARSS is digitized by the Tracor-Northern 1710 Multichannel Analyzer System. A single photomultiplier and gated analog-to-digital conversion provide integrated intensity information for each of the four CARS signals generated.

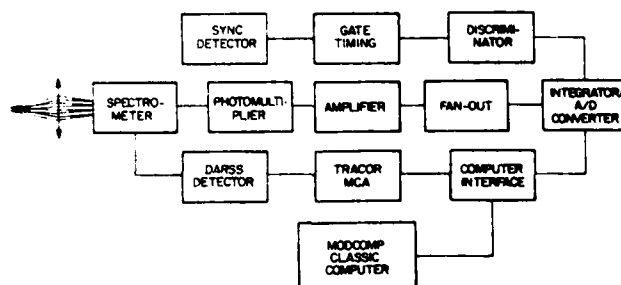


Figure 3. Signal-Detection and Data-Collection Electronics Configuration.

Data Reduction

The N_2 spectral information stored during acquisition is reduced with the aid of a computer program to arrive at a "best-fit" temperature. The reduction program incorporates a nonlinear least-squares fitting¹² routine which iteratively adjusts the frequency and temperature estimate of the experimental spectrum by comparing it to precalculated spectra from a library of N_2 spectra produced at various temperatures. Three such best-fit single-shot temperatures, representing three distinct ranges of temperatures encountered during the reported measurements, are illustrated in Fig. 4. Once the temperature determination has been made, the integrated intensities of the N_2 and O_2 CARS signals can be used to determine the concentration of these species present during the measurement pulse. However, for the purpose of this study, concentration measurements were not made.

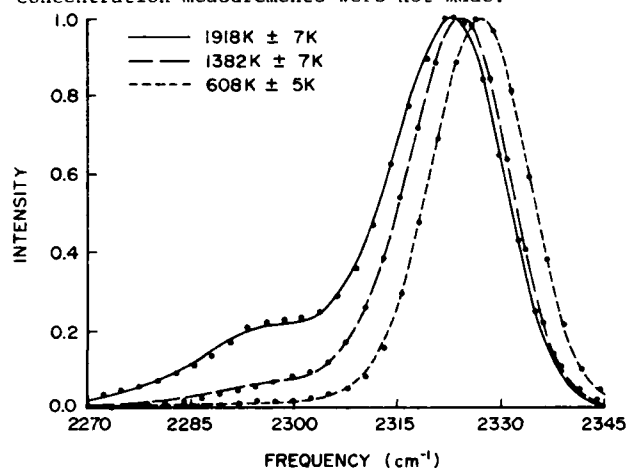


Figure 4. Best-Fit Temperature Results for Three Single-Shot N_2 Spectra. Experimental Data (+).

Luminosity-Data-Collection System

The luminous emissions from the combustor gases were monitored through the use of an EG&G UV-100B photodiode. As indicated in Fig. 1, the diode, a collecting lens, and a field stop were positioned normal to the CARS optical axis and approximately 10 cm above the sampled volume. This configuration collected light emitted from within a 1.1-deg. half-angle cone of view, resulting in a cross sectional diameter of 9 mm at the sample point.

Signals from the photodetector were amplified and selectively filtered by bandpass filters ranging in value from 100 Hz to 100 kHz. The amplified signal was digitized by a 0 to 10 V, 12-bit binary-coded-decimal (BCD), analog-to-digital converter being cycled at a 10-kHz rate by a free-running pulse generator. Each digitization of luminous intensity was accompanied by a 16-bit computer word containing the output of a 12-bit binary counter, which maintains a count of the CARS laser pulses, plus two additional bits—one to identify the word as a "count" word and the other to mark the "event" of a CARS measurement. The collection of luminosity data and laser shot number was accomplished continuously to yield a time history of flame luminosity (see Fig. 8). However, in order to reduce the large amount of disk storage

space required for continuous 10-kHz data acquisition, windowed-emission data collection was employed during most of this study. This mode of operation enabled emission-data acquisition only during a 5-ms window which opened symmetrically about the CARS measurement event and resulted in a factor-of-200 reduction in necessary disk storage space, thus allowing large sample sizes without sacrificing data pertinent to conditional sampling. The correlation between a given CARS measurement and the luminous emission during that measurement was accomplished through the laser-shot counter/event marker. That is, although the CARS and luminosity data-acquisition cycles proceed asynchronously, they are initiated from a common manual command. From the commencement of acquisition, synchronization of a CARS measurement to the coincident emission is accomplished through the laser-shot counter contained in each data stream.

One of the difficulties in interpreting the luminosity data was the determination of the signal level which represents the base line or zero flame emission. Depending upon such factors as amplifier gain, filter bandwidth, and the amount of scattered light, the photodiode base-line signal varied from 0 to ≈ 200 counts of the 999-count range of the three-digit BCD emission word. For the purpose of the conditional sampling of data presented in this paper, the dividing line between the presence and absence of flame was defined as the percentage of the maximum value of recorded emission above which the density of emission values decreased uniformly throughout the spectrum of observed temperatures.

Test Conditions

Experiments were conducted with the combustor operating under the various air- and fuel-flow conditions given in Tables I and II, respectively. The annulus-air and fuel-exit velocities for each experiment are given in the Results and Discussion Section. The combustor was operated at an ambient pressure of 0.98 bars. Measurements to determine

Table I.
Air-Flow Conditions

Air Flow	Inlet Temp.	Ann. Vel.	Duct Vel.	Air Re. No.*
(kg/s)	(K)	(m/s)	(m/s)	($\cdot 10^{-3}$)
0.50	294	11.6	8.2	0.76
1.00	294	23.3	16.4	1.52
1.50	294	34.9	24.6	2.27
2.00	294	46.6	32.8	3.02

*Calculated using duct velocity and centerbody diameter.

Table II.
Fuel-Flow Conditions

Fuel Flow	Inlet Temp.	Fuel Vel.	Fuel Tube Re. No.
(kg/hr)	(K)	(m/s)	($\cdot 10^{-4}$)
6.0	400	69.6	4.20
8.0	391	91.0	5.71
10.0	382	110.8	7.29
12.0	378	141.4	9.50
14.0	366	168.1	11.9

the optimum sample size for the combustion environments examined indicated that although the average of the temperatures measured did not change significantly after 500 samples, their pdf's became stable only after approximately 1500 samples. Thus, the CARS data presented are the result of more than 1500 individual measurements.

Results and Discussion

Comparison of CARS and Thermocouple Measurements

To establish the reliability of the CARS temperature measurements, comparisons were made between the CARS and thermocouple-derived radial and axial temperature profiles. Figure 5 presents a comparison (at an axial position of $Z/D = 2.86$) of the

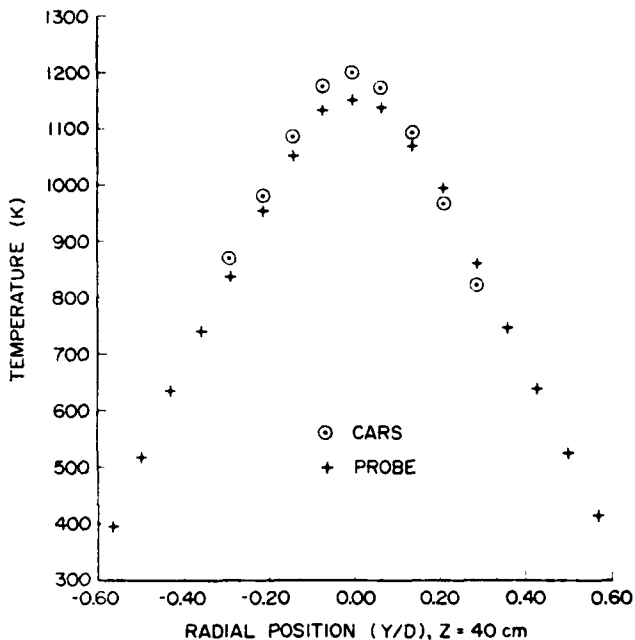


Figure 5. Comparisons of CARS and Thermocouple Radial Temperature Profiles at an Axial Location of 40 cm (2.86D) for an Annulus-Air Velocity of 23.3 m/s and a Fuel-Exit Velocity of 69.6 m/s.

average CARS temperature profile obtained along an X-axis radial scan and the average thermocouple-indicated temperature profile obtained on a Y-axis radial scan. This plot indicates not only that the temperatures obtained by the two methods agree, well within an anticipated $\approx 10\%$ precision of the CARS measurements in the indicated temperature range, but also that the combustion process is proceeding on a time-averaged basis symmetrically about the tunnel axis. The centerline average-temperature profiles compared in Fig. 6 also show quite good agreement between the two methods.

Ciné Pictures

The radial and axial profiles of average temperature given in Figs. 5 and 6 are well-behaved functions and appear to be similar to those measured in

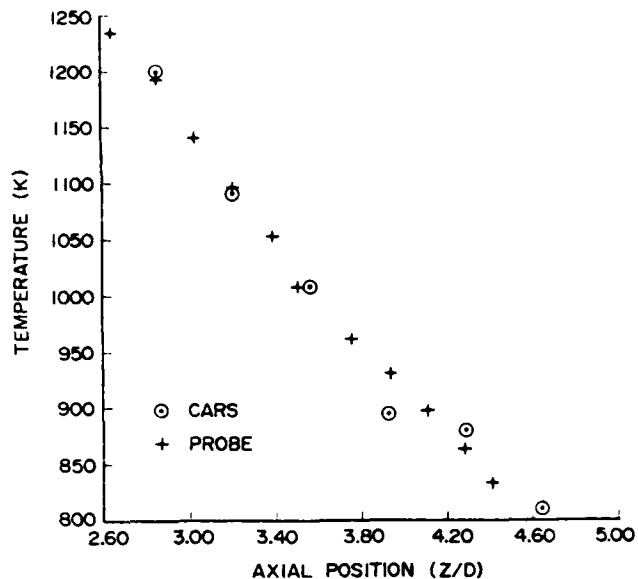


Figure 6. Comparisons of CARS and Thermocouple Centerline Axial Temperature Profiles for an Annulus-Air Velocity of 23.3 m/s and a Fuel-Exit Velocity of 69.6 m/s.

many non-recirculating combustor flows. Unfortunately, such profiles do not provide clear insight into the underlying, more basic dynamic processes that give rise to the time-averaged results. A view of the dynamic process responsible for the time-averaged profiles is shown in the high-speed ciné pictures in Fig. 7. The color ciné pictures were made at a rate of 500 frames/s; however, only every other frame is presented in the figure to illustrate the pertinent flame structures. The recirculation zone established behind the bluff-body was confined to the region viewed through window W1 (see Fig. 1). The time-averaged temperature profiles in Figs. 5 and 6 were made downstream of the recirculation zone in the region viewed through window W3. This region was characterized by large flame structures (flame turbules) as shown between locations 3D and 5D in Fig. 7(k) and small flame structures as at 3D in Fig. 7(f). The large structures can maintain their identity over many centerbody diameters downstream. The bright part of the flame was due to blackbody radiation of soot particles which show up on the color photographs as yellow. Sometimes, blue flames, which were free of soot particles, were observed in Window W3. Such small blue-flame structures exist at the axial locations 3D and 4D in the original color photographs for Figs. 7(a) and 7(b), but they are barely noticeable on the black-and-white frames. Careful study of the high-speed ciné pictures shows that the flame turbules formed downstream of the recirculation zone were often the direct result of toroidal vortices being shed from the bluff-body.⁵ At times, the flame turbules were actually shed vortices that had picked up burning fuel near the end of the recirculation zone as they moved downstream. Figure 7 shows that the average temperatures obtained in this flame are the result of a combination of various-size flame structures and the interconnecting noncombusting regions which alternately pass through the measurement location.

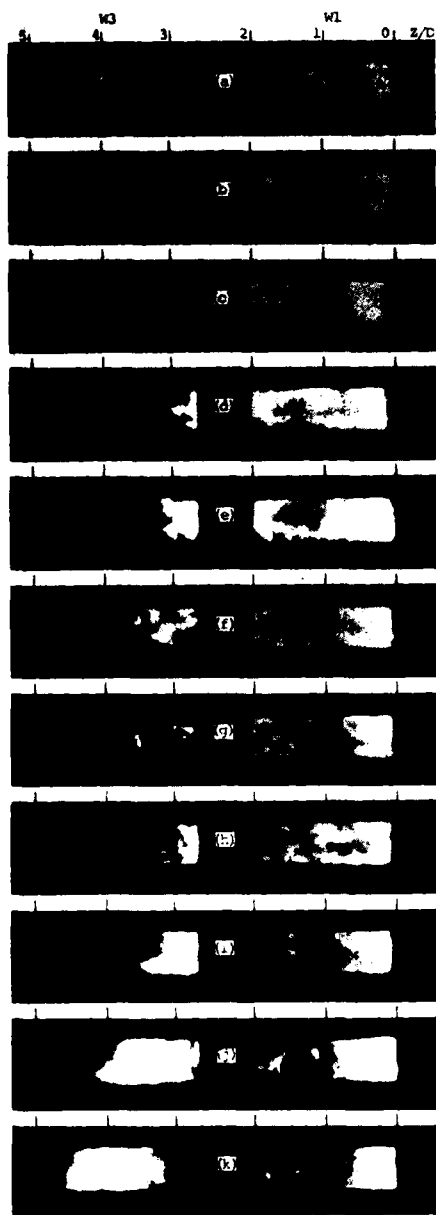


Figure 7. High-Speed (500 Frames/s) Ciné Photographs of the Flame for an Annulus-Air Velocity of 23.3 m/s and a Fuel-Exit Velocity of 69.6 m/s. Alternate frames are shown.

Flame Luminosity

Figure 8 is an intensity-vs-time trace of flame luminosity recorded at an axial location of 40 cm (2.86D) by the emission photodiode. The temporal relation of the CARS measurement event and flame luminosity is indicated by the marker within this 102.4-ms emission data sample. A flame turbule can be identified by the electrical pulse that is produced as the turbule is convected past the field-of-view of the photodetector. The non-luminous

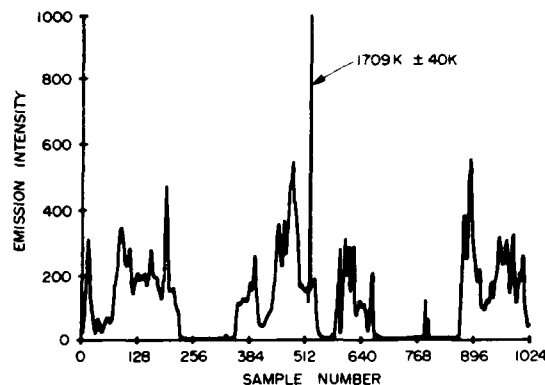


Figure 8. Continuously Sampled (10-kHz) Flame-Luminosity Data at an Axial Location of 40 cm (2.86D) for an Annulus-Air Velocity of 23.3 m/s and a Fuel-Exit Velocity of 69.6 m/s. The labeled marker indicates a CARS measurement event.

regions between the flame turbules are clearly evident from the constant voltage regions between the pulses. It should be noted that although the spectral sensitivity of the photodiode extends from 350 to 1000 nm, it is possible that comparatively low intensity emission (e.g., blue flame) could be indistinguishable from the background-emission noise level. The different time widths noted in Fig. 8 are due to the different sizes or velocities of the turbules. The high-frequency fluctuations riding on some of the pulses may be due to the small flame structures shown in Figs. 7(e) to 7(g). These small structures are close together and are moving with the same velocity as the larger flame turbule, thus possibly producing high-frequency luminosity fluctuations.

PDF Variation with Axial Location

A Lagrangian description of the dynamic processes shown in Fig. 7 seems appropriate in that the downstream motion of the flame and nonflame regions can be tracked over rather large distances. However, thermocouple, flame-luminosity, and CARS devices provide an Eulerian description of the processes since they record events as they are convected past a stationary measurement point. The interpretation of the Eulerian-type measurements in terms of the Lagrangian-type processes is not always straightforward and can often be confusing. For example, without the aid of the ciné pictures in Fig. 7, which provide a Lagrangian view of the flow, it would be difficult to envision the probable cause of the high-frequency fluctuations noted in Fig. 8. Conditional sampling can potentially aid in this interpretation by identifying Eulerian-type data that result from certain specific Lagrangian-type events. It is easy to envision from Fig. 8 that CARS measurements made in the flame turbules can be distinguished from those made in the non-luminous regions. Such a distinction can aid in obtaining a Lagrangian description of the dynamic processes responsible for the time-averaged temperature profiles given in Figs. 5 and 6.

An experiment was conducted to: (1) determine how the temperature pdf's changed with axial location and (2) to examine the potential value of using flame luminosity for conditional sampling of the CARS data. The combustor operating conditions were

the same as those under which the time-averaged axial temperature profile data in Fig. 6 were taken. The results from this experiment are shown in Fig. 9. The CARS temperature measurements were made on the combustor centerline at axial locations of 40 cm (2.86D), 50 cm (3.57D), and 60 cm (4.29D). The CARS data in Figs. 9(a) and 9(c) were conditionally sampled using simultaneous flame-luminosity measurements as previously described in the section entitled, "Luminosity - Data Collection System." The pdf's of the CARS temperature data taken when the flame turbules were present as well as those taken in the non-luminous regions are presented in these figures. The reproducibility of the pdf's can be noted by comparing three different sets of

measurements in Figs. 9(a), 10(a), and 11(a) which were made under the same test conditions. The average temperature from these three repeat measurements was 1289 K to a precision of ± 67 K. The standard deviation in the average temperatures indicated in all figures is representative of the dynamic nature of the flames studied.

Some background information is needed before discussing the temperature pdf's. The pdf's can be thought of as representing the fraction of time that different temperature intervals exist at the measurement point within the combustor flow, with the temperature interval or bin width being chosen to correspond to the uncertainty in the CARS temperature measurements. The bimodal shape of the pdf's presented in this paper suggests that at least two Lagrangian-type processes are occurring in the flow. The cine films suggest that these two modes correspond to the convection of the flame turbules and the non-luminous regions through the measurement volume. These events will be referred to as the hot and cold modes. For all pdf's presented in this paper, it appears that the hot mode is characterized by a temperature of 1100 K and above and the cold mode by temperatures below 1100 K. Using this criterion, the fraction of time which the flow spends in the hot mode can be calculated by summing up the probabilities of having temperatures of 1100 K and above. The fraction of the time during which the cold mode exists can be calculated in a similar way. Of course, the sum of the two time fractions must be 1.0.

The axial profile in Fig. 6 shows that the average centerline temperature decreases with increasing axial location. The pdf's in Fig. 9 give some insight into the processes responsible for this effect. Inspection of Fig. 9 shows that the cold mode always peaks at 300 K, whereas the hot-mode peak--or, more appropriately, the hot-mode average temperature--shifts to somewhat lower values farther downstream. Also, the fraction of time that the hot mode exists decreases with increasing axial location. Thus, the axial decay in average temperature is the combined effect of the decrease in the hot-mode temperature and in the fraction of time during which these temperatures exist. This implies that cold air is being entrained and mixed with products within the flame turbules as they move downstream, thus lowering the average temperature in the turbule. Also, some of the flame turbules burn out or the reactions are quenched as they move downstream, thus reducing the fraction of time during which the hotter temperatures exist. It should also be noted that the average temperature occurs in the trough between the hot and cold modes, indicating that the flow field is actually at this temperature a small (less than 3%) fraction of the time.

The conditionally sampled data in Figs. 9(a) and 9(c) provide some additional insight into the dynamic processes responsible for the time-averaged temperatures. Although it is generally true that when the flame is present, the temperatures are in the hot mode and when the flame is absent, the temperatures are in the cold mode, this is not always the case. The conditionally sampled data in Fig. 9 show that at times, no flame is present but the temperatures are in the hot mode, and at other times, flame is present but the temperatures are in the cold mode. This apparent anomaly is undoubtedly due, in part, to the fact that the flame luminosity can be detected at any location along the line-of-sight of the photodetector, whereas the CARS

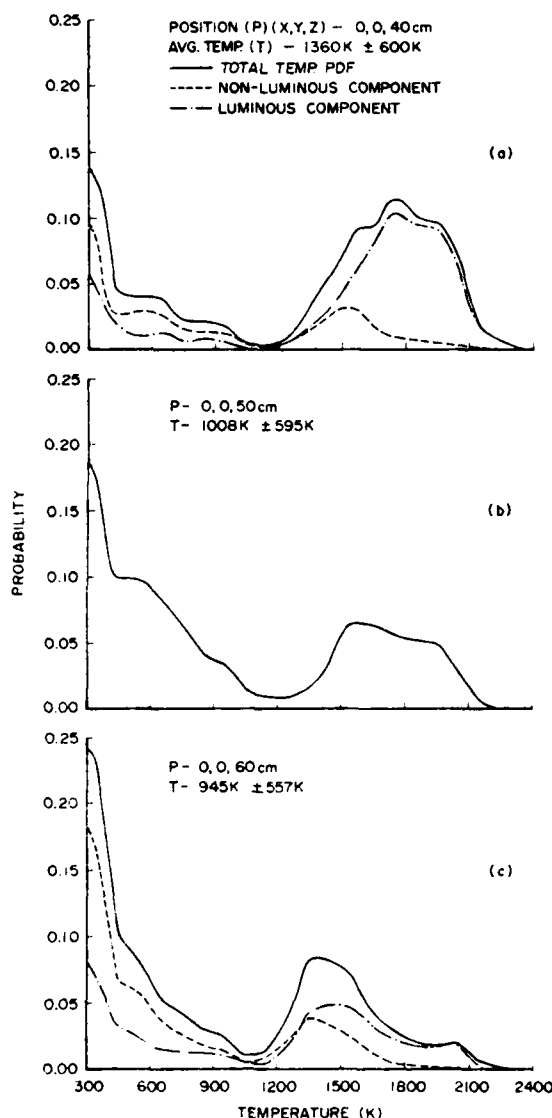


Figure 9. Conditionally Sampled Axial Temperature PDF's for an Annulus-Air Velocity of 23.3 m/s and a Fuel-Exit Velocity of 69.6 m/s at Axial Locations of (a) 40 cm (2.86D), (b) 50 cm (3.57D), and (c) 60 cm (4.29D).

measurement is made at a point contained within the field-of-view of the detector. With this in mind, some explanations of the conditionally sampled data can be offered--but unfortunately cannot be verified.

The conditionally sampled data suggest that the hot mode is composed of at least two types of events, one corresponding to the presence of flame and the other to the absence of flame. The hot mode which is associated with the non-luminous regions peaks at about 1500 K in both Figs. 9(a) and 9(c). This mode is believed to be caused by the hot product gases from a flame turbule that have consumed all or almost all of the fuel just prior to passing through the measurement location. The width of the hot mode associated with the nonluminous events is believed to be determined by the time available for mixing before the product gases pass through the measurement location. Relatively long mixing times could account for the positive skewness of the cold, non-luminous mode. The width of the hot mode, associated with measurements taken when the flame was present, suggests that the large flame turbules may consist of smaller packets of burning fuel separated by non-reacting regions of product gases and entrained air. The degree of mixing between the entrained air and the product gases within a flame turbule could account for the broad distribution of the hot mode and the distribution in the cold mode associated with the flame measurements.

PDF Variation with Radial Location

Figure 10 shows pdf's obtained at X locations of 0 cm, -2 cm, and -4 cm at an axial location of 40 cm. The air- and fuel-flow-rate conditions are the same as those in which the time-averaged radial profile data in Fig. 5 were collected. These pdf's have a very similar bimodal shape to those obtained at various axial stations. In fact, much of the previous discussion with reference to Fig. 9 seems to apply to Fig. 10. The average temperature is located between the hot and cold modes, and the flow field is at this temperature only a small fraction of the time. The decrease in average temperature with increasing radius appears to be primarily due to a decrease in the fraction of time during which the hot mode is present. Some shifting of the hot-mode distribution to slightly lower temperatures takes place as the radius is increased, but this appears to be a secondary effect. These pdf's suggest that the entrainment and mixing decrease significantly as the flow moves toward the centerline. The distribution of the cold-mode temperatures reflects the various degrees of mixing of products and entrained air that have taken place prior to their passing through the measurement volume.

PDF Variations with Air- and Fuel-Flow Rates

Figure 11 shows how the temperature pdf's change with fuel-flow rate at a fixed axial location and a fixed air-flow rate. The shaded regions represent the temperature distributions in the absence of flame. The bimodal structure is apparent for each of the three fuel-flow rates. The decrease in the standard deviations with increasing fuel-flow rate is a result of the increase in the hot-mode contribution of the pdf's, whereby the hot mode becomes more like a single mode. The non-luminous contribution to the hot mode increases in magnitude as

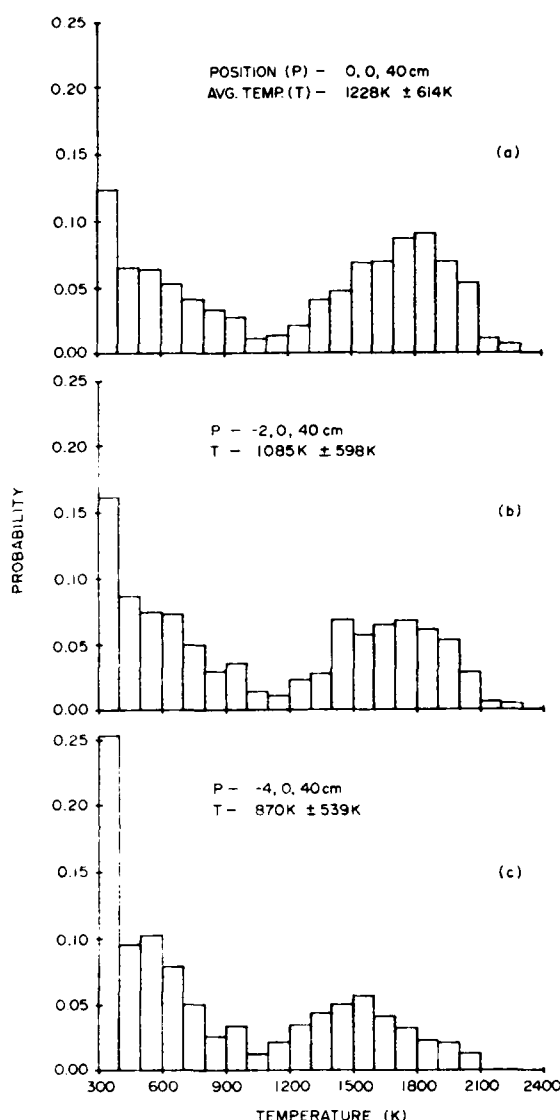


Figure 10. Temperature PDF's for an Annulus-Air Velocity of 23.3 m/s and a Fuel-Exit Velocity of 69.6 m/s for an Axial Location of 40 cm (2.86D) and Radial (X) Locations of (a) 0.0 cm (0.143D), (b) -2.0 cm (0.143D), (c) -4.0 cm (0.286D).

well as shifts to higher temperatures with increasing fuel-flow rate. The increase in fuel-flow rate does not appreciably change the fraction of time during which unmixed inlet air is present. However, the degree of mixing and heat diffusion is significantly reduced as the fuel-flow rate is increased, as indicated by the increased probabilities of the cold-mode temperatures other than the 300-K bin.

The fraction of time during which inlet air is present is greatly increased when the air-flow rate is increased. This is shown in Fig. 12 by noting the fraction of the time during which combustor

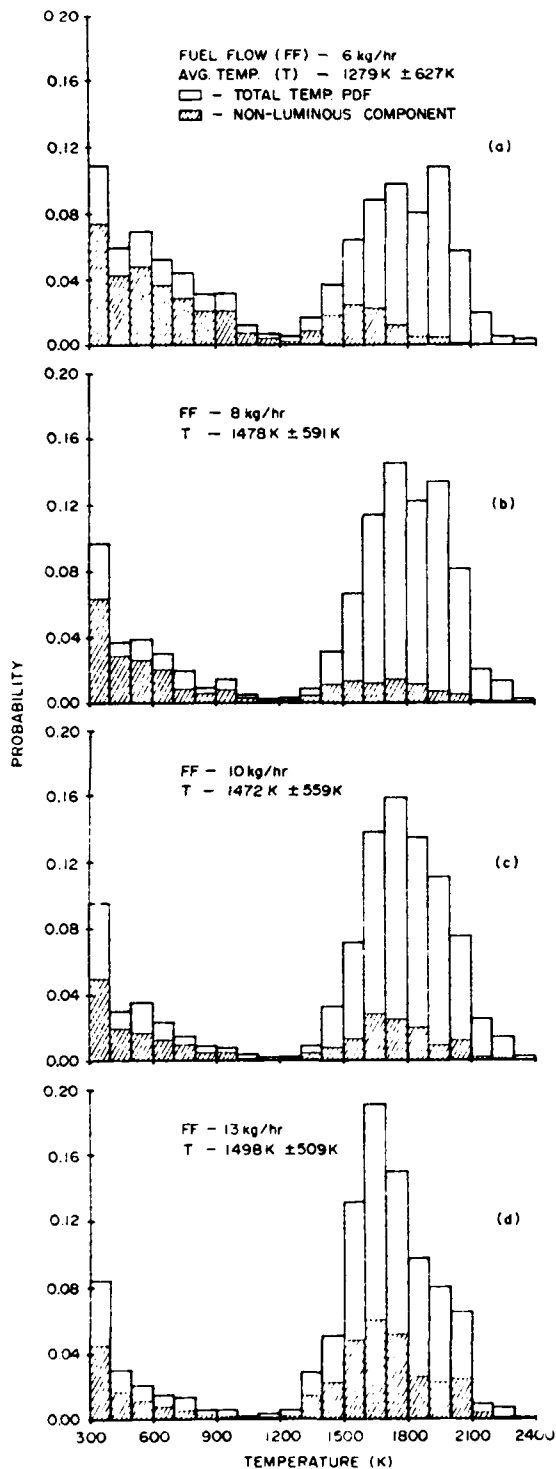


Figure 11. Conditionally Sampled Temperature PDF's at a Radial Location of 0.0 cm and Axial Location of 40 cm (2.86D) for an Annulus-Air Velocity of 23.3 m/s and Fuel-Exit Velocities of (a) 69.6 m/s, (b) 91.0 m/s, (c) 110.8, (d) 141.4 m/s.

inlet temperatures (300-K bin) are present for the four different air-flow rates. It is also evident that the non-luminous contribution to the 300-K peak also increases significantly with increasing air-flow rate. A factor-of-four increase in air-flow rate results in a factor-of-two decrease in average temperature. This is primarily due to the increase in entrained cold air and the increase in the cold air mixing with products, as indicated by the increased probabilities of the other cold-mode temperatures. The temperature fluctuations increase as the air-flow rate increases from 0.5 to 1.5 kg/s because the distribution becomes more bimodal; however, as the air-flow rate continues to increase, the cold mode dominates and the temperature fluctuations decrease. A surprising feature is that the hot-mode distribution becomes more uniform as the air-flow rate increases. The cause is not understood, but it is probably related to changes in the internal structure of the flame turbules.

A comparison of Fig. 12(d) and Fig. 13 shows how the pdf's change with increasing fuel-flow rate at an air-flow rate of 2 kg/s. Trends similar to those noted in the discussion of Fig. 11 are observed. The average temperature increased with increasing fuel-flow rate, and the temperature fluctuations decreased slightly. The 300-K peak does not change, whereas the probabilities for the other cold-mode temperature decrease with increasing fuel-flow rate. This indicates that the degree of mixing is reduced.

Summary and Conclusions

The feasibility of using a BOXCARS-configured CARS system for making instantaneous (10-ns) temperature measurements at a point (1 mm³) at a rate of 10 Hz in a large-scale research combustor has been demonstrated. CARS measurements of axial and radial temperature profiles in a highly sooting flame compared favorably with profiles measured with a Type-R shielded thermocouple probe. The CARS system was also used to investigate the dynamic processes in the bluff-body, turbulent diffusion flame which are responsible for the time-averaged temperature profiles. High-speed ciné pictures suggest that the average temperature results from the convection of large flame structures and non-luminous regions past the measurement point. Flame-luminosity measurements made simultaneously with the CARS temperature measurements were used to distinguish the CARS data taken within the flame structures from those taken in the non-luminous regions. The temperature pdf's determined at different axial and radial locations for different air- and fuel-flow rates were bimodal. The cold mode peaked at the combustor inlet temperature (300 K), and the hot mode was distributed between 1100 and 2200 K. The conditionally sampled data showed that both the hot and cold modes could be resolved into two additional modes, one consisting of temperatures measured in the presence of flame and the other consisting of temperatures measured in the absence of flame. However, it is generally true that the hot mode is dominated by those temperatures measured in the presence of flame and that the cold mode is made up predominantly of temperatures measured when the flame is not present. The results of this study show that the CARS technique is a valuable tool for studying dynamic combustion processes and that conditional sampling of the CARS data using flame luminosity enhances its value.

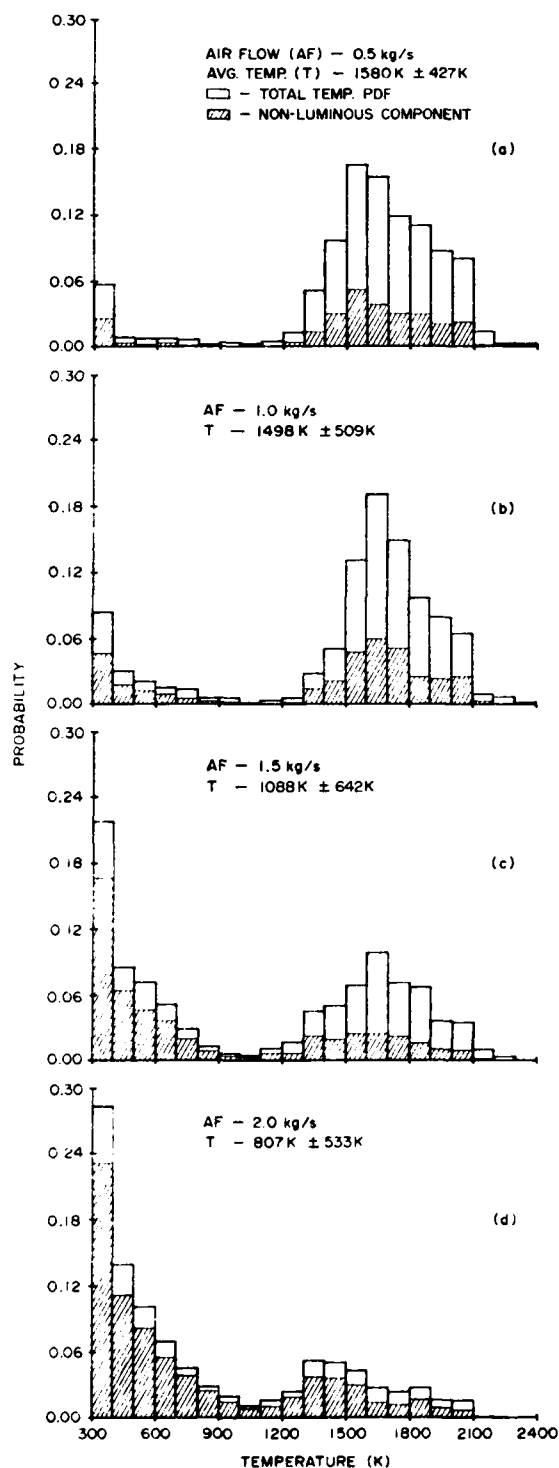


Figure 12. Conditionally Sampled Temperature PDF's at a Radial Location of 0.0 cm and Axial Location of 40 cm (2.86D) for a Fuel-Exit Velocity of 141.4 m/s and Annulus-Air Velocity of (a) 11.6 m/s, (b) 23.3 m/s, (c) 34.9 m/s, and (d) 46.6 m/s.

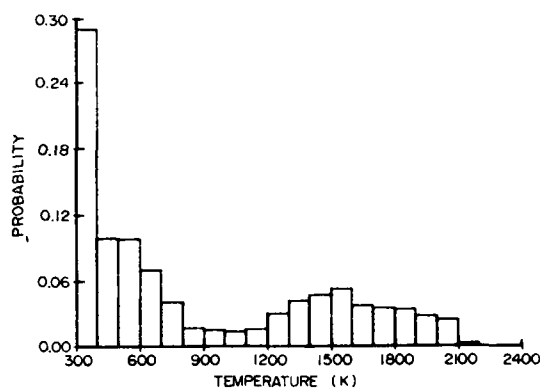


Figure 13. Temperature PDF at a Radial Location of 0.0 cm and Axial Location of 40 cm (2.86D) for an Annulus-Air Velocity of 46.6 m/s, a Fuel-Exit Velocity of 168.1 m/s, and an Average Temperature of 876 K \pm 587 K.

Acknowledgements

The authors wish to thank Ron Britton for setting up and participating in the luminosity measurements and for preparing several figures used in this paper. The authors would also like to thank Melvin Russell for operating the combustion tunnel. This work was performed as part of Air Force Contract F33615-80-C-2054 and Aero Propulsion Laboratory In-House Work Unit 30480590.

References

1. W. M. Roquemore, R. P. Bradley, J. S. Stutrud, C. M. Reeves, and L. Krishnamurthy, "Preliminary Evaluation of a Combustor for Use in Modeling and Diagnostic Development," ASME Publication 80-GT-93, March 1980.
2. G. I. Switzer, W. M. Roquemore, R. P. Bradley, P. W. Schreiber, and W. B. Roh, "CARS Measurements in a Bluff-Body Stabilized Diffusion Flame," *Appl. Opt.* **18**, 2343 (1979).
3. G. I. Switzer, L. P. Goss, W. M. Roquemore, R. P. Bradley, P. W. Schreiber, and W. B. Roh, "Application of CARS to Simulated Practical Combustion Systems," *J. Energy* **4**, 209 (1980).
4. W. M. Roquemore, R. L. Britton, and S. A. Sandhu, "Investigation of The Dynamic Behavior of a Bluff-Body Diffusion Flame Using Flame Emission," *AIAA-82-0178*, January 1982.
5. W. M. Roquemore, R. P. Bradley, J. S. Stutrud, C. M. Reeves, R. L. Britton, S. A. Sandhu, and R. S. Archer, "Influence of the Vortex Shedding Process on a Bluff-Body Diffusion Flame," *AIAA-83-0335*, January 1983.

6. P. D. Magill, A. J. Lightman, C. E. Orr, R. P. Bradley, and W. M. Roquemore, "Simultaneous Velocity and Emission Measurements in a Bluff-Body Combustor," AIAA-82-0883, June 1982.
7. L. P. Goss, D. D. Trump, G. L. Switzer, and B. G. MacDonald, "CARS Thermometry and N_2 Number Density Measurements in a Turbulent Diffusion Flame," AIAA-83-1480, June 1983.
8. G. E. Glaw, R. Holnda, and F. N. Krause, "Recovery and Radiation Corrections and Time Constants of Several Sizes of Shielded and Unshielded Thermocouple Probes for Measuring Gas Temperatures," NACA-TP-1099, January 1978.
9. A. C. Eckbreth, "BOXCARS: Crossed-Beam-Phase-Matched CARS Generation in Gases," Appl. Phys. Lett. 32, 421 (1978).
10. G. L. Switzer and L. P. Goss, "A Hardened CARS System for Temperature and Species Concentration Measurements in Practical Combustion Environments," Temperature its Measurement and Control in Science and Industry, Vol. 5 (1982) pp. 583-587 (Ed., James F. Schooley).
11. L. P. Goss, G. L. Switzer, and D. D. Trump, "Temperature and Species Concentration Measurements in Turbulent Diffusion Flames by the CARS Technique," Paper No. AIAA-82-0240 presented at the 20th Aerospace Science Meeting, Orlando, FL, 11-14 January 1982.
12. A. Kim, "Computer Programming in Physical Chemistry Laboratory: Least Squares Analysis," J. Chem. Ed. 47, 120 (1970).

Considerable effort was expended to determine the cause of the difficulty in obtaining proper species-concentration data. The result of this effort was the identification of a severe beam-steering effect which is created by the thermally induced index-of-refraction gradients present in the large turbulent combusting medium. This phenomenon influences the CARS signal strength in two ways. First, it causes relative beam steering and defocusing of the three (single species) or four (two species) laser beams entering the CARS sample volume, thus affecting the amount of CARS signal produced. Secondly, the CARS signals produced in the sampled volume are steered through the remainder of the flame diameter before exiting the test tunnel. The subsequent beam steering can cause a portion of the CARS signal to be deflected out of the acceptance angle of the 200- μm -diam. optical-fiber pickup. Efforts to reduce the degree of beam steering experienced going into the sample volume included changing optical geometries from folded BOXCARS to planar BOXCARS to USED CARS (i.e., more collinear). These experiments yielded no significant improvement in concentration determination, with an addition of lowered spatial-volume resolution. Since no convenient method of correcting or compensating for the beam-steering problem could be implemented, the decision was made that, temporarily, less emphasis would be placed upon concentration measurements and that temperature profiling in the flame should continue.

A final measurement program was undertaken to provide CARS-temperature mapping of the fuel-rich near-wake region of the bluff-body combustor. The resulting CARS-temperature pdf map is presented in Fig. 26. During this program two very significant problems were identified. The first of these involved the error in the CARS temperature determination which was induced by the large nonresonant CARS background signal which was being generated from unburnt fuel. This problem was solved by employing a software scheme to compensate

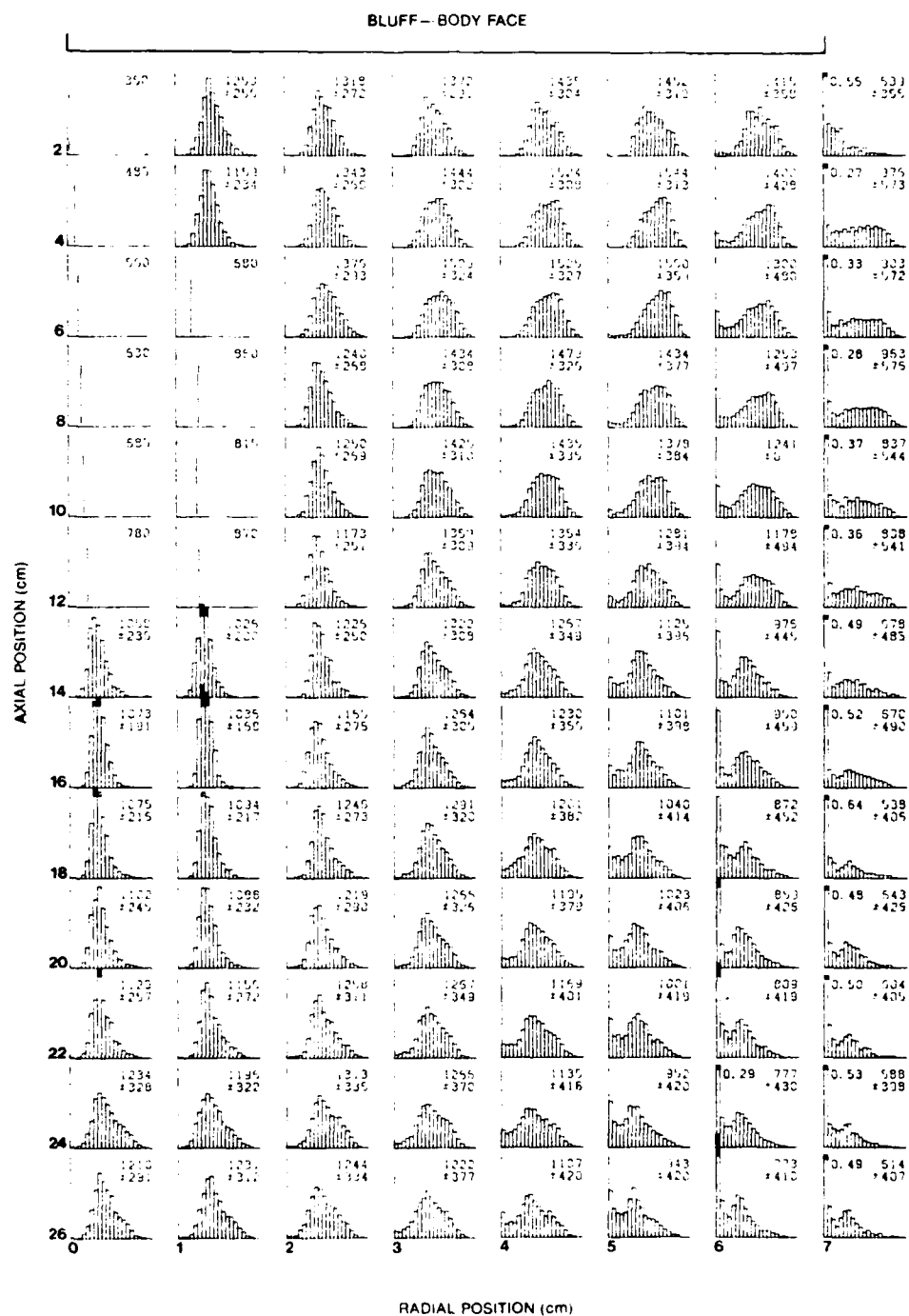


Figure 26. CARS Temperature pdf's in the Near-Wake Region of the Bluff Body.

for background contributions during theoretical spectra development. The second problem identified in this region of the flame was related to the accuracy of the thermocouple probe data in the highly recirculating-flow field. It was found that the shape, size, and orientation of probe geometries could have a profound effect upon indicated temperatures. A description of the measurements and results of this program are contained in a paper entitled, "CARS Measurements in the Near-Wake Region of an Axisymmetric Bluff-Body Combustor," which follows.

AIAA'85

AIAA-85-1106

CARS Measurements in the Near-Wake Region of an Axisymmetric Bluff-Body Combustor

G. L. Switzer, L. P. Goss, and D. D. Trump, Systems Research Laboratories, Inc., Dayton, OH 45440-3696; C. M. Reeves, J. S. Stutrud, R. P. Bradley, and W. M. Roquemore, AFWAL Aero Propulsion Laboratory, Wright-Patterson AFB, OH 45433-6503.

**AIAA/SAE/ASME/ASEE 21st Joint
Propulsion Conference**

July 8-10, 1985 / Monterey California

For permission to copy or republish, contact the American Institute of Aeronautics and Astronautics
1633 Broadway, New York, NY 10019

G.L. Switzer, L.P. Goss, D.D. Trump
Systems Research Laboratories, Inc.
Dayton, OH 45440-3696

C.M. Reeves, J.S. Stutrud, R.P. Bradley and W.M. Roquemore
Air Force Wright Aeronautical Laboratories
Aero Propulsion Laboratory
Wright-Patterson AFB, OH 45433-6563

Abstract

The Coherent Anti-Stokes Raman Spectroscopy (CARS) technique has been employed to measure temperatures in the near-wake recirculating flow region of a bluff-body stabilized diffusion flame. Time-averaged temperature profiles and probability distribution functions (pdf's) are discussed in terms of the flow field characteristics. Velocity information obtained by Laser Doppler Anemometry (LDA) is employed along with the theoretical predictions of temperature and velocity as aids in interpreting the time averaged CARS data. Temperature measurements, made with CARS and three thermocouples of different design, are compared. Several problems affecting CARS in the fuel-rich regions are identified and discussed. Among these problems are the effects of nonresonant background CARS generation, beam steering and detector aging.

Introduction

Results of CARS diagnostic experiments being conducted in a simulated practical combustor environment at the Combustion Research Facility at the Air Force Wright Aeronautical Laboratories/Aero Propulsion Laboratory have been reported previously.^{1,2} The research objectives and the facilities which have been assembled to conduct this research have also been documented.^{3,4} The published CARS results were obtained in a highly sooting bluff-body-stabilized diffusion flame at a position well downstream of the recirculation zone established by the bluff-body combustor. It was believed that both the CARS and thermocouple measurement techniques would be most applicable in this combustion zone; indeed, results of the average-temperature measurement, are in good agreement for the two techniques.⁴

The CARS diagnostics efforts discussed in this paper are a continuation of these experiments through examination of the near-wake region behind the bluff-body where intense mixing occurs. During this study, two effects, which are crucial to the CARS and probe diagnostic capability in this flame environment, were identified. The first of these involved the effect upon CARS temperature measurements of the contribution of the nonresonant background CARS signal generated from the unburnt propane fuel. Although several other problems were encountered which influenced the CARS results, this was the most severe.

Even after nonresonant background effects and other CARS related problems were minimized, a discrepancy between CARS and thermocouple probe temperatures remained. The second effect upon the diagnostic capability--and the one believed to be responsible for the remaining temperature discrepancy--was the intrusive nature of a thermocouple probe being inserted. The consequences of the physical body of a thermocouple probe disturbing or having secondary effects upon the temperature measurement process were examined by comparing results for several probe geometries.

This paper identifies the problems influencing the CARS and thermocouple temperature diagnostic capabilities in the fuel-rich recirculation zone encountered during this measurement program and discusses the solutions which have been implemented. CARS temperature profiles are presented and compared with thermocouple and model predictions. Flow velocities obtained from LDA data and model predictions are employed along with temperature pdf's as aids in interpreting the processes believed to be occurring in the recirculation zone.

Combustion Tunnel Facility

The axisymmetric bluff-centerbody research combustor, as configured for these experiments, is diagrammed in Fig. 1. The centerbody is 79 cm long and has a diameter (D) of 14 cm. Gaseous propane fuel is injected from the center of the bluff-body face through a 4.8 mm diameter nozzle. Annular air flow is conditioned using a honeycomb flow straightener and screens. The centerbody is mounted in a 25.4 cm diameter duct equipped with 30.5 X 7.6 cm viewing ports which provide either probe or optical access to the combustion regions. To facilitate optical access, these ports are covered with 2.5 cm thick optical windows; whereas, metal ports are used for probe access. Additional details of the combustion tunnel facility can be found in Ref. 3.

All the experiments were conducted at one test condition. The annulus air velocity was 23.3 m/s which corresponds to a Reynolds number of 1.5×10^5 , based on the bluff-body diameter and an inlet temperature of 294 K. The gaseous propane fuel jet exit velocity was 69.6 m/s with a Reynolds number of 4.2×10^5 based on the jet diameter and inlet temperature of 400 K. This condition was chosen because of the understanding gained in previous high speed motion picture

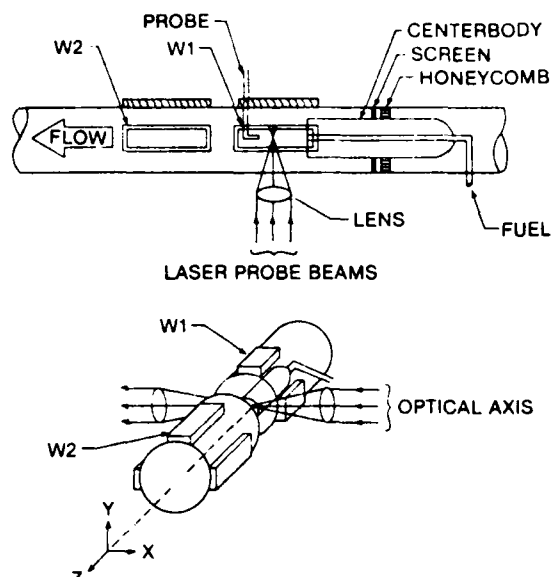


Fig. 1. Schematic diagram of the combustion tunnel, the centerbody combustor and probe arrangements.

flame studies of the flow field^{4,16} and because the computations of Sturgess and Syed suggested that the measured vortex shedding frequency observed at this condition was far removed from the calculated acoustical resonances of the tunnel.

Theoretical Predictions

Theoretical predictions are presented to aid in the understanding of the complex flow field in the near-wake region of the bluff-body. The predictions were made using a computer code developed at Imperial College as a teaching aid (TEACH) and is described in Ref. 5. The code uses a hybrid upwind finite differencing scheme to solve the Reynolds' averaged equations. Closure is obtained by using the k- ϵ turbulence model with the standard constants. A simple one step chemical reaction is assumed. Flat velocity

and turbulence intensity inlet profiles were used for boundary conditions. The computational grid had 41 axial nodes and 39 radial nodes and extends 4D downstream. Grid independence of the solution was not determined and no attempts were made to improve on the calculations, since the predictions are primarily used to give qualitative insights to the flow field.

Figure 2 is a vector diagram of velocity predicted by the TEACH code for the combustor flow and is presented to acquaint the reader with the complex flow field being studied. The diagram shows two recirculation zones, one driven by the entrainment of the central jet and the other is driven by the annular air flow. The centerline velocity decreases as the fuel travels downstream and, at about one centerbody diameter downstream, it begins to increase as it comes in contact with the higher velocity air from the annulus. Some of the fuel near the edge of the jet is captured by the reverse flowing air and carried back upstream where it is either entrained into the fuel jet or into the annulus air flow. Although the quantitative aspects of the predictions are not correct, the general qualitative picture of this flow field is consistent with the data presented in this and other studies.

Large toroidal vortex structures are known to be shed from the bluff body. An illustration of the shed vortices is superimposed on the time averaged flow field calculation in Fig. 2 as a reminder that the dynamic events are important in discussing the processes occurring in the near-wake region of the bluff-body. As will be discussed later, these vortices are believed to have a major impact on the temperature field behind the bluff-body.

Instrumentation

Thermocouples

It is well recognized that probes can interfere with their environment to the extent that the temperature at the point of measurement when the probe is present can be quite different than the temperature when the probe is absent. This is particularly true in the combustor recirculation zone behind a bluff body. Since

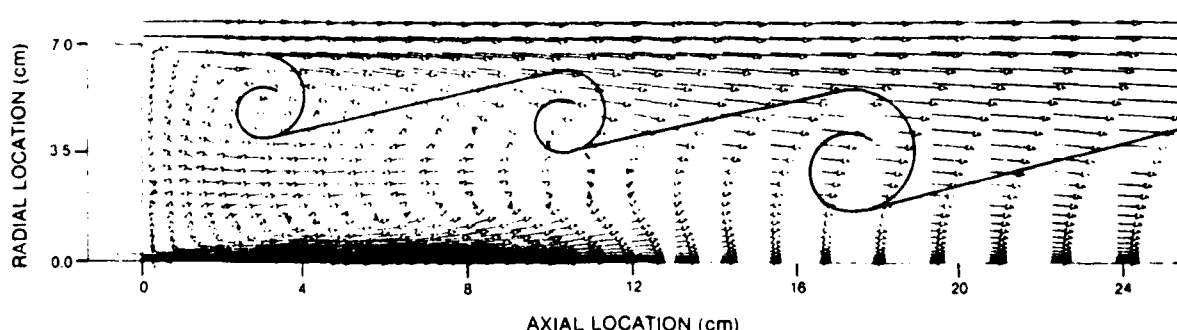


Fig. 2. Vector plot of the TEACH Code predictions for one half of the time averaged velocity field in the near-wake region of the bluff body with an illustration of shed vortices.

the direction of the flow field changes dramatically with time and location, as illustrated in Fig. 2, probes must be as small as possible to minimize their blockage while at the same time they must be sufficiently robust to survive the high temperature environment. It is not always clear how to configure the probe to accomplish this. In this study, three thermocouple probe designs were evaluated in the near-wake region of the bluff body.

Envelopes of the three thermocouple designs are shown in Fig. 3. They all have a sheath diameter of 4.76 mm near the tip. The portion of the NAT thermocouple that is perpendicular to the tunnel centerline is 6.35 mm in diameter. These dimensions are large with respect to the 4.76 mm diameter of the fuel jet, but it is small in comparison to the diameter of the bluff body. Hence, one might expect all the probes to significantly interfere with the flow near the fuel jet but to be less of a problem when they are far downstream or removed from the jet flow. All three thermocouples are made from platinum alloys. Probe NAT and R4 are type R thermocouples and POLST is a type S.

Probe POLST in Fig 3a was designed to minimize the effects of the stem. It is uncooled and has an exposed tip made from 22 gauge wire. NAT in Figure 3b is a shielded thermocouple with a platinum alloy sheath that is in the shape of a rotated T. Hot gases pass over the tip of the thermocouple and pass out through holes in the shield. The stem is water cooled to a distance of about 3 cm above the thermocouple where the platinum tip starts. The extension of the probe below the thermocouple has been shown to be beneficial in establishing symmetry in temperature measurements made in parabolic flows while experience has shown that the end-on design of probe R4 (Fig. 3c) causes the peak temperature in a radial profile to shift away from the direction of the stem. R4 is a barewire thermocouple (20 gauge) and is uncooled.

LDA System

The velocity data presented in this paper were obtained by Lightman et al. using a two-component Laser Doppler Anemometer (LDA). This system was especially designed for use in the combustion tunnel facility. It is a real-fringe system with a three-beam optical configuration. The fringe spacing is 10 μ m. The scattered light is collected 10 degrees from the forward direction by a parabolic mirror. The length of the measurement volume is 3 mm. Polarization is used to distinguish the two orthogonal velocity components. The optical beam, which is common to both LDA channels, is frequency shifted so that both positive and negative velocities can be measured. The scattered light is separated according to polarization and transmitted through optical fibers to two photomultipliers. The electrical signals are processed by two Model 1990 TSI counter processors. Each velocity realization is stored in the facility computer for future processing.

Both the annulus air and the fuel were seeded with alumina particles using fluidized-bed

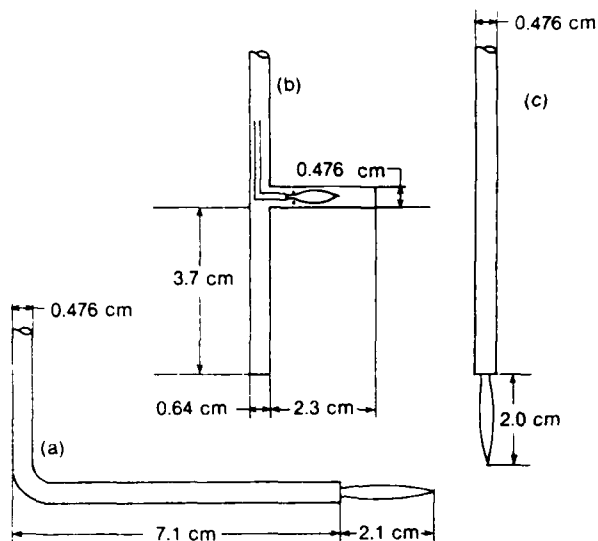


Fig. 3. Illustration of three thermocouple configurations used for temperature comparison: (a) uncooled right angle tip (POLST), (b) water cooled, T shape tip (NAT), and (c) uncooled end-on tip (R4).

seeders. Five thousand velocity realizations were obtained for each point measurement. In practice it is very difficult to provide equal seed densities to the fuel and air streams and no attempt was made to do so for these measurements. Experiments in cold flows, where the extreme variations in results were obtained by the use of one seeder and then the other, indicated that the precision of the velocity measurements was about 10% except near stagnation regions where much larger percentage errors can occur. The precision was not determined for the combustor flow. A detailed description of the LDA system and the test procedures are given in Ref. 7.

Radial profiles of axial velocity are presented for axial locations of 4 and 8 cm. These data are not sufficiently detailed to describe the combustion flow field in the near-wake region of the bluff body. However, they do provide some insights that aid in interpreting the CARS temperature measurements and they also lend some credibility to the trends of the theoretical predictions.

CARS System

A detailed description of the optical and electronic configuration of the basic CARS system employed in these experiments can be found elsewhere.¹⁸ Several modifications to the basic system were made for the present study. The CARS system employs a frequency-doubled neodymium-YAG laser which produces a 6-ns (FWHM) pulse at a 10-Hz repetition rate. A planar BOXCAR optical configuration was employed in conjunction with a broadband H_2 Stokes dye laser to obtain single-shot H_2 temperature information from a spatial volume on the order of 1 mm³. A beam expansion

telescope was added to the ω_1 pump beams in order to decrease their energy density as they pass through the combustion-tunnel access windows. This modification allowed a radial scan range sufficient to probe the total combustor flow plus the major portion of the annular air flow without causing damage to the window material.

The CARS signal generated in the sampled volume is collected in a 200- μm diameter fiber-optic transmission line and introduced into a 0.64-m spectrometer. Dispersion of the CARS information within the spectrometer is accomplished with a 2400 g/mm holographic grating, and detection of the resultant spectral content is provided by a Tracor-Northern Model TN 6132 Diode Array Rapid Scan Spectrometer (DARSS) detector head. The detector is an intensified, gateable, 1024-element silicon photodiode array which exhibits sufficient linearity that only one optical split of the CARS signal is required to accommodate the dynamic-range enhancement scheme necessary to follow the signal fluctuations which occur within the turbulent combustor medium. This grating and detector represent the remaining modifications to the basic CARS system with respect to the 1200 g/mm grating and the TN 1223IG detector described previously. This combination exhibits a hybrid Gaussian/Lorentzian slit function and produces an overall system resolution of 4.1 cm^{-1} FWHM.

Results and Discussion

Initial attempts to make CARS temperature measurements within the highly recirculating flow in the near-wake region of the bluff-body combustor resulted in temperature indications that in some areas of the flame were as much as 500 or 600 K higher than those indicated by thermocouple measurements. Inspection of the single-shot CARS spectra in those areas revealed that a large nonresonant CARS background signal was being generated which was contributing to the N_2 spectral signature. This background signal is primarily due to the nonresonant susceptibility of the high concentration of unburnt propane. Since the least-squares temperature-fitting procedure, being employed to fit the CARS spectra, is sensitive to frequency and resonant CARS spectral shape only, it became evident that many temperatures in the predominantly fuel-rich combustion environment were being fit artificially high.

For a more accurate prediction of the composite N_2 spectra being generated experimentally, a technique similar to that described by Hall and Boedecker¹¹ was incorporated into the temperature-fitting procedure. This technique provides for the expression of CARS intensities as a function of two independent parameters, namely, temperature and a concentration factor which consists of the ratio of N_2 concentration to background nonresonant susceptibility. With this modification, consideration can be given to the relative effects due to the concentration of probe-to-background species rather than assuming a predominant resonant N_2 contribution and a constant relatively small background component. The magnitude of the effect of the background-concentration factor upon temperature determina-

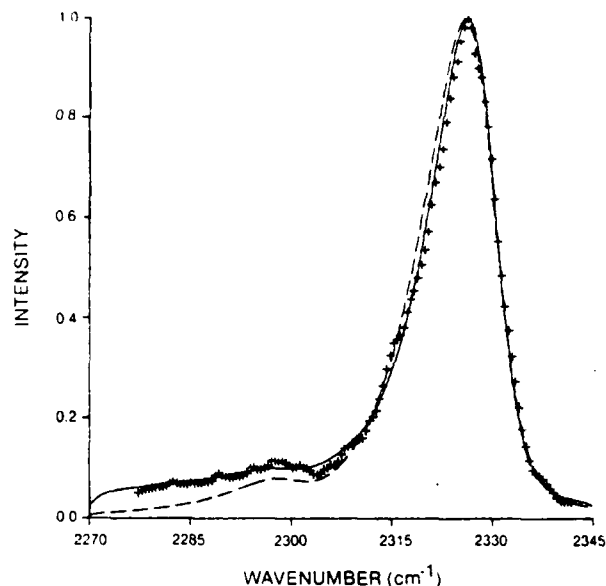


Fig. 4. Effect of background-concentration consideration on temperature fitting. (+) Experimentally observed spectrum. (—) Best fit 1080 K, theoretical spectrum obtained with fitting to background concentration. (---) Best fit 1430 K, theoretical spectrum without background variation.

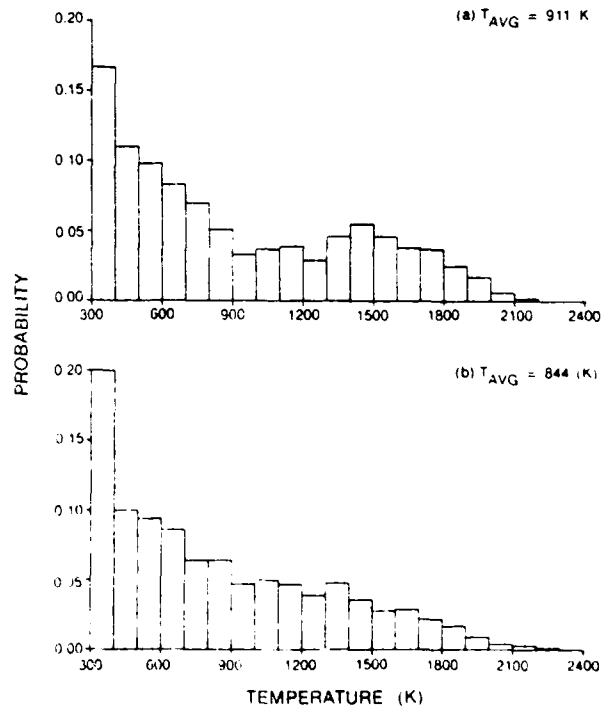


Fig. 5. Influence of background fitting procedure upon temperature pdf. (a) Distribution of temperatures without background fitting. (b) Temperature distribution when variable background considered.

tion is illustrated in Fig. 4. Here, the theoretical spectra with and without background-concentration are fit to an experimentally observed spectrum. The extreme shift in the lower-wavenumber tail of the 1060 K spectrum of Fig. 4 relative to the 1430 K spectrum is due primarily to a decrease of approximately 77% in the value of the concentration factor below that which would be expected in a stoichiometric environment. The addition of this parameter into the temperature-reduction procedure necessitated only slight modification to the existing software but increased the time required for fitting a temperature to a single spectrum from 1 to 3 seconds on the MODCOMP Classic computer system.

The decrease in CARS temperatures obtained by fitting to the background concentration can be interpreted in terms of the characteristic shape of the temperature pdf of Fig. 5. Here, the temperature pdf at a point 40 cm downstream of the combustor face is shown without (a) and with (b) consideration of background-susceptibility modification. It is apparent that the average temperature decrease from 911 to 844 K results when the correction for background shifts the hotter temperatures in the 1500 K region to lower values. This shift in a relatively small number of temperature determinations has the effect of smoothing the pdf profile, thus making the apparent bimodal structure much less predominant. The magnitude of the shift in average temperature and the distortions in the pdf resulting from background considerations can be interpreted as a measure of the degree of penetration of combustion reactants within the combustion region.

Another phenomenon, which produced an effect upon the CARS temperature measurements, was observed within the Tracor-Northern 6132 detector. It became apparent that a relatively short-duration overexposure of the diode array resulted in a permanent nonuniform decrease in sensitivity of the affected diodes. One of the consequences of this desensitization was that the spectral profiles were artificially broadened, thus producing an apparent increase in temperature. This effect was especially noticeable at lower temperatures where the spectral width is most critical in temperature fitting. For instance, what would normally have been a 400 K spectrum could be distorted to indicate a temperature 50 to 200 K higher.

Since overexposure of the detector diodes cannot be avoided at present, particularly near the edge of the flame in a turbulent combustion environment, several steps were taken to minimize its potential effect. The sampled spectra were moved to new areas of the 1024-element array having uniform response and sensitivity. Subsequent overexposure time of the detector was kept to a minimum by input filtering. Daily calibration to room temperature and to a standard flame provided a check for variation in detector sensitivity. These steps effectively eliminated the influence of detector "aging" upon the measurement process and helped to ensure the reliability of the CARS data.

In addition to its nonuniform contribution to the CARS spectral information, the turbulent combustion environment in the near-wake region of the flame presents another problem to CARS

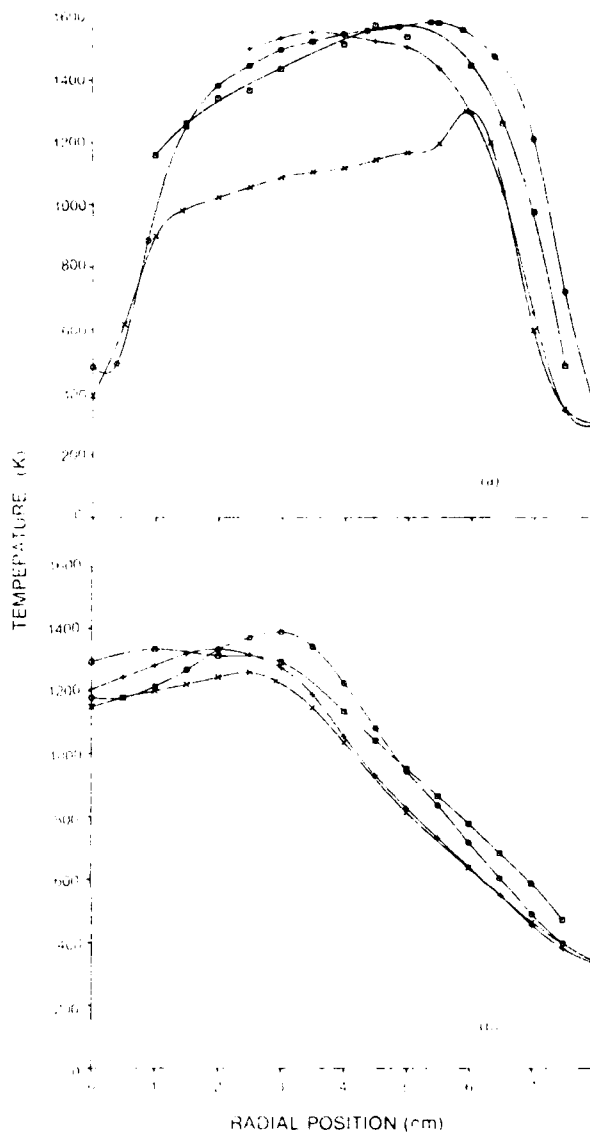


Fig. 6. Radial profile of temperature for CARS and thermocouples at axial locations of (a) 40 cm (0.29z/D) and (b) 24 cm (1.71z/D). (\square) CARS, (\circ) POLST, (\times) NAT, (+) R4

diagnostics. Large thermally induced index-of-refraction gradients are present between the mixing cold fuel and the hot combustion products. These gradients cause considerable bending of the optical beams in transit through the flame. Since each of the three laser beams (two of frequency ω_1 and one of frequency ω_2) entering the sample focal volume experiences a different optical path, each is steered independently and there is relative movement of the beam centers. This defocusing causes a decrease in CARS intensity. While this intensity does not detract from the spectral content (i.e., temperature-dependent information), it does prohibit determination of O_2 concentration by relative intensities. Thus, until a scheme for compensation of turbulent beam steering can be implemented, the CARS concen-

tration measurement capability will not be reliable for the near-wake recirculating combust- ing flow.

As stated earlier, a large discrepancy between temperatures, determined by CARS and the NAT thermocouple probe remained after the CARS temperature reducing procedure was modified to fit nonresonant background contributions. To help identify the source of this discrepancy, the type, geometry and orientation of the thermo- couple were varied. Some of the results of these

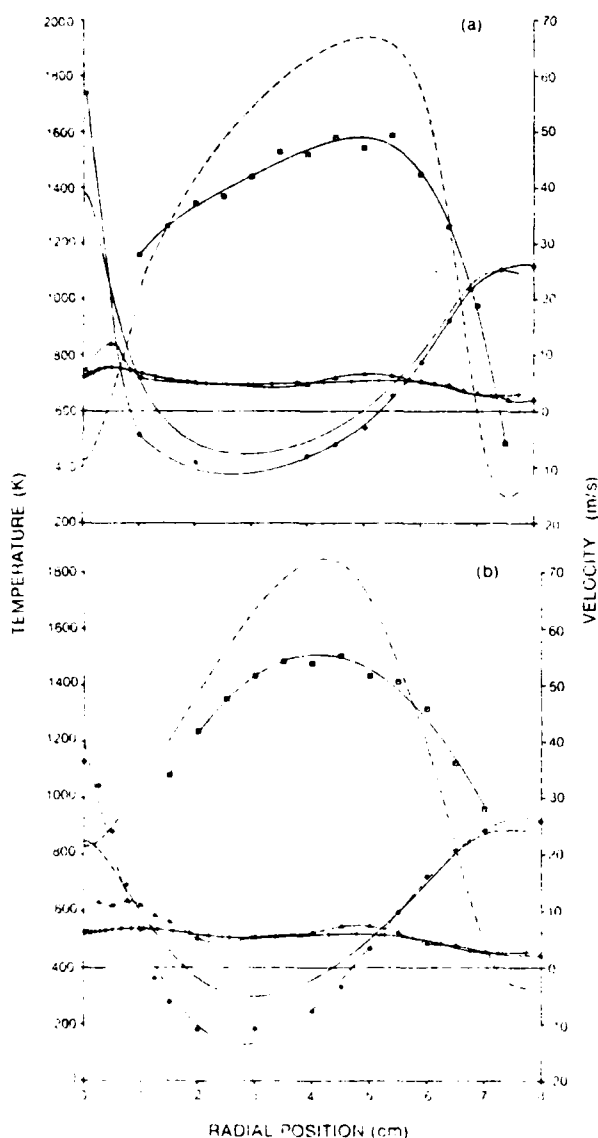


Fig. 7. A comparison of time averaged CARS temperatures and averaged and rms LDA axial velocities with TEACH code predictions at axial locations of: (a) $z=4\text{ cm}$ ($0.29 z/D$) and (b) $z=8\text{ cm}$ ($0.57 z/D$). (---) TEACH Temperature, (\square) CARS Temperature, (—) TEACH Average Velocity, (\circ) LDA Average Velocity, (+) TEACH RMS Velocity, (\triangle) LDA RMS Velocity.

experiments are shown in Fig. 6. The radial profiles give a comparison of the CARS temperatures to those obtained from the three thermocouple probes identified in Fig. 3. The NAT and POLST probes were oriented parallel to the flow and facing upstream. The R4 probe was inserted from the top and normal to the flow axis. The data of Fig. 6a reveals that the error between the CARS and NAT temperatures is due to probe characteristics. The distinct departure of the NAT profile from the other thermocouple data suggests that this probe exhibits a large perturbing presence in the combust- ing media. The cause of this perturbation becomes apparent if one considers that at an axial location of 4 cm the combust- ing flow is highly recirculating as will be discussed presently. Thus, the body of the NAT probe located downstream of the thermocouple tip plays a definite role in blocking the transport of the reverse flowing combust- ing gases that would otherwise be present at the measurement location. Although the POLST and R4 probe temperature profiles of Fig. 6a exhibit similar shapes, there is sufficient spread in the data to cause concern that perhaps one or both of these probes also perturb the characteristics of the measurement volume by their presence in a recirculating flow field.

The temperature profiles of Fig. 6b, obtained at an axial location of 24 cm, show a marked convergence of the four profiles. This convergence is thought to occur because this measurement location is downstream of the recirculation zone and thus the thermocouple is influenced to a lesser degree by the presence of the physical body of the probe. Secondary effects such as heat conduction away from the thermocouple through its leads or probe body and radiation from the heated probe body may contribute to the probe inaccuracies but their effect is believed to be much less severe. The convergence of these profiles are believed to continue as the measurement location moves further downstream. This is suggested because at $z=40\text{ cm}$, where the flow is parabolic, point-to-point temperature differences of less than 50 K between CARS and the NAT probe have been measured. Additional measurements with the other thermocouples are needed at this location to determine if they all give the same results.

Figure 7 shows measured and predicted radial profiles of average temperature, axial velocity, and rms velocity at axial locations of 4 and 8 cm. This figure is presented to illustrate the qualitative agreement between TEACH code predictions and experiment. It also offers some insights into the processes that are occurring. It is our intent to give only a qualitative assessment of the TEACH code predictions since measured inlet conditions have not been used and the necessary checks on the numerical accuracy of the computations have not been made. It should be noted that, if precise inlet conditions are desired, inlet velocity and turbulence intensity data for this combustor are contained in Ref. 4. Also, recent studies have shown that LDA velocity data, when not collected at a constant time interval, are Favre averaged (density weighted); whereas, the TEACH predictions are time average. This difference must be taken into account if quantitative assessments of the model are to be made.



Fig. 8. A comparison of time averaged CARS temperature measurements and TEACH predictions of temperature and velocity with an illustration of shed vortices.

Qualitative agreement between the theory and experiment is most evident when comparing the temperature plots in Fig. 7. At $z=4$ cm, the temperature profile in Fig. 7a has a broad peak that is skewed towards the centerline for both prediction and measurement. At $z=8$ cm, the theoretical and measured temperature peaks in Fig. 7b are more rounded. The peak temperature occurs at a radial location very near that of the zero velocity point in both Figs. 7a and 7b. The broadness in the temperature profile and the radial location of the peak appears to be related to the width of the reverse flow (negative velocity) region. The TEACH code predicts and the LDA measurements show that the reverse flow region is considerably larger at $z=4$ cm than at $z=8$ cm. The radial locations of the peak temperature and the zero velocity are also farther from the centerline at the 4 cm location than at the 8 cm location. The change in width of the reverse flow region with axial location is clearly evident in Fig. 2.

The temperature decreases very rapidly at radial locations greater than the peak temperature location in both Fig. 7a and 7b. Since this occurs just as the flow changes direction, the rapid decay is most likely due to the mixing of cold downstream flowing annular air with the hot products and burning fuel. This view is supported by the small peak in the measured rms velocity fluctuations, which indicated enhanced mixing near the outer velocity stagnation point. The TEACH code predictions also show a small peak in the rms velocity near the stagnation point. However, it is not very evident in Fig. 7 because of the chosen velocity scale. The TEACH code predictions of average and rms velocities and temperature appear to give very good qualitative agreement with the measured data.

Measured and predicted temperature isotherms along with the predicted velocity field are shown

in Fig. 8. The average CARS temperatures on a 0.5 cm radial by 2 cm axial grid (for $r=0$ to 7 cm and $z=2$ to 26 cm) were used to produce the upper half of the temperature contour plot. For comparison, and to assist in interpretation, TEACH code predictions of temperature and velocity are presented in the lower half of the figure. For clarity, some of the velocity vectors have been omitted from the fuel jet, otherwise, they would obscure the temperature isotherms in this region. Since the absolute temperatures measured using CARS and predicted by TEACH are different, the scale shown in Fig. 8 is normalized to the maximum temperature in each half (1587 K for CARS and 1994 K for predictions). This approach allows for more convenient comparisons of the qualitative features.

The strong similarity between the CARS measured and TEACH predicted temperatures in Fig. 8 suggests that the predictions contain the important qualitative features of the entire temperature field. For example, each isotherm shows that the coal fuel is heated as it moves downstream and radially out. Also, each map shows that there are two hot spots which are labeled by their normalized temperature. The one located downstream and near the centerline will be referred to as the fuel jet hot spot and the other near the face of the stagnation point will be referred to as the annular jet hot spot. The fuel jet hot spot is identified in the CARS data as considerably cooler than that predicted by TEACH and it is displaced further downstream. This displacement differential might be due to the fact that this hot spot is associated with the central jet and the TEACH code, with the stagnation point, normally would predict the location of the field and would predict the development of the annular jet flow.

Figure 9 shows that the TEACH code predicts that the annular jet hot spot is located near the centerline and near the stagnation point, which is

supported by the measured data in Fig. 7. The maximum temperature measured in the flow field is located at an axial location of 4 cm and is shown in Fig. 7a. As noted earlier, the measured peak temperature is very near the radial location where the measured axial velocity is zero. From observations of high speed movies of the flame, it was determined that this is very near the vortex center.

The apparent connection between the velocity and temperature fields suggests that the dominant mechanism of heat transport is convection. An examination of the TEACH predictions showed that the magnitude of convective heat transport in the shear layer of the bluff body is at least an order of magnitude larger than that due to the turbulent diffusion transport at all but a few locations in the flow field. The qualitative agreement between the predictions and experiment suggests that the measured temperature field might also be interpreted in terms of the convective heat transfer. To this end, a qualitative explanation of the TEACH code predictions of the temperature field, based on the mean velocity field, will be presented as a reasonable interpretation of the time averaged CARS data.

The zero axial velocity surface of the annular jet vortex, which is observed in the lower half of Fig. 8, is believed to be important for understanding the cause of the associated hot spot. Judging from the velocity plot, the zero axial velocity surface extends about one bluff body diameter downstream. This surface, which is near the outer edge of the 0.80 to 0.87 isotherm, is believed to be very important because it separates the gases flowing upstream from those flowing downstream. The fluid elements on either side of the surface have very different time histories. The downstream flow, which is outside the surface, contains mostly cold annulus air and some hot products very near the surface. Inside the surface, the ignited fuel and hot products are convected upstream by the mean flow. By tracking the velocity vectors and isotherms near the fuel jet, it is seen that combustion is sustained in the upstream flow region by the continuous supply of hot fuel from the outer shear layer of the fuel jet. Also, the fuel, which is transported near the zero velocity surface of the annular jet vortex, must linger for a relatively long time because of the very low velocities. In effect, the long residence time insures sustained high temperatures in this region.

The fuel jet hot spot, as noted in Fig. 8, is also located in a region where the velocities are very low. The velocity vector plot in Fig. 8 shows that the fuel jet penetrates the recirculation zone established by the annular jet. Tracking the magnitude of the velocity vectors near the centerline, it is seen that as the fuel travels downstream, the velocity decays to a minimum value and then starts increasing. The fuel jet hot spot is located in this region of low velocity. Studies of high speed movies of the flame also show that the fuel jet penetrates the recirculation zone and that the fuel jet hot spot is located in a region where the axial velocities are very low.

The fuel jet is heated by the entrainment of hot products. The vortex associated with the central jet (see Fig. 2) also has a zero axial velocity surface which separates the fuel and hot products moving downstream from the products and reactants moving upstream. Some of the hot products moving upstream are entrained into the fuel jet near the bluff body face, thus heating the fuel as it moves downstream. By the time the fuel near the centerline reaches the minimum velocity it has started to react because of the entrained hot products. Since this burning fuel spends considerable time where the velocity is low, the temperatures will be high in this region. The TEACH predictions indicate that the radial extent of the downstream hot spot is determined by the cooling effects of the radial penetration of the annular jet shear layer. This is evident by tracking the velocity vectors in the shear layer of the bluff body as they move downstream.

The discussions have considered a time average view of the near wake region. However, it must be remembered that the flow is really very dynamic with large toroidal vortices (illustrated in Fig. 8) being shed from the bluff body. The impact of the dynamic motions on the temperature field are shown in Fig. 9. In this figure, each pdf consists of at least 1500 temperature samples. The probability axis height is 0.2 and the temperature axis ranges from 300 to 2400 K with 100 K temperature bin widths (same as Fig. 5). Temperature probabilities ranging from 0.2 to 0.27 are represented by darkened bin segments and temperature bins exceeding a probability of 0.27 are clipped at 0.2 on the plot and labeled with their actual value. Those plots consisting of a single line indicate only "best estimate" values of the thermocouple temperatures. CARS measurements were not made in these locations due to the large nonresonant signal generation from the unburnt propane in the fuel jet. The time average and rms temperatures for the particular pdf are given in the upper right-hand corner of each plot.

It should be noted that the averaged CARS temperatures represented in Fig. 8 might differ somewhat from those given in Fig. 9. This is because the temperatures for the isotherms are the result of averaging from 6 to 8 sets of 1500 individual CARS measurements while those shown with the pdf's in Fig. 7 are just for one set of data. The worst case precision of the experiment, as indicated by averaging 6 CARS data sets taken on different days in the shear layer of the annular jet, was 80 K. For most locations, the experiment was repeatable to 40 K.

The pdf's in Fig. 9 provide a map of the transported annular air into the near-wake region. The 300 K temperatures can serve as a marker for the annulus air that is unmixed and thus, unheated by the combustion process. By tracking the radial locations where the probability of measuring 300 K temperatures approaches zero (from the high side), one can tell how far the annulus air extends into the near-wake region without being mixed. The probability of the 300 K bin gives the fraction of time that this occurs. An examination of the pdf's for an axial location of 4 cm, shows that

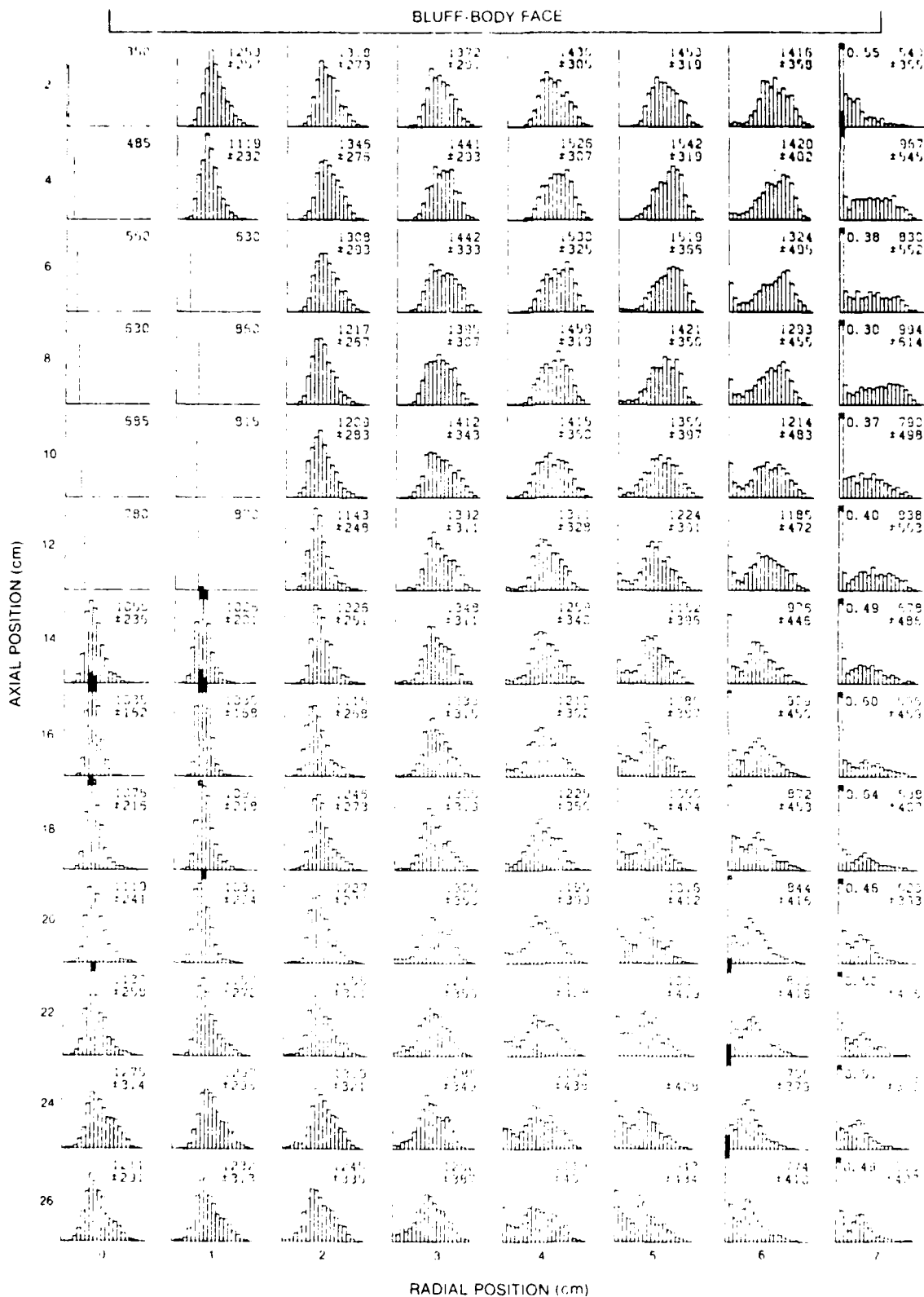


Fig. 9. CARS temperature pdf's in the near-wake region of the bluff body.

at a radial location of 5 cm or less, there is zero probability of measuring a temperature of 300 K; whereas, at 6 and 7 cms, 300 K temperatures will be measured some of the time. This implies that the annular flow penetration into the near-wake region at $z=4$ cm is between 5 and 6 cm. Figure 7a confirms this since the measured zero axial velocity location separating downstream and upstream moving gases is at 5.3 cm. At the $z=8$ cm axial location, the annular air does extend to the 5 cm radial location as interpreted by the nonzero probability of measuring 300 K. The location of the zero axial velocity point is 4.7 cm according to the LDA data in Fig. 7b. Thus, by tracking the probability of measuring a temperature of 300 K, one can determine to what extent and the fraction of time unmixed annular air penetrates into the near-wake region.

The temperature pdf's in Fig. 9 support the view, established by the study of high speed movies in Ref. 16, that shed vortices are actually responsible for the transport of annular air and heat (mixed air and hot products) into the wake of the bluff body. The presence of the 300 K inlet temperatures some of the time and very high temperatures at other times, indicate that the flow is intermittent. Indeed, the probability of observing the presence of annular air is a measure of the intermittence. The study of high speed movies suggest that the cause of the intermittence is the occurrence of large scale shed vortices. By imagining the observed large scale vortices being convected downstream as depicted in Fig. 8, one can more easily visualize the events leading to the transport of unmixed annular air into the near-wake region. As the vortex rolls up, an interface, which separates annular air and products, is formed. As the vortex is convected downstream, the rotational motion towards the centerline transports unmixed annular air, at the interface, deep into the shear layer of bluff body. As the vortex continues to rotate, it transports reactants, hot products and air radially outward. The bimodal shapes of the pdf's indicate the presence of these large toroidal vortices and the influence they have on the temperature field.

High speed movies of the flame indicate that the fuel is burned in discrete packets, surrounded by hot products and air.¹⁶ Studies of high speed movies of a laser sheet-lit view of a cold reacting flow in a vertically mounted centerbody, suggest that the discrete packets of reacting fuel are vortices that are shed from the fuel jet. The convection of these packets of burning fuel past the measurement point is also believed to be responsible in part for the shape of the temperature pdf's in Fig. 9.

Summary and Conclusions

CARS temperature measurements have been extended into the recirculating, near-wake region of a bluff-body stabilized diffusion flame. Corrections for nonresonant background, due primarily to the presence of unburned fuel, had to be made to obtain what is considered valid CARS data. Attempts to establish the accuracy of the measurements in this environment failed due

to a lack of a suitable standard technique for comparing time averaged temperatures. Thermocouples, which have been used in the past to check the performance of averaged CARS temperature measurements in parabolic flows, perturbed the near-wake flow field to the extent that their measurements were unreliable. This was determined by making measurements with three differently shaped thermocouples.

CARS temperature pdf's were most useful in providing insights into the dynamic nature of the turbulent combustion processes occurring in the near-wake region of the bluff body. By tracking the probability of measuring the inlet air temperature, it was determined that: (1) unheated and unmixed annular air is transported into the near-wake region towards the peak time averaged temperature and (2) the transport is intermittent. The bimodal shape of the temperature pdf's and previous studies of high speed movies of the flame, suggest that the transport mechanism of heat, air, and products in the shear layer of the bluff body is due to the convective nature of large scale vortices shed from the bluff body.

A quantitative comparison of experimental results and TEACH code predictions was not attempted in this study because sufficient checks have not been made on the numerical accuracy of the calculations. However, the TEACH code did successfully predict many of the qualitative features of the mean temperature and axial velocity data. The success of the predictions is believed to be due to the fact that the TEACH calculated radial convective transport is considerably larger at almost all locations in the shear layer of the bluff body than the calculated transport by turbulent diffusion via the eddy viscosity model. Also, it is very doubtful that the TEACH code would provide accurate quantitative predictions of the temperature field, unless intermittency and mixing, due to the large scale shed vortices, are taken into account.

Acknowledgements

The authors would like to thank Mr. M. Russell for assisting in the operation of the combustion tunnel. We also express appreciation to Dr. Robert Piccirelli, Dr. L.D. Chen and Dr. D.R. Ballal for their useful discussions. Appreciation is extended to Ms Marion Whitaker for assisting with the figures and Ms Roma Bush for typing the manuscript. This research was sponsored by the Air Force Wright Aeronautical Laboratories, Aero Propulsion Laboratory on contract F33615-80-C-2054, W.U. 30480502 with Systems Research Laboratories, Inc. and by the Air Force Office of Scientific Research on W.U. 23085705.

References

1. G.L. Switzer, L.P. Goss, W.M. Roquemore, R.P. Bradley, P.W. Schreiber, and W.B. Roh, "Application of CARS to Simulated Practical Combustion Systems," *J. Energy* 4, 209 (1980).
2. G.L. Switzer, D.D. Trump, L.P. Goss, W.M. Roquemore, R.P. Bradley, J.S. Stutrud, and C.M. Reeves, "Simultaneous CARS and Luminosity Measurements in a Bluff-Body Combustor," *AIAA Paper* 83-1481, June 1983.
3. W.M. Roquemore, R.P. Bradley, J.S. Stutrud, C.M. Reeves, and L. Krishnamurthy, "Preliminary Evaluation of a Combustor for Use in Modeling and Diagnostic Development," *ASME Publication* 80-GT-93, March 1980.
4. W.M. Roquemore, R.P. Bradley, J.S. Stutrud, C.M. Reeves, C.A. Obringer, and R.L. Britton, "Utilization of Laser Diagnostics to Evaluate Combustor Models," *AGARD CP-333 "Combustion Problems in Turbine Engines,"* 19, 1151-1157, 1983.
5. G.J. Sturgess, and S.A. Syed, "Dynamic Behavior of Turbulent Flow in a Widely-Spaced Co-Axial Jet Diffusion Flame Combustor" Paper No. AIAA-83-0575, AIAA 21st Aerospace Meeting, Reno, Nevada, January 1983.
6. A.D. Gosman and F.J.K. Ideriah, "TEACH-T: A General Computer Program for Two-Dimensional Turbulent Recirculating Flows," Imperial College, Department of Mechanical Engineering Report, June 1976.
7. A. Lightman, P.D. Magill, and R.J. Andrews, Laser Diagnostics Development and Measurements and Modeling of Turbulent Flowfields of Jets and Wakes, AFWAL-TR-832044, Part I, June 1983.
8. G.L. Switzer and L.P. Goss, "A Hardened CARS System for Temperature and Species-Concentration Measurements in Practical Combustion Environments," in Temperature: Its Measurement and Control in Science and Industry, Vol. 5 (J.F. Schooley, ed.) (AIP, New York, 1982), pp. 583-587.
9. A.C. Eckbreth, "BOXCARS" Crossed-Beam-Phase-Matched CARS Generation in Gases," *Appl. Phys. Lett.* 32 421 (1978).
10. L.P. Goss, G.L. Switzer, and D.D. Trump, "Temperature and Species Concentration Measurements in Turbulent Diffusion Flames by the CARS Technique," *AIAA Paper* 82-0240.
11. R.J. Hall and L.R. Boedicker, "CAKS Thermometry in Fuel-Rich Combustion Zones," *Appl. Opt.* 23 1340 (1984).
12. G.J. Sturgess, "Aerothermal Modeling Program-Phase I: Final Report," *NACA CR* 168202, May 1983.
13. P.D. Magill, A.J. Lightman, E.E. Orr, R.P. Bradley, and W.M. Roquemore, "Simultaneous Velocity and Emission Measurements in a Bluff-Body Combustor," *AIAA-82-0603*, June 1982.
14. M.V. Heitor, A.M.K.P. Taylor, and J.H. Whitelaw, "Simultaneous Velocity and Temperature Measurements in a Premixed Flame," *ASME AMD-Vol. 66: Experimental Measurements and Techniques in Turbulent Reactive and Non-Reactive Flows*, Eds. R.M.C. So, J.H. Whitelaw, and M. Lapp, pp 243, Dec. 1984.
15. L.P. Goss, D.D. Trump, and W.M. Roquemore, "A Combined CARS/LDA Instrument for Simultaneous Temperature and Velocity Measurements," To Be Published.
16. W.M. Roquemore, R.P. Bradley, J.S. Stutrud, C.M. Reeves, and R.L. Britton, "Influence of Vortex Shedding Process on a Bluff-Body Diffusion Flame," *AIAA-83-0225*, AIAA 21st Aerospace Sciences Meeting, January 1983.
17. W.M. Roquemore, R.S. Tankin, H.H. Chiu, and S.A. Lottes, "The Role of Vortex Shedding in a Bluff-Body Combustor," *ASME AMD-Vol. 66: Experimental Measurements and Techniques in Turbulent Reactive and Non-Reactive Flows*, Eds. R.M.C. So, J.H. Whitelaw, and M. Lapp, pp. 159, December 1984.

REFERENCES

1. L. P. Goss, G. L. Switzer, D. D. Trump, and P. W. Schreiber, "Temperature and Species-Concentration Measurements in Turbulent Diffusion Flames by the CARS Technique," AIAA Paper 82-0240, Presented at the AIAA 20th Aerospace Sciences Meeting, Orlando, FL, 11-14 January 1982.
2. "Laser Optics/Combustion Diagnostics," Quarterly R&D Status Report 6603-9 under Contract F33615-80-C-2054, covering the period 3 September 1982 - 2 December 1982 (Systems Research Laboratories, Inc. Dayton, OH, 16 February 1983).
3. D. Klick, K. A. Marko, and L. Rimal, "Temperature Measurements for Combustion Diagnostics from High-Resolution Single-Pulse CARS N_2 Spectra," in Temperature: Its Measurement and Control in Science and Industry, Vol. 5 (J. F. Schooley, Ed.) (American Institute of Physics, New York, 1982).
4. L. P. Goss, G. L. Switzer, and P. W. Schreiber, "Flame Studies with the Coherent Anti-Stokes Raman Technique," AIAA J. Energy 7, 389 (1983).
5. W. M. Tolles and R. D. Turner, Appl. Spectrosc. 31, 96 (1977).
6. G. Herzberg, Molecular Spectra and Molecular Structure: Vol. 1 Spectra of Diatomic Molecules (D. Van Nostrand Co., Inc., London, 1950).
7. L. P. Goss, G. L. Switzer, D. D. Trump, and P. W. Schreiber, AIAA Paper No. 82-0240.
8. "Laser Optics/Combustion Diagnostics," Quarterly R&D Status Report 6603-8 under Contract F33615-80-C-2054, covering the period 3 June 1982 - 2 September 1982 (Systems Research Laboratories, Inc., Dayton, OH, 16 September 1982).
9. L. P. Goss, G. L. Switzer, D. D. Trump, and P. W. Schreiber, AIAA Paper No. 82-0240.
10. L. A. Rahn, L. J. Zych, and P. L. Mattern, Opt. Comm. 30, 249 (1979).
11. A. C. Eckbreth and R. J. Hall, Comb. Sci. Technol. 25, 175 (1981).
12. "Laser Optics/Combustion Diagnostics," Quarterly R&D Status Report 6603-3 under Contract F33615-80-C-2054, covering the period 3 March 1981 - 2 June 1981 (Systems Research Laboratories, Inc., Dayton, OH, 29 July 1981).
13. L. P. Goss and P. W. Schreiber, "Assessment of the Application of CARS to Combustion Diagnostics," in Proceedings of the International Conference on Lasers '80 (held in New Orleans, LA, 15-19 July 1980), pp. 220-235.

14. S. Gordon and B. J. McBride, "Computer Program for Calculation of Complex Equilibrium Composition Rocket Performance, Incident and Reflected Shocks, and Chapman-Junget Detonations," NASA SP273 (National Aeronautics and Space Administration, 1971) NTIS N71-37775.
15. R. R. Dils, "NBS Develops High Temperature Optical Fiber Thermometer," U. S. Department of Commerce News (September 21, 1982) TN-5387.
16. "Award-Winning Fiber Temperature Sensor Slated for Commercial Production," Laser Focus/Electro-Optics 19, 66 (December 1983).
17. R. R. Dils and D. Tchenor, "A Fiberoptic Probe for Measuring High Frequency Temperature Fluctuations in Combustion Gases," SAND83-8871 (Sandia National Laboratories, Livermore, CA, February 1984).
18. L. P. Goss, D. D. Trump, B. G. MacDonald, and G. L. Switzer, "10-Hz Coherent Anti-Stokes Raman Apparatus for Turbulent Combustion Studies," Rev. Sci. Instrum. 54, 563 (1983).
19. E. R. G. Eckert and R. M. Drake, Heat and Mass Transfer (McGraw-Hill, New York, 1959), p. 761.
20. H. S. Carslaw and J. C. Jaeger, Combustion of Heat in Solids, 2nd Ed. (Clarendon Press, Oxford, 1959), p. 73.
21. L. P. Goss, G. L. Switzer, D. D. Trump, and P. W. Schreiber, AIAA Paper 82-0240.

END 11-86